

ATOMIC LAYER DEPOSITION OF NONMETALS AND METAL OXIDES

PRECURSOR AND REACTIVITY DEVELOPMENT FOR
THE DEPOSITION OF MAIN GROUP ELEMENT AND
GROUP 4 METAL OXIDE THIN FILMS

By MAJEDA AL HARERI, H.B.Sc.

A Thesis Submitted to the School of Graduate Studies in Partial Fulfillment
of the Requirements for the Degree Doctor of Philosophy

McMaster University © Copyright by Majeda Al Hareri, June 2023

DOCTOR OF PHILOSOPHY (2023)

McMaster University

(Department of Chemistry and Chemical Biology)

Hamilton, Ontario

TITLE: Precursor and Reactivity Development for the Deposition of Main Group
Element and Group 4 Metal Oxide Thin Films

AUTHOR: Majeda Al Hareri

SUPERVISOR: Prof. Dr. David J. H. Emslie

NUMBER OF PAGES: xlv, 188, A83

Lay Abstract

The focus of this work is the development of new processes to deposit ultra-thin films of main group elements and transition metal oxides. The deposition method utilized in this work is atomic layer deposition (ALD), which involves the use of a precursor molecule (which contains the target element) and a co-reactant. These chemical species must be appropriately reactive towards one another, and display adequate volatility and thermal stability. The feasibility of a precursor/co-reactant combination can be assessed using solution-state reactivity studies.

For main group element ALD, silyl-containing compounds ($E(\text{SiR}_3)_3$, $E = \text{Sb, B}$) have been investigated as precursors in combination with EX_3 ($X = \text{F, Cl, Br, I}$) co-reactants, due to the potential for thermodynamically favourable Si-X bond formation to drive the required surface-based reactions. For metal oxide ALD (MO_2 ; $M = \text{Hf, Zr}$), new ALD methods have been proposed to enable gap-free filling of narrow trenches on the surface of a silicon wafer. This work involved the design, synthesis, and evaluation of new ALD precursor molecules and reactions, ALD reactor studies for thin film deposition, and characterization of the resulting films.

Abstract

Atomic layer deposition (ALD) is a technique by which surface-based reactions between a precursor molecule (often metal-containing) and a co-reactant (e.g. H₂O, O₂ or H₂) yield highly uniform and conformal (ultra-)thin films. The precursor and co-reactant are each delivered in the gas phase, separated from one another by inert gas purge steps. The self-limiting nature of these surface-based reactions allows the thickness of the film to be controlled solely by the number of 'precursor – purge – co-reactant – purge' cycles. This nano-scale control of film thickness allows for a large number of applications such as in flat panel displays, fuel and solar cells, and microelectronic devices.

The first goal of this project was the pursuit of new low-temperature methods for main group elemental ALD using silyl-substituted precursor molecules. The second goal of the project was the development of alternative methods for thin film deposition of group 4 (M = Hf, Zr) oxides that would encourage effective (ie. void-free) filling of narrow (<20 nm) trenches in high-aspect-ratio (HAR) substrates. This thesis includes the development of new precursor molecules and reaction pathways, evaluation of precursor molecular structures, thermal stability, volatility and solution reactivity, identification of appropriate experimental conditions for ALD, and characterization of the resulting thin films.

ALD of elemental antimony was achieved on hydrogen-terminated silicon (H-Si) and SiO₂/Si substrates using Sb(SiMe₃)₃ (**2-1**) and SbCl₃ in the temperature range 23-65 °C. The mirror-like films were confirmed to be composed of crystalline antimony by XPS (for the film deposited at 35 °C) and XRD, with low impurity levels and strong preferential orientation of crystal growth relative to the substrate surface. To the best of

our knowledge, this is the first example of room temperature thermal ALD (with demonstrated self-limiting growth) of a pure element. Film growth at 35 °C exhibited a substrate-enhanced mechanism, characterized by faster film growth for the first ~125 ALD cycles, where substantial deposition is occurring on the original substrate surface (GPC (growth-per-cycle) = 1.3 Å on SiO₂/Si, and 1.0 Å on H-Si), and slower film growth (GPC = 0.40 Å on SiO₂/Si, and 0.27 Å on H-Si) after ~125 cycles, once much of the initial substrate surface has been covered. Films deposited using 500-2000 ALD cycles were shown to be continuous by SEM. The use of less than 250 cycles afforded discontinuous films. However, in this initial growth phase, when deposition is occurring primarily on the original substrate surface, in-situ surface pre-treatment by Sb(SiMe₃)₃ or SbCl₃ (50 x 0.4 or 0.8 s pulses), followed by the use of longer precursor pulses (0.4 or 0.8 s) during the first 50 ALD cycles resulted in improved nucleation. For example, on H-Si, a continuous 6.7 nm thick film was produced after initial pre-treatment with 50 x 0.8 s pulses of SbCl₃, followed by 50 ALD cycles using 0.8 s pulses. The use of longer ALD pulses in the first 50 ALD cycles following surface pre-treatment is likely required in order to achieve complete reactivity with an increased density of reactive surface sites.

Boranes featuring bulky silyl or sterically unencumbered trimethylgermyl groups, in combination with a stabilizing dimethylamido group, were pursued as potential precursors for ALD of elemental boron. This ALD process would employ a boron trihalide (BX₃; X = F, Cl, Br, I) co-reactant, exploiting the thermodynamically favourable formation of tetrel-halide bonds as a driving force. This work required multistep syntheses of alkali metal silyl reagents, {(Me₃Si)₃Si}Li(THF)₂ (**3-1**) and ^tBu₃SiNa(THF)_n (**3-2**), and previously un-isolated [Me₃GeLi(THF)₂]₂ (**3-3**), and their reactions with B(NMe₂)Cl₂ (**3-4**). The

boranes $\{(\text{Me}_3\text{Si})_3\text{Si}\}_2\text{B}(\text{NMe}_2)$ (**3-8**) and $(\text{tBu}_3\text{Si})(\text{Me}_3\text{Ge})\text{B}(\text{NMe}_2)$ (**3-12**) were successfully synthesized, spectroscopically and crystallographically characterized, and assessed for their suitability as precursor molecules for boron ALD. Unfortunately, deposition attempts on SiO_2/Si using **3-8** and BCl_3 led to minor film growth (GPC = 0.01 Å). However, the enhanced volatility and solution-state reactivity of **3-12** in comparison to **3-8** makes it a promising precursor candidate for future ALD reactor studies. Attempts to synthesize bis(trimethylgermyl)(dimethylamido)borane from the 2:1 reaction of **3-3** with **3-4** resulted in the formation of a lithium trigermylamidoborate, $\{(\text{Me}_3\text{Ge})_3\text{B}(\text{NMe}_2)\}_2\text{Li}(\text{THF})_2$ (**3-13**).

ALD can give rise to uniquely uniform and conformal ultra-thin films, but voids often remain after attempted filling of narrow high-aspect-ratio trenches. To achieve void-free trench-filling, ALD (or CVD; chemical vapour deposition) methods which deposit a flowable material are desirable, and this initially-deposited material can be converted to the target material (e.g. a metal oxide) by post-deposition annealing, or potentially at the deposition temperature on a longer timescale than flowable behaviour. In this work, a new HfO_2 ALD process was developed using $[\text{Hf}(\text{NMeEt})_4]$ in combination with β -hydroxyisovaleric acid (IVA; $\text{CMe}_2(\text{OH})\text{CH}_2\text{CO}_2\text{H}$) that introduces the potential for flowability. Self-limiting growth was observed at 100, 250, and 300 °C, with a GPC of 1.5-2.2 Å on planar SiO_2 substrates. Films deposited at 100 °C consisted of amorphous HfO_2 with significant carbon content (~22 at%) and <1 at% nitrogen. After annealing at 400 °C *in vacuo* for 1 hour, the films were composed of amorphous HfO_2 with low (<1 at%) carbon content. The co-reactant in this work, β -hydroxyisovaleric acid, was chosen with the following criteria in mind: Firstly, the carboxylic acid group may be sufficiently acidic to

cleave linkages between chemisorbed hafnium species and the surface, generating flowable non-surface-tethered hafnium carboxylate species (with low volatility, so that they are not lost from the surface). Secondly, the hydroxyl groups of the ligands can potentially serve as reactive sites for the hafnium precursor delivered in the next pulse. Thirdly, fairly low-energy pathways should exist for deprotonated IVA ligands to decompose to generate oxide or hydroxide ligands with release of volatile by-products, such as CO₂ and isobutene, or acetone and ketene. Experiments to gain insight into the nature of reactivity between [Hf(NMeEt)₄] and IVA and a structurally similar carboxylic acid are described. These include (a) solution-state reactions between [Hf(NMeEt)₄] and IVA or pivalic acid (*t*BuCO₂H), with formation of [H₂NMeEt]₂[Hf(κ²-O₂CCH₂CMe₂OH)₂(κ²-OC(O)CH₂CMe₂O)₂] (**4-1**) and [Hf₅(μ₃-O)₄(κ²-O₂C^{*t*}Bu)₄(μ-O₂C^{*t*}Bu)₈] (**4-2**), (b) attempted ALD using pivalic acid (which lacks a hydroxyl group) in place of IVA, and (c) room-temperature solution reactions between [Hf(NMeEt)₄] and 4 equiv. of IVA to form **4-1**, followed by removal of volatiles, heating at 200 °C, and volatile/soluble product analysis by NMR spectroscopy and GC-MS headspace analysis. Compounds **4-1** and **4-2** were isolated and crystallographically characterized.

Heteroleptic zirconium(IV) complexes were designed, synthesized, spectroscopically and crystallographically characterized, and assessed as potential precursor molecules to enable flowable ZrO₂ ALD. The envisaged process would operate via the deposition of oligomeric, one-dimensional chains that, if grown untethered on a functionalized substrate, could potentially flow to the bottoms of trenches. Reaction of one equivalent of H₂(*acn*), H₂(*cis*-Cyacn) or H₂(*trans*-Cyacn) with [Zr(CH₂SiMe₃)₄] at room temperature afforded [Zr(*acn*)(CH₂SiMe₃)₂] (**5-1**), [Zr(*cis*-Cyacn)(CH₂SiMe₃)₂] (**5-**

2) or $[\text{Zr}(\textit{trans}\text{-Cyacen})(\text{CH}_2\text{SiMe}_3)_2]$ (**5-3**), respectively (acen = $\text{C}_2\text{H}_4(\text{NCMeCHC}(\text{O})\text{Me})_2$; Cyacen = $1,2\text{-C}_6\text{H}_{10}(\text{NCMeCHC}(\text{O})\text{Me})_2$). These alkyl compounds are trigonal prismatic in the solid state, and whereas **5-1** and **5-3** decomposed without sublimation above $120\text{ }^\circ\text{C}$ (5-10 mTorr), **5-2** sublimed in >95% yield at $85\text{ }^\circ\text{C}$ (5-10 mTorr). However, heating solid **5-2** at $88\text{ }^\circ\text{C}$ under static argon for 24 hours resulted in extensive decomposition to afford $\text{H}_2(\textit{cis}\text{-Cyacen})$ and SiMe_4 as the soluble products. Compound **5-2** reacted cleanly with two equivalents of $t\text{BuOH}$ to afford $[\text{Zr}(\textit{cis}\text{-Cyacen})(\text{O}^t\text{Bu})_2]$ (**5-4**), but excess $t\text{BuOH}$ caused both SiMe_4 and $\text{H}_2(\textit{cis}\text{-Cyacen})$ elimination. The 1:1 reaction of $\text{H}_2(\text{acen})$ with $[\text{Zr}(\text{NMeEt})_4]$ did not proceed cleanly, and 8-coordinate $[\text{Zr}(\text{acen})_2]$ (**5-5**) was identified as a by-product; this complex was isolated from the 2:1 reaction. A zirconium amido complex, $[\text{Zr}(\text{acen})(\text{NMeEt})_2]$ (**5-6**) was accessed via the reaction of **1** with two equiv. or excess HNMeEt , but decomposed readily in solution at room temperature. More sterically hindered $[\text{Zr}(\text{acen})\{\text{N}(\text{SiMe}_3)_2\}_2]$ (**5-7**) was synthesized via the reaction of $[\text{Zr}(\text{acen})\text{Cl}_2]$ with two equivalents of $\text{Li}\{\text{N}(\text{SiMe}_3)_2\}$, but was also thermally unstable as a solid and in solution at room temperature. Compounds **5-1** to **5-3**, **5-5** and **5-7** were crystallographically characterized.

Acknowledgements

I must begin by expressing my gratitude to my supervisor, Prof. David J. H. Emslie, for his constant support and mentorship over my graduate career. You have taught me how to become an independent researcher while still being there for me whenever I needed support, and somehow managed to always be incredibly friendly! For these reasons and for so many more, I am eternally grateful. Additional thanks must be expressed to my supervisory committee members, Prof. Gary Schrobilgen and Prof. Jonathan Bradley, for their encouragement and kindness throughout the years, and to our Intel collaborators (Dr. Scott Clendenning, Dr. James Blackwell, and Dr. Charles Mokhtarzadeh) for all of the useful discussions over the years and contribution of materials.

Additionally, I am grateful to past and current members of the Emslie group for being a wonderful family away from family. Specifically, Dr. Jeffrey Price, Dr. Aathith Vasanthakumar, Dr. Blossom Yan, Katarina Paskaruk, Novan Gray, Nicholas Hoffman, Aya Kadri, Declan Dejordy, Maia Murphy, and Andrew Broomfield: you have made grad school a blast with all the days inside and outside the lab spent together, especially when we should've been doing work but just couldn't find the time to, for some reason. To McMaster facility members (Dr. James Britten, Vicky Jarvis, Dr. Bob Berno, Dr. Hilary Jenkins, Dr. Kirk Green, and Megan Fair), I am truly thankful for all the help in training, sample running, and answering of endless questions you have provided. A special thanks to Prof. Melanie Pilkington and Dr. Emma Stares for their mentorship and friendship during the beginning of my research journey at Brock University!

Lastly, I must thank all my siblings, in-laws, nieces, and nephews – Majid, Amjad, Majdoulin, Majed, Majdi, Sajed, Afraa, Mohammad, Mayas, Abdulmajed, Jamal, Rana, Mohammed, Melek, Mariam, and Maisoon – from the bottom of my heart for the limitless love and support you have each shown me in your own way throughout my life and especially during my schooling. Above all, my deepest gratitude must be expressed to my parents. Thank you to my mother, Rana, for teaching me to reach for the stars without limits, and for pushing me through the hardest moments. Thank you to my father, Abdulmajed, for instilling in me a deep love for education from an early age, and although you are not here with me to celebrate this conclusion, you have been my inspiration from the beginning, and I dedicate this work to you.

Table of Contents

Lay Abstract	iii
Abstract	iv
Acknowledgements	ix
Table of Contents	xi
List of Figures	xv
List of Schemes	xxxv
List of Tables	xxxviii
List of Compounds (Observed)	xl
List of Abbreviations, Acronyms, and Symbols	xlii
Declaration of Academic Achievement	xliv
Chapter 1: Introduction	
1.1 – Introduction to Thermal ALD.....	1
1.2 – Other Deposition Methods Related to Thermal ALD.....	8
1.3 – Requirements for ALD Precursors.....	11
1.4 – Materials Grown by Thermal ALD.....	13
1.4.1 – ALD of Pure Elements and its Challenges.....	13
1.4.1.1 – ALD of Main Group Elements.....	14
1.4.2 – ALD of Group 4 Metal Oxides and its Challenges.....	17
1.5 – Thesis Goals.....	19
1.6 – References for Chapter 1.....	22
Chapter 2: Room-Temperature Atomic Layer Deposition of Elemental Antimony	
2.1 – Introduction to Chapter 2.....	27
2.2 – Synthesis and Solution-State Reactivity of Tris(trimethylsilyl)antimony ... (2-1)	30
2.3 – ALD Studies using Sb(SiMe ₃) ₃ (2-1) and SbCl ₃	32
2.4 – Nucleation Enhancement by In Situ Surface Pre-Treatment.....	39
2.5 – Summary and Conclusions for Chapter 2.....	43
2.6 – Future Work for Chapter 2.....	45
2.7 – References for Chapter 2.....	47

Chapter 3: Synthesis of Silyl- and Germylboranes and Investigation of their Suitability as Precursors for Boron Atomic Layer Deposition

3.1 – Introductory Preface.....	52
3.1.1 – ALD of Boron-Containing Films.....	53
3.1.2 – Previously Reported Silylboron and Germylboron Compounds.....	58
3.2 – Synthesis of Silyl- and Germyl-Substituted Boranes.....	66
3.2.1 – Starting Material Synthesis.....	68
3.2.1.1 – Alkali Metal Silyl Reagents.....	68
3.2.1.2 – Trimethylgermyllithium.....	71
3.2.1.3 – Dimethylamidodihaloboranes.....	73
3.2.2 – Hypersilyl-Substituted Boranes.....	74
3.2.3 – Supersilyl-Substituted Boranes.....	78
3.2.4 – Germyl-Substituted Boranes.....	83
3.3 – Testing Bis(tetrel)amidoboranes as Precursors for Boron ALD.....	86
3.3.1 – Volatility, Thermal Stability, and Reactivity of $\{(Me_3Si)_3Si\}_2B(NMe_2)$	86
(3-8)	
3.3.2 – Attempted ALD using $\{(Me_3Si)_3Si\}_2B(NMe_2)$ (3-8) and BCl_3	88
3.3.3 – Volatility, Thermal Stability, and Reactivity of $(^tBu_3Si)(Me_3Ge)B(NMe_2)$.	89
(3-12)	
3.4 – Summary and Conclusions for Chapter 3.....	91
3.5 – Future Work for Chapter 3.....	92
3.6 – References for Chapter 3.....	94

Chapter 4: Flowable Atomic Layer Deposition of HfO_2 Using a Carboxylic Acid as the Co-Reactant

4.1 – Introduction to Chapter 4.....	98
4.2 – Results.....	103
4.2.1 – Deposition Using $[Hf(NMeEt)_4]$ and IVA.....	106
4.2.2 – Solution-State Studies.....	113
4.2.3 – Decomposition Studies.....	123
4.3 – Summary and Conclusions for Chapter 4.....	128
4.4 – Future Work for Chapter 4.....	129

4.5 – References for Chapter 4.....	131
Chapter 5: Synthesis, Structures, and Thermal Stability of Dialkyl and Bis(amido) Zirconium(IV) Acen Complexes	
5.1 – Introduction to Chapter 5.....	135
5.2 – Synthesis and Structures of Dialkyl Zirconium(IV) Acen Complexes.....	138
5.3 – Investigation of the Thermal Stability and Reactivity of Dialkyl.....	145
Zirconium(IV) Acen Complexes	
5.4 – Synthesis of Bis(amido) Zirconium(IV) Acen Complexes.....	146
5.5 – Summary and Conclusions for Chapter 5.....	150
5.6 – Future Work for Chapter 5.....	151
5.7 – References for Chapter 5.....	153
Chapter 6: Experimental Methods	
6.1 – General Methods.....	157
6.1.1 – ALD Reactor.....	158
6.1.2 – Solvents	159
6.1.3 – Instrumentation and Analysis.....	160
6.1.4 – Materials Characterization.....	161
6.2 – Starting Materials, Synthetic Procedures, and Characterization.....	164
Pertaining to the Work of Chapter 2	
6.2.1 – Starting Materials.....	164
6.2.2 – ALD Experiments using $\text{Sb}(\text{SiMe}_3)_3$ (2-1) and SbCl_3	165
6.3 – Starting Materials, Synthetic Procedures, and Characterization.....	166
Pertaining to the Work of Chapter 3	
6.3.1 – Starting Material Synthesis.....	166
6.3.2 – Silyl- and Germyl-Substituted Boranes.....	172
6.3.3 – Attempted ALD using $\{(\text{Me}_3\text{Si})_3\text{Si}\}_2\text{B}(\text{NMe}_2)$ (3-8) and BCl_3	176
6.4 – Starting Materials, Synthetic Procedures, and Characterization.....	177
Pertaining to the Work of Chapter 4	
6.4.1 – Starting Materials.....	177
6.4.2 – Synthetic Procedures and Characterization.....	178
6.4.3 – ALD Experiments using $[\text{Hf}(\text{NMeEt})_4]$ and IVA.....	179

6.4.4 – Attempted ALD using [Hf(NMeEt) ₄] and Pivalic Acid (tBuCO ₂ H).....	180
6.5 – Starting Materials, Synthetic Procedures, and Characterization.....	181
Pertaining to the Work of Chapter 5	
6.5.1 – Starting Materials.....	181
6.5.2 – Synthetic Procedures and Characterization.....	181
6.6 – References for Chapter 6.....	187
Appendix – Supplementary Information	
A1 – Crystal Structure and Refinement Data of Compounds Reported in.....	A1
Chapters 2 to 5	
A2 – Supplementary Information Related to Chapter 2.....	A10
A3 – Supplementary Information Related to Chapter 3.....	A32
A4 – Supplementary Information Related to Chapter 4.....	A47
A5 – Supplementary Information Related to Chapter 5.....	A71

List of Figures

Figure 1.1: The most common graphical demonstrations of ALD. (a) Dependency of growth-per-cycle (GPC) or film thickness on the reactant pulse time. (b) Dependency of film thickness on the number of ALD cycles. (c) Dependency of GPC or film thickness on deposition temperature.

Figure 1.2: Diagram of deposition using ALD versus other deposition methods. Adapted from Atomic Limits image library (2020).

Figure 1.3: Schematic diagram depicting the bottom-up, self-aligned patterning achievable by AS-ALD.

Figure 1.4: Histogram showing the number of records referring to “atomic layer deposition” and either “TiO₂”, “ZrO₂”, or “HfO₂” using the Web of Science platform.

Figure 1.5: Colour-coded periodic table, adapted from the Atomic Limits database, depicting reported thermal and plasma ALD processes. Elements that have been reported to be deposited in the elemental form by thermal ALD are enclosed in solid boxes. Elements enclosed in dashed boxes have been proposed to be deposited by thermal ALD with only an oxide detected due to instantaneous oxidation upon exposure to air.

Figure 2.1: (a) ¹H NMR spectra of the NMR-scale reaction of Sb(SiMe₃)₃ (**2-1**) and SbCl₃ in C₆D₆ (600 MHz, 298 K). The reaction was monitored before and after addition of 1 equivalent of SbCl₃. After complete consumption of Sb(SiMe₃)₃, Me₃SiCl was added to the NMR tube to verify the identify the reaction product. (b) X-ray diffractogram of Sb powder generated from the 1:1 reaction of **2-1** and SbCl₃ in hexanes.

Figure 2.2: XPS depth analysis of Sb films grown on (a) H-Si and (b) SiO₂/Si at 35 °C using 2000 cycles and 0.1 second pulse times.

Figure 2.3: X-ray diffractograms of Sb films grown on (a) H-Si and (b) SiO₂/Si at 35 °C using 2000 cycles and 0.1 second pulse times.

Figure 2.4: Dependence of film thickness and GPC on Sb(SiMe₃)₃ and/or SbCl₃ pulse times for Sb deposition on H-Si (circles) and SiO₂/Si (squares). All experiments employed

1000 cycles and a deposition temperature of 35 °C. Red data points indicate experiments in which the pulse time (on the x-axis) applies to both $\text{Sb}(\text{SiMe}_3)_3$ and SbCl_3 . Gray or black coloured data points indicate experiments in which the pulse time (on the x-axis) applies only to $\text{Sb}(\text{SiMe}_3)_3$ or SbCl_3 , respectively (the pulse time of the other reactant was fixed at 0.1 s).

Figure 2.5: Dependence of film thickness on the number of cycles for Sb ALD on H-Si (circles) and SiO_2/Si (squares) substrates at 35 °C. Reactant pulse times were kept constant at 0.1 s. The inset shows an expanded view of the region from 0 to 250 cycles.

Figure 2.6: FESEM images of films grown on H-Si at 35 °C using (a) 125, (b) 250, (c) 500 and (d) 1000 ALD cycles. Film thicknesses are average values determined by VASE.

Figure 2.7: Dependence of film thickness and GPC on Sb deposition temperature on H-Si (circles) and SiO_2/Si (squares). All films were deposited using 1000 cycles and 0.4 second reactant pulse times.

Figure 2.8: FESEM images of films grown on H-Si at 35 °C with or without 50 pulses of $\text{Sb}(\text{SiMe}_3)_3$ or SbCl_3 prior to carrying out 50 ALD cycles: (a) 50 ALD cycles (0.1 s pulses) without any pre-treatment, (b) pre-treatment with $\text{Sb}(\text{SiMe}_3)_3$ (50×0.4 s pulses), followed by 50 ALD cycles (using 0.4 s pulses), (c) pre-treatment with $\text{Sb}(\text{SiMe}_3)_3$ (50×0.8 s pulses), followed by 50 ALD cycles (using 0.8 s pulses), (d) pre-treatment with SbCl_3 (50×0.4 s pulses), followed by 50 ALD cycles (using 0.4 s pulses), and (e) pre-treatment with SbCl_3 (50×0.8 s pulses), followed by 50 ALD cycles (using 0.8 s pulses). Film thicknesses are average values determined by VASE.

Figure 2.9: Film thickness versus the number of ALD cycles for 35 °C deposition on H-Si using: (i; black) standard ALD parameters (no pre-treatment, all cycles using 0.1 s pulses), (ii; red) ALD with $\text{Sb}(\text{SiMe}_3)_3$ pre-treatment (surface pre-treatment with 50×0.4 s pulses of $\text{Sb}(\text{SiMe}_3)_3$, followed by 50 ALD cycles using 0.4 s pulses, and all remaining ALD cycles using 0.1 s pulses), or (iii; blue) ALD with SbCl_3 pre-treatment (surface pre-treatment with 50×0.4 s pulses of SbCl_3 , followed by 50 ALD cycles using 0.4 s pulses, and all remaining ALD cycles using 0.1 s pulses).

Figure 2.10: X-ray diffractograms of Sb films grown on H-Si (35 °C; 2000 cycles) using (a) the standard ALD method (no pre-treatment, all 0.1 s precursor pulses), (b) ALD with Sb(SiMe₃)₃ pre-treatment (surface pre-treatment with 50 x 0.4 s pulses of Sb(SiMe₃)₃, followed by 50 ALD cycles using 0.4 s pulses, and then 1950 cycles using 0.1 s pulses), or (c) ALD with SbCl₃ pre-treatment (surface pre-treatment with 50 x 0.4 s pulses of SbCl₃, followed by 50 ALD cycles using 0.4 s pulses, and then 1950 cycles using 0.1 s pulses).

Figure 3.1: Chemical structure of MTp₂ and MTp^{Et}₂.

Figure 3.2: X-ray crystal structure of (tBu₃Si)Na(THF)₂ (**3-2**) with ellipsoids set at 50% probability. Space group P2₁/c. All hydrogen atoms have been omitted for clarity. R₁ = 0.0549. Only one of three independent molecules in the unit cell is shown. Each of the molecules displayed disorder at the carbon atoms of the THF rings and/or the methyl carbons of the tert-butyl groups.

Figure 3.3: X-ray crystal structure of [Me₃GeLi(THF)₂]₂ (**3-3**) with ellipsoids set at 50% probability. Space group P-1. All hydrogen atoms have been omitted for clarity. R₁ = 0.0232.

Figure 3.4: ¹¹B{¹H} NMR spectrum of a stock solution of **3-4** in heptane (C₆D₆, 193 MHz, 298 K).

Figure 3.5: X-ray crystal structure of {(Me₃Si)₃Si}₂B(NMe₂) (**3-8**) with ellipsoids set at 50% probability. Space group Pn. All hydrogen atoms have been omitted for clarity. (a) A view facing the boron center's trigonal plane. (b) A view down the B-N bond. R₁ = 0.0721.

Figure 3.6: ¹¹B{¹H} NMR spectra from the NMR-scale reaction of dimethylamido-dichloroborane (**3-4**) and 1.5 equivalents of supersilylsodium (**3-2**) to produce supersilyldimethylamidochloroborane (**3-9**) (C₆D₆, 193 MHz, 298 K). Top: **3-4** before the addition of **3-2**; middle: 18 hours after the addition of **3-2**; bottom: after heating at 50 °C for 4 hours.

Figure 3.7: ¹¹B{¹H} (left) and ¹⁹F NMR (right) spectra monitoring the reaction of (tBu₃Si)B(NMe₂)F (**3-10**) with tBu₃SiNa(THF)_n (**3-2**) (C₆D₆, 193 MHz (¹¹B{¹H}), 565 MHz (¹⁹F), 298 K). From top to bottom: **3-10** before addition of **3-2**; 24 hours after the addition

of excess **3-2** to **3-10** and heating at 100 °C; after heating for an additional 5 days at 100 °C.

Figure 3.8: X-ray crystal structure of $({}^t\text{Bu}_3\text{Si})(\text{Me}_3\text{Ge})\text{B}(\text{NMe}_2)$ (**3-12**) with ellipsoids set at 50% probability. Space group *Pnma*. H atoms are omitted for clarity. Only one of two independent molecules in the unit cell is shown. (a) A view facing the boron center's trigonal plane. (b) A view down the B-N bond. $R_1 = 0.1081$.

Figure 3.9: ${}^{11}\text{B}\{^1\text{H}\}$ NMR spectrum of the NMR-scale test reaction between 1 equivalent of $\text{B}(\text{NMe}_2)\text{Cl}_2$ (**3-4**) and 2 equivalents of $\text{Me}_3\text{GeLi}(\text{THF})_2$ (**3-3**) 15 minutes after addition at room temperature. The chemical shifts of the two major peaks from this reaction are indicated.

Figure 3.10: X-ray crystal structure of $\{(\text{Me}_3\text{Ge})_3\text{B}(\text{NMe}_2)\}\text{Li}(\text{THF})_2$ (**3-13**), with atoms displayed isotropically and bond metrics not included due to a combination of weak data and a high level of unmodeled disorder and twinning. One of six independent molecules (that with least amount of disorder) is shown, and H atoms are omitted for clarity. Space group *P1*. $R_1 = 0.0764$.

Figure 3.11: TGA of $\{(\text{Me}_3\text{Si})_3\text{Si}\}_2\text{B}(\text{NMe}_2)$ (**3-8**) and $({}^t\text{Bu}_3\text{Si})(\text{Me}_3\text{Ge})\text{B}(\text{NMe}_2)$ (**3-12**). Ramp rate = 10 °C/min; starting weights = 3.481 mg (**3-8**), 3.306 mg (**3-12**).

Figure 3.12: Comparison of the X-ray diffractogram of the powder generated from the reaction of $({}^t\text{Bu}_3\text{Si})(\text{Me}_3\text{Ge})\text{B}(\text{NMe}_2)$ (**3-12**) and BBr_3 at room temperature (bottom) to elemental boron (top).

Figure 3.13: Molecular design of future bis(tetrel)amidoborane compounds as precursors for boron ALD.

Figure 4.1: (a) Schematic diagram depicting the development of voids in a deposition process on a narrow trench substrate due to the growth of overhangs on the top of the trench. (b) Schematic diagram depicting the proposed development of a void-free film through deposition of monometallic complexes or oligomeric clusters and subsequent thermal conversion to HfO_2 .

Figure 4.2: Example cross-sectional TEM (a and c) and SEM (b) images of gap-filled trenches.

Figure 4.3: Thermogravimetric analysis (TGA) of β -hydroxyisovaleric acid (IVA). Ramp rate = 10 °C/min; starting weight = 4.286 mg.

Figure 4.4: Dependence of average film thickness and GPC on $[\text{Hf}(\text{NMeEt})_4]$ and IVA pulse times at various deposition temperatures. All films were deposited using 500 cycles, and thicknesses/GPC values are for un-annealed films.

Figure 4.5: Dependence of average film thickness and GPC on deposition temperature without (gray) and with (red) in situ post-deposition thermal annealing. All films were deposited using 500 cycles and 0.6 s reactant pulse times.

Figure 4.6: XPS depth analysis of films grown without (a) and with (b) an in situ post-deposition thermal annealing step. Thin films were grown at 100 °C using 500 cycles and 1.0 s reactant pulse times and 20 s purge times. For this preliminary data, initial experimental conditions used argon flow rates totaling 260 sccm (providing an internal pressure of 630 mTorr during operation), and IVA was delivered at 50 °C.

Figure 4.7: (a) Top-down and (b) cross-sectional FESEM images of as-deposited films grown at 100 °C. (c) Top-down and (d) cross-sectional FESEM images of post-deposition annealed films, using 500 cycles and 0.6 s pulse times. Film thicknesses are average values determined by VASE.

Figure 4.8: X-ray crystal structure of $[\text{EtMeNH}_2]_2[\text{Hf}(\kappa^2\text{-O}_2\text{CCH}_2\text{CMe}_2\text{OH})_2(\kappa^2\text{-OC(O)CH}_2\text{CMe}_2\text{O})_2]$ (**4-1**) with ellipsoids set at 50% probability. Space group P-1. View (a) shows only the anionic portion of the molecule, and view (b) shows the extended hydrogen-bonded structure, with intramolecular and intermolecular hydrogen bonds coloured green and blue, respectively. For clarity, most hydrogen atoms have been omitted, and disorder in the O(6) atom and neighbouring methyl groups are not shown. $R_1 = 0.0422$.

Figure 4.9: ^1H NMR spectra of pure $[\text{EtMeNH}_2]_2[\text{Hf}(\kappa^2\text{-O}_2\text{CCH}_2\text{CMe}_2\text{OH})_2(\kappa^2\text{-OC(O)CH}_2\text{CMe}_2\text{O})_2]$ (**4-1**) after heating the sample as a solid *in vacuo* at the indicated temperatures for 4 hours (C_6D_6 , 500 MHz, 298 K).

Figure 4.10: X-ray crystal structure of $[\text{Hf}_5(\mu_3\text{-O})_4(\kappa^2\text{-O}_2\text{C}^t\text{Bu})_4(\mu\text{-O}_2\text{C}^t\text{Bu})_8]\cdot 3\text{C}_6\text{H}_6$ (**4-2**) (C_6H_6)₃) with ellipsoids set at 50% probability. Space group C2/c. For clarity, hydrogen atoms and lattice solvent are omitted, and pivalate anions are depicted in wireframe. $R_1 = 0.0529$.

Figure 4.11: Variable temperature ^1H NMR spectra of $[\text{Hf}_5(\mu_3\text{-O})_4(\kappa^2\text{-O}_2\text{C}^t\text{Bu})_4(\mu\text{-O}_2\text{C}^t\text{Bu})_8]$ (**4-2**; $d_8\text{-THF}$, 500 MHz).

Figure 4.12: ^1H NMR spectra confirming the generation of *N*-ethyl-*N*-methylpivalamide (top) in the NMR-scale reaction between 1 equivalent of $[\text{Hf}(\text{NMeEt})_4]$ and 3.2 equivalents of pivOH (middle) (C_6D_6 , 500 MHz, 298 K) required for the formation of $[\text{Hf}_5(\mu_3\text{-O})_4(\kappa^2\text{-O}_2\text{C}^t\text{Bu})_4(\mu\text{-O}_2\text{C}^t\text{Bu})_8]$ (**4-2**). In the bottom spectrum, an independently-synthesized sample of the amide was added to the NMR tube, to verify the identity of the reaction by-product.

Figure 4.13: ^1H NMR spectra of the by-products (coloured red) from the thermal decomposition of a crude sample of **4-1** at 200 °C for 4 hours under dynamic vacuum (C_6D_6 , 600 MHz, 298 K). Top: Room temperature-volatile by-products vacuum transferred into a degassed J. Young tube containing C_6D_6 . Bottom: Non-room temperature-volatile by-products dissolved in C_6D_6 .

Figure 4.14: Headspace gas chromatograph of room temperature-volatile by-products (coloured red) formed from heating a crude sample of **4-1** at 200 °C for 4 hours under dynamic vacuum (bottom) and of the experimental blank (top). Figure (b) is the same as Figure (a) except that the baseline is magnified in order to display minor thermal decomposition by-products.

Figure 4.15: Dependence of average film thickness and GPC on $[\text{Hf}(\text{X})_4]$ ($\text{X} = \text{NMeEt}$, NMe_2 , O^tBu) and IVA pulse times at various deposition temperatures. All films were deposited using 500 cycles, and thicknesses/GPC values are for un-annealed films.

Figure 5.1: (a) X-ray crystal structure of $[\text{Zr}(\text{acen})(\text{CH}_2\text{SiMe}_3)_2]$ (**5-1**) with ellipsoids at 50% probability. The Zr-CH₂ hydrogen atoms were located from the difference map and refined isotropically; all other hydrogen atoms are omitted for clarity. $R_1 = 0.0330$.

Figure 5.2: X-ray crystal structure of $[\text{Zr}(\text{cis-Cyacen})(\text{CH}_2\text{SiMe}_3)_2]$ (**5-2**; two views are shown to facilitate comparison of the structure of **5-2** with those of **5-1** and **5-3**). Ellipsoids are set at 50% probability. The Zr-CH₂ hydrogen atoms were located from the difference map and refined isotropically; all other hydrogen atoms have been omitted for clarity. $R_1 = 0.0312$.

Figure 5.3: X-ray crystal structure of $[\text{Zr}(\text{trans-Cyacen})(\text{CH}_2\text{SiMe}_3)_2]$ (**5-3**; only one of two independent and essentially isostructural molecules in the unit cell is shown; both molecules in the unit cell displayed disorder at the cyclohexyl ring, one nitrogen donor atom, and one of the *trans*-Cyacen ligand's CH₃ and CH groups). Ellipsoids are set at 50% probability. The Zr-CH₂ hydrogen atoms were located from the difference map and refined isotropically; all other hydrogen atoms have been omitted for clarity. $R_1 = 0.0289$.

Figure 5.4: (a) Variable temperature ¹H NMR spectra of $[\text{Zr}(\text{cis-Cyacen})(\text{CH}_2\text{SiMe}_3)_2]$ (**5-2**) from 188-348 K in *d*₈-toluene (500 MHz). (b,c,d) Expanded regions of the ¹H NMR spectra featuring the (b) ZrCH₂Si(CH₃)₃, (c) NCH, and (d) CH proton peaks.

Figure 5.5: X-ray crystal structure of $[\text{Zr}(\text{acen})_2]$ (**5-5**) with ellipsoids set at 50% probability and all hydrogen atoms omitted for clarity. $R_1 = 0.0679$.

Figure 5.6: ¹H NMR spectrum of $[\text{Zr}(\text{acen})(\text{NMeEt})_2]$ (**5-6**) generated in situ from the reaction of **5-1** with excess HNMeEt in *d*₈-toluene (500 MHz, 249 K). Unassigned peaks in the spectrum are the residual solvent signal, H grease, and silicone grease.

Figure 5.7: X-ray crystal structure of $[\text{Zr}(\text{acen})\{\text{N}(\text{SiMe}_3)_2\}_2]$ (**5-7**) with ellipsoids set at 50% probability and hydrogen atoms omitted for clarity. $R_1 = 0.0192$.

Figure 6.1: Schematic diagram of the home-built ALD reactor used in this research.

Figure A2.1: ¹³C{¹H} and ²⁹Si NMR (1-dimensional projection from ²⁹Si/¹H-HMBC NMR) spectra of the NMR-scale reaction of Sb(SiMe₃)₃ (**2-1**) and SbCl₃ in C₆D₆ (151 and 119

MHz, respectively; 298 K). The reaction was monitored before (top) and after (middle) addition of 1 equivalent of SbCl_3 . After complete consumption of $\text{Sb}(\text{SiMe}_3)_3$, Me_3SiCl was added to the NMR tube to verify the identify the reaction product (bottom).

Figure A2.2: XPS survey spectrum of the surface of an Sb film (before sputtering into the film) grown on H-Si at 35 °C using 2000 cycles and 0.1 second pulses.

Figure A2.3: XPS survey spectrum of the surface of an Sb film (before sputtering into the film) grown on SiO_2/Si at 35 °C using 2000 cycles and 0.1 second pulses.

Figure A2.4: XPS data at Etch Level 3 of the Sb film grown on H-Si (35 °C, 2000 cycles, 0.1 second pulses) in the energy regions for (a) Sb4d, (b) Sb4s and Si2s, (c) Cl2p, (d) C1s, and (e) Sb3d and O1s. Orange lines represent the backgrounds, and red and blue lines represent the fitted model of the Sb peaks.

Figure A2.5: XPS data at Etch Level 2 of the Sb film grown on SiO_2/Si (35 °C, 2000 cycles, 0.1 second pulses) in the energy regions for (a) Sb4d, (b) Sb4s and Si2s, (c) Cl2p, (d) C1s, and (e) Sb3d and O1s. Orange lines represent the backgrounds, and red and blue lines represent the fitted model of the Sb peaks.

Figure A2.6: FESEM images of films grown on H-Si using (a) 125, (b) 250, (c) 500, (d) 1000, and (e) 2000 ALD cycles (35 °C deposition temperature; 0.1 second pulse times). Film thicknesses are average values determined by VASE.

Figure A2.7: FESEM images of films grown on SiO_2/Si using (a) 125, (b) 250, (c) 500, (d) 1000, and (e) 2000 ALD cycles (35 °C deposition temperature; 0.1 second pulse times). Black dots in figures (b), (d), and (e) are due to post deposition surface contamination which developed over time from storage in a glove box (see Figure S9). Film thicknesses are average values determined by VASE.

Figure A2.8: FESEM images of Sb films grown on H-Si using 2000 cycles (35 °C deposition temperature; 0.1 second pulse times). FESEM images (a) were obtained within 2 months of depositing the film, while (b) were taken after 5 months. In both cases, films were stored in a glove box. Therefore, black spots in films depicted here and in Figure S8 are most likely due to surface contamination from long storage times in a glove box.

Figure A2.9: Photographs of films grown on SiO₂/Si and H-Si at variable growth temperatures. All films were grown using 1000 cycles and 0.4 second precursor and co-reactant pulse times. The loss of appearance of pristine, mirror-like silver films at higher temperatures indicates a decay of uniformity (of the films photographed, ALD growth occurred only at 35 and 65 °C).

Figure A2.10: X-ray diffractograms of Sb films grown on H-Si at deposition temperatures ranging from 23 to 150 °C using 0.4 second reactant pulse times and 1000 cycles.

Figure A2.11: Dependence of average film thickness and growth rate on Sb(SiMe₃)₃ and SbCl₃ pulse times at a given deposition temperature. All films were deposited on H-Si using 1000 cycles.

Figure A2.12: FESEM images of films grown on H-Si at (a) 35 °C, (b) 95 °C, (c) 125 °C, and (d) 150 °C using 1000 cycles and 0.4 second reactant pulse times (except for (a) which used 0.1 second pulses). Film thicknesses are average values determined by VASE.

Figure A2.13: X-ray diffractograms of Sb films grown on SiO₂/Si at deposition temperatures ranging from 23 to 150 °C using 0.4 second reactant pulse times and 1000 cycles.

Figure A2.14: Dependence of average film thickness and growth rate on Sb(SiMe₃)₃ and SbCl₃ pulse times at a given deposition temperature. All films were deposited on SiO₂/Si using 1000 cycles.

Figure A2.15: XPS depth analysis of a Sb film grown on SiO₂/Si at 95 °C using 1000 cycles and 0.4 second reactant pulse times.

Figure A2.16: Comparison of FESEM images of ultra-thin films deposited on H-Si at 35 °C using 50 pre-treatment cycles of SbCl₃ (pulse times are indicated in row headings) and 50 ALD cycles of Sb(SiMe₃)₃ and SbCl₃ (pulse times are indicated in column headings). Film thicknesses are average values determined by VASE.

Figure A2.17: Comparison of FESEM images of ultra-thin films deposited on H-Si at 35 °C using 50 pre-treatment cycles of Sb(SiMe₃)₃ (pulse times are indicated in row

headings) and 50 ALD cycles of $\text{Sb}(\text{SiMe}_3)_3$ and SbCl_3 (pulse times are indicated in column headings). Film thicknesses are average values determined by VASE.

Figure A2.18: Comparison of FESEM images of ultra-thin films deposited on SiO_2/Si at 35 °C using 50 pre-treatment cycles of SbCl_3 (pulse times are indicated in row headings) and 50 ALD cycles of $\text{Sb}(\text{SiMe}_3)_3$ and SbCl_3 (pulse times are indicated in column headings). Film thicknesses are average values determined by VASE.

Figure A2.19: Comparison of FESEM images of ultra-thin films deposited on SiO_2/Si at 35 °C using 50 pre-treatment cycles of $\text{Sb}(\text{SiMe}_3)_3$ (pulse times are indicated in row headings) and 50 ALD cycles of $\text{Sb}(\text{SiMe}_3)_3$ and SbCl_3 (pulse times are indicated in column headings). Film thicknesses are average values determined by VASE.

Figure A2.20: X-ray diffractograms of Sb films grown on SiO_2/Si (35 °C; 2000 cycles) using (a) the standard ALD method (no pre-treatment, all 0.1 s precursor pulses), (b) ALD with $\text{Sb}(\text{SiMe}_3)_3$ pre-treatment (surface pre-treatment with 50 × 0.4 s pulses of $\text{Sb}(\text{SiMe}_3)_3$, followed by 50 ALD cycles using 0.4 s pulses, and then 1950 ALD cycles using 0.1 s pulses), or (c) ALD with SbCl_3 pre-treatment (surface pre-treatment with 50 × 0.4 s pulses of SbCl_3 , followed by 50 ALD cycles using 0.4 s pulses, and then 1950 ALD cycles using 0.1 s pulses).

Figure A2.21: Film thickness versus the number of ALD cycles for 35 °C deposition on SiO_2/Si using: (i; black) standard ALD parameters (no pre-treatment, all cycles using 0.1 s pulses), (ii; red) ALD with $\text{Sb}(\text{SiMe}_3)_3$ pre-treatment (surface pre-treatment with 50 × 0.4 s pulses of $\text{Sb}(\text{SiMe}_3)_3$, followed by 50 ALD cycles using 0.4 s pulses, and all remaining ALD cycles using 0.1 s pulses), or (iii; blue) ALD with SbCl_3 pre-treatment (surface pre-treatment with 50 × 0.4 s pulses of SbCl_3 , followed by 50 ALD cycles using 0.4 s pulses, and all remaining ALD cycles using 0.1 s pulses).

Figure A2.22: Dependence of film thickness on purge times (for each data point, purge times are those following each of the two precursor pulses). All films were grown on SiO_2/Si at 35 °C using 1000 cycles. Data points coloured black indicate films grown using 0.1 s reactant pulse times, while gray indicates films grown using 0.4 s pulse times.

Figure A2.23: Dependence of film thickness and growth rate on $\text{Sb}(\text{SiEt}_3)_3$ and SbCl_3 pulse times on SiO_2/Si (squares) and H-Si (circles). Cycle number was kept constant (1000) as well as deposition temperature (95 °C) and delivery temperatures (85 °C for $\text{Sb}(\text{SiEt}_3)_3$, 30 °C for SbCl_3).

Figure A2.24: FESEM images of films grown on H-Si: (a) 50 $\text{Sb}(\text{SiEt}_3)_3/\text{SbCl}_3$ ALD cycles at 95 °C (using 2 second pulse times); (b) 50 $\text{Sb}(\text{SiMe}_3)_3/\text{SbCl}_3$ ALD cycles at 95 °C (using 0.1 second pulse times); (c) 50 $\text{Sb}(\text{SiMe}_3)_3/\text{SbCl}_3$ ALD cycles at 35 °C (using 0.1 second pulse times). Film thicknesses are average values determined by VASE.

Figure A2.25: (a) Cross-sectional FESEM image of Sb film grown on SiO_2/Si at 35 °C using 1000 ALD cycles and 0.1 second and 30 second pulse and purge times, respectively. The average of three different thickness measurements along the film (47 nm) correlates well with the average thickness measurement obtained from VASE (47.03 nm). (b) AFM image of Sb film grown on SiO_2/Si at 35 °C using 1000 ALD cycles and 0.1 second and 30 second pulse and purge times, respectively (note: Kapton tape was adhered to the right side of the film before deposition and removed after deposition). The thickness measurement from AFM step analysis (44 nm) correlates well with the average thickness measured obtained from VASE (47.03 nm).

Figure A2.26: Measured values of Psi (Ψ , solid lines) and Delta (Δ , dashed lines) as a function of wavelength for a Sb film grown on H-Si at 35 °C (1000 cycles, 0.1 second pulse and 30 second purge times).

Figure A2.27: Measured values of Psi (Ψ , solid lines) and Delta (Δ , dashed lines) as a function of wavelength for a Sb film grown on SiO_2/Si at 35 °C (1000 cycles, 0.1 second pulse and 30 second purge times).

Figure A2.28: Photo showing the precursor bubbler design used in this work (in this case, the bubbler containing SbCl_3 is shown, but the same type was used for $\text{Sb}(\text{SiMe}_3)_3$). Bubblers are of a flow-through design, with a dip tube that is short enough to avoid contact with the precursor upon loading of the bubbler.

Figure A3.1: ^1H NMR spectrum of $[\text{Me}_3\text{GeLi}(\text{THF})_2]_2$, **3-3** (C_6D_6 , 600 MHz, 298 K).

Figure A3.2: $^{13}\text{C}\{^1\text{H}\}$ NMR spectrum of $[\text{Me}_3\text{GeLi}(\text{THF})_2]_2$, **3-3** (C_6D_6 , 151 MHz, 298 K).

Figure A3.3: ^1H NMR spectrum of $\{(\text{Me}_3\text{Si})_3\text{Si}\}_2\text{B}(\text{NMe}_2)$, **3-8** (C_6D_6 , 600 MHz, 298 K).

Figure A3.4: $^{13}\text{C}\{^1\text{H}\}$ NMR spectrum of $\{(\text{Me}_3\text{Si})_3\text{Si}\}_2\text{B}(\text{NMe}_2)$, **3-8** (C_6D_6 , 151 MHz, 298 K).

Figure A3.5: $^{11}\text{B}\{^1\text{H}\}$ NMR spectrum of $\{(\text{Me}_3\text{Si})_3\text{Si}\}_2\text{B}(\text{NMe}_2)$, **3-8** (C_6D_6 , 193 MHz, 298 K).

Figure A3.6: $^{29}\text{Si}-^1\text{H}$ HMBC NMR spectrum of $\{(\text{Me}_3\text{Si})_3\text{Si}\}_2\text{B}(\text{NMe}_2)$, **3-8** (C_6D_6 , 600/119 MHz, 298 K). F1 axis is an internal ^{29}Si NMR projection.

Figure A3.7: ^1H NMR spectrum of $(^t\text{Bu}_3\text{Si})\text{B}(\text{NMe}_2)\text{Cl}$, **3-9** (C_6D_6 , 600 MHz, 298 K). Peaks labeled with a double dagger correspond to the impurity that consistently arose during $(^t\text{Bu}_3\text{Si})\text{Na}(\text{THF})_n$ synthesis.

Figure A3.8: $^{13}\text{C}\{^1\text{H}\}$ NMR spectrum of $(^t\text{Bu}_3\text{Si})\text{B}(\text{NMe}_2)\text{Cl}$, **3-9** (C_6D_6 , 151 MHz, 298 K). Peaks labeled with a double dagger correspond to the impurity that consistently arose during $(^t\text{Bu}_3\text{Si})\text{Na}(\text{THF})_n$ synthesis.

Figure A3.9: $^{11}\text{B}\{^1\text{H}\}$ NMR spectrum of $(^t\text{Bu}_3\text{Si})\text{B}(\text{NMe}_2)\text{Cl}$, **3-9** (C_6D_6 , 193 MHz, 298 K).

Figure A3.10: $^{29}\text{Si}-^1\text{H}$ HMBC NMR spectrum of $(^t\text{Bu}_3\text{Si})\text{B}(\text{NMe}_2)\text{Cl}$, **3-9** (C_6D_6 , 600/119 MHz, 298 K). F1 axis is an internal ^{29}Si NMR projection. Peaks labeled with a double dagger correspond to the impurity that consistently arose during $(^t\text{Bu}_3\text{Si})\text{Na}(\text{THF})_n$ synthesis.

Figure A3.11: ^1H NMR spectrum of $(^t\text{Bu}_3\text{Si})\text{B}(\text{NMe}_2)\text{F}$, **3-10** (C_6D_6 , 500 MHz, 298 K). Peaks labeled with a double dagger correspond to the impurity that consistently arose during $(^t\text{Bu}_3\text{Si})\text{Na}(\text{THF})_n$ synthesis.

Figure A3.12: $^{13}\text{C}\{^1\text{H}\}$ NMR spectrum of $(^t\text{Bu}_3\text{Si})\text{B}(\text{NMe}_2)\text{F}$, **3-10** (C_6D_6 , 126 MHz, 298 K). Peaks labeled with a double dagger correspond to the impurity that consistently arose during $(^t\text{Bu}_3\text{Si})\text{Na}(\text{THF})_n$ synthesis.

Figure A3.13: $^{11}\text{B}\{^1\text{H}\}$ NMR spectrum of $(^t\text{Bu}_3\text{Si})\text{B}(\text{NMe}_2)\text{F}$, **3-10** (C_6D_6 , 161 MHz, 298 K).

Figure A3.14: ^{19}F NMR spectrum of $(^t\text{Bu}_3\text{Si})\text{B}(\text{NMe}_2)\text{F}$, **3-10** (C_6D_6 , 471 MHz, 298 K).

Figure A3.15: ^{29}Si - ^1H HMBC NMR spectrum of $(^t\text{Bu}_3\text{Si})\text{B}(\text{NMe}_2)\text{F}$, **3-10** (C_6D_6 , 500/99 MHz, 298 K). F1 axis is an internal ^{29}Si NMR projection. Peaks labeled with a double dagger correspond to the impurity that consistently arose during $(^t\text{Bu}_3\text{Si})\text{Na}(\text{THF})_n$ synthesis.

Figure A3.16: ^1H NMR spectrum of $(^t\text{Bu}_3\text{Si})\text{BCl}_2$, **3-11** (C_6D_6 , 600 MHz, 298 K). Peaks labeled with a double dagger correspond to the impurity that consistently arose during $(^t\text{Bu}_3\text{Si})\text{Na}(\text{THF})_n$ synthesis.

Figure A3.17: $^{13}\text{C}\{^1\text{H}\}$ NMR spectrum of $(^t\text{Bu}_3\text{Si})\text{BCl}_2$, **3-11** (C_6D_6 , 151 MHz, 298 K).

Figure A3.18: $^{11}\text{B}\{^1\text{H}\}$ NMR spectrum of $(^t\text{Bu}_3\text{Si})\text{BCl}_2$, **3-11** (C_6D_6 , 193 MHz, 298 K).

Figure A3.19: ^{29}Si - ^1H HMBC NMR spectrum of $(^t\text{Bu}_3\text{Si})\text{BCl}_2$, **3-11** (C_6D_6 , 600/119 MHz, 298 K). F1 axis is an internal ^{29}Si NMR projection. Peaks labeled with a double dagger correspond to the impurity that consistently arose during $(^t\text{Bu}_3\text{Si})\text{Na}(\text{THF})_n$ synthesis.

Figure A3.20: ^1H NMR spectrum of $(^t\text{Bu}_3\text{Si})(\text{Me}_3\text{Ge})\text{B}(\text{NMe}_2)$, **3-12** (C_6D_6 , 600 MHz, 298 K).

Figure A3.21: $^{13}\text{C}\{^1\text{H}\}$ NMR spectrum of $(^t\text{Bu}_3\text{Si})(\text{Me}_3\text{Ge})\text{B}(\text{NMe}_2)$, **3-12** (C_6D_6 , 151 MHz, 298 K).

Figure A3.22: $^{11}\text{B}\{^1\text{H}\}$ NMR spectrum of $(^t\text{Bu}_3\text{Si})(\text{Me}_3\text{Ge})\text{B}(\text{NMe}_2)$, **3-12** (C_6D_6 , 193 MHz, 298 K).

Figure A3.23: ^{29}Si - ^1H HMBC NMR spectrum of $(^t\text{Bu}_3\text{Si})(\text{Me}_3\text{Ge})\text{B}(\text{NMe}_2)$, **3-12** (C_6D_6 , 600/119 MHz, 298 K). F1 axis is an internal ^{29}Si NMR projection.

Figure A3.24: ^1H NMR spectrum of $\{(\text{Me}_3\text{Ge})_3\text{B}(\text{NMe}_2)\}\text{Li}(\text{THF})_2$, **3-13** (C_6D_6 , 600 MHz, 298 K).

Figure A3.25: $^{13}\text{C}\{^1\text{H}\}$ NMR spectrum of $\{(\text{Me}_3\text{Ge})_3\text{B}(\text{NMe}_2)\}\text{Li}(\text{THF})_2$, **3-13** (C_6D_6 , 151 MHz, 298 K).

Figure A3.26: $^{11}\text{B}\{^1\text{H}\}$ NMR spectrum of $\{(\text{Me}_3\text{Ge})_3\text{B}(\text{NMe}_2)\}\text{Li}(\text{THF})_2$, **3-13** (C_6D_6 , 193 MHz, 298 K).

Figure A3.27: Monitoring the NMR-scale test reaction between $\{(Me_3Si)_3Si\}_2B(NMe_2)$ (**3-8**) and excess BCl_3 (1M in heptane) in C_6D_6 , with C_6Me_6 as an internal standard. Identified NMR signals (based on known compounds in literature) are labelled throughout. (a) 1H NMR spectra (500 MHz, 298 K); (b) $^{11}B\{^1H\}$ NMR spectra (126 MHz, 298 K).

Figure A3.28: Monitoring the NMR-scale test reaction between $(^iBu_3Si)(Me_3Ge)B(NMe_2)$ (**3-12**) and excess BBr_3 in C_6D_6 , with C_6Me_6 as an internal standard. Identified NMR signals (based on known compounds in literature) are labelled throughout. (a) 1H NMR spectra (500 MHz, 298 K); (b) $^{11}B\{^1H\}$ NMR spectra (126 MHz, 298 K).

Figure A4.1: Dependence of average film thickness and growth rate on $[Hf(NMeEt)_4]$ and IVA pulse times at a given deposition temperature. All films were deposited on SiO_2/Si using 500 cycles and annealed *in situ* at 400 °C for 1 hour.

Figure A4.2: Measured values of Psi (Ψ , solid lines) and Delta (Δ , dashed lines) as a function of wavelength for an as-deposited HfO_2 film grown on SiO_2/Si at 100 °C (500 cycles, 0.6 second pulse and 60 second purge times).

Figure A4.3: Measured values of Psi (Ψ , solid lines) and Delta (Δ , dashed lines) as a function of wavelength for an annealed HfO_2 film grown on SiO_2/Si at 100 °C (500 cycles, 0.6 second pulse and 60 second purge times), followed by *in situ* annealing at 400 °C for 1 hour.

Figure A4.4: XPS data at Etch Level 20 of the as-deposited film grown on SiO_2/Si in the energy regions for (a) Hf4f, (b) O1s, (c) C1s, and (d) N1s. Thin films were grown at 100 °C using 500 cycles and 1 s reactant pulse times and 20 s purge times. For this preliminary data, initial deposition conditions used argon flow rates totaling 260 sccm (providing an internal pressure of 630 mTorr during operation), and IVA was delivered at 50 °C.

Figure A4.5: XPS data at Etch Level 12 of the thermally annealed film grown on SiO_2/Si in the energy regions for (a) Hf4f, (b) O1s, (c) C1s, and (d) N1s. Thin films were grown at 100 °C using 500 cycles and 1 s reactant pulse times and 20 s purge times. For this preliminary data, initial deposition conditions used argon flow rates totaling 260 sccm

(providing an internal pressure of 630 mTorr during operation), and IVA was delivered at 50 °C.

Figure A4.6: ^1H NMR spectrum of $[\text{EtMeNH}_2]_2[\text{Hf}(\kappa^2\text{-O}_2\text{CCH}_2\text{CMe}_2\text{OH})_2(\kappa^2\text{-OC(O)CH}_2\text{CMe}_2\text{O})_2]$ (**4-1**) in C_6D_6 (500 MHz, 298 K).

Figure A4.7: $^{13}\text{C}\{^1\text{H}\}$ NMR spectrum of $[\text{EtMeNH}_2]_2[\text{Hf}(\kappa^2\text{-O}_2\text{CCH}_2\text{CMe}_2\text{OH})_2(\kappa^2\text{-OC(O)CH}_2\text{CMe}_2\text{O})_2]$ (**4-1**) in C_6D_6 (126 MHz, 298 K).

Figure A4.8: Select areas of the ^{13}C - ^1H HMBC NMR spectrum of $[\text{EtMeNH}_2]_2[\text{Hf}(\kappa^2\text{-O}_2\text{CCH}_2\text{CMe}_2\text{OH})_2(\kappa^2\text{-OC(O)CH}_2\text{CMe}_2\text{O})_2]$ (**4-1**) in C_6D_6 (600/151 MHz, 298 K) for the assignment of the (a) $\text{CMe}_2(\text{OH})\text{Me}_2$ and (b) O_2CCH_2 ^{13}C NMR signals.

Figure A4.9: Variable temperature ^1H NMR spectra of $[\text{EtMeNH}_2]_2[\text{Hf}(\kappa^2\text{-O}_2\text{CCH}_2\text{CMe}_2\text{OH})_2(\kappa^2\text{-OC(O)CH}_2\text{CMe}_2\text{O})_2]$ (**4-1**) in $d_8\text{-tol}$ (500 MHz). (b) Magnified regions of the ^1H NMR spectra.

Figure A4.10: ^1H NMR spectrum of $[\text{Hf}_5(\text{O})_4(\mu\text{-O}_2\text{C}^t\text{Bu})_8(\kappa^2\text{-O}_2\text{C}^t\text{Bu})_4]$ (**4-2**) in $d_8\text{-THF}$ (600 MHz, 298 K).

Figure A4.11: $^{13}\text{C}\{^1\text{H}\}$ NMR spectrum of $[\text{Hf}_5(\text{O})_4(\mu\text{-O}_2\text{C}^t\text{Bu})_8(\kappa^2\text{-O}_2\text{C}^t\text{Bu})_4]$ (**4-2**) in $d_8\text{-THF}$ (151 MHz, 298 K).

Figure A4.12: Select areas of the ^{13}C - ^1H HMBC NMR spectrum of $[\text{Hf}_5(\text{O})_4(\mu\text{-O}_2\text{C}^t\text{Bu})_8(\kappa^2\text{-O}_2\text{C}^t\text{Bu})_4]$ (**4-2**) in $d_8\text{-THF}$ (600/151 MHz, 298 K) for the assignment of the (a) $\text{O}_2\text{CC}(\text{CH}_3)_3$ and (b) $\text{O}_2\text{CC}(\text{CH}_3)_3$ ^{13}C NMR signals.

Figure A4.13: Low-temperature $^{13}\text{C}\{^1\text{H}\}$ NMR spectrum of $[\text{Hf}_5(\text{O})_4(\mu\text{-O}_2\text{C}^t\text{Bu})_8(\kappa^2\text{-O}_2\text{C}^t\text{Bu})_4]$ (**4-2**) in $d_8\text{-THF}$ (151 MHz, 176 K).

Figure A4.14: Select area of the low-temperature ^{13}C - ^1H HSQC NMR spectrum of $[\text{Hf}_5(\text{O})_4(\mu\text{-O}_2\text{C}^t\text{Bu})_8(\kappa^2\text{-O}_2\text{C}^t\text{Bu})_4]$ (**4-2**) in $d_8\text{-THF}$ (600/151 MHz, 176 K) for the assignment of the $\text{O}_2\text{CC}(\text{CH}_3)_3$ ^{13}C NMR signals.

Figure A4.15: Select areas of the low-temperature ^{13}C - ^1H HMBC NMR spectrum of $[\text{Hf}_5(\text{O})_4(\mu\text{-O}_2\text{C}^t\text{Bu})_8(\kappa^2\text{-O}_2\text{C}^t\text{Bu})_4]$ (**4-2**) in d_8 -THF (600/151 MHz, 176 K) for the assignment of the (a) $\text{O}_2\text{CC}(\text{CH}_3)_3$ and (b) $\text{O}_2\text{CC}(\text{CH}_3)_3$ ^{13}C NMR signals.

Figure A4.16: FT-IR spectrum of $[\text{Hf}_5(\text{O})_4(\mu\text{-O}_2\text{C}^t\text{Bu})_8(\kappa^2\text{-O}_2\text{C}^t\text{Bu})_4]$ (**4-2**) in a Nujol mull.

Figure A4.17: (a) $^{13}\text{C}\{^1\text{H}\}$ NMR spectra of the by-products (coloured red) from the thermal decomposition of a crude sample of **4-1** at 200 °C for 4 hours under dynamic vacuum (C_6D_6 , 151 MHz, 298 K). Top: Room temperature-volatile by-products vacuum transferred into a degassed J. Young tube containing C_6D_6 . Bottom: Non-room temperature-volatile by-products dissolved in C_6D_6 . (b and c) Magnified regions of (a). Unidentified peaks are labeled with a question mark.

Figure A4.18: Gas chromatogram (mass selective detector) of non-room temperature-volatile by-products (coloured red) formed from heating a crude sample of **4-1** at 200 °C for 4 hours under dynamic vacuum (bottom) and of the experimental blank (top). Peaks at 7.9 and 8.5 min are tentatively assigned based on their MS fragmentation patterns.

Figure A4.19: Mass spectrum of carbon dioxide detected in the headspace GC-MS sample after heating a crude sample of **4-1** at 200 °C for 4 hours under dynamic vacuum.

Figure A4.20: Mass spectrum of isobutene detected in the headspace GC-MS sample after heating a crude sample of **4-1** at 200 °C for 4 hours under dynamic vacuum.

Figure A4.21: Mass spectrum of *N*-ethyl-*N*-methylamine detected in the headspace GC-MS sample after heating a crude sample of **4-1** at 200 °C for 4 hours under dynamic vacuum.

Figure A4.22: Mass spectrum of acetone detected in the headspace GC-MS sample after heating a crude sample of **4-1** at 200 °C for 4 hours under dynamic vacuum.

Figure A4.23: Mass spectrum of mesityl oxide detected in the headspace GC-MS sample after heating a crude sample of **4-1** at 200 °C for 4 hours under dynamic vacuum.

Figure A4.24: Mass spectrum of *N*-ethyl-*N*-methylacetamide detected in the headspace GC-MS sample after heating a crude sample of **4-1** at 200 °C for 4 hours under dynamic vacuum.

Figure A4.25: Mass spectrum of the unknown compound detected in the headspace GC-MS sample after heating a crude sample of **4-1** at 200 °C for 4 hours under dynamic vacuum.

Figure A4.26: Mass spectrum of IVA detected in the GC-MS sample after heating a crude sample of **4-1** at 200 °C for 4 hours under dynamic vacuum.

Figure A4.27: Mass spectrum of *N*-ethyl-*N*,3-dimethylbut-3-enamide detected in the GC-MS sample after heating a crude sample of **4-1** at 200 °C for 4 hours under dynamic vacuum. The identity of this compound is tentatively assigned based on the fragmentation pattern.

Figure A4.28: Mass spectrum of *N*-ethyl-3-hydroxy-*N*,3-dimethylbutanamide detected in the GC-MS sample after heating a crude sample of **4-1** at 200 °C for 4 hours under dynamic vacuum. The identity of this compound is tentatively assigned based on the fragmentation pattern.

Figure A4.29: (a) Central coordination network of Hf metal centres and bridging oxo ligands observed in the X-ray crystal structure of **4-2(C₆H₆)₃**. (b) Coordination geometry about the apical, square antiprismatic Hf(1) centre of complex **4-2(C₆H₆)₃**. (c) Coordination geometry about the 7-coordinate Hf(2) and Hf(3) centres of complex **4-2(C₆H₆)₃**.

Figure A.30: X-ray crystal structure of $[\text{Hf}_5(\mu_3\text{-O})_4(\mu\text{-Opiv})_8(\kappa^2\text{-Opiv})_4]$ (**4-2**) with ellipsoids set at 50% probability. Space group C2/c. Hydrogen atoms were refined isotropically and omitted for clarity. Pivalate ligands are depicted in wireframe for clarity. $R_1 = 0.0830$.

Figure A4.31: (a) Central coordination network of Hf ions and bridging oxo ligands observed in the X-ray crystal structure of **4-2**. (b) Coordination geometry about the apical, square antiprismatic Hf(1) centre of complex **4-2**. (c) Coordination geometry about the 7-coordinate Hf(2) and Hf(3) centres of complex **4-2**.

Figure A5.1: ^1H NMR spectrum of $[\text{Zr}(\text{acen})(\text{CH}_2\text{SiMe}_3)_2]$ (**5-1**) in C_6D_6 (500 MHz, 298 K). Unassigned peaks in the spectrum are the residual solvent signal, H grease, and tetramethylsilane.

Figure A5.2: $^{13}\text{C}\{^1\text{H}\}$ NMR spectrum of $[\text{Zr}(\text{acen})(\text{CH}_2\text{SiMe}_3)_2]$ (**5-1**) in C_6D_6 (126 MHz, 298 K). Unassigned peaks in the spectrum are the residual solvent signal, and tetramethylsilane.

Figure A5.3: Non-decoupled $^{13}\text{C}-^1\text{H}$ HSQC NMR spectrum of $[\text{Zr}(\text{acen})(\text{CH}_2\text{SiMe}_3)_2]$ (**5-1**) in C_6D_6 (126/500 MHz, 298 K). The $^1J_{\text{CH}}$ coupling constant of the CH_2SiMe_3 group is displayed on the right.

Figure A5.4: $^{29}\text{Si}-^1\text{H}$ HMBC NMR spectrum of $[\text{Zr}(\text{acen})(\text{CH}_2\text{SiMe}_3)_2]$ (**5-1**) in C_6D_6 (99/500 MHz, 298 K). F1 axis is an internal ^{29}Si NMR projection.

Figure A5.5: ^1H NMR spectrum of $[\text{Zr}(\text{cis-Cyacen})(\text{CH}_2\text{SiMe}_3)_2]$ (**5-2**) in C_6D_6 (600 MHz, 298 K). Unassigned peaks in the spectrum are the residual solvent signal, H grease, and tetramethylsilane.

Figure A5.6: (a) Variable temperature ^1H NMR spectra of $[\text{Zr}(\text{cis-Cyacen})(\text{CH}_2\text{SiMe}_3)_2]$ (**5-2**) from 188-348 K in d_8 -toluene (500 MHz). (b,c,d) Expanded regions of the ^1H NMR spectra featuring the (b) $\text{ZrCH}_2\text{Si}(\text{CH}_3)_3$, (c) NCH , and (d) CH proton peaks.

Figure A5.7: $^{13}\text{C}\{^1\text{H}\}$ NMR spectrum of $[\text{Zr}(\text{cis-Cyacen})(\text{CH}_2\text{SiMe}_3)_2]$ (**5-2**) in C_6D_6 (151 MHz, 298 K). Unassigned peaks in the spectrum are the residual solvent signal, H grease, and tetramethylsilane.

Figure A5.8: Non-decoupled $^{13}\text{C}-^1\text{H}$ HSQC NMR spectrum of $[\text{Zr}(\text{cis-Cyacen})(\text{CH}_2\text{SiMe}_3)_2]$ (**5-2**) in C_6D_6 (126/500 MHz, 298 K). The $^1J_{\text{CH}}$ coupling constant of the CH_2SiMe_3 group is displayed on the right.

Figure A5.9: $^{29}\text{Si}-^1\text{H}$ HMBC NMR spectra of $[\text{Zr}(\text{cis-Cyacen})(\text{CH}_2\text{SiMe}_3)_2]$ (**5-2**) in d_8 -toluene at 238 K (99/500 MHz). F1 axis is an internal ^{29}Si NMR projection.

Figure A5.10: ^1H NMR spectrum of $[\text{Zr}(\text{trans-Cyacen})(\text{CH}_2\text{SiMe}_3)_2]$ (**5-3**) in C_6D_6 (500 MHz, 298 K). Unassigned peaks in the spectrum are the residual solvent signal, H grease, and tetramethylsilane.

Figure A5.11: $^{13}\text{C}\{^1\text{H}\}$ NMR spectrum of $[\text{Zr}(\textit{trans}\text{-Cyacen})(\text{CH}_2\text{SiMe}_3)_2]$ (**5-3**) in C_6D_6 (126 MHz, 298 K). Unassigned peaks in the spectrum are the residual solvent signal, H grease, and tetramethylsilane.

Figure A5.12: Non-decoupled $^{13}\text{C}\text{-}^1\text{H}$ HSQC NMR spectrum of $[\text{Zr}(\textit{trans}\text{-Cyacen})(\text{CH}_2\text{SiMe}_3)_2]$ (**5-3**) in C_6D_6 (126/500 MHz, 298 K). The $^1J_{\text{CH}}$ coupling constant of the CH_2SiMe_3 group is displayed on the right.

Figure A5.13: $^{29}\text{Si}\text{-}^1\text{H}$ HMBC NMR spectrum of $[\text{Zr}(\textit{trans}\text{-Cyacen})(\text{CH}_2\text{SiMe}_3)_2]$ (**5-3**) in C_6D_6 (99/500 MHz, 298 K). F1 axis is an internal ^{29}Si NMR projection.

Figure A5.14: ^1H NMR spectrum of $[\text{Zr}(\textit{cis}\text{-Cyacen})(\text{O}^t\text{Bu})_2]$ (**5-4**) generated in situ via the reaction of **2** with 2 equiv. of $^t\text{BuOH}$ in C_6D_6 in the presence of naphthalene as an internal standard (500 MHz, 298 K). Unassigned peaks in the spectrum are the residual solvent signal, naphthalene, and silicone grease.

Figure A5.15: $^{13}\text{C}\{^1\text{H}\}$ NMR spectrum of $[\text{Zr}(\textit{cis}\text{-Cyacen})(\text{O}^t\text{Bu})_2]$ (**5-4**) generated in situ via the reaction of **2** with 2 equiv. of $^t\text{BuOH}$ in C_6D_6 (126 MHz, 298 K). Unassigned peaks in the spectrum are the residual solvent signal, naphthalene, silicone grease, and tetramethylsilane.

Figure A5.16: ^1H NMR spectrum of $[\text{Zr}(\textit{acen})_2]$ (**5-5**) in C_6D_6 (600 MHz, 298 K). Unassigned peaks in the spectrum are the residual solvent signal and H grease.

Figure A5.17: $^{13}\text{C}\{^1\text{H}\}$ NMR spectrum of $[\text{Zr}(\textit{acen})_2]$ (**5-5**) in C_6D_6 (151 MHz, 298 K). Unassigned peaks in the spectrum are the residual solvent signal and H grease.

Figure A5.18: $^{13}\text{C}\{^1\text{H}\}$ NMR spectrum of $[\text{Zr}(\textit{acen})(\text{NMeEt})_2]$ (**5-6**) generated in situ from the reaction of **1** with excess HNMeEt in d_8 -toluene (126 MHz, 249 K). Unassigned peaks in the spectrum are the residual solvent signal, H grease, and silicone grease.

Figure A5.19: ^1H NMR spectrum of $[\text{Zr}(\textit{acen})\{\text{N}(\text{SiMe}_3)_2\}_2]$ (**5-7**) in d_8 -THF (500 MHz, 249 K). Unassigned peaks in the spectrum are the residual solvent signal.

Figure A5.20: $^{13}\text{C}\{^1\text{H}\}$ NMR spectrum of $[\text{Zr}(\textit{acen})\{\text{N}(\text{SiMe}_3)_2\}_2]$ (**5-7**) in d_8 -THF (126 MHz, 249 K). Unassigned peaks in the spectrum are the residual solvent signal.

Figure A5.21: ^{29}Si - ^1H HMBC NMR spectrum of $[\text{Zr}(\text{acen})\{\text{N}(\text{SiMe}_3)_2\}_2]$ (**5-7**) in d_8 -THF (99/500 MHz, 249 K). F1 axis is an internal ^{29}Si NMR projection.

List of Schemes

Scheme 1.1: Schematic diagram displaying one ALD cycle consisting of (1) precursor pulse, (2) purge, (3) co-reactant pulse, and (4) purge. Adapted from emsliegroup.mcmaster.ca/orf-re/ald.

Scheme 1.2: Schematic diagram displaying once cycle of alucone MLD.

Scheme 1.3: Schematic diagram displaying one cycle of alumina ALE.

Scheme 1.4: Surface-based reaction schemes for reported nonmetal ALD processes.

Scheme 2.1: Proposed reaction of a tri(silyl)antimony precursor with antimony trichloride.

Scheme 2.2: Synthesis of $\text{Sb}(\text{SiMe}_3)_3$ (**2-1**; DME= 1,2-dimethoxyethane).

Scheme 2.3: Proposed reaction of a main group tris(trimethylsilyl) compound as the precursor and an element chloride as the co-reactant to deposit the pure main group element.

Scheme 3.1: Proposed reaction of a tri(silyl)borane or tri(germyl)borane precursor with a boron trihalide co-reactant.

Scheme 3.2: Reaction for the generation of hexagonal boron nitride (h-BN) via ALD using trichloroborazine and hexamethyldisilazane to form a polyborazylene, and subsequent thermal annealing under a partial atmosphere of ammonia.

Scheme 3.3: Reaction scheme for the preparation of silyl(silylene)diboranes (Entries 27 and 28 in Table 3.3).

Scheme 3.4: Reaction scheme for the preparation of disilylborane (Entry 29 in Table 3.3) and silaborinine compounds.

Scheme 3.5: Literature methods for the preparation of trimethylsilyllithium.

Scheme 3.6: Potential reactivity for boron ALD using $(\text{R}_3\text{E})_2\text{B}(\text{NR}_2)$ precursors.

Scheme 3.7: Synthetic route for the preparation of hypersilyllithium (**3-1**).

Scheme 3.8: Synthetic route for the preparation of supersilylsodium (**3-2**).

Scheme 3.9: Synthetic route for the preparation of trimethylgermyllithium (**3-3**).

Scheme 3.10: Synthetic route for the preparation of dimethylamidodihaloboranes (**3-4**, **3-5**).

Scheme 3.11: Synthetic route for the preparation of hypersilyldichloroborane, **3-7**.

Scheme 3.12: Synthetic route for the synthesis of bis(hypersilyl)amidoborane (**3-8**).

Scheme 3.13: Synthetic route for the synthesis of supersilyldimethylamidohaloboranes [X = Cl (**3-9**), F (**3-10**)] and supersilyldichloroborane (**3-11**).

Scheme 3.14: Synthetic route for the preparation of supersilyl(trimethylgermyl)-(dimethylamido)borane, **3-12**.

Scheme 3.15: Synthetic route for the isolation of $\{(Me_3Ge)_3B(NMe_2)\}Li(THF)_2$ (**3-13**).

Scheme 4.1: Schematic diagram of the proposed process to deposit monometallic complexes on the substrate surface using $[Hf(NMeEt)_4]$ and IVA. Scenarios (a) and (b) differ based on whether the first monolayer remains covalently tethered to the substrate surface. This idealized scheme does not consider other possible coordination modes of the IVA ligand, or oxo bridge formation due to thermal decomposition of the IVA ligand.

Scheme 4.2: Proposed transformations involving a singly or doubly deprotonated IVA ligand coordinated to hafnium. [Hf] indicates hafnium(IV) coordinated by other ligands, and (H) indicates a proton which may or may not be present, depending on whether IVA in the starting complex has been singly or doubly deprotonated.

Scheme 4.3: Synthesis of $[EtMeNH_2]_2[Hf(\kappa^2-O_2CCH_2CMe_2OH)_2(\kappa^2-OC(O)CH_2CMe_2O)_2]$ (**4-1**) by amine elimination.

Scheme 4.4: Intramolecular nucleophilic addition producing *N*-ethyl-*N*-methylpivalamide during the formation of **4-2**. [Hf] indicates hafnium(IV) coordinated by other ligands.

Scheme 4.5: Proposed decomposition pathways for a singly or doubly deprotonated IVA ligand that is κ^2 -coordinated to hafnium; these pathways generate the thermal decomposition products (coloured red) observed by NMR spectroscopy and GC-MS

headspace analysis. [Hf] indicates hafnium(IV) coordinated by other ligands, and (H) indicates a proton which may or may not be present, depending on whether IVA in the starting complex has been singly or doubly deprotonated.

Scheme 5.1: Proposed process for ALD of non-surface-tethered, Zr-containing one-dimensional chains on a functionalized substrate surface using $[(\text{acen}^{\text{R}})\text{ZrX}_2]$ complexes as the precursor.

Scheme 5.2: Synthesis of dialkyl complexes **5-1** to **5-3** by SiMe_4 elimination.

Scheme 5.3: Isomerization, involving interconversion between trigonal prismatic and octahedral structures, proposed to explain the apparent C_{2v} symmetry of compound **5-1** in solution at room temperature. The two equivalent alkyl groups are labelled R^{a} and R^{b} .

Scheme 5.4: Reaction of **5-2** with $t\text{BuOH}$ to afford $[\text{Zr}(\text{cis-Cyacen})(\text{O}^t\text{Bu})_2]$ (**5-4**).

Scheme 5.5: Syntheses of $[\text{Zr}(\text{acen})_2]$ (**5-5**) and the bis(amido) complexes $[\text{Zr}(\text{acen})(\text{NMeEt})_2]$ (**5-6**) and $[\text{Zr}(\text{acen})\{\text{N}(\text{SiMe}_3)_2\}_2]$ (**5-7**).

List of Tables

Table 3.1: Reported thermal ALD processes to deposit boron-containing films.

Table 3.2: Reported boranes or borates of the type $(R_3E)_3B$, $[(R_3E)_4B]^-$, and $[(R_3E)_3BX]^-$, where E = Si or Ge, and X = any other atom. The ^{11}B NMR chemical shifts, B-E bond distances, and E-B-E bond angles are listed if the ^{11}B NMR spectrum or X-ray crystal structure of the compound has been reported.

Table 3.3: Reported boranes or borates of the type $(R_3E)_2BX$ or $[(R_3E)_2BX_2]^-$, where E = Si or Ge, and X = any other atom. The ^{11}B NMR chemical shifts, B-E bond distances, and E-B-E bond angles are listed if the ^{11}B NMR spectrum or X-ray crystal structure of the compound has been reported.

Table 3.4: ^{11}B NMR chemical shifts, B-N bond distances, and CNC/EBE interplanar angles for crystallographically characterized $(R_3E)_2B(NR_2)$ compounds, where E = Si or Ge. H_3B-NH_3 and $[Li(THF)_4][(Me_3Sn)_3B(NMePh)]$ are listed as examples of nitrogen-boron single bonded compounds. Compounds **3-8** and **3-12** are included for comparison.

Table 3.5: Summary of volatility, thermal stability, and reactivity of precursor candidates $\{(Me_3Si)_3Si\}_2B(NMe_2)$ (**3-8**) and $(^tBu_3Si)(Me_3Ge)B(NMe_2)$ (**3-12**).

Table 4.1: Select Hf-containing precursors (left) and all co-reactants (right) used for reported HfO_2 thermal ALD processes.

Table 5.1: Comparison of the continuous shape measure (CSM) values for trigonal prismatic (TPR-6) and octahedral (OC-6) geometry and twist angles of complexes **5-1** to **5-3** and **5-7**, as well as crystallographically characterized literature examples of 6-coordinate zirconium(IV) acen^R complexes.

Table A1.1: Crystal data for $^tBu_3SiNa(THF)_2$ (**3-2**) and $[Me_3GeLi(THF)_2]_2$ (**3-3**).

Table A1.2: Crystal data for $\{(Me_3Si)_3Si\}_2B(NMe_2)$ (**3-8**), $(^tBu_3Si)(Me_3Ge)B(NMe_2)$ (**3-12**), and $\{(Me_3Ge)_3B(NMe_2)\}Li(THF)_2$ (**3-13**).

Table A1.3: Crystal data for [EtMeNH₂]₂[Hf(O₂CCH₂CMe₂OH)₂(OC(O)CH₂CMe₂O)₂] (**4-1**), [Hf₅(O)₄(O₂C^tBu)₁₂·3C₆H₆] (**4-2(C₆H₆)₃**), and [Hf₅(O)₄(O₂C^tBu)₁₂] (**4-2**).

Table A1.4: Crystal data for [Zr(acen)(CH₂SiMe₃)₂] (**5-1**), [Zr(*cis*-Cyacen)(CH₂SiMe₃)₂] (**5-2**), and [Zr(*trans*-Cyacen)(CH₂SiMe₃)₂] (**5-3**).

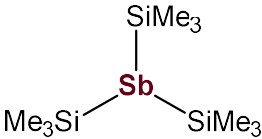
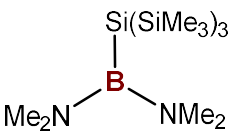
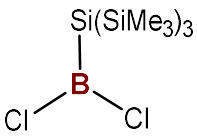
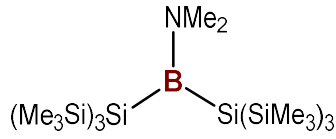
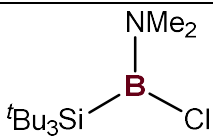
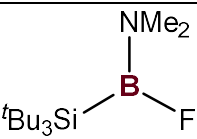
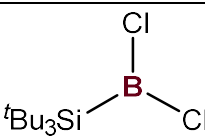
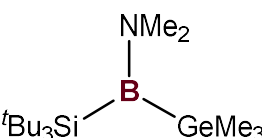
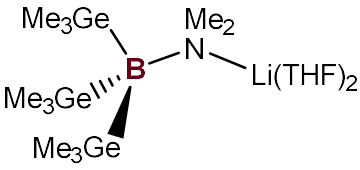
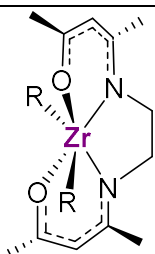
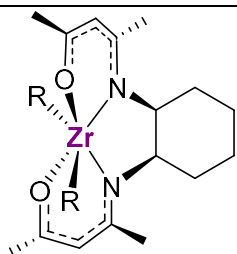
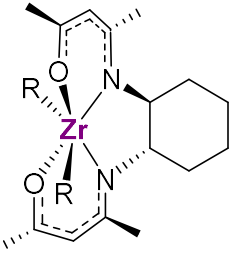
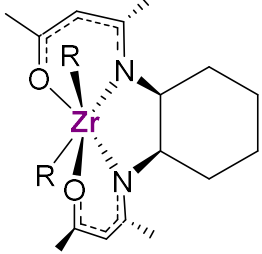
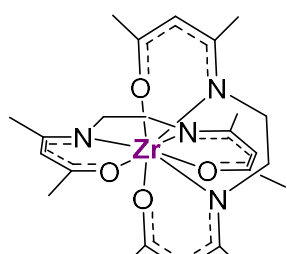
Table A1.5: Crystal data for [Zr(acen)₂] (**5-5**) and [Zr(acen){N(SiMe₃)₂]₂] (**5-7**).

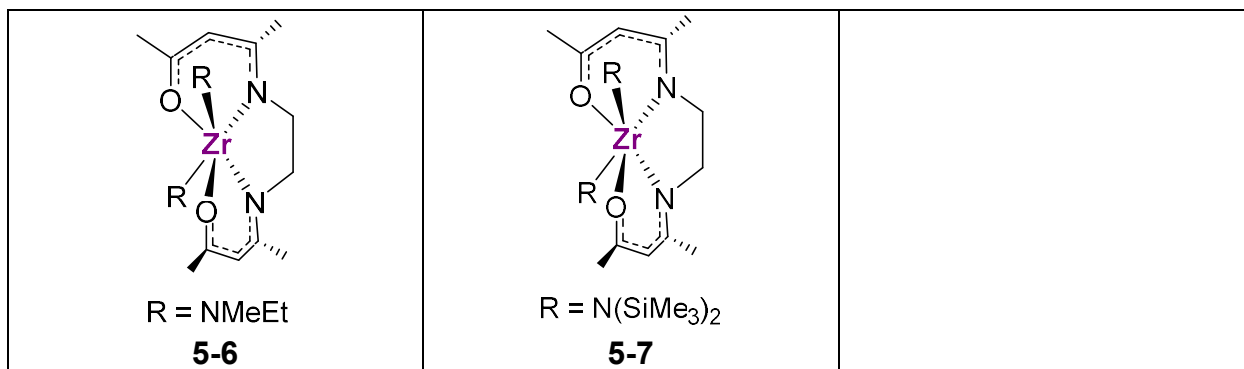
Table A4.1: Continuous shape measures (CSMs) of the 7-coordinate hafnium coordination polyhedra in the X-ray crystal structures of **4-1**, **4-2(C₆H₆)₃**, and **4-2**. The bolded values indicate the ideal polyhedron that best fit the coordination geometry.

Table A4.2: Continuous shape measures (CSMs) of the 8-coordinate Hf(3) coordination polyhedra in the X-ray crystal structures of **4-1**, **4-2(C₆H₆)₃**, and **4-2**. The bolded values indicate the ideal polyhedron that best fit the coordination geometry.

Table A5.1: Continuous shape measures (CSMs) of the 6-coordinate zirconium coordination polyhedra in the X-ray crystal structures of **5-1** to **5-3** and **5-7**. The bolded values indicate the ideal polyhedron that best fit the coordination geometry.

List of Compounds (Observed)

 <p style="text-align: center;">2-1</p>	<p style="text-align: center;">$\{(\text{Me}_3\text{Si})_3\text{Si}\}\text{Li}(\text{THF})_3$</p> <p style="text-align: center;">3-1</p>	<p style="text-align: center;">${}^t\text{Bu}_3\text{SiNa}(\text{THF})_n$ ($n = 2-3$)</p> <p style="text-align: center;">3-2</p>
<p style="text-align: center;">$[\text{Me}_3\text{GeLi}(\text{THF})_2]_2$</p> <p style="text-align: center;">3-3</p>	<p style="text-align: center;">$[\text{B}(\text{NMe}_2)\text{Cl}_2]_n$</p> <p style="text-align: center;">3-4 ($n = 1$), 3-4' ($n = 2$)</p>	<p style="text-align: center;">$[\text{B}(\text{NMe}_2)\text{F}_2]_2$</p> <p style="text-align: center;">3-5</p>
 <p style="text-align: center;">3-6</p>	 <p style="text-align: center;">3-7</p>	 <p style="text-align: center;">3-8</p>
 <p style="text-align: center;">3-9</p>	 <p style="text-align: center;">3-10</p>	 <p style="text-align: center;">3-11</p>
 <p style="text-align: center;">3-12</p>	 <p style="text-align: center;">3-13</p>	<p style="text-align: center;">$[\text{EtMeNH}_2]_2$ $[\text{Hf}(\kappa^2\text{-O}_2\text{CCH}_2\text{CMe}_2\text{OH})_2$ $(\kappa^2\text{-O}_2\text{CCH}_2\text{CMe}_2\text{O})_2]$</p> <p style="text-align: center;">4-1</p>
<p style="text-align: center;">$[\text{Hf}_5(\mu_3\text{-O})_4(\kappa^2\text{-O}_2\text{C}^t\text{Bu})_4$ $(\mu\text{-O}_2\text{C}^t\text{Bu})_8] \cdot n\text{C}_6\text{H}_6$</p> <p style="text-align: center;">4-2 ($n = 0$) 4-2(C₆H₆)₃ ($n = 3$)</p>	 <p style="text-align: center;">$\text{R} = \text{CH}_2\text{SiMe}_3$</p> <p style="text-align: center;">5-1</p>	 <p style="text-align: center;">$\text{R} = \text{CH}_2\text{SiMe}_3$</p> <p style="text-align: center;">5-2</p>
 <p style="text-align: center;">$\text{R} = \text{CH}_2\text{SiMe}_3$</p> <p style="text-align: center;">5-3</p>	 <p style="text-align: center;">$\text{R} = \text{O}^t\text{Bu}$</p> <p style="text-align: center;">5-4</p>	 <p style="text-align: center;">5-5</p>



List of Abbreviations, Acronyms, and Symbols

General

α – Twist Angle	DED – Deposition/Etch/Deposition
Δ – Heat	DFT – Density Functional Theory
Δ – Delta (phase component of VASE data)	DSC – Differential Scanning Calorimetry
2θ – 2-Theta	EA – Elemental Analysis
κ – Denticity	EI – Electron Ionization
κ – Permittivity (Dielectric) Constant	equiv. - Equivalent
λ – Wavelength	FEALD – Flash-Enhanced ALD
μ – Bridging Ligand	FESEM – Field Emission SEM
ρ – Density	FT-IR – Fourier Transform-Infrared
Ψ – Psi (amplitude component of VASE data)	GC-MS – Gas Chromatography-Mass Spectrometry
1D, 2D, 3D – 1-, 2-, 3-Dimensional	GPC – Growth-Per-Cycle
4PP – Four Point Probe	HAR – High-Aspect-Ratio
AFM – Atomic Force Micrography	HDP-CVD – High-Density Plasma CVD
ALD – Atomic Layer Deposition	h-BN – Hexagonal Boron Nitride
ALE – Atomic Layer Epitaxy	HMBC – Heteronuclear Multiple Bond Correlation
ALE – Atomic Layer Evaporation	H-Si – Hydrogen-Terminated Silicon
ALE – Atomic Layer Etching	HSQC – Heteronuclear Single Quantum Coherence
AS-ALD – Area-Selective ALD	LALD – Laser-Assisted ALD
BDD – Boron-Doped Diamond	MD – Molecular Deposition
B:ZnO – Boron-Doped Zinc Oxide	MFC – Mass Flow Controller
CMOS – Complementary Metal-Oxide-Semiconductor	ML – Molecular Layering
CVD – Chemical Vapour Deposition	MLD – Molecular Layer Deposition
CSM – Continuous Shape Measurement	MLD – Monolayer Doping
cf. – confer	MLE – Molecular Layer Epitaxy

MOCVD – Metal-Organic CVD	photo-ALD – Photo-Assisted ALD
MOF – Metal-Organic Framework	PVD – Physical Vapour Deposition
MOSFET – Metal-Oxide-Semiconductor Field-Effect Transistor	PXRD – Powder XRD
NMR – Nuclear Magnetic Resonance	QCM – Quartz Crystal Microbalance
s – singlet	QMS – Quadrupole Mass Spectrometry
d – doublet	RT – Room Temperature
t – triplet	SEM – Scanning Electron Microscope
q – quartet	Si(100) – Silicon(100)
sept – septet	SiO ₂ /Si – Silica on Silicon
m – multiplet	TGA – Thermogravimetric Analysis
bs – broad singlet	USSR – Union of Soviet Socialist Republics
<i>J</i> – coupling constant	UV - Ultraviolet
δ – chemical shift	VASE – Variable Angle Spectroscopic Ellipsometry
NTPALD – Non-thermal Plasma ALD	VHPA – Virtual Project on the History of ALD
PAALD – Plasma-Assisted ALD	XPS – X-ray Photoelectron Spectroscopy
PCM – Phase Change Memory	XRD – X-ray Diffraction
PEALD – Plasma-Enhanced ALD	
PE-CVD – Plasma-Enhanced CVD	

Units

at% – atomic percent	
mA – milliampere	μL , mL – microlitre, millilitre
cm^{-1} - wavenumber	nm, μm , mm, cm, m – nanometre, micrometre, millimetre, centimetre, metre
eV – electron volt	
mg, g – milligram, gram	mmol, mol – millimole, mole
Hz, MHz – hertz, megahertz	m/z – mass-to-charge ratio
K – Kelvin	

ppm – parts per million

ppt – parts per trillion

s, min, hr – second, minute, hour

sccm – standard cubic centimetre per minute

mTorr, Torr – millitorr, torr

kV – kilovolt

W, kW – watt, kilowatt

Ω – ohm

$^{\circ}$ – degree

$^{\circ}\text{C}$ – degrees Celsius

% – percent

\AA – Angstrom

Chemical Species

18C6 – 18-Crown-6

acen – *N,N*-Ethylenebis-(acetylacetonimine)

AcOH – Acetic Acid

Ar – Aryl

ⁿBu – *n*-Butyl

^tBu – *tert*-Butyl

Cp – Cyclopentadienyl

Cp* – Pentamethylcyclopentadienyl

MeCp – Methylcyclopentadienyl

Cy – Cyclohexyl

DHP – 1,4-Dihydropyrazine

Dipp – 2,6-Diisopropylphenyl

DME – 1,2-Dimethoxyethane

Dur – Duryl (2,3,5,6-tetramethylphenyl)

Et – Ethyl

Et-APTMS – (Diethylaminopropyl)-trimethoxysilane

HMPA – Hexamethylphosphoramide

IVA – β -Hydroxyisovaleric Acid

Me – Methyl

mp – 3-Methyl-3-pentoxide

mmp – 1-Methoxy-2-methyl-2-propoxy

NHSi – *N*-Heterocyclic Silylene

Ph – Phenyl

ⁱPr – Isopropyl

PTFE – Polytetrafluoroethylene

THF – Tetrahydrofuran

tmhd – 2,2,6,6-Tetramethyl-heptanedionate

TMP – 2,2,5,5-Tetramethylpiperidine

Trp – Tris(pyrazolyl)borate

TPPA – Tris(*N,N*-tetramethylene)-phosphoric triamide

UPW – Ultrapure Water

Xyl – Xylyl

Declaration of Academic Achievement

Dr. James Britten (of the McMaster Analytical X-ray Diffraction Facility) was responsible for the structure solution and refinement for (^tBu₃Si)Na(THF)₂ (**3-2**) and {(Me₃Ge)₃B(NMe₂)}Li(THF)₂ (**3-13**). Dr. Kirk Green and Megan Fair were responsible for the collection of GC-MS data for the thermal decomposition products of [EtMeNH₂]₂[Hf(κ²-O₂CCH₂CMe₂OH)₂(κ²-OC(O)CH₂CMe₂O)₂] (**4-1**). Travis Casagrande and Chris Butcher (of the Canadian Centre for Electron Microscopy) were responsible for obtaining all FESEM images of thin films throughout this work, and Nicholas Hoffman was responsible for obtaining AFM images of Sb thin films discussed in Chapter 2. Dr. Jeffrey Price and Novan Gray were responsible for obtaining variable-temperature NMR data on complexes [Zr(*cis*-Cyacen)(CH₂SiMe₃)₂] (**5-2**) and [Hf₅(μ₃-O)₄(κ²-O₂C^tBu)₄(μ-O₂C^tBu)₈] (**4-2**), respectively. Jian Li at the University of Calgary was responsible for running all combustion elemental analyses in this work. Dr. Nicholas Hein (of GreenCentre Canada) and Nicholas Hoffman were responsible for obtaining thermogravimetric analysis data on the bis(tetrel)amidoborane compounds [{"(Me₃Si)₃Si}₂B(NMe₂) (**3-8**) and (^tBu₃Si)(Me₃Ge)B(NMe₂) (**3-12**)] and β-hydroxyisovaleric acid (IVA), respectively. Dr. Rana Sodhi (of Surface Interface Ontario) was responsible for obtaining XPS of all Sb and Hf-containing films in this work. All other results were obtained by Majeda Al Hareri.

Chapter 1 - Introduction

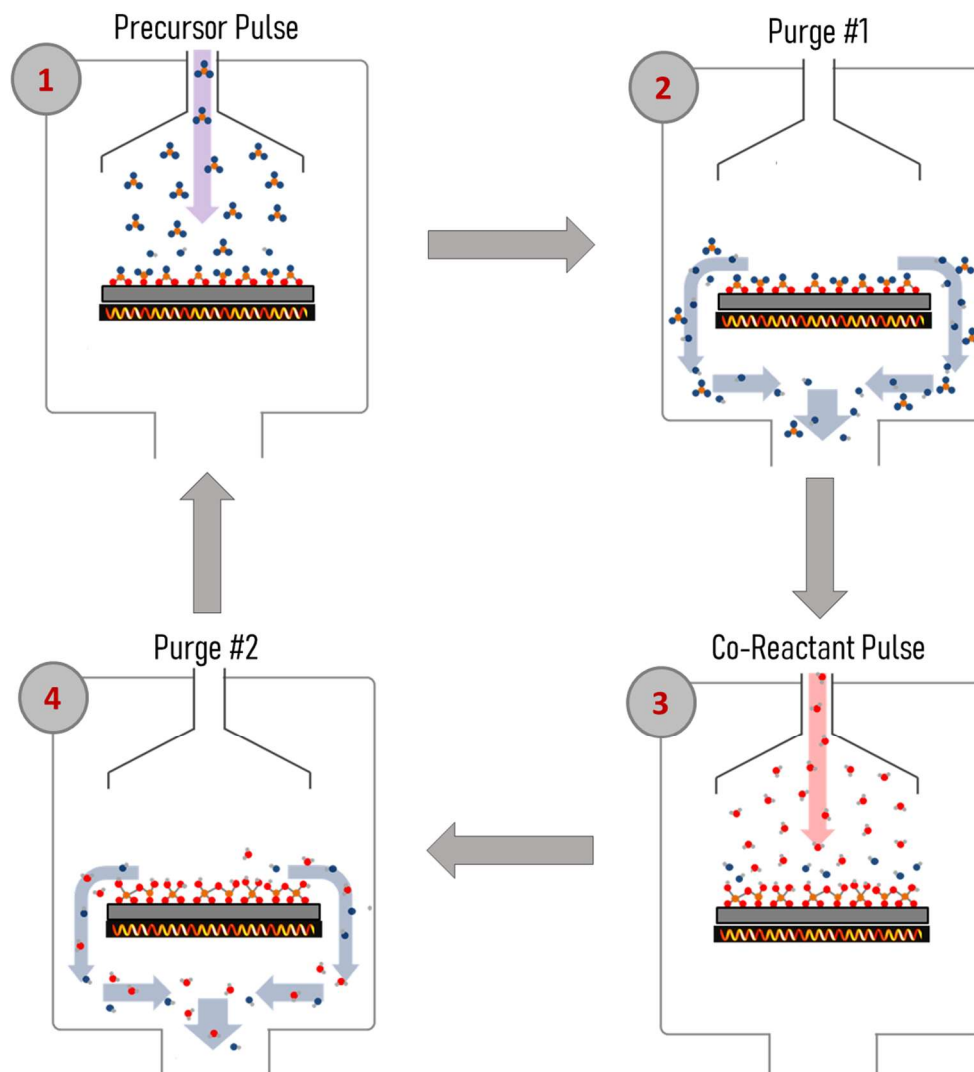
1.1 – Introduction to Thermal ALD

In 1965, Gordon E. Moore, the co-founder of Fairchild Semiconductor, and later of Intel, postulated that the number of components that can fit into a semiconductor device would double every year for the next decade. While he hypothesized that by 1975, the number of transistors within one integrated circuit would reach 65,000, he had also stated that this rate of increase seemed “uncertain” over a longer term.^[1] However, his prediction held true well past 1975, as evidenced by the number of transistors in a single microprocessor reaching over 50 billion in 2021.^[2,3] This observation, referred to as Moore’s Law, has guided and continues to guide advancements in the semiconductor industry, with the layers in critical device components (e.g. transistors) expected to reach thicknesses as low as 2 nm.^[4-6] The continued miniaturization of device sizes, as predicted by Moore’s Law, has established a necessity for advanced fabrication processes. One major feat in reaching this target was achieved by Gurtej Singh Sandhu in the 2000s by implementing a deposition process known as atomic layer deposition (ALD) to fabricate thin films of high- κ dielectrics such as HfO_2 as layers in transistors of complementary metal-oxide-semiconductor (CMOS) devices. ^[4,7]

ALD is a deposition technique that yields highly uniform and conformal thin films through the use of repeated, self-terminating reactions.^[8,9] In this chapter, the term ALD is used to refer specifically to thermal ALD whereby all reactants are stable molecules. Different ALD processes will be touched on briefly in Section 1.2. ALD is described as a

derivative of chemical vapour deposition (CVD), but unlike CVD, it does not rely on thermal decomposition of the reactants for film growth. The inception of the field of ALD is convoluted, but substantial effort has been made by the ALD community through the virtual project on the history of ALD (VPHA) to explicate its founding.^[10] ALD is generally considered to have been discovered twice independently: firstly by USSR researchers, Aleskovskii and Koltsov in the 1960s [using the term molecular layering (ML)], and secondly by Finnish researcher, Suntola in the 1970s [using the term atomic layer epitaxy (ALE)].^[11] Other terminology used in the past to denote ALD includes atomic layer evaporation (ALE), molecular deposition (MD), and molecular layer epitaxy (MLE).

In a typical ALD process (Scheme 1.1), a precursor, which contains the target element for deposition, is introduced into a reaction chamber under reduced pressure in the vapour phase and chemisorbs onto the surface of the substrate. During this process, the substrate is maintained at a temperature that is suitable to promote chemisorption of the precursor while avoiding decomposition of the precursor, which would lead to other forms of deposition such as CVD.^[12] This chemisorption involves a reaction with the substrate surface, typically resulting in the loss of one or more of the ligands on the precursor molecule (e.g. by dissociation of a neutral ligand and/or protonolysis/ σ -bond metathesis reactivity involving an anionic ligand).^[8] This reactivity consumes reactive functional groups on the surface, leading to monolayer formation and preventing chemisorption of additional precursor molecules, rendering the reaction between the precursor and substrate surface “self-limiting”.



Scheme 1.1: Schematic diagram displaying one ALD cycle consisting of (1) precursor pulse, (2) purge, (3) co-reactant pulse, and (4) purge. Adapted from emsliegroup.mcmaster.ca/orf-re/ald.

An inert gas or vacuum purge is then introduced to the system to remove all reaction by-products (which must be volatile) and excess precursor molecules. Following this, a co-reactant is introduced into the chamber which reacts with the precursor species on the

surface of the substrate, also in a self-limiting fashion, to convert the adsorbed monolayer to the desired film composition. A second purge step is then applied to remove excess co-reactant and all reaction by-products (which must be volatile). This ‘precursor pulse – purge – co-reactant pulse – purge’ sequence is repeated a specified number of times in order to develop a film of a desired thickness. The precise thickness control achievable with ALD is attributed to the self-limiting nature of its surface reactions. Unlike CVD processes, the precursor molecules will no longer deposit once the surface of the substrate has been saturated. Once this saturation point has been reached, the thickness of the film obtained after a specific number of cycles will be identical, even if the length of the precursor and/or co-reactant pulse is increased.

The self-limiting growth mechanism characteristic of ALD can be demonstrated in multiple ways, the most common of which are shown in Figure 1.1. Plotting the film thickness or growth-per-cycle (commonly referred to as the growth rate or GPC) against the pulse duration of the precursor and/or co-reactant will display a plateau after the point of surface saturation (Figure 1.1a). This allows the thickness of the film to be dependent solely on the number of ALD cycles, as exhibited by a linear growth rate (Figure 1.1b) with varying cycle numbers. The slope of this plot equates to the constant GPC observed in Figure 1.1a. Although an ideal ALD process will intercept at 0 cycles, a substrate-enhanced process (occurring due to a higher growth rate during nucleation) or substrate-inhibited process (occurring due to a lower growth rate or delay during nucleation) will result in a positive or negative y-intercept, respectively.^[12] Lastly, the self-limiting nature of an ALD process is sometimes characterized by a constant growth rate within a

temperature range known as “the ALD window” (Figure 1.1c). However, it has been remarked on previously that the GPC for an ALD process can be nonconstant yet still show self-limiting growth within the ALD window range due to the effect the deposition temperature can have on the availability of surface sites and the types of reactions that can take place.^[12,13] Increased GPCs observed at higher deposition temperatures than a process’s ALD window are sometimes described as an ALD process with a CVD component arising from precursor decomposition.^[8] Non-ALD behaviour can also be observed at high temperature due to precursor desorption, or at low temperature due to precursor condensation or incomplete nucleation during the investigated range of pulse durations (Figure 1.1c).

Although the self-limiting nature of ALD processes means that ALD requires relatively much more time to produce a film of equal thickness to a CVD process, there are numerous advantages to ALD. Thin films deposited by ALD feature high thickness uniformity and conformality, which makes it the preferred method for thin film deposition on high-aspect-ratio (HAR) substrates (Figure 1.2). Additionally, the surface-based reactions by which ALD operates can potentially allow for the preferential deposition of film on one area of a sample composed of multiple substrate materials (e.g. selective deposition on an oxide versus a metal surface).^[14] Furthermore, as this process does not depend on precursor thermal decomposition, deposition can often be achieved at much lower temperatures than those required in CVD methods, which can limit degradation of film quality arising due to agglomeration at high temperatures, and can potentially allow for deposition on temperature-sensitive substrates such as polymers. Due to these

advantages, ALD has gained interest in a large variety of industrial and exploratory applications, including microprocessors and memory storage devices in the semiconductor industry, solar and fuel cells, heterogeneous catalysis, nanoparticle synthesis, and biosensors.^[5,6,15-20]

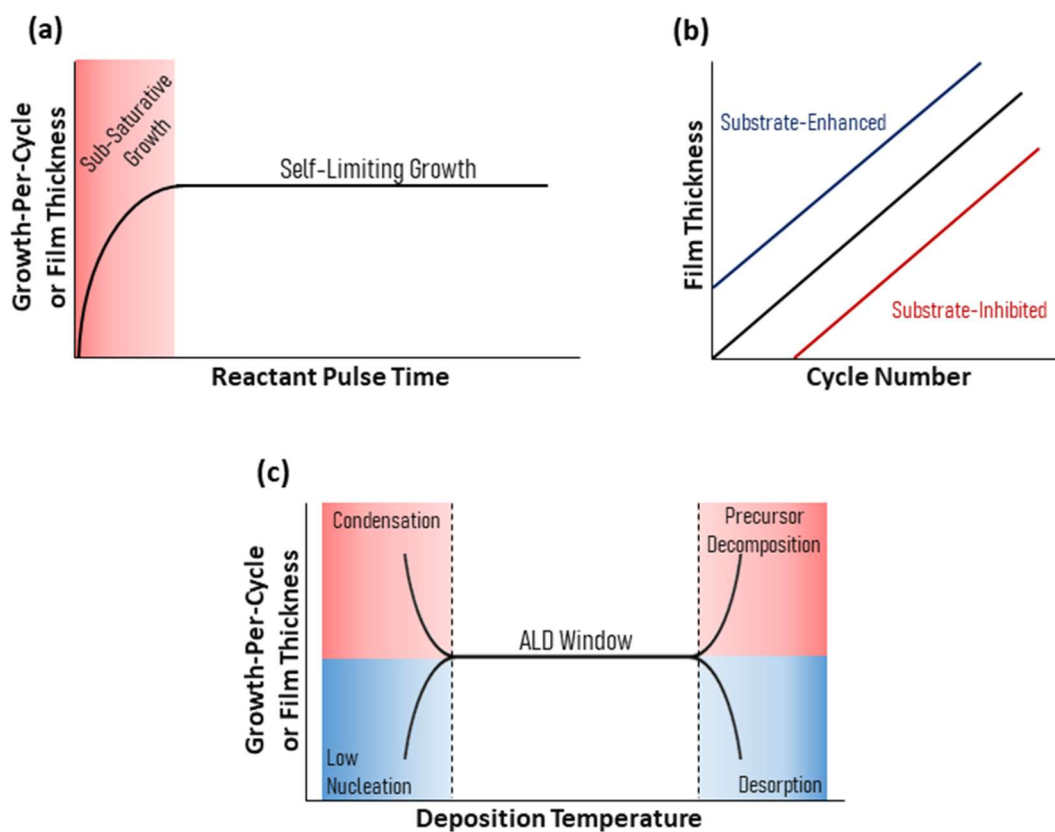


Figure 1.1: The most common graphical demonstrations of ALD. (a) Dependency of growth-per-cycle (GPC) or film thickness on the reactant pulse time. (b) Dependency of film thickness on the number of ALD cycles. (c) Dependency of GPC or film thickness on deposition temperature.

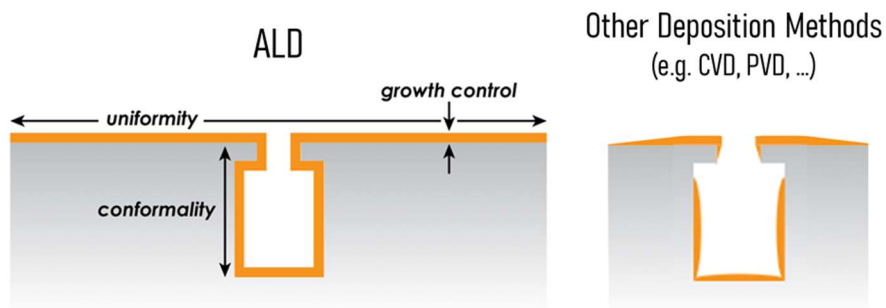


Figure 1.2: Diagram of deposition using ALD versus other deposition methods. Adapted from Atomic Limits image library (2020).

Despite the inclination to describe ALD in its most ideal form, it should be noted that, in actuality, there have been an array of unideal behaviours observed in reported ALD processes.^[12] For instance, film growth, which is idealized to be single monolayer growth per ALD cycle, oftentimes will display growth that is less than or greater than one monolayer per cycle. In cases where the substrate is fairly unreactive with the reactants, island formation can occur due to preferential nucleation on the deposited material rather than the substrate, although with additional ALD cycles, the growing islands may coalesce to form an overall uniform film.^[21] Furthermore, some ALD processes have exhibited lower growth rates with prolonged purge durations due to desorption of weakly adsorbed surface species, which will be discussed in further detail in Chapter 2.

Alongside unideal ALD behaviours, films prepared by reported ALD processes may possess adverse characteristics for a target application. These can include undesired crystallinity or morphology, and slow nucleation resulting from the use of large precursor and/or co-reactant molecules bearing sterically bulky ligands. Additionally, due to ALD

being a reaction-based process, it can result in a narrow temperature window, necessitating more accurate temperature control at the surface of the substrate, or it may only occur on a narrow range of substrate materials which, depending on what is desired, can be disadvantageous. Therefore, further investigation on previously discovered ALD processes to alleviate these limitations can be as beneficial as discovering unknown processes. The concept of ALD non-ideality and improvement of known ALD processes will be explored in further detail in Chapters 2 and 4.

1.2 – Other Deposition Methods Related to Thermal ALD

Although this work focuses solely on thermal ALD processes, this section will briefly discuss important methods related to thermal ALD.

ALD processes are often categorized as either thermal ALD or plasma ALD (which includes the terms plasma-enhanced ALD (PEALD), plasma-assisted ALD (PAALD), non-thermal plasma ALD (NTPALD), and remote- or direct plasma ALD). In plasma ALD, at least one of the reactants is an unstable entity within a plasma.^[22-25] The high reactivity of the plasma species can allow for the deposition of a large variety of materials at temperatures lower than that of thermal ALD. However, the application of this process adds complexity in the design of an ALD reactor, and the harsh deposition process can cause damage to the substrate. Furthermore, conformal deposition on HAR substrates is more difficult using plasma methods due to high radical recombination rates from surface collisions leading to loss of reactive species.^[25]

Since ALD involves surface-based reactions with a substrate, it can offer the potential for substrate-selective deposition. This feature has been exploited in the field of area-selective ALD (AS-ALD), whereby nucleation and film growth occur in desired areas, allowing for self-aligned fabrication of patterned materials by a bottom-up approach, removing the need for an added process to remove deposited film from undesired areas (Figure 3.3).^[14,26]

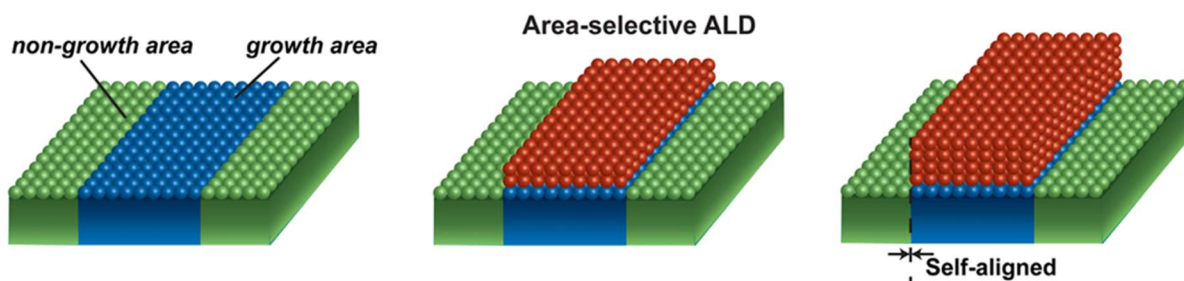
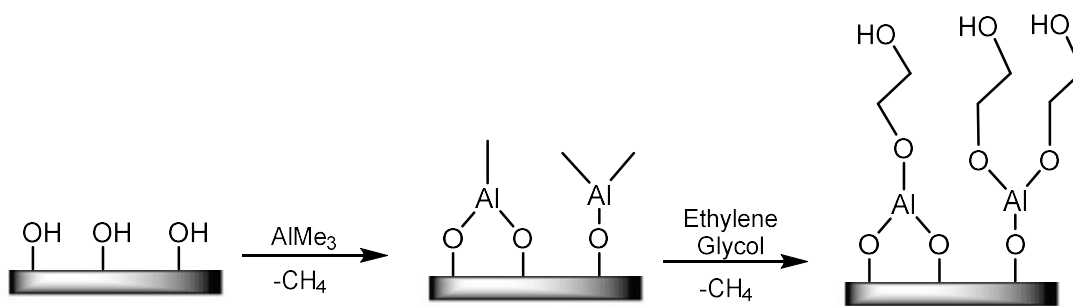


Figure 3.3: Schematic diagram depicting the bottom-up, self-aligned patterning achievable by AS-ALD. Reprinted (adapted) with permission from reference [26].

A lesser-used process (possibly due to challenges in reactor design) known as photo-assisted ALD (photo-ALD) involves irradiation of the substrate by ultraviolet (UV) or visible light during deposition to enhance surface reactivity, allowing for potentially lower deposition temperatures than comparable thermal ALD processes.^[27,28] AS-ALD has also been achieved using photo-ALD by obscuring light within the area of undesired deposition.^[28] Flash-enhanced ALD (FEALD) has been described as a process similar to photo-ALD, except that high-intensity visible or infrared light is pulsed during deposition

to heat the surface and drive reactions, whereas photo-ALD utilizes photolysis to reduce the deposition temperature.^[29]

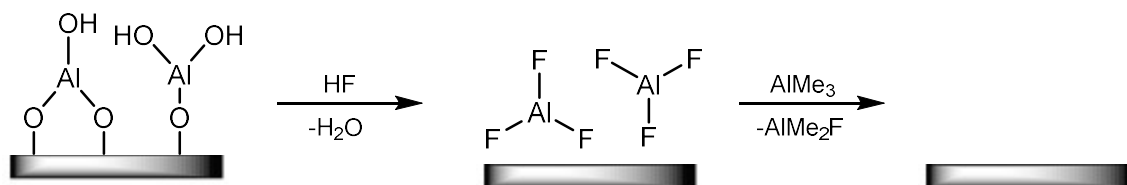
Molecular layer deposition (MLD) is often coined as the sister technique of ALD for the deposition of organic polymers or hybrid organic-inorganic polymers through the use of organic co-reactants.^[30-33] The technique was first introduced by Yoshimura and coworkers in the 1990s, exclusively for the fabrication of organic polymers,^[34] but the field has since extended to include hybrid organic-inorganic polymers.^[32] A notable example is that of alucone MLD which involves sequential, self-limiting reactions of trimethylaluminum and ethylene glycol (Scheme 1.2).^[35] MLD-grown materials can take the form of one-dimensional polymeric chains such as polyimides,^[34] or three-dimensional networks such as metal-organic frameworks (MOFs).^[36,37]



Scheme 1.2: Schematic diagram displaying once cycle of alucone MLD. Adapted with permission from reference [35].

Atomic layer etching (ALE) is an etching method in which alternating and sequential surface-based reactions remove a monolayer of substrate in each cycle in a self-limiting fashion (Scheme 1.3).^[38-41] Similarly to ALD, ALE processes display constant

etch rates upon prolonged reactant exposure, and are dichotomized into thermal and plasma methods. The first report of ALE was in a patent in 1988^[42] but the method has been gaining traction in the last decade due to its complementary role in semiconductor device miniaturization.



Scheme 1.3: Schematic diagram displaying one cycle of alumina ALE. Adapted with permission from reference [41].

1.3 – Requirements for ALD Precursors

Original work in the development of ALD processes utilized simple and commercially available chemicals as precursors, notably metal halides and alkoxides.^[13,30] However, these precursors often resulted in significant limitations which illustrated the need to design and synthesize new molecules as potential ALD precursors. For instance, metal halides, while being very thermally stable and reactive, generally display low volatility and reactivity resulting in halide incorporation. In contrast, small metal alkoxides have generally exhibited poor thermal stability and reactivity.^[13,43-45]

In order for a compound to be used as a precursor for thermal ALD, there are a number of requirements that must be met. The precursor candidate must: (i) display adequate volatility in order to allow delivery within the reactor in the vapour phase; (ii) possess sufficient thermal stability to avoid decomposition, either in the precursor delivery bubbler

(on a timescale of weeks or months) or on the substrate surface (on a timescale of seconds or minutes); (iii) demonstrate high surface reactivity towards the chosen co-reactant, and; (iv) yield only volatile by-products in its reaction with the co-reactant so they may also be removed from the reaction chamber during purge steps.^[8]

The chemical characterization of new precursor molecules must therefore involve determining whether a target molecule exhibits these properties before its evaluation in an ALD reactor. The volatility and thermal stability of a molecule can be analyzed using differential scanning calorimetry (DSC) and thermogravimetric analysis (TGA) in order to observe the temperatures at which phase transitions and decomposition occur, and mass loss as a function of temperature. Alternatively, volatility can be assessed by a molecule's ability to sublime or distill *in vacuo*, while thermal stability can be determined on a longer timescale by periodic monitoring of a heated sample of the neat precursor by nuclear magnetic resonance (NMR) spectroscopy. The reactivity of a precursor with a co-reactant can be assessed based on the reactivity displayed in solution, typically by NMR spectroscopy combined with powder X-ray diffraction (PXRD) or X-ray photoelectron spectroscopy (XPS) to analyze insoluble reaction products. However, it should be noted that while solution reaction studies are useful to determine whether a particular precursor and co-reactant are highly reactive or poorly reactive towards one another, the detailed reaction pathways followed in solution versus on a substrate surface can often differ from one another.^[8,46] Additionally, to deposit a pure material via solution reactivity, the reaction by-product must be soluble, whereas for ALD, the reaction by-products must be volatile.

1.4 – Materials Grown by Thermal ALD

The variety of materials grown thus far by ALD is as diverse as the type of molecules and reactions employed to fabricate them. Figure 1.6 contains a schematic diagram adapted from the ALD database, Atomic Limits, which encapsulates all materials grown by thermal or plasma ALD (although details regarding substrate selection and deposition temperature are not highlighted).^[47] For the deposition of any given material by ALD, a precursor and co-reactant are selected based on their reactivity towards one another, which is highly dependent on the nature of the target material. Details on the processes and challenges of some materials that are most relevant to this thesis are described in the following sections.

1.4.1 – ALD of Pure Elements and its Challenges

To achieve elemental ALD, a precursor, often containing a metal or nonmetal in a positive oxidation state, must be reduced to its zerovalent state by the co-reactant.^[8,46] This process is relatively facile for noble metals that are inherently resistant to oxidation; for example, elemental Ru, Os, Rh, Ir, Pd, and Pt have been grown by ALD at high temperatures (>200 °C) using O₂ or O₃ as co-reactants to oxidize the precursor ligands.^[48] For other transition metals, a range of reactivity has been employed, such as reduction using dihydrogen,^[49,50] and σ -bond metathesis or oxidative addition followed by reductive elimination using main group hydrides (e.g. Si₂H₆, B₂H₆).^[51,52]

This becomes increasingly challenging to achieve as the electropositivity of the target element increases, as illustrated by the scarcity of processes for early transition metal ALD. As an example of electropositive transition metal ALD, Winter and coworkers reported two low-temperature Ti ALD processes using TiCl_4 in combination with 1,4-bis(trimethylsilyl)-2-methyl-2,5-cyclohexadiene (110-240 °C) or 1,4-bis(trimethylsilyl)-1,4-dihydropyrazine (90-100 °C) through the observed elimination of chlorotrimethylsilane and toluene or pyrazine, respectively.^[53]

1.4.1.1 – ALD of Main Group Elements

In recent years, interest in main group element ALD has increased. All reported main group element ALD processes are described herein (Scheme 1.4).

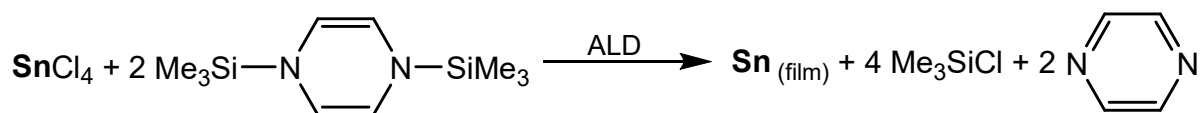
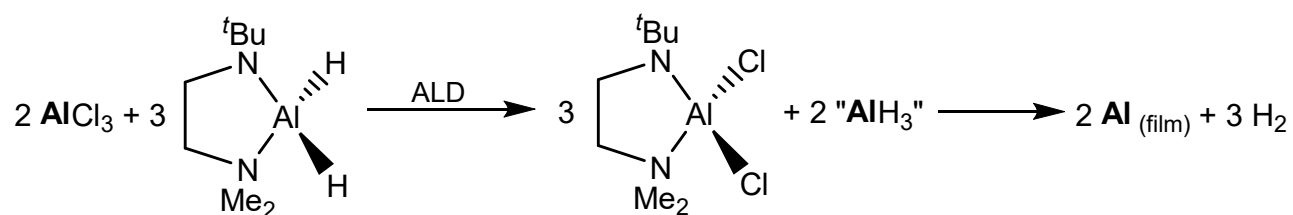
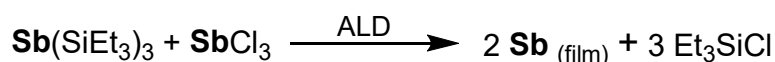
In 1990, Nishizawa and coworkers reported the deposition of elemental silicon on Si(100) using alternating pulses of SiCl_2H_2 and H_2 with a constant growth rate observed at 825 and 850 °C when the precursor and/or co-reactant pulse was varied.^[54] However, the authors noted that long exposures of SiCl_2H_2 at higher pressures with no H_2 precursor did result in film deposition where “the molecular layer growth is never realized”, which they attribute to decomposition of the precursor. Yokoyama and coworkers later reported Si ALD on Si(100) and Si(111) using Si_2H_6 and SiCl_4 in the temperature range of 355-385 °C (~0.12 nm growth rate) through elimination of HCl.^[55] Similar to Nishizawa’s Si ALD process, the authors reported observable film growth within the claimed ALD window when the surface was only exposed to Si_2H_6 , due to thermal dissociation of the precursor

into SiH_4 and SiH_2 . Therefore, these two processes would be more appropriately defined as CVD processes (or ALD processes with a CVD component).

In 2011, Pore and coworkers reported the first ALD process for a nonmetal utilizing tris(triethylsilyl)antimony ($\text{Sb}(\text{SiEt}_3)_3$) and SbCl_3 to deposit pure and conformal elemental antimony. Film growth was observed at 95-250 °C, and self-limiting growth was demonstrated at 95 °C (GPC = 0.45 Å).^[56] This was achieved by dehalosilylation to form volatile chlorotriethylsilane which was observed by quadrupole mass spectrometry (QMS). Cheng and coworkers later reported the deposition of elemental tellurium using $\text{Te}(\text{SiMe}_3)_2$ and $\text{Te}(\text{OEt})_4$ at 60 °C (the only tested deposition temperature) on Si by elimination of volatile Me_3SiOEt .^[57] The process exhibited a slightly reduced growth rate with prolonged $\text{Te}(\text{SiMe}_3)_2$ duration which the authors attributed to loss of reactive surface sites due to either reversible adsorption or self-passivation. Additionally, the authors incorporated Te ALD cycles into a GeTe ALD process to generate GeTe_x ($x > 1$) films with controllable Te content.

In 2018, Winter and coworkers reported a low-temperature aluminum ALD process using AlCl_3 as the precursor and the novel LAlH_2 co-reactant $\{\text{L}=(^i\text{BuN})\text{CH}_2\text{CH}_2(\text{NMe}_2)\}$ as a hydride source.^[58] The authors proposed that a ligand exchange would occur, producing the volatile dichloride by-product, LAlCl_2 , and a surface-bound Al-H species which would reductively eliminate to form Al and H_2 . Self-limiting growth was observed at 140 °C on TiN, and a semi-constant growth rate of 3.5-4.1 Å was observed within the temperature range of 100-140 °C.

Also in 2018, Parsons and coworkers reported the deposition of elemental tin by ALD on SiO₂ and Si substrates by utilizing SnCl₄ as the precursor and 1,4-bis(trimethylsilyl)-1,4-dihydropyrazine (DHP) as the co-reactant.^[59] A linear growth rate of approximately 0.3 Å at 190 °C was determined by in situ quartz crystal microbalance (QCM) mass change data, and an ALD window of 170-210 °C was reported. The authors proposed that DHP would bind with two surface-bound SnCl_x (x<4) species (forming chlorotrimethylsilane as a by-product) which reduces the SnCl_x species to form Sn-Sn bonds through elimination of pyrazine.



Scheme 1.4: Surface-based reaction schemes for reported nonmetal ALD processes. Adapted from references [56-59].

1.4.2 – ALD of Group 4 Metal Oxides and its Challenges

ALD of group 4 metal oxides ($M = \text{Ti, Zr, Hf}$) has been extensively studied within the past two decades, as shown in Figure 1.3. These numerous ALD processes have been the subject of reviews that have highlighted the variety of precursors utilized and potential applications of the materials.^[4,13,60,61] In general, inorganic compounds (e.g. MCl_4 ^[62]), organometallic complexes (e.g. MCp_2Me_2 ^[63]) and coordination complexes (e.g. $\text{M}(\text{O}^i\text{Pr})_2(\text{NMe}_2)_2$ ^[64]) have been utilized as group 4 metal oxide precursors. These are commonly employed alongside classical oxygen source co-reactants (e.g. H_2O , O_2 , O_3 , etc.) to deposit metal oxides by relatively facile ligand exchange or combustion reactions. Table 4.1 (page 103) provides examples of commonly reported precursors for HfO_2 ALD.

The primary use for ALD-grown metal oxides has been as a replacement for SiO_2 as the gate dielectric in metal-oxide-semiconductor field-effect transistors (MOSFETs) due to their higher permittivity constant (κ), and their thermodynamic stability (especially HfO_2) in direct contact with Si, which is a desirable quality for any SiO_2 substitute in order to eliminate the need for an interfacial layer.^[61] This shift, first announced by Intel in 2007, has made possible the continued miniaturization of semiconductor devices.^[65] Doped TiO_2 ALD processes have also gained a large amount of interest in the field of photocatalysis.^[66]

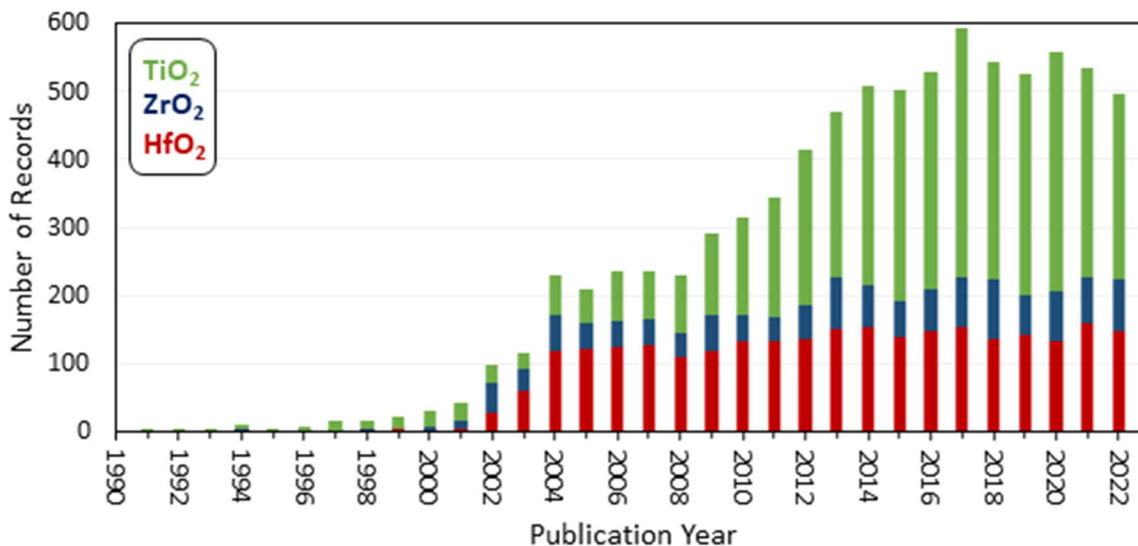


Figure 1.4: Histogram showing the number of records referring to “atomic layer deposition” and either “TiO₂”, “ZrO₂”, or “HfO₂” using the Web of Science platform.

High-k dielectric materials inherently possess high gate capacitance that allows them to retain electric charge without current leakage at reduced thicknesses.^[4,61] However, as device sizes continue to decrease and dielectric thicknesses are further reduced, film discontinuity and nonuniformity, especially on nonplanar substrates, becomes a more prevalent challenge leading to device failure. An additional challenge is that amorphous dielectrics are preferred because crystallization can expedite current leakage. Since most SiO₂ substitute candidates, including group 4 metal oxides, are crystalline at elevated temperatures, investigations in this field include incorporation of dopants to reduce the tendency for crystallization.^[61]

1.5 – Thesis Goals

This work details the development and evaluation of new precursors and co-reactants for ALD, as well as the development of new ALD processes, with a focus on the deposition of main group elements (ALD of Sb on hydrogen-terminated silicon, and ALD of B) and investigation of new processes for group 4 metal oxide (HfO_2 and ZrO_2) ALD in HAR substrates without the formation of voids.

Tris(trimethylsilyl)antimony was synthesized and evaluated using solution-state studies and ALD reactor studies for elemental antimony ALD in combination with SbCl_3 (Chapter 2). Portions of Chapter 2 have been reprinted (adapted) with permission from: M. Al Hareri, D. J. H. Emslie, Room-Temperature Atomic Layer Deposition of Elemental Antimony. *Chemistry of Materials* **2022**, *34*, 2400-2409. Copyright 2022 American Chemical Society.^[67] Boron-containing compounds were synthesized and evaluated as potential precursors for elemental boron ALD in combination with boron trihalides (Chapter 3). Solution-state and ALD reactor studies were conducted for HfO_2 ALD utilizing an unusual carboxylic acid as a co-reactant with a view towards HfO_2 ALD for void-free trench filling (Chapter 4). Zirconium-containing complexes were synthesized and evaluated as potential precursors for ZrO_2 ALD (Chapter 5). Portions of Chapter 5 have been reprinted (adapted) with permission from: M. Al Hareri, D. J. H. Emslie, Synthesis, Structures, and Thermal Stability of Dialkyl and Bis(amido) Zirconium(IV) Acen Complexes. *European Journal of Inorganic Chemistry* **2022**, *26*, 202200594 (7 pages). Copyright 2022 John Wiley & Sons.^[68] Introductions specific to each of these areas of

research are provided at the start of Chapters 2-5 (pages 27-30, 52-65, 98-103, and 135-137).

The evaluation of potential new precursors involved examination of their volatility, thermal stability, and solution reactivity towards a chosen co-reactant. The development of new ALD processes involved deposition and characterization of thin films to determine self-limiting growth, the ALD temperature window, and the thickness, composition, and morphology of the deposited films.

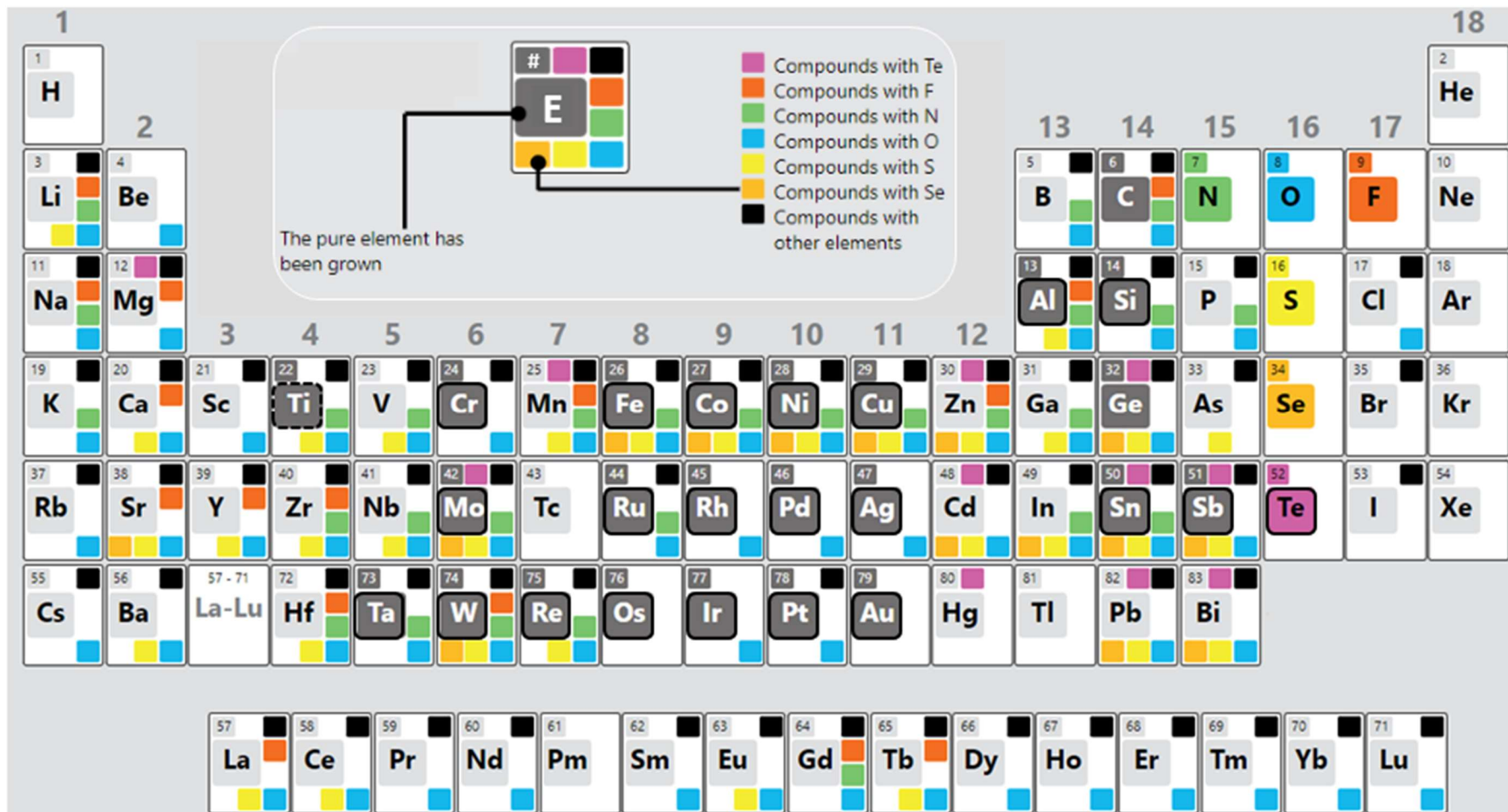


Figure 1.5: Colour-coded periodic table, adapted from the Atomic Limits database (DOI: 10.6100/alddatabase), depicting reported thermal and plasma ALD processes. Elements that have been reported to be deposited in the elemental form by thermal ALD are enclosed in solid boxes. Elements enclosed in dashed boxes have been proposed to be deposited by thermal ALD with only an oxide detected due to instantaneous oxidation upon exposure to air.

1.6 – References for Chapter 1

- [1] G. E. Moore (1965). "Cramming more components onto integrated circuits." *Electronics* 8, 38.
- [2] K. Rupp (2022). "Transistors per Microprocessor." from www.ourworldindata.org/grapher/transistors-per-microprocessor.
- [3] K. Rupp (2022). "42 Years of Microprocessor Trend Data." from www.karlrupp.net/2018/02/42-years-of-microprocessor-trend-data.
- [4] W. Jeon. Recent advances in the understanding of high-*k* dielectric materials deposited by atomic layer deposition for dynamic random-access memory capacitor applications. *J. Mater. Res.* **2019**, 35, 775-794.
- [5] T. Nam, H. Kim. Atomic layer deposition for nonconventional nanomaterials and their applications. *J. Mater. Res.* **2019**, 35, 656-680.
- [6] P. O. Oviroh, R. Akbarzadeh, D. Pan, R. A. M. Coetzee, T. C. Jen. New development of atomic layer deposition: Processes, methods and applications. *Sci. Technol. Adv. Mater.* **2019**, 20, 465-496.
- [7] G. S. Sandhu, R. P. Thakur (2007). "Process for Growing a Dielectric Layer on a Silicon-Containing Surface Using a Mixture of N₂O and O₃." Micron Technology, Inc., USA: Patent No. 0207573 A1.
- [8] D. J. H. Emslie, P. Chadha, J. S. Price. Metal ALD and pulsed CVD: Fundamental reactions and links with solution chemistry. *Coord. Chem. Rev.* **2013**, 257, 3282-3296.
- [9] S. M. George. Atomic Layer Deposition: An Overview. *Chem. Rev.* **2010**, 110, 111-131.
- [10] E. Ahvenniemi, A. R. Akbashev, S. Ali, M. Bechelany, M. Berdova, S. Boyadjiev, D. C. Cameron, R. Chen, M. Chubarov, V. Cremers, A. Devi, V. Drozd, L. Elnikova, G. Gottardi, K. Grigoras, D. M. Hausmann, C. S. Hwang, S.-H. Jen, T. Kallio, J. Kanervo, I. Khmel'nitskiy, D. H. Kim, L. Klibanov, Y. Koshtyal, A. O. I. Krause, J. Kuhs, I. Kärkkäinen, M.-L. Kääriäinen, T. Kääriäinen, L. Lamagna, A. A. Łapicki, M. Leskelä, H. Lipsanen, J. Lyytinen, A. Malkov, A. Malygin, A. Mennad, C. Militzer, J. Molarius, M. Norek, Ç. Özgüt-Akgün, M. Panov, H. Pedersen, F. Pierrat, G. Popov, R. L. Puurunen, G. Rampelberg, R. H. A. Ras, E. Rauwel, F. Roozeboom, T. Sajavaara, H. Salami, H. Savin, N. Schneider, T. E. Seidel, J. Sundqvist, D. B. Suyatin, T. Törndahl, J. R. van Ommen, C. Wiemer, O. M. E. Ylivaara, O. Yurkevich. Review Article: Recommended reading list of early publications on atomic layer deposition—Outcome of the "Virtual Project on the History of ALD". *J. Vac. Sci. Technol., A* **2017**, 35, 010801.
- [11] R. L. Puurunen. A Short History of Atomic Layer Deposition: Tuomo Suntola's Atomic Layer Epitaxy. *Chem. Vap. Deposition* **2014**, 20, 332-344.
- [12] R. L. Puurunen. Surface chemistry of atomic layer deposition: A case study for the trimethylaluminum/water process. *J. Appl. Phys.* **2005**, 97, 121301.

- [13] T. Blanquart, J. Niinistö, M. Ritala, M. Leskelä. Atomic Layer Deposition of Groups 4 and 5 Transition Metal Oxide Thin Films: Focus on Heteroleptic Precursors. *Chem. Vap. Deposition* **2014**, *20*, 189-208.
- [14] G. N. Parsons, R. D. Clark. Area-Selective Deposition: Fundamentals, Applications, and Future Outlook. *Chem. Mater.* **2020**, *32*, 4920-4953.
- [15] O. Graniel, M. Weber, S. Balme, P. Miele, M. Bechelany. Atomic layer deposition for biosensing applications. *Biosens. Bioelectron.* **2018**, *122*, 147-159.
- [16] M. A. Waghmare, M. Naushad, Z. A. Alothman, A. U. Ubale, H. M. Pathan. Zirconium oxide films: deposition techniques and their applications in dye-sensitized solar cells. *J. Solid State Electrochem.* **2017**, *21*, 2531-2545.
- [17] R. W. Johnson, A. Hultqvist, S. F. Bent. A brief review of atomic layer deposition: From fundamentals to applications. *Mater. Today* **2014**, *17*, 236-246.
- [18] H. Kim, H.-B.-R. Lee, W. J. Maeng. Applications of atomic layer deposition to nanofabrication and emerging nanodevices. *Thin Solid Films* **2009**, *517*, 2563-2580.
- [19] M. Ritala, J. Niinistö. Industrial Applications of Atomic Layer Deposition. *ECS Trans.* **2009**, *25*, 641-652.
- [20] A. W. Weimer. Particle atomic layer deposition. *J. Nanopart. Res.* **2019**, *21*, 9.
- [21] R. L. Puurunen, W. Vandervorst. Island growth as a growth mode in atomic layer deposition: A phenomenological model. *J. Appl. Phys.* **2004**, *96*, 7686-7695.
- [22] W. Chiappim, B. B. Neto, M. Shiotani, J. Karnopp, L. Gonçalves, J. P. Chaves, A. D. S. Sobrinho, J. P. Leitão, M. Fraga, R. Pessoa. Plasma-Assisted Nanofabrication: The Potential and Challenges in Atomic Layer Deposition and Etching. *Nanomaterials* **2022**, *12*, 3497.
- [23] H. Kim, I.-K. Oh. Review of plasma-enhanced atomic layer deposition: Technical enabler of nanoscale device fabrication. *Jpn. J. Appl. Phys.* **2014**, *53*, 03DA01.
- [24] H. C. M. Knoops, T. Faraz, K. Arts, W. M. M. Kessels. Status and prospects of plasma-assisted atomic layer deposition. *J. Vac. Sci. Technol., A* **2019**, *37*, 030902.
- [25] H. B. Profijt, S. E. Potts, M. C. M. van de Sanden, W. M. M. Kessels. Plasma-Assisted Atomic Layer Deposition: Basics, Opportunities, and Challenges. *J. Vac. Sci. Technol., A* **2011**, *29*, 050801.
- [26] A. J. M. Mackus, M. J. M. Merckx, W. M. M. Kessels. From the Bottom-Up: Toward Area-Selective Atomic Layer Deposition with High Selectivity. *Chem. Mater.* **2019**, *31*, 2-12.
- [27] V. Miikkulainen, K. Väyrynen, V. Kilpi, Z. Han, M. Vehkamäki, K. Mizohata, J. Räisänen, M. Ritala. Photo-assisted ALD: Process Development and Application Perspectives. *ECS Trans.* **2017**, *80*, 49-60.
- [28] V. Miikkulainen, K. Väyrynen, K. Mizohata, J. Räisänen, M. Vehkamäki, M. Ritala. Photoassisted atomic layer deposition of oxides employing alkoxides as single-source precursors. *J. Vac. Sci. Technol., A* **2019**, *37*, 060911.
- [29] T. Henke, M. Knaut, C. Hossbach, M. Geidel, L. Rebohle, M. Albert, W. Skorupa, J. W. Bartha. Flash-Enhanced Atomic Layer Deposition: Basics, Opportunities,

- Review, and Principal Studies on the Flash-Enhanced Growth of Thin Films. *ECS J. Solid State Sci. Technol.* **2015**, *4*, P277-P287.
- [30] H. Van Bui, F. Grillo, J. R. van Ommen. Atomic and molecular layer deposition: Off the beaten track. *Chem. Commun.* **2016**, *53*, 45-71.
- [31] P. Sundberg, M. Karppinen. Organic and inorganic-organic thin film structures by molecular layer deposition: A review. *Beilstein J. Nanotechnol.* **2014**, *5*, 1104-1136.
- [32] S. M. George, B. Yoon, A. A. Dameron. Surface Chemistry for Molecular Layer Deposition of Organic and Hybrid Organic-Inorganic Polymers. *Acc. Chem. Res.* **2009**, *42*, 498-508.
- [33] X. Meng. An overview of molecular layer deposition for organic and organic-inorganic hybrid materials: Mechanisms, growth characteristics, and promising applications. *J. Mater. Chem. A* **2017**, *5*, 18326-18378.
- [34] T. Yoshimura, S. Tatsuura, W. Sotoyama. Polymer films formed with monolayer growth steps by molecular layer deposition. *Appl. Phys. Lett.* **1991**, *59*, 482-484.
- [35] A. A. Dameron, D. Seghete, B. B. Burton, S. D. Davidson, A. S. Cavanagh, J. A. Bertrand, S. M. George. Molecular Layer Deposition of Alucone Polymer Films Using Trimethylaluminum and Ethylene Glycol. *Chem. Mater.* **2008**, *20*, 3315-3326.
- [36] E. Ahvenniemi, M. Karppinen. Atomic/molecular layer deposition: A direct gas-phase route to crystalline metal-organic framework thin films. *Chem. Commun.* **2016**, *52*, 1139-1142.
- [37] L. D. Salmi, M. J. Heikkilä, E. Puukilainen, T. Sajavaara, D. Grosso, M. Ritala. Studies on atomic layer deposition of MOF-5 thin films. *Microporous Mesoporous Mater.* **2013**, *182*, 147-154.
- [38] A. Fischer, A. Routzahn, S. M. George, T. Lill. Thermal atomic layer etching: A review. *J. Vac. Sci. Technol., A* **2021**, *39*, 030801.
- [39] K. J. Kanarik, S. Tan, R. A. Gottscho. Atomic Layer Etching: Rethinking the Art of Etch. *J. Phys. Chem. Lett.* **2018**, *9*, 4814-4821.
- [40] S. M. George. Mechanisms of Thermal Atomic Layer Etching. *Acc. Chem. Res.* **2020**, *53*, 1151-1160.
- [41] Y. Lee, J. W. DuMont, S. M. George. Trimethylaluminum as the Metal Precursor for the Atomic Layer Etching of Al₂O₃ Using Sequential, Self-Limiting Thermal Reactions. *Chem. Mater.* **2016**, *28*, 2994-3003.
- [42] M. N. Yoder (1988). "Atomic Layer Etching." The United States of America as represented by the Secretary of the Navy, USA: Patent No. 4,756,794.
- [43] T. Hatanpää, M. Ritala, M. Leskelä. Precursors as enablers of ALD technology: Contributions from University of Helsinki. *Coord. Chem. Rev.* **2013**, *257*, 3297-3322.
- [44] H. H. Sønsteby, J. E. Bratvold, V. A. L. K. Killi, D. Choudhury, J. W. Elam, H. Fjellvåg, O. Nilsen. *tert*-Butoxides as precursors for atomic layer deposition of alkali metal containing thin films. *J. Vac. Sci. Technol., A* **2020**, *38*, 060804.

- [45] M. Madadi, J. Heiska, J. Multia, M. Karppinen. Atomic and Molecular Layer Deposition of Alkali Metal Based Thin Films. *Acs Applied Materials & Interfaces* **2021**, *13*, 56793-56811.
- [46] D. J. Hagen, M. E. Pemble, M. Karppinen. Atomic layer deposition of metals: Precursors and film growth. *Appl. Phys. Rev.* **2019**, *6*, 041309.
- [47] "ALD Database" (2023) 10.6100/alddatabase:10.6100/alddatabase. www.atomiclimits.com/alddatabase.
- [48] J. Hämäläinen, M. Ritala, M. Leskelä. Atomic Layer Deposition of Noble Metals and Their Oxides. *Chem. Mater.* **2013**, *26*, 786-801.
- [49] P. Mårtensson, J.-O. Carisson. Atomic Layer Epitaxy of Copper: Growth and Selectivity in the Cu(II)-2,2,6,6-tetramethyl-3,5-heptanedionate/H₂ Process. *J. Electrochem. Soc.* **1998**, *145*, 2926-2931.
- [50] B. S. Lim, A. Rahtu, R. G. Gordon. Atomic layer deposition of transition metals. *Nat. Mater.* **2003**, *2*, 749-754.
- [51] D. Seghete, G. B. Rayner, A. S. Cavanagh, V. R. Anderson, S. M. George. Molybdenum Atomic Layer Deposition Using MoF₆ and Si₂H₆ as the Reactants. *Chem. Mater.* **2011**, *23*, 1668-1678.
- [52] S.-H. Kim, N. Kwak, J. Kim, H. Sohn. A Comparative Study of the Atomic-Layer Deposited Tungsten Thin Films as Nucleation Layers for W-Plug Deposition. *J. Electrochem. Soc.* **2006**, *153*, G887-G893.
- [53] J. P. Klesko, C. M. Thrush, C. H. Winter. Thermal Atomic Layer Deposition of Titanium Films Using Titanium Tetrachloride and 2-Methyl-1,4-bis(trimethylsilyl)-2,5-cyclohexadiene or 1,4-Bis(trimethylsilyl)-1,4-dihydropyrazine. *Chem. Mater.* **2015**, *27*, 4918-4921.
- [54] J.-i. Nishizawa, K. Aoki, S. Suzuki, K. Kikuchi. Silicon Molecular Layer Epitaxy. *J. Electrochem. Soc.* **1990**, *137*, 1898-1904.
- [55] S. Yokoyama, K. Ohba, A. Nakajima. Self-limiting atomic-layer deposition of Si on SiO₂ by alternate supply of Si₂H₆ and SiCl₄. *Appl. Phys. Lett.* **2001**, *79*, 617-619.
- [56] V. Pore, K. Knapas, T. Hatanpää, T. Sarnet, M. Kemell, M. Ritala, M. Leskelä, K. Mizohata. Atomic Layer Deposition of Antimony and its Compounds Using Dechlorosilylation Reactions of Tris(trimethylsilyl)antimony. *Chem. Mater.* **2011**, *23*, 247-254.
- [57] L. Cheng, V. Adinolfi, S. L. Weeks, S. V. Barabash, K. A. Littau. Conformal deposition of GeTe films with tunable Te composition by atomic layer deposition. *J. Vac. Sci. Technol., A* **2019**, *37*, 020907.
- [58] K. J. Blakeney, C. H. Winter. Atomic Layer Deposition of Aluminum Metal Films Using a Thermally Stable Aluminum Hydride Reducing Agent. *Chem. Mater.* **2018**, *30*, 1844-1848.
- [59] E. C. Stevens, M. B. M. Mousa, G. N. Parsons. Thermal atomic layer deposition of Sn metal using SnCl₄ and a vapor phase silyl dihydropyrazine reducing agent. *J. Vac. Sci. Technol., A* **2018**, *36*, 06A106.

- [60] G. Y. Lee, S. Yeo, S. H. Han, B. K. Park, T. Eom, J. H. Kim, S. H. Kim, H. Kim, S. U. Son, T. M. Chung. Group IV Transition Metal (M = Zr, Hf) Precursors for High- κ Metal Oxide Thin Films. *Inorg. Chem.* **2021**, *60*, 17722-17732.
- [61] G. He, Z. Sun, G. Li, L. Zhang. Review and Perspective of Hf-based High- k Gate Dielectrics on Silicon. *Crit. Rev. Solid State Mater. Sci.* **2012**, *37*, 131-157.
- [62] M. Ritala, M. Leskelä. Zirconium dioxide thin films deposited by ALE using zirconium tetrachloride as precursor. *Appl. Surf. Sci.* **1994**, *75*, 333-340.
- [63] J. Niinistö, M. Putkonen, L. Niinistö, K. Arstila, T. Sajavaara, J. Lu, K. Kukli, M. Ritala, M. Leskelä. HfO₂ Films Grown by ALD Using Cyclopentadienyl-Type Precursors and H₂O or O₃ as Oxygen Source. *J. Electrochem. Soc.* **2006**, *153*, F39-F45.
- [64] T. Blanquart, J. Niinistö, M. Gavagnin, V. Longo, V. R. Pallem, C. Dussarrat, M. Ritala, M. Leskelä. Novel Heteroleptic Precursors for Atomic Layer Deposition of TiO₂. *Chem. Mater.* **2012**, *24*, 3420-3424.
- [65] Intel, 2007. "Intel's Fundamental Advance in Transistor Design Extends Moore's Law, Computing Performance", Santa Clara, Calif., USA.
- [66] J.-P. Niemelä, G. Marin, M. Karppinen. Titanium dioxide thin films by atomic layer deposition: A review. *Semicond. Sci. Technol.* **2017**, *32*, 093005.
- [67] M. Al Hareri, D. J. H. Emslie. Room-Temperature Atomic Layer Deposition of Elemental Antimony. *Chem. Mater.* **2022**, *34*, 2400-2409.
- [68] M. Al Hareri, D. J. H. Emslie. Synthesis, Structures, and Thermal Stability of Dialkyl and Bis(amido) Zirconium(IV) Acen Complexes. *Eur. J. Inorg. Chem.* **2022**, *26*, 202200594.

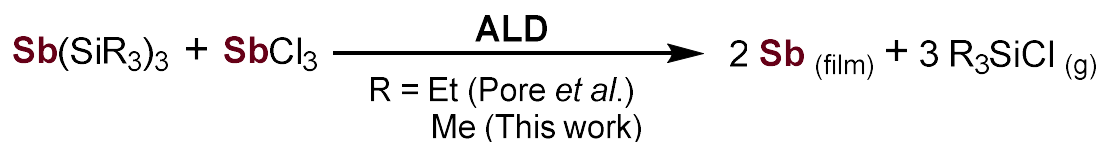
Chapter 2

Room-Temperature Atomic Layer Deposition of Elemental Antimony

Portions of this chapter have been reprinted (adapted) with permission from M. Al Hareri, D. J. H. Emslie, Room-Temperature Atomic Layer Deposition of Elemental Antimony. *Chemistry of Materials* **2022**, *34*, 2400-2409. Copyright 2022 American Chemical Society.

2.1 – Introduction to Chapter 2

ALD methods have been reported for a range of materials,^[1] including pure elements. Most of element ALD research has focused on the transition metals,^[2-4] although ALD of main group elements such as Al,^[5] Sn,^[6] Sb^[7] and Te^[8] has also been described. Antimony ALD was achieved using Sb(SiEt₃)₃ and SbCl₃ (Scheme 2.1); film growth was observed at 95-250 °C, and self-limiting growth was demonstrated at 95 °C.^[7]



Scheme 2.1: Proposed reaction of a tri(silyl)antimony precursor with antimony trichloride.

Thin films of elemental antimony have recently seen a flurry of interest^[9-13] in the context of phase change memory (PCM), where data storage is achieved by switching between crystalline and amorphous states.^[14-16] The use of elemental antimony as a monoatomic PCM material was made possible by confinement of a 3-10 nm thick

antimony film between oxide or nitride layers. Use of a pure element for PCM avoids problems with more complex PCM materials, such as deviations from ideal stoichiometry, which can be introduced during film deposition, or can occur as a result of compositional partitioning under operating conditions. The programmable optical nonlinearity of thin antimony films has also been investigated, demonstrating high potential for applications in nanophotonics and optoelectronics.^[17]

Additionally, ultra-thin films of Sb could potentially find application for in-situ n-doping of semiconductor materials such as silicon. In recent years, monolayer doping (MLD) has been developed as a method for doping of silicon or germanium with group 15 (or group 13) elements.^[18-21] This method involves surface functionalization with a monolayer of a dopant-containing molecule, followed by application of a capping layer such as SiO₂ (to minimize loss of dopant atoms to the surroundings during the next step), rapid thermal annealing to cause diffusion of the chemisorbed dopant atoms into the semiconductor material, and removal of the capping layer. MLD can enable ultra-shallow doping, and doping of 3-D structures without crystal damage. However, several drawbacks of MLD have been noted, including: (a) almost all of the molecules used for monolayer formation contain carbon, leading to inevitable carbon incorporation into the semiconductor, in some cases significantly deactivating the electrical activity of the dopant atoms,^[19,20,22] (b) dopant concentrations higher than those provided by a monolayer of dopant-containing molecules are not readily achieved,^[18,23] and (c) monolayer formation typically requires prolonged reaction with the dopant-containing molecule (liquid, or in solution) at elevated temperature.^[20] ALD-fabricated ultra-thin films of group 15 elements could potentially

circumvent these issues, providing (via thermal annealing) access to films with high dopant concentrations and minimal carbon contamination.

Herein we report thermal ALD of antimony on H-Si (hydrogen-terminated silicon) and SiO₂/Si (Si(100) with a layer of oxide) substrates at 23-65 °C using the precursors Sb(SiMe₃)₃ and SbCl₃ (Scheme 2.1). This precursor combination also resulted in improved nucleation on H-Si (at 35 °C), relative to the previously reported higher temperature Sb ALD method {Sb(SiEt₃)₃/SbCl₃ at 95 °C}.

Thermal ALD processes capable of operation at room temperature are scarce, given that it requires: (a) precursors which are volatile enough to allow room temperature delivery, (b) precursors with sufficient reactivity to enable rapid surface-based reactivity during each ALD cycle, and (c) ALD reaction by-products which are volatile enough to be efficiently removed from the substrate surface. Most other materials to have been deposited by room temperature thermal ALD are metal oxides (e.g. Al₂O₃,^[24,25] B₂O₃,^[26,27] ZnO,^[24] SiO₂^[28,29] and TiO₂^[24]), with deposition utilizing H₂O (or rarely O₃)^[25] as the co-reactant. To the best of our knowledge, a pure element has not previously been deposited by thermal ALD (with demonstrated self-limiting growth) at room temperature.^[30,31] Room temperature ALD processes are of particular interest as a means to enable deposition on thermally-sensitive substrates,^[25] to minimize problems with agglomeration of low-melting films (e.g. Cu),^[32] and to enable ALD using less complex (and less expensive) ALD reactors. Room temperature thermal ALD methods can also be beneficial for high-throughput roll-to-roll ALD techniques,^[25] and for area-selective ALD using small molecule

inhibitors,^[33] where inhibitor desorption and undesired reactivity can be minimized at low temperature.

We also describe the use of in situ surface (H-Si or SiO₂/Si) pre-treatment with Sb(SiMe₃)₃ or SbCl₃ as a method to improve nucleation during the initial growth phase of ALD. Deposition in ALD is highly dependent on the chemical nature of the surface, and surface pre-treatment has previously been reported as a means to improve nucleation, or to improve selectivity in area-selective ALD (AS-ALD),^[33,34] either by promoting or inhibiting growth on a particular material. For example, AlMe₃, AlMe₂Cl or ZnEt₂ pre-treatment has been used to enhance nucleation during Pt ALD (using MeCpPtMe₃ with O₂ or O₂ plasma) on oxide surfaces such as SiO₂,^[35-37] and AlMe₃ pre-treatment has been shown to enhance nucleation during Ru ALD (using RuO₄ and H₂) on SiO₂.^[38] Conversely, pre-treatment with Me₂Si(NMe₂)₂ has been used to preferentially inhibit ALD growth of Ru (and to a lesser extent Pt) on SiO₂ while still permitting growth on H-Si or MoS₂,^[39] and dodecanethiol pre-treatment has been used to inhibit ALD on copper, while allowing ALD on SiO₂ and TaN.^[40]

2.2 – Synthesis and Solution-State Reactivity of Tris(trimethylsilyl)antimony (2-1)

Trialkylchlorosilane elimination reactivity between Sb(SiMe₃)₃ (**2-1**) and SbCl₃ was investigated as a means to achieve room temperature thermal ALD of elemental antimony. This reactivity mirrors that previously reported by Pore *et al.* at 95-250 °C,^[7] but utilizes substantially more volatile and reactive Sb(SiMe₃)₃ in place of Sb(SiEt₃)₃ (the

former precursor is substantially less sterically hindered, given that it features 9 methyl groups in place of ethyl groups). The required precursor, $\text{Sb}(\text{SiMe}_3)_3$, was prepared as a colourless, pyrophoric and light-sensitive oil in 90% yield (Scheme 2.2) via the reaction of 3 equiv. of Na with Sb in 1,2-dimethoxyethane (in the presence of naphthalene as a catalyst) to form Na_3Sb , followed by the addition of 3 equiv. of Me_3SiCl .



Scheme 2.2: Synthesis of $\text{Sb}(\text{SiMe}_3)_3$ (**2-1**; DME= 1,2-dimethoxyethane).

As an initial test of the feasibility of the proposed ALD method, the solution reactivity of $\text{Sb}(\text{SiMe}_3)_3$ with SbCl_3 was investigated. This reaction proceeded at room temperature in C_6D_6 , affording a black precipitate of elemental antimony (confirmed by PXRD; Figure 2.1b), accompanied by Me_3SiCl as the only soluble byproduct (confirmed by ^1H , ^{13}C and ^{29}Si NMR spectroscopy; Figure 2.1a and A2.1). The formation of R_3SiCl as the solution reaction by-product mirrors the observations of Pore *et al.* during ALD (Scheme 2.1), who used in situ quadrupole mass spectrometry (QMS) to identify the byproduct from the $\text{Sb}(\text{SiEt}_3)_3/\text{SbCl}_3$ ALD process as Et_3SiCl .^[7]

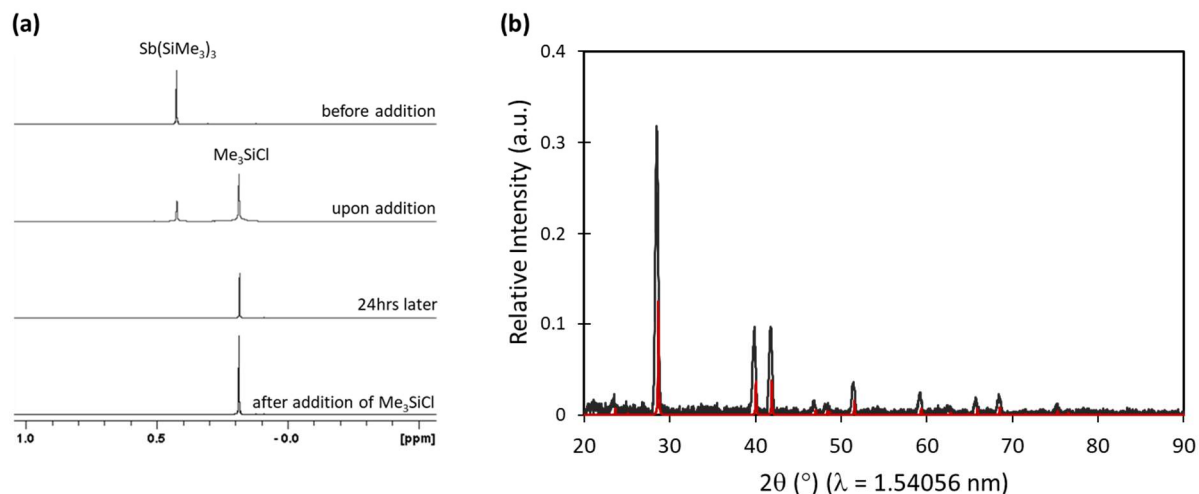


Figure 2.1: (a) ^1H NMR spectra of the NMR-scale reaction of $\text{Sb}(\text{SiMe}_3)_3$ (**2-1**) and SbCl_3 in C_6D_6 (600 MHz, 298 K). The reaction was monitored before and after addition of 1 equivalent of SbCl_3 . After complete consumption of $\text{Sb}(\text{SiMe}_3)_3$, Me_3SiCl was added to the NMR tube to verify the identify the reaction product. (b) X-ray diffractogram of Sb powder generated from the 1:1 reaction of **2-1** and SbCl_3 in hexanes.

2.3 – ALD Studies using $\text{Sb}(\text{SiMe}_3)_3$ (**2-1**) and SbCl_3

To enable accurate temperature control, initial ALD experiments were carried out utilizing $\text{Sb}(\text{SiMe}_3)_3$ and SbCl_3 bubbler temperatures of 30°C , and a substrate temperature of 35°C (see later for discussion of deposition at 23°C). Substrates were hydrogen-terminated silicon (H-Si) and Si(100) with 100 nm of thermal oxide (SiO_2/Si). After 2000 ALD cycles using 0.1 s pulses, mirror-like films were obtained on both substrates, which were confirmed to be composed of elemental antimony by XPS and XRD. After sputtering to remove surface contaminants and antimony oxides, XPS revealed elemental antimony with low impurity levels (Figure 2.2).

All peaks in the X-ray diffractograms (Figure 2.3) can be indexed to rhombohedral Sb (R-3m) with strong preferential orientation (i.e. crystallographic texture) apparent through the loss of some expected peaks and deviation of observed peaks from their ideal relative intensities. The resistivity of an Sb film grown on undoped SiO₂/Si using 3000 ALD cycles was 93 $\mu\Omega\cdot\text{cm}$ (determined by 4-point probe), which is approximately double the literature value for bulk antimony (41.5 $\mu\Omega\cdot\text{cm}$),^[41] and is comparable with the values (60-100 $\mu\Omega\cdot\text{cm}$) reported by Pore *et al.* for Sb films deposited using Sb(SiEt₃)₃/SbCl₃ at 95-200 °C.^[7]

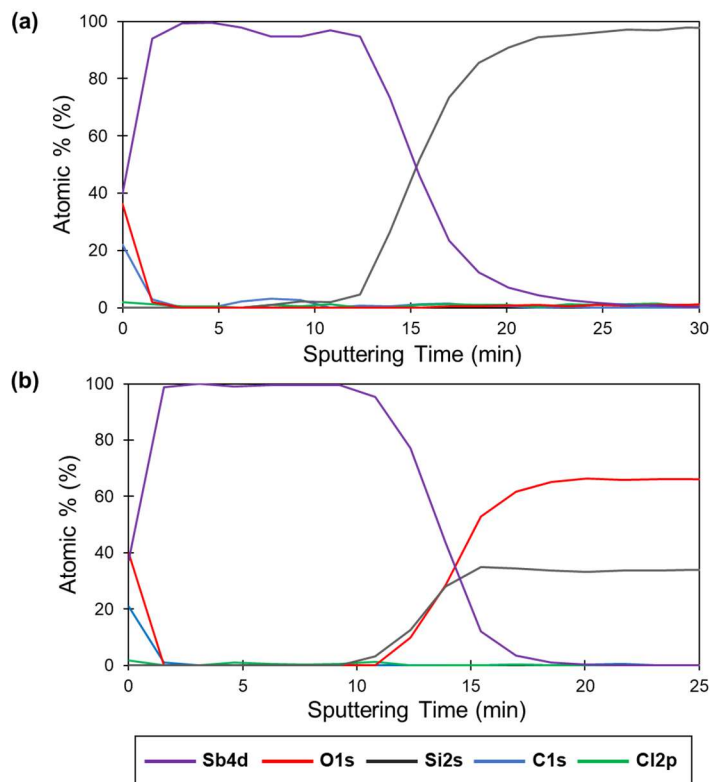


Figure 2.2: XPS depth analysis of Sb films grown on (a) H-Si and (b) SiO₂/Si at 35 °C using 2000 cycles and 0.1 second pulse times.

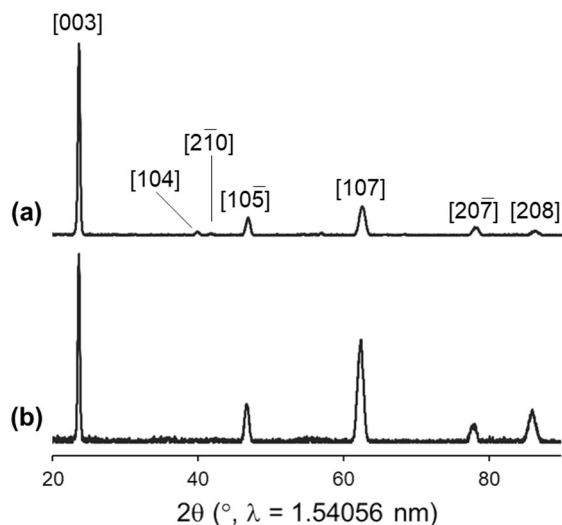


Figure 2.3: X-ray diffractograms of Sb films grown on (a) H-Si and (b) SiO₂/Si at 35 °C using 2000 cycles and 0.1 second pulse times.

The conditions for self-limiting growth at 35 °C on SiO₂/Si and H-Si were assessed by varying the pulse lengths of both Sb(SiMe₃)₃ and SbCl₃ from 0.03 to 1.0 s (Figure 2.4; variable angle spectroscopic ellipsometry (VASE) was used to determine film thickness). On SiO₂/Si, the growth rate remained constant at 0.48 Å using pulse times of at least 0.03 s and 0.05 s for Sb(SiMe₃)₃ and SbCl₃, respectively. On H-Si a growth rate of 0.36 Å was obtained utilizing Sb(SiMe₃)₃ and SbCl₃ pulses of at least 0.05 s. Sb deposition was also carried out with the bubblers and substrate at room temperature (23 °C), and self-limiting growth was verified through the observation of the same film thickness using precursor pulses of 0.1, 0.4 and 1.0 s, affording after 1000 cycles a GPC of 0.45 Å on SiO₂ and 0.37 Å on H-Si.

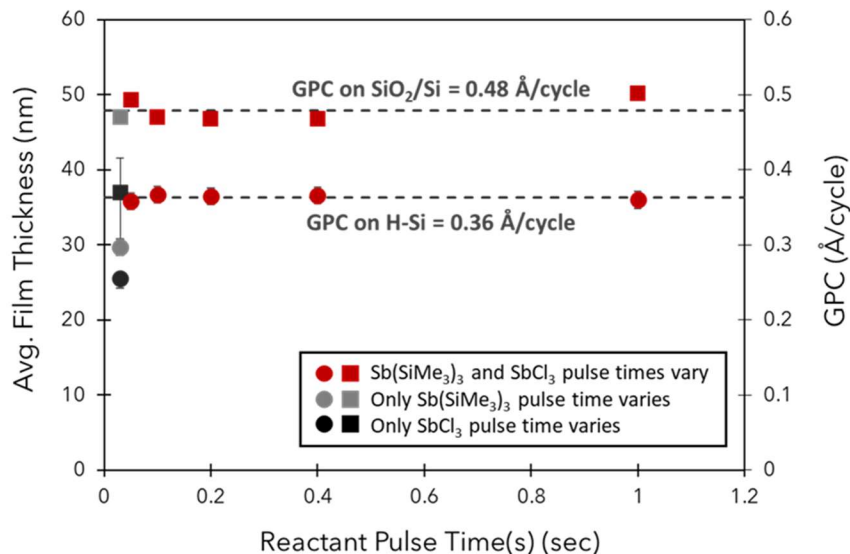


Figure 2.4: Dependence of film thickness and GPC on $\text{Sb}(\text{SiMe}_3)_3$ and/or SbCl_3 pulse times for Sb deposition on H-Si (circles) and SiO_2/Si (squares). All experiments employed 1000 cycles and a deposition temperature of 35 °C. Red data points indicate experiments in which the pulse time (on the x-axis) applies to both $\text{Sb}(\text{SiMe}_3)_3$ and SbCl_3 . Gray or black coloured data points indicate experiments in which the pulse time (on the x-axis) applies only to $\text{Sb}(\text{SiMe}_3)_3$ or SbCl_3 , respectively (the pulse time of the other reactant was fixed at 0.1 s).

Film thickness varied linearly when the number of deposition cycles was varied from 125 to 2000 at 35 °C (Figure 2.5). The y-axis intercept in this graph is greater than zero, indicative of a substrate-enhanced growth mechanism^[42-44] in which a higher GPC is achieved during the initial growth phase (when substantial deposition is occurring on the SiO_2/Si or H-Si substrate surface, rather than the growing Sb film); experiments with 50-125 cycles afforded a GPC of 1.3 Å on SiO_2/Si , and 1.0 Å on H-Si (cf. 0.40 Å on SiO_2/Si , and 0.27 Å on H-Si for the region from 250-2000 cycles after the original substrate surface has been covered^[45]).

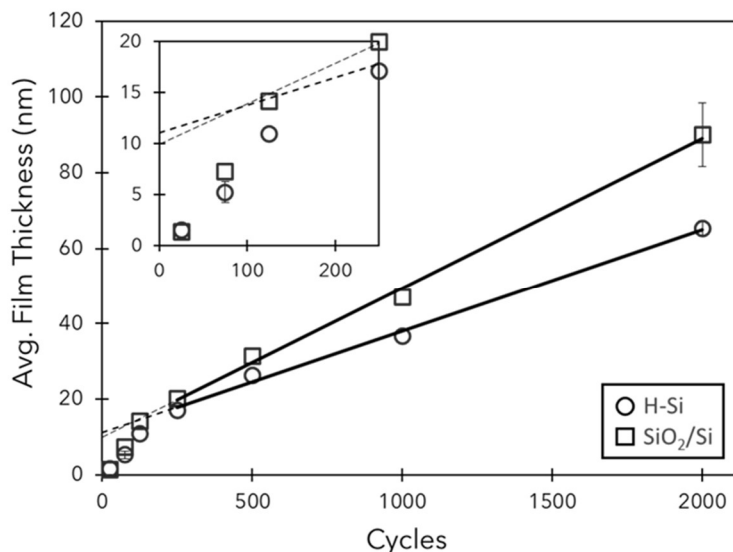


Figure 2.5: Dependence of film thickness on the number of cycles for Sb ALD on H-Si (circles) and SiO₂/Si (squares) substrates at 35 °C. Reactant pulse times were kept constant at 0.1 s. The inset shows an expanded view of the region from 0 to 250 cycles.

For films deposited using 500-2000 ALD cycles, continuous films were observed by SEM (films deposited on H-Si are shown in Figures 2.6 and A2.6; SEMs of films deposited on SiO₂/Si are provided in Figure A2.7). However, films deposited using 1000 or 2000 cycles on H-Si had increased surface roughness due to the formation of grains (100-300 nm in diameter) on the surface of the underlying antimony film; analogous behaviour was reported for Sb ALD at 95 °C using Sb(SiEt₃)₃/SbCl₃.⁴ With 125 or 250 cycles, films composed of individual grains or grains in the process of coalescence, respectively, were observed.

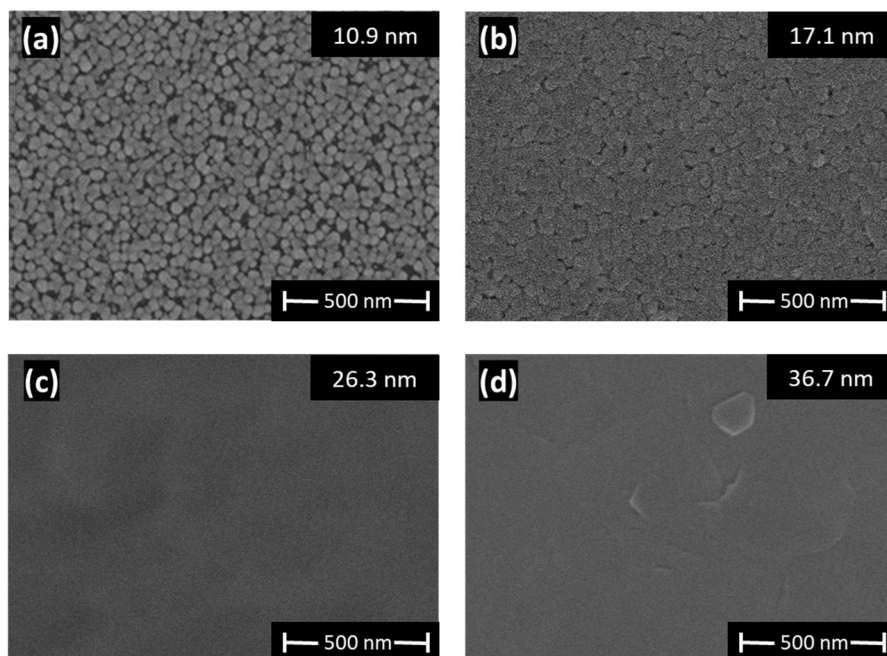


Figure 2.6: FESEM images of films grown on H-Si at 35 °C using (a) 125, (b) 250, (c) 500 and (d) 1000 ALD cycles. Film thicknesses are average values determined by VASE.

Deposition experiments were performed at temperatures ranging from 23 to 150 °C to determine the ALD window of the $\text{Sb}(\text{SiMe}_3)_3/\text{SbCl}_3$ process on SiO_2/Si and H-Si (Figure 2.7; 1000 cycles, 0.4 s precursor pulses). Film growth was observed at all temperatures with the highest GPC occurring at 65 °C (0.39 Å) on H-Si and 95 °C (0.53 Å) on SiO_2/Si . All films were shown to be composed of elemental Sb by XRD (Figures A2.10 and A2.13), as well as XPS for the film deposited on SiO_2/Si at 95 °C (Figure A2.15). However, films deposited above 95 °C on either substrate exhibited a decrease in the extent of crystallographic orientation relative to the substrate surface. On both substrates, ALD growth was found to occur up to 65 °C, as determined by an

independence of growth rate on precursor pulse times (Figures A2.11 and A2.14) and the formation of reflective silver-coloured films (Figure A2.9) with uniform thickness by VASE. By contrast, films deposited at 95, 125 and 150 °C (using 0.4 s pulse times) appeared visibly non-uniform (Figure A2.9), and VASE indicated substantial variations in film thickness at different points on the wafer. These observations are inconsistent with ALD growth at 95-150 °C, and SEM also revealed a change in morphology, from smooth continuous films, to discontinuous grains (Figure A2.12).^[46]

Consequently, the $\text{Sb}(\text{SiMe}_3)_3/\text{SbCl}_3$ ALD process is complementary to the previously reported $\text{Sb}(\text{SiEt}_3)_3/\text{SbCl}_3$ ALD process, in that the former enables low temperature (room temperature to 65 °C) deposition, whereas the latter operates at temperatures of 95°C and above. It is also notable that the low-temperature $\text{Sb}(\text{SiMe}_3)_3/\text{SbCl}_3$ ALD process (0.1s pulses) resulted in more effective nucleation on H-Si than ALD at 95 °C using $\text{Sb}(\text{SiEt}_3)_3/\text{SbCl}_3$ (2.0 s pulses; Figures A2.23-24). This could perhaps be due to improved physisorption at low temperature, or the greater reactivity and reduced steric bulk of $\text{Sb}(\text{SiMe}_3)_3$ versus $\text{Sb}(\text{SiEt}_3)_3$.

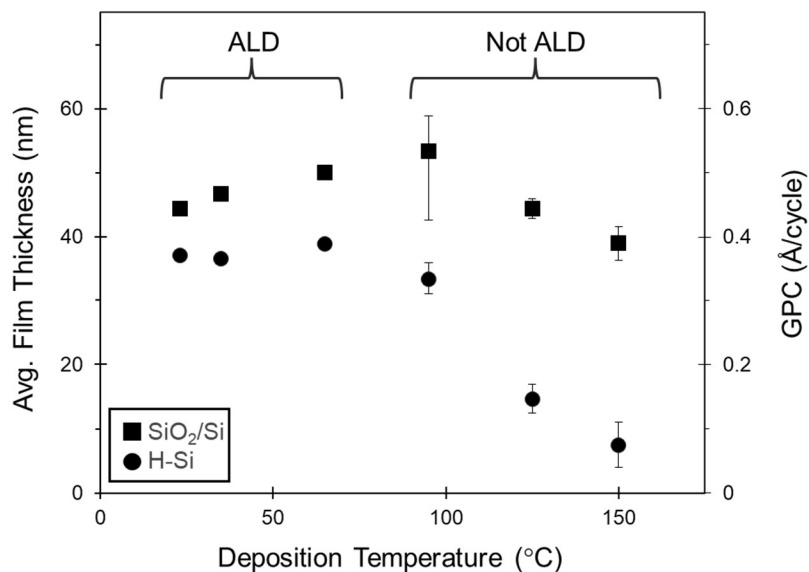


Figure 2.7: Dependence of film thickness and GPC on Sb deposition temperature on H-Si (circles) and SiO₂/Si (squares). All films were deposited using 1000 cycles and 0.4 second reactant pulse times.

2.4 – Nucleation Enhancement by In Situ Surface Pre-Treatment

As illustrated in Figures 2.8a and A2.6-7, films deposited at 35 °C using ≤ 250 ALD cycles were composed of isolated grains. However, we wondered whether in-situ pre-treatment of the H-Si or SiO₂/Si surface with Sb(SiMe₃)₃ or SbCl₃ might generate additional nucleation sites leading to more continuous film growth at low cycle numbers. Consequently, the surface was treated with 50 \times 0.1-0.8 s pulses of Sb(SiMe₃)₃ or SbCl₃ prior to carrying out 50 ALD cycles (Figures A2.16-19; the reactor was placed under vacuum for 2-5 minutes between pre-treatment and ALD; use of an additional 20 minute argon purge between pre-treatment and the start of ALD afforded nearly identical film

thicknesses;^[47] no film deposition was observed by VASE after surface pre-treatment alone). In these experiments, significantly more continuous films were obtained using 50 x 0.4 s pulses of $\text{Sb}(\text{SiMe}_3)_3$ or SbCl_3 as the pre-treatment, and 0.4 s pulses during ALD (b and d in Figure 2.8). Additionally, films of the same thickness, but with further improved surface coverage, were obtained using 50 x 0.8 s pulses of $\text{Sb}(\text{SiMe}_3)_3$ or SbCl_3 as the pre-treatment, and 0.8 s pulses during ALD (c and e in Figure 2.8). For example, on H-Si, a continuous 6.7 nm thick film was produced after initial pre-treatment with 50 x 0.8 s pulses of SbCl_3 , followed by 50 ALD cycles using 0.8 s pulses.

The use of longer ALD pulses in the first 50 ALD cycles after surface pre-treatment is likely required in order to achieve complete reactivity with an increased density of reactive surface sites. The effect of surface pre-treatment and longer ALD pulses during the first 50 cycles was probed by carrying out depositions (at 35 °C) utilizing 50 x 0.4 s pulses of $\text{Sb}(\text{SiMe}_3)_3$ or SbCl_3 for pre-treatment, followed by between 50 and 2000 ALD cycles, where the first 50 cycles utilized 0.4 s precursor pulses, and any remaining cycles utilized 0.1 s precursor pulses. Plots of film thickness versus cycle number are provided in Figure 2.9 for deposition on H-Si, and Figure A2.21 for deposition on SiO_2/Si . These plots indicate that during the initial ALD growth phase (the first ~125 cycles) surface pre-treatment results in a further increased GPC, but after this point, the GPC matches that for depositions carried out without the use of surface pre-treatment.

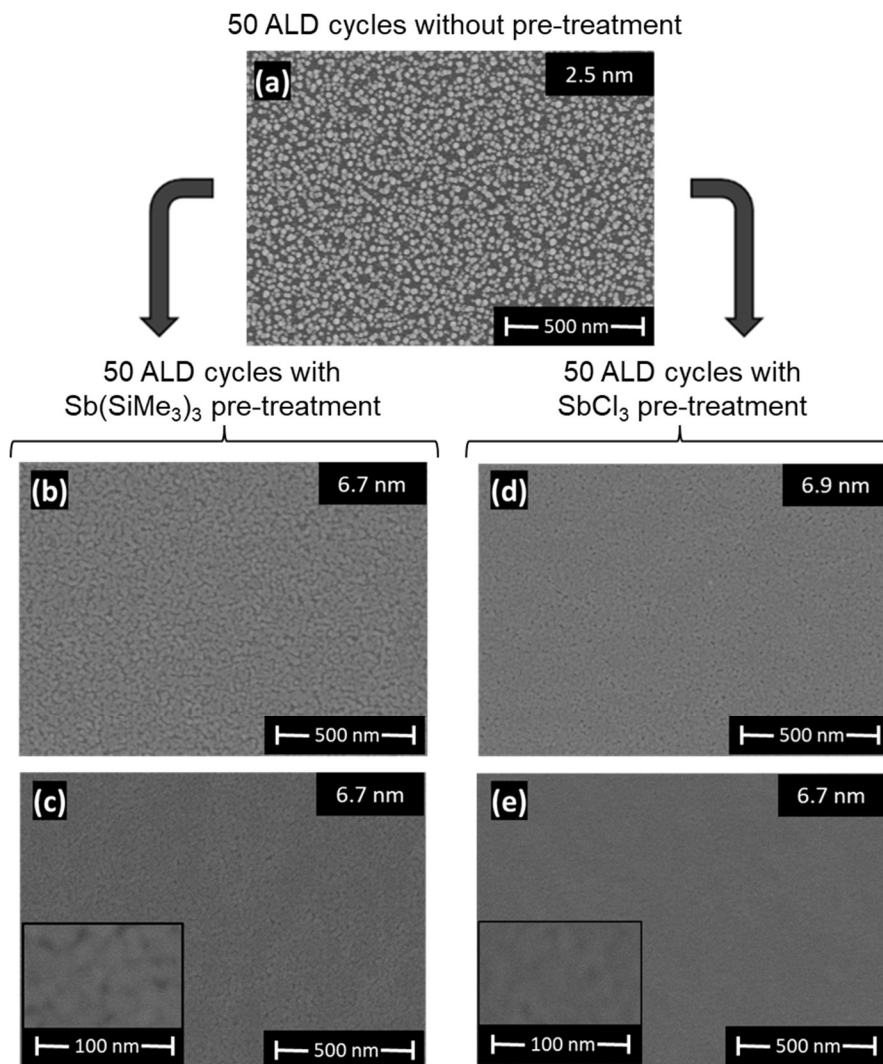


Figure 2.8: FESEM images of films grown on H-Si at 35 °C with or without 50 pulses of $\text{Sb}(\text{SiMe}_3)_3$ or SbCl_3 prior to carrying out 50 ALD cycles: (a) 50 ALD cycles (0.1 s pulses) without any pre-treatment, (b) pre-treatment with $\text{Sb}(\text{SiMe}_3)_3$ (50×0.4 s pulses), followed by 50 ALD cycles (using 0.4 s pulses), (c) pre-treatment with $\text{Sb}(\text{SiMe}_3)_3$ (50×0.8 s pulses), followed by 50 ALD cycles (using 0.8 s pulses), (d) pre-treatment with SbCl_3 (50×0.4 s pulses), followed by 50 ALD cycles (using 0.4 s pulses), and (e) pre-treatment with SbCl_3 (50×0.8 s pulses), followed by 50 ALD cycles (using 0.8 s pulses). Film thicknesses are average values determined by VASE.

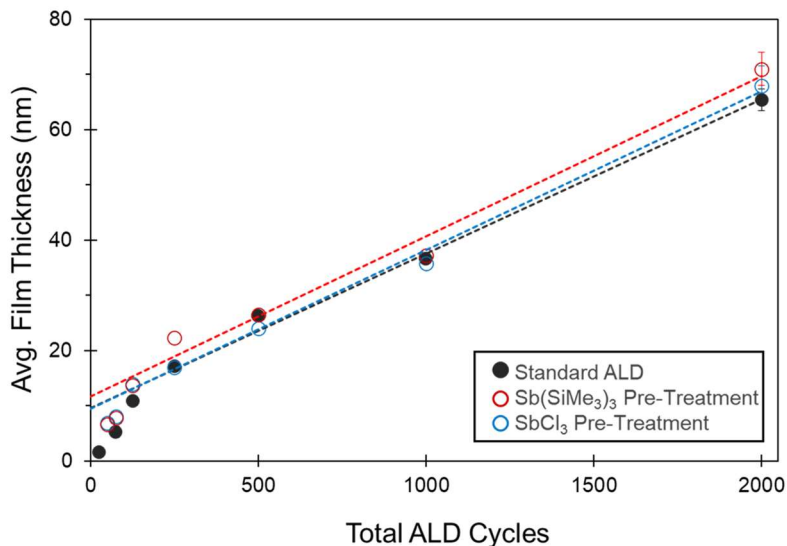


Figure 2.9: Film thickness versus the number of ALD cycles for 35 °C deposition on H-Si using: (i; black) standard ALD parameters (no pre-treatment, all cycles using 0.1 s pulses), (ii; red) ALD with Sb(SiMe₃)₃ pre-treatment (surface pre-treatment with 50 x 0.4 s pulses of Sb(SiMe₃)₃, followed by 50 ALD cycles using 0.4 s pulses, and all remaining ALD cycles using 0.1 s pulses), or (iii; blue) ALD with SbCl₃ pre-treatment (surface pre-treatment with 50 x 0.4 s pulses of SbCl₃, followed by 50 ALD cycles using 0.4 s pulses, and all remaining ALD cycles using 0.1 s pulses).

However, it is interesting to note that films deposited using surface pre-treatment prior to ALD (35 °C; 2000 cycles) exhibited a change in crystallographic texture (for X-ray diffractograms, see Figures 2.10 and A2.20). The resistivities of films obtained using initial SbCl₃ or Sb(SiMe₃)₃ pre-treatment (35 °C; undoped SiO₂/Si substrates; 2000 ALD cycles) were 91 μΩ·cm and 98 μΩ·cm, respectively (cf. 93 μΩ·cm for the film deposited without pre-treatment).

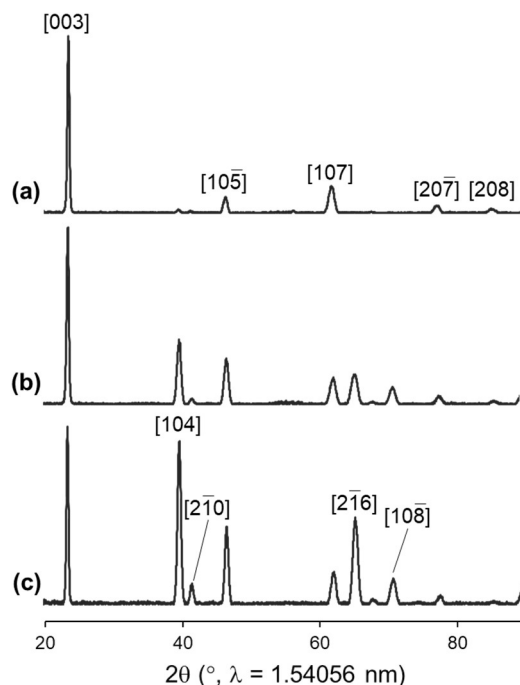


Figure 2.10: X-ray diffractograms of Sb films grown on H-Si (35 °C; 2000 cycles) using (a) the standard ALD method (no pre-treatment, all 0.1 s precursor pulses), (b) ALD with $\text{Sb}(\text{SiMe}_3)_3$ pre-treatment (surface pre-treatment with 50 x 0.4 s pulses of $\text{Sb}(\text{SiMe}_3)_3$, followed by 50 ALD cycles using 0.4 s pulses, and then 1950 cycles using 0.1 s pulses), or (c) ALD with SbCl_3 pre-treatment (surface pre-treatment with 50 x 0.4 s pulses of SbCl_3 , followed by 50 ALD cycles using 0.4 s pulses, and then 1950 cycles using 0.1 s pulses).

2.5 – Summary and Conclusions for Chapter 2

Room temperature thermal ALD of elemental antimony was achieved using $\text{Sb}(\text{SiMe}_3)_3$ (**2-1**) and SbCl_3 . This was made possible by (a) the high volatility of both precursors, which enables room temperature delivery (using a reactor pressure of ~1.0 Torr), (b) the high reactivity of this precursor combination, which facilitates rapid surface-based reactivity within each ALD cycle, and (c) the volatility of the Me_3SiCl reaction

byproduct, which enables efficient byproduct removal from the surface of the growing film, even at room temperature.

Antimony ALD had previously been reported in the 95-250 °C range (with self-limiting growth demonstrated at 95 °C) using SbCl_3 in combination with $\text{Sb}(\text{SiEt}_3)_3$,^[7] which is less volatile and less reactive than $\text{Sb}(\text{SiMe}_3)_3$. The $\text{Sb}(\text{SiMe}_3)_3/\text{SbCl}_3$ ALD process provided uniform films of crystalline antimony on H-Si or SiO_2/Si in the temperature range of 23-65 °C. On SiO_2/Si substrates, ALD using $\text{Sb}(\text{SiMe}_3)_3/\text{SbCl}_3$ at 35 °C afforded films with a similar morphology and thickness to those deposited using $\text{Sb}(\text{SiEt}_3)_3/\text{SbCl}_3$ at 95 °C. By contrast, on hydrogen terminated silicon (H-Si), improved nucleation was achieved using the former low-temperature process.

Film growth using $\text{Sb}(\text{SiMe}_3)_3/\text{SbCl}_3$ at 35 °C proceeded via a substrate-enhanced growth mechanism^[42-44] in which a higher GPC is achieved during the initial growth phase (when substantial deposition is occurring on the SiO_2/Si or H-Si substrate surface, rather than the growing Sb film). The use of 250 ALD cycles, or less, afforded films composed of isolated grains. However, in this initial growth stage, in-situ surface pre-treatment by $\text{Sb}(\text{SiMe}_3)_3$ or SbCl_3 (50 x 0.4 or 0.8 s pulses) combined with the use of longer precursor pulses (0.4 or 0.8 s) during the first 50 ALD cycles resulted in improved nucleation. For example, on H-Si, a continuous 6.7 nm thick film was produced after initial pre-treatment with 50 x 0.8 s pulses of SbCl_3 , followed by 50 ALD cycles using 0.8 s pulses. The use of longer ALD pulses in the first 50 ALD cycles after surface pre-treatment is likely required in order to achieve complete reactivity with an increased density of reactive surface sites.

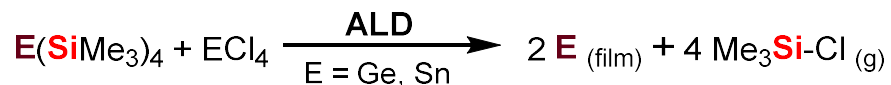
ALD processes capable of operating at room temperature are scarce, and to the best of our knowledge, a pure element has not previously been deposited by thermal ALD (with demonstrated self-limiting growth) at room temperature. Room temperature ALD processes are of particular interest as a means to enable deposition on thermally-sensitive substrates,^[25] to minimize problems with agglomeration of low-melting films (e.g. Cu),^[32] and to enable ALD using less complex (and less expensive) ALD reactors. Room temperature thermal ALD methods can also be beneficial for high-throughput roll-to-roll ALD techniques,^[25] and for area-selective ALD using small molecule inhibitors,^[33] where inhibitor desorption and undesired reactivity can be minimized at low temperature.

Thin (<10 nm) ALD-grown antimony films may find applications in monoatomic phase change memory, nanophotonics, optoelectronics, or for the preparation of antimony-doped silicon or germanium.

2.6 – Future Work Pertaining to Chapter 2

Tris(trimethylsilyl)antimony (**2-1**) was utilized in combination with SbCl_3 to deposit elemental antimony on silica and hydrogen-terminated silicon by ALD at deposition temperatures of 23-65 °C. The successful utilization of dechlorosilylation as a thermodynamic driving force for element deposition could potentially be expanded to other main group elements. For example, elemental tin or germanium ALD may be achievable using a combination of $\text{Sn}(\text{SiMe}_3)_4$ and SnCl_4 or $\text{Ge}(\text{SiMe}_3)_4$ and GeCl_4 (Scheme 2.3). At present, there is no reported thermal ALD process for germanium, and

the single reported process for tin has been discussed in Section 1.4.1.1. The synthesis of these silyl compounds has been previously reported^[48-53] but their volatility and thermal stability has not previously been investigated.



Scheme 2.3: Proposed reaction of a main group tris(trimethylsilyl) compound as the precursor and an element chloride as the co-reactant to deposit the pure main group element.

2.7 – References for Chapter 2

- [1] V. Miikkulainen, M. Leskelä, M. Ritala, R. L. Puurunen. Crystallinity of inorganic films grown by atomic layer deposition: Overview and general trends. *J. Appl. Phys.* **2013**, *113*, 021301.
- [2] D. J. Hagen, M. E. Pemble, M. Karppinen. Atomic layer deposition of metals: Precursors and film growth. *Appl. Phys. Rev.* **2019**, *6*, 041309.
- [3] D. J. H. Emslie, P. Chadha, J. S. Price. Metal ALD and pulsed CVD: Fundamental reactions and links with solution chemistry. *Coord. Chem. Rev.* **2013**, *257*, 3282-3296.
- [4] T. J. Knisley, L. C. Kalutarage, C. H. Winter. Precursors and chemistry for the atomic layer deposition of metallic first row transition metal films. *Coord. Chem. Rev.* **2013**, *257*, 3222-3231.
- [5] K. J. Blakeney, C. H. Winter. Atomic Layer Deposition of Aluminum Metal Films Using a Thermally Stable Aluminum Hydride Reducing Agent. *Chem. Mater.* **2018**, *30*, 1844-1848.
- [6] E. C. Stevens, M. B. M. Mousa, G. N. Parsons. Thermal atomic layer deposition of Sn metal using SnCl₄ and a vapor phase silyl dihydropyrazine reducing agent. *J. Vac. Sci. Technol., A* **2018**, *36*, 06A106.
- [7] V. Pore, K. Knapas, T. Hatanpää, T. Sarnet, M. Kemell, M. Ritala, M. Leskelä, K. Mizohata. Atomic Layer Deposition of Antimony and its Compounds Using Dechlorosilylation Reactions of Tris(triethylsilyl)antimony. *Chem. Mater.* **2011**, *23*, 247-254.
- [8] L. X. Cheng, V. Adinolfi, S. L. Weeks, S. V. Barabash, K. A. Littau. Conformal deposition of GeTe films with tunable Te composition by atomic layer deposition. *J. Vac. Sci. Technol., A* **2019**, *37*, 020907.
- [9] M. Salinga, B. Kersting, I. Ronneberger, V. P. Jonnalagadda, X. T. Vu, M. Le Gallo, I. Giannopoulos, O. Cojocaru-Mirédin, R. Mazzarello, A. Sebastian. Monatomic phase change memory. *Nat. Mater.* **2018**, *17*, 681-685.
- [10] W. Zhang, E. Ma. Single-element glass to record data. *Nat. Mater.* **2018**, *17*, 654-655.
- [11] Y. F. Hu, Q. Q. Qiu, X. Q. Zhu, T. S. Lai. Ultrafast crystallization in nanoscale phase change film of monobasic antimony. *Appl. Surf. Sci.* **2020**, *505*, 144337.
- [12] F. Y. Jiao, B. Chen, K. Y. Ding, K. L. Li, L. Wang, X. R. Zeng, F. Rao. Monatomic 2D phase-change memory for precise neuromorphic computing. *Applied Materials Today* **2020**, *20*, 100641.
- [13] J. B. Xu, Y. F. Hu, T. S. Lai, Y. K. Xu, S. Sun. Improved thermal stability and contact of antimony film by the interlayer HfO₂. *J. Mater. Sci. Mater. Electron.* **2020**, *31*, 8052-8058.
- [14] P. Noé, C. Vallée, F. Hippert, F. Fillot, J.-Y. Raty. Phase-change materials for non-volatile memory devices: from technological challenges to materials science issues. *Semicond. Sci. Technol.* **2018**, *33*, 013002.

- [15] M. Wuttig, H. Bhaskaran, T. Taubner. Phase-change materials for non-volatile photonic applications. *Nat. Photon.* **2017**, *11*, 465-476.
- [16] For a review on the use of ALD to deposit phase change memory materials, see: Lee, Y. K.; Yoo, C.; Kim, W.; Jeon, J. W.; Hwang, C. S. Atomic layer deposition of chalcogenides for next-generation phase change memory, *J. Mater. Chem. C* **2021**, *9*, 3708-3725.
- [17] Z. G. Cheng, T. Milne, P. Salter, J. S. Kim, S. Humphrey, M. Booth, H. Bhaskaran. Antimony thin films demonstrate programmable optical nonlinearity. *Science Advances* **2021**, *7*, eabd7097.
- [18] L. Ye, M. P. de Jong, T. Kudernac, W. G. van der Wiel, J. Huskens. Doping of semiconductors by molecular monolayers: monolayer formation, dopant diffusion and applications. *Mater. Sci. Semicond. Process.* **2017**, *62*, 128-134.
- [19] J. O'Connell, S. Biswas, R. Duffy, J. D. Holmes. Chemical approaches for doping nanodevice architectures. *Nanotechnology* **2016**, *27*, 342002.
- [20] C. F. Zhang, S. N. Chang, Y. P. Dan. Advances in ultrashallow doping of silicon. *Adv. Phys.: X* **2021**, *6*, 1871407.
- [21] Most MLD studies have focused on phosphorus or boron as the dopant. However, monolayer doping (MLD) of germanium by antimony has been reported: Alphazan, T.; Alvarez, A. D.; Martin, F.; Grampeix, H.; Enyedi, V.; Martinez, E.; Rochat, N.; Veillerot, M.; Dewitte, M.; Nys, J. P.; Berthe, M.; Stiévenard, D.; Thieuleux, C.; Grandidier, B. Shallow Heavily Doped n++ Germanium by Organo-Antimony Monolayer Doping, *ACS Appl. Mater. Interfaces* **2017**, *9*, 20179-20187. Additionally, related nanometer-scale doping of silicon with antimony has been described: Popere, B. C.; Russ, B.; Heitsch, A. T.; Trefonas, P.; Segalman, R. A. Large-Area, Nanometer-Scale Discrete Doping of Semiconductors via Block Copolymer Self-Assembly, *Adv. Mater. Interfaces* **2015**, *2*, 1500421.
- [22] Carbon-free monolayer doping (MLD) of an OH-terminated silicon surface was recently achieved using PCl_3 as the dopant-carrying molecule: Li, K.; Zhang, J. Y.; Chang, S. N.; Wei, H.; Zhang, J. J.; Dan, Y. P. Full Activation of Dopants by Carbon-free Self-Assembled Molecular Monolayer Doping, *ACS Appl. Electron. Mater.* **2021**, *3*, 3346-3351.
- [23] For doping of silicon with boron via MLD, an elegant strategy to increase the level of doping involved the use of carborane clusters containing ten boron atoms: Ye, L.; Gonzalez-Campo, A.; Nunez, R.; de Jong, M. P.; Kudernac, T.; van der Wiel, W. G.; Huskens, J. Boosting the Boron Dopant Level in Monolayer Doping by Carboranes, *ACS Appl. Mater. Interfaces* **2015**, *7*, 27357-27361.
- [24] T. Nam, J. M. Kim, M. K. Kim, H. Kim, W. H. Kim. Low-temperature Atomic Layer Deposition of TiO_2 , Al_2O_3 , and ZnO Thin Films. *J. Korean Phys. Soc.* **2011**, *59*, 452-457.
- [25] S. E. Potts, H. B. Profijt, R. Roelofs, W. M. M. Kessels. Room-Temperature ALD of Metal Oxide Thin Films by Energy-Enhanced ALD. *Chem. Vap. Deposition* **2013**, *19*, 125-133.

- [26] M. Putkonen, L. Niinisto. Atomic layer deposition of B₂O₃ thin films at room temperature. *Thin Solid Films* **2006**, *514*, 145-149.
- [27] A. Pilli, J. Jones, V. Lee, N. Chugh, J. Kelber, F. Pasquale, A. LaVoie. In situ XPS study of low temperature atomic layer deposition of B₂O₃ films on Si using BCl₃ and H₂O precursors. *J. Vac. Sci. Technol., A* **2018**, *36*, 061503.
- [28] J. D. Ferguson, E. R. Smith, A. W. Weimer, S. M. George. ALD of SiO₂ at room temperature using TEOS and H₂O with NH₃ as the catalyst. *J. Electrochem. Soc.* **2004**, *151*, G528-G535.
- [29] D. Arl, V. Roge, N. Adjeroud, B. R. Pistillo, M. Sarr, N. Bahlawane, D. Lenoble. SiO₂ thin film growth through a pure atomic layer deposition technique at room temperature. *RSC Adv.* **2020**, *10*, 18073-18081.
- [30] Thermal ALD of tungsten has been reported at 152-327 °C (using WF₆/Si₂H₆). Room temperature tungsten deposition (using WF₆/Si₂H₆) was also investigated, but extremely long WF₆ pulses were required to achieve saturation, and the authors noted that the WF₆ reaction did not proceed to completion. See: (a) Klaus, J. W.; Ferro, S. J.; George, S. M. Atomic layer deposition of tungsten using sequential surface chemistry with a sacrificial stripping reaction, *Thin Solid Films* **2000**, *360*, 145-153; (b) Elam, J. W.; Nelson, C. E.; Grubbs, R. K.; George, S. M. Kinetics of the WF₆ and Si₂H₆ surface reactions during tungsten atomic layer deposition, *Surf. Sci.* **2001**, *479*, 121-135.
- [31] Room temperature copper deposition by an ALD-like process has been reported (using Cu(hfac)₂/pyridine/H₂), but self-limiting growth was not demonstrated: Kang, S.-W.; Yun, J.-Y.; Chang, Y. H. Growth of Cu Metal Films at Room Temperature Using Catalyzed Reactions, *Chem. Mater.* **2010**, *22*, 1607-1609.
- [32] Z. Guo, H. Li, Q. Chen, L. J. Sang, L. Z. Yang, Z. W. Liu, X. W. Wang. Low-Temperature Atomic Layer Deposition of High Purity, Smooth, Low Resistivity Copper Films by Using Amidinate Precursor and Hydrogen Plasma. *Chem. Mater.* **2015**, *27*, 5988-5996.
- [33] G. N. Parsons, R. D. Clark. Area-Selective Deposition: Fundamentals, Applications, and Future Outlook. *Chem. Mater.* **2020**, *32*, 4920-4953.
- [34] J. Yarbrough, A. B. Shearer, S. F. Bent. Next generation nanopatterning using small molecule inhibitors for area-selective atomic layer deposition. *J. Vac. Sci. Technol., A* **2021**, *39*, 021002.
- [35] Y. Hwang, B. M. Nguyen, S. A. Dayeh. Atomic layer deposition of platinum with enhanced nucleation and coalescence by trimethylaluminum pre-pulsing. *Appl. Phys. Lett.* **2013**, *103*, 263115.
- [36] C. de Paula, N. E. Richey, L. Zeng, S. F. Bent. Mechanistic Study of Nucleation Enhancement in Atomic Layer Deposition by Pretreatment with Small Organometallic Molecules. *Chem. Mater.* **2020**, *32*, 315-325.
- [37] C. de Paula, D. Bobb-Semple, S. F. Bent. Increased selectivity in area-selective ALD by combining nucleation enhancement and SAM-based inhibition. *J. Mater. Res.* **2021**, *36*, 582-591.

- [38] M. M. Minjauw, H. Rijckaert, I. Van Driessche, C. Detavemier, J. Dendooven. Nucleation Enhancement and Area-Selective Atomic Layer Deposition of Ruthenium Using RuO₄ and H₂ Gas. *Chem. Mater.* **2019**, *31*, 1491-1499.
- [39] R. Khan, B. Shong, B. G. Ko, J. K. Lee, H. Lee, J. Y. Park, I. K. Oh, S. S. Raya, H. M. Hong, K. B. Chung, E. J. Luber, Y. S. Kim, C. H. Lee, W. H. Kim, H. B. R. Lee. Area-Selective Atomic Layer Deposition Using Si Precursors as Inhibitors. *Chem. Mater.* **2018**, *30*, 7603-7610.
- [40] T. L. Liu, K. L. Nardi, N. Draeger, D. M. Hausmann, S. F. Bent. Effect of Multilayer versus Monolayer Dodecanethiol on Selectivity and Pattern Integrity in Area-Selective Atomic Layer Deposition. *ACS Appl. Mater. Interfaces* **2020**, *12*, 42226-42235.
- [41] N. N. Greenwood, A. Earnshaw, In *Chemistry of the Elements*, 2nd Ed.; Butterworth-Heinemann, Oxford, **1998**; p 522.
- [42] R. L. Puurunen. Surface chemistry of atomic layer deposition: A case study for the trimethylaluminum/water process. *J. Appl. Phys.* **2005**, *97*, 121301.
- [43] R. L. Puurunen, W. Vandervorst. Island growth as a growth mode in atomic layer deposition: A phenomenological model. *J. Appl. Phys.* **2004**, *96*, 7686-7695.
- [44] Some examples of ALD processes exhibiting substrate-enhanced growth are: (a) W ALD on Al₂O₃, (b) Sb₂Se₃ ALD on ZnS, (c) Al₂O₃ ALD on Si₃N₄, and (d) TiO₂ ALD on Ru (when O₃ is used as the co-reactant). See: (a) Wind, R. W.; Fabreguette, F. H.; Sechrist, Z. A.; George, S. M. Nucleation period, surface roughness, and oscillations in mass gain per cycle during W atomic layer deposition on Al₂O₃, *J. Appl. Phys.* **2009**, *105*, 074309. (b) Mahuli, N.; Halder, D.; Paul, A.; Sarkar, S. K. Atomic Layer Deposition of an Sb₂Se₃ Photoabsorber Layer Using Selenium Dimethyldithiocarbamate as a New Se Precursor, *Chem. Mater.* **2019**, *31*, 7434-7442. (c) Lamagna, L.; Wiemer, C.; Perego, M.; Spiga, S.; Rodríguez, J.; Coll, D. S.; Grillo, M. E.; Klejna, S.; Elliott, S. D. Mechanisms for Substrate-Enhanced Growth during the Early Stages of Atomic Layer Deposition of Alumina onto Silicon Nitride Surfaces, *Chem. Mater.* **2012**, *24*, 1080-1090. (d) Lee, S. W.; Han, J. H.; Kim, S. K.; Han, S.; Lee, W.; Hwang, C. S. Role of Interfacial Reaction in Atomic Layer Deposition of TiO₂ Thin Films Using Ti(O-*i*Pr)₂(tmhd)₂ on Ru or RuO₂ Substrates, *Chem. Mater.* **2011**, *23*, 976-983.
- [45] After the initial substrate has been covered, the different GPCs observed on H-Si and SiO₂/Si could perhaps be due to subtle differences in morphology or crystallinity at the surface of the growing antimony film. Similar phenomena have been reported for thermal or plasma-enhanced ALD of Ru, NiO and TiO₂. See: (a) Hwang, J. M.; Han, S. M.; Yang, H.; Yeo, S.; Lee, S. H.; Park, C. W.; Kim, G. H.; Park, B. K.; Byun, Y.; Eom, T.; Chung, T. M. Atomic layer deposition of a ruthenium thin film using a precursor with enhanced reactivity, *J. Mater. Chem. C* **2021**, *9*, 3820-3825, (b) Song, S. J.; Lee, S. W.; Kim, G. H.; Seok, J. Y.; Yoon, K. J.; Yoon, J. H.; Hwang, C. S.; Gatineau, J.; Ko, C. Substrate Dependent Growth Behaviors of Plasma-Enhanced Atomic Layer Deposited Nickel Oxide Films for Resistive Switching Application, *Chem. Mater.* **2012**, *24*, 4675-4685, (c) Won, S. J.; Suh, S.;

- Lee, S. W.; Choi, G. J.; Hwang, C. S.; Kim, H. J. Substrate Dependent Growth Rate of Plasma-Enhanced Atomic Layer Deposition of Titanium Oxide Using N₂O Gas, *Electrochem. Solid-State Lett.* **2010**, *13*, G13-G16.
- [46] At 95, 125 and 150 °C, pulse times of 1.0 or 2.0 s were also investigated for deposition on H-Si. At 95 °C, 1.0 and 2.0 s pulses led to slightly thicker films (after 1000 cycles, average film thickness values of 39 and 41 nm were obtained, respectively, vs 33 nm using 0.4 s pulses). The films now appeared visibly uniform, and VASE showed minimal variation in film thickness at different points on the wafer. By contrast, at 125 and 150 °C, 1.0s pulses still led to visibly patchy films, and VASE indicated substantial variations in film thickness at different points on the wafer.
- [47] Use of an additional 20 minute argon purge between pre-treatment and the start of ALD was tested for (a) deposition on H-Si using SbCl₃ pre-treatment (50 x 0.8s pulses) prior to ALD (50 cycles using 0.8s pulses), and (b) deposition on SiO₂/Si using Sb(SiMe₃)₃ pre-treatment (50 x 0.4s pulses) prior to ALD (50 cycles using 0.4s pulses). The former yielded a film thickness of 6.5 nm (*cf.* 6.7 nm without the 20 minute argon purge), and the latter yielded a film thickness of 7.2 nm (*cf.* 7.1 nm without the 20 minute argon purge).
- [48] L. Rösch, H. Neumann. Synthese und Eigenschaften der ersten Organosilyl-Gallium-Verbindungen. *Angew. Chem.* **1980**, *92*, 62-63.
- [49] A. G. Brook, F. Abdesaken, H. Söllradl. Synthesis of Some Tris(trimethylsilyl)germyl Compounds. *J. Organomet. Chem.* **1986**, *299*, 9-13.
- [50] H. Gilman, C. L. Smith. Tetrakis(trimethylsilyl)silane. *J. Organomet. Chem.* **1967**, *8*, 245-253.
- [51] N. Auner, U. Klingbiel, Synthetic Methods in Organometallic and Inorganic Chemistry. Vol. 2, Thieme Medical Publishers, **1996**.
- [52] T. Hatanpää, V. Pore, M. Ritala, M. Leskelä. Alkylsilyl Compounds of Selenium and Tellurium: New Precursors for ALD. *ECS Trans.* **2009**, *25*, 609-616.
- [53] A. N. Beecher, X. Yang, J. H. Palmer, A. L. LaGrassa, P. Juhas, S. J. Billinge, J. S. Owen. Atomic Structures and Gram Scale Synthesis of Three Tetrahedral Quantum Dots. *J. Am. Chem. Soc.* **2014**, *136*, 10645-10653.

Chapter 3

Synthesis of Silyl- and Germylboranes and Investigation of their Suitability as Precursors for Boron Atomic Layer Deposition

3.1 – Introductory Preface

Elemental boron and boron-containing materials have a number of applications in industry and research. For instance, boron nitride is used as a ceramic or a protective coating layer due to its extreme hardness, high thermal conductivity, and corrosion-resistant properties.^[1] Due to its hygroscopicity, boron oxide is not utilized as a pure binary material, but it is a budding material of interest as an alternative Group 13 oxide dopant in place of indium oxide.^[2,3]

Boron is utilized as an elemental semiconductor and p-type dopant for Si semiconductors.^[4] In the last decade, boron-doped diamond (BDD) has gained traction as a superconducting Group-IV electrode material, possessing the largest known electrochemical potential window.^[5-8] The incorporation of boron atoms into the diamond lattice in concentrations around 3×10^{20} B atoms per cm^3 lowers the very wide band gap of diamond and the resultant material demonstrates metal-like conductivity tunable based on the dopant concentration.

Boron thin films in the semiconductor industry are currently fabricated using high-temperature PVD or CVD methods. These techniques often employ B_2H_6 or BCl_3 as boron sources and deposition temperatures over 1,000 K.^[9] Deposition of BDD currently requires plasma-assisted CVD of a carbon-containing gas such as methane in the presence of hydrogen and B_2H_6 , with plasma being generated by microwaves or hot

filaments, requiring high plasma and substrate temperatures (2,500 and 1,200 K, respectively) for deposition.^[6]

The development of a new process for elemental boron deposition by thermal ALD would provide a novel low-temperature, plasma-free technique. This chapter focuses on the design and attempted syntheses of silyl- and/or germlyboranes (e.g. B(ER₃)₃; E = Si or Ge) to be utilized as precursors, in combination with boron halides as co-reactants, for ALD of elemental boron. This process (Scheme 3.1) mirrors the ALD process discussed in Chapter 2 (Scheme 2.1), which also exploits the thermodynamically favourable formation of tetrel-halide bonds as a driving force.



Scheme 3.1: Proposed reaction of a tri(silyl)borane or tri(germyl)borane precursor with a boron trihalide co-reactant.

3.1.1 – ALD of Boron-Containing Films

Boron-containing films grown by ALD can be divided into three categories: boron nitride (BN), boron oxide (B₂O₃), and metal boron oxides, as summarized in Table 3.1.

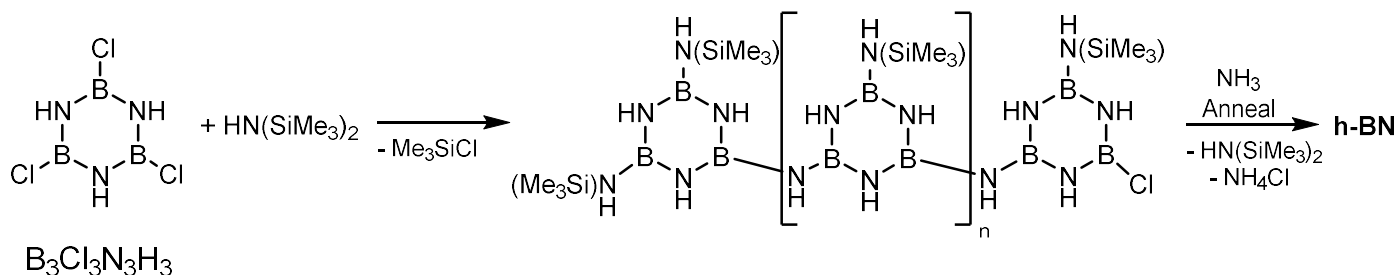
Table 3.1: Reported thermal ALD processes to deposit boron-containing films.

Material	Boron Precursor	Co-Reactant(s)	Year
BN	BCl ₃	NH ₃	2002 ^[10]
	BBr ₃	NH ₃	2002 ^[11]
			2005 ^[12]
	B ₃ Cl ₃ N ₃ H ₃	HN(SiMe ₃) ₂	2017 ^[13]
B ₂ O ₃	BBr ₃	H ₂ O	2006 ^[14]
	BCl ₃	H ₂ O, O ₂	2018 ^[15]
Li ₃ BO ₃ -Li ₂ CO ₃	B(O ^t Pr) ₃	Li(O ^t Bu), O ₃	2018 ^[16]
CaB ₂ O ₄	CaTp ₂	H ₂ O	2010 ^[17]
SrB _x O _y	SrTp ₂	H ₂ O	2011 ^[18]
BaB ₂ O ₄	Ba(Tp ^{Et2}) ₂	H ₂ O	2009 ^[19]
Mn ₂ (BO ₃) ₂	MnTp ₂	O ₃	2016 ^[20]
CoB ₂ O ₄	CoTp ₂	O ₃	2016 ^[20]
ZnB _x O _y	B ₂ H ₆	ZnEt ₂ , H ₂ O	1997 ^[21]
	B(O ^t Pr) ₃	ZnEt ₂ , H ₂ O	2015 ^[2]

In 2002, two new processes for BN ALD were separately reported. Uniform and conformal BN film deposition was observed at 500 K on ZrO₂ particles using separated pulses of BCl₃ and NH₃.^[10] Although the authors described the deposition as an ALD process, self-limiting growth was not investigated. BN films were also deposited on silica at 400 and 750 K using BBr₃ and NH₃.^[11] Self-limiting growth (0.45 Å) was observed at

both temperatures, and films grown at 400 K were amorphous while those grown at 750 K were turbostratic (a crystal lattice form featuring disordered basal planes^[22]). The authors later demonstrated that the GPC of this process can be increased to 1.2 Å while maintaining self-limiting growth by photochemical activation of BBr_3 in a process called laser-assisted atomic layer deposition (LALD), whereby a gaseous reactant is irradiated by a laser beam focused above and parallel to the substrate surface which can induce the reactant's dissociation into more reactive radical species;^[12] laser irradiation of NH_3 made no difference to the GPC.

Newer research in BN ALD includes deposition on membranes for applications in nanofluidics.^[23] Additionally, Marichy and coworkers reported an alternative process for BN ALD that avoids the use and production of highly corrosive chemicals by employing the reaction of trichloroborazine ($\text{B}_3\text{Cl}_3\text{N}_3\text{H}_3$) with hexamethyldisilazane ($\text{HN}(\text{SiMe}_3)_2$), followed by high temperature annealing under an atmosphere of argon and ammonia.^[13] The process proposed based on solution-state deposition experiments involves elimination of trimethylchlorosilane upon exposure of hexamethyldisilazane to the $\text{BCl}_3\text{N}_3\text{H}_3$ -treated substrate. The resulting polyborazylene (Scheme 3.2) is then thermally annealed (600 °C) under a partial atmosphere of NH_3 to form hexagonal BN. Uniform and conformal films were observed after deposition at 80-150 °C and post-deposition annealing (1.85 Å growth rate). The authors state that the self-limiting nature of the process was demonstrated by the linear relationship between film thickness and the number of cycles, and the reproducibility of deposition; however, the effect of varying pulse times of either reagent was not investigated.



Scheme 3.2: Reaction for the generation of hexagonal boron nitride (h-BN) via ALD using trichloroborazine and hexamethyldisilazane to form a polyborazylene, and subsequent thermal annealing under a partial atmosphere of ammonia. Adapted from reference [13].

ALD of boron oxide (B_2O_3) thin films was first reported using BBr_3 and H_2O .^[14] Self-limiting growth was observed at 20 °C deposition temperature (0.75 Å), while minimal growth occurred at 50 °C and no film deposited between 100-400 °C which the authors state is likely due to the formation of H_3BO_3 at higher temperatures (which is volatile in the presence of H_2O vapours). The hygroscopic B_2O_3 layer was protected by an ALD-grown Al_2O_3 layer before exposure to air. Over a decade later, a second room temperature B_2O_3 ALD process was reported by Kelber and coworkers using BCl_3 and H_2O ,^[15] which resulted in a significantly higher GPC of 2.5 Å, although minor Cl contamination was observed at the Si/ B_2O_3 interface. The authors also investigated BCl_3/O_2 as a potential B_2O_3 ALD process but found that there was negligible growth at room temperature, and at 650 K, Cl contamination was observed in the growing film.

Boron-doped ZnO (B:ZnO) thin films were studied before the development of the first B_2O_3 ALD process.^[21] Yamada and coworkers grew ZnO thin films by ALD at temperatures between 105 and 165 °C using diethylzinc ($ZnEt_2$) and H_2O . B-doped ZnO was obtained by pulsing B_2H_6 during the $ZnEt_2$ pulses. While the self-limiting nature of the ZnO process was confirmed, the same was not done for B:ZnO.

A new process for depositing B:ZnO thin films at 150 °C was developed using triisopropoxyborane ($B(O^iPr)_3$) as a safe alternative to B_2H_6 .^[2] In this process, $B(O^iPr)_3$ was pulsed after each $ZnEt_2/H_2O$ cycle and was followed by a second water pulse, essentially forming a supercycle consisting of one ZnO cycle and one B_2O_3 cycle. The authors noted that it was possible to grow B_2O_3 dopant layers incorporated into a supercycle at elevated temperatures despite their and previous researchers' previously unsuccessful attempts at metal-free B_2O_3 deposition using BCl_3 or $B(O^iPr)_3$ in combination with H_2O .^[2,15]

Lithium borate-carbonate films grown by ALD were investigated for use as a glassy solid electrolyte for Li batteries using supercycles consisting of one $Li(O^iBu)/O_3$ cycle and one $B(O^iPr)_3/O_3$ cycle.^[16] Self-limiting Li_3BO_3 - Li_2CO_3 growth was observed at the tested substrate temperatures (200-260 °C), and the ratio of Li_3BO_3 to Li_2CO_3 in the films could be controlled by the deposition temperature. Negligible growth was observed by QCM for the binary $B(O^iPr)_3/O_3$ process, consistent with previous reports.^[2,15]

The development of metal boron oxide ALD has been dominated by metal precursors featuring tris(pyrazolyl)borate (Tp; Figure 3.1) ligands; an approach first utilized for ALD by the Winter group.^[17-20] Metal complexes of the type $MTpR_2$ were shown to have an optimal combination of thermal stability, volatility, and reactivity towards oxygen-containing co-reactants (H_2O or O_3).^[24] Additionally, the precursors contain a 1:2 metal to boron ratio that is maintained during the ALD processes, with the exception of $Mn_3(BO_3)_2$ and $SrB_{1.65}O_{3.29}$ ALD. In the case of $Mn_3(BO_3)_2$ ALD, the authors attributed the 3:2 metal to boron ratio to loss of B_2O_3 at high deposition temperatures, arising from the oxidizing ability of the high valent metal (Mn^{n+} , $n>2$) species present after oxidation of one

Tp ligand by oxo species on the substrate surface. Metal boron oxide ALD using MTp^{R_2} precursors ($\text{M} = \text{Ca}, \text{Sr}, \text{Ba}, \text{Mn}, \text{Co}$), in combination with H_2O or O_3 (Table 3.1), was observed at deposition temperatures ranging from 250 to 375 °C.^a

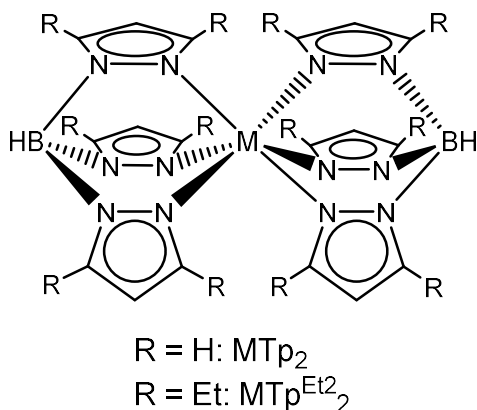


Figure 3.1: Chemical structure of MTp_2 and $\text{MTp}^{\text{Et}_2}_2$.

3.1.2 – Previously Reported Silylboron and Germylboron Compounds

The aim of this section is to provide an overview of research in the field of oligosilyl- and oligogermylboron compounds, with a focus on their synthesis and characterization. Tables 3.2 and 3.3 provide a comprehensive list of all reported boron-containing molecules featuring two or more Si-B and/or Ge-B bonds. It should be noted that the entries are limited to small molecules; in particular, molecules containing boron or silicon clusters have been excluded.^[25-27] The molecules discussed consist nearly exclusively of oligosilylboron compounds as there are presently no reported mixed silylgermylboron

^a In these reports, Winter and coworkers identified self-limiting growth by demonstrating a constant growth rate with varying pulse times at one deposition temperature. They then demonstrated nearly constant growth rates over a range of temperatures. The exception to this method was CoB_2O_4 ALD, for which only 325 °C deposition was investigated.

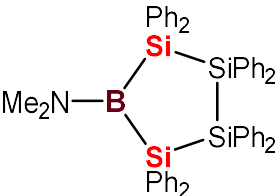
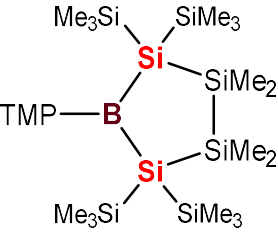
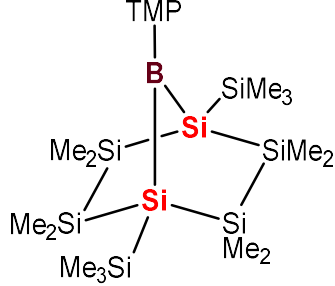
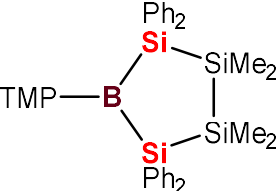
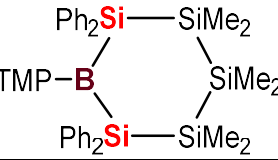
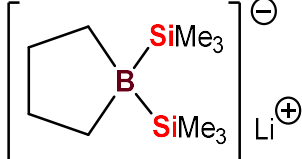
compounds, and only one digermylborane, $(\text{Ph}_3\text{Ge})_2\text{B}(\text{TMP})$,^[28] reported by Nöth and coworkers (the same group has reported a mixed germylstannylborane^[29] which will not be discussed further).

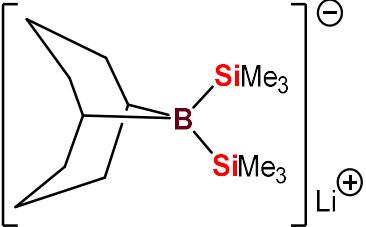
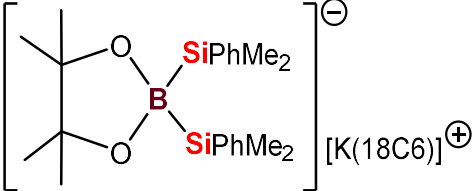
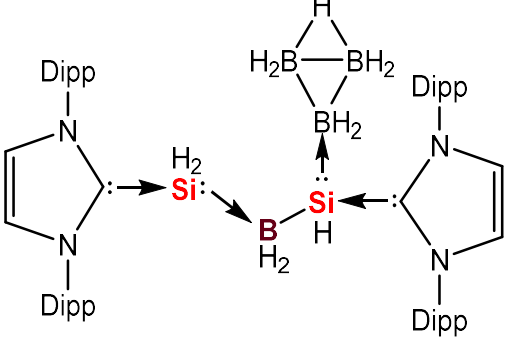
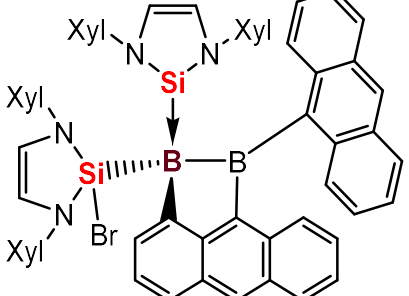
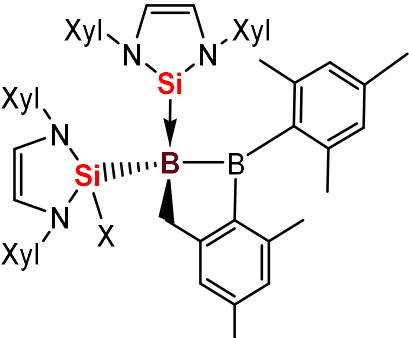
Table 3.2: Reported boranes or borates of the type $(\text{R}_3\text{E})_3\text{B}$, $[(\text{R}_3\text{E})_4\text{B}]^-$, and $[(\text{R}_3\text{E})_3\text{BX}]^-$, where E = Si or Ge, and X = any other atom. The ^{11}B NMR chemical shifts, B-E bond distances, and E-B-E bond angles are listed if the ^{11}B NMR spectrum or X-ray crystal structure of the compound has been reported.

Entry	Compound	^{11}B NMR chemical shifts (ppm)	B-E (Å); E-B-E (°)	Year
1	$\text{Li}[(\text{Me}_3\text{Si})_3\text{B}(\text{NMe}_2)]$	-21.7 ($^1J_{\text{B,Si}} = -54$ Hz)	-	1981 ^[30]
2	$\text{Li}[(\text{Me}_3\text{Si})_4\text{B}]$	-53.4 (C_6D_6) ($^1J_{\text{B,Si}} = -48$ Hz)	2.025(2)-2.027(2); avg. 109.3	1982 ^[31] , 1999 ^[32]
3	$\text{Li}[(\text{Me}_3\text{Si})_3\text{B}(\text{CH}_3)]$	-45.4 (C_6D_6) ($^1J_{\text{B,Si}} = -53$ Hz)	2.017(2)-2.034(2); avg. 109.2	1982 ^[31] , 1999 ^[32]
4	$(\text{Ph}_3\text{Si})_3\text{B}$	-	-	1984 ^[33,34]
5	$\text{Li}[(\text{PhMe}_2\text{Si})_3\text{B}(\text{OMe})]$	-7.5 (C_6D_6)	2.043(5)-2.073(5); 105.9(2)-110.6(2)	2017 ^[35]
6	$\text{Li}[(\text{PhMe}_2\text{Si})_3\text{B}(\text{O}^i\text{Pr})]$	-7.8 (C_6D_6)	2.040(2)-2.048(2); 108.0(1)-109.4(1)	2017 ^[35]

Table 3.3: Reported boranes or borates of the type $(\text{R}_3\text{E})_2\text{BX}$ or $[(\text{R}_3\text{E})_2\text{BX}_2]^-$, where E = Si or Ge, and X = any other atom. The ^{11}B NMR chemical shifts, B-E bond distances, and E-B-E bond angles are listed if the ^{11}B NMR spectrum or X-ray crystal structure of the compound has been reported.

Entry	Compound	^{11}B NMR chemical shifts (ppm)	B-E (Å); E-B-E (°)	Year
7	$(\text{Ph}_3\text{Si})_2\text{B}(\text{NEt}_2)$	-	-	1966 ^[36]
8	$(\text{Me}_3\text{Si})_2\text{B}(\text{NMe}_2)$	57.6	-	1981 ^[30]
9	$(\text{Me}_3\text{Si})_2\text{B}(\text{NEt}_2)_2$	56.4	-	1981 ^[30]
10	$(\text{PhMe}_2\text{Si})_2\text{B}(\text{NEt}_2)$	55.7 (C_6D_6)	-	1995 ^[37]
11	$(\text{Ph}_3\text{Si})_2\text{B}(\text{CH}_3)$	-	-	1984 ^[33,34]
12	$(\text{Ph}_3\text{Si})_2\text{B}(\text{Mes})$	-	-	1984 ^[33,34]
13	$(\text{Ph}_3\text{Ge})_2\text{B}(\text{TMP})$	64.0 (C_6D_6)	2.118(3), 2.160(3); 109.5(1)	2001 ^[28]
14	$\{(\text{Me}_3\text{Si})_3\text{Si}\}_2\text{B}(\text{NMe}_2)$	61.0	-	1981 ^[38]
15	$\{(\text{Me}_3\text{Si})_3\text{Si}\}_2\text{B}(\text{OMe})$	36.6 (CDCl_3)	-	1981 ^[38]

Entry	Compound	^{11}B NMR chemical shifts (ppm)	B-E (Å); E-B-E (°)	Year
16	$(t\text{Bu}_3\text{Si})_2\text{BX}$ (X = Cl or F)	F: 106.7 (C_6D_6) (d in hexane, $^1J_{\text{B,F}} = 203$ Hz) Cl: 135.0 (C_6D_6)	F: 2.126(4), 2.103(3); 151.1(2) Cl: 2.127(1); 151.9(1)	2001 ^[39]
17		-	-	1973 ^[40]
18		72.1 (C_6D_6)	2.109(6), 2.112(5); 110.4(2)	2004 ^[41]
19		66.0 (C_6D_6)	-	2004 ^[41]
20		63.77 (CD_2Cl_2)	2.072(2), 2.117(2); 105.44(7)	2019 ^[42]
21		66.30 (CD_2Cl_2)	2.065(2), 2.131(3); 108.5(1)	2019 ^[42]
22		-31.2 (C_6D_6)	-	1982 ^[31]

Entry	Compound	^{11}B NMR chemical shifts (ppm)	B-E (Å); E-B-E (°)	Year
23		-25.3 (C_6D_6)	-	1982 ^[31]
24	$\text{Li}[(\text{Me}_3\text{Si})_2\text{B}(\text{CH}_3)_2]$	-36.9 (C_6D_6) ($^1J_{\text{B,Si}} = -67$ Hz)	-	1982 ^[31] , 1999 ^[32]
25		9.2 (d_8 -THF)	2.094(3); 107.5(2)	2013 ^[43]
26		-29.91 (d_8 -THF)	Single (S): 1.994(8), Dative (D): 1.922(7); 109.1(4)	2011 ^[44]
27		-17.3 (C_6D_6)	S: 2.003(1), D: 1.982(3); 113.1(1)	2017 ^[45]
28		X = F: -28;8 (C_6D_6) X = Cl: -23.2 (C_6D_6)	X = F: S: 1.991(3), D: 1.947(3); 112.2(1) X = Cl: S: 1.998(3), D: 1.969(2); 110.8(1)	2017 ^[45]

Entry	Compound	^{11}B NMR chemical shifts (ppm)	B-E (Å); E-B-E (°)	Year
29		X = Cl: 100 X = Br: 99.2 (solid-state)	X = Cl: 2.025(2), 126.2(2) X = Br: 2.052(3), 2.049(3); 120.1(1)	2016 ^[46]

Mes = Mesityl; TMP = 2,2,6,6-tetramethylpiperidyl; 18C6 = 18-crown-6; Dipp = 2,6-diisopropylphenyl; Xyl = 2,6-dimethylphenyl (xylyl).

The majority of oligosilylboranes have been prepared via a salt metathesis reaction between a haloborane and silyl anion. For example, the only neutral trisilylborane, $(\text{Ph}_3\text{Si})_3\text{B}$ (Entry 4), was reported by Pechaly and West in 1984 from the reaction of boron tribromide and 3 equivalents of triphenylsilyllithium at room temperature.^[33,34] It should be noted that although this compound was successfully isolated in 64% yield and a flame test confirmed the absence of lithium, there is no reported ^{11}B NMR chemical shift nor X-ray crystal structure to corroborate its assignment (titrimetric analysis determined its boron content to be 1.44% in comparison to the theoretical value of 1.37%).

Attempts to form tris(trimethylsilyl)borane from trimethylsilyllithium and trimethoxyborane resulted in the formation of lithium tetrakis(trimethylsilyl)borate (Entry 2) and small amounts of $\text{Li}[(\text{Me}_3\text{Si})_3\text{B}(\text{Me})]$ (Entry 3).^[31] Nöth and coworkers later reported the crystal structure of both lithium borates from their 1:1 co-crystallization.^[32] Nöth continued to report oligosilylboranes and borates for over three decades, with all initial work focused on reactions of trimethylsilyllithium (prepared from the organomercury

precursor, $[\text{Hg}(\text{SiMe}_3)_2]$.^[30] Over time, more boranes and borates were reported featuring bulkier silyl groups such as dimethylphenylsilyl,^[37] tris(trimethylsilyl)silyl ($\{\text{Me}_3\text{Si}\}_3\text{Si}$ -, hypersilyl),^[38] and tri-*tert*-butylsilyl ($t\text{Bu}_3\text{Si}$ -, supersilyl) groups.^[39] Additionally, these compounds often incorporated an amido (R_2N -) substituent bonded to the boron center^[36,37] to promote stability through π -donation from nitrogen to the vacant p orbital on boron.

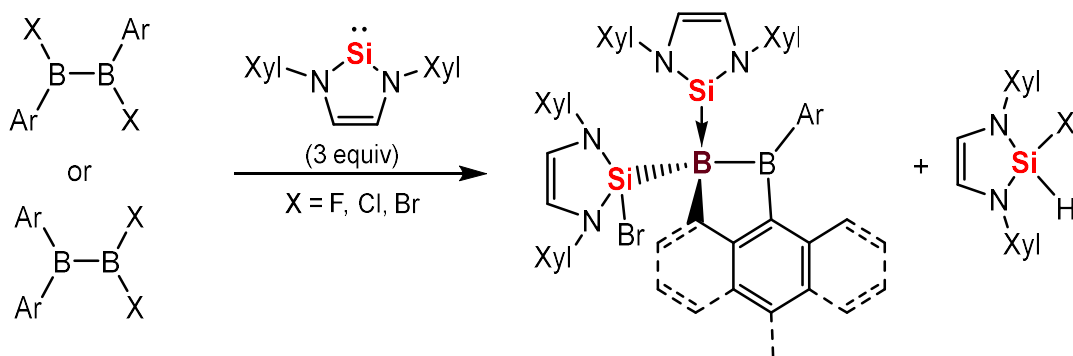
A subset of cyclic and bicyclic disilylamidoboranes have been reported over the last two decades,^[41,42] with a single earlier example from 1974.^[40] These compounds were synthesized via salt metathesis reactions between the corresponding disilyl dianion and an amidodihaloborane (in one report, MgBr_2 was added to the reaction, and was shown to suppress undesired ring fragmentation^[42]). Klausen and coworkers characterized the optical properties of the deeply coloured $(\text{Me}_2\text{Si})_n(\text{Ph}_2\text{Si})_2\text{B}(\text{TMP})$ [$n = 2$ (Entry 20), 3 (Entry 21)] compounds and supported their assignments using DFT analysis.^[42]

The ^{11}B NMR chemical shifts of the three-coordinate boranes and four-coordinate borates were typically in the range of 35 to 70 ppm and -50 to 10 ppm, respectively. Notable exceptions are the reported chemical shifts of $t\text{Bu}_3\text{Si}_2\text{BX}$ (Entry 16; $\text{X} = \text{F}$ or Cl) which were 107 and 135 ppm, respectively.^[39] The reported Si-B bond lengths of the boranes and borates described thus far ranged between 2.017(2) and 2.131(3) Å. The reported E-B-E bond angles varied greatly depending on the steric bulk of the silyl groups and other substituents on boron (105.44(7)-151.9(1)° for boranes; 105.9(2)-110.6(2)° for borates).

A unique class of compounds that has emerged in the last decade feature bonding between boron and one or two silylenes. Silylenes have one lone pair of electrons and one vacant p orbital, but are poorer σ -donors and stronger π -acceptors than carbenes.^[45,47] However, the syntheses of silylene-containing boranes (Entries 26-28) or disilylboranes from silylenes (Entry 29) are not as straightforward as examples discussed earlier in this section, and in some cases their mechanisms are not fully established.

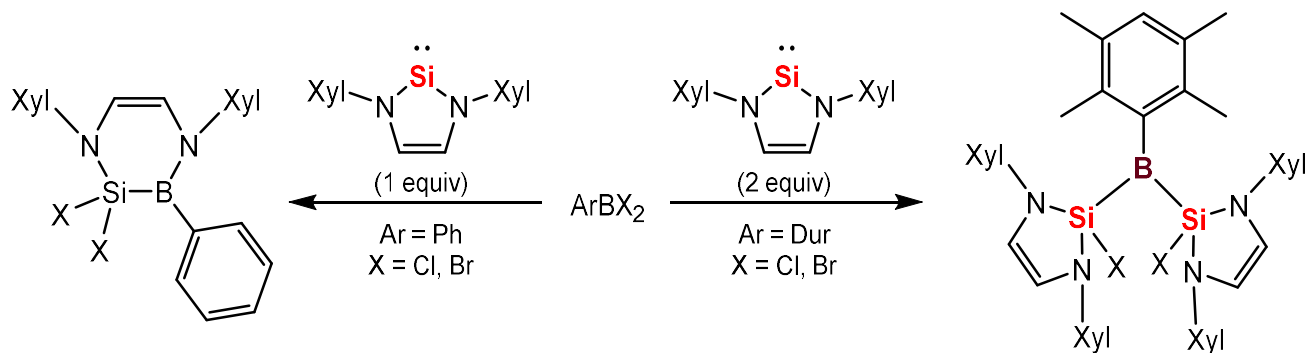
In 2011, Robinson and coworkers reported the reaction of an NHC-stabilized disilicon compound, $\text{LSi}=\text{SiL}$ ($\text{L} = \text{:C}\{\text{N}(2,6\text{-}i\text{Pr}_2\text{C}_6\text{H}_3)\text{CH}_2\}_2$), with $\text{BH}_3\cdot\text{THF}$, resulting in cleavage of the $\text{Si}=\text{Si}$ double bond and insertion of BH_3 to form a (silylene)silyldihydroborane (Entry 26), which was described by the authors as featuring one boron-silicon single bond and one dative bond between the silylene silicon and boron.^[44]

Braunschweig and coworkers synthesized a series of silyl(silylene)diborane complexes (Entries 27 and 28) via the reactions of 3 equivalents of an N-heterocyclic silylene (NHSi) with one equivalent of a dihalodiborane(4).^[45] This reaction involves (a) B-X insertion upon the nucleophilic addition of the first 2 equivalents of the NHSi to the diborane, and (b) C-H borylation, which proceeds by addition of a third NHSi equivalent, activation of an aryl C-H bond, and release of one equivalent of a hydrohalosilane (Scheme 3.3).



Scheme 3.3: Reaction scheme for the preparation of silyl(silylene)diboranes (Entries 27 and 28 in Table 3.3). Adapted from reference [45].

Additionally, Braunschweig and coworkers prepared disilylboranes (Entry 29) via the reactions between 2 equivalents of an NHSi and (Dur)BX₂ (Dur = 2,3,5,6-tetramethylphenyl; X = Cl or Br).^[46] By contrast, the authors found that utilizing a smaller aryldihaloborane, PhBX₂, led to the rapid formation of a six-membered silaborinine (Scheme 3.4).

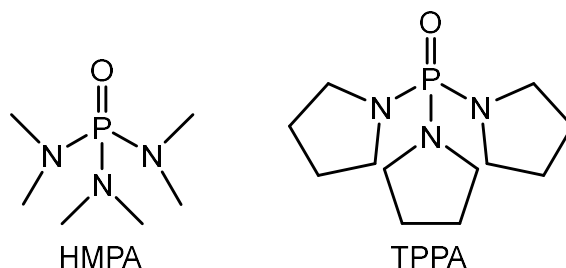


Scheme 3.4: Reaction scheme for the preparation of disilylborane (Entry 29 in Table 3.3) and silaborinine compounds. Adapted from reference [46].

3.2 – Synthesis of Silyl- and Germyl-Substituted Boranes

Possessing a firm grasp on the history of oligosilyl- and germylboron chemistry will facilitate the design of boron ALD precursors. Boranes featuring three silyl or germyl groups ($B(ER_3)_3$; E = Si or Ge) are of particular interest as ALD precursors, given that they could potentially react with a boron trihalide (e.g. BCl_3 or BBr_3) to afford elemental boron and a volatile halosilane by-product (Scheme 3.1). This reactivity mirrors that utilized for antimony ALD using tris(trimethylsilyl)antimony in combination with antimony trichloride (Scheme 2.1).

Given that previous attempts to prepare $B(SiMe_3)_3$ resulted in the formation of silylborates, this work focused on the synthesis of boranes bearing at least one sterically bulky tris(trimethylsilyl)silyl [$(Me_3Si)_3Si-$; hypersilyl] or tri-*tert*-butylsilyl [$(Me_3C)_3Si-$; supersilyl] group in combination with smaller trimethylgermyl (Me_3Ge-) groups. Trimethylgermyl substituents were employed in this work rather than trimethylsilyl substituents because $[(Me_3Ge)Li(THF)_2]_2$ can be prepared (*vide infra*) in good yield without the use of highly toxic organomercury reagents. By contrast, trimethylsilyllithium is only accessible via $[Hg(SiMe_3)_2]$,^[30] or as an adduct with strongly coordinating hexamethylphosphoramide (HMPA) or tris(*N,N*-tetramethylene)phosphoric triamide (TPPA; Scheme 3.5).^[48,49]

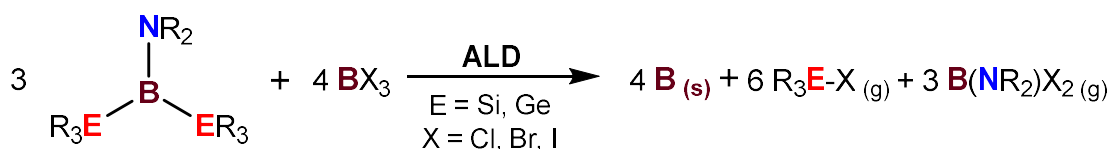


Scheme 3.5: Literature methods for the preparation of trimethylsilyllithium.^[30,48,49]

It is also worth noting that previous research in the Emslie group explored alternative methods for the preparation of R_3SiM ($\text{R} = \text{Me, Et}$; $\text{M} = \text{Li, Na, K, Cs}$); however, all attempts to do so were unsuccessful. These attempts included reactions between Si_2Me_6 or Et_3SiH with strong reducing agents or Lewis bases – such as metal hydrides, benzyl potassium, potassium graphite, sodium naphthalenide, *tert*-butyllithium, and elemental cesium – in the presence or absence of a crown ether.

Boranes bearing a combination of bulky silyl and sterically unencumbered trimethylgermyl groups may be particularly suitable as ALD precursors because the bulky silyl groups can be expected to impart thermal stability, while the less-hindered B-GeMe₃ linkages can serve as sites for initial reactivity. Furthermore, these boranes can be expected to be more volatile than boranes bearing three bulky silyl groups, due to their lower molecular weight. Functional groups bearing phenyl rings were not pursued due to their tendency to decrease volatility by engaging in π -stacking. Hypersilyl and supersilyl groups may be the most suitable choice for providing thermal stability while maintaining adequate volatility.

That said, boranes bearing one amido group in combination with two silyl or germyl groups [(R₃E)₂B(NR₂); E = Si or Ge] may be anticipated to be both (a) more straightforwardly synthesized, and (b) more thermally robust, due to π -donation from nitrogen to boron. These compounds may also be useful for elemental boron ALD, since BCl₃ is a common reagent to replace an amido group on boron with a chloro substituent, potentially allowing for boron ALD as indicated in Scheme 3.6. Consequently, (R₃E)₂B(NR₂) compounds are also a focus in this work.



Scheme 3.6: Potential reactivity for boron ALD using (R₃E)₂B(NR₂) precursors.

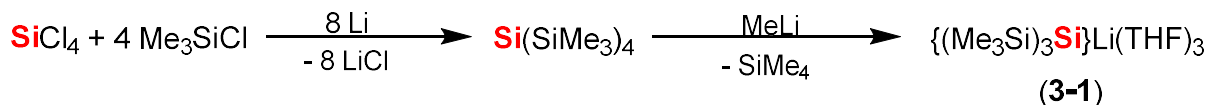
The following sections (3.2.1 – 3.3.3) describe the synthesis, structures, and reactivity of (a) the alkali metal silyl and germyl reagents required in this work, (b) the previously synthesized but not crystallographically characterized hypersilyl compound {(Me₃Si)₃Si}₂B(NMe₂) (**3-8**), (c) the supersilyl and supersilyl/trimethylgermyl compounds (^tBu₃Si)B(NMe₂)X [X = Cl (**3-9**) or F (**3-10**)], (^tBu₃Si)BCl₂ (**3-11**), and (^tBu₃Si)(Me₃Ge)B(NMe₂) (**3-12**), and (d) the tris(trimethylgermyl)dimethylamidoborate {(Me₃Ge)₃B(NMe₂)}Li(THF)₂ (**3-13**).

3.2.1 – Starting Material Synthesis

3.2.1.1 – Alkali Metal Silyl Reagents

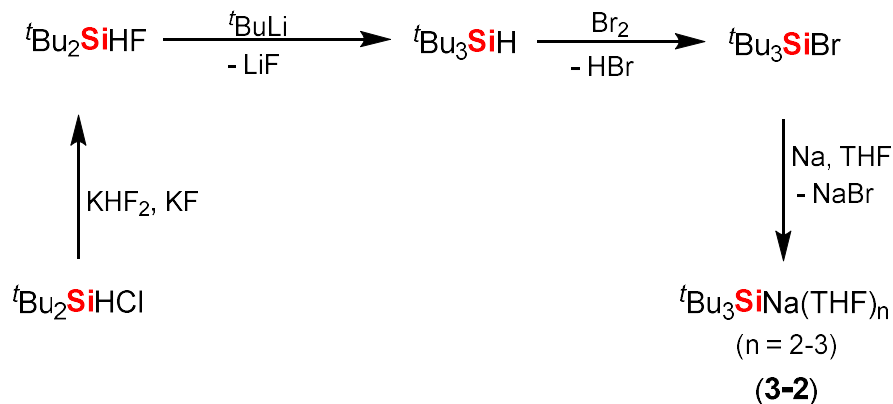
Hypersilyllithium (**3-1**) was prepared using the two-step procedure described in literature^[50] involving the reaction of lithium and chlorotrimethylsilane with silicon

tetrachloride in THF to form tetrakis(trimethylsilyl)silane, which was subsequently reacted with equimolar methyllithium in diethyl ether to form **3-1** in 70% yield after crystallization from hexanes at $-30\text{ }^{\circ}\text{C}$ (Scheme 3.7).



Scheme 3.7: Synthetic route for the preparation of hypersilyllithium (**3-1**).

Supersilylsodium, $(t\text{Bu}_3\text{Si})\text{Na}(\text{THF})_n$ (**3-2**; $n = 2-3$), was prepared from the multistep synthesis first reported by Wiberg and coworkers (Scheme 3.8).^[51] Its preparation began with the fluorination of di-*tert*-butylchlorosilane by potassium fluoride and potassium hydrogen fluoride to yield di-*tert*-butylfluorosilane in nearly quantitative yield as a clear, faintly yellow liquid. This then underwent a salt metathesis reaction with *tert*-butyllithium to insert a third *tert*-butyl group on the silicon center. Tri-*tert*-butylsilane was then brominated at $0\text{ }^{\circ}\text{C}$ in pentane, and the crude solid was purified by distillation to quantitatively yield tri-*tert*-butylbromosilane as a white crystalline solid. This was then reacted with a large excess of thinly cut sodium in THF to produce **3-2**, which can be crystallized from hexanes in very high yields. The synthesis of the donor-free form of **3-2** has been reported by Nöth and coworkers^[39], but its yield and solubility is significantly lower than that of the THF adduct and was therefore not pursued in this project.



Scheme 3.8: Synthetic route for the preparation of supersilylsodium (**3-2**).

The number of THF molecules in **3-2** varied between each large-scale synthesis ($n = 2-3$). Additionally, it should be noted that the position of the peak associated with the $\text{Si}(\text{CH}_3)_3$ protons of **3-2** ranged between 1.1 and 1.5 ppm in the ^1H NMR spectrum in C_6D_6 , depending on the concentration of the sample. This observation had been noted previously in literature.^[51] Single crystals of $({}^t\text{Bu}_3\text{Si})\text{Na}(\text{THF})_2$ were grown from a saturated hexanes solution stored at $-30\text{ }^\circ\text{C}$ (Figure 3.2). The unit cell of **3-2** contains 6 independent molecules, and all bond distances are unremarkable. The average sum of the C-Si-C angles in the tri-*tert*-butylsilyl group of **3-2** (314.4°) is larger than the sum of Si-Si-Si angles observed in the reported crystal structure of **3-1** (307.25°), which is perhaps due to increased steric hindrance in **3-2**.^[50]

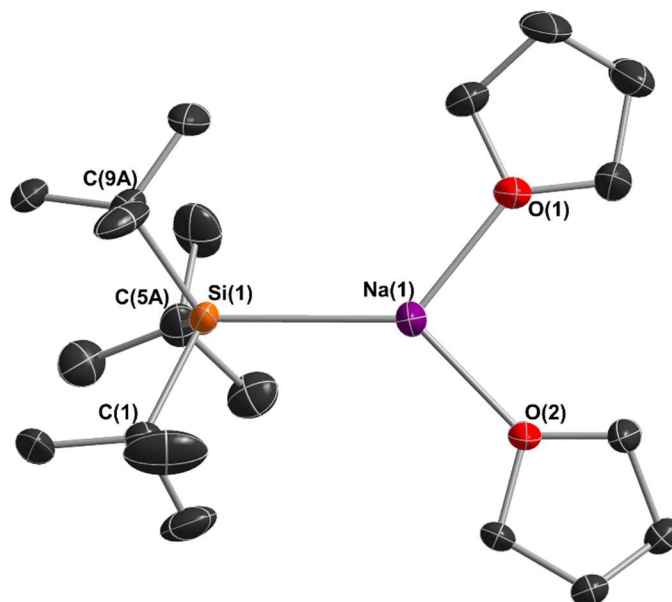
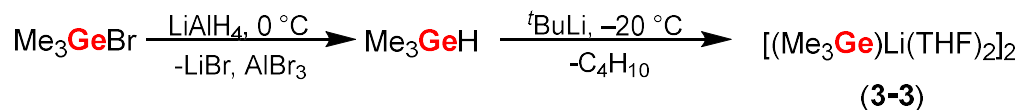


Figure 3.2: X-ray crystal structure of $(t\text{Bu}_3\text{Si})\text{Na}(\text{THF})_2$ (**3-2**) with ellipsoids set at 50% probability. Space group $P2_1/c$. All hydrogen atoms have been omitted for clarity. $R_1 = 0.0549$. Only one of three independent molecules in the unit cell is shown. Each of the molecules displayed disorder at the carbon atoms of the THF rings and/or the methyl carbons of the *tert*-butyl groups. Select bond distances (Å) and angles ($^\circ$): Na(1)-Si(1) 2.912(1); Na(1)-O(1) 2.293(2); Na(1)-O(2) 2.286(2); C(1)-Si(1)-C(5A) 101.6(1); C(5A)-Si(1)-C(9A) 103.5(2); C(9A)-Si(1)-C(1) 109.3(1).

3.2.1.2 – Trimethylgermyllithium

Isolation and crystallographic crystallization of trimethylgermyllithium (**3-3**) has not been published, but its in situ synthesis has been described by Piers and Lemieux,^[52] and preparation of solid **3-3** from Me_3GeH was developed by Dr. Patricio Romero at Intel Corporation. Compound **3-3** was synthesized from the reaction of trimethylgermylbromide with excess lithium aluminum hydride in THF at $0\text{ }^\circ\text{C}$ (Scheme 3.9). The resulting trimethylgermane was distilled (along with the reaction solvent) into a second flask, and was converted to trimethylgermyllithium by reaction with *tert*-butyllithium, as described by Romero (personal communication).^[52,53] Compound **3-3** was

isolated as a white solid, which decomposed upon prolonged exposure (e.g. over one hour) to vacuum, presumably via initial loss of THF.



Scheme 3.9: Synthetic route for the preparation of trimethylgermyllithium (**3-3**).

Single crystals of **3-3** were grown from a concentrated solution in hexanes at $-30\text{ }^\circ\text{C}$ (Figure 3.3). In the solid state, **3-3** is dimeric with the trimethylgermyl anions bridging between the lithium cations in a rhombus shape. The asymmetric unit consists of one half of the dimer with a Ge-Li bond distance that is marginally shorter than the other Ge-Li bond comprising the dimer [2.731(2) vs 2.746(2) Å]. The sum of the C-Ge-C bond angles in the trimethylgermyl groups in **3-3** (295.7°) is significantly less than the analogous Si-Si-Si angles in the hypersilyl groups in **3-1**, and the sum of the C-Si-C angles in the supersilyl groups of **3-2** (*vide supra*), likely due to much lower steric hindrance in **3-3** and the coordination number of five at germanium.

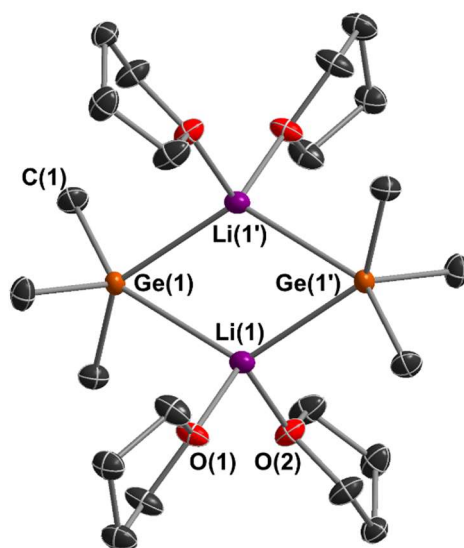
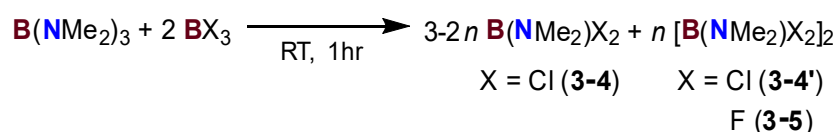


Figure 3.3: X-ray crystal structure of $[\text{Me}_3\text{GeLi}(\text{THF})_2]_2$ (**3-3**) with ellipsoids set at 50% probability. Space group $P-1$. All hydrogen atoms have been omitted for clarity. $R_1 = 0.0232$. Select distances (Å) and angles ($^\circ$): Ge(1)-Li(1) 2.731(2); Ge(1)-Li(1') 2.746(2); Ge(1)-Ge(1') 4.7579(8); Li(1)-Li(1') 2.714(4); Li(1)-O(1) 1.941(2); Li(1)-O(2) 1.938(3); Li(1)-Ge(1)-Li(1') 59.40(8); Ge(1)-Li(1)-Ge(1') 120.60(8); O(1)-Li(1)-O(2) 102.8(1).

3.2.1.3 – Dimethylamidodihaloboranes

Dimethylamidodichloroborane (**3-4**) was used for the synthesis of various compounds in this chapter. This compound was prepared following the previously reported substituent redistribution reaction between tris(dimethylamino)borane and excess boron trichloride in heptane (Scheme 3.10).^[54] Compound **3-4** was kept dissolved in heptane at room temperature and used as a stock solution for all further reactions, to minimize the extent to which **3-4** converted to the less reactive dimeric form, $[\text{B}(\text{NMe}_2)\text{Cl}_2]_2$ (**3-4'**). Nevertheless, this dimer crystallized out of solution over time, and so the concentration of the solution was determined by ^1H NMR spectroscopy (by integration of the $\text{N}(\text{CH}_3)_2$ NMR signal relative to the CH_3 signal of heptane) before utilization in any reactions. The ^1H and ^{11}B NMR spectra of the stock solutions consistently

indicated that the solutions contained small amounts (~5%) of the dimer (**3-4'**) in solution (Figure 3.4). $[\text{B}(\text{NMe}_2)\text{F}_2]_2$ (**3-5**) was prepared from the 2:1 reaction of $\text{BF}_3 \cdot \text{OEt}_2$ and tris(dimethylamino)borane, which is a modification of the literature procedure which utilizes gaseous BF_3 . Unlike the chlorine analogue, which can exist as a monomer (**3-4**) or dimer (**3-4'**) at room temperature, this compound was only present as a dimer at room temperature, as described previously in literature.^[55]



Scheme 3.10: Synthetic route for the preparation of dimethylamidodihaloboranes (**3-4**, **3-5**).

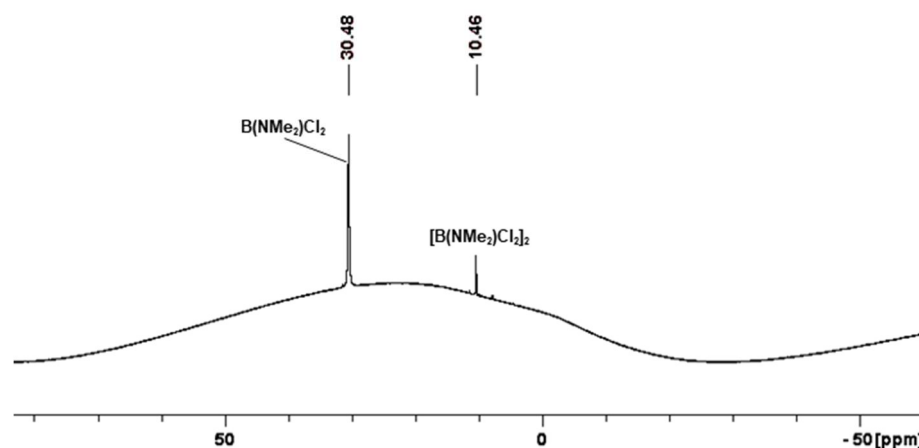
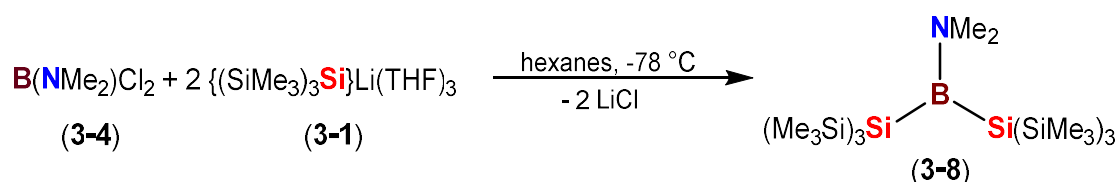


Figure 3.4: $^{11}\text{B}\{^1\text{H}\}$ NMR spectrum of a stock solution of **3-4** in heptane (C_6D_6 , 193 MHz, 298 K).

3.2.2 – Hypersilyl-Substituted Boranes

The salt metathesis reaction of hypersilyllithium (**3-1**) with bis(dimethylamido)bromoborane formed hypersilylbis(dimethylamido)borane (**3-6**; Scheme 3.11), and subsequent reaction with 2 equivalents of BCl_3 (1M solution in

30.48 ppm in **3-1** to -112.81 and 60.65 ppm in **3-8**, respectively. The previously unreported X-ray crystal structure of **3-8** (Figure 3.5) features a 3-coordinate boron center bound to the dimethylamido group and two hypersilyl groups in a trigonal planar geometry, with the sum of angles totaling 360.0° . The most obtuse angle about the boron center is that between the two bulky hypersilyl groups ($129.92(4)^\circ$).



Scheme 3.12: Synthetic route for the synthesis of bis(hypersilyl)amidoborane (**3-8**).

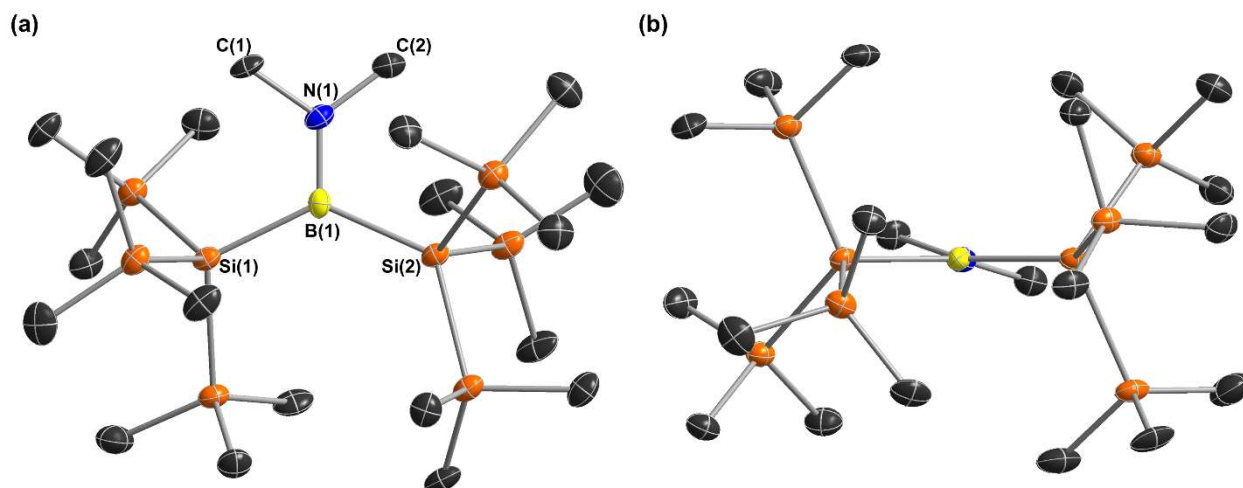
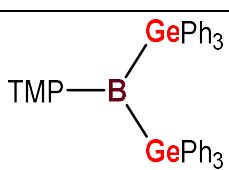
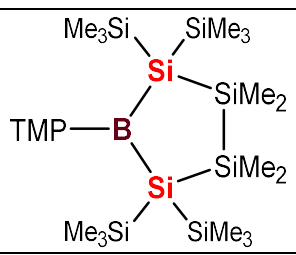
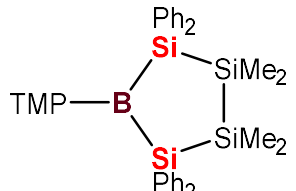
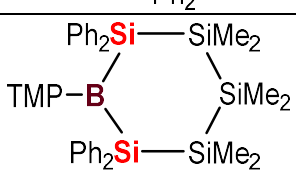


Figure 3.5: X-ray crystal structure of $\{(\text{Me}_3\text{Si})_3\text{Si}\}_2\text{B(NMe}_2)$ (**3-8**) with ellipsoids set at 50% probability. Space group Pn . All hydrogen atoms have been omitted for clarity. (a) A view facing the boron center's trigonal plane. (b) A view down the B-N bond. $R_1 = 0.0721$. Select bond lengths (\AA) and angles ($^\circ$): B(1)-N(1) 1.422(1); B(1)-Si(1) 2.075(9); B(1)-Si(2) 2.100(7); N(1)-C(1) 1.474(8); N(1)-C(2) 1.44(1); Si(1)-B(1)-Si(2) $129.92(4)$; Si(2)-B(1)-N(1) $114.3(5)$; N(1)-B(1)-Si(1) $115.8(5)$; C(1)-N(1)-C(2) $109.5(5)$.

While the B-Si bond distances in **3-8** are within the range reported for other silylboranes, the B-N bond (1.422(1) Å) is significantly shorter than the single B-N bond distance in H₃B-NH₃ (1.58(2) Å) and [Li(THF)₄][(Me₃Sn)₃B(NMePh)] (1.545(8) Å).^[57] This can be attributed to π -donation from the nitrogen lone pair to the empty p orbital on boron, resulting in double bond character between boron and nitrogen. This is consistent with the trigonal planar geometry about the nitrogen atom, although the CNC plane is rotated slightly (18.7°) out of the SiBSi plane, likely to accommodate the steric bulk of the hypersilyl groups. The extent to which the sterically unencumbered NMe₂ group is rotated out of the SiBSi plane is significantly less than in previously structurally characterized (R₃E)₂B(NR₂) compounds, all of which bear a sterically bulky TMP (2,2,6,6-tetramethylpiperidyl) group (see Table 3.4).

Table 3.4: ¹¹B NMR chemical shifts, B-N bond distances, and CNC/EBE interplanar angles for crystallographically characterized (R₃E)₂B(NR₂) compounds, where E = Si or Ge. H₃B-NH₃ and [Li(THF)₄][(Me₃Sn)₃B(NMePh)] are listed as examples of nitrogen-boron single bonded compounds. Compounds **3-8** and **3-12** are included for comparison.

Compound	¹¹ B NMR chemical shift (ppm)	B-N distance (Å)	Interplanar Angle (°)	References
H ₃ B-NH ₃	41.4 (CH ₃ CN)	1.58(2)	-	[55,57]
[Li(THF) ₄][(Me ₃ Sn) ₃ B(NMePh)]	-13.1 d (¹ J _{BSn} = 580 Hz) (C ₆ D ₆)	1.545(8)	-	[29]
	64.0 (C ₆ D ₆)	1.409(3)	34.5	[28]

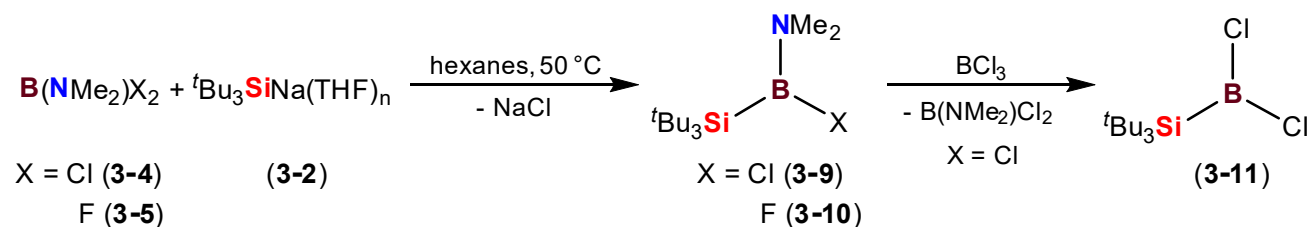
Compound	^{11}B NMR chemical shift (ppm)	B-N distance (Å)	Interplanar Angle (°)	References
	72.1 (C ₆ D ₆)	1.406(7)	40.4	[41]
	63.77 (CD ₂ Cl ₂)	1.408(2)	31.6	[42]
	66.30 (CD ₂ Cl ₂)	1.409(3)	36.1	[42]
3-8	60.65 (C ₆ D ₆)	1.422(1)	18.7	<i>This work</i>
3-12	59.88 (C ₆ D ₆)	1.395(1) 1.386(1)	2.33 6.56	<i>This work</i>

TMP = 2,2,6,6-tetramethylpiperidyl.

3.2.3 – Supersilyl-Substituted Boranes

In an attempt to synthesize bis(supersilyl)dimethylamidoborane (the supersilyl analogue of **3-8**) the reaction between two equivalents of supersilylsodium (**3-2**) and one equivalent of dimethylamidodichloroborane (**3-4**) was conducted and monitored by ^1H and $^{11}\text{B}\{^1\text{H}\}$ NMR spectroscopy. However, only the installation of a single supersilyl group was successful (Scheme 3.13). This outcome can be attributed to the greater steric bulk of supersilyl versus hypersilyl substituents, preventing installation of two supersilyl groups on the borane. A slight excess of **3-2** and mild heating of the reaction was required in order to isolate pure ($^t\text{Bu}_3\text{Si}$)B(NMe₂)Cl (**3-9**) free from unreacted [B(NMe₂)Cl₂]₂ (**3-4'**)

dimer (Figure 3.6). The synthesis of a small number of silylamidohaloboranes have been previously reported and they display very similar ^{11}B NMR signals as that observed for **3-9**.^[30,37,41,58,59]



Scheme 3.13: Synthetic route for the synthesis of supersilyldimethylamidohaloboranes [X = Cl (**3-9**), F (**3-10**)] and supersilyldichloroborane (**3-11**).

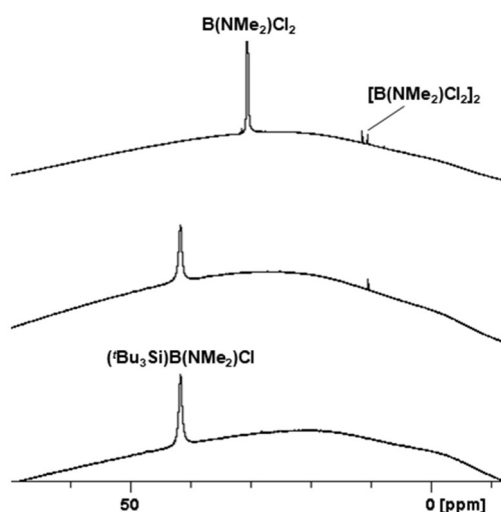


Figure 3.6: $^{11}\text{B}\{^1\text{H}\}$ NMR spectra from the NMR-scale reaction of dimethylamido-dichloroborane (**3-4**) and 1.5 equivalents of supersilylsodium (**3-2**) to produce supersilyldimethylamidochloroborane (**3-9**) (C_6D_6 , 193 MHz, 298 K). Top: **3-4** before the addition of **3-2**; middle: 18 hours after the addition of **3-2**; bottom: after heating at 50°C for 4 hours.

Although $(\text{}^t\text{Bu}_3\text{Si})\text{B}(\text{NMe}_2)\text{Cl}$ (**3-9**) did not react with additional equivalents of $\text{}^t\text{Bu}_3\text{SiNa}(\text{THF})_n$ (**3-2**) at room temperature or elevated temperatures, its reaction with BCl_3

generated supersilyldichloroborane (**3-11**; Scheme 3.13). This compound has been reported by Nöth and coworkers^[39] from the reaction between BCl_3 and base-free supersilylsodium. However, our synthesis is more convenient, given that the yield of THF-free ${}^t\text{Bu}_3\text{SiNa}$ is significantly less than that of the THF adduct.

The reaction of one equivalent of ${}^t\text{Bu}_3\text{SiNa}(\text{THF})_n$ (**3-2**) with ${}^t\text{Bu}_3\text{SiBCl}_2$ (**3-11**) in C_6D_6 was also explored in an attempt to generate bis(supersilyl)chloroborane. However, this reaction led to considerable precipitation and the formation of multiple boron-containing species in minor concentrations relative to remaining **3-11**. Reactions between supersilyldichloroborane (**3-11**) and trimethylgermyllithium (**3-3**) (using varying stoichiometries and reaction conditions) were also conducted and monitored by NMR spectroscopy, targeting the generation of supersilyltrimethylgermylboranes. However, multiple ${}^{11}\text{B}$ NMR signals and multiple singlets in the region of 0-1 ppm in the ${}^1\text{H}$ NMR spectra were consistently observed.

$({}^t\text{Bu}_3\text{Si})\text{B}(\text{NMe}_2)\text{F}$ (**3-10**) was synthesized in the hope that the salt metathesis reaction to generate bis(supersilyl)dimethylamidoborane would be more favourable when **3-10** is employed rather than **3-9** due to the greater lattice enthalpy of sodium fluoride over sodium chloride.^[60] Compound **3-10** was synthesized as a clear and colourless oil (93% yield) via the reaction between supersilylsodium (**3-2**) and $[\text{B}(\text{NMe}_2)\text{F}_2]_2$ (**3-5**, synthesized analogously to **3-4**^[54,61]).

Similarly to $({}^t\text{Bu}_3\text{Si})\text{B}(\text{NMe}_2)\text{Cl}$ (**3-9**), the preparation of **3-10** required the addition of a slight excess of **3-2** in order to fully consume the dimeric borane precursor (although for the synthesis of **3-10**, heating was not required). The transformation of the four-coordinate boron starting material into a heteroleptic three-coordinate

amidosilylfluoroborane resulted in significant positive shifts in the ^{11}B and ^{19}F NMR signals from 0.98 and -161.85 ppm in **3-5** to 34.35 and -70.95 ppm, respectively (Figure 3.7).

The addition of 2 equivalents of ${}^t\text{Bu}_3\text{SiNa}(\text{THF})_n$ (**3-2**) to a solution of $({}^t\text{Bu}_3\text{Si})\text{B}(\text{NMe}_2)\text{F}$ (**3-10**) in C_6D_6 yielded no reaction at room temperature. Heating this reaction to $100\text{ }^\circ\text{C}$ for 24 hours lead to considerable precipitation and generation of a promising new peak at 49.3 ppm in the $^{11}\text{B}\{^1\text{H}\}$ NMR spectrum, but further heating to consume remaining **3-10** lead to the generation of multiple boron-containing decomposition products (Figure 3.7).

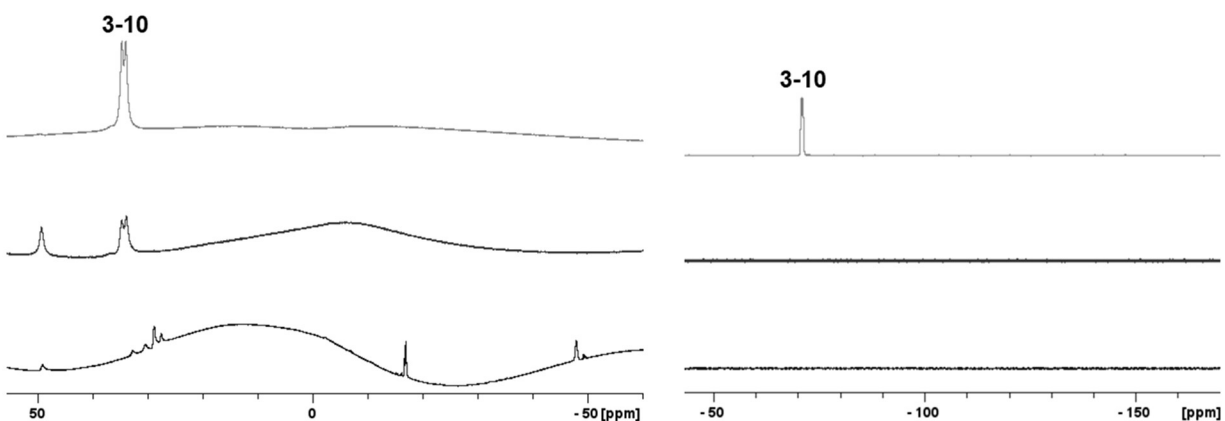
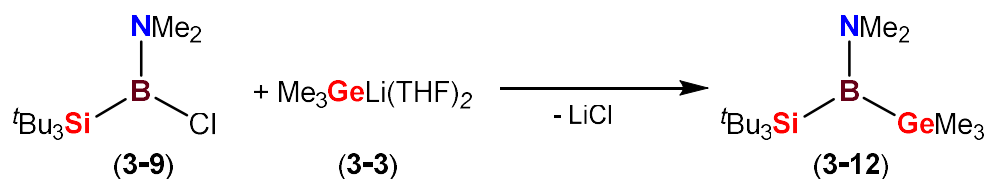


Figure 3.7: $^{11}\text{B}\{^1\text{H}\}$ (left) and ^{19}F NMR (right) spectra monitoring the reaction of $({}^t\text{Bu}_3\text{Si})\text{B}(\text{NMe}_2)\text{F}$ (**3-10**) with ${}^t\text{Bu}_3\text{SiNa}(\text{THF})_n$ (**3-2**) (C_6D_6 , 193 MHz ($^{11}\text{B}\{^1\text{H}\}$), 565 MHz (^{19}F), 298 K). From top to bottom: **3-10** before addition of **3-2**; 24 hours after the addition of excess **3-2** to **3-10** and heating at $100\text{ }^\circ\text{C}$; after heating for an additional 5 days at $100\text{ }^\circ\text{C}$.

The mixed tetrel borane, supersilyl(trimethylgermyl)(dimethylamido)borane (**3-12**), was prepared from the 1:1 salt metathesis reaction between

supersilyl(dimethylamido)chloroborane (**3-9**) and trimethylgermyllithium (**3-3**) at room temperature (Scheme 3.14). To isolate pure **3-12** from this reaction, it was found to be critical that $\text{B}(\text{NMe}_2)\text{Cl}_2$ (**3-4**) be completely consumed during the preparation of **3-9**, as trace amounts of remaining **3-4** result in the formation of a product with a $^{11}\text{B}\{^1\text{H}\}$ NMR chemical shift of -13 ppm, which was identified as $\{(\text{Me}_3\text{Ge})_3\text{B}(\text{NMe}_2)\}\text{Li}(\text{THF})_2$ (**3-13**, *vide infra*).



Scheme 3.14: Synthetic route for the preparation of supersilyl(trimethylgermyl)-(dimethylamido)borane, **3-12**.

Single crystals of **3-12** grew at room temperature within the oil (crude reaction product) remaining after centrifugation and removal of all volatiles. The X-ray crystal structure of **3-12** features a 3-coordinate boron center bound to the dimethylamido, supersilyl, and trimethylgermyl groups in a trigonal planar geometry, with the sum of angles totaling 360.0° (Figure 3.8). The B-N bond distance ($1.395(1)$ Å) is shorter than that of any reported $(\text{R}_3\text{E})_2\text{B}(\text{NR}_2)$ compound (including **3-8**), and is the first $(\text{R}_3\text{E})_2\text{B}(\text{NR}_2)$ compound to approach coplanarity between the CNC and EBE planes (Table 3.4). Altogether, these observations suggest a greater amount of π -interaction between the boron and nitrogen atoms due to a decrease in the steric hindrance about the central boron atom.

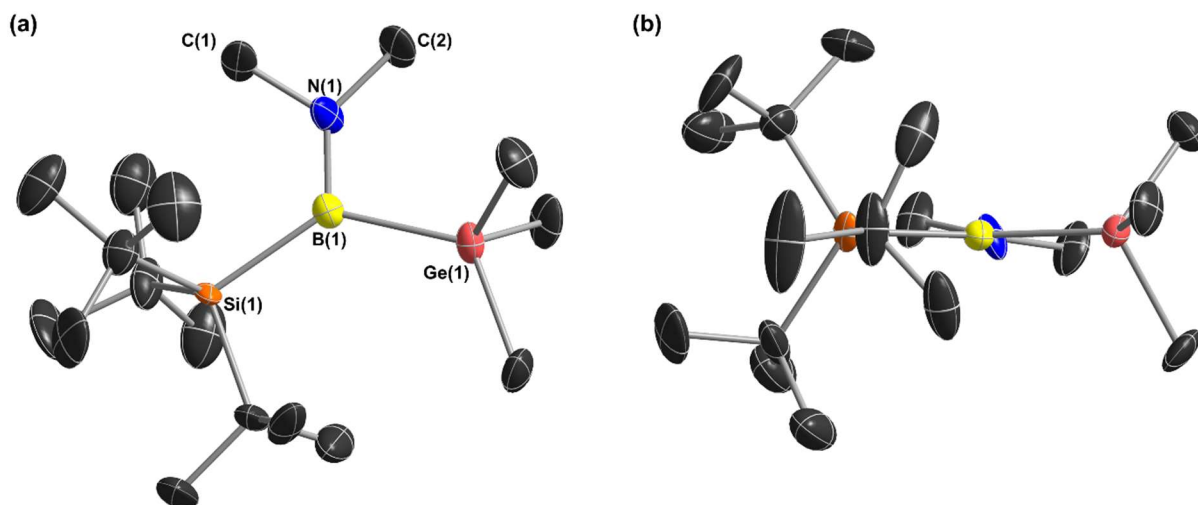


Figure 3.8: X-ray crystal structure of $(t\text{Bu}_3\text{Si})(\text{Me}_3\text{Ge})\text{B}(\text{NMe}_2)$ (**3-12**) with ellipsoids set at 50% probability. Space group $Pnma$. H atoms are omitted for clarity. Only one of two independent molecules in the unit cell is shown. (a) A view facing the boron center's trigonal plane. (b) A view down the B-N bond. $R_1 = 0.1081$. Select bond lengths (\AA) and angles ($^\circ$): B(1)-N(1) 1.395(1); B(1)-Si(1) 2.12(3); B(1)-Ge(1) 2.14(3); N(1)-C(1) 1.49(3); N(1)-C(2) 1.43(3); Si(1)-B(1)-Ge(1) 132.3(9); Ge(1)-B(1)-N(1) 104.4(2); N(1)-B(1)-Si(1) 123.3(2); C(1)-N(1)-C(2) 104.4(2).

3.2.4 – Germyl-Substituted Boranes

Given the successful synthesis of $\{(\text{Me}_3\text{Si})_3\text{Si}\}_2\text{B}(\text{NMe}_2)$ (**3-8**) and $(t\text{Bu}_3\text{Si})(\text{Me}_3\text{Ge})\text{B}(\text{NMe}_2)$ (**3-12**), we were interested to determine whether less sterically encumbered $(\text{Me}_3\text{Ge})_2\text{B}(\text{NMe}_2)$ might be accessible. Therefore, the NMR-scale reaction between 2 equivalents of trimethylgermyllithium (**3-3**) and 1 equivalent of dimethylamidodichloroborane (**3-4**) was carried out, resulting in the rapid formation of a white precipitate and a complex mixture of species in the $^{11}\text{B}\{^1\text{H}\}$ NMR spectrum, including two major peaks: a broad peak at 45 ppm and a sharp peak at -12 ppm (Figure 3.9). This reaction was repeated on a larger scale and modified such that **3-4** was added to a solution of **3-3** in toluene at -78 $^\circ\text{C}$. After removal of volatiles *in vacuo*, redissolving

in pentane and filtration, colourless needle crystals suitable for X-ray diffraction studies grew from the supernatant stored at $-30\text{ }^{\circ}\text{C}$.

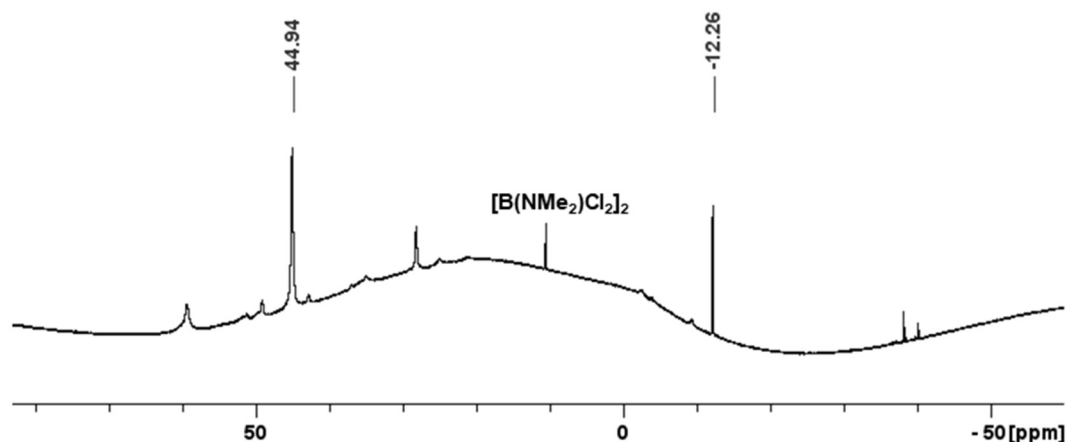


Figure 3.9: $^{11}\text{B}\{^1\text{H}\}$ NMR spectrum of the NMR-scale test reaction between 1 equivalent of $\text{B}(\text{NMe}_2)\text{Cl}_2$ (**3-4**) and 2 equivalents of $\text{Me}_3\text{GeLi}(\text{THF})_2$ (**3-3**) 15 minutes after addition at room temperature. The chemical shifts of the two major peaks from this reaction are indicated.

The product was determined to be a lithium borate, $\{(\text{Me}_3\text{Ge})_3\text{B}(\text{NMe}_2)\}\text{Li}(\text{THF})_2$ (**3-13**; Figure 3.10), which features 4-coordinate boron bonded to three trimethylgermyl substituents and one dimethylamido group, accompanied by a solvated lithium cation forming a contact ion pair. The Li-N distance is less than the sum of the ionic radii and is within the range previously reported for lithium amidoborate compounds (1.969(3) – 2.326(3) Å).^[62] This reactivity is similar to that observed by Nöth and coworkers, who observed that the reaction of trimethylsilyllithium and trimethoxyborane in varying stoichiometries did not result in the formation of silylboranes, but rather lithium silylborates, $\text{Li}[(\text{Me}_3\text{Si})_n\text{B}(\text{Me})_{4-n}]$.^[31,32]

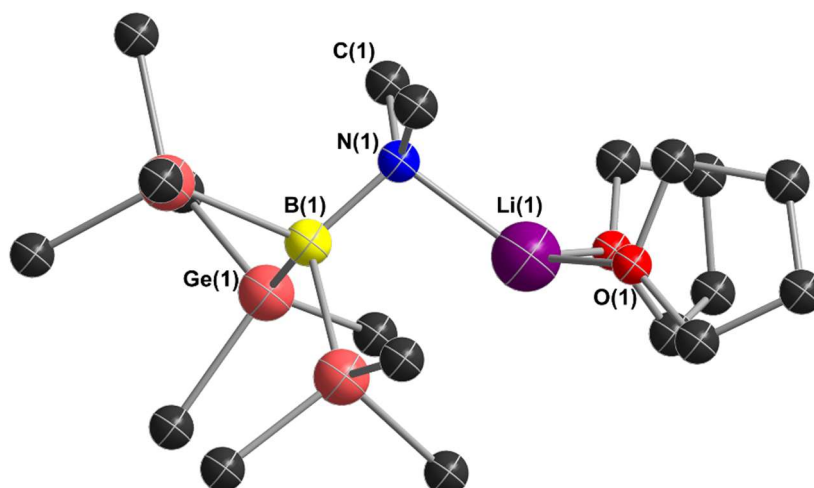
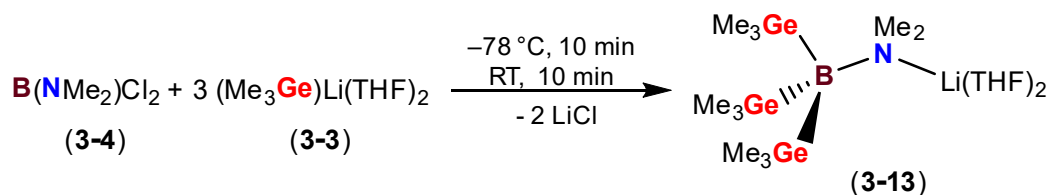


Figure 3.10: X-ray crystal structure of $\{(\text{Me}_3\text{Ge})_3\text{B}(\text{NMe}_2)\}\text{Li}(\text{THF})_2$ (**3-13**), with atoms displayed isotropically and bond metrics not included due to a combination of weak data and a high level of unmodeled disorder and twinning. One of six independent molecules (that with least amount of disorder) is shown, and H atoms are omitted for clarity. Space group $P1$. $R_1 = 0.0764$.

Pure borate **3-13** was isolated in reasonable yield from the 1:3 reaction between $\text{B}(\text{NMe}_2)\text{Cl}_2$ (**3-4**) and trimethylgermyllithium (**3-3**) (Scheme 3.15) and features a sharp peak in the $^{11}\text{B}\{^1\text{H}\}$ NMR spectrum at -13 ppm. The identity of the broad ^{11}B NMR peak at 45 ppm from the 1:2 reaction remains unknown but may be bis(trimethylgermyl)(dimethylamido)borane. However, all attempts to isolate this compound have been unsuccessful.



Scheme 3.15: Synthetic route for the isolation of $\{(\text{Me}_3\text{Ge})_3\text{B}(\text{NMe}_2)\}\text{Li}(\text{THF})_2$ (**3-13**).

3.3 – Testing Bis(tetrel)amidoboranes as Precursors for Boron ALD

3.3.1 – Volatility, Thermal Stability, and Reactivity of $\{(\text{Me}_3\text{Si})_3\text{Si}\}_2\text{B}(\text{NMe}_2)$ (**3-8**)

The volatility and thermal stability of **3-8**, and the reactivity of **3-8** with boron trihalides was assessed to determine its viability as a precursor for elemental boron ALD (summarized in Table 3.5). Solid **3-8** cleanly sublimed at 85 °C over the span of 1-2 hours at a pressure of 10 mTorr. The thermal stability of **3-8** was determined by heating a solid sample in a J. Young NMR tube under static argon for 24 hours at increasing temperatures (from 25 to 155 °C), and monitoring changes by ^1H NMR spectroscopy. These tests revealed that **3-8** is stable for 24 hours at up to 155 °C.

Thermogravimetric analysis (TGA) carried out on **3-8** between 40 and 400 °C (Figure 3.11) revealed the onset of volatilization at atmospheric pressure to occur at 254 °C. The bulk of sample mass loss (~72%) was observed within a 50 °C temperature window, and 99% mass loss was observed by the end of the run which suggests that **3-8** efficiently volatilized without decomposition residue.

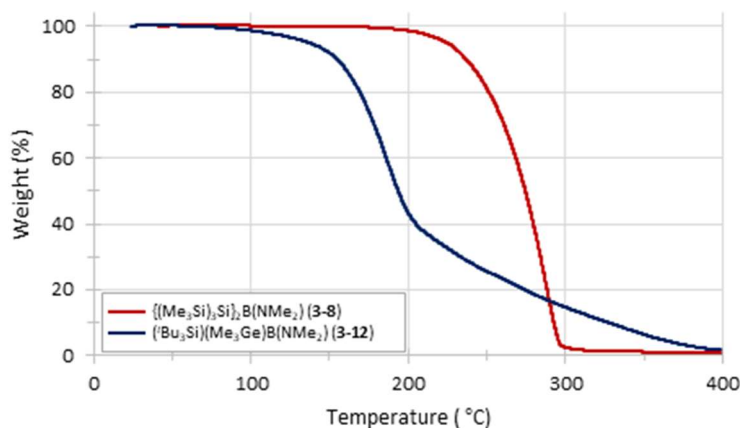


Figure 3.11: TGA of $\{(\text{Me}_3\text{Si})_3\text{Si}\}_2\text{B}(\text{NMe}_2)$ (**3-8**) and $(^t\text{Bu}_3\text{Si})(\text{Me}_3\text{Ge})\text{B}(\text{NMe}_2)$ (**3-12**). Ramp rate = 10 °C/min; starting weights = 3.481 mg (**3-8**), 3.306 mg (**3-12**).

NMR-scale reactions were conducted and monitored by ^1H and $^{11}\text{B}\{^1\text{H}\}$ NMR spectroscopy between **3-8** and excess $\text{BF}_3\cdot\text{OEt}_2$, BCl_3 (1M solution in heptane), BBr_3 , and BI_3 , the results of which are summarized in Table 3.5. Compound **3-8** failed to react completely with $\text{BF}_3\cdot\text{OEt}_2$ (a small amount of **3-8** remained, even after heating at 100 °C for 16 hours) but gave a complex mixture of products that were mostly removed *in vacuo* at room temperature. Reaction with BCl_3 , BBr_3 , and BI_3 resulted in slow consumption of **3-8** at room temperature to form a complex mixture of by-products that were not all volatile at room temperature (see Figure A3.27 as an example). Of the multiple by-products observed, $[\text{B}(\text{NMe}_2)\text{X}_2]_n$ ($\text{X} = \text{F}, \text{Cl}, \text{Br}, \text{I}; n = 1 \text{ or } 2$) and $\{(\text{Me}_3\text{Si})_3\text{Si}\}\text{BX}_2$ ($\text{X} = \text{Cl}$ confirmed, and $\text{X} = \text{Br}, \text{I}$ tentatively assigned based on the $^{11}\text{B}\{^1\text{H}\}$ NMR chemical shift) were identified. No significant precipitation was observed other than in the case of BI_3 . The number of products formed in these reactions suggests that cleavage of Si-Si bonds within the hypersilyl ligand may have occurred, rather than the formation of $(\text{Me}_3\text{Si})_3\text{SiX}$ ($\text{X} = \text{F}, \text{Cl}, \text{Br}, \text{I}$) by-products proposed in Scheme 3.6.

Table 3.5: Summary of volatility, thermal stability, and reactivity of precursor candidates $\{(\text{Me}_3\text{Si})_3\text{Si}\}_2\text{B}(\text{NMe}_2)$ (**3-8**) and $(^t\text{Bu}_3\text{Si})(\text{Me}_3\text{Ge})\text{B}(\text{NMe}_2)$ (**3-12**).

	$\{(\text{Me}_3\text{Si})_3\text{Si}\}_2\text{B}(\text{NMe}_2)$ (3-8)	$(^t\text{Bu}_3\text{Si})(\text{Me}_3\text{Ge})\text{B}(\text{NMe}_2)$ (3-12)
Volatility at 10 mTorr	85 °C, sublimation	45 °C, distillation
Thermal Stability	Stable at 155 °C for 24 hours	Decomposition after heating at 100 °C for 4 days

	{(Me₃Si)₃Si}₂B(NMe₂) (3-8)		(^tBu₃Si)(Me₃Ge)B(NMe₂) (3-12)	
Reactivity with:	Observations	By-products	Observations	By-products
BF₃·OEt₂	Incomplete consumption of 3-8 up to 100 °C; no precipitate	Complex mixture, mostly RT-volatile	3-12 slowly consumed at 80 °C; no precipitate	Multiple products, not all RT-volatile
BCl₃ (1M in heptane)	3-8 slowly consumed at RT; no precipitate	Multiple products including {(Me ₃ Si) ₃ Si}BCl ₂ and B(NMe ₂)Cl ₂ , some RT-volatile ^a	3-12 quickly consumed at RT; no precipitate	Multiple products including ^t Bu ₃ SiBCl ₂ and B(NMe ₂)Cl ₂ , not all RT-volatile ^a
BBr₃	3-8 slowly consumed at RT; no precipitate	Complex mixture, mostly RT-volatile	3-12 quickly consumed at RT; off-white precipitate	Multiple products including ^t Bu ₃ SiBr, ^t Bu ₃ SiBBr ₂ and B(NMe ₂)Br ₂ , not all RT-volatile ^a
BI₃	3-8 slowly consumed at RT; gray precipitate	Complex mixture, some RT-volatile	3-12 quickly consumed at RT; gray precipitate	Complex mixture including B(NMe ₂)I ₂ , mostly RT-volatile ^a

^a = product identified based on ¹H, ¹¹B, ¹³C, and/or ²⁹Si chemical shifts of known compounds^[39,56,63,64]

3.3.2 – Attempted ALD using {(Me₃Si)₃Si}₂B(NMe₂) (3-8) and BCl₃

With borane **3-8** proven to display the thermal stability and volatility, and perhaps also the reactivity, required for an ALD precursor, deposition experiments were conducted in a home-built ALD reactor using BCl₃ as the co-reactant. With an internal reactor pressure of approximately 1 Torr (using a total argon flow of 500 sccm), **3-8** was delivered at 135 °C and gaseous BCl₃ was delivered with a gas flow of 5 sccm. Deposition on a

substrate of SiO₂ on Si was attempted at temperatures between 150 and 300 °C using 2000 cycles and pulse times for **3-8** and BCl₃ of 1-2 seconds and 1-10 seconds, respectively. A scarce amount of deposition (~2 nm determined by VASE) was observed between 150 and 300 °C, corresponding to a GPC of approximately 0.01 Å, and the thickness of the deposited film did not improve with increased precursor or co-reactant pulse times. The results within this temperature window reveal a lack of significant film growth, perhaps due to undesirable reactivity at the Si-Si bonds, as observed by NMR spectroscopy during solution-state reactivity tests.

3.3.3 – Volatility, Thermal Stability, and Reactivity of (^tBu₃Si)(Me₃Ge)B(NMe₂)

(3-12)

Bis(tetrel)amidoborane **3-12** distilled at 45 °C at a pressure of 10 mTorr and possesses a melting point near room temperature. Thermal stress tests, conducted and monitored by NMR spectroscopy (in a method analogous to that previously outlined for compound **3-8** in Section 3.3.1), demonstrated the sample's stability for 24-hour periods at temperatures up to 100 °C. However, **3-12** was significantly decomposed (~50%) after 4 days at 100 °C, demonstrating reduced thermal stability relative to **3-8** (Table 3.5). TGA carried out on **3-12** between 40 and 400 °C at atmospheric pressure revealed the onset of volatilization to occur at 157 °C but exhibited a gradual loss of sample mass over a temperature window of approximately 140 °C (Figure 3.11). This illustrates that sample decomposition may be taking place slowly after the onset of volatilization, unlike **3-8** which exhibited rapid volatilization. Nevertheless, over 98.5% of the sample mass was lost by the end of the run which suggests that any decomposition by-products also volatilize.

The solution-state reactivity of **3-12** with excess boron trihalides ($\text{BF}_3 \cdot \text{OEt}_2$, BCl_3 (1M solution in heptane), BBr_3 , or BI_3) was screened by NMR spectroscopy. Compound **3-12** showed room temperature reactivity with BCl_3 , BBr_3 and BI_3 , but required elevated temperatures to completely react with $\text{BF}_3 \cdot \text{OEt}_2$. Multiple by-products were observed, including ${}^t\text{Bu}_3\text{SiX}$ ($\text{X} = \text{Br}$ confirmed), $[\text{B}(\text{NMe}_2)\text{X}_2]_n$ ($\text{X} = \text{F}, \text{Cl}, \text{Br}, \text{I}; n = 1 \text{ or } 2$), and ${}^t\text{Bu}_3\text{SiBX}_2$ ($\text{X} = \text{Cl}, \text{Br}$). The reaction of **3-12** and BBr_3 was the most promising (see Figure A3.28) as it reacted quickly at room temperature and formed an off-white precipitate; however – as expected, given the colour of the precipitate - elemental boron was not observed by powder X-ray diffractometry, as seen by its comparison to the most common allotrope of elemental boron (Figure 3.12).^[65] The diffractogram did not match any known material in the International Centre for Diffraction Database, and crystallization attempts were unsuccessful.

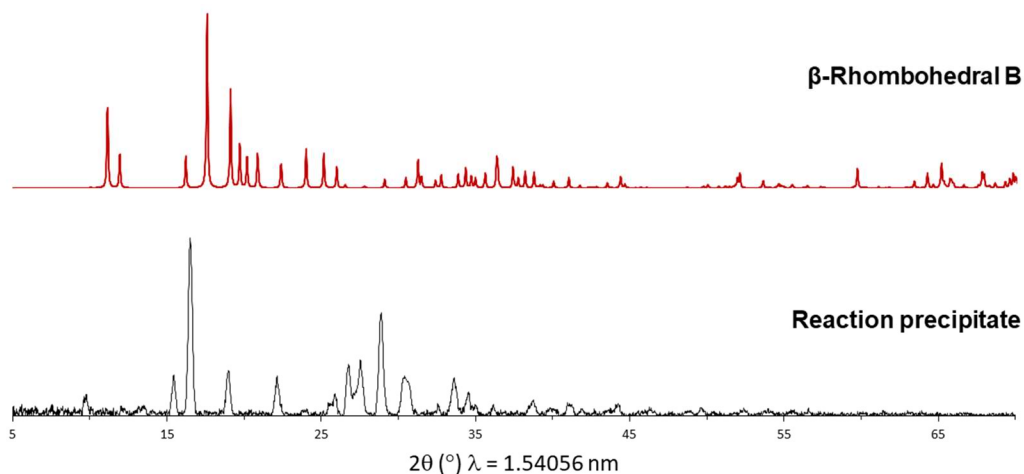


Figure 3.12: Comparison of the X-ray diffractogram of the powder generated from the reaction of $({}^t\text{Bu}_3\text{Si})(\text{Me}_3\text{Ge})\text{B}(\text{NMe}_2)$ (**3-12**) and BBr_3 at room temperature (bottom) to elemental boron (top).

The solution-state reactivity of **3-12** at room temperature suggests that reactivity towards a BX_3 reagent would be thermodynamically favourable on a substrate surface. In fact, the reactivity on a substrate surface could be envisaged to be much different than what has been observed by solution-state studies since some functional groups will be cleaved in order for the precursor to bind to the surface, and elevated temperatures and reduced pressures can facilitate the removal of by-products. Therefore, despite the reduced thermal stability of **3-12** in comparison to **3-8**, its enhanced volatility, in combination with the presence of a reactive $GeMe_3$ group and the absence of Si-Si linkages, makes it an interesting and potentially viable precursor candidate for elemental boron ALD.

3.4 – Summary and Conclusions for Chapter 3

In this research, boranes featuring bulky hypersilyl, supersilyl, and/or trimethylgermyl substituents were pursued as potential precursors to develop the first process for thermal ALD of elemental boron. The required alkali metal silyl reagents $\{(Me_3Si)_3Si\}Li(THF)_2$ (**3-1**) and $tBu_3SiNa(THF)_n$ (**3-2**) had previously been reported, but an X-ray crystal structure was obtained for **3-2**. In addition, previously un-isolated $[Me_3GeLi(THF)_2]_2$ (**3-3**) was prepared via the reaction of trimethylgermane with *tert*-butyllithium, and was crystallography and spectroscopically characterized.

$\{(Me_3Si)_3Si\}_2B(NMe_2)$ (**3-8**) and $(tBu_3Si)(Me_3Ge)B(NMe_2)$ (**3-12**) were successfully synthesized from the 2:1 reaction of hypersilyllithium (**3-1**) with dimethylamidodichloroborane (**3-4**), and the 1:1 reaction of

supersilyl(dimethylamido)chloroborane (**3-9**) with trimethylgermyllithium (**3-3**), respectively. Attempts to synthesize bis(trimethylgermyl)(dimethylamido)borane from the 2:1 reaction of trimethylgermyllithium (**3-3**) and dimethylamidodichloroborane (**3-4**) resulted in the formation of a lithium trigermylamidoborate (**3-13**). Compounds **3-8**, **3-12**, and **3-13** were crystallographically characterized.

Compounds **3-8** and **3-12** displayed the volatility, thermal stability, and solution-state reactivity towards boron trihalides to be considered promising potential ALD precursors. Unfortunately, deposition attempts at temperatures between 150 and 300 °C using **3-8** and BCl₃ led to poor film growth, with a GPC of approximately 0.01 Å.

3.5 – Future Work Pertaining to Chapter 3

While some promising reactivity was observed during solution-state studies of $\{(\text{Me}_3\text{Si})_3\text{Si}\}_2\text{B}(\text{NMe}_2)$ (**3-8**), attempts at film deposition utilizing BCl₃ as a co-reactant were unsuccessful. In the future, deposition studies will be conducted using $(^t\text{Bu}_3\text{Si})(\text{Me}_3\text{Ge})\text{B}(\text{NMe}_2)$ (**3-12**) in combination with BCl₃ or BBr₃. In comparison to **3-8**, compound **3-12** possesses a small and highly reactive trimethylgermyl group that may prove key to propagating film growth past the nucleation phase. Additionally, small modifications to the target precursor design allow access to a wider range of bis(tetrel)amidoboranes (Figure 3.13). For example, the use of less sterically encumbered SiⁱBu₂Me or SiⁱBuMe₂ groups in place of SiⁱBu₃ could possibly allow for the formation of bis(silyl)(dimethylamido)borane analogues of **3-8**. Additionally, replacement of the dimethylamido substituent with a bulkier amido group, such as a 2,2,5,5-

tetramethylpiperidyl (TMP) or hexamethyldisilazyl [(Me₃Si)₂N] group, may allow for the formation of potentially highly reactive bis(trimethylgermyl)amidoborane, or supersilyl-(trimethylgermyl)amidoborane compounds analogous to **3-12**.

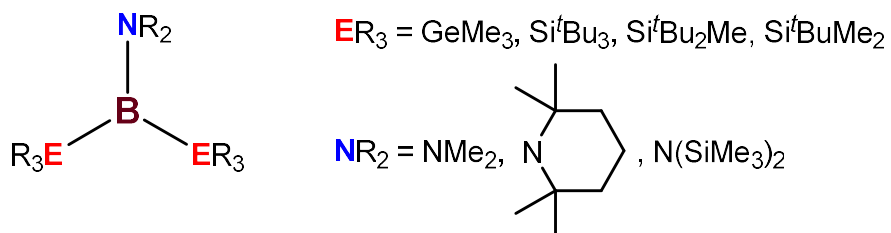


Figure 3.13: Molecular design of future bis(tetrel)amidoborane compounds as precursors for boron ALD.

3.6 – References for Chapter 3

- [1] R. T. Paine, C. K. Narula. Synthetic Routes to Boron Nitride. *Chem. Rev.* **1990**, *90*, 73-91.
- [2] D. Garcia-Alonso, S. E. Potts, C. A. A. van Helvoirt, M. A. Verheijen, W. M. M. Kessels. Atomic layer deposition of B-doped ZnO using triisopropyl borate as the boron precursor and comparison with Al-doped ZnO. *J. Mater. Chem. C* **2015**, *3*, 3095-3107.
- [3] X. L. Chen, B. H. Xu, J. M. Xue, Y. Zhao, C. C. Wei, J. Sun, Y. Wang, X. D. Zhang, X. H. Geng. Boron-doped zinc oxide thin films for large-area solar cells grown by metal organic chemical vapor deposition. *Thin Solid Films* **2007**, *515*, 3753-3759.
- [4] B. G. Yacobi, Semiconductor Materials: An Introduction to Basic Principles. Springer, **2003**; pp. 239.
- [5] X. Blase, E. Bustarret, C. Chapelier, T. Klein, C. Marcenat. Superconducting group-IV semiconductors. *Nat. Mater.* **2009**, *8*, 375-382.
- [6] S. J. Cobb, Z. J. Ayres, J. V. Macpherson. Boron Doped Diamond: A Designer Electrode Material for the Twenty-First Century. *Annu. Rev. Anal. Chem.* **2018**, *11*, 463-484.
- [7] J. M. Freitas, T. D. C. Oliveira, R. A. A. Munoz, E. M. Richter. Boron Doped Diamond Electrodes in Flow-Based Systems. *Front. Chem.* **2019**, *7*, 1-21.
- [8] K. Muzyka, J. Sun, T. H. Fereja, Y. Lan, W. Zhang, G. Xu. Boron-doped diamond: current progress and challenges in view of electroanalytical applications. *Anal. Methods* **2019**, *11*, 397-414.
- [9] B. Schurink, W. T. E. van den Beld, R. M. Tiggelaar, R. W. E. van de Kruijs, F. Bijkerk. Synthesis and Characterization of Boron Thin Films Using Chemical and Physical Vapor Depositions. *Coatings* **2022**, *12*, 685-702.
- [10] J. D. Ferguson, A. W. Weimer, S. M. George. Atomic layer deposition of boron nitride using sequential exposures of BCl₃ and NH₃. *Thin Solid Films* **2002**, *413*, 16-25.
- [11] B. Mårlid, M. Ottosson, U. Pettersson, K. Larsson, J.-O. Carlsson. Atomic layer deposition of BN thin films. *Thin Solid Films* **2002**, *402*, 167-171.
- [12] J. Olander, L. M. Ottosson, P. Heszler, J.-O. Carlsson, K. M. E. Larsson. Laser-Assisted Atomic Layer Deposition of Boron Nitride Thin Films. *Chem. Vap. Deposition* **2005**, *11*, 330-337.
- [13] W. Hao, C. Marichy, C. Journet, A. Brioude. A Novel Two-Step Ammonia-Free Atomic Layer Deposition Approach for Boron Nitride. *ChemNanoMat* **2017**, *3*, 656-663.
- [14] M. Putkonen, L. Niinistö. Atomic layer deposition of B₂O₃ thin films at room temperature. *Thin Solid Films* **2006**, *514*, 145-149.
- [15] A. Pilli, J. Jones, V. Lee, N. Chugh, J. Kelber, F. Pasquale, A. LaVoie. In situ XPS study of low temperature atomic layer deposition of B₂O₃ films on Si using BCl₃ and H₂O precursors. *J. Vac. Sci. Technol., A* **2018**, *36*, 061503.
- [16] E. Kazyak, K.-H. Chen, A. L. Davis, S. Yu, A. J. Sanchez, J. Lasso, A. R. Bielinski, T. Thompson, J. Sakamoto, D. J. Siegel, N. P. Dasgupta. Atomic layer deposition

- and first principles modeling of glassy $\text{Li}_3\text{BO}_3\text{--Li}_2\text{CO}_3$ electrolytes for solid-state Li metal batteries. *J. Mater. Chem. A* **2018**, *6*, 19425-19437.
- [17] M. J. Saly, F. Munnik, C. H. Winter. Atomic layer deposition of CaB_2O_4 films using bis(tris(pyrazolyl)borate)calcium as a highly thermally stable boron and calcium source. *J. Mater. Chem.* **2010**, *20*, 9995-10000.
- [18] M. J. Saly, F. Munnik, C. H. Winter. The Atomic Layer Deposition of SrB_2O_4 - Films Using the Thermally Stable Precursor Bis(tris(pyrazolyl)borate)strontium. *Chem. Vap. Deposition* **2011**, *17*, 128-134.
- [19] M. J. Saly, F. Munnik, R. J. Baird, C. H. Winter. Atomic Layer Deposition Growth of BaB_2O_4 Thin Films from an Exceptionally Thermally Stable Tris(pyrazolyl)borate-Based Precursor. *Chem. Mater.* **2009**, *21*, 3742-3744.
- [20] J. P. Klesko, J. A. Bellow, M. J. Saly, C. H. Winter, J. Julin, T. Sajavaara. Unusual stoichiometry control in the atomic layer deposition of manganese borate films from manganese bis(tris(pyrazolyl)borate) and ozone. *J. Vac. Sci. Technol., A* **2016**, *34*, 051515.
- [21] A. Yamada, B. Sang, M. Konagai. Atomic layer deposition of ZnO transparent conducting oxides. *Appl. Surf. Sci.* **1997**, *112*, 216-222.
- [22] J. J. Thomas, N. E. Weston, T. E. O'Connor. Turbostratic Boron Nitride, Thermal Transformation to Ordered-layer-lattice Boron Nitride. *J. Am. Chem. Soc.* **1963**, *84*, 4619-4622.
- [23] M. Weber, B. Koonkaew, S. Balme, I. Utke, F. Picaud, I. Iatsunskyi, E. Coy, P. Miele, M. Bechelany. Boron Nitride Nanoporous Membranes with High Surface Charge by Atomic Layer Deposition. *ACS Appl. Mater. Interfaces* **2017**, *9*, 16669-16678.
- [24] M. J. Saly, M. J. Heeg, C. H. Winter. Volatility, High Thermal Stability, and Low Melting Points in Heavier Alkaline Earth Metal Complexes Containing Tris(pyrazolyl)borate Ligands. *Inorg. Chem.* **2009**, *48*, 5303-5312.
- [25] L. Wesemann, M. Trinkaew, U. Englert, J. Müller. Silaborates with an Unprecedented Cluster Geometry. *Organometallics* **1999**, *18*, 4654-4659.
- [26] H. Wang, L. Wu, Z. Lin, Z. Xie. Transition-Metal-Like Behavior of Monovalent Boron Compounds: Reduction, Migration, and Complete Cleavage of CO at a Boron Center. *Angew. Chem. Int. Ed.* **2018**, *57*, 8708-8713.
- [27] Y. Heider, P. Willmes, V. Huch, M. Zimmer, D. Scheschkewitz. Boron and Phosphorus Containing Heterosiliconoids: Stable p- and n-Doped Unsaturated Silicon Clusters. *J. Am. Chem. Soc.* **2019**, *141*, 19498-19504.
- [28] T. Habereeder, H. Nöth. Synthesis and Structures of Amino(triphenylgermyl) Boranes and Trihydro(triphenylgermyl) Borates. *Z. Anorg. Allg. Chem.* **2001**, *627*, 1003-1012.
- [29] T. Habereeder, H. Nöth. Synthesis and Structures of some Trisorganylstannyl Boranes and Triorganylstannyl Borates. *Z. Anorg. Allg. Chem.* **2001**, *627*, 789-796.
- [30] W. Biffar, H. Nöth, R. Schwerthöffer. Synthesis and Reactivity of Trimethylsilylboranes. *Liebigs Ann. Chem.* **1981**, 2067-2080.
- [31] W. Biffar, H. Nöth. (Trimethylsilyl)borates from Alkoxyboranes and Trimethylsilyllithium. *Chem. Ber.* **1982**, *115*, 934-945.

- [32] W. Lippert, H. Nöth, W. Ponikwar, T. Seifert. Preparation and Structural Characterization of Lithium Silylborates. *Eur. J. Inorg. Chem.* **1999**, 817-823.
- [33] B. Pachaly, R. West. Photochemische Erzeugung von Triphenylsilylborandiyl (C_6H_5)₃B: aus Organosilylboranen. *Angew. Chem.* **1984**, *96*, 444-445.
- [34] B. Pachaly, R. West. Photochemical Generation of Triphenylsilylborandiyl (C_6H_5)₃B: from Organosilylboranes. *Angew. Chem. Int. Ed.* **1984**, *23*, 454-455.
- [35] A. Tsurusaki, K. Yoshida, S. Kyushin. Synthesis and structures of lithium alkoxytris(dimethylphenylsilyl)borates. *Dalton Trans.* **2017**, *46*, 8705-8708.
- [36] H. Nöth, G. Höllerer. Organosilyl-borane. *Chem. Ber.* **1966**, *99*, 2197-2205.
- [37] J. D. Buynak, B. Geng. Synthesis and Reactivity of Silylboranes. *Organometallics* **1995**, *14*, 3112-3115.
- [38] W. Biffar, H. Nöth. Tris(trimethylsilyl)silyl Boranes and Tris(trimethylsilyl)silyl Borates. *Z. Anorg. Allg. Chem. B* **1981**, *36*, 1509-1515.
- [39] N. Wiberg, K. Amelunxen, T. Blank, H.-W. Lerner, K. Polborn, H. Nöth, R. Littger, M. Rackl, M. Schmidt-Amelunxen, H. Schwenk-Kircher, M. Warchold. Supersilyltrialanes $R^*_nEHal_{3-n}$ (E = Triel, $R^* = Si^tBu_3$): Syntheses, Characterization, Reactions, Structures. *Z. Anorg. Allg. Chem. B* **2001**, *56*, 634-651.
- [40] E. Hengge, D. Wolfer. Boracyclopentasilan, ein neuer Typ heterocyclischer Silane. *Angew. Chem.* **1973**, *7*, 304.
- [41] J. Markov, R. Fischer, H. Wagner, N. Noormofidi, J. Baumgartner, C. Marschner. Open, cyclic, and bicyclic compounds of double silylated phosphorus and boron. *Dalton Trans.* **2004**, 2166-2169.
- [42] T. K. Purkait, E. M. Press, E. A. Marro, M. A. Siegler, R. S. Klausen. Low-Energy Electronic Transition in SiB Rings. *Organometallics* **2019**, *38*, 1688-1698.
- [43] C. Kleeberg, C. Borner. On the Reactivity of Silylboranes toward Lewis Bases: Heterolytic B–Si Cleavage vs. Adduct Formation. *Eur. J. Inorg. Chem.* **2013**, *2013*, 2799-2806.
- [44] M. Y. Abraham, Y. Wang, Y. Xie, P. Wei, H. F. Schaefer, III, P. v. R. Schleyer, G. H. Robinson. Cleavage of Carbene-Stabilized Disilicon. *J. Am. Chem. Soc.* **2011**, *133*, 8874-8876.
- [45] H. Braunschweig, T. Brückner, A. Deißberger, R. D. Dewhurst, A. Gackstatter, A. Gärtner, A. Hofmann, T. Kupfer, D. Prieschl, T. Thiess, S. R. Wang. Reaction of Dihalodiboranes(4) with a N-Heterocyclic Silylene: Facile Construction of 1-Aryl-2-Silyl-1,2-Diboraindanes. *Chem. Eur. J.* **2017**, *23*, 9491-9494.
- [46] A. Gackstatter, H. Braunschweig, T. Kupfer, C. Voigt, N. Arnold. N-Heterocyclic Silylenes in Boron Chemistry: Facile Formation of Silylboranes and Silaborinines. *Chem. Eur. J.* **2016**, *22*, 16415-16419.
- [47] M. Asay, C. Jones, M. Driess. N-Heterocyclic Carbene Analogues with Low-Valent Group 13 and Group 14 Elements: Syntheses, Structures, and Reactivities of a New Generation of Multitalented Ligands. *Chem. Rev.* **2011**, *111*, 354-396.
- [48] W. C. Still. Conjugate Addition of Trimethylsilyllithium. A Preparation of 3-Silyl Ketones. *J. Org. Chem.* **1976**, *41*, 3063-3064.
- [49] S. Kamio, T. Imagawa, M. Nakamoto, M. Oestreich, H. Yoshida. HMPA-Free Generation of Trialkylsilyllithium Reagents and Its Applications to the Synthesis of Silylboronic Esters. *Synthesis* **2021**, *53*, 4678-4681.

- [50] A. Heine, R. Herbst-Irmer, G. M. Sheldrick, D. Stalke. Structural Characterization of Two Modifications of Tris(tetrahydrofuran)(tris(trimethylsilyl)silyl)lithium: A Compound with a ^{29}Si - ^7Li NMR Coupling. *Inorg. Chem.* **1993**, *32*, 2694-2698.
- [51] N. Wiberg, K. Amelunxen, H.-W. Lemer, H. Schuster, H. Nöth, I. Krossing, M. Schmidt-Amelunxen, T. Seifert. Donorfreie und donorhaltige Supersilylalkalimetalle $^t\text{Bu}_3\text{SiM}$: Synthesen, Charakterisierung, Strukturen. *J. Organomet. Chem.* **1997**, *542*, 1-18.
- [52] E. Piers, R. Lemieux. Reaction of (Trimethylgermyl)copper(I)-Dimethyl Sulfide with Acyl Chlorides: Efficient Syntheses of Functionalized Acyltrimethylgermanes. *Organometallics* **1995**, *14*, 5011-5012.
- [53] P. Romero, Intel Corporation, Adapted from Private Communication.
- [54] A. J. Banister, N. N. Greenwood, B. P. Straughan, J. Walker. Monomeric Dimethylaminoboron Dihalides. *J. Chem. Soc.* **1964**, 995-1000.
- [55] C. W. Heitsch. The Nuclear Magnetic Resonance Spectra of Some Boron Complexes. *Inorg. Chem.* **1965**, *4*, 1019-1024.
- [56] H. Braunschweig, M. Colling, C. Kollann, U. Englert. The first silyl- and germylboryl complexes: synthesis from novel (dichloro)silyl- and (dichloro)germylboranes, structure and reactivity. *J. Chem. Soc., Dalton Trans.* **2002**, 2289-2296.
- [57] E. L. Lippert, W. N. Lipscomb. The Structure of H_3NBH_3 . *J. Am. Chem. Soc.* **1956**, *78*, 503-504.
- [58] M. Fan, R. T. Paine, E. N. Duesler, H. Nöth. Synthesis and Molecular Structure of Tris[(trimethylsilyl)silyl](diisopropylamino)(diphenylphosphino)borane. *Z. Anorg. Allg. Chem.* **2006**, *632*, 2443-2446.
- [59] M. Haase, U. Klingebiel, R. Boese, M. Polk. Stabilisierung und Reaktionen von Iminoboranen Kristallstruktur von (*tert*-Butylimino)tris(trimethylsilyl)silyl]boran. *Chem. Ber.* **1986**, *119*, 1117-1126.
- [60] Lattice Energies. In *CRC Handbook of Chemistry and Physics*, 103 Ed.; J. R. Rumble, Ed. Taylor & Francis Group, **2022-2023**.
- [61] A. C. Hazell. The Crystal Structure of Dimethylaminoboron Difluoride. *J. Chem. Soc. A* **1966**, 1392-1394.
- [62] Bond distance range based on a search of the Cambridge Structural Database for lithium amidoborate compounds. 96% of the Li-N distances in the CSD fall within the range described. CSD accessed via conquest CSD on December 21, 2022; version 2020.3.0, updated November 2020.
- [63] H. Nöth, H. Vahrenkamp. Monomeren-Dimeren-Gleichgewichte bei Aminoboranen. *Chem. Ber.* **1967**, *100*, 3353-3362.
- [64] C. Mechtler, M. Zirngast, J. Baumgartner, C. Marschner. Synthesis and Reactions of Alkynyl Oligosilanes. *Eur. J. Inorg. Chem.* **2004**, *2004*, 3254-3261.
- [65] M. J. v. Setten, M. A. Uijtewaal, G. A. d. Wijs, R. A. d. Groot. Thermodynamic Stability of Boron: The Role of Defects and Zero Point Motion. *J. Am. Chem. Soc.* **2007**, *129*, 2458-2465.

Chapter 4

Flowable Atomic Layer Deposition of HfO_2 using a Carboxylic Acid as the Co-Reactant

4.1 – Introduction to Chapter 4

An overarching challenge arising in the field of device fabrication, due to the ongoing miniaturization of device sizes, is effective gap filling of trenches without the formation of voids (Figure 4.1a) during the deposition of thin films (especially in sub-20 nm high-aspect-ratio structures). Shallow trench isolation, a method used in the semiconductor industry to prevent current leakage by using trenches to isolate active elements, has utilized processes such as deposition/etch/deposition (DED) and dynamic reflow to fill the trenches with a dielectric.^[1,2] DED utilizes cyclic deposition and etching steps to remove material overhang so that the entrance of the trench is reopened to allow partial filling at every deposition step.^[3,4] However, challenges associated with deposition and etching uniformity are common when utilizing the DED method, especially as the number of cycles required continues to increase as trench sizes decrease.^[4] In dynamic reflow, the deposited material, which is relatively low-melting (e.g. copper), is exposed to high temperatures and vacuum to fill the trenches, and then the surface is polished back so that the deposited material remains only within the trenches.^[5,6] Common challenges associated with this process include non-uniformity and sensitivity of materials to polishing and/or high temperatures.

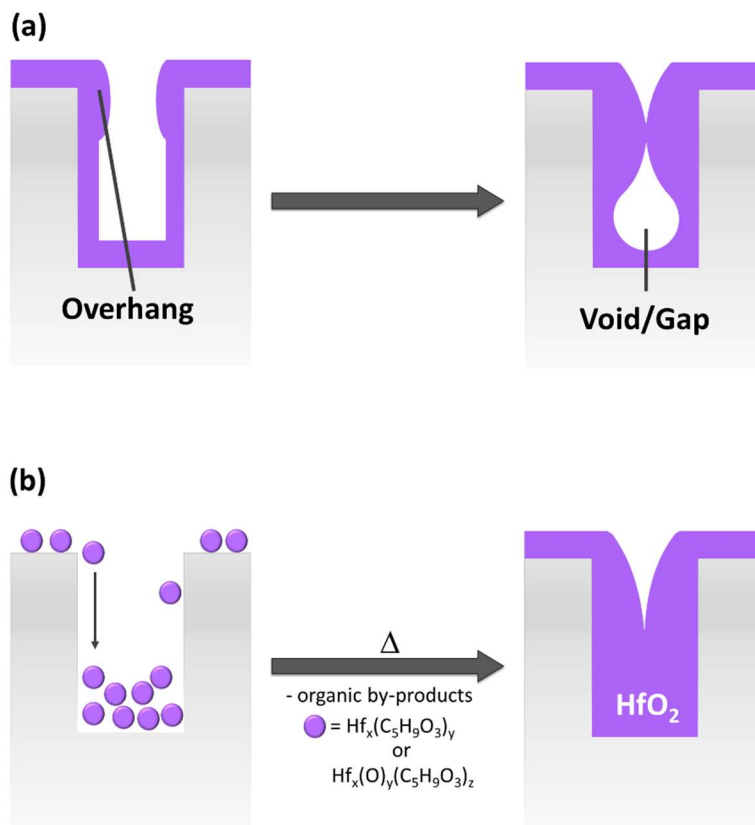


Figure 4.1: (a) Schematic diagram depicting the development of voids in a deposition process on a narrow trench substrate due to the growth of overhangs on the top of the trench. (b) Schematic diagram depicting the proposed development of a void-free film through deposition of monometallic complexes or oligomeric clusters and subsequent thermal conversion to HfO₂.

Alternative deposition methods focusing on the void-free filling of trenches have been reported, the majority of which aimed to deposit SiO₂. In most cases, the methods involved a preliminary step of low temperature deposition of an intermediary species exhibiting a capability of flowing to the bottom of the trench, due to a low molecular weight arising from their oligomeric nature, or sufficiently low viscosity, followed by a post deposition treatment involving a combination of heat, UV, and/or plasma exposure to

remove organic functional groups, leading to film shrinkage and densification (similar to that proposed in Figure 4.1b).^[7-13] The initially deposited films were prepared from a variety of methods including CVD (sometimes referred to in this context as flowable CVD),^[9,11] PE-CVD,^[7,8,10] HDP-CVD,^[13] and spin-coating.^[12] In the cases where the target material was SiO₂, a silicon-containing precursor such as trisilylamine (N(SiH₃)₃) was employed, and initial deposition of the flowable intermediary species occurred at low temperatures (ie. 100-250 °C) and sometimes in combination with a stable (e.g. NH₃, O₃) and/or plasma species as a co-reactant. Details about the intermediary species formed had not been ascertained. It is worth mentioning that major evidence of gap-filling capabilities in these processes utilized substrates containing non-parallel trenches that were tapered towards the bottom, which may inaccurately portray the lack of void formation as there is less possibility for overhangs to develop in such structures.

Vapour-phase methods for gap-free trench filling that do not involve flowable films have also been reported, and three prominent examples are discussed in this paragraph. Lee and coworkers reported the filling of 40 nm-wide trenches by the post-deposition tellurization annealing of ALD-grown Ge-Sb films using di-*tert*-butyltellurium.^[14] As the tellurization temperature increased, the Te at% concentration increased, resulting in expansion in the film volume. Complete trench filling was observed after tellurization at 230 °C (Figure 4.2a); however, a void was observed at the bottom of the trench at 250 °C. Poodt and coworkers recently reported the gap-filling capability of alucone deposited in high-aspect-ratio trenches by molecular layer deposition (MLD) with a CVD component due to insufficient outgassing of trimethylaluminum from the bottom of the trenches. This

CVD component provided a higher deposition growth rate within the trenches, thereby preventing gap formation during trench filling (Figure 4.2b).^[15] Nguyen, Cho, and coworkers achieved void-free filling of three-dimensional holes (50 nm wide at the bottom) by a gradient TiO₂ area-selective ALD (AS-ALD) process which utilized a molecular surface inhibitor, [TiCp*(OMe)₃], to prevent deposition of TiO₂ at the top of the substrate structure (Figure 4.2c).^[16] This was done to prevent blocking of the hole opening and allow for anisotropic TiO₂ film growth as there are a greater number of reactive surface sites at the bottom of the holes.

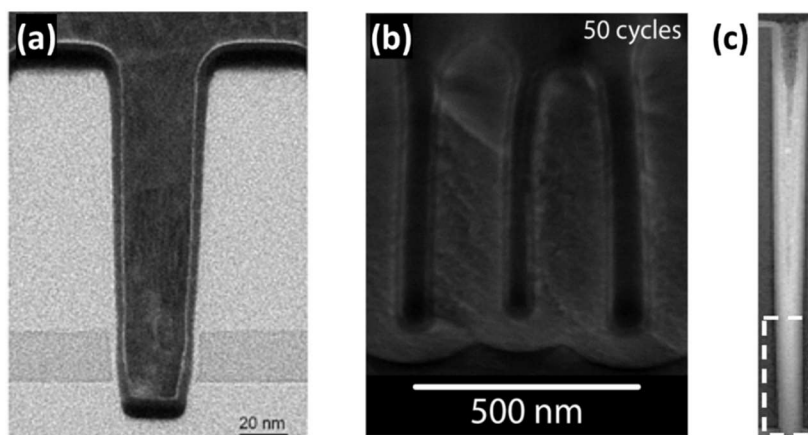


Figure 4.2: Example cross-sectional TEM (a and c) and SEM (b) images of gap-filled trenches. These images were adapted with permission from references [14], [15], and [16] for (a), (b), and (c), respectively.

In this work, we present efforts towards the development of a flowable ALD process for HfO₂ deposition. Previously reported HfO₂ thermal ALD processes have involved the use of homoleptic or heteroleptic Hf complexes as precursors bearing the

following ligands: halides, alkoxides, amides, cyclopentadienyls, alkyls, borohydrides, guanidates, hydroxylamides, and alkoxy carboximidates.^[17-20] The most frequently reported HfO₂ ALD precursors are depicted in Table 4.1. These processes all used classical co-reactants (H₂O, O₂, H₂O₂, and O₃) as oxygen sources, with a small number of notable exceptions that are described in the following paragraph.

Pinna and coworkers employed small carboxylic acids as alternative oxygen sources for the deposition of group 4 oxides that pose less risk of oxidation of the substrate surface.^[21,22] A constant growth rate of 0.5 Å was obtained between 175 and 250 °C using Hf(O^tBu)₄ and acetic acid, and XPS revealed low carbon content in the films. The use of formic acid led to a narrower ALD window at lower temperatures (100-125 °C), which the authors attributed to the higher reactivity and lower thermal stability of the acid. Jeon and coworkers investigated the use of N₂O gas versus N₂O plasma, in combination with [Hf(NEt₂)₄], for HfO₂ ALD.^[23] Although self-limiting growth was not confirmed by varying reactant pulse times, both processes displayed a linear growth rate with varying cycle number at 340 °C, and a constant growth rate was observed within a temperature window of 330 to 360 °C for N₂O gas (1.3 Å) and 300 to 360 °C for N₂O plasma (1.8 Å). The films obtained from the PEALD process were polycrystalline and displayed improved electronic properties (e.g. low leakage current density and carbon incorporation) over the amorphous films deposited by thermal ALD.

Table 4.1: Select Hf-containing precursors (left) and all co-reactants (right) used for reported HfO₂ thermal ALD processes.

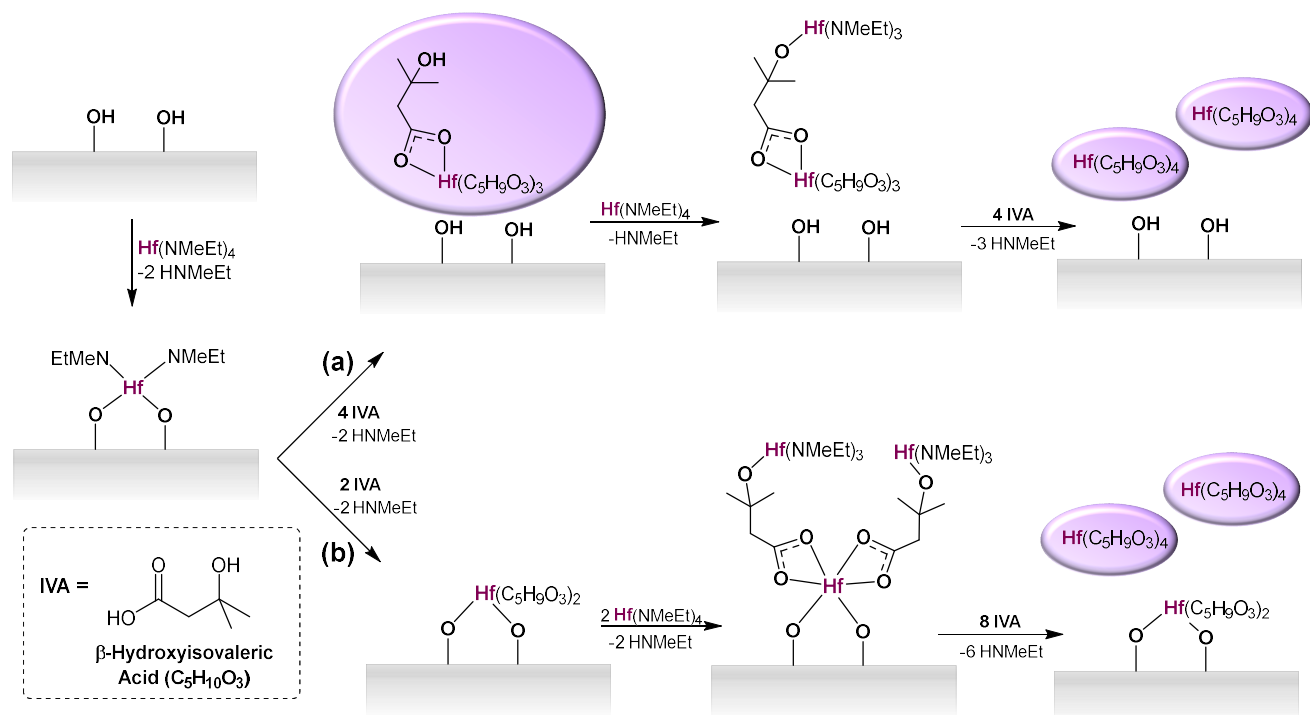
Precursors				Oxygen Sources				
HfCl_4	$\text{Hf}(\text{O}^t\text{Bu})_4$	$\text{Hf}(\text{mp})_4$	$\text{Hf}(\text{mmp})_4$	O_2	O_3	H_2O	H_2O_2	N_2O
				O_2	O_3	H_2O	H_2O_2	N_2O
				<i>This work</i>				

4.2 – Results

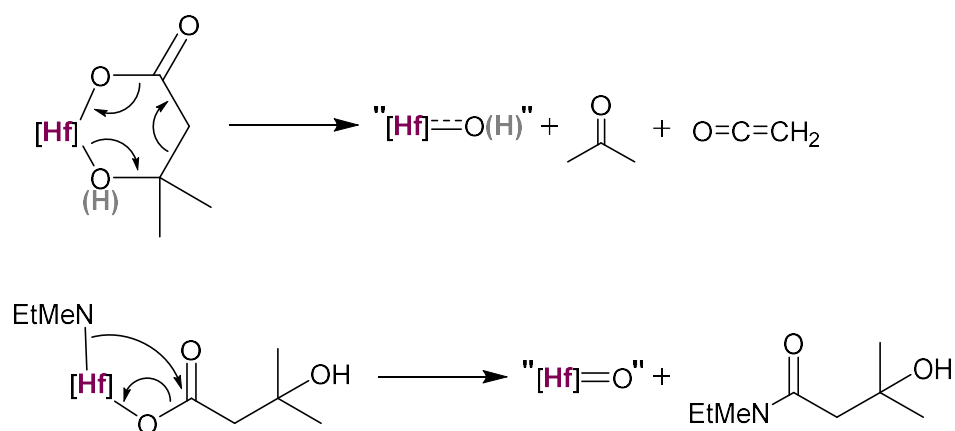
In this work, we investigate the use of β -hydroxyisovaleric acid (IVA) as an unusual oxygen source in combination with $[\text{Hf}(\text{NMeEt})_4]$ for HfO₂ ALD on SiO₂ substrates. Initial deposition studies discussed in this chapter utilized planar substrates, and future work will employ substrates featuring HAR trenches. It is rationalized that this carboxylic acid may allow for the deposition of non-volatile hafnium complexes and/or clusters which are not covalently tethered to the substrate surface, and could therefore diffuse to the bottom of HAR trenches and fill the trench in a void-free manner (Figure 4.1b). As shown in Scheme 4.1a, the acidity of the carboxyl group of IVA is expected to allow for the cleavage of the amido groups remaining after nucleation of $[\text{Hf}(\text{NMeEt})_4]$ onto the substrate surface, as well as Hf-O_{substrate} bonds, to form a non-volatile $[\text{Hf}(\text{C}_5\text{H}_9\text{O}_3)_4]$ complex. The β -hydroxyl group of the co-reactant acts as a secondary reactive site for incoming $[\text{Hf}(\text{NMeEt})_4]$ molecules which propagates the formation of additional $[\text{Hf}(\text{C}_5\text{H}_9\text{O}_3)_4]$ molecules. If the carboxyl group of IVA is unable to cleave the Hf-O_{substrate} bonds, then the first monolayer

would remain covalently tethered to the substrate surface. However, $[\text{Hf}(\text{C}_5\text{H}_9\text{O}_3)_4]$ molecules could still deposit over the newly formed monolayer due to the acidity of the carboxyl groups of oncoming IVA relative to that of the β -hydroxyl group tethering Hf centers to the passivated surface (Scheme 4.1b).

Furthermore, intramolecular transformations involving the IVA ligand, such as rearrangement of a 6-membered metallacycle to form acetone and ketene, may provide a mechanism for thermal conversion of the deposited material to HfO_2 , either during deposition on a longer timescale than flowability, or during post-deposition annealing. It is also worth noting that amide elimination caused by nucleophilic attack on a β -hydroxyisovalerate ligand by a neighbouring amido ligand (Scheme 4.2) could potentially result in the formation of oxo bridges, leading to larger, non-volatile $[\text{Hf}_x\text{O}_y(\text{C}_5\text{H}_9\text{O}_3)_z]$ clusters. The low temperature window accessible by thermal ALD in comparison to CVD may prove to be beneficial in maximizing flowability behaviour and avoiding premature conversion to the oxide species.^[8] A post-deposition treatment (e.g. wet or dry thermal anneal) may be required for conversion to the pure oxide.



Scheme 4.1: Schematic diagram of the idealized process to deposit monometallic complexes on the substrate surface using $[\text{Hf}(\text{NMeEt})_4]$ and IVA. Scenarios (a) and (b) differ based on whether the first monolayer remains covalently tethered to the substrate surface. This idealized scheme does not consider other possible coordination modes of the IVA ligand, or oxo bridge formation due to thermal decomposition of the IVA ligand.



Scheme 4.2: Proposed transformations involving a singly or doubly deprotonated IVA ligand coordinated to hafnium. $[\text{Hf}]$ indicates hafnium(IV) coordinated by other ligands, and (H) indicates a proton which may or may not be present, depending on whether IVA in the starting complex has been singly or doubly deprotonated.

4.2.1 – Deposition Using [Hf(NMeEt)₄] and IVA

Deposition studies were carried out using [Hf(NMeEt)₄] as the metal containing precursor and β-hydroxyisovaleric acid (IVA) as the co-reactant, delivered at 70 °C and 100 °C, respectively. Thermogravimetric analysis carried out on IVA (dried over 4Å molecular sieves) between 35 and 400 °C revealed the bulk of the mass loss (85%) occurred within a 50 °C window and >99% mass loss was observed by the end of the run (Figure 4.3). These data suggest that IVA efficiently volatilizes without decomposition within the short timeframe of TGA analysis. A neat sample of IVA was continuously heated at 100 °C in a sealed J. Young tube for one month to gauge its thermal stability over a longer timescale. The sample displayed approximately 20% decomposition by ¹H NMR spectroscopy. Therefore, IVA was determined to be thermally stable enough to be used as a co-reactant, but caution was exercised to ensure that the liquid was not heated at 100 °C for excessively long periods of time.

The walls of the ALD reactor were maintained at 100 °C, the temperature of the substrate stage varied between 100 and 300 °C, and a cycle number of 500 was kept constant. All deposition studies were on flat 100 nm SiO₂/Si substrates, and the pressure during reactor operation was 250 mTorr unless otherwise specified.

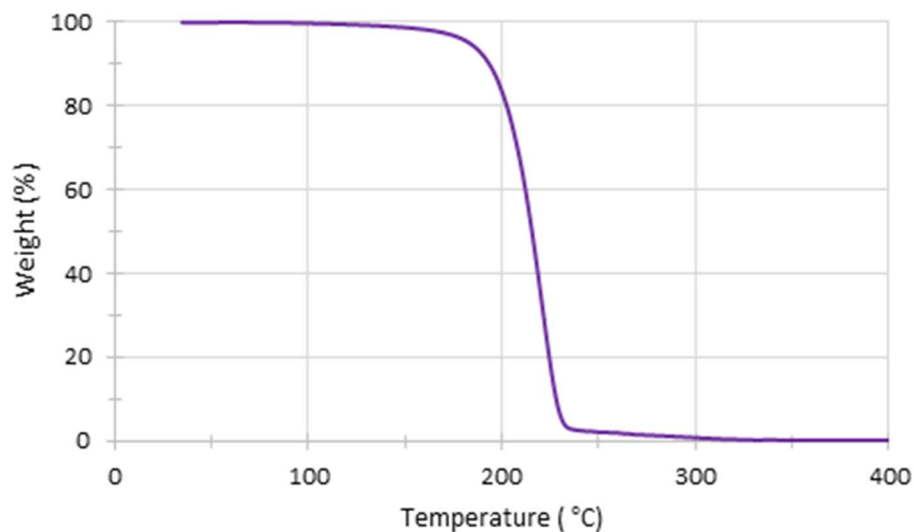


Figure 4.3: Thermogravimetric analysis (TGA) of β -hydroxyisovaleric acid (IVA). Ramp rate = 10 °C/min; starting weight = 4.286 mg.

At a deposition temperature of 100 °C, film growth was determined to be self-limiting (ie. GPC values remained constant within 0.1 Å) based on variable angle spectroscopic ellipsometry (VASE) measurements, giving rise to a GPC of 2.3 ± 0.1 Å when pulse durations (for both precursors) of 0.4, 0.6 and 1.0 seconds were employed, respectively (Figure 4.4). At 150 °C, the GPC increased significantly to 3.4 Å with 0.6 s pulse times, and did not exhibit self-limiting growth when pulse times were increased to 1.0 s (ie. the change in GPC was greater than 0.1 Å). The growth rate at 200 °C using 0.6 s pulse times was nearly equal to that obtained at 100 °C (2.2 Å); however, self-limiting growth was also not exhibited at this temperature. By contrast, at 250 and 300 °C, self-limiting growth was again achieved, affording GPCs of 1.6 ± 0.0 and 1.5 ± 0.05 Å, respectively, using pulse durations of 0.6 or 1.0 s.

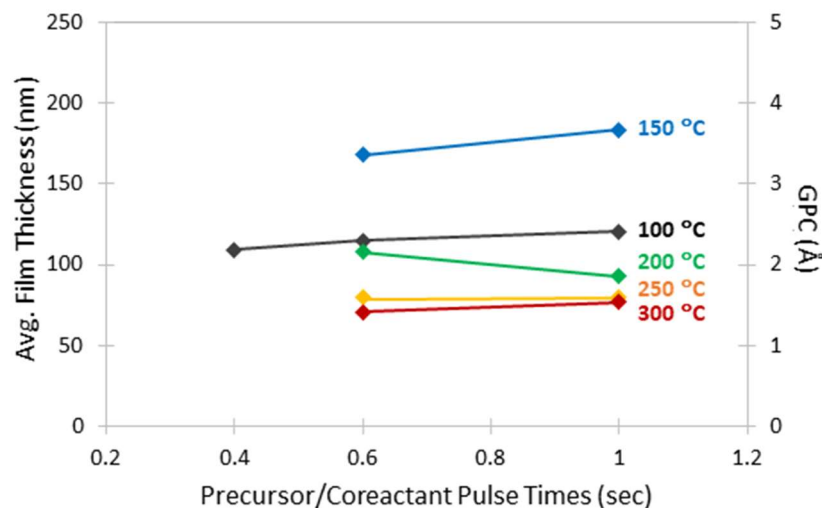


Figure 4.4: Dependence of average film thickness and GPC on [Hf(NMeEt)₄] and IVA pulse times at various deposition temperatures. All films were deposited using 500 cycles, and thicknesses/GPC values are for un-annealed films.

The variation in GPC as a function of temperature (using pulse durations of 0.6 s) is plotted in Figure 4.5, highlighting a maximum GPC at 150 °C. This figure also shows changes in film thickness that occur upon annealing *in vacuo* at 400 °C for 1 hour (the intent of annealing is to convert the initially deposited material into HfO₂). The effective GPCs for the annealed films range from 1.2 to 2.5 Å, depending on the deposition temperature; for comparison, GPC values previously reported for HfO₂ ALD using homoleptic or heteroleptic Hf precursors listed in Table 4.1 typically range from 0.5 to 1.2 Å.^[19] Similar to the as-deposited films, the thicknesses of annealed films grown at 100, 250, and 300 °C corresponded to self-limiting growth when pulse durations were increased from 0.6 to 1.0 s (Figure A4.1).

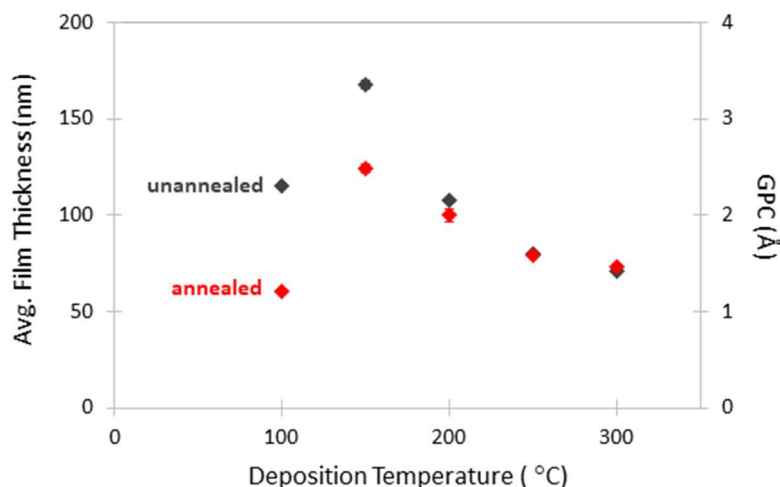


Figure 4.5: Dependence of average film thickness and GPC on deposition temperature without (gray) and with (red) in situ post-deposition thermal annealing. All films were deposited using 500 cycles and 0.6 s reactant pulse times.

All as-deposited films were silvery gold in appearance and were found to be amorphous by XRD. Many previous reports of HfO_2 thermal ALD also afforded amorphous HfO_2 , especially at temperatures below 300 °C.^[24,25] XPS depth analysis of a film grown at 100 °C revealed a Hf to O ratio of 1:2.1, and approximately 22 at% carbon content (Figure 4.6a).¹ The binding energy of Hf4f (17.4 eV; combined $4f_{5/2}$ and $4f_{7/2}$) fits within the range of energies previously reported for both HfO_2 ^[18,26,27] and hafnium carboxylates,^[28,29] and therefore the nature of the hafnium species cannot be established. The O1s region detected in the film consisted of one major peak and one shoulder peak

¹ Thin films analyzed by XPS depth analysis were deposited using slightly different preliminary experimental conditions than those for thin films discussed thus far. Initially, IVA was delivered at 50 °C, 20 s purge times were utilized for both reactants, and the total argon flow rate was 260 sccm, making the internal pressure during reactor operation 630 mTorr. As-deposited films grown at 100 °C using updated reactor conditions (higher IVA delivery temperature, longer purge times, lower flow rates) had little effect on the Hf:O atomic ratio or carbon concentration observed by XPS.

with binding energies of 531.8 and 530.0 eV, respectively (Figure A4.4). The smaller shoulder peak matches the reported O1s binding energy for HfO₂,^[26] and the larger broad peak could be attributed to either a metal carbonate or an organic hydroxyl species. In the C1s region of the sputtered levels of the as-deposited film, one major peak was observed with a binding energy of 280.0 eV which matches well with that reported for hafnium carbide.^[30]

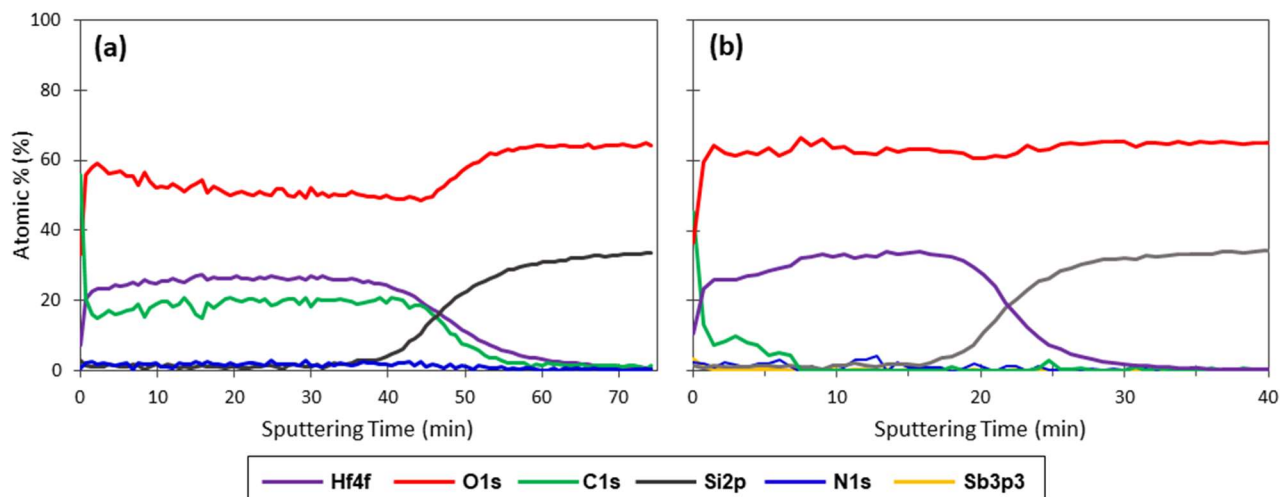


Figure 4.6: XPS depth analysis of films grown without (a) and with (b) an in situ post-deposition thermal annealing step. Thin films were grown at 100 °C using 500 cycles and 1.0 s reactant pulse times and 20 s purge times. For this preliminary data, initial experimental conditions used argon flow rates totaling 260 sccm (providing an internal pressure of 630 mTorr during operation), and IVA was delivered at 50 °C.

The atomic composition of the films deposited at 100 °C was not significantly sensitive to other experimental conditions. For example, carbon content between 22 and 28 at% was observed for films deposited using varying pulse times (0.6-1.0 s), purge times (20-60 s), and argon flow rates (260 or 80 sccm in total; corresponding to a reactor operating

pressure of 630 and 250 mTorr, respectively). Furthermore, the carbon content of films deposited at lower temperatures could be greatly decreased by thermal annealing at 400 °C *in vacuo* for 1 hour, resulting in films containing <1 at% carbon (after sputtering to remove surface contamination; Figure 4.6b). Thermal annealing afforded mirror-like silver-coloured films which, for films deposited at 100 °C, were found to be composed of HfO₂ by XPS, based on a Hf:O ratio very close to 1:2, and Hf4f and O1s peaks with binding energies of 17.8 and 530.0 eV, respectively (Figure A4.5), consistent with literature values for HfO₂.^[26,27] Thermal annealing resulted in a significant decrease in film thickness: 47.2, 26.0 and 7.4% for films deposited at 100, 150 and 200 °C, respectively, compared to <0.1% for films deposited at 250 and 300 °C (Figure 4.5).

FESEM images of the as-deposited film grown using 500 cycles at 100 °C show large circular grains (40-180 nm in diameter) atop a smooth and uniform continuous film (a and b in Figure 4.7). As yet, it is still unclear whether the grains are intrinsic to the deposition process, or whether nucleation is occurring on particles present due to reactor contamination. The overall morphology of the films did not change noticeably upon annealing (c and d in Figure 4.7).

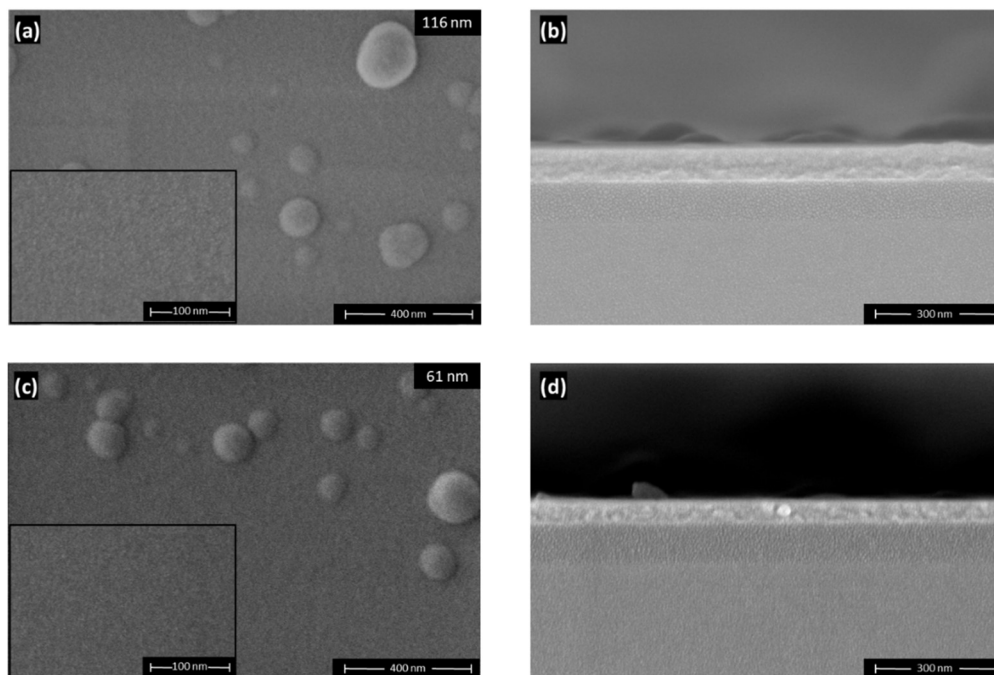
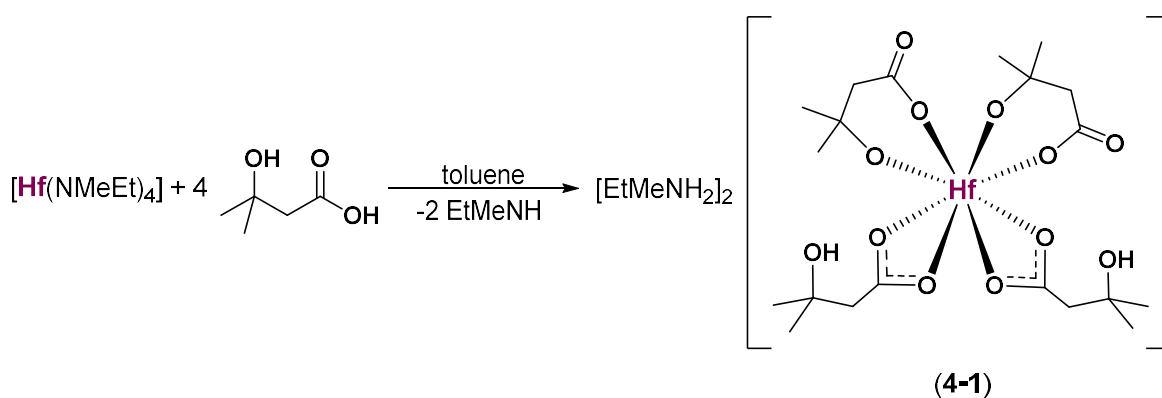


Figure 4.7: (a) Top-down and (b) cross-sectional FESEM images of as-deposited films grown at 100 °C. (c) Top-down and (d) cross-sectional FESEM images of post-deposition annealed films, using 500 cycles and 0.6 s pulse times. Film thicknesses are average values determined by VASE.

The co-reactant β -hydroxyisovaleric acid (IVA) provides a new method for thermal ALD of HfO_2 (either directly at 250 or 300 °C, or in the case of films deposited at 100 °C, after post-deposition annealing *in vacuo*). The β -hydroxyl group is considered to be essential to the effectiveness of IVA as a co-reactant, by providing reactive sites to react with $[\text{Hf}(\text{NMeEt})_4]$ in the next precursor pulse and/or by providing a relatively low-energy pathway for transformation of IVA-derived ligands to oxide or hydroxide ligands. Consistent with this hypothesis, attempted deposition of HfO_2 using $[\text{Hf}(\text{NMeEt})_4]$ and pivalic acid ($t\text{BuCO}_2\text{H}$) was unsuccessful at 100-250 °C.

4.2.2 – Solution-State Studies

In order to gain insight into the type of molecular structures that might form during deposition, solution-state reactions were conducted between 1 equivalent of $[\text{Hf}(\text{NMeEt})_4]$ and 1, 2, or 4 equivalents of IVA. In most cases, a gelatinous precipitate formed during the reaction or during crystallization attempts, which may be due to cross-linking via the hydroxyl group of IVA resulting in polymeric products. However, slow room-temperature vapour diffusion of hexanes into a toluene solution of the crude product from the 1:4 reaction afforded colourless plates of $[\text{EtMeNH}_2]_2[\text{Hf}(\kappa^2\text{-O}_2\text{CCH}_2\text{CMe}_2\text{OH})_2(\kappa^2\text{-OC(O)CH}_2\text{CMe}_2\text{O})_2]$ (**4-1**), in which two singly deprotonated IVA ligands are κ^2 -coordinated via the carboxylate group, and two doubly deprotonated IVA ligands are κ^2 -coordinated via one oxygen of the carboxylate group and the alkoxide oxygen, forming a 6-membered metallacycle (Scheme 4.3). The 8-coordinate Hf centre displays triangular dodecahedral geometry (Figure 4.8).



Scheme 4.3: Synthesis of $[\text{EtMeNH}_2]_2[\text{Hf}(\kappa^2\text{-O}_2\text{CCH}_2\text{CMe}_2\text{OH})_2(\kappa^2\text{-OC(O)CH}_2\text{CMe}_2\text{O})_2]$ (**4-1**) by amine elimination.

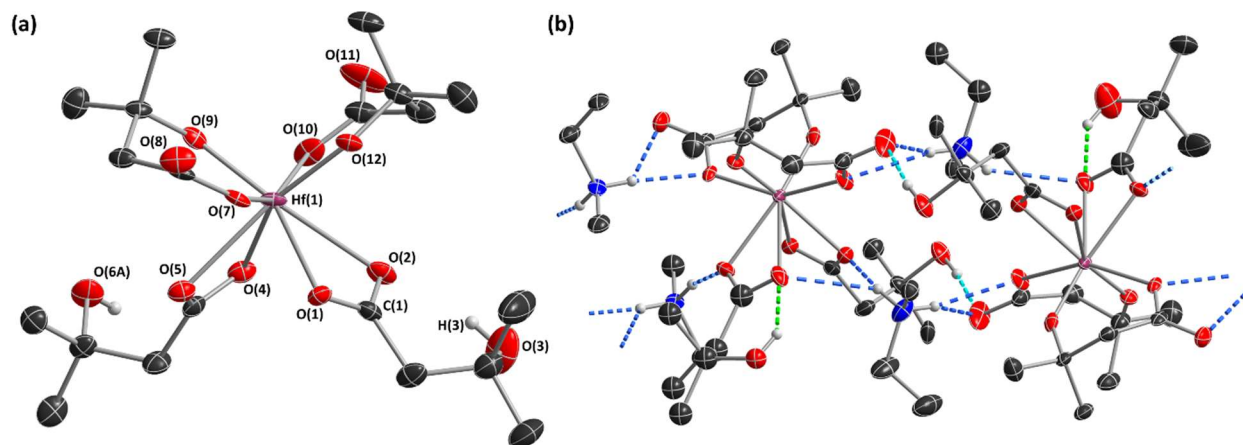


Figure 4.8: X-ray crystal structure of $[\text{EtMeNH}_2]_2[\text{Hf}(\kappa^2\text{-O}_2\text{CCH}_2\text{CMe}_2\text{OH})_2(\kappa^2\text{-OC(O)CH}_2\text{CMe}_2\text{O})_2]$ (**4-1**) with ellipsoids set at 50% probability. Space group P-1. View (a) shows only the anionic portion of the molecule, and view (b) shows the extended hydrogen-bonded structure, with intramolecular and intermolecular hydrogen bonds coloured green and blue, respectively. For clarity, most hydrogen atoms have been omitted, and disorder in the O(6) atom and neighbouring methyl groups are not shown. $R_1 = 0.0422$. Selected bond lengths (Å) and angles ($^\circ$): Hf(1)-O(1) 2.243(4), Hf(1)-O(2) 2.650(4), Hf(1)-O(4) 2.231(4), Hf(1)-O(5) 2.493(5), Hf(1)-O(7) 2.179(4), Hf(1)-O(9) 1.951(4), Hf(1)-O(10) 2.178(5), Hf(1)-O(12) 1.984(4), O(1)-Hf(1)-O(2) 52.2(1), O(1)-C(1)-O(2) 119.7(6), O(7)-Hf(1)-O(9) 82.1(2).

All Hf–O_{carboxylate} and Hf–O_{alkoxide} distances (2.178(5)–2.650(4) and 1.951(4)–1.984(4) Å, respectively) are in the expected ranges,^[31,32] confirming the extent of ligand deprotonation. Compound **4-1** exists as 1-dimensional chains involving four distinct types of hydrogen bonding interaction. One intramolecular interaction occurs between a dangling β -hydroxyl hydrogen {H(3)} and an oxygen atom of the carboxylate group {O(2)} within the same monoanionic ligand. The β -hydroxyl hydrogen atom of the second monoanionic ligand interacts with a carboxylate oxygen of a dianionic ligand of a neighbouring molecule. Two intermolecular interactions involving the 2 hydrogen atoms of the ethylmethylammonium counter cations are present: one hydrogen atom interacts

with one oxygen atom of a carboxyl group {O(1)} of a monoanionic ligand, and the other hydrogen atom interacts with the two carboxylate oxygen atoms of a dianionic ligand.

Room temperature ^1H and ^{13}C NMR spectra of **4-1** in C_6D_6 show one set of NCH_2CH_3 and NCH_3 signals, one set of $\text{O}_2\text{CCH}_2\text{CMe}_2\text{O}(\text{H})$ signals, and very broad NH and OH signals (Figures 4.10 and A4.6-8). These data are indicative of a rapid fluxional process which renders both the dianionic $\text{O}_2\text{CCH}_2\text{CMe}_2\text{O}^{2-}$ and monoanionic $\text{O}_2\text{CCH}_2\text{CMe}_2\text{OH}^-$ ligands equivalent on the NMR timescale; perhaps via protonation of $\text{O}_2\text{CCH}_2\text{CMe}_2\text{O}^{2-}$ ligands by the H_2NMeEt^+ cations (forming HNMeEt), followed by deprotonation of $\text{O}_2\text{CCH}_2\text{CMe}_2\text{OH}^-$ ligands by HNMeEt , with associated changes in the ligand binding mode (*vide supra*). Attempts were made to observe two sets of $\text{O}_2\text{CCH}_2\text{CMe}_2\text{O}(\text{H})$ signals (one for the $\text{O}_2\text{CCH}_2\text{CMe}_2\text{O}^{2-}$ ligands, and one for the $\text{O}_2\text{CCH}_2\text{CMe}_2\text{OH}^-$ ligands) by conducting ^1H NMR experiments at low temperatures (278-188 K) in *d*₈-toluene; however, this led only to peak broadening with some initial splitting observed for the $\text{O}_2\text{CCH}_2\text{CMe}_2\text{O}(\text{H})$ signal (Figure A4.9).

All hydrogen atoms in the X-ray crystal structure of **4-1** were added with AFIX constraints; however, q-peaks too weak to refine were observed in the tetrahedral positions of both nitrogen atoms. This observation, in combination with the short Hf- $\text{O}_{\text{alkoxide}}$ bond lengths and the relative integration of the NH and OH signals in the ^1H NMR spectrum of **4-1** at room temperature (Figure 4.10) and below (Figure A4.9), provide firm support that the structure of **4-1** contains two ethylmethyllummonium cations rather than neutral ethylmethyllumine.

Complex **4-1** can be considered to result, at least conceptually, from initial formation of $[\text{Hf}(\kappa^2\text{-O}_2\text{CCH}_2\text{CMe}_2\text{OH})_4]$, followed by deprotonation of the hydroxyl group in two of the β -hydroxyisovalerate ligands by the methylethylamine by-product, likely after initial coordination of the hydroxyl groups to hafnium, rendering them more acidic. However, it is notable that this reaction is more complex than might be anticipated, given that an unidentified hafnium-containing precipitate is initially formed (all signals stemming from IVA are absent in the ^1H NMR spectrum).

The structure of **4-1** illustrates the potential for (a) double deprotonation of IVA, (b) κ^2 -coordination of doubly deprotonated IVA via one carboxylate oxygen atom and the alkoxide group, and (c) ammonium salt formation via acid/base reactivity involving the ethylmethylethylamine reaction by-product. To probe the potential for ethylmethylethylamine loss, solid **4-1** (crystals) was heated *in vacuo* in 20 °C temperature intervals up to 100 °C for 4 hours. ^1H NMR spectra of the sample indicated that product decomposition occurred before complete loss of signals attributed to the *N*-methyl and *N*-ethyl groups (Figure 4.9). Heating pure **4-1** at 200 °C for 4 hours under dynamic vacuum led to complete decomposition, with no signals observable by ^1H NMR spectroscopy of the residue.

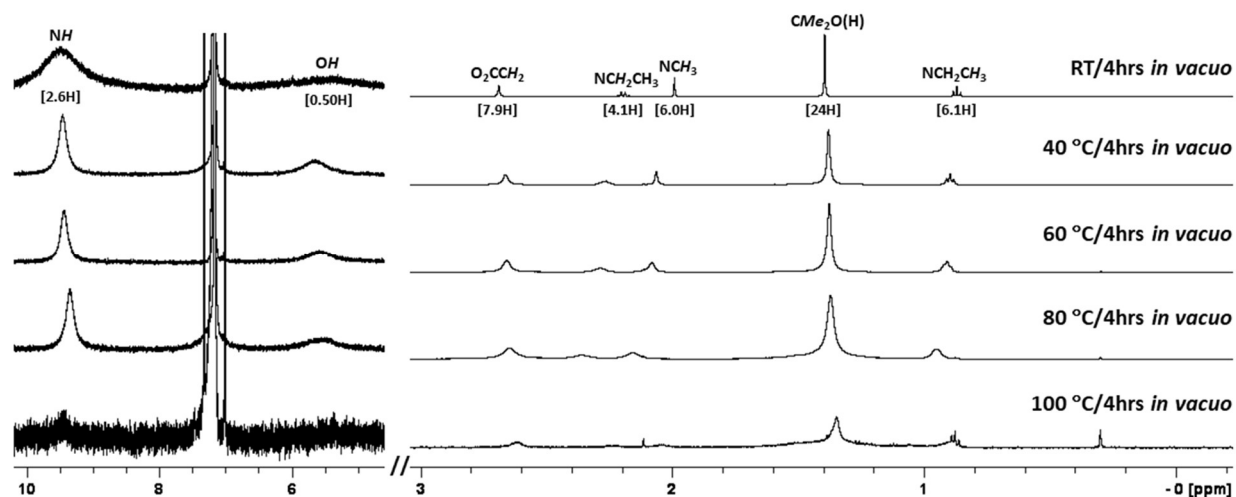


Figure 4.9: ^1H NMR spectra of pure $[\text{EtMeNH}_2]_2[\text{Hf}(\kappa^2\text{-O}_2\text{CCH}_2\text{CMe}_2\text{OH})_2(\kappa^2\text{-OC(O)CH}_2\text{CMe}_2\text{O})_2]$ (**4-1**) after heating the sample as a solid *in vacuo* at the indicated temperatures for 4 hours (C_6D_6 , 500 MHz, 298 K).

It is unlikely that ammonium salts similar to **4-1** play a significant role during ALD within the 100–300 °C temperature range, given that minimal (~1%) nitrogen was detected by XPS depth analysis in the as-deposited film grown at 100 °C (Figure 4.6a). The complex proposed in the 1:4 reaction of $[\text{Hf}(\text{NMeEt})_4]$ and IVA, or an oligomeric form of the complex formed from reactions involving the ligand's β -hydroxyl group ($[\text{Hf}(\kappa^2\text{-O}_2\text{CCH}_2\text{CMe}_2\text{OH})_4]_n$, $n \geq 1$), is more likely to be a possible surface species.

To further probe the reactivity of $[\text{Hf}(\text{NMeEt})_4]$ with carboxylic acids, reactions were conducted utilizing pivalic acid ($t\text{BuCO}_2\text{H}$) as a hydroxyl-free alternative. The 1:4 reaction of $[\text{Hf}(\text{NMeEt})_4]$ with pivalic acid in benzene afforded crystals of $[\text{Hf}_5(\mu_3\text{-O})_4(\kappa^2\text{-O}_2\text{C}^i\text{Bu})_4(\mu\text{-O}_2\text{C}^i\text{Bu})_8] \cdot 3\text{C}_6\text{H}_6$ (**4-2**(C_6H_6)₃). This compound features five hafnium centres linked by four μ_3 -oxo bridges, resulting in a square-based pyramidal

arrangement of the hafnium centres (Figure 4.10). Each hafnium centre in the basal plane {Hf(2), Hf(3), Hf(2') and Hf(3')}, is also κ^2 -coordinated to one pivalate ligand. Furthermore, four pivalate anions bridge between the four hafnium centres in the basal plane, and a pivalate anion bridges between each of the four hafnium centres in the basal plane and Hf(1) in the apical site. Consequently, Hf(1) is 8-coordinate, with a square antiprismatic geometry, whereas the hafnium centres in the basal plane are 7-coordinate, with a geometry best described as capped trigonal prismatic. Residual density located in the difference map near the oxo bridges and below the basal plane is attributed to whole molecule disorder. The absence of O-H stretches in the FT-IR spectrum of **4-2**(C₆H₆)₃ confirms the assignment of O(1) and O(2) as oxo groups rather than hydroxyl groups (Figure A4.16).

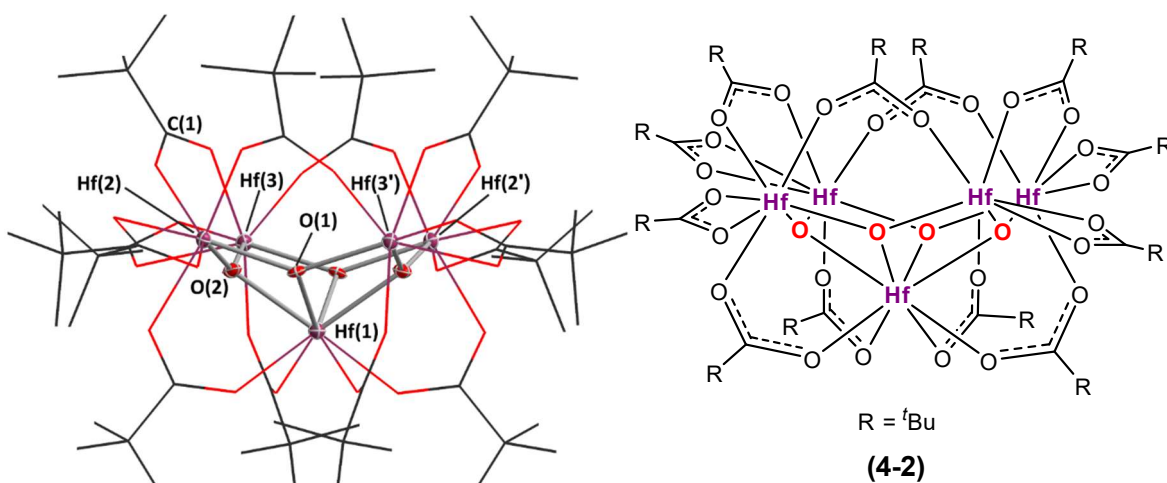


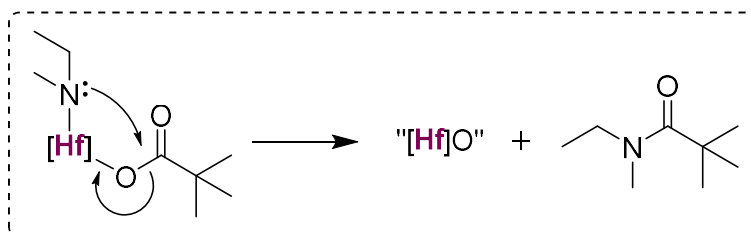
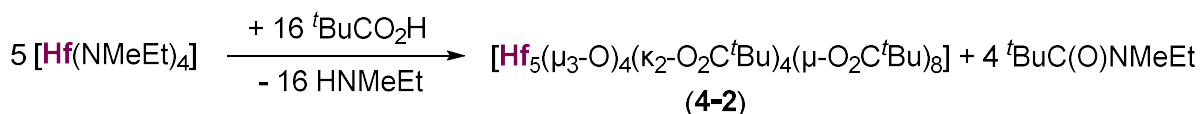
Figure 4.10: X-ray crystal structure of [Hf₅(μ₃-O)₄(κ²-O₂C^tBu)₄(μ-O₂C^tBu)₈] \cdot 3C₆H₆ (**4-2**(C₆H₆)₃) with ellipsoids set at 50% probability. Space group C2/c. For clarity, hydrogen atoms and lattice solvent are omitted, and pivalate anions are depicted in wireframe. R₁ = 0.0529. Selected bond lengths (Å) and angles (°): Hf(1)-O(1) 2.171(4); Hf(1)-O(2) 2.157(5); Hf(2)-O(1) 2.064(5); Hf(2)-O(2) 2.007(5); Hf(3)-O(1) 2.019(5); Hf(3)-O(2) 2.089(5); O(1)-Hf(1)-O(2) 71.20(2); O(1)-Hf(1)-O(1') 113.1(2); O(2)-Hf(1)-O(2') 110.9(3);

Hf(1)-O(2)-Hf(2) 102.3(2), Hf(1)-O(2)-Hf(3) 103.9(2), Hf(2)-O(2)-Hf(3) 143.4(2); Hf(2)-O(2)-Hf(3') 144.8(3).

Hf(1) is positioned 1.82 Å away from the basal Hf(2)/Hf(3)/Hf(2')/Hf(3') plane. The bridging oxo ligands bond more closely to the basal hafnium centers, Hf(2) and Hf(3), (Hf-O_{oxo} = 2.007(5)-2.089(5) Å) than the apical hafnium centre, Hf(1) (Hf-O_{oxo} = 2.157(5) and 2.171(4) Å). Bonds between the bridging pivalate ligands and Hf(2) or Hf(3) (Hf-O_{piv} = 2.138(5)-2.153(5) Å) are also shorter than those to 8-coordinate Hf(1) (Hf-O_{piv} = 2.216(5) and 2.227(5) Å). The Hf-O_{oxo} bond distances are within the range previously reported for hafnium complexes containing μ_3 -oxo ligands (2.02(2)-2.25(2) Å).^[33] Additionally, the Hf-O_{carboxylate} distances and O-C-O angles are within the reported range for κ^2 -coordinated (2.18(1)-2.320(5) Å; 115.2(9)-118.2(7)°) and bridging (2.11(2)-2.281(5) Å; 120.4(3)-130.2(2)°) carboxylate ligands in hafnium complexes, respectively.^[34,35] Boyle and coworkers have synthesized and structurally characterized a series of group 4 carboxylate complexes for nanowire production from reactions of [M(O^tBu)₄] (M = Ti, Zr, Hf) and pivalic acid, including [Hf₂(μ -O₂C^tBu)₄(κ^2 -O₂C^tBu)₄] and [Hf₄(μ_3 -O)₂(μ -O₂C^tBu)₈(μ , κ^2 -O₂C^tBu)₂(κ^2 -O₂C^tBu)₂], although the quality of the latter structure was poor due to significant ligand disorder.^[36] The bond metrics of the former structure are very similar to those of complex **4-2(C₆H₆)₃** (e.g. O-C-O angles of bridging pivalate ligands = 121.4(1)-124.9(2) versus 121.9(6)-123.3(6), respectively).

The formation of **4-2(C₆H₆)₃**, under strictly anhydrous conditions, is likely due to intramolecular nucleophilic attack of an ethylmethyamido ligand (EtMeN⁻) on the

carbonyl carbon of a pivalate ligand, forming an oxo ligand and an organic amide by-product ($t\text{BuC(O)NMeEt}$; *N*-ethyl-*N*-methylpivalamide). This reactivity requires a 1:3.2 ratio of $[\text{Hf}(\text{NMeEt})_4]$ to pivOH (Scheme 4.4), and indeed, crystals of **4-2** (solvent-free; Figure A4.30; this solid-state structure is isostructural to that of **4-2(C₆H₆)₃**, so is not discussed further) were isolated in reasonable yield using this stoichiometry, followed by crystallization from diethyl ether at $-30\text{ }^\circ\text{C}$.



Scheme 4.4: Intramolecular nucleophilic addition producing *N*-ethyl-*N*-methylpivalamide during the formation of **4-2**. [Hf] indicates hafnium(IV) coordinated by other ligands.

The ^1H NMR spectra of crystals of **4-2(C₆H₆)₃** and **4-2** consist primarily of one (in C_6D_6) or two (in $d_8\text{-THF}$) broad signals (Figure A4.10) which is likely due to dynamic exchange occurring in solution on the NMR timescale,^[37] as has been observed previously in reports of Hf-containing clusters of similar size (e.g. $[\text{Hf}_2(\text{O}_2\text{C}^t\text{Bu})_8]$,^[36] $[\text{Hf}_4(\text{O})_2(\text{O}_2\text{C}_4\text{H}_5)_{12}]$, and $[\text{Hf}_6(\text{O})_4(\text{OH})_4(\text{O}_2\text{C}_4\text{H}_5)_{12}(n\text{BuOH})]$ ^[28,38]). The room temperature ^1H and $^{13}\text{C}\{^1\text{H}\}$ NMR spectra for **4-2** in $d_8\text{-THF}$ show one sharp set of $t\text{Bu}$ signals, and one broad set of signals, suggesting that of the three chemically distinct $t\text{Bu}$ environments in **4-2**, one remains static

on the NMR timescale, while two are in rapid exchange. However, an alternative explanation is that **4-2** dissolves to afford a mixture of two different clusters (presumably **4-2** and an undetected species), and fluxional processes render the environments in each of the clusters equivalent. At 188 K, four broad ^tBu singlets are observed in the ¹H NMR spectrum with a 2:4:4:2 integration ratio (Figure 4.11), and four major CMe₃, CMe₃, and CO₂ signals were also observed in the ¹³C{¹H} NMR spectrum (Figure A4.12-15). Given that **4-2** would be expected to give rise to a maximum of three ^tBu signals, the low temperature data seems more consistent with the presence of two different clusters in solution.

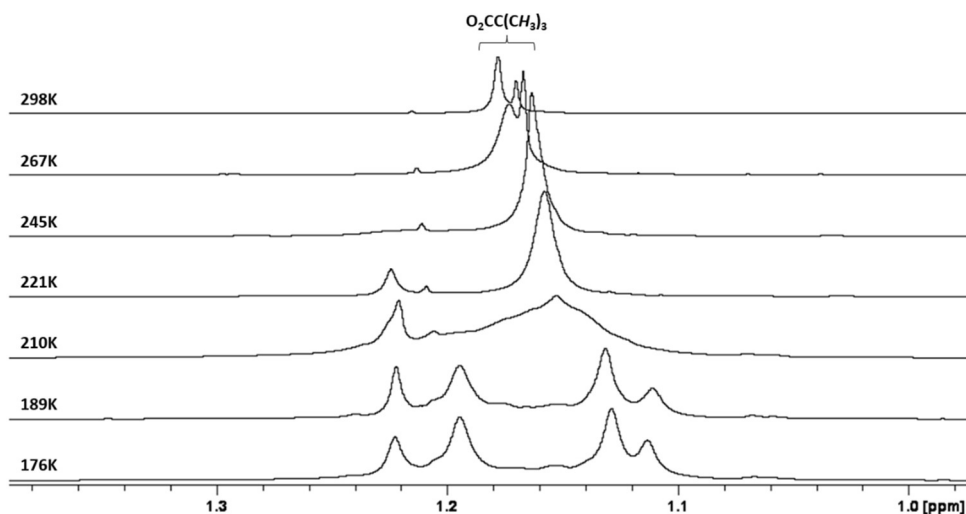


Figure 4.11: Variable temperature ¹H NMR spectra of [Hf₅(μ₃-O)₄(κ²-O₂C^tBu)₄(μ-O₂C^tBu)₈] (**4-2**; d₈-THF, 500 MHz).

Consistent with the proposed reaction pathway for the formation of **4-2**, the expected *N*-ethyl-*N*-methylpivalamide by-product was observed (4 equiv. relative to **4-2**) in the 1:3.2

reaction between $[\text{Hf}(\text{NMeEt})_4]$ and ${}^t\text{BuCO}_2\text{H}$ (Figure 4.12). By contrast, in the 1:4 reaction between $[\text{Hf}(\text{NMeEt})_4]$ and ${}^t\text{BuCO}_2\text{H}$, the amide by-product was formed in much smaller amounts (~ 0.1 equiv. relative to the free amine), indicating that oxo ligand formation becomes more significant under conditions where ${}^t\text{BuCO}_2\text{H}$ is in deficit (< 4 equiv.), because oxo ligand formation requires reactivity between pivalate ligands and *remaining* amido ligands. To the best of our knowledge, **4-2** represents the first reported example of a pentahafnium oxo complex, and of a group 4 oxo complex prepared by amide elimination.^[37,39]

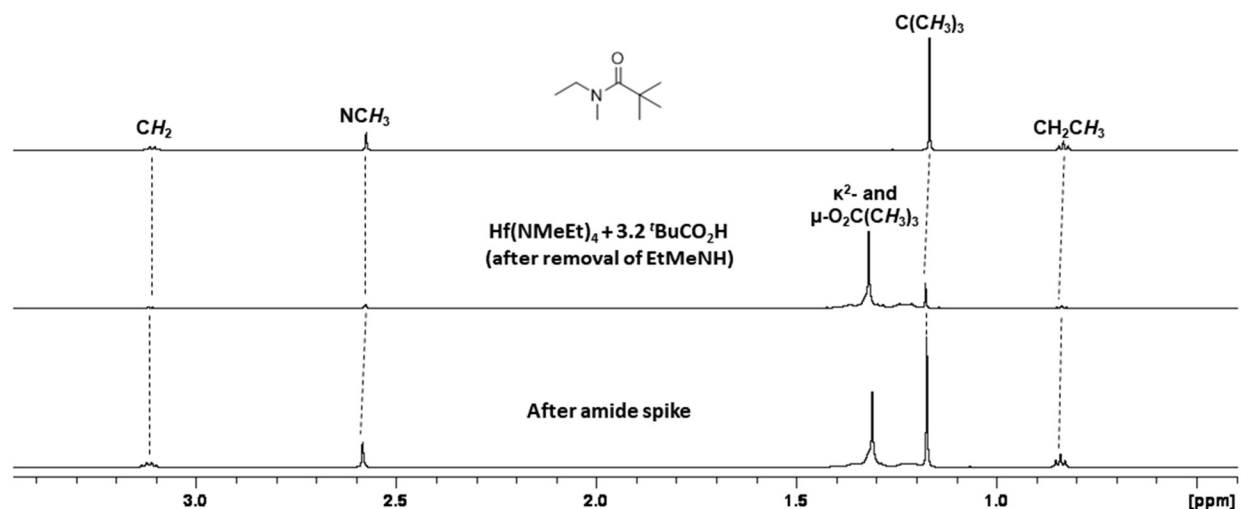


Figure 4.12: ${}^1\text{H}$ NMR spectra confirming the generation of *N*-ethyl-*N*-methylpivalamide (top) in the NMR-scale reaction between 1 equivalent of $[\text{Hf}(\text{NMeEt})_4]$ and 3.2 equivalents of pivOH (middle) (C_6D_6 , 500 MHz, 298 K) required for the formation of $[\text{Hf}_5(\mu_3\text{-O})_4(\kappa^2\text{-O}_2\text{C}^t\text{Bu})_4(\mu\text{-O}_2\text{C}^t\text{Bu})_8]$ (**4-2**). In the bottom spectrum, an independently-synthesized sample of the amide was added to the NMR tube, to verify the identity of the reaction by-product.

The carbon (22 at%), and nitrogen (<1 at%) content of the film deposited at 100 °C might indicate the formation of surface species similar to the proposed complex $[\text{Hf}(\text{O}_2\text{CCH}_2\text{CMe}_2\text{OH})_4]$ (61 at% carbon not including hydrogen) or pentahafnium cluster **4-2** (57 at% carbon not including hydrogen, if all pivalate ligands are replaced with isovalerate ligands), with some ligand decomposition occurring to reduce the carbon content over the duration of the deposition experiment.

4.2.3 – Decomposition Studies

Studies were carried out to identify reaction pathways that might be involved in the decomposition of singly or doubly deprotonated IVA ligands, either during ALD or in a subsequent annealing step. Specifically, $[\text{Hf}(\text{NMeEt})_4]$ was reacted with 4 equiv. of IVA in solution for 24 hours at room temperature, and the reaction mixture was then evaporated to dryness *in vacuo*. This residue, which consisted almost exclusively of compound **4-1** by ^1H NMR spectroscopy, was heated at 200 °C, and then analyzed as follows: after heating for 4 hours under dynamic vacuum in a flask with an attached –196 °C cold-trap to collect volatiles, room temperature-volatile by-products were (a) vacuum transferred into a degassed J. Young NMR tube and analyzed by ^1H or ^{13}C NMR spectroscopy in C_6D_6 , or (b) vacuum transferred into a 2-neck round bottom flask sealed with a rubber septum and analyzed by headspace gas chromatography-mass spectrometry (GC-MS). Products that remained in the collection flask were analyzed by NMR spectroscopy and GC-MS. The residual amorphous solid in the original flask contained only insoluble compounds (i.e. no signals were detected by ^1H NMR spectroscopy in C_6D_6), but contained approximately 23.5% carbon by combustion elemental analysis.

The major decomposition by-products from headspace GC-MS analysis were ethylmethanamine, isobutene, and acetone, accompanied by smaller amounts of CO₂, *N*-ethyl-*N*-methanacetamide (MeC(O)NMeEt), mesityl oxide (MeC(O)CH=CMe₂), and an unidentified product with a retention time of 19.92 minutes (Figure 4.14). All of the by-products observed by GC-MS were also identified (in comparable ratios to one another) by ¹H and/or ¹³C NMR spectroscopic analysis of the volatile reaction products produced under dynamic vacuum (Figure 4.13 and A4.17).

The major non-room temperature-volatile product that remained in the collection flask (as determined by ¹H and ¹³C{¹H} NMR spectroscopy) was the amide formed from the reaction of IVA and ethylmethanamine (*N*-ethyl-3-hydroxy-*N*,3-dimethylbutanamide; Figure 4.14). This product, as well as the dehydrated derivative of the amide (*N*-ethyl-*N*,3-dimethylbut-3-enamide; presumably formed during the high-temperature injection of the GC-MS sample) and minor amounts of free IVA, was observed by GC-MS (Figure A4.18). The identification of these two amides was tentatively assigned based on the fragmentation patterns in their mass spectra (Figures A4.27-28).

The formation of isobutene and CO₂ is proposed to occur via κ^2 -coordination of singly or doubly deprotonated IVA to form a 6-membered metallacycle (as observed in the X-ray crystal structure of **4-1**), followed by electrocyclic rearrangement (Scheme 4.5). Furthermore, rearrangement in the opposite direction would afford acetone and ketene, and the latter highly reactive product would be expected to react with methylethylamine to afford the observed *N*-ethyl-*N*-methanacetamide. Aldol condensation of 2 equivalents of acetone would result in the formation of the observed mesityl oxide (Scheme 4.5). Both

of these rearrangements generate a hydroxide or oxide ligand on hafnium, depending on whether the starting ligand is monoanionic or dianionic (i.e. whether the H atom shown in brackets in Scheme 4.5 is present or absent), respectively, and any hydroxide ligands can then convert to oxide ligands via elimination of water ($2 [\text{Hf}]\text{OH} \rightarrow [\text{Hf}]_2\text{O} + \text{H}_2\text{O}$).

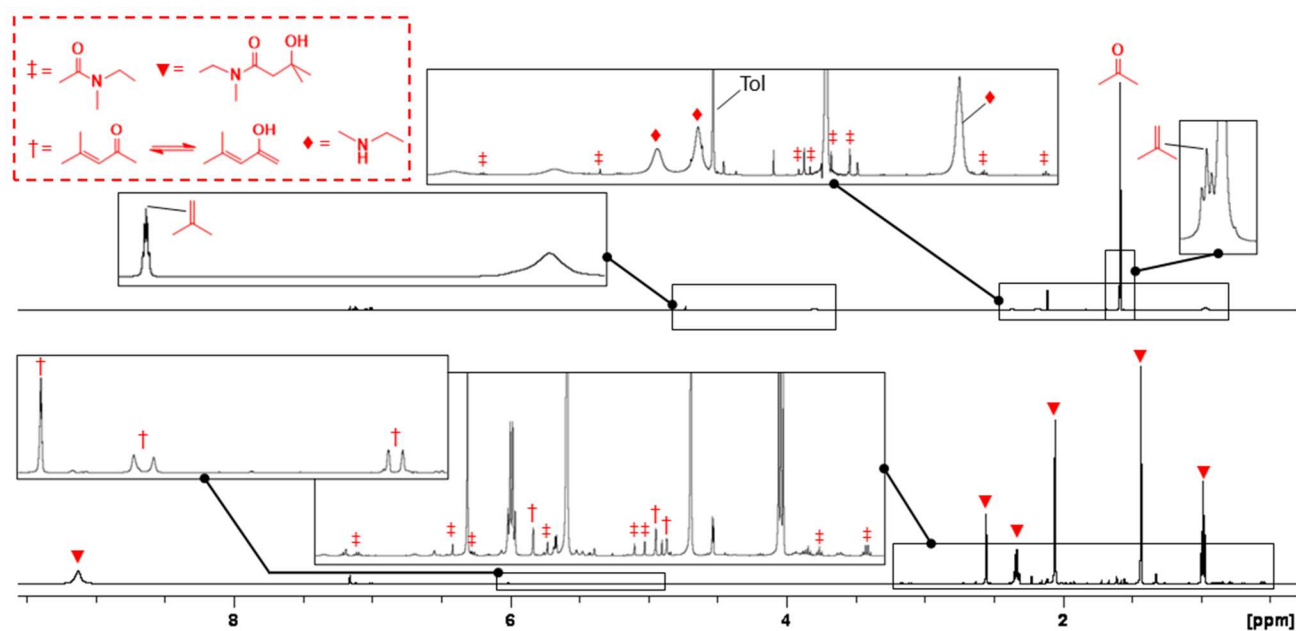


Figure 4.13: ¹H NMR spectra of the by-products (coloured red) from the thermal decomposition of a crude sample of **4-1** at 200 °C for 4 hours under dynamic vacuum (C₆D₆, 600 MHz, 298 K). Top: Room temperature-volatile by-products vacuum transferred into a degassed J. Young tube containing C₆D₆. Bottom: Non-room temperature-volatile by-products dissolved in C₆D₆.

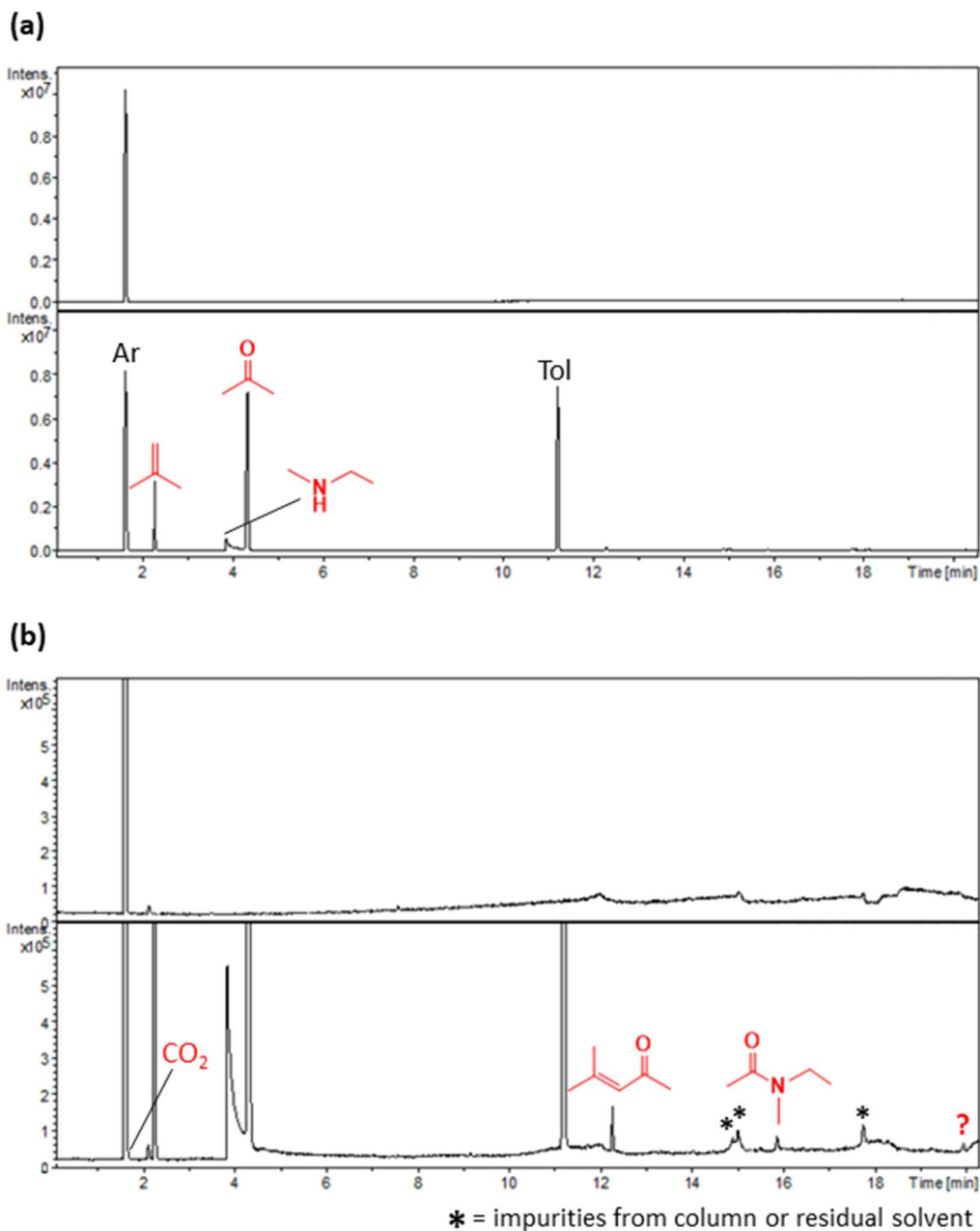
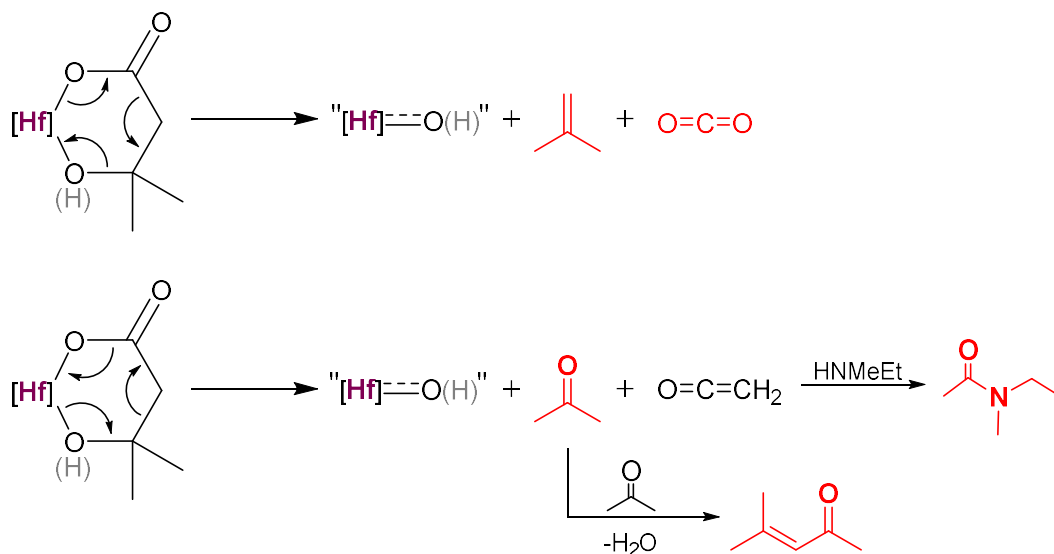


Figure 4.14: Headspace gas chromatograph of room temperature-volatile by-products (coloured red) formed from heating a crude sample of **4-1** at 200 °C for 4 hours under dynamic vacuum (bottom) and of the experimental blank (top). Figure (b) is the same as Figure (a) except that the baseline is magnified in order to display minor thermal decomposition by-products.

GC-MS and NMR spectroscopy data illustrate substantially more acetone than isobutene (~4.5:1 ratio), indicating that electrocyclic rearrangement to form acetone and CO₂ is the dominant ligand decomposition pathway. However, isobutene and CO₂ should be formed in a 1:1 ratio, and acetone and products derived from ketene (e.g. *N*-ethyl-*N*-methylacetamide) should be formed in a 1:1 ratio, which is not the case; substantially more acetone and isobutene was observed than CO₂ and *N*-ethyl-*N*-methylacetamide. This may be due to other unidentified reactions consuming CO₂ and ketene, such as reactions of CO₂ with oxo ligands to form carbonate,^[20,40-42] or ketene polymerization.^[43,44]



Scheme 4.5: Proposed decomposition pathways for a singly or doubly deprotonated IVA ligand that is κ^2 -coordinated to hafnium; these pathways generate the thermal decomposition products (coloured red) observed by NMR spectroscopy and GC-MS headspace analysis. [Hf] indicates hafnium(IV) coordinated by other ligands, and (H) indicates a proton which may or may not be present, depending on whether IVA in the starting complex has been singly or doubly deprotonated.

4.3 – Summary and Conclusions for Chapter 4

Thermal ALD of carbon-contaminated HfO₂ on SiO₂/Si was achieved at 100 °C using [Hf(NMeEt)₄] as the precursor and β-hydroxyisovaleric (IVA) acid as the co-reactant. Deposition was observed between 100 and 300 °C, but a constant growth rate characteristic of ALD was only observed at 100, 250, and 300 °C. *In situ* thermal annealing after 100 °C deposition yielded a carbon-free, amorphous HfO₂ film. This new ALD method may generate flowable molecular (monometallic or oligomeric) species on the surface, enabling flowable ALD with gap-filling capabilities.

While most solution-state reactions involving [Hf(NMeEt)₄] and IVA produced gel-like precipitates, single crystals of [EtMeNH₂]₂[Hf(κ²-O₂CCH₂CMe₂OH)₂(κ²-OC(O)CH₂CMe₂O)₂] (**4-1**) were obtained which featured monoanionic and dianionic IVA ligands and *N*-ethyl-*N*-methylammonium counter cations. Analogous reactions employing pivalic acid (*t*BuCO₂H) as a substitute for IVA led to the formation of a small molecular cluster, [Hf₅(μ₃-O)₄(κ²-O₂C^{*t*}Bu)₄(μ-O₂C^{*t*}Bu)₈] (**4-2**). These complexes provide insight into the nature of potential surface species formed during ALD.

The carbon content in the potential surface species, [Hf(O₂CCH₂CMe₂OH)₄] and [Hf₅(O)₄(O₂CCH₂CMe₂OH)₁₂], is significantly higher than that observed in the 100 °C as-deposited film, which indicates that thermal decomposition must occur during deposition. Heating of crude **4-1** yielded multiple thermal decomposition by-products which were identified by NMR spectroscopy and GC-MS. Major products were acetone and isobutene, indicative of thermally induced electrocyclic fragmentation of β-

hydroxyisovalerate or β -alkoxyisovalerate ligands on hafnium. By-products observed in minor amounts were CO_2 , *N*-ethyl-*N*-methylacetamide, *N*-ethyl-*N*-methylamine, and mesityl oxide.

4.4 – Future Work Pertaining to Chapter 4

To investigate the gap-filling capabilities of the $[\text{Hf}(\text{NMeEt})_4]/\text{IVA}$ process, deposition of Hf-containing thin films will be conducted on HAR Si and SiO_2 substrates. A variety of deposition conditions must be tested, such as the deposition temperature and the pulse and purge durations. Additionally, XPS depth analysis will be performed on films grown on planar substrates at temperatures of 150-300 °C to analyze their carbon content and to determine whether carbon content correlates with the percentage decrease in film thickness that occurs upon post-deposition annealing of the films. In order to assess the suitability of the $[\text{Hf}(\text{NMeEt})_4]/\text{IVA}$ process for applications in the semiconductor industry, it will also be important to obtain information regarding the deposited material's film density and crystallization temperature.

Furthermore, future work in this research will involve utilizing alternative hafnium precursors in combination with IVA to assess the viability of the process for flowable ALD. Initial efforts in this avenue utilized $[\text{Hf}(\text{NMe}_2)_4]$ and $[\text{Hf}(\text{O}^t\text{Bu})_4]$ to deposit thin films at 100 °C (Figure 4.15). Preliminary results revealed that the $[\text{Hf}(\text{O}^t\text{Bu})_4]/\text{IVA}$ process yielded films of similar thickness to those deposited by the $[\text{Hf}(\text{NMeEt})_4]/\text{IVA}$ process, and the process displayed self-limiting growth characteristic of ALD ($2.0 \pm 0.1 \text{ \AA}$). However,

the $[\text{Hf}(\text{NMeEt})_4]/\text{IVA}$ process differed greatly, with the film deposited using 0.6 s pulse durations nearly double the thickness of the $[\text{Hf}(\text{NMeEt})_4]/\text{IVA}$ films grown in the same conditions, and non-ALD growth observed with increased pulse durations. XPS depth analysis of the deposited films in combination with solution-state reactions involving the alternative hafnium precursors and IVA may provide insight into the nature of the potential surface species.

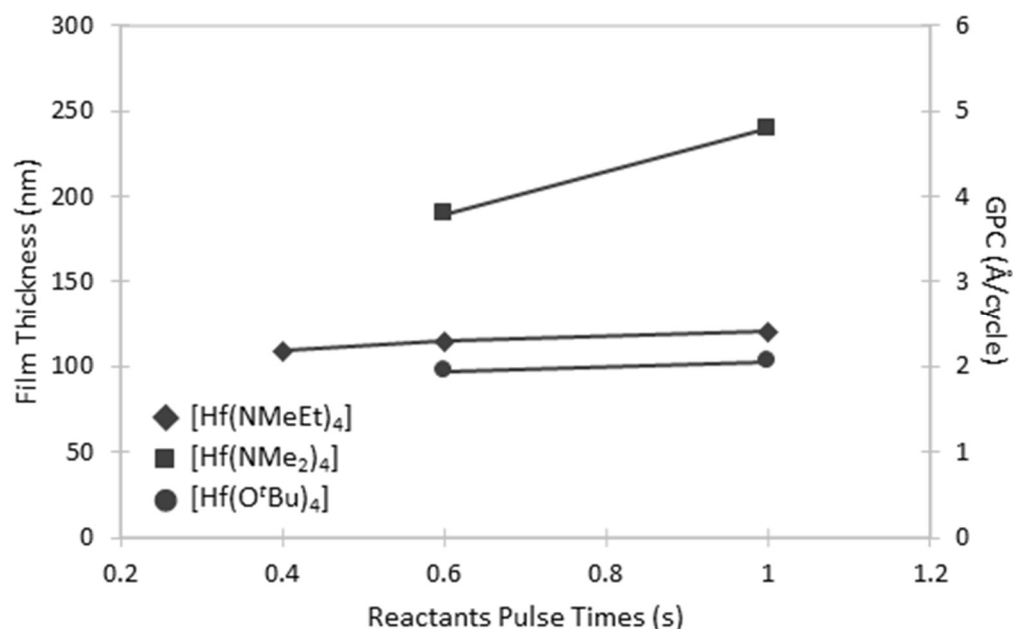


Figure 4.15: Dependence of average film thickness and GPC on $[\text{Hf}(\text{X})_4]$ ($\text{X} = \text{NMeEt}$, NMe_2 , O^tBu) and IVA pulse times at various deposition temperatures. All films were deposited using 500 cycles, and thicknesses/GPC values are for un-annealed films.

4.5 – References for Chapter 4

- [1] J. C. Chen, Y. Chen, R. Gao, C. Cheng, X. Li, G. Zhao, D. Chan, T. Lee. Evolution of STI Gap fill Technology. *ECS Trans.* **2011**, *34*, 479-482.
- [2] R. Srinivasan, P. V. R. Dandu, S. V. Babu. Shallow Trench Isolation Chemical Mechanical Planarization: A Review. *ECS J. Solid State Sci. Technol.* **2015**, *4*, P5029-P5039.
- [3] D. Chen, J. Robert A. Shepherd, V. Gauri, G. D. Papasouliotis (2005). "Multi-Step Deposition and Etch Back Gap Fill Process." 1-8. Novellus Systems, Inc., USA: Patent No. 6,867,086 B1.
- [4] B.-J. Lee, D.-W. Seo, J.-W. Choi. A Study on the Gap-Fill Process Deposited by the Deposition/Etch/Deposition Method in the Space-Divided PE-ALD System. *Coatings* **2023**, *13*, 48-60.
- [5] L. Chen, D. Ando, Y. Sutou, J. Koike. CuAl₂ thin films as a low-resistivity interconnect material for advanced semiconductor devices. *J. Vac. Sci. Technol., B* **2019**, *37*, 031215.
- [6] D. S. Gardner (2003). "Copper Reflow Process." Intel Corporation, United States of America: Patent No. 6,599,828 B1.
- [7] D. Ishikawa, A. Nakano, S. Ueda, H. Kou, H. Arai, A. Kobayashi, K. Matsushita, N. Kobayashi (2014). Plasma-Enhanced CVD Low-k Process Enabling Global Planarity by Controlling Flowability. IEEE International Interconnect Technology Conference, San Jose, CA, USA, 135-138.
- [8] Y. Yana, B. Zhanga, H. Denga, L. Chena, L. Xiaoa, B. Zhanga, Y. Chen. Flowable CVD Process Application for Gap Fill at Advanced Technology. *ECS Trans.* **2014**, *60*, 503-506.
- [9] Q. Xu, G. Wang, W. Xiong, T. Ye. Novel gap filling technique of shallow trench isolation structure in 16/14 nm FinFET using sub-atmospheric chemical vapor deposition. *J. Mater. Sci. Mater. Electron.* **2020**, *31*, 9796-9802.
- [10] S.-W. Chung, S.-T. Ahn, H.-C. Sohn, J. Ku, S. Park, Y.-W. Song, H.-S. Park, S.-D. Lee (2002). Novel shallow trench isolation process using flowable oxide CVD for sub-100nm DRAM. Digest. International Electron Devices Meeting, San Francisco, CA, USA, 233-236.
- [11] H. Kim, S. Lee, J.-W. Lee, B. Bae, Y. Choi, Y.-H. Koh, H. Yi, E. Hong, M. Kang, S. W. Nam, H.-K. Kang, C. C. J. Park, N. Cho, S. Lee (2012). Novel Flowable CVD Process Technology for sub-20nm Interlayer Dielectrics. 2012 IEEE International Interconnect Technology Conference, San Jose, CA, USA, 1-3.
- [12] L. Zhang, J.-F. de Marneffe, A. Lesniewska, P. Verdonck, N. Heylen, G. Murdoch, K. Croes, J. Boemmels, Z. Tokei, S. De Gendt, M. R. Baklanov. Cu passivation for integration of gap-filling ultralow-k dielectrics. *Appl. Phys. Lett.* **2016**, *109*, 232901.
- [13] C. C. Lai, L. Y. Li, W. L. Wang, T. B. Huang, H. J. Chien, T. H. Ying. The improvement of MOSFET performance by the optimization of STI HDP-CVD integration process. *Microelectron. Eng.* **2016**, *149*, 9-13.

- [14] Y. Kim, B. Han, Y. J. Kim, J. Shin, S. Kim, R. Hidayat, J. M. Park, W. Koh, W. J. Lee. Atomic layer deposition and tellurization of Ge-Sb film for phase-change memory applications. *RSC Adv.* **2019**, *9*, 17291-17298.
- [15] H. Jain, M. Creatore, P. Poodt. Molecular layer deposition of alucone in high aspect ratio trenches: The effect of TMA outgassing on step-coverage. *J. Vac. Sci. Technol., A* **2023**, *41*, 012401.
- [16] C. T. Nguyen, E.-H. Cho, B. Gu, S. Lee, H.-S. Kim, J. Park, N.-K. Yu, S. Shin, B. Shong, J. Y. Lee, H.-B.-R. Lee. Gradient area-selective deposition for seamless gap-filling in 3D nanostructures through surface chemical reactivity control. *Nat. Commun.* **2022**, *13*, 7597.
- [17] A. C. Jones, H. C. Aspinall, P. R. Chalker, R. J. Potter, T. D. Manning, Y. F. Loo, R. O'Kane, J. M. Gaskell, L. M. Smith. MOCVD and ALD of High- κ Dielectric Oxides Using Alkoxide Precursors. *Chem. Vap. Deposition* **2006**, *12*, 83-98.
- [18] W. Cho, K. S. An, T. M. Chung, C. G. Kim, B. S. So, Y. H. You, J. H. Hwang, D. Jung, Y. Kim. ALD of Hafnium Dioxide Thin Films Using the New Alkoxide Precursor Hafnium 3-Methyl-3-pentoxide, $\text{Hf}(\text{mp})_4$. *Chem. Vap. Deposition* **2006**, *12*, 665-669.
- [19] T. Blanquart, J. Niinistö, M. Ritala, M. Leskelä. Atomic Layer Deposition of Groups 4 and 5 Transition Metal Oxide Thin Films: Focus on Heteroleptic Precursors. *Chem. Vap. Deposition* **2014**, *20*, 189-208.
- [20] K. Xu, A. P. Milanov, H. Parala, C. Wenger, C. Baristiran-Kaynak, K. Lakribssi, T. Toader, C. Bock, D. Rogalla, H.-W. Becker, U. Kunze, A. Devi. Atomic Layer Deposition of HfO_2 Thin Films Employing a Heteroleptic Hafnium Precursor. *Chem. Vap. Deposition* **2012**, *18*, 27-35.
- [21] E. Rauwel, G. Clavel, M. G. Willinger, P. Rauwel, N. Pinna. Non-aqueous routes to metal oxide thin films by atomic layer deposition. *Angew. Chem. Int. Ed.* **2008**, *47*, 3592-3595.
- [22] E. Rauwel, M.-G. Willinger, F. Ducroquet, P. Rauwel, I. Matko, D. Kiselev, N. Pinna. Carboxylic Acids as Oxygen Sources for the Atomic Layer Deposition of High- κ Metal Oxides. *J. Phys. Chem. C* **2008**, *112*, 12754-12759.
- [23] Y. Lee, S. Kim, J. Koo, I. Kim, J. Choi, H. Jeon, Y. Wonb. Effect of Nitrogen Incorporation in HfO_2 Films Deposited by Plasma-Enhanced Atomic Layer Deposition. *J. Electrochem. Soc.* **2006**, *153*, G353-G537.
- [24] V. Miikkulainen, M. Leskelä, M. Ritala, R. L. Puurunen. Crystallinity of inorganic films grown by atomic layer deposition: Overview and general trends. *J. Appl. Phys.* **2013**, *113*, 021301.
- [25] T. Gougousi. Low-Temperature Dopant-Assisted Crystallization of HfO_2 Thin Films. *Crystal Growth & Design* **2021**, *21*, 6411-6416.
- [26] D. Barreca, A. Milanov, R. A. Fischer, A. Devi, E. Tondello. Hafnium oxide thin film grown by ALD: An XPS study. *Surf. Sci. Spectra* **2007**, *14*, 34-40.
- [27] J. P. Lehan, Y. Mao, B. G. Bovard, H. A. Macleod. Optical and Microstructural Properties of Hafnium Dioxide Thin Films. *Thin Solid Films* **1991**, *203*, 227-250.

- [28] P.-C. Liao, P.-H. Chen, Y.-F. Tseng, T.-A. Shih, T.-A. Lin, T.-S. Gau, B.-J. Lin, P.-W. Chiu, J.-H. Liu. Partial decarboxylation of hafnium oxide clusters for high resolution lithographic applications. *J. Mater. Chem. C* **2022**, *10*, 15647-15655.
- [29] T. E. G. Alivio, L. R. De Jesus, R. V. Dennis, Y. Jia, C. Jaye, D. A. Fischer, U. Singisetti, S. Banerjee. Atomic Layer Deposition of Hafnium(IV) Oxide on Graphene Oxide: Probing Interfacial Chemistry and Nucleation by using X-ray Absorption and Photoelectron Spectroscopies. *Chemphyschem* **2015**, *16*, 2842-2848.
- [30] L. Ramqvist, K. Hamrin, G. Johansson, A. Fahlman, C. Nordling. Charge Transfer in Transition Metal Carbides and Related Compounds Studied by ESCA. *J. Phys. Chem. Solids* **1969**, *30*, 1835-1847.
- [31] Hf-O_{carboxyl} bond distance range based on a search of the Cambridge Structural Database. 95% of the Hf-O distances in the CSD fall within the range described. CSD accessed via conquest CSD on April 15, 2023; version 2020.3.0, updated November 2020.
- [32] Hf-O_{alkoxide} bond distance range based on a search of the Cambridge Structural Database. 97% of the Hf-O distances in the CSD fall within the range described. CSD accessed via conquest CSD on April 15, 2023; version 2020.3.0, updated November 2020.
- [33] Hf-O_{oxo} bond distance range based on a search of the Cambridge Structural Database for hafnium compounds containing μ_3 -oxo ligands. 94% of the Hf-O distances in the CSD fall within the range described. CSD accessed via conquest CSD on April 15, 2023; version 2020.3.0, updated November 2020.
- [34] Hf-O bond distance and O-C-O bond angle range based on a search of the Cambridge Structural Database for hafnium complexes containing κ^2 -coordinated carboxylate ligands. 91% of the Hf-O distances and 88% of the O-C-O angles in the CSD fall within the range described. CSD accessed via conquest CSD on April 15, 2023; version 2020.3.0, updated November 2020.
- [35] Hf-O bond distance and O-C-O bond angle range based on a search of the Cambridge Structural Database for hafnium complexes containing μ -coordinated carboxylate ligands. 97% of the Hf-O distances and 91% of the O-C-O angles in the CSD fall within the range described. CSD accessed via conquest CSD on April 15, 2023; version 2020.3.0, updated November 2020.
- [36] T. J. Boyle, D. T. Yonemoto, T. Q. Doan, T. M. Alam. Synthesis and Structural Characterization of Group 4 Metal Carboxylates for Nanowire Production. *Inorg. Chem.* **2014**, *53*, 12449-12458.
- [37] D. Van den Eynden, R. Pokratath, J. De Roo. Nonaqueous Chemistry of Group 4 Oxo Clusters and Colloidal Metal Oxide Nanocrystals. *Chem. Rev.* **2022**, *122*, 10538-10572.
- [38] G. Kickelbick, M. Puchberger, U. Schubert, S. Gross. Mono-, Di-, and Trimetallic Methacrylate-substituted Metal Oxide Clusters Derived from Hafnium Butoxide. *Monatsh. Chem.* **2003**, *134*, 1053-1063.

- [39] Y. Zhang, F. de Azambuja, T. N. Parac-Vogt. The forgotten chemistry of group(IV) metals: A survey on the synthesis, structure, and properties of discrete Zr(IV), Hf(IV), and Ti(IV) oxo clusters. *Coord. Chem. Rev.* **2021**, *438*, 213886.
- [40] T. Gougousi, D. Niu, R. W. Ashcraft, G. Parsons. Carbonate formation during post-deposition ambient exposure of high-*k* dielectrics. *Appl. Phys. Lett.* **2003**, *83*, 3543-3545.
- [41] T. Gougousi, G. N. Parsons. Postdeposition reactivity of sputter-deposited high-dielectric-constant films with ambient H₂O and carbon-containing species. *J. Appl. Phys.* **2004**, *95*, 1391-1396.
- [42] T. Gougousi, D. Barua, E. D. Young, G. N. Parsons. Metal Oxide Thin Films Deposited from Metal Organic Precursors in Supercritical CO₂ Solutions. *Chem. Mater.* **2005**, *17*, 5093-5100.
- [43] A. T. Williamson. The Polymerization and Thermal Decomposition of Ketene. *J. Am. Chem. Soc.* **1934**, *56*, 2216-2218.
- [44] S. M. Mitchell, K. A. Niradha Sachinthani, R. Pulukkody, E. B. Pentzer. Polymerization of Cumulated Bonds: Isocyanates, Allenes, and Ketenes as Monomers. *ACS Macro Lett.* **2020**, *9*, 1046-1059.

Chapter 5

Synthesis, Structures, and Thermal Stability of Dialkyl and Bis(amido)

Zirconium(IV) Acen Complexes

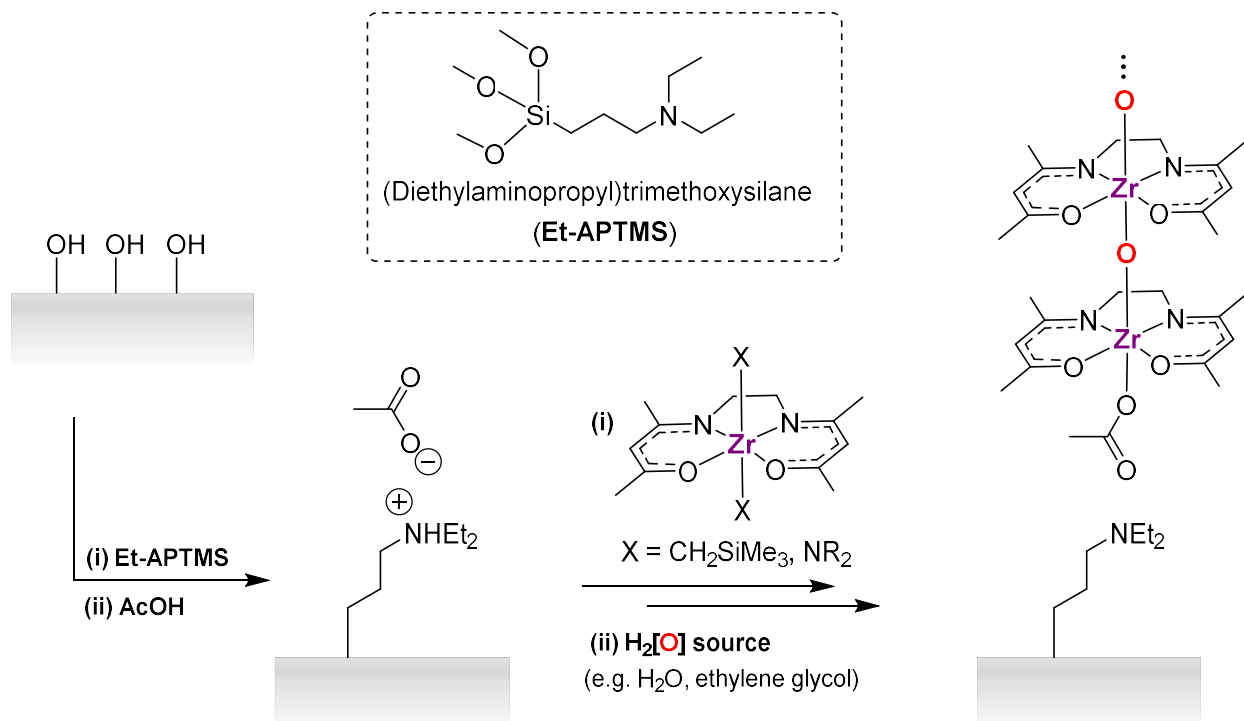
Portions of this chapter have been reprinted (adapted) with permission from M. Al Hareri, D. J. H. Emslie, Synthesis, Structures, and Thermal Stability of Dialkyl and Bis(amido) Zirconium(IV) Acen Complexes. *European Journal of Inorganic Chemistry* **2022**, 26, 202200594 (7 pages). Copyright 2022 John Wiley & Sons.

5.1 – Introduction to Chapter 5

This chapter focuses on the design, synthesis, and investigation of the structure and thermal stability of new Zr(IV) complexes as potential precursors for flowable ZrO₂ ALD. The process discussed herein was conceived as an alternative strategy to deposit thin films into narrow high-aspect-ratio trenches (<20 nm widths) without the formation of voids, as introduced in Section 4.1. We present efforts towards the development of suitable precursor molecules to enable a flowable ALD process for ZrO₂ through the deposition of oligomeric one-dimensional chains that, if grown untethered on a functionalized substrate,^[1] could potentially flow to the bottoms of trenches.

The proposed process involves the use of an octahedral Zr(IV) complex as a precursor molecule, which features a tetradentate ligand coordinated in the equatorial plane and two *trans*-disposed, monodentate anionic ligands that could be selectively removed by protonation, allowing for preferential growth in the axial direction (Scheme 5.1). We considered that [(acen^R)ZrX₂] (X = alkyl or amido) complexes could be suitable

candidates for use as ALD precursors for the deposition of one-dimensional Zr-containing chains.



Scheme 5.1: Proposed process for ALD of non-surface-tethered, Zr-containing one-dimensional chains on a functionalized substrate surface using [(acen^R)ZrX₂] complexes as the precursor.

Acen^R ligands are tetradentate dianions featuring two β-ketiminate units, with the general formula [1,2-C₂R_x(NCR'CR''C(O)R''')₂]²⁻, where the CR''CR''' unit is not part of an aromatic ring (from herein, acen^R is used to refer to ligands with any substitution pattern, whereas acen is used to refer only to C₂H₄(NMeCHC(O)Me)₂). They have been used to prepare a broad range of complexes from throughout the periodic table.^[2-8] Previously reported zirconium acen^R complexes include [(acen^R)ZrCl₂], [(acen^R)ZrCl₂(THF)],^[9] [(acen^R)Zr(CH₂^tBu)₂]^[10] (acen^R = acen or acen-F₆ {C₂H₄(NMeCHC(O)CF₃)₂}) and

$[\text{Zr}(\text{acen-F}_6)_2]$,^[11] as well as cationic alkyl derivatives such as $[(\text{acen-F}_6)\text{Zr}(\text{CH}_2^t\text{Bu})\text{L}_x][\text{B}(\text{C}_6\text{F}_5)_4]$ ($\text{L} = \text{NMe}_2\text{Ph}$, PMe_2Ph , PMe_3 or NCMe).^[10]

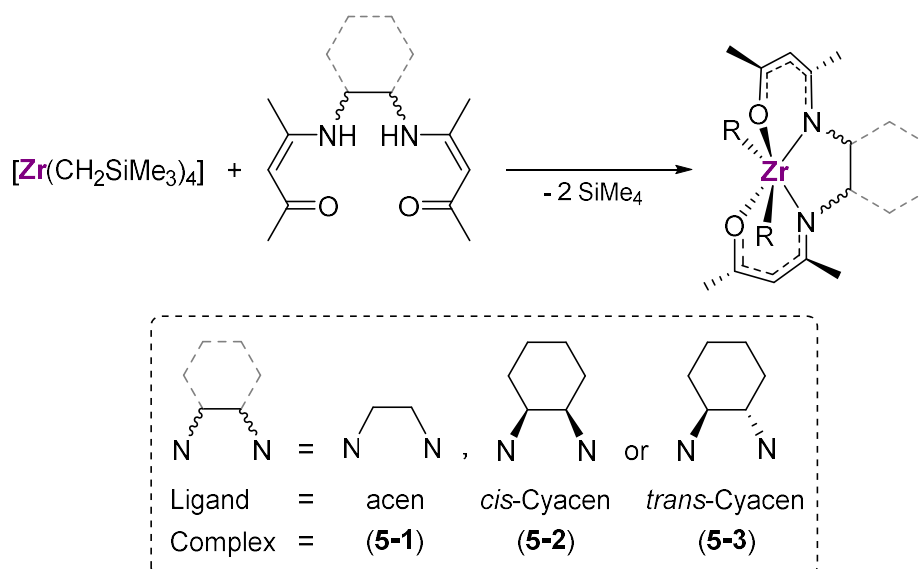
For use in ALD, precursor molecules should be sufficiently volatile for delivery into the reactor in the vapour phase (typically at a pressure between 0.1 and 1 Torr), and thermally stable enough to withstand weeks of heating at the delivery temperature. Consequently, we set out to prepare $[(\text{acen}^R)\text{ZrX}_2]$ ($\text{X} = \text{alkyl}$ or amido) complexes bearing acen {1,2- $\text{C}_2\text{H}_4(\text{NCMeCHC}(\text{O})\text{Me})_2$ } ligands, due to their low molecular weight, and *cis*- and *trans*- Cycacen ligands (Scheme 5.1), given that the more rigid *cis*- or *trans*-1,2-disubstituted cyclohexane linker might be expected to afford complexes with enhanced thermal stability. A phenylene linker would perhaps have a similar effect, but such ligands were not pursued due to the propensity of aryl rings to engage in π -stacking, resulting in decreased volatility.

Several acen^R complexes have previously been utilized as CVD or ALD precursors. For example, $[\text{Cu}(\text{acen})]$ has been used, in combination with H_2 or O_2 to deposit metallic copper or copper oxide thin films by ALD,^[12,13] $[\text{Ni}(\text{acen})]$ has been employed for the deposition of elemental nickel films as well as Ni/TiO_2 and Ni/CrN composite thin films by plasma-assisted MOCVD,^[14,15] and $[\text{Ga}(\text{acen})\text{H}]$, $[\text{Ga}(\text{acen-Ph}_2)(\text{Me})]$ ($\text{acen-Ph}_2 = \text{C}_2\text{H}_4(\text{NCMeCHC}(\text{O})\text{Ph})_2$), and $[\text{Al}(\text{acen})(\text{O}^i\text{Pr})]$ have been investigated as precursors for gallium and aluminium oxide deposition by aerosol-assisted chemical vapour deposition.^[16,17] Additionally, $[\text{Zr}(\text{acen-F}_6)_2]$ was found to be an effective MOCVD precursor for the growth of yttrium-stabilized ZrO_2 using $\text{Y}(\text{tmhd})_3$ ($\text{tmhd} =$

tetramethylheptanedionate) as the co-precursor and H₂O-saturated N₂O gas as the co-reactant.^[18]

5.2 – Synthesis and Structures of Dialkyl Zirconium(IV) Acen Complexes

Reaction of one equivalent of H₂(acen), H₂(*cis*-Cyacen) or H₂(*trans*-Cyacen) with [Zr(CH₂SiMe₃)₄] at room temperature afforded red [Zr(acen)(CH₂SiMe₃)₂] (**5-1**), dark yellow [Zr(*cis*-Cyacen)(CH₂SiMe₃)₂] (**5-2**) or yellow [Zr(*trans*-Cyacen)(CH₂SiMe₃)₂] (**5-3**), respectively (Scheme 5.2).



Scheme 5.2: Synthesis of dialkyl complexes **5-1** to **5-3** by SiMe₄ elimination.

X-ray quality crystals of **5-1** were obtained from toluene/hexanes at –30 °C. The crystal structure of **5-1** (Figure 5.1) revealed a distorted trigonal prismatic coordination geometry, with each triangular face consisting of a nitrogen, an oxygen, and a carbon donor atom. This geometry was assigned based on the smaller continuous shape measurement (CSM) value of 1.58 for trigonal prismatic geometry versus 11.53 for

octahedral geometry (Table 5.1). Consistent with this geometry, the twist angles (α ; c in Figure 5.1) are 6.49° , 6.98° and 23.89° , which are much closer to 0° (expected for a trigonal prism) than to 60° (expected for an octahedron). Zirconium is approximately equidistant from the two triangular faces (Zr-centroid = 1.380 and 1.389 Å), and the angle between the planes of the two NO-chelates within the acen ligand is 36.8° .

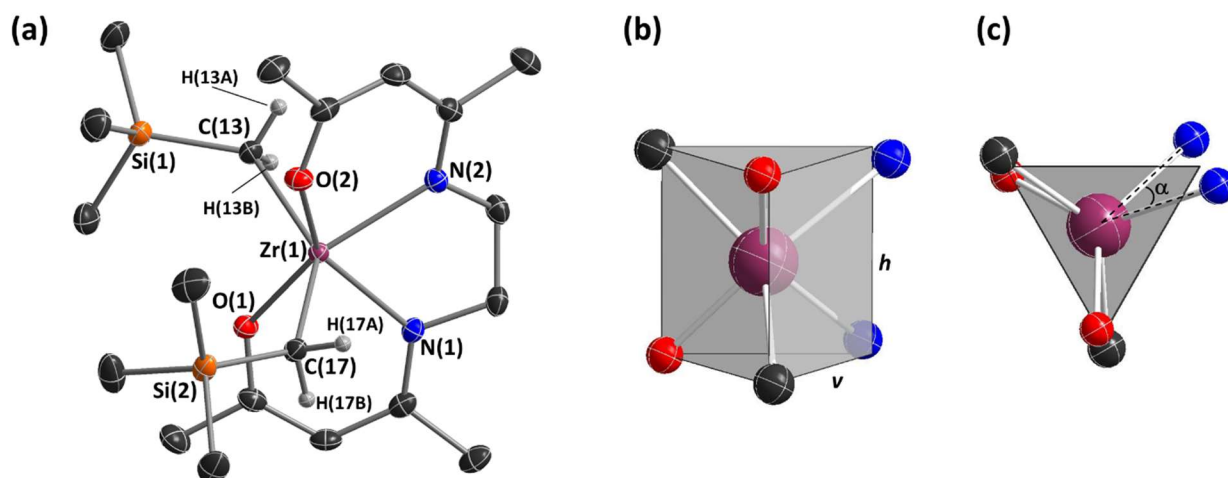


Figure 5.1: (a) X-ray crystal structure of [Zr(acen)(CH₂SiMe₃)₂] (**5-1**) with ellipsoids at 50% probability. Space group P2₁/n. The Zr-CH₂ hydrogen atoms were located from the difference map and refined isotropically; all other hydrogen atoms are omitted for clarity. R₁ = 0.0330. Selected bond lengths (Å) and angles (°): Zr(1)-O(1) 2.096(1), Zr(1)-O(2) 2.107(1), Zr(1)-N(1) 2.275(1), Zr(1)-N(2) 2.268(1), Zr(1)-C(13) 2.265(1), Zr(1)-C(17) 2.280(1), N(1)-Zr(1)-N(2) 74.19(4), C(13)-Zr(1)-C(17) 139.96(5), Zr(1)-C(13)-Si(1) 129.58(7), Zr(1)-C(17)-Si(2) 128.25(7), Zr(1)-C(13)-H(13A) 103(1), Zr(1)-C(13)-H(13B) 100(1), Zr(1)-C(17)-H(17A) 100(1), Zr(1)-C(17)-H(17B) 100(1). (b)-(c) Coordination geometry around Zr in **5-1** superimposed on the ideal trigonal prism calculated by the SHAPE program.

Table 5.1: Comparison of the continuous shape measure (CSM) values for trigonal prismatic (TPR-6) and octahedral (OC-6) geometry and twist angles of complexes **5-1** to **5-3** and **5-7**, as well as crystallographically characterized literature examples of 6-coordinate zirconium(IV) acen^R complexes.

Complex	TPR-6 CSM	OC-6 CSM	Twist angles, α (°) ^[a]
5-1	1.576	11.532	6.49, 6.98, 23.89 ^[b]
5-2	1.645	15.785	3.19, 3.23, 18.67 ^[b]
5-3	4.459	11.225	8.40, 9.36, 35.78 ^[b]
	5.465	10.911	9.80, 10.89, 39.41 ^[b]
5-7	3.472	8.508	7.84 ^[b] , 27.93, 27.93
[Zr(acen)Cl ₂] ^[9]	11.242	3.141	37.85, 44.38, 50.17
[Zr(acen-F ₆)(CH ₂ ^t Bu) ₂] ^[10]	1.348	15.446	0.01, 3.98, 17.28 ^[b]
[Zr(acen-F ₆)(CH ₂ ^t Bu)(NMe ₂ Ph)][B(Ar ^F) ₄] ^[10]	7.371	7.540	18.45, 24.73, 49.07 ^[b]

^[a]The ideal twist angles for a trigonal prism are 0°, compared with 60° for an octahedron.

^[b]Twist angle associated with the N donor atoms.

The Zr–C distances {2.265(1) and 2.280(2) Å} are within the usual range for 6-coordinate zirconium bis(trimethylsilylmethyl) complexes {2.224(3)-2.36(2) Å}, whereas the Zr–C–Si bond angles of 128.25(7)° and 129.58(7)° lie at the upper end of the reported range {113.96(8)-127.8(2)°},^[19] likely due to steric hindrance or the presence of α -agostic interactions. The ¹J_{C,H} NMR coupling constant for **5-1** is 106 Hz, which is at the upper end of the range for early transition metal and *f*-element complexes for which α -agostic interactions have been proposed,^[20-26] and the Zr–C–H angles {100(1)°} are not especially acute, more consistent with a steric origin for the moderately expanded Zr–C–

Si angle.^[27-33] For comparison, the $^1J_{C,H}$ NMR coupling constants for $[(acen^R)Zr(CH_2CMe_3)_2]$ ($acn^R = acn-F_6$ or acn) are 109.8 and 112.5 Hz, respectively, and the Zr–C–C angles in the solid state structure of the former complex are $124.7(3)^\circ$ and $128.1(3)^\circ$.^[10]

Additionally, the Zr–O {2.097(1) and 2.107(1) Å} and Zr–N {2.268(1) and 2.275(1) Å} distances are within the range for previously reported 6-coordinate Zr acn^R complexes {Zr–O = 1.977(3)–2.138(3); Zr–N = 2.217(4)–2.347(4)}.^[9,10] In comparison to isostructural $[Zr(acn-F_6)(CH_2^tBu)_2]$, complex **5-1** features shorter Zr–O, Zr–N, and Zr–C bonds, consistent with reduced steric hindrance, and a more obtuse C–Zr–C bond angle.^[10]

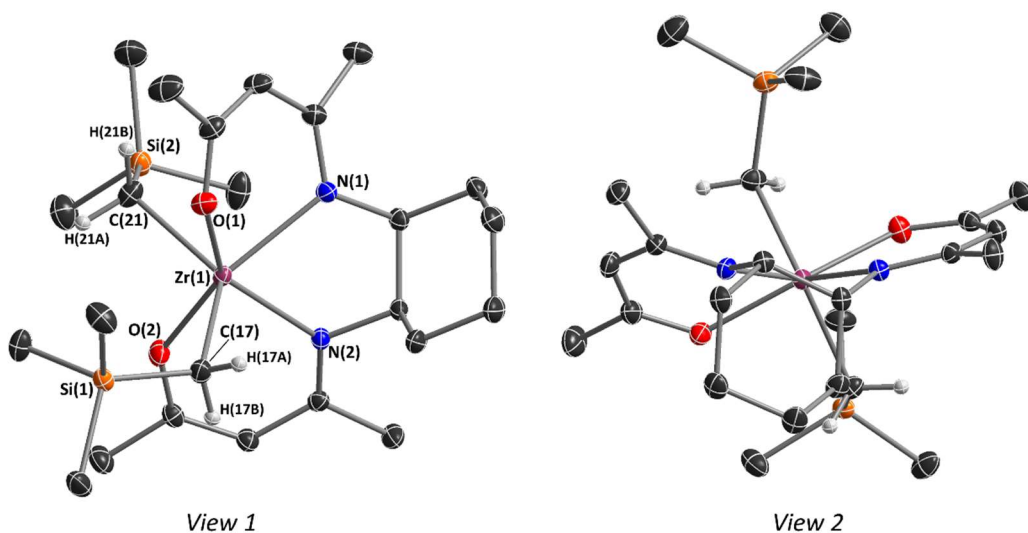


Figure 5.2: X-ray crystal structure of $[Zr(cis-Cyacen)(CH_2SiMe_3)_2]$ (**5-2**; two views are shown to facilitate comparison of the structure of **5-2** with those of **5-1** and **5-3**). Space group $Pbca$. Ellipsoids are set at 50% probability. The Zr–CH₂ hydrogen atoms were located from the difference map and refined isotropically; all other hydrogen atoms have been omitted for clarity. $R_1 = 0.0312$. Selected bond lengths (Å) and angles ($^\circ$): Zr(1)–O(1) 2.135(1), Zr(1)–O(2) 2.110(1), Zr(1)–N(1) 2.273(1), Zr(1)–N(2) 2.290(1), Zr(1)–C(17) 2.281(2), Zr(1)–C(21) 2.288(2), N(1)–Zr(1)–N(2) $72.55(4)$, C(17)–Zr(1)–C(21) $127.09(6)$,

Zr(1)-C(17)-Si(1) 120.11(8), Zr(1)-C(21)-Si(2) 119.73(8), Zr(1)-C(17)-H(17A) 105(2), Zr(1)-C(17)-H(17B) 105(2), Zr(1)-C(21)-H(21A) 102(2), Zr(1)-C(21)-H(21B) 109(2).

Pale yellow, needle-like crystals of **5-2** and yellow block crystals of **5-3** were obtained from concentrated hexanes solutions at $-30\text{ }^{\circ}\text{C}$. The structure of **5-2** (Figure 5.2) is analogous to that of **5-1**, with similar CSM and α values (Table 5.1), Zr–C {2.281(2) and 2.288(2) Å}, Zr–O {2.110(1) and 2.135(1) Å} and Zr–N {2.273(1) and 2.290(1) Å} distances, and slightly less obtuse Zr–C–Si angles {119.74(8) $^{\circ}$ and 120.11(8) $^{\circ}$; $^1J_{\text{C,H}}$ is 105 Hz}. Compound **5-3** (Figure 5.3) is also trigonal prismatic, but differs significantly from **5-1** and **5-2** in that the Zr, N and O atoms lie approximately in a plane. The angle between the planes of the two NO-chelates within the *trans*-Cyacen ligand is 70.4 and 69.3 $^{\circ}$ in the two molecules in the unit cell, and the Zr–C {2.251(1)-2.294(1) Å}, Zr–O {2.120(1)-2.143(1)}, and Zr–N {2.236(1)-2.288(2) Å} distances and Zr–C–Si angles {123.71(7)-125.74(7)} are similar to those in **5-1** and **5-2** ($^1J_{\text{C,H}}$ is ~ 110 Hz for **5.3**).

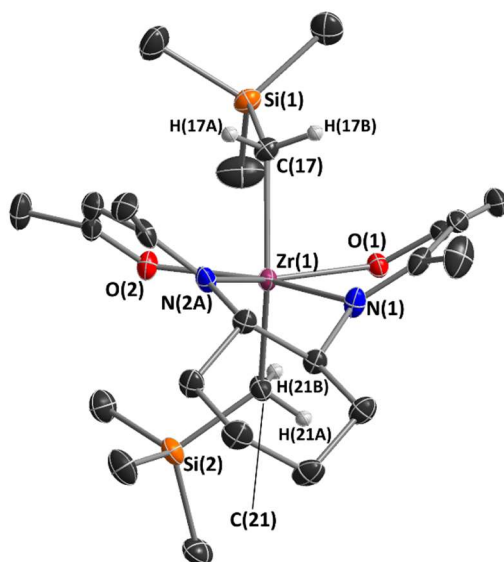
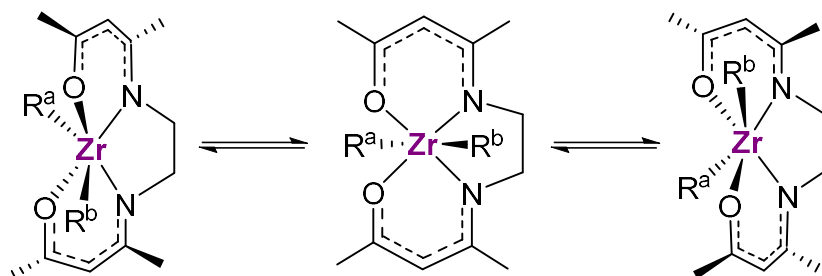


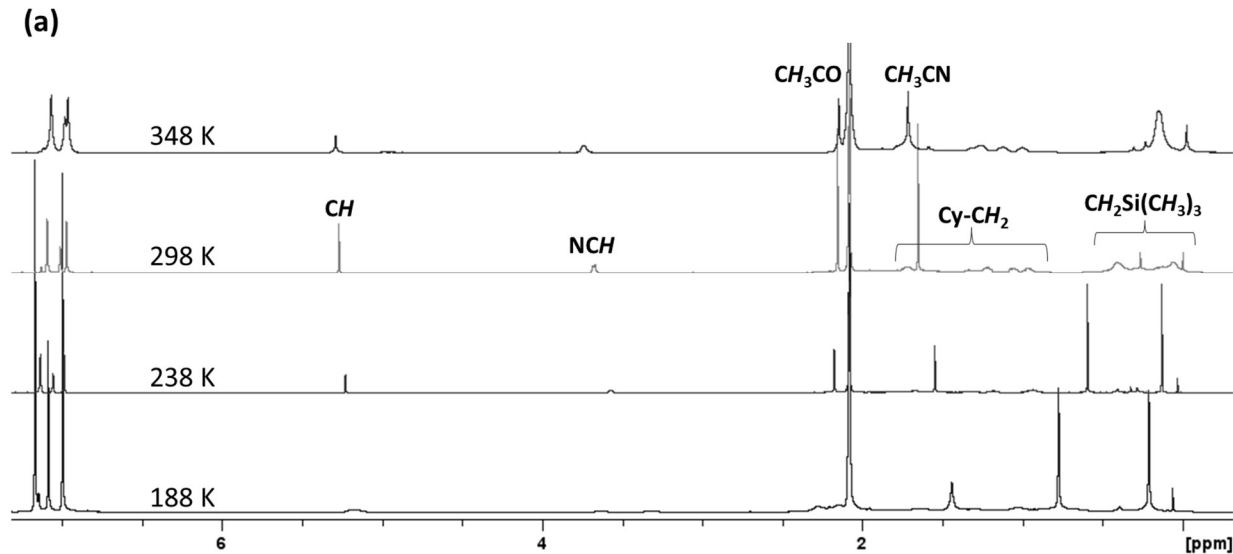
Figure 5.3: X-ray crystal structure of $[\text{Zr}(\text{trans-Cyacen})(\text{CH}_2\text{SiMe}_3)_2]$ (**5-3**; only one of two independent and essentially isostructural molecules in the unit cell is shown; both molecules in the unit cell displayed disorder at the cyclohexyl ring, one nitrogen donor atom, and one of the *trans*-Cyacen ligand's CH_3 and CH groups). Ellipsoids are set at 50% probability. Space group P-1. The Zr- CH_2 hydrogen atoms were located from the difference map and refined isotropically; all other hydrogen atoms have been omitted for clarity. $R_1 = 0.0289$. Selected bond lengths (Å) and angles ($^\circ$): Zr(1)-O(1) 2.143(1), Zr(1)-O(2) 2.129(1), Zr(1)-N(1) 2.235(1), Zr(1)-N(2A) 2.288(1), Zr(1)-C(17) 2.251(1), Zr(1)-C(21) 2.278(1), N(1)-Zr(1)-N(2A) 70.38(6), C(17)-Zr(1)-C(21) 135.70(5), Zr(1)-C(17)-Si(1) 125.74(7), Zr(1)-C(21)-Si(2) 124.32(7), Zr(1)-C(17)-H(17A) 100(1), Zr(1)-C(17)-H(17B) 104(1), Zr(1)-C(21)-H(21A) 100(1), Zr(1)-C(21)-H(21B) 105(1).

Complexes **5-1** to **5-3** formed pale to vivid yellow solutions when dissolved in benzene or toluene. Complex **5-1** has approximate C_2 symmetry in the solid state, but gave rise to single $\text{N}(\text{CH}_2)_2\text{N}$ and ZrCH_2 environments in the ^1H NMR spectrum, indicative of apparent C_{2v} symmetry in solution, presumably due to a fluxional process involving trigonal prismatic and octahedral structures as shown in Scheme 5.3. The ZrCH_2 ^1H and ^{13}C NMR signals for **5-1** were observed at 0.18 ppm and 54.61 ppm, respectively.



Scheme 5.3: Isomerization, involving interconversion between trigonal prismatic and octahedral structures, proposed to explain the apparent C_{2v} symmetry of compound **5-1** in solution at room temperature. The two equivalent alkyl groups are labelled R^a and R^b .

By contrast, **5-2** is C_1 symmetric, and the two trimethylsilylmethyl groups are inequivalent at room temperature and below, giving rise (at 298 K) to broad $ZrCH_2$ signals at 0.39 and 0.21 ppm in the 1H NMR spectrum, and 57.02 and 54.78 ppm in the ^{13}C NMR spectrum. At high temperature (348 K), the two trimethylsilylmethyl groups were rendered equivalent by an unidentified fluxional process. At low temperature (188 K) the two NCH and $CH(CMe)_2$ environments became inequivalent, presumably due to slowing of a fluxional process involving ring flip of the cyclohexane ring in the ligand backbone (Figure 5.4). Conversely, **5-3** has approximate C_2 symmetry at room temperature, but the $ZrCH_2$ protons are diastereotopic, affording doublets ($^2J_{H,H} = 10.6$ Hz) at 0.31 and 0.12 ppm in the 1H NMR spectrum, and a single ^{13}C NMR signal at 56.39 ppm.



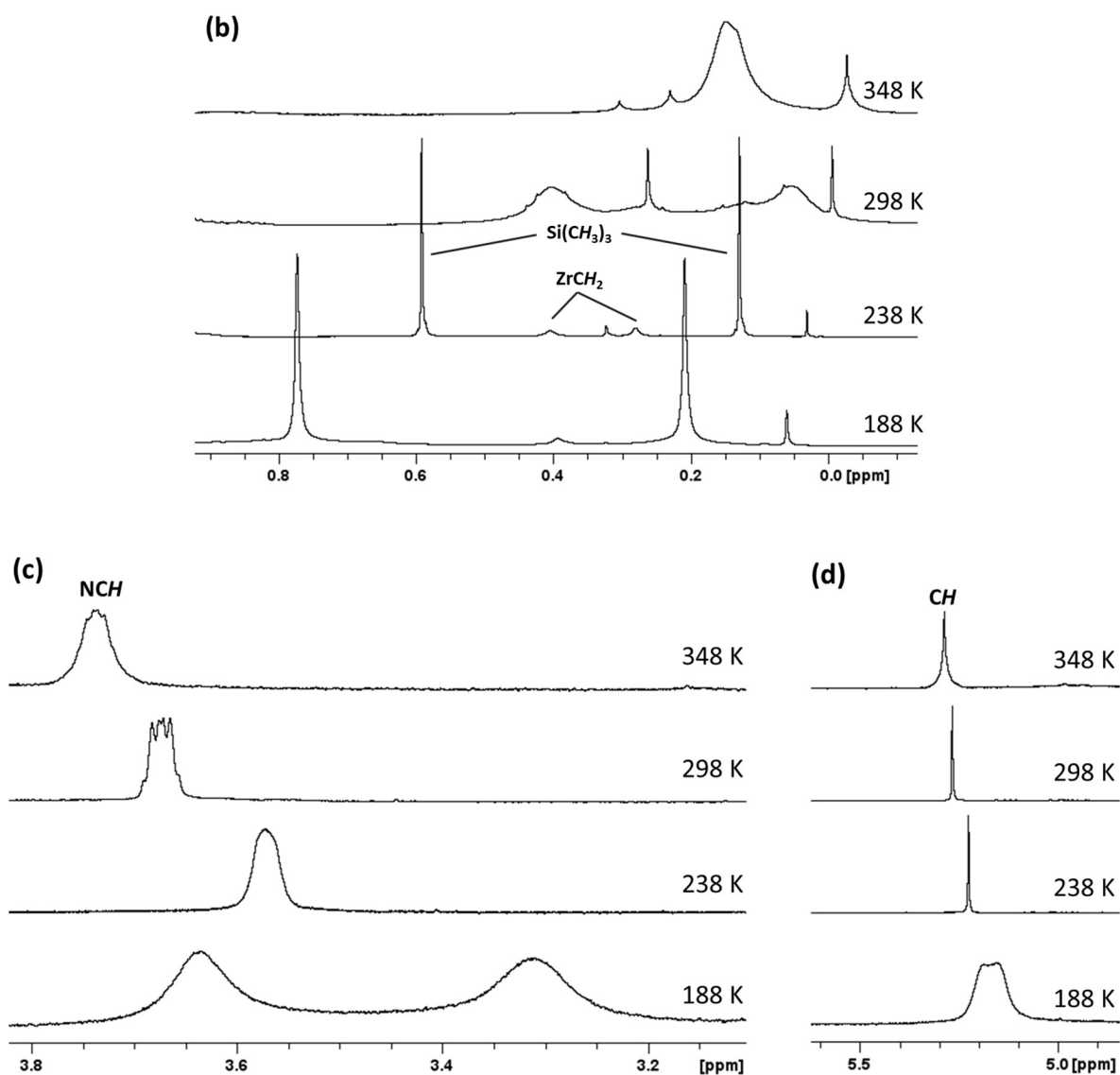
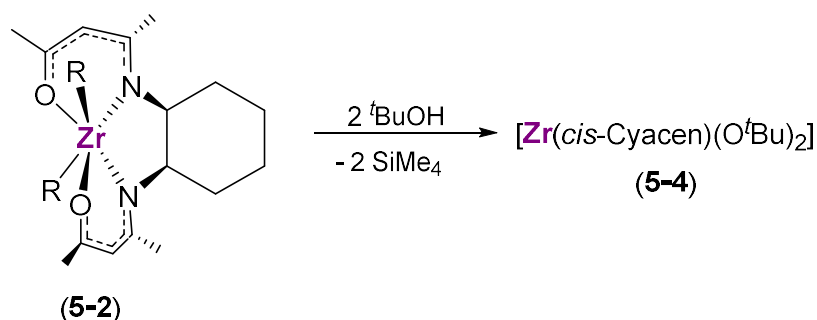


Figure 5.4: (a) Variable temperature ^1H NMR spectra of $[\text{Zr}(\text{cis-Cyacen})(\text{CH}_2\text{SiMe}_3)_2]$ (5-2) from 188-348 K in d_8 -toluene (500 MHz). (b,c,d) Expanded regions of the ^1H NMR spectra featuring the (b) $\text{ZrCH}_2\text{Si}(\text{CH}_3)_3$, (c) NCH, and (d) CH proton peaks.

5.3 – Investigation of Thermal Stability and Reactivity of Dialkyl Zirconium(IV)

Acen Complexes

Compound **5-2** reacted cleanly with 2 equivalents of ^tBuOH to afford [Zr(*cis*-Cyacen)(O^tBu)₂] (**5-4**; Scheme 5.4), which was characterized in solution, demonstrating that the alkyl groups could be selectively removed by protonation (Figure A5.14). However, reaction of **5-2** with excess ^tBuOH resulted in both SiMe₄ and H₂(*cis*-Cyacen) formation. The volatility and thermal stability of **5-1** to **5-3** was evaluated by attempted sublimation at 5-10 mTorr. Compounds **5-1** and **5-3** decomposed without sublimation at 140 and 130 °C, respectively. By contrast, compound **5-2** sublimed in >95% yield at 85 °C. However, heating pure **5-2** at 88 °C under static argon for 24 hours resulted in extensive decomposition to afford H₂(*cis*-Cyacen) and SiMe₄ as the soluble products, indicating that **5-2** lacks the long-term thermal stability typically required for an ALD precursor.

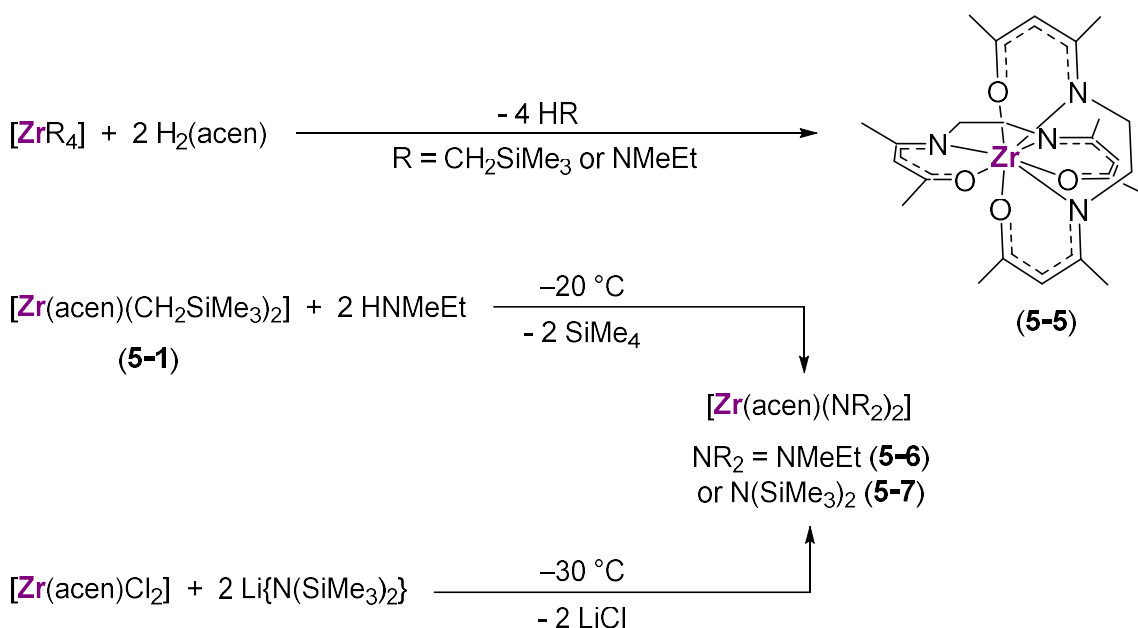


Scheme 5.4: Reaction of **5-2** with ^tBuOH to afford [Zr(*cis*-Cyacen)(O^tBu)₂] (**5-4**).

5.4 – Synthesis of Bis(amido) Zirconium(IV) Acen Complexes

As a potential means to improve the thermal stability of the target precursors, bis-amido Zr(IV) acen^R complexes were pursued in place of dialkyl complexes. Initial attempts to synthesize such complexes via amine elimination proved unsuccessful. For example, reaction of H₂(acen) and [Zr(NMeEt)₄] in a 1:1 molar ratio resulted in a mixture of products, one of which was identified as [Zr(acen)₂] (**5-5**; *vide infra*). Reactions of [Zr(NMeEt)₄] with 1 equiv. of H₂(*cis*-Cyacen) or H₂(*trans*-Cyacen) also yielded multiple unidentified products, as did reactions of [(acen)ZrCl₂] with 2 equiv. of LiNMeEt.

Complex **5-5** was formed in good yield from the 2:1 reaction of H₂acen with either [Zr(CH₂SiMe₃)₄] or [Zr(NMeEt)₄] (Scheme 5.5), and yellow-orange single crystals of **5-5** were obtained from toluene at –30 °C (complex **5-5** could also be purified by sublimation). This complex features two κ⁴-coordinated acen ligands (Figure 5.5), zirconium and the N and O donors of each acen ligand lie approximately in a plane, and the angle between the ONNO planes of the two ligands is nearly orthogonal (87.8°), analogous to the bonding situation in [Zr(acen-F₆)₂] (88.5°).^[11] The geometry of **5-5** is intermediate between square antiprismatic and triangular dodecahedral, but the structure is not of sufficient quality for more detailed discussion of bond metrics.



Scheme 5.5: Syntheses of $[\text{Zr}(\text{acen})_2]$ (**5-5**) and the bis(amido) complexes $[\text{Zr}(\text{acen})(\text{NMeEt})_2]$ (**5-6**) and $[\text{Zr}(\text{acen})\{\text{N}(\text{SiMe}_3)_2\}_2]$ (**5-7**).

The target $[\text{Zr}(\text{acen})(\text{NMeEt})_2]$ complex, **5-6**, was ultimately synthesized via the reaction of excess HNMeEt with $[\text{Zr}(\text{acen})(\text{CH}_2\text{SiMe}_3)_2]$ (**5-1**) in C_6D_6 or d_8 -toluene (Scheme 5.5). When this reaction was carried out at room temperature, partial product decomposition was evident after 30 minutes (even when only 2 equivalents of HNMeEt were used in the reaction). However, **5-6** was generated cleanly by stirring at room temperature for 10 minutes in d_8 -toluene followed by cooling to $-20 \text{ }^\circ\text{C}$ or below, enabling in-situ characterization by ^1H (Figure 5.6) and $^{13}\text{C}\{^1\text{H}\}$ NMR spectroscopy (Figure A5.19). The thermal instability of **5-6** is surprising, and attempts to isolate or obtain X-ray quality crystals of **5-6** were unsuccessful.

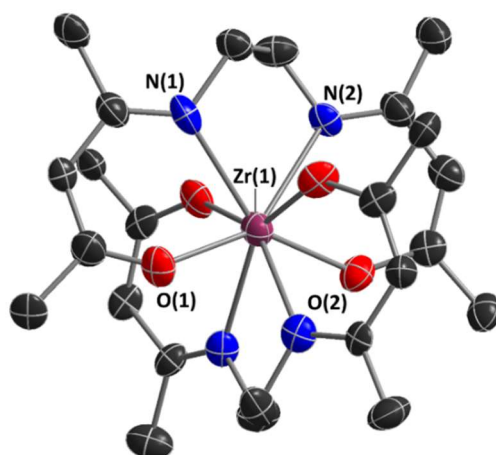


Figure 5.5: X-ray crystal structure of $[\text{Zr}(\text{acen})_2]$ (**5-5**) with ellipsoids set at 50% probability and all hydrogen atoms omitted for clarity. Space group $P2_1/n$. $R_1 = 0.0679$.

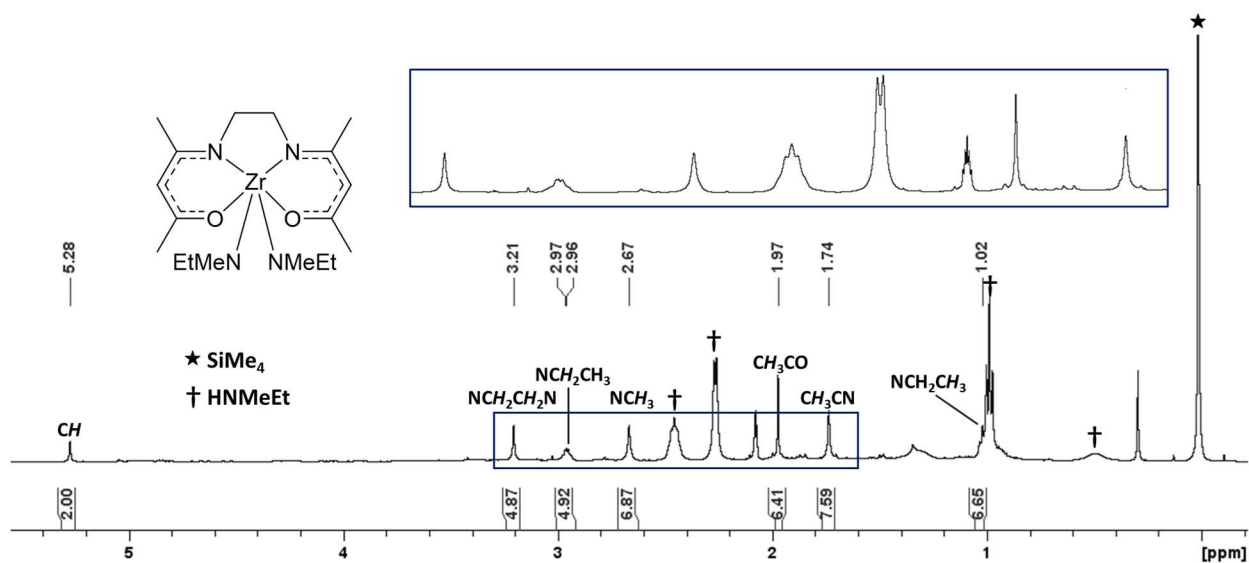


Figure 5.6: ^1H NMR spectrum of $[\text{Zr}(\text{acen})(\text{NMeEt})_2]$ (**5-6**) generated in situ from the reaction of **5-1** with excess HNMeEt in d_8 -toluene (500 MHz, 249 K). Unassigned peaks in the spectrum are the residual solvent signal, H grease, and silicone grease.

In an effort to access a bis-amido complex with increased thermal stability, a more sterically encumbered bis(trimethylsilyl)amido analogue of **5-6** was pursued. Compound

5-1 failed to react with excess $\text{HN}(\text{SiMe}_3)_2$ at room temperature or $50\text{ }^\circ\text{C}$. By contrast, reaction of $[\text{Zr}(\text{acen})\text{Cl}_2]$ with 2 equiv. of $\text{Li}\{\text{N}(\text{SiMe}_3)_2\}$ at $-30\text{ }^\circ\text{C}$ afforded the target product, $[\text{Zr}(\text{acen})\{\text{N}(\text{SiMe}_3)_2\}_2]$ (**5-7**; Scheme 5.5), which was isolated by crystallization at $-30\text{ }^\circ\text{C}$. Compound **5-7** is thermally unstable both as a solid and in solution at room temperature. However, it was characterized by ^1H , ^{13}C and ^{29}Si NMR spectroscopy at 249 K in d_8 -THF, revealing one singlet for the $\text{NCH}_2\text{CH}_2\text{N}$ protons, one SiMe_3 environment, and one CH signal, presumably due to a fluxional process analogous to that proposed for dialkyl complex **5-1** (Scheme 5.3).

Large yellow crystals of **5-7** were obtained from toluene/hexanes at $-30\text{ }^\circ\text{C}$. The structure features a κ^4 -coordinated acen ligand and two bis(trimethylsilyl)amido ligands, affording a distorted trigonal prismatic geometry (Figure 5.7; Table 5.1). The twist angles of the prism are 7.84 , 27.93 , and 27.93° , but unlike acen^{R} complexes **5-1** to **5-3**, the smallest twist angle is associated with the $\text{NCH}_2\text{CH}_2\text{N}$ bridge as a consequence of a larger angle of 73.5° between the planes of the two NO-chelates within the acen^{R} ligand (cf. 36.8° in **5-1**). This likely arises to alleviate unfavourable steric interactions between the acen dianion and the bulky amido ligands. Consistent with significant steric hindrance in compound **5-7**, the $\text{N}(2)\text{--Zr--N}(2')$ angle between the amido groups ($114.87(4)^\circ$) is far more acute than the $139.96(5)^\circ$ C--Zr--C angle between the alkyl groups in **5-1**. Nevertheless, the $\text{Zr--N}_{\text{acen}}$ and Zr--O distances in **5-7** $\{2.3271(8)$ and $2.1435(6)\text{ \AA}$, respectively} are only marginally longer than those in **5-1**, and the $\text{Zr--N}_{\text{amido}}$ bond distance in **5.7** $\{2.1242(7)\text{ \AA}\}$ falls within the typical range for $\text{Zr--N}(\text{SiMe}_3)_2$ linkages $\{2.020(2) \text{ -- } 2.180(3)\text{ \AA}\}$.^[34]

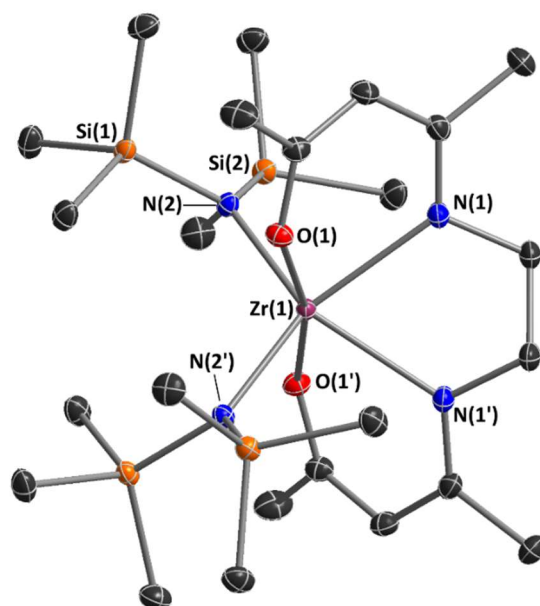


Figure 5.7: X-ray crystal structure of $[\text{Zr}(\text{acen})\{\text{N}(\text{SiMe}_3)_2\}_2]$ (**5-7**) with ellipsoids set at 50% probability and hydrogen atoms omitted for clarity. Space group $C2/c$. $R_1 = 0.0192$. Selected bond lengths (Å) and angles ($^\circ$): $\text{Zr}(1)\text{-O}(1)$ 2.1435(6), $\text{Zr}(1)\text{-N}(1)$ 2.3271(8), $\text{Zr}(1)\text{-N}(2)$ 2.1242(7), $\text{N}(1)\text{-Zr}(1)\text{-N}(1')$ 69.61(4), $\text{N}(2)\text{-Zr}(1)\text{-N}(2')$ 114.87(4), $\text{Zr}(1)\text{-N}(2)\text{-Si}(1)$ 124.85(4), $\text{Zr}(1)\text{-N}(2)\text{-Si}(2)$ 118.87(4).

5.5 – Summary and Conclusions for Chapter 5

This work presents the synthesis of reactive dialkyl and bis(amido) zirconium complexes employing acen, *cis*-Cyacen and *trans*-Cyacen ligands. Key findings include: (a) the *cis*-Cyacen ligand afforded a zirconium dialkyl complex with greater thermal stability and volatility than the acen or *trans*-Cyacen analogues; the *cis*-Cyacen compound, **5-3**, sublimed cleanly at 85 $^\circ\text{C}$ *in vacuo*, (b) the acen^R dialkyl complexes, **5-1** to **5-3**, are significantly more thermally robust than the acen bis(amido) complexes, **5-6** and **5-7**, which decomposed at room temperature; the unexpectedly low thermal stability of these complexes may explain the absence of group 4 bis(amido) acen^R complexes in

the literature, (c) in the solid state, the dialkyl and bis(amido) complexes are best described as trigonal prismatic rather than octahedral, although fluxional NMR behaviour indicates facile access to octahedral structures in solution, (d) the acen^R ligand in zirconium dialkyl complexes is susceptible to protonolysis even by weakly acidic reagents such as *t*BuOH, limiting the potential of such complexes for ALD involving selective reactivity at the monodentate ligands, (e) reaction of one equiv. of H₂(acen) with [Zr(NMeEt)₄] failed to cleanly generate [(acen)Zr(NMeEt)₂], although this product could be accessed cleanly via the reaction of [(acen)Zr(CH₂SiMe₃)₂] with two or more equiv. of HNMeEt; by contrast, [(acen)Zr(CH₂SiMe₃)₂] did not react with excess HN(SiMe₃)₂, even at 50 °C, and (f) reaction of [(acen)ZrCl₂] with two equiv. of LiNMeEt afforded a mixture of unidentified products, whereas the analogous reaction with Li{N(SiMe₃)₂} generated [(acen)Zr{N(SiMe₃)₂}₂] in high yield, highlighting the sensitivity of these reactions to the nature of the amido ligand.

5.6 – Future Work Pertaining to Chapter 5

The zirconium(IV) acen complexes prepared in this research bearing monodentate alkyl or amido ligands lacked the volatility and/or thermal stability required to be suitable ALD precursor candidates. However, synthetically facile modifications to the acen ligand backbone could potentially give rise to more thermally robust complexes. Potential modifications include the addition of sterically bulky isopropyl or *tert*-butyl groups to the β-ketiminate units or to the cyclohexyl rings of the Cyacen derivatives. Fluorination of the methyl groups of the β-ketiminate units may also instill greater volatility in the target

precursor molecule. Furthermore, utilizing monodentate alkoxides in place of alkyl or amido ligands also enhance thermal stability while retaining the promising reactivity observed for **5-2**.

5.7 – References for Chapter 5

- [1] M. Zhu, M. Z. Lerum, W. Chen. How to Prepare Reproducible, Homogeneous, and Hydrolytically Stable Aminosilane-Derived Layers on Silica. *Langmuir* **2012**, *28*, 416-423.
- [2] F. Corazza, C. Floriani, A. Chiesi-Villa, C. Guastini, S. Ciurli. Five-co-ordinate Magnesium Complexes: Synthesis and Structure of Quadridentate Schiff-base Derivatives. *J. Chem. Soc. Dalton Trans.* **1988**, 2341-2345.
- [3] A. Pasini, M. Gullotti. Schiff Base Complexes of Oxocations Part II Oxovanadium(IV) Complexes with Tetridentate Optically Active Schiff Bases. *J. Coord. Chem.* **1974**, *3*, 319-332.
- [4] B. J. Kennedy, K. S. Murray. Magnetic Properties and Zero-Field Splitting in High-Spin Manganese(III) Complexes. 1. Mononuclear and Polynuclear Schiff-Base Chelates. *Inorg. Chem.* **1985**, *24*, 1552-1557.
- [5] B. J. Kennedy, A. C. McGrath, K. S. Murray, B. W. Skelton, A. H. White. Variable-Temperature Magnetic, Spectral, and X-ray Crystallographic Studies of “Spin-Crossover” Iron(III) Schiff-Base-Lewis-Base Adducts. Influence of Noncoordinated Anions on Spin-State Interconversion Dynamics in [Fe(salen)(imd)₂]Y Species (Y = ClO₄⁻, BF₄⁻, PF₆⁻, BPh₄⁻; imd = Imidazole). *Inorg. Chem.* **1987**, *26*, 483-495.
- [6] M. North, C. Young. Bimetallic aluminium(acen) complexes as catalysts for the synthesis of cyclic carbonates from carbon dioxide and epoxides. *Catal. Sci. Technol.* **2011**, *1*, 93-99.
- [7] Y.-P. Cai, H.-Z. Ma, B.-S. Kang, C.-Y. Su, W. Zhang, J. Sun, Y.-L. Xiong. Partially cyclopentadienyl-substituted tetranuclear lanthanide Schiff base complexes. *J. Organomet. Chem.* **2001**, *628*, 99-106.
- [8] V. Mougel, P. Horeglad, G. Nocton, J. Pécaut, M. Mazzanti. Cation-Cation Complexes of Pentavalent Uranyl: From Disproportionation Intermediates to Stable Clusters. *Chem. Eur. J.* **2010**, *16*, 14365-14377.
- [9] F. Corazza, E. Solari, C. Floriani, A. Chiesi-Villa, C. Guastini. cis- and trans-Dichloro-derivatives of six- and seven-co-ordinate zirconium and hafnium bonded to quadridentate Schiff-base ligands. Crystal structures of [Zr(acen)Cl₂(thf)], [M(salphen)Cl₂(thf)]·0.5thf, [M(acen)Cl₂], (M = Zr or Hf) and [Zr(msal)Cl₂]. *J. Chem. Soc. Dalton Trans.* **1990**, 1335-1344.
- [10] E. B. Tjaden, D. C. Swenson, R. F. Jordan, J. L. Petersen. Synthesis, Structures, and Reactivity of (R₆-acen)ZrR'₂ and (R₆-acen)Zr(R')⁺ Complexes (R = H, F; R' = CH₂CMe₃, CH₂Ph). *Organometallics* **1995**, *14*, 371-386.
- [11] A. Bastianini, G. A. Battiston, F. Benetollo, R. Gerbasi, M. Porchia. Synthesis and crystal structure of zirconium complexes with fluorinated tetridentate beta-ketoiminate ligands. *Polyhedron* **1997**, *16*, 1105-1110.
- [12] T. Gerfin, M. Becht, K.-H. Dahmen. Preparation of copper and copper oxide films by metal-organic chemical vapour deposition using beta-ketoiminate complexes. *Mater. Sci. Eng., B* **1993**, *17*, 97-100.
- [13] G. G. Condorelli, G. Malandrino, I. L. Fragalà. Nucleation and growth of copper oxide films in MOCVD processes using the beta-ketoiminate precursor 4,4'-(1,2-

- ethanediyldinitrilo)bis(2-pentanone) copper(II). *Chem. Vap. Deposition* **1999**, *5*, 237-244.
- [14] P. A. Premkumar, A. Dasgupta, P. Kuppasami, P. Parameswaran, C. Mallika, K. S. Nagaraja, V. S. Raghunathan. Synthesis and Characterization of Ni and Ni/CrN Nanocomposite Coatings by Plasma Assisted Metal-Organic CVD. *Chem. Vap. Deposition* **2006**, *12*, 39-45.
- [15] S. Arockiasamy, V. S. Raghunathan, P. A. Premkumar, P. Kuppasami, A. Dasgupta, P. Parameswaran, C. Mallika, K. S. Nagaraja. Plasma-Assisted MOCVD of Titanium Oxide and its Composite Coatings Using Metallo-organic Precursors. *Chem. Vap. Deposition* **2007**, *13*, 691-697.
- [16] D. Pugh, P. Marchand, I. P. Parkin, C. J. Carmalt. Group 13 beta-ketoiminate compounds: gallium hydride derivatives as molecular precursors to thin films of Ga₂O₃. *Inorg. Chem.* **2012**, *51*, 6385-6395.
- [17] C. E. Knapp, P. Marchand, C. Dyer, I. P. Parkin, C. J. Carmalt. Synthesis and characterisation of novel aluminium and gallium precursors for chemical vapour deposition. *New J. Chem.* **2015**, *39*, 6585-6592.
- [18] J. A. Belot, R. J. McNeely, A. Wang, C. J. Reedy, T. J. Marks, G. P. A. Yap, A. L. Rheingold. Expedient route to volatile zirconium metal-organic chemical vapor deposition precursors using amide synthons and implementation in yttria-stabilized zirconia film growth. *J. Mater. Res.* **1999**, *14*, 12-15.
- [19] Bond distance and angle range based on a search of the Cambridge Structural Database for 6-coordinate zirconium bis(trimethylsilylmethyl) complexes. 100% of the Zr-C distances and Zr-C-Si angles in the CSD fall within the range described. CSD accessed via conquest CSD on September 13, 2022; version 5.42, updated November 2020).
- [20] J. W. Bruno, G. M. Smith, T. J. Marks, C. K. Fair, A. J. Schultz, J. M. Williams. C-H Activation Mechanisms and Regioselectivity in the Cyclometalation Reactions of Bis(pentamethylcyclopentadienyl)thorium Dialkyl Complexes. *J. Am. Chem. Soc.* **1986**, *108*, 40-56.
- [21] Z. Guo, D. C. Swenson, R. F. Jordan. Cationic Zirconium and Hafnium Isobutyl Complexes as Models for Intermediates in Metallocene-Catalyzed Propylene Polymerizations. Detection of an α -Agostic Interaction in (C₅Me₅)₂Hf(CH₂CHMe₂)(PMe₃)⁺. *Organometallics* **1994**, *13*, 1424-1432.
- [22] A. F. Dunlop-Brière, P. H. M. Budzelaar, M. C. Baird. α - and β -Agostic Alkyl-Titanocene Complexes. *Organometallics* **2012**, *31*, 1591-1594.
- [23] J. Jaffart, M. Etienne, F. Maseras, J. E. McGrady, O. Eisenstein. Equilibria between α - and β -Agostic Stabilized Rotamers of Secondary Alkyl Niobium Complexes. *J. Am. Chem. Soc.* **2001**, *123*, 6000-6013.
- [24] D. L. Clark, S. K. Grumbine, B. L. Scott, J. G. Watkin. Sterically Demanding Aryloxides as Supporting Ligands in Organoactinide Chemistry. Synthesis, Structural Characterization, and Reactivity of Th(O-2,6-*t*-Bu₂C₆H₃)₂(CH₂SiMe₃)₂ and Formation of the Trimeric Thorium Hydride Th₃H₆(O-2,6-*t*-Bu₂C₆H₃)₆. *Organometallics* **1996**, *15*, 949-957.

- [25] L. Turculet, T. D. Tilley. Zirconium Amide, Halide, and Alkyl Complexes Supported by Tripodal Amido Ligands Derived from *cis,cis*-1,3,5-Triaminocyclohexane. *Organometallics* **2002**, *21*, 3961-3972.
- [26] C. A. Cruz, D. J. H. Emslie, L. E. Harrington, J. F. Britten, C. M. Robertson. Extremely Stable Thorium(IV) Dialkyl Complexes Supported by Rigid Tridentate 4,5-Bis(anilido)xanthene and 2,6-Bis(anilidomethyl)pyridine Ligands. *Organometallics* **2007**, *26*, 692-701.
- [27] D. M. Amorose, R. A. Lee, J. L. Petersen. 1-Sila-3-metallacyclobutanes, Precursors for the Generation of Highly Electrophilic Group 4 Metallocene Alkyl Cations. Spectroscopic and Structural Evidence of a Weakly Bound THF Ligand in [(C₅Me₅)₂Zr(CH₂SiMe₃)(THF)][BPh₄]. *Organometallics* **1991**, *10*, 2191-2198.
- [28] In metal (M) alkyl complexes with CH₂ER₃ (E = Si or C) ligands, the interpretation of expanded M-C-E angles and ¹J_{C,H} coupling constants should be approached with caution, given that larger M-C-E angles can arise due to steric effects, potentially giving rise to smaller ¹J_{C,H} coupling constants due to decreased s-character in the C-H bonds (see refs. 23 and 24). Furthermore, ¹J_{C,H} coupling constants are diminished when the carbon atom is attached to an electropositive substituent, as predicted by Bent's rule (see ref. 32). For example, the ¹J_{C,H} coupling for SiMe₄ is 118 Hz, compared with 124 Hz for CMe₄ (see ref. 33), and the ¹J_{C,H} coupling for the methyl ligands in [(MgMe₂(μ-1,4-dioxane))_n] (in d₈-THF) is 106 Hz (see ref. 34), compared with 115.5 Hz for the terminal methyl groups in Al₂Me₆ (see ref. 35), and 125 Hz for methane (see ref. 36).
- [29] H. A. Bent. An Appraisal of Valence-Bond Structures and Hybridization in Compounds of the First-Row Elements. *Chem. Rev.* **1961**, *61*, 275-311.
- [30] R. B. Nazarski, W. Makulski. ¹J_{CH} couplings in Group 14/IVA tetramethyls from the gas-phase NMR and DFT structural study: a search for the best computational protocol. *Phys. Chem. Chem. Phys.* **2014**, *16*, 15699-15708.
- [31] R. Fischer, H. Görls, P. R. Meisinger, R. Suxdorf, M. Westerhausen. Structure-Solubility Relationship of 1,4-Dioxane Complexes of Di(hydrocarbyl)magnesium. *Chem. Eur. J.* **2019**, *25*, 12830-12841.
- [32] O. Yamamoto. ²⁷Al-¹³C coupling constants in trimethylaluminum dimer and its derivatives. *J. Chem. Phys.* **1975**, *63*, 2988-2995.
- [33] N. Muller, D. E. Pritchard. C¹³ Splittings in Proton Magnetic Resonance Spectra. I. Hydrocarbons. *J. Chem. Phys.* **1959**, *31*, 768-771.
- [34] Bond distance range based on a search of the Cambridge Structural Database for zirconium bis(trimethylsilyl)amido complexes. 96% of the Zr-N distances in the CSD fall within the range described. CSD accessed via conquest CSD on September 13, 2022; version 5.42, updated November 2020).

Chapter 6 – Experimental Methods

6.1 – General Details

All reactions were conducted under an atmosphere of argon, with the exception of the preparation of $t\text{Bu}_3\text{SiBr}$ which was carried out under N_2 on a Schlenk line containing a mineral oil bubbler rather than a mercury bubbler, and the synthesis of the $\text{H}_2\text{acen}^{\text{R}}$ proligands which were carried out in air. An argon-filled Innovative Technology PureLab HE glovebox equipped with a $-30\text{ }^\circ\text{C}$ freezer was employed for the manipulation and storage of all oxygen- and moisture-sensitive compounds. Air-sensitive syntheses were performed on a double-manifold high-vacuum line (with mercury bubblers) equipped with an Edwards R12 vacuum pump using standard techniques. The vacuum was measured periodically using a Kurt J. Lesker 275i convection enhanced Pirani gauge.

Commonly utilized specialty glassware included thick-walled flasks equipped with Teflon taps leading to a 24/40 glass joint (bombs), or J. Young or Wilmad LPV NMR tubes. Centrifugation was performed using a Fisher Scientific model 228 centrifuge [using Kimble 15 mL glass centrifuge tubes (21020-684) and Wheaton PTFE-lined phenolic caps (240463)] located within the glovebox. Glass-to-glass connections were lubricated using H grease (Apiezon) or silicone grease (Dow Corning). Argon cylinders (Linde) of 99.998% and 99.999% purity were used for the ALD reactor and vacuum lines, respectively. Argon supplied to the vacuum lines was purified to below 0.1 ppm of O_2 and 0.5 ppm H_2O using an Oxisorb-W scrubber from Matheson Gas Products. Argon supplied to the ALD reactor was purified to below 100 ppt of O_2 and H_2O using an SAES MC450-902F purifier.

6.1.1 – ALD Reactor

All ALD experiments were conducted in a home-built, flow-type temporal ALD reactor (Figure 6.1). The reactor consists of a reaction chamber (a 4.5" conflat cube) housed within an oven ("Oven 1"). This reaction chamber contains a flange-mounted 1-inch heated substrate stage (Heatwave Labs) which can be heated independently to a temperature equal to or above the temperature of the surrounding oven. The reaction chamber is connected to an Edwards R12 vacuum pump (located within a fume hood) via a heated foreline (a section is heated to ~300 °C, but most of the foreline is at 100-150 °C) with several manual bellows valves, and a 4Å molecular sieve trap (MDC vacuum products) to prevent oil backstreaming from the pump. The foreline also connects to a Convection Enhanced Pirani Vacuum Gauge (not connected during ALD).

Four separate precursor lines attach to the top of the reaction chamber. One line can be used for room temperature precursor delivery ("RT Bubbler"). One can be used for gaseous precursor delivery. Two lines lead to heated bubblers of a flow-through design (but with a dip tube short enough to avoid contact with the precursor upon initial loading of the bubbler; see Figure A2.28); one heated bubbler is housed within the same oven that contains the reaction chamber, while the second is housed in an adjacent oven (connected to the oven that contains the reaction chamber via a short section of tubing which can be independently heated). Purified argon is supplied to each of the four precursor lines via a mass flow controller and a pneumatically actuated diaphragm valve ("ALD valve").

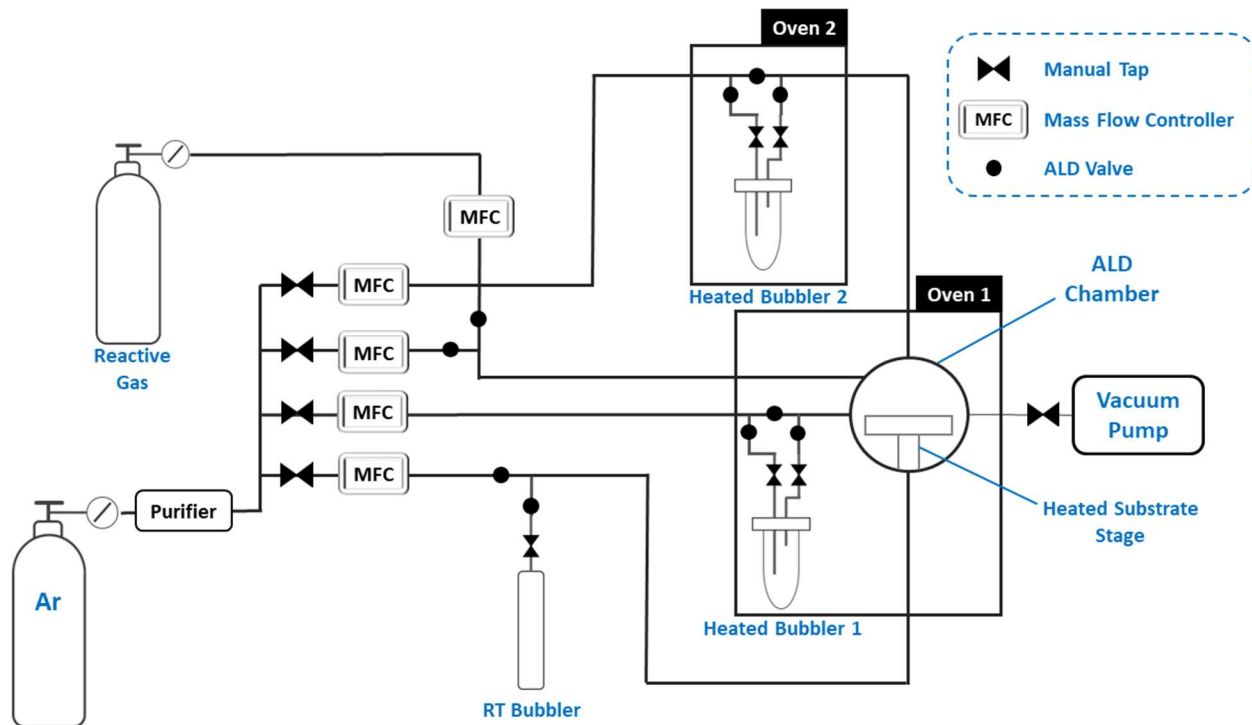


Figure 6.1: Schematic diagram of the home-built ALD reactor used in this research.

6.1.2 – Solvents

Other than d_8 -toluene and d_8 -THF (which were purchased from Cambridge Isotope Laboratories), all solvents (1,2-dimethoxyethane (DME), hexanes, pentane, benzene, toluene, tetrahydrofuran (THF), diethyl ether (Et₂O), C₆D₆) were purchased from Sigma-Aldrich. All solvents were initially dried over an appropriate drying agent (DME, benzene = 4Å mol. sieves followed by Na/benzophenone (Ph₂CO); hexanes, pentane = Na/Ph₂CO/tetraglyme; THF, Et₂O, C₆D₆, d_8 -tol, d_8 -THF = Na/Ph₂CO; toluene = Na followed by Na/Ph₂CO), and then distilled.

6.1.3 – Instrumentation and Analysis

Solution NMR spectroscopy (nuclei: ^1H , ^{13}C , ^{11}B , ^{29}Si , ^{19}F) was performed on a Bruker AV-600 at 298 K and a Bruker AV-500 NMR spectrometer between 188 and 248 K. All ^1H and $^{13}\text{C}\{^1\text{H}\}$ NMR spectra were directly referenced relative to SiMe_4 through the resonance of the proto impurity in C_6D_6 , $d_8\text{-tol}$, or $d_8\text{-THF}$ (for ^1H NMR; 7.16 ppm, 2.08 (CH_3), and 3.58 (OCH_2) ppm, respectively) or the resonance of C_6D_6 , $d_8\text{-tol}$, or $d_8\text{-THF}$ (for ^{13}C NMR; 128.06 ppm, 20.43 (CD_3), and 67.21 (OCD_2) ppm, respectively). $^{11}\text{B}\{^1\text{H}\}$, ^{29}Si , and ^{19}F NMR spectra were indirectly referenced by conversion of the spectral frequency of the ^1H NMR spectrum using the frequency ratio (Ξ) of each nuclei to ^1H , as described by Harris *et al.*^[1] The frequency ratio is defined as the percentage of measured frequency of a specific isotope to that of the measured ^1H NMR frequency of TMS, and is a known value for all commonly used NMR nuclei (e.g. ^1H : 100, ^{13}C : 25.145004, ^{11}B : 32.083974, ^{29}Si : 19.867187, ^{19}F : 94.094008%). Heteronuclear NMR spectra can therefore be indirectly referenced by multiplying the frequency ratio by the spectrometer frequency of the ^1H NMR spectrum ($\nu_{\text{nuclei}2} = \nu_{^1\text{H}} \times \Xi_{\text{nuclei}2} \div 100$). Direct referencing using an external standard was performed periodically to validate spectral frequency values. All reported ^{29}Si NMR chemical shifts were located from crosspeaks in 2D ^{29}Si - ^1H HMBC NMR spectra.

Combustion elemental analyses were performed at the University of Calgary using a Perkin Elmer Model 2400 series II analyzer. An FTIR spectrum of solid **5-2** in a Nujol mull sealed between two CaCl_2 windows was obtained using a Thermo Scientific Nicolet iS5 FTIR spectrometer equipped with a Thermo Scientific iD1 Transmission accessory, and processed using Thermo Scientific OMNIC Series software. Gas chromatography-

mass spectrometry (GC-MS) was obtained on an Agilent 6890 GC coupled to Agilent 5973 mass spectrometer (column: Phenomenex ZB624Plus, 30 m, ID 250 μm , film thickness 1.4 μm). Helium was used as a carrier gas with a constant flow (0.8 mL/min, split 30:1), 200 μL of sample was injected, and the oven temperature program was as follows: an initial temperature of 35 $^{\circ}\text{C}$ was held for 4 minutes, and then ramped to 180 $^{\circ}\text{C}$ at a rate of 10 $^{\circ}\text{C}/\text{min}$, and held at the final temperature for 2 minutes.

Single crystal X-ray diffraction studies were conducted on crystals coated in Paratone oil and mounted on either (a) a SMART APEX II diffractometer with a 3 kW sealed-tube Mo generator and SMART6000 CCD detector (**3-8**, **4-2**, **5-1**, **5-2**, **5-3**, **5-7**), or (b) a STOE IPDS II diffractometer with an image plate detector (**3-2**, **3-3**, **3-12**, **3-13**, **4-1**, **5-5**) in the McMaster Analytical X-ray diffraction (MAX) facility. Raw data was processed using XPREP (as part of the APEX v2.2.0 software) and solved by an intrinsic method (SHELXT).^[2,3] In all cases, non-hydrogen atoms were refined anisotropically and hydrogen atoms were generated in ideal positions and then updated with each refinement cycle (except for all ZrCH_2 hydrogen atoms in complexes **5-1**, **5-2**, and **5-3** which were located from the difference map and refined isotropically). All structure solutions and refinements were performed using Olex2.^[4] Geometries were assigned through the use of continuous shape measure (CSM) analysis using the SHAPE program.^[5]

6.1.4 – Materials Characterization

Powder and thin film X-ray diffraction (XRD) was carried out using a Bruker D8 Discover diffractometer equipped with a Vantec 500 area detector and a focused Cu source with K_{α} radiation ($\lambda = 1.5418 \text{ \AA}$) operated at 40 kV and 40 mA. Thin films and

powders were measured using a 2θ (thin film) or θ - 2θ (powders) scan with Φ rotation and a fixed θ angle of 5° (6 frames with exposure times of 300 seconds per frame) to produce a continuous 2θ range of 10 - 130° . A reference Sb and B diffractogram was produced using Mercury software with data retrieved from the Inorganic Crystal Structure Database (ICSD collection codes 64695 and 68104, respectively). Experimental diffractograms were generated and analyzed using GADDS, Diffrac.EVA, and Topas.

Average film thicknesses were determined by variable angle spectroscopic ellipsometry (VASE) using a J. A. Woolam M-2000 spectroscopic ellipsometer. Measurements were taken from 55° to 75° at 5° increments with an acquisition time of 10 seconds. Experimental data were modeled using the CompleteEase software provided with the spectrometer. For Sb films deposited on SiO_2/Si , the model used to fit the experimental data consisted of a Si substrate with a SiO_2 layer of fixed thickness (thickness determined by VASE analysis of the bare substrates) followed by a B-Spline model with starting material parameters set to Sb. Sb films deposited on H-Si were treated analogously, but without the SiO_2 layer in the model. Models utilized data obtained in the angle and wavelength ranges 65 - 70° and 300 - 900 nm. For Hf-containing films deposited on SiO_2/Si , the fitting model consisted of a Si substrate with a SiO_2 layer followed by a Cauchy model layer, and utilized data obtained in the angle and wavelength ranges 55 - 60° and 300 - 900 nm.

In all cases, VASE measurements were carried out at 3 points on the wafer, and quoted thickness values are an average of all three measurements (where film thickness data is represented graphically, vertical bars indicate the range of the 3 obtained values; only shown if the range extends >1 nm from the average value). Average thickness values

from VASE were periodically confirmed by AFM step analysis (immediately before placing inside the reaction chamber, a strip of 1/8" wide Kapton tape was neatly stuck to one side of the substrate; after deposition, the tape was peeled off to reveal the bare substrate, which was cleaned with isopropanol and hexanes to remove any tape residue) and/or cross-sectional SEM.

In addition to XRD, film composition was analyzed by X-ray photoelectron spectroscopy (XPS) using a Thermofisher Scientific Escalab 250Xi (monochromatic Al- $K\alpha$ source) with a nominal spot size of 900 μm . Sputtering depth profiles were obtained using 2000 eV monoatomic Ar^+ ion bombardment at a high current density with a 90 s cycle time rastered over an area of 4.5 mm by 4.5 mm. Electron micrographs were obtained using a FEI Magellan 400 and analyzed using ImageJ software. All average thickness values depicted on the top right corner of FESEM images were obtained from VASE. Atomic force micrographs were obtained using a Bruker Dimension Icon AFM and analyzed using Nanoscope Analysis software. Surface resistivity of selected films (those deposited on undoped Si(100) wafers with 2 nm of oxide) were measured using a Jandel cylindrical four-point-probe (CYL-1.0-45-TC-250-8; 1 mm tip spacing; tungsten carbide tips with 0.25mm tip radius) and Jandel HM20 4PP test meter.

6.2 – Starting Materials, Synthetic Procedures, and Characterization Pertaining to the Work of Chapter 2

6.2.1 – Starting Materials

Antimony powder, sodium, naphthalene, Me_3SiCl , and SbCl_3 were purchased from Sigma-Aldrich and stored under argon. All reagents were used without further purification.

Sb(SiMe₃)₃ (2-1) was prepared using a modification of the previously reported syntheses,^[6,7] based on the syntheses of $\text{Sb}(\text{SiEt}_3)_3$ ^[8] and $\text{Sb}(\text{Si}^i\text{Pr}_3)_3$ ^[9] (note: all work conducted outside of a glove box was carried out in a fume hood): In a thick-walled 500 mL bomb, a mixture of Sb powder (7.35 g; 0.060 mol), thin ribbons of Na (4.18 g; 0.182 mol) and naphthalene (300 mg; 2.34 mmol) in DME (200 mL) was stirred at 100 °C for 2 days to afford a black-coloured slurry of Na_3Sb . After cooling to room temperature, trimethylchlorosilane (27 mL; 0.213 mol) was added dropwise with vigorous stirring over 30 minutes. The mixture was then heated at 100 °C for 3 days. The volume of the black slurry was halved *in vacuo*, before the mixture was brought into a glovebox and centrifuged. The solid residue was washed with 30 mL of hexanes, followed by centrifugation. The combined mother liquors were transferred to a 250 mL bomb, attached to a vacuum line, and cooled to 0 °C. Remaining solvent was slowly distilled from the solution (through the vacuum line) into a receiving bomb cooled to -78 °C under static vacuum. This afforded $\text{Sb}(\text{SiMe}_3)_3$ as a pale yellow oil (18.5 g, 0.054 mol, 90%), which was brought into a glovebox and stored at -30 °C as a solid. $\text{Sb}(\text{SiMe}_3)_3$ is light sensitive and seemingly reactive towards polypropylene centrifuge tubes (presumably due to reaction with additives). Therefore, glass centrifuge tubes should be used, and $\text{Sb}(\text{SiMe}_3)_3$ should be stored in the dark. ¹H NMR (C₆D₆, 600 MHz, 298 K): δ 0.43 (s, 27H,

CH_3) ppm; $^{13}C\{^1H\}$ (C_6D_6 , 151 MHz, 298 K) NMR: δ 5.03 (CH_3) ppm; ^{29}Si NMR (C_6D_6 , 199 MHz, 298 K): δ -8.68 (s) ppm.

6.2.2 – ALD Experiments using $Sb(SiMe_3)_3$ (2-1) and $SbCl_3$

For all ALD experiments, argon flows of 50 sccm were used on the two inactive lines, and flows of 200 sccm were used on the two in-use lines, resulting in a reactor pressure of ~630 mTorr during ALD.

The $SbCl_3$ and $Sb(SiMe_3)_3$ bubblers^[10] were maintained at 30 °C in all experiments except for room temperature deposition experiments in which all heaters were turned off. Substrate temperatures ranged from room temperature (~23 °C) to 150 °C. For all depositions in this work, the purge time following each precursor pulse was 30 s (the ALD reactor used in this work requires longer pulses than most commercial ALD reactors due to the significantly larger reaction chamber volume). Note: the GPC for the $Sb(SiMe_3)_3/SbCl_3$ ALD process (at 35 °C) shows significant dependence on purge duration, as shown in Figure A2.22. This is presumably due to some desorption of weakly adsorbed precursor during the purge step, and analogous behaviour was previously observed, by in situ QCM, for Sb ALD using $Sb(SiEt_3)_3/SbCl_3$ at 98 °C.^[8] Analogous behaviour was also observed during Sb_2Te_3 ALD using $Te(SiEt_3)_2/SbCl_3$.^[11,12]

All ALD experiments used double side polished Si(100) wafers with a layer (~100 or 5 nm) of oxide, or freshly prepared hydrogen-terminated Si(100) substrates. Si(100) substrates with a layer of oxide (SiO_2/Si) were plasma cleaned (air plasma) for 10 minutes immediately prior to being loaded into the ALD reactor and placed under vacuum. Plasma cleaning was carried out using a Basic Plasma Cleaner (PDC-32G) from Harrick Plasma

connected to a 3.6 cfm Edwards nXDS6i scroll pump. A leak valve (to air) was used to set the pressure in the plasma cleaner to 600-650 mTorr during plasma cleaning (RF coil set to 18 W).

Hydrogen-terminated Si(100) (H-Si) substrates were prepared using the following procedure: 1 cm x 1 cm sections of a Si(100) wafer with a ≤ 5 nm layer of native oxide were placed in a beaker containing 85 °C piranha (3:1 H₂O₂/H₂SO₄) for 10 minutes, followed by a quick rinse under a stream of ultrapure water (UPW). The wafer was then placed in a PTFE beaker containing 2% HF_(aq) for 1-2 minutes,^[13-15] rinsed in a stream of UPW, and dried under a rapid flow of nitrogen or argon. The wafer was then quickly (within 2 or 3 minutes) loaded into the ALD reactor and placed under vacuum. 48% HF (used to prepare 2% HF solutions), 30% H₂O₂, and conc. H₂SO₄ were purchased from Sigma-Aldrich. Ultrapure water was produced using a Milli-Q Direct Water Purification System.

6.3 – Starting Materials, Synthetic Procedures, and Characterization Pertaining to the Work of Chapter 3

6.3.1 – Starting Material Synthesis

The multistep preparations of THF-solvated hypersilyllithium^[16,17] (**3-1**) and supersilylsodium^[18,19] (**3-2**) were conducted according to literature procedures with some modifications to the purification steps. Trimethylgermyllithium (**3-3**) was prepared following an unpublished procedure by Dr. Patricio Romero at Intel Corporation based on the in situ synthesis described by Piers and Lemieux.^[20] The preparations of dimethylamidodichloroborane (**3-4**) and dimethylamidodifluoroborane (**3-5**) were slightly

modified from the literature procedures^[21] to avoid the handling of gaseous BX_3 . Their detailed synthesis and characterization are described below. All commercial reagents (Li, Na, Me_3SiCl , $SiCl_4$, $MeLi$ (1.6M in Et_2O), tBu_2SiHCl , KF , KHF_2 , $tBuLi$ (1.7M in pentane), Br_2 , $LiAlH_4$, Me_3GeBr , BCl_3 (1.0M in heptane), $BF_3 \cdot OEt_2$, BBr_3 , BI_3 , $B(NMe_2)_3$, $B(NMe_2)_2Br$) were purchased from Sigma Aldrich, stored under argon, and used without further purification.

$Si(SiMe_3)_4$. To a 50 mL THF suspension of Li (4.58 g, 660 mmol) in a 2-neck round-bottomed flask was added 41.9 mL (330 mmol) of trimethylchlorosilane. A 50 mL THF solution of silicon tetrachloride (7.56 mL, 66 mmol) was added dropwise to the vigorously stirring mixture using an addition funnel. After stirring at room temperature for 2 days under dynamic argon, the dark brown mixture was gravity filtered to remove unreacted Li and LiCl. A mixture of crushed ice and hydrochloric acid (50 mL) was added to the brown solution, and the organic layer was extracted with 3×15 mL Et_2O and dried over $MgSO_4$. The crude product was purified by sublimation at $90\text{ }^\circ\text{C}/10\text{ mTorr}$ as a white solid (7.5 g, 35%). 1H NMR (C_6D_6 , 600 MHz, 298 K): δ 0.27 (s, 36H, $Si(CH_3)_3$) ppm. $^{13}C\{^1H\}$ NMR (C_6D_6 , 151 MHz, 298 K): δ 2.88 ($Si(CH_3)_3$) ppm. ^{29}Si NMR (C_6D_6 , 119 MHz, 298 K): δ -10.24 (s, $SiMe_3$), -136.11 (s, $Si(SiMe_3)_4$) ppm.

$\{(Me_3Si)_3Si\}Li(THF)_3$ (3-1). A solution of Tetrakis(trimethylsilyl)silane (2.00 g, 6.23 mmol) in 45 mL of THF was prepared in a 100 mL bomb. A solution of 4.15 mL (1.6 M) methyllithium in diethyl ether was added dropwise with vigorous stirring. After stirring the reaction mixture at room temperature for 24 hours, approximately half of the solvent was removed *in vacuo*, and then the reaction was left to stir for 3 additional days at room temperature. All remaining solvent was removed *in vacuo* which left a pale yellow residue.

The crude product was purified by crystallization from 5 mL of hexanes at $-30\text{ }^{\circ}\text{C}$ to afford **3-1** as large orange crystals (1.53 g, 70%). ^1H NMR (C_6D_6 , 600 MHz, 298 K): δ 3.46 (t, 12H, $\text{CH}_2\text{CH}_2\text{O}$), 1.34 (m, 12H, $\text{CH}_2\text{CH}_2\text{O}$), 0.62 (s, 27H, SiMe_3) ppm. $^{13}\text{C}\{^1\text{H}\}$ NMR (C_6D_6 , 151 MHz, 298 K): δ 68.33 ($\text{CH}_2\text{CH}_2\text{O}$), 25.39 ($\text{CH}_2\text{CH}_2\text{O}$), 6.90 ($\text{Si}(\text{CH}_3)_3$) ppm. ^{29}Si NMR (C_6D_6 , 119 MHz, 298 K): δ -5.60 (s, SiMe_3), -185.78 (s, $\text{Si}(\text{SiMe}_3)_3$) ppm.

$^t\text{Bu}_2\text{SiHF}$. Di-*tert*-butylchlorosilane (7.54 g, 0.042 mol), potassium fluoride (1.30 g, 0.021 mol), and potassium hydrogenfluoride (3.41 g, 0.043 mol) were added to a 100 mL round-bottomed flask. The reagents were stirred neat at $70\text{ }^{\circ}\text{C}$ overnight, and then the clear and colourless liquid product was distilled into a 50 mL bomb cooled to $-78\text{ }^{\circ}\text{C}$ (6.58 g, 96%). ^1H NMR (C_6D_6 , 600 MHz, 298 K): δ 4.33 (d, 1H, $^2J_{\text{H,F}} = 48.5\text{ Hz}$, SiH), 0.98 (s, 18H, CH_3) ppm. $^{13}\text{C}\{^1\text{H}\}$ NMR (C_6D_6 , 151 MHz, 298 K): δ 26.39 (CMe_3), 19.26 (CH_3) ppm. ^{19}F NMR (C_6D_6 , 565 MHz, 298 K): δ -188.78 (d, $^2J_{\text{F,H}} = 48.2\text{ Hz}$) ppm. ^{29}Si NMR (C_6D_6 , 119 MHz, 298 K): δ 23.25 (d, $^1J_{\text{Si,F}} = 293\text{ Hz}$) ppm.

$^t\text{Bu}_3\text{SiH}$. A solution of *tert*-butyllithium (2.47 g, 0.039 mol) in 10 mL of hexanes was added dropwise to a stirring solution of di-*tert*-butylfluorosilane (6.03 g, 0.037 mol) in 15 mL of pentane in a 100 mL bomb. The dropwise addition was carried out sufficiently slowly to limit heat generation. After the addition had completed, the reaction mixture was stirred at $60\text{ }^{\circ}\text{C}$ overnight under static argon. Upon cooling to room temperature, all volatiles were removed slowly *in vacuo*, leaving behind a colourless liquid accompanied by a white precipitate. The white precipitate (LiF) was removed by centrifugation to isolate the pure product as a clear and colourless liquid (6.18 g, 83%). ^1H NMR (C_6D_6 , 600 MHz, 298 K): δ 3.53 (s, 1H, SiH), 1.13 (s, 27H, $\text{C}(\text{CH}_3)_3$) ppm. $^{13}\text{C}\{^1\text{H}\}$ NMR (C_6D_6 , 151 MHz,

298 K): δ 30.92 (CMe₃), 21.07 (CH₃) ppm. ²⁹Si NMR (C₆D₆, 119 MHz, 298 K): δ 17.18 (s) ppm.

^tBu₃SiBr. A solution of tri-*tert*-butylsilane (8.03 g, 40 mmol) in 70 mL of pentane was cooled to 0 °C on a mineral oil bubbler Schlenk line. In the dark, 4.2 mL of bromine (82 mmol) was added slowly via syringe to the vigorously stirring solution. The reaction mixture was warmed to room temperature over an hour and stirred for at least 24 hours under dynamic argon. Once the reaction was complete, all volatiles were removed *in vacuo*, leaving a light beige residue with red spots. The crude product was purified by sublimation at 80 °C/10 mTorr through a short distillation neck to a 2-neck flask cooled to –78 °C. This afforded the pure product as a stark white solid (11.1 g, 99%). ¹H NMR (C₆D₆, 600 MHz, 298 K): δ 1.14 (s, 27H, C(CH₃)₃) ppm. ¹³C{¹H} NMR (C₆D₆, 151 MHz, 298 K): δ 30.17 (CMe₃), 24.58 (CH₃) ppm. ²⁹Si NMR (C₆D₆, 119 MHz, 298 K): δ 41.07 (s) ppm.

^tBu₃SiNa(THF)_n; n = 2-3 (3-2). Thin pieces of sodium (8.58 g, 373 mmol) and tri-*tert*-butylbromosilane (11.1 g, 40 mmol) in a suspension of 50 mL of THF were heated at 65 °C in a sealed 500 mL bomb. The mixture was vigorously stirred at this temperature for 8 hours before cooling to room temperature and removing all volatiles *in vacuo*. The residue was redissolved in approximately 20 mL of pentane and centrifuged for 30 minutes to remove precipitates (NaBr, excess Na). The crude product remaining after removal of volatiles *in vacuo* was purified by crystallization from hexanes at –30 °C to afford **3-2** as large brown-orange crystals (13.6 g, 93%). *Note: a trace amount (< 5%) of an impurity (likely ^tBu₃SiH) was consistently present after recrystallizations, and appeared in small amounts in products prepared from 3-2.* ¹H NMR (C₆D₆, 600 MHz, 298 K): δ 3.39

(t, 8-12H, CH₂CH₂O), 1.53 (s, 27H, C(CH₃)₃) *note: peak position concentration-dependent*, 1.34 (m, 8 12H, CH₂CH₂O), 1.13 (s, <1.5H, impurity) ppm. ¹³C{¹H} NMR (C₆D₆, 151 MHz, 298 K): δ 67.83 (CH₂CH₂O), 34.62 (CMe₃), 25.56 (CH₂CH₂O), 24.11 (C(CH₃)₃), 30.89 and 20.81 (impurity) ppm. ²⁹Si NMR (C₆D₆, 119 MHz, 298 K): δ 45.82 (s), 17.27 (s, impurity) ppm.

[Me₃GeLi(THF)₂]₂ (3-3). To a suspension of LiAlH₄ (580 mg, 15.3 mmol) in THF (25 ml) was added a THF solution (15 mL) of trimethylgermanium bromide (2.97 g, 15.1 mmol) dropwise via syringe at 0 °C. The mixture was warmed to room temperature after addition, at which point all volatiles were distilled into a receiving flask at –78 °C. After warming the resulting Me₃GeH solution to –20 °C, a 1.7M solution of *tert*-butyllithium (1.06, 16.5 mmol) in pentane (10 mL) was added dropwise to the stirring solution via syringe over 5 minutes. The yellow reaction mixture was stirred at –10 °C for 10 minutes and then kept at the same temperature to remove volatiles *in vacuo*. Once the mixture appeared as a thick slurry, the flask was warmed to room temperature and the mixture was further evacuated for 30 minutes until a solid pale yellow residue was left. The crude product was washed with 3×5 mL of hexanes, and the supernatant was stored at –30 °C overnight to yield the pure product as a white solid (3.3 g, 82%). X-ray quality single crystals were grown from a hexanes solution at –30 °C as colourless needles. *Note: although the product is stable at room temperature under argon for a few weeks, it decomposes under vacuum over a few hours.* ¹H NMR (C₆D₆, 600 MHz, 298 K): δ 3.61 (t, 8H, CH₂CH₂O), 1.36 (m, 8H, CH₂CH₂O), 0.62 (s, 9H, Ge(CH₃)₃) ppm. ¹³C{¹H} NMR (C₆D₆, 151 MHz, 298 K): δ 68.66 (CH₂CH₂O), 25.44 (CH₂CH₂O), 7.42 (Ge(CH₃)₃) ppm.

C₂₂H₅₀Ge₂Li₂O₄ (537.78 g·mol⁻¹): calcd. C 49.14, H 9.37, N 0.00%; found. C 49.49, H 9.03, N 0.26%.

B(NMe₂)Cl₂ (3-4). A 1.0M solution of boron trichloride in heptane (21.6 mL; 21.6 mmol of BCl₃) was added dropwise via syringe to a vigorously stirring solution of tris(dimethylamido)borane (1.23 g, 8.62 mmol) in 30 mL of pentane in a 100 mL bomb. The clear and colourless solution was stirred at room temperature for one hour, at which point the reaction was cooled to 0 °C. Volatiles were then removed *in vacuo* until approximately one third of the volume remained. The solution was centrifuged for 10 minutes to remove any solid dimer ([B(NMe₂)Cl₂]₂) before storing the colourless solution of dimethylamidodichloroborane at -30 °C. *Note: the concentration of the solution was determined by integration of the ¹H NMR signal of the product relative to heptane before use in reactions.* ¹H NMR (C₆D₆, 500 MHz, 298 K): δ 2.34 (s, 6H, N(CH₃)₂), 1.28 (m, heptane), 0.90 (m, heptane) ppm. ¹³C{¹H} NMR (C₆D₆, 151 MHz, 298 K): δ 39.36 (s, 6H, N(CH₃)₂), 32.37, 29.56, 23.17, and 14.36 (heptane) ppm. ¹¹B{¹H} NMR (C₆D₆, 161 MHz, 298 K): δ 30.48 (s) ppm.

[B(NMe₂)Cl₂]₂ (3-4'). Solutions of **3-4** at room temperature always contained some dimer (**3-4'**) which would precipitate slowly out of solution as large colourless block crystals. ¹H NMR (C₆D₆, 500 MHz, 298 K): δ 2.19 (sep, 6H, N(CH₃)₂, ²J_{H,H} = 3.3 Hz) ppm. ¹³C{¹H} NMR (C₆D₆, 126 MHz, 298 K): δ 34.56 (N(CH₃)₂) ppm. ¹¹B{¹H} NMR (C₆D₆, 161 MHz, 298 K): δ 10.40 (s) ppm.

[B(NMe₂)F₂]₂ (3-5). The dimer of dimethylamidodifluoroborane was prepared analogously to B(NMe₂)Cl₂ using B(NMe₂)₃ (442 mg, 3.09 mmol) and BF₃·OEt₂ (0.80 mL, 6.48 mmol). Monomeric B(NMe₂)F₂ dimerizes and rapidly precipitates out of solution. The

precipitate was dried *in vacuo* to obtain the pure dimer as a white crystalline solid (846 mg, 98%). $^1\text{H NMR}$ (C_6D_6 , 600 MHz, 298 K): δ 1.98 (s, 6H, $\text{N}(\text{CH}_3)_2$) ppm. $^{13}\text{C}\{^1\text{H}\}$ NMR (C_6D_6 , 151 MHz, 298 K): δ 38.31 ($\text{N}(\text{CH}_3)_2$) ppm. $^{11}\text{B}\{^1\text{H}\}$ NMR (C_6D_6 , 161 MHz, 298 K): δ 0.98 (m) ppm. $^{19}\text{F NMR}$ (C_6D_6 , 565 MHz, 298 K): δ -161.85 (m) ppm.

6.3.2 – Silyl- and Germyl-Substituted Boranes

Hypersilylbis(dimethylamido)borane (**3-6**), hypersilyldichloroborane (**3-7**), and bis(hypersilyl)dimethylamidoborane (**3-8**) were prepared following literature procedures (the X-ray crystal structure of **3-8** has not been previously reported).^[22,23] Supersilyldichloroborane (**3-11**) has previously been observed by NMR spectroscopy from the reaction of THF-free ($t\text{Bu}_3\text{Si}$)Na and BCl_3 , but had not previously been isolated. Their detailed synthesis and characterization, as well as those of new supersilyl- and/or germyl-containing boron compounds (**3-9**, **3-10**, **3-12**, **3-13**) are described below.

$\{(\text{Me}_3\text{Si})_3\text{Si}\}\text{B}(\text{NMe}_2)_2$ (3-6**)**. A solution of $\{(\text{Me}_3\text{Si})_3\text{Si}\}\text{Li}(\text{THF})_3$ (**3-1**) (2.00 g, 4.25 mmol) in 100 mL of hexanes was cooled to 0 °C in a 250 mL bomb. A solution of bromobis(dimethylamido)borane (0.80 g, 4.46 mmol) in 5 mL of hexanes was added dropwise with vigorous stirring. The reaction mixture was warmed back to room temperature over 30 minutes, and further stirred at room temperature for 1 hour. The precipitate (LiBr) was then separated by centrifugation for 20 minutes. After removal of the solvent *in vacuo*, the white residue was purified by sublimation at 80 °C/10 mTorr to afford the product as a white solid (1.25 g, 83%). $^1\text{H NMR}$ (C_6D_6 , 600 MHz, 298 K): δ 2.62 (s, 12H, $\text{N}(\text{CH}_3)_2$), 0.36 (s, 27H, $\text{Si}(\text{CH}_3)_3$) ppm. $^{13}\text{C}\{^1\text{H}\}$ NMR (C_6D_6 , 151 MHz, 298 K): δ 42.56 ($\text{N}(\text{CH}_3)_2$), 4.14 ($\text{Si}(\text{CH}_3)_3$) ppm. $^{11}\text{B}\{^1\text{H}\}$ NMR (C_6D_6 , 193 MHz, 298 K): δ 38.19 (s) ppm. $^{29}\text{Si NMR}$ (C_6D_6 , 119 MHz, 298 K): δ -10.94 (s, SiMe_3) ppm, $\text{Si}(\text{SiMe}_3)_3$ unobserved.

$\{(Me_3Si)_3Si\}BCl_2$ (3-7). A solution of 1.00 g (2.89 mmol) of hypersilylbis(dimethylamido)borane (**3-6**) in 50 mL of hexanes was cooled to $-78\text{ }^\circ\text{C}$ in a 100 mL bomb. A 1.0M solution of boron trichloride in heptane (5.78 mL) was added dropwise via syringe to the vigorously stirring solution. The white suspension was warmed to room temperature over 2 hours and stirred overnight. The volatiles were removed *in vacuo* and the pale yellow residue was purified by sublimation at $60\text{ }^\circ\text{C}/5\text{ mTorr}$ onto a dry-ice cold finger to afford the product as a white solid (0.69 g, 75%). $^1\text{H NMR}$ (C_6D_6 , 600 MHz, 298 K): δ 0.26 (s, 27H, $Si(CH_3)_3$) ppm. $^{13}\text{C}\{^1\text{H}\}$ NMR (C_6D_6 , 151 MHz, 298 K): δ 1.94 ($Si(CH_3)_3$) ppm. $^{11}\text{B}\{^1\text{H}\}$ NMR (C_6D_6 , 193 MHz, 298 K): δ 78.90 (s) ppm. $^{29}\text{Si NMR}$ (C_6D_6 , 119 MHz, 298 K): δ -10.67 (s, $SiMe_3$) ppm, $Si(SiMe_3)_3$ unobserved.

$\{(Me_3Si)_3Si\}_2B(NMe_2)$ (3-8). A solution of $\{(Me_3Si)_3Si\}Li(THF)_3$ (**3-1**) (0.724 g, 1.54 mmol) in 10 mL of hexanes was cooled to $-78\text{ }^\circ\text{C}$ in a round-bottom flask. 0.64 g of the prepared $B(NMe_2)Cl_2$ solution (**3-4**; 0.769 mmol) in heptane was added dropwise to the stirring solution. The reaction mixture was then slowly warmed back to room temperature and left to stir overnight. All volatiles were removed *in vacuo*, leaving behind a pale yellow residue. The crude product was purified by recrystallization from hexanes at $-30\text{ }^\circ\text{C}$ (after centrifugation to remove LiCl precipitate), affording **3-8** as a white crystalline solid (0.41 g, 97%). $^1\text{H NMR}$ (C_6D_6 , 600 MHz, 298 K): δ 2.97 (s, 6H, $N(CH_3)_2$), 0.37 (s, 54H, $Si(CH_3)_3$) ppm. $^{13}\text{C}\{^1\text{H}\}$ NMR (C_6D_6 , 151 MHz, 298 K): δ 50.61 ($N(CH_3)_2$), 5.13 ($Si(CH_3)_3$) ppm. $^{11}\text{B}\{^1\text{H}\}$ NMR (C_6D_6 , 193 MHz, 298 K): δ 60.65 (s) ppm. $^{29}\text{Si NMR}$ (C_6D_6 , 119 MHz, 298 K): δ -9.55 (s, $Si(SiMe_3)_3$), -112.81 (s, $Si(SiMe_3)_3$) ppm. **$C_{20}H_{60}BNSi_8$ (550.20 g·mol $^{-1}$):** calcd. C 43.66, H 10.99, N 2.55%; found. C 43.28, H 11.03, N 2.48%.

(^tBu₃Si)B(NMe₂)Cl (3-9). To a bright yellow/orange solution of ^tBu₃SiNa(THF)₂ (**3-2**; 4.442 g, 12.1 mmol) in 15 mL of hexanes was added dropwise a heptane solution of B(NMe₂)Cl₂ (**3-4**; 9.7 mmol; diluted with approximately 5 mL of hexanes). Upon addition, the reaction mixture immediately began to lighten in colour, forming a cloudy light yellow solution, and then a nearly colourless solution with a white precipitate. The reaction mixture was stirred at 50 °C overnight to allow for complete consumption of [B(NMe₂)Cl₂]₂ (**3-4'**), some of which was always present in solutions of **3-4**. All volatiles were removed *in vacuo* and the pale yellow residue was redissolved in 5 mL of hexanes and centrifuged to remove NaCl. Upon removal of solvent *in vacuo*, the clear and colourless oil was purified by distillation at 90 °C/10 mTorr as a colourless oil (2.52 g, 72%). ¹H NMR (C₆D₆, 600 MHz, 298 K): δ 2.70 (s, 6H, N(CH₃)₂), 1.31 (s, 27H, C(CH₃)₃) ppm. ¹³C{¹H} NMR (C₆D₆, 151 MHz, 298 K): δ 45.02 (N(CH₃)₂), 41.19 (CMe₃), 32.84 (C(CH₃)₃) ppm. ¹¹B{¹H} NMR (C₆D₆, 193 MHz, 298 K): δ 41.61 (s) ppm. ²⁹Si NMR (C₆D₆, 119 MHz, 298 K): δ 2.18 (m) ppm. **C₁₄H₃₃BCINSi (289.77 g·mol⁻¹):** calcd. C 58.03, H 11.48, N 4.83%; found. C 57.93, H 11.37, N 4.70%.

(^tBu₃Si)B(NMe₂)F (3-10). To a room temperature suspension of [B(NMe₂)F₂]₂ (**3-5**; 114.2 mg, 0.615 mmol) in 2 mL of hexanes was added dropwise a solution of ^tBu₃SiNa(THF)₂ (**3-2**; 238.4 mg, 0.922 mmol) in hexanes (10 mL). After roughly 1 hour of stirring, the yellow-orange solution turned nearly colourless. The reaction was left to stir for 2 hours total at room temperature before centrifugation and removal of solvent *in vacuo*. The residue was redissolved in pentane (4 mL) and stored at –30 °C overnight to crystallize unreacted [B(NMe₂)F₂]₂. The solution was decanted and dried under vacuum to obtain (^tBu₃Si)B(NMe₂)F as a clear and colourless oil (235.6 mg, 93%). The product

can be distilled at 50 °C/10 mTorr. ^1H NMR (C_6D_6 , 600 MHz, 298 K): δ 2.52 (dd, $^2J_{\text{H,H}} = 2$ Hz, $^4J_{\text{H,F}} = 61$ Hz, 6H, $\text{N}(\text{CH}_3)_2$), 1.26 (s, 27H, $\text{C}(\text{CH}_3)_3$) ppm. $^{13}\text{C}\{^1\text{H}\}$ NMR (C_6D_6 , 151 MHz, 298 K): δ 39.55 (d, $^3J_{\text{CF}} = 4.6$ Hz) and 35.58 (d, $^3J_{\text{CF}} = 13.8$ Hz) ($\text{N}(\text{CH}_3)_2$), 32.15 ($\text{C}(\text{CH}_3)_3$), 22.70 (CMe_3) ppm. $^{11}\text{B}\{^1\text{H}\}$ NMR (C_6D_6 , 193 MHz, 298 K): δ 34.35 (d, $^1J_{\text{B,F}} = 130$ Hz). ^{19}F NMR (C_6D_6 , MHz, 298 K): δ -70.95 (m) ppm. ^{29}Si NMR (C_6D_6 , 119 MHz, 298 K): δ 2.28 (m) ppm. **$\text{C}_{14}\text{H}_{33}\text{BFNSi}$ (273.32 g·mol⁻¹):** calcd. C 61.52, H 12.17, N 5.12%; found. C 61.53, H 12.02, N 5.55%.

(^tBu₃Si)BCl₂ (3-11). To a stirring 10 mL hexanes solution of (^tBu₃Si)B(NMe₂)Cl (**3-9**; 1.38 mmol) cooled to -78 °C was added boron trichloride (1.50 mL, 1M solution in heptane) dropwise via syringe. The reaction mixture was warmed to room temperature over 1 hour and stirred overnight to yield a pale yellow solution with a white precipitate. After the slow removal of all volatiles *in vacuo*, the product was obtained as a beige-brown solid (0.28 g, 72%). ^1H NMR (C_6D_6 , 600 MHz, 298 K): δ 1.18 (s, 27H, $\text{C}(\text{CH}_3)_3$) ppm. $^{13}\text{C}\{^1\text{H}\}$ NMR (C_6D_6 , 151 MHz, 298 K): δ 31.59 ($\text{C}(\text{CH}_3)_3$), 22.70 (CMe_3) ppm. $^{11}\text{B}\{^1\text{H}\}$ NMR (C_6D_6 , 193 MHz, 298 K): δ 77.43 (s) ppm. ^{29}Si NMR (C_6D_6 , 119 MHz, 298 K): δ -1.58 (m) ppm.

(^tBu₃Si)(Me₃Ge)B(NMe₂) (3-12). To a stirring solution of (^tBu₃Si)B(NMe₂)Cl (**3-9**; 307.4 mg, 1.06 mmol) in hexanes (4 mL) at room temperature was added a benzene solution (8 mL) of Me₃GeLi(THF)₂ (**3-3**; 285.2 mg, 1.06 mmol) dropwise via syringe. After one hour, the clear colourless solution became a translucent, pale yellow mixture and was left to stir at room temperature overnight. The solution was centrifuged to remove LiCl and dried *in vacuo* to remove solvents. The crude, pale yellow waxy solid was distilled at 45 °C/10 mTorr to afford **3-12** as a clear and colourless oil that solidifies into a waxy

crystalline solid over approximately one hour at room temperature (302.5 mg, 77%). ^1H NMR (C_6D_6 , 600 MHz, 298 K): δ 2.96 and 2.82 (s, $2 \times 3\text{H}$, $\text{N}(\text{CH}_3)_2$), 1.27 (s, 27H, $\text{C}(\text{CH}_3)_3$), 0.46 (s, 9H, $\text{Ge}(\text{CH}_3)_3$) ppm. $^{13}\text{C}\{^1\text{H}\}$ NMR (C_6D_6 , 151 MHz, 298 K): δ 53.25 and 47.84 ppm ($\text{N}(\text{CH}_3)_2$), 33.32 ($\text{SiC}(\text{CH}_3)_3$), 23.64 (SiCMe_3), 5.11 ($\text{Ge}(\text{CH}_3)_3$) ppm. $^{11}\text{B}\{^1\text{H}\}$ NMR (C_6D_6 , 193 MHz, 298 K): δ 59.88 (s) ppm. ^{29}Si NMR (C_6D_6 , 119 MHz, 298 K): δ 4.43 (m) ppm. **$\text{C}_{17}\text{H}_{42}\text{BNGeSi}$ (372.06 g·mol⁻¹)**: calcd. C 54.88, H 11.38, N 2.91%; found. C 55.25, H 11.05, N 3.30%.

$\{(\text{Me}_3\text{Ge})_3\text{B}(\text{NMe}_2)\}\text{Li}(\text{THF})_2$ (3-13). To a stirring toluene solution (5 mL) of $\text{Me}_3\text{GeLi}(\text{THF})_2$ (**3-3**; 258 mg, 0.960 mmol) at -78 °C was added a heptane solution of $\text{B}(\text{NMe}_2)\text{Cl}_2$ (**3-4**; 0.320 mmol, diluted with 5 mL of hexanes) dropwise via syringe. Upon addition, the mixture became translucent white in colour. The mixture was slowly warmed to room temperature and kept stirring for an additional hour at room temperature before removal of volatiles *in vacuo*. 5 mL of pentane was added to the crude residue and the mixture was centrifuged to remove LiCl. Colourless needle crystals of **3-13** were obtained upon storing the supernatant at -30 °C (242 mg, 45%). ^1H NMR (C_6D_6 , 600 MHz, 298 K): δ 3.32 (m, 8H, $\text{CH}_2\text{CH}_2\text{O}$), 2.41 (m, 6H, $\text{N}(\text{CH}_3)_2$), 1.24 (m, 8H, $\text{CH}_2\text{CH}_2\text{O}$), 0.48 (s, 27H, $\text{C}(\text{CH}_3)_3$) ppm. $^{13}\text{C}\{^1\text{H}\}$ NMR (C_6D_6 , 151 MHz, 298 K): δ 68.21 ($\text{CH}_2\text{CH}_2\text{O}$), 47.91 ($\text{N}(\text{CH}_3)_2$), 25.43 ($\text{CH}_2\text{CH}_2\text{O}$), 4.04 ($\text{Si}(\text{CH}_3)_3$) ppm. $^{11}\text{B}\{^1\text{H}\}$ NMR (C_6D_6 , 193 MHz, 298 K): δ -13.25 (s) ppm.

6.3.3 – Attempted ALD using $\{(\text{Me}_3\text{Si})_3\text{Si}\}_2\text{B}(\text{NMe}_2)$ (3-8) and BCl_3

Typical ALD experiments using $\{(\text{Me}_3\text{Si})_3\text{Si}\}_2\text{B}(\text{NMe}_2)$ (**3-8**) and BCl_3 followed the method outlined below:

Wafers of 100 nm SiO₂/Si(100) and 5 nm SiO₂/Si(100) were cut into squares approximately 1.5 cm x 0.5 cm in size. The wafers were then sprayed with argon gas to remove any silica shards and then plasma cleaned for 10 minutes immediately before use. The wafers were mounted onto the substrate holder and placed inside the reaction chamber, which was evacuated to a pressure of roughly 5 mTorr. Oven 1, which contains the bubbler of **3-8** and the reaction chamber, was held at a temperature of 135 °C. A cylinder of BCl₃ was attached through a room temperature delivery line with a gas flow of 5 sccm. The substrate heater, which can be independently heated, was set at various temperatures above 135 °C. Carrier argon flows were set to 50 and 200 sccm for inactive and active lines, respectively, resulting in a total argon flow of 500 sccm and an internal pressure of ~630 mTorr during operation.

For all deposition experiments in this work, the pulse time of **3-8** was varied between 1-2 seconds and the purge time was kept at 30 seconds. The BCl₃ pulse time was varied between 1-10 seconds and the purge time was kept at 30 seconds. The substrate temperatures varied between 150 and 300 °C. The cycle number was kept constant at 2000.

6.4 – Starting Materials, Synthetic Procedures, and Characterization Pertaining to the Work of Chapter 4

6.4.1 – Starting Materials

Pivalic acid (*t*BuCO₂H) was purchased from Sigma-Aldrich, β-hydroxyisovaleric acid (IVA) was purchased from Alfa Aesar, and [Hf(NMeEt)₄] was purchased from Strem Chemicals.

Warmed (40-50 °C) ^tBuCO₂H and IVA were stirred over 4Å molecular sieves for over two weeks and distilled before use. All other reagents were used without further purification.

6.4.2 – Synthetic Procedures and Characterization

[EtMeNH₂]₂[Hf(κ²-O₂CCH₂CMe₂OH)₂(κ²-OC(O)CH₂CMe₂O)₂] (4-1). To a 10 mL solution of IVA (1.4266 g, 12 mmol) in toluene stirring under dynamic argon was added dropwise a solution of [Hf(NMeEt)₄] (1.2405, 3 mmol) in 10 mL of toluene via syringe. After stirring the translucent white solution for 2 days under dynamic argon, all volatiles were removed *in vacuo* to obtain a waxy white residue consisting almost exclusively of compound **4-1** by NMR spectroscopy. Single crystals of **4-1** were obtained in trace amounts from vapour diffusion at room temperature of a dilute toluene solution of the crude solid with hexanes. ¹H NMR (C₆D₆, 600 MHz, 298 K): δ 9.49 (bs, ~4H, NH), 5.31 (bs, ~1H, OH), 2.69 (s, 8H, O₂CCH₂), 2.19 (q, 4H, NCH₂CH₃), 1.99 (s, 6H, NCH₃), 1.39 (s, 24H, C(OH)(CH₃)₂), 0.87 (t, 6H, NCH₂CH₃) ppm. ¹³C{¹H} NMR (C₆D₆, 151 MHz, 298 K): δ 180.26 (O₂C), 71.38 (C(OH)(CH₃)₂), 50.78 (O₂CCH₂), 43.28 (NCH₂CH₃), 31.38 (NCH₃), 30.84 (C(OH)(CH₃)₂), 10.78 (NCH₂CH₃) ppm. **C₂₆H₅₄N₂O₁₂Hf (765.21 g·mol⁻¹):** calcd. C 40.81, H 7.11, N 3.66%; found. C 40.76, H 6.71, N 4.06%.

[Hf₅(μ₃-O)₄(κ²-O₂C^tBu)₄(μ-O₂C^tBu)₈] (4-2). To a cooled (-78 °C) 6 mL solution of ^tBuCO₂H (137.7 mg, 1.348 mmol) in Et₂O under dynamic argon was added dropwise a solution of [Hf(NMeEt)₄] (167.9 mg, 0.409 mmol) in 3 mL of Et₂O via syringe. After slowly warming to room temperature, the clear and colourless solution is left to stir under dynamic argon for 1-2 days. All volatiles were removed *in vacuo* to obtain a light yellow-beige solid residue. Large, colourless plate crystals of **4-2** were obtained from a

concentrated Et₂O solution of the crude solid stored at –30 °C (60.0 mg, 33.8%). ¹H NMR (d₈-THF, 600 MHz, 298 K): δ 1.18 (bs, 72H, O₂CC(CH₃)₃), 1.17 (bs, 36H, O₂CC(CH₃)₃) ppm. ¹³C{¹H} NMR (d₈-THF, 151 MHz, 298 K): δ 191.73 (O₂CC(CH₃)₃), 187.69 (O₂CC(CH₃)₃), 40.04 (O₂CC(CH₃)₃), 27.76 (O₂CC(CH₃)₃), 27.29 (O₂CC(CH₃)₃) ppm. **C₆₀H₁₀₈O₂₈Hf₅ (2169.95 g·mol⁻¹):** calcd. C 33.21, H 5.02, N 0.00%; found. C 32.94, H 4.68, N 0.21%.

General procedure for thermal decomposition of crude 4-1 under dynamic vacuum: Approximately 50-100 mg of crude **4-1** was placed in a 25 mL round-bottomed-flask connected to a 2-neck flask by an adapter. The solid was heated at 200 °C under dynamic vacuum for 4 hours, and the 2-neck flask was kept cool at –196 °C to collect volatile decomposition by-products. Room temperature-volatile by-products were distilled under vacuum either into a degassed J. Young tube containing C₆D₆ and analyzed by NMR spectroscopy, or into a 2-neck round bottom flask sealed with a rubber septum and analyzed by headspace GC-MS. Non-room temperature-volatile by products were either dissolved in C₆D₆ and analyzed by NMR spectroscopy, or dissolved in toluene and analyzed by GC-MS. The solid powder residue was amorphous by XRD and there were no soluble products observed by NMR spectroscopy (avg found. C 23.54, H 2.45, N 0.77% by combustion EA).

6.4.3 – ALD Experiments using [Hf(NMeEt)₄] and IVA

The [Hf(NMeEt)₄] and IVA bubblers were maintained at 70 and 100 °C, respectively, in all experiments. Substrate temperatures ranged from 100 °C to 300 °C during deposition. Carrier argon flows were set to 20 sccm for inactive and active lines,

respectively, resulting in a total argon flow of 80 sccm and an internal pressure 250 mTorr during operation. The $[\text{Hf}(\text{NMeEt})_4]$ and IVA pulse times were varied between 0.4 and 1 seconds. For all depositions in this work, the purge time following each precursor pulse was 60 s, unless otherwise stated (the ALD reactor used in this work requires longer pulses than most commercial ALD reactors due to the significantly larger reaction chamber volume), and the cycle number was kept constant at 500. Thermal annealing (400 °C for 1 hour) was performed in the reactor chamber after deposition with minimal to no exposure to air in between deposition and annealing.

6.4.4 – Attempted ALD using $[\text{Hf}(\text{NMeEt})_4]$ and Pivalic Acid (tBuCO_2H)

Typical ALD experiments using $[\text{Hf}(\text{NMeEt})_4]$ and tBuCO_2H followed the method outlined below:

The $[\text{Hf}(\text{NMeEt})_4]$ and tBuCO_2H bubblers were maintained at 90 and 50 °C, respectively. The substrate heater was set at temperatures of 100-250 °C, and deposition was attempted on SiO_2/Si substrates. Carrier argon flows were set to 50 and 200 sccm for inactive and active lines, respectively, resulting in a total argon flow of 500 sccm and an internal pressure of 630 mTorr during operation. The $[\text{Hf}(\text{NMeEt})_4]$ and IVA pulse times were varied between 0.4 and 1 seconds, and the purge time after each reactant was kept at 20 seconds. The cycle number was kept constant at 500.

6.5 – Starting Materials, Synthetic Procedures, and Characterization Pertaining to the Work of Chapter 5

6.5.1 – Starting Materials

ZrCl₄, LiCH₂SiMe₃ (1.0M in pentane) ethylenediamine, *cis*- and *trans*-1,2-diaminocyclohexane, acetylacetonone, ethylmethylamine, methyllithium (1.6M in Et₂O), lithium hexamethyldisilazide (Li{N(SiMe₃)₂}) and *tert*-butanol were purchased from Sigma-Aldrich. [Zr(NMeEt)₄] was purchased from Strem Chemicals. ZrCl₄ was stored under argon and freshly sublimed before each use. Ethylmethylamine and *t*-butanol were dried over 4Å mol. sieves, degassed, and stored under argon in a storage flask. All other reagents were used without further purification. H₂(acen), [Zr(acen)Cl₂], and [Zr(CH₂SiMe₃)₄], were prepared using literature procedures.^[24,25] LiNMeEt was prepared by the addition of HNMeEt to a solution *n*BuLi in hexanes at –78 °C and the removal of all volatiles *in vacuo* after stirring at room temperature overnight to obtain the desired product as a white solid. H₂(*cis*-Cyacen) and H₂(*trans*-Cyacen) were prepared using the same method as H₂(acen) (similar to the previously reported method, but starting with pure *cis*- or *trans*-1,2-diaminocyclohexane).^[26] The proligands H₂(acen), H₂(*cis*-Cyacen), and H₂(*trans*-Cyacen) were dissolved in toluene and dried over 4Å molecular sieves for 2 weeks before use.

6.5.2 – Synthetic Procedures and Characterization

[Zr(acen)(CH₂SiMe₃)₂] (5-1). A solution of H₂(acen) (116 mg, 0.52 mmol) in toluene (10 mL) was added dropwise to a solution of [Zr(CH₂SiMe₃)₄] (228 mg, 0.52 mmol) in hexanes (5 mL) at room temperature, whereupon the clear, pale yellow solution turned

bright yellow in colour. The reaction darkened to a clear, red solution while stirring overnight at room temperature. Volatiles were removed *in vacuo* to obtain a dark red solid that was >95% pure by NMR spectroscopy (229 mg, 89%). Analytically pure and X-ray quality single crystals were grown by layering hexanes onto a saturated toluene solution (1:3) and cooling to $-30\text{ }^{\circ}\text{C}$ (95 mg, 38%). Compound **5-1** decomposed without sublimation at $140\text{ }^{\circ}\text{C}$. No decomposition was observed by NMR spectroscopy after heating solid **5-1** at $120\text{ }^{\circ}\text{C}$ *in vacuo* for 6 hours. ^1H NMR (C_6D_6 , 500 MHz, 298K): δ 5.27 (s, 2H, CH), 3.02 (s, 4H, NCH_2), 2.16 (s, 6H, CH_3CO), 1.50 (s, 6H, CH_3CN), 0.29 (s, 18H, $\text{CH}_2\text{Si}(\text{CH}_3)_3$), 0.18 (s, 4H, CH_2SiMe_3) ppm. $^{13}\text{C}\{^1\text{H}\}$ NMR (C_6D_6 , 126 MHz, 298K): δ 181.44 (C=O), 171.63 (C=N), 102.68 (CH), 54.61 (CH_2SiMe_3), 53.07 (NCH_2), 25.50 (CH_3CO), 22.94 (CH_3CN), 3.38 ($\text{CH}_2\text{Si}(\text{CH}_3)_3$) ppm. ^{29}Si NMR (C_6D_6 , 99 MHz, 298 K): δ -3.7 ppm. **$\text{C}_{20}\text{H}_{40}\text{N}_2\text{O}_2\text{Si}_2\text{Zr}$ (487.95 g mol $^{-1}$):** calcd. C 49.23, H 8.26, N 5.74%; found. C 49.36, H 8.09, N 6.00%.

[Zr(*cis*-Cyacen)(CH_2SiMe_3) $_2$] (5-2). A solution of $\text{H}_2(\textit{cis}\text{-Cyacen})$ (131.6 mg, 0.47 mmol) in toluene (10 mL) was added dropwise to a solution of $[\text{Zr}(\text{CH}_2\text{SiMe}_3)_4]$ (208.1 mg, 0.47 mmol) in hexanes (5 mL) at room temperature, whereupon the clear, pale yellow solution turned bright yellow in colour. Volatiles were removed *in vacuo* after stirring at room temperature overnight. A dark yellow powder was obtained that was >95% pure by NMR spectroscopy (220 mg, 86%). Analytically pure and X-ray quality single crystals were grown from a concentrated hexanes solution at $-30\text{ }^{\circ}\text{C}$ as pale yellow needles (107 mg, 42%). Compound **5-2** sublimed in >95% yield at $85\text{ }^{\circ}\text{C}$. However, heating **5-2** at $88\text{ }^{\circ}\text{C}$ under static argon for 24 hours resulted in extensive decomposition to afford $\text{H}_2(\textit{cis}\text{-Cyacen})$ and SiMe_4 as the soluble products. ^1H NMR (C_6D_6 , 600 MHz, 298K): δ 5.29 (s,

2H, CH), 3.66 (m, 2H, NCH), 2.18 (s, 6H, CH₃CO), 1.71 (m, 2H) and 1.04 (m, 2H, CH₂CH₂CH), 1.63 (s, 6H, CH₃CN), 1.21 (m, 2H) and 0.94 (m, 2H, CH₂CH₂CH), 0.49 and 0.12 (2 bs, 18H, CH₂Si(CH₃)₃), 0.39 and 0.21 (2 bs, 4H, CH₂SiMe₃) ppm. ¹³C{¹H} NMR (C₆D₆, 151 MHz, 298K): δ 180.90 (C=O), 171.22 (C=N), 103.81 (CH), 62.72 (NCH), 57.02 and 54.78 (CH₂SiMe₃), 31.13 (CH₂CH₂CH), 25.40 (CH₃CO), 22.87 (CH₃CN), 22.38 (CH₂CH₂CH), 3.41 (CH₂Si(CH₃)₃) ppm. ²⁹Si NMR (d₈-toluene, 99 MHz, 238 K): δ -4.01 and -3.53 ppm. **C₂₄H₄₆N₂O₂Si₂Zr (542.04 g mol⁻¹):** calcd. C 53.18, H 8.55, N 5.17%; found. C 53.17, H 8.36, N 5.40%.

[Zr(*trans*-Cyacen)(CH₂SiMe₃)₂] (5-3). A solution of H₂(*trans*-Cyacen) (210.1 mg, 0.48 mmol) in toluene (10 mL) was added dropwise to a solution of [Zr(CH₂SiMe₃)₄] (132.9 mg, 0.48 mmol) in hexanes (10 mL) at room temperature, whereupon the clear, pale yellow solution turned bright yellow in colour. Volatiles were removed *in vacuo* after stirring at room temperature overnight. A yellow powder was obtained that was >95% pure by NMR spectroscopy (220 mg, 90%). Analytically pure and X-ray quality single crystals were grown from a concentrated hexanes solution at -30 °C as yellow blocks (126 mg, 49%). Compound **5-3** decomposed without sublimation at 130 °C. No decomposition was observed by NMR spectroscopy after heating solid **5-3** at 120 °C *in vacuo* for 6 hours. ¹H NMR (C₆D₆, 500 MHz, 298K): δ 5.23 (s, 2H, CH), 3.36 (m, 2H, NCH), 2.23 (s, 6H, CH₃CO), 1.67 (m, 2H) and 1.18 (m, 2H, CH₂CH₂CH), 1.62 (s, 6H, CH₃CN), 1.31 (m, 2H) and 0.80 (m, 2H, CH₂CH₂CH), 0.39 (s, 18H, CH₂Si(CH₃)₃), 0.31 and 0.12 (2 d, 2×2H, ²J_{H,H} = 10.6 Hz) ppm. ¹³C{¹H} NMR (C₆D₆, 126 MHz, 298K): δ 181.20 (C=O), 169.12 (C=N), 104.08 (CH), 66.14 (NCH), 56.39 (CH₂SiMe₃), 33.31 (CH₂CH₂CH), 25.64 (CH₃CO), 25.62 (CH₂CH₂CH), 23.38 (CH₃CN), 3.62 (CH₂Si(CH₃)₃) ppm. ²⁹Si NMR

(C₆D₆, 99 MHz, 298 K): δ -3.8 ppm. **C₂₄H₄₆N₂O₂Si₂Zr (542.04 g mol⁻¹):** calcd. C 53.18, H 8.55, N 5.17%; found. C 53.75, H 8.71, N 5.21%.

[Zr(*cis*-Cyacen)(O^tBu)₂] (5-4). A solution of **5-2** (15.5 mg, 0.028 mmol) dissolved in C₆D₆ (0.4 mL) was prepared in a NMR tube sealed with a rubber septum and parafilm. A 0.52M solution of *tert*-butanol in C₆D₆ (0.12 mL, 0.063 mmol) was added via syringe through the rubber septum. Upon addition, the pale yellow solution instantly became colourless, and complete conversion of **5-2** to **5-4** was observed by NMR spectroscopy. ¹H NMR (C₆D₆, 500 MHz, 298K): δ 5.01 (s, 2H, CH), 3.60 (bs, 2H, NCH), 2.41 (m, 2H) and 1.29 (m, 2H, CH₂CH₂CH), 1.98 (s, 6H, CH₃CO), 1.65 (s, 6H, CH₃CN), 1.52 (m, 2H) and 1.12 (m, 2H, CH₂CH₂CH) ppm, 1.39 (s, 18H, OC(CH₃)₃) ppm. ¹³C{¹H} NMR (C₆D₆, 126 MHz, 298K): δ 179.21 (C=O), 169.70 (C=N), 102.89 (CH), 74.35 (OC(CH₃)₃), 60.65 (NCH), 32.90 (OC(CH₃)₃), 30.41 (CH₂CH₂CH), 25.63 (CH₃CO), 22.30 (CH₂CH₂CH), 21.66 (CH₃CN) ppm.

[Zr(acen)₂] (5-5). A solution of [Zr(NMeEt)₄] (139.3 mg, 0.43 mmol) in toluene (5 mL) was added dropwise to a solution of H₂(acen) (193.1 mg, 0.86 mmol) in toluene (10 mL) at room temperature. The yellow solution was stirred at room temperature for 2 days and turned red. Volatiles were removed *in vacuo*, and the solid residue was washed with hexanes and then dried *in vacuo* to obtain a red solid that was >95% pure by NMR spectroscopy (170 mg, 74%). Analytically pure and X-ray quality single crystals were grown from a concentrated toluene solution at -30 °C as yellow-orange needles (68 mg, 29%). Complex **5-5** could also be purified by sublimation at 105 °C at 10 mTorr, and no decomposition was detected by NMR after heating solid **5-5** for 24 hours under static argon at 145 °C. ¹H NMR (C₆D₆, 600 MHz, 298K): δ 4.86 (s, 4H, CH), 3.80 (s, 8H, NCH₂),

1.75 (s, 12H, CH_3CO), 1.71 (s, 12H, CH_3CN) ppm. $^{13}\text{C}\{^1\text{H}\}$ NMR (C_6D_6 , 151 MHz, 298K): δ 172.02 (C=O), 162.97 (C=N), 100.38 (CH), 51.82 (NCH₂), 25.03 (CH_3CO), 22.24 (CH_3CN) ppm. **$\text{C}_{24}\text{H}_{36}\text{N}_4\text{O}_4\text{Zr}$ (535.80 g mol⁻¹):** calcd. C 53.80, H 6.77, N 10.46%; found. C 54.14, H 6.90, N 10.38%.

[Zr(acen)(NMeEt)₂] (5-6). A solution of **5-1** (13.2 mg, 0.027 mmol) in *d*₈-toluene was prepared in a NMR tube sealed with a rubber septum secured with parafilm. A 1.16M solution of HNMeEt in C_6D_6 (0.09 mL, 0.105 mmol) was added via syringe through the rubber septum. The mixture was allowed to react at room temperature for 10 minutes and then immersed in a -78 °C cold bath before inserting into an NMR spectrometer held at -20 °C. ^1H NMR (*d*₈-toluene, 500 MHz, 249K): δ 5.28 (s, 2H, CH), 3.21 (s, 4H, NCH₂CH₂N), 2.97 (q, 4H, NCH₂CH₃), 2.67 (s, 6H, NCH₃), 1.97 (s, 6H, CH_3CO), 1.74 (s, 6H, CH_3CN), 1.02 (t, 6H, NCH₂CH₃) ppm. $^{13}\text{C}\{^1\text{H}\}$ NMR (*d*₈-toluene, 126 MHz, 249K): δ 171.18 (C=O), 165.16 (C=N), 102.03 (CH), 52.01 (NCH₂CH₂N), 51.41 (NCH₂CH₃), 41.11 (NCH₃), 25.45 (CH_3CO), 23.03 (CH_3CN), 14.54 (NCH₂CH₃) ppm.

[Zr(acen){N(SiMe₃)₂]₂] (5-7). Note: all glassware, solvents, and reagents were cooled to -30 °C before this reaction was conducted. A solution of Li{N(SiMe₃)₂} (21.7 mg, 0.130 mmol) in toluene (1 mL) was added dropwise to a slurry of [Zr(acen)Cl₂] (24.9 mg, 0.065 mmol) in toluene (0.5 mL) at -30 °C in a 4 mL vial. The reaction was shaken approximately every 5 minutes and left at -30 °C until the starting material dissolved and LiCl precipitated. The dark red-orange mixture was filtered through a pasteur pipette packed with glass wool and celite to obtain a clear, vivid red solution. Large, yellow block crystals were obtained by layering the toluene solution with 3 mL of hexanes and storing

at $-30\text{ }^{\circ}\text{C}$. (35 mg, 85%). ^1H NMR (d_8 -THF, 500 MHz, 249K): δ 5.54 (s, 2H, CH), 3.69 (s, 4H, NCH₂), 2.07 (s, 6H, CH₃CO), 2.06 (s, 6H, CH₃CN), 0.04 (s, 36H, Si(CH₃)₃) ppm. $^{13}\text{C}\{^1\text{H}\}$ NMR (d_8 -THF, 126 MHz, 249K): δ 178.84 (C=O), 172.32 (C=N), 105.86 (CH), 53.74 (NCH₂), 25.37 (CH₃CO), 23.02 (CH₃CN), 6.88 (Si(CH₃)₃) ppm. ^{29}Si NMR (d_8 -THF, 99 MHz, 242 K): δ -7.3 ppm. **C₂₄H₅₄N₄O₂Si₄Zr (634.29 g mol⁻¹):** calcd. C 45.45, H 8.58, N 8.88%; found. C 45.16, H 8.36, N 8.91%.

6.6 – References for Chapter 6

- [1] R. K. Harris, E. D. Becker, S. M. C. d. Menezes, R. Goodfellow, P. Granger. NMR Nomenclature. Nuclear Spin Properties and Conventions for Chemical Shifts. *Pure Appl. Chem.* **2001**, *73*, 1795-1818.
- [2] G. M. Sheldrick. SHELXT - Integrated space-group and crystal-structure determination. *Acta Crystallogr. Sect. A: Found. Crystallogr.* **2015**, *71*, 3-8.
- [3] G. M. Sheldrick. Crystal structure refinement with SHELXL. *Acta Crystallogr. Sect. C: Cryst. Struct. Commun.* **2015**, *71*, 3-8.
- [4] O. V. Dolomanov, L. J. Bourhis, R. J. Gildea, J. A. K. Howard, H. Puschmann. OLEX2: A complete structure solution, refinement and analysis program. *J. Appl. Crystallogr.* **2009**, *42*, 339-341.
- [5] H. Zabrodsky, S. Peleg, D. Avnir. Continuous Symmetry Measures. *J. Am. Chem. Soc.* **1992**, *114*, 7843-7851.
- [6] C. M. Evans, S. L. Castro, J. J. Worman, R. P. Raffaele. Synthesis and use of tris(trimethylsilyl)antimony for the preparation of InSb quantum dots. *Chem. Mater.* **2008**, *20*, 5727-5730.
- [7] E. Amberger, R. W. Salazar G. Mixed Organometallic Compounds of Group V. I. Synthesis of Tris(trimethyl-group-IV)stibines. *J. Organomet. Chem.* **1967**, *8*, 111-114.
- [8] V. Pore, K. Knapas, T. Hatanpää, T. Sarnet, M. Kemell, M. Ritala, M. Leskelä, K. Mizohata. Atomic Layer Deposition of Antimony and its Compounds Using Dechlorosilylation Reactions of Tris(triethylsilyl)antimony. *Chem. Mater.* **2011**, *23*, 247-254.
- [9] C. von Hanisch. The Tris(triisopropylsilyl)pnikogenes: Synthesis and Characterization of E(SiⁱPr₃)₃ (E = P, As, Sb). *Z. Anorg. Allg. Chem.* **2001**, *627*, 1414-1416.
- [10] Precursor bubblers (where argon flows through the bubbler during delivery, but does not actually bubble through the precursor; see Figure S29) rather than cylinders (which connect to the reactor via a single ALD valve) were used for all experiments. At room temperature (~23 °C), insufficient delivery was achieved when ALD was attempted with the precursors in cylinders, even with pulse durations of 10s.
- [11] T. Eom, S. Choi, B. J. Choi, M. H. Lee, T. Gwon, S. H. Rha, W. Lee, M.-S. Kim, M. C. Xiao, I. Buchanan, D.-Y. Cho, C. S. Hwang. Conformal Formation of (GeTe₂)_(1-x)(Sb₂Te₃)_x Layers by Atomic Layer Deposition for Nanoscale Phase Change Memories. *Chem. Mater.* **2012**, *24*, 2099-2110.
- [12] K. Knapas, T. Hatanpää, M. Ritala, M. Leskelä. In Situ Reaction Mechanism Studies on Atomic Layer Deposition of Sb₂Te₃ and GeTe from (Et₃Si)₂Te and Chlorides. *Chem. Mater.* **2010**, *22*, 1386-1391.
- [13] J. M. Buriak. Organometallic chemistry on silicon and germanium surfaces. *Chem. Rev.* **2002**, *102*, 1271-1308.
- [14] S. Jayachandran, A. Delabie, A. Billen, H. Dekkers, B. Douhard, T. Conard, J. Meersschaut, M. Caymax, W. Vandervorst, M. Heyns. Deposition of O atomic

- layers on Si(100) substrates for epitaxial Si-O superlattices: investigation of the surface chemistry. *Appl. Surf. Sci.* **2015**, *324*, 251-257.
- [15] Q. Y. Sun, L. de Smet, B. van Lagen, A. Wright, H. Zuilhof, E. J. R. Sudholter. Covalently attached monolayers on hydrogen terminated Si(100): Extremely mild attachment by visible light. *Angew. Chem. Int. Ed.* **2004**, *43*, 1352-1355.
- [16] A. Heine, R. Herbst-Irmer, G. M. Sheldrick, D. Stalke. Structural Characterization of Two Modifications of Tris(tetrahydrofuran)(tris(trimethylsilyl)silyl)lithium: A Compound with a ^{29}Si - ^7Li NMR Coupling. *Inorg. Chem.* **1993**, *32*, 2694-2698.
- [17] H. Gilman, C. L. Smith. Tetrakis(trimethylsilyl)silane. *J. Organomet. Chem.* **1967**, *8*, 245-253.
- [18] N. Wiberg, K. Amelunxen, H.-W. Lemer, H. Schuster, H. Nöth, I. Krossing, M. Schmidt-Amelunxen, T. Seifert. Donorfreie und donorhaltige Supersilylalkalimetalle $t\text{Bu}_3\text{SiM}$: Synthesen, Charakterisierung, Strukturen. *J. Organomet. Chem.* **1997**, *542*, 1-18.
- [19] M. Weidenbruch, H. Pesel, W. Peter, R. Steichen. Silicium-Verbindungen Mit Starken Intramolekularen Sterischen Wechselwirkungen. VI. Darstellung Und Eigenschaften Des Tri-*t*-butylsilans Und Der Tri-*t*-butylhalogensilane. *J. Organomet. Chem.* **1977**, *141*, 9-21.
- [20] E. Piers, R. Lemieux. Reaction of (Trimethylgermyl)copper(I)-Dimethyl Sulfide with Acyl Chlorides: Efficient Syntheses of Functionalized Acyltrimethylgermanes. *Organometallics* **1995**, *14*, 5011-5012.
- [21] A. J. Banister, N. N. Greenwood, B. P. Straughan, J. Walker. Monomeric Dimethylaminoboron Dihalides. *J. Chem. Soc.* **1964**, 995-1000.
- [22] W. Biffar, H. Nöth. Tris(trimethylsilyl)silyl Boranes and Tris(trimethylsilyl)silyl Borates. *Z. Anorg. Allg. Chem. B* **1981**, *36*, 1509-1515.
- [23] H. Braunschweig, M. Colling, C. Kollann, U. Englert. The first silyl- and germylboryl complexes: synthesis from novel (dichloro)silyl- and (dichloro)germylboranes, structure and reactivity. *J. Chem. Soc., Dalton Trans.* **2002**, 2289-2296.
- [24] F. Corazza, E. Solari, C. Floriani, A. Chiesi-Villa, C. Guastini. *cis*- and *trans*-Dichloro-derivatives of six- and seven-co-ordinate zirconium and hafnium bonded to quadridentate Schiff-base ligands. Crystal structures of $[\text{Zr}(\text{acen})\text{Cl}_2(\text{thf})]$, $[\text{M}(\text{salphen})\text{Cl}_2(\text{thf})] \cdot 0.5\text{thf}$, $[\text{M}(\text{acen})\text{Cl}_2]$, (M = Zr or Hf) and $[\text{Zr}(\text{msal})\text{Cl}_2]$. *J. Chem. Soc. Dalton Trans.* **1990**, 1335-1344.
- [25] M. R. Collier, M. F. Lappert, R. Pearce. Silylmethyl and Related Complexes. Part I. Kinetically Stable Alkyls of Titanium(IV), Zirconium(IV), and Hafnium(IV). *J. Chem. Soc. Dalton Trans.* **1973**, 445-451.
- [26] C. H. Huang, L. F. Hsueh, P. C. Kuo, H. M. Lee, C. L. Uno, J. H. Huang, C. Y. Tu, C. H. Hu, G. H. Lee, C. H. Hung. Aluminum Complexes Containing Cyclohexane-1,2-diyl Linked Bis(ketiminato) Ligands and Proton-Promoted Demethylation. *Eur. J. Inorg. Chem.* **2008**, *2008*, 3000-3008.

Appendix – Supplementary Information

A1 – Crystal Structure and Refinement Data of Compounds Reported in Chapters 2 to 5

Table A1.1: Crystal data for 3-2 and 3-3.

	^tBu₃SiNa(THF)₂ (3-2)	[Me₃GeLi(THF)₂]₂ (3-3)
Empirical Formula	C ₂₀ H ₄₃ NaO ₂ Si	C ₁₁ H ₂₅ GeLiO ₂
Formula Weight	366.62	268.84
Temp, K	100.0(1)	100.0(1)
Crystal system	Monoclinic	Triclinic
Space group	P2 ₁ /c	P-1
a, Å	16.062(4)	8.908(2)
b, Å	12.162(8)	9.576(1)
c, Å	36.188(6)	10.069(2)
α, °	90	94.46(2)
β, °	100.07(2)	114.16(1)
γ, °	90	109.13(2)
Volume, Å ³	6960(5)	717.7(2)
Z	12	2
ρ _{calc} , g/cm ³	1.050	1.244
μ, mm ⁻¹	0.129	2.115
F(000)	2448.0	284.0
Crystal size, mm ³	0.35×0.02×0.02	0.30×0.15×0.02
Radiation	MoKα (λ = 0.71073)	

2 θ range for data collection, °	3.13 to 57.398	4.574 to 59.19
Index ranges	-21 ≤ h ≤ 21 -15 ≤ k ≤ 16 -48 ≤ l ≤ 46	-11 ≤ h ≤ 12 -12 ≤ k ≤ 13 -13 ≤ l ≤ 13
Reflections collected	74944	8037
Independent reflections	17896 [R _{int} = 0.0676, R _{sigma} = 0.0690]	3929 [R _{int} = 0.0126, R _{sigma} = 0.0266]
Data/restraints /parameters	17896/1113/779	3929/0/236
Goodness-of-fit on F ²	1.019	1.081
Final R indexes [I ≥ 2σ (I)]	R ₁ = 0.0549 wR ₂ = 0.1310	R ₁ = 0.0232 wR ₂ = 0.0598
Final R indexes (all data)	R ₁ = 0.1037 wR ₂ = 0.1526	R ₁ = 0.0265 wR ₂ = 0.0606
Largest diff. peak/hole, eÅ ⁻³	0.59/-0.64	0.69/-0.47

Table A1.2: Crystal data for 3-8, 3-12, and 3-13.

	{(Me₃Si)₃Si}₂B(NMe₂) (3-8)	(^tBu₃Si)(Me₃Ge)B(NMe₂) (3-12)	{(Me₃Ge)₃B(NMe₂)} Li(THF)₂ (3-13)
Empirical Formula	C ₂₀ H ₆₀ BNSi ₈	C ₁₇ H ₄₂ BGeNSi	C ₁₉ H ₄₉ BGe ₃ LiNO ₂
Formula Weight	550.22	372.00	559.11
Temp, K	100.0(1)	100.0(1)	100.0(1)
Crystal system	Monoclinic	Orthorhombic	Triclinic
Space group	Pn	Pna2 ₁	P1
a, Å	9.500(8)	18.135(8)	9.168(4)

b, Å	16.06(1)	12.872(7)	15.409(2)
c, Å	12.27(1)	18.80(1)	29.432(7)
α , °	90	90	90
β , °	109.83(2)	90	90.20(2)
γ , °	90	90	90
Volume, Å ³	1761(3)	4390(4)	4158(2)
Z	2	8	6
ρ_{calc} , g/cm ³	1.037	1.126	1.340
μ , mm ⁻¹	0.315	1.447	3.244
F(000)	608.0	1616.0	1740.0
Crystal size, mm ³	0.30×0.10×0.05	0.50×0.05×0.05	0.40×0.20×0.10
Radiation	MoK α (λ = 0.71073)		
2 θ range for data collection, °	2.536 to 52.724	3.834 to 54.538	3.828 to 59.254
Index ranges	-11 ≤ h ≤ 11 -19 ≤ k ≤ 20 -15 ≤ l ≤ 15	-23 ≤ h ≤ 23 -16 ≤ k ≤ 16 -22 ≤ l ≤ 24	-12 ≤ h ≤ 10 -21 ≤ k ≤ 20 -40 ≤ l ≤ 40
Reflections collected	3586	40878	51764
Independent reflections	3586 [R _{int} = 0.1366, R _{sigma} = 0.0869]	9611 [R _{int} = 0.1853, R _{sigma} = 0.1702]	37046 [R _{int} = 0.0452, R _{sigma} = 0.1400]
Data/restraints /parameters	3586/2/291	9611/468/258	37046/621/828
Goodness-of-fit on F ²	0.988	1.038	1.062
Final R indexes [I ≥ 2 σ (I)]	R ₁ = 0.0626 wR ₂ = 0.1328	R ₁ = 0.1053 wR ₂ = 0.2280	R ₁ = 0.0764 wR ₂ = 0.1899

Final R indexes (all data)	R ₁ = 0.0906 wR ₂ = 0.1430	R ₁ = 0.1949 wR ₂ = 0.2658	R ₁ = 0.0831 wR ₂ = 0.1948
Largest diff. peak/hole, eÅ ⁻³	1.15/-0.34	1.11/-1.51	1.99/-0.84

Table A1.3: Crystal data for **4.1**, **4-2(C₆H₆)₃**, and **4-2**.

	[EtMeNH₂]₂[Hf(O₂CCH₂CMe₂OH)₂(OC(O)CH₂CMe₂O)₂] (4-1)	[Hf₅(O)₄(O₂C^tBu)₁₂·3C₆H₆] (4-2(C₆H₆)₃)	[Hf₅(O)₄(O₂C^tBu)₁₂] (4-2)
Empirical Formula	C ₂₆ H ₅₄ HfN ₂ O ₁₂	C ₇₈ H ₁₂₆ Hf ₅ O ₂₈	C ₃₀ H ₅₄ Hf ₅ O ₁₄
Formula Weight	762.50	2404.23	1084.95
Temp, K	100.0(1)	100.0(1)	100.0(1)
Crystal system	Triclinic	Monoclinic	Monoclinic
Space group	P-1	C2/c	C2/c
a, Å	10.253(3)	24.236(3)	23.371(7)
b, Å	10.810(6)	17.863(2)	18.769(5)
c, Å	15.695(5)	22.978(3)	22.283(7)
α, °	77.94(2)	90	90
β, °	87.606(18)	111.037(2)	107.56(3)
γ, °	77.81(3)	90	90
Volume, Å ³	1662.7(12)	9285(2)	9319(5)
Z	2	4	8
ρ _{calc} , g/cm ³	1.528	1.720	1.547

μ , mm ⁻¹	3.195	5.639	5.609
F(000)	784.0	4712.0	4208.0
Crystal size, mm ³	0.31×0.30×0.05	0.30×0.20×0.18	0.5×0.04×0.04
Radiation	MoK α (λ = 0.71073)		
2 θ range for data collection, °	4.064 to 59.284	2.906 to 60.954	2.838 to 56.796
Index ranges	-14 ≤ h ≤ 14 -14 ≤ k ≤ 15 -21 ≤ l ≤ 17	-34 ≤ h ≤ 26 -25 ≤ k ≤ 25 -32 ≤ l ≤ 30	-31 ≤ h ≤ 30 -25 ≤ k ≤ 25 -29 ≤ l ≤ 29
Reflections collected	16623	34139	93123
Independent reflections	8998 [R _{int} = 0.0616, R _{sigma} = 0.1728]	13939 [R _{int} = 0.0575, R _{sigma} = 0.0801]	11578 [R _{int} = 0.0867, R _{sigma} = 0.0497]
Data/restraints /parameters	8998/370/397	13939/0/520	11578/0/438
Goodness-of-fit on F ²	0.838	1.021	1.171
Final R indexes [I ≥ 2 σ (I)]	R ₁ = 0.0423 wR ₂ = 0.1002	R ₁ = 0.0529 wR ₂ = 0.1191	R ₁ = 0.0830 wR ₂ = 0.2113
Final R indexes (all data)	R ₁ = 0.0576 wR ₂ = 0.1018	R ₁ = 0.0828 wR ₂ = 0.1340	R ₁ = 0.1276 wR ₂ = 0.2670
Largest diff. peak/hole, eÅ ⁻³	3.44/-2.82	7.86/-1.34	12.13/-3.93

Table A1.4: Crystal data for **5-1** to **5-3**.

	[Zr(acen) (CH₂SiMe₃)₂] (5-1)	[Zr(cis-Cyacen) (CH₂SiMe₃)₂] (5-2)	[Zr(trans-Cyacen) (CH₂SiMe₃)₂] (5-3)
Empirical Formula	C ₂₀ H ₄₀ N ₂ O ₂ Si ₂ Zr	C ₂₄ H ₄₆ N ₂ O ₂ Si ₂ Zr	C ₂₄ H ₄₆ N ₂ O ₂ Si ₂ Zr
Formula Weight	487.94	542.03	542.03
Temp, K	100.0(1)	100.0(1)	100.0(1)
Crystal system	Monoclinic	Orthorhombic	Triclinic
Space group	P2 ₁ /n	Pbca	P-1
a, Å	14.543(1)	15.727(1)	10.8111(9)
b, Å	10.2255(8)	18.738(1)	15.933(1)
c, Å	18.554(1)	19.745(2)	18.557(2)
α, °	90	90	100.160(1)
β, °	112.510(3)	90	104.927(1)
γ, °	90	90	104.406(1)
Volume, Å ³	2548.9(3)	5818.5(8)	2891.1(4)
Z	4	8	4
ρ _{calc} , g/cm ³	1.272	1.238	1.245
μ, mm ⁻¹	0.541	0.481	0.484
F(000)	1032.0	2304.0	1152.0
Crystal size, mm ³	0.5 x 0.22 x 0.2	0.52 x 0.44 x 0.27	0.35 x 0.24 x 0.18
Radiation	MoKα (λ = 0.71073)		

2 θ range for data collection, °	3.052 to 65.606	3.96 to 61.142	3.112 to 61.47
Index ranges	-22 $\leq h \leq$ 22 -15 $\leq k \leq$ 15 -27 $\leq l \leq$ 28	-22 $\leq h \leq$ 22 -26 $\leq k \leq$ 26 -28 $\leq l \leq$ 28	-15 $\leq h \leq$ 15 -22 $\leq k \leq$ 22 -26 $\leq l \leq$ 26
Reflections collected	101692	105117	83934
Independent reflections	9174 [R _{int} = 0.0664, R _{sigma} = 0.0353]	8894 [R _{int} = 0.0266, R _{sigma} = 0.0122]	17858 [R _{int} = 0.0196, R _{sigma} = 0.0163]
Data/restraints /parameters	9174/0/270	8894/0/306	17858/16/696
Goodness-of-fit on F ²	1.064	1.092	1.085
Final R indexes [I \geq 2 σ (I)]	R ₁ = 0.0330 wR ₂ = 0.0483	R ₁ = 0.0312 wR ₂ = 0.0750	R ₁ = 0.0289 wR ₂ = 0.0702
Final R indexes (all data)	R ₁ = 0.0483 wR ₂ = 0.0768	R ₁ = 0.0397 wR ₂ = 0.0827	R ₁ = 0.0346 wR ₂ = 0.0727
Largest diff. peak/hole, eÅ ⁻³	0.75/-0.36	1.03/-0.25	0.65/-0.58

Table A1.5: Crystal data for **5-5** and **5-7**.

	[Zr(acen)₂] (5-5)	[Zr(acen){N(SiMe₃)₂]₂] (5-7)
Empirical Formula	C ₂₄ H ₃₆ N ₄ O ₄ Zr	C ₂₄ H ₅₄ N ₄ O ₂ Si ₄ Zr
Formula Weight	535.79	634.29
Temp, K	100.0(1)	100.0(1)
Crystal system	Monoclinic	Monoclinic
Space group	P2 ₁ /n	C2/c
a, Å	8.48(3)	20.5455(9)
b, Å	12.46(5)	10.4996(5)
c, Å	26.6(1)	16.2027(8)
α, °	90	90
β, °	95.31(8)	110.703(2)
γ, °	90	90
Volume, Å ³	2803(19)	3269.5(3)
Z	4	4
ρ _{calc} , g/cm ³	1.270	1.289
μ, mm ⁻¹	0.425	0.509
F(000)	1120.0	1352.0
Crystal size, mm ³	0.35 x 0.02 x 0.02	0.42 x 0.3 x 0.29
Radiation	MoKα (λ = 0.71073)	
2θ range for data collection, °	3.612 to 34.452	4.238 to 61.408
Index ranges	-7 ≤ h ≤ 7 -10 ≤ k ≤ 10	-29 ≤ h ≤ 29 -15 ≤ k ≤ 15

	$-22 \leq l \leq 22$	$-23 \leq l \leq 23$
Reflections collected	6601	63009
Independent reflections	1696 [$R_{\text{int}} = 0.2037$, $R_{\text{sigma}} = 0.1898$]	5050 [$R_{\text{int}} = 0.0167$, $R_{\text{sigma}} = 0.0067$]
Data/restraints /parameters	1696/334/ 298	5050/0/167
Goodness-of-fit on F^2	0.948	1.097
Final R indexes [$I \geq 2\sigma(I)$]	$R_1 = 0.0679$ $wR_2 = 0.1512$	$R_1 = 0.0192$ $wR_2 = 0.0536$
Final R indexes (all data)	$R_1 = 0.1217$ $wR_2 = 0.1768$	$R_1 = 0.0204$ $wR_2 = 0.0546$
Largest diff. peak/hole, $e\text{\AA}^{-3}$	0.64/-0.5	0.55/-0.34

A2 – Supplementary Information Related to Chapter 2

Contents	Pages
NMR spectra of the solution reaction between $\text{Sb}(\text{SiMe}_3)_3$ and SbCl_3	A11
XPS data for Sb films deposited by ALD at 35 °C	A11-14
FESEM images of Sb films deposited at 35 °C using variable ALD cycle numbers	A14-17
Photographs of Sb films grown on H-Si and SiO_2/Si at variable temperatures	A17
X-ray diffractograms, plots of film thickness versus pulse length, and FESEMs of Sb films grown at variable temperatures	A18-20
XPS depth profile of an Sb film grown at 95 °C on SiO_2/Si	A21
FESEM images of ultrathin films grown at 35 °C using surface pre-treatment steps	A22-25
X-ray diffractograms and plots of film thickness versus number of cycles for Sb films grown on SiO_2/Si at 35 °C using the standard ALD method vs the methods employing initial surface pre-treatment	A26
Plots of film thickness versus purge time for Sb films grown at 35 °C on SiO_2/Si	A27
Plots of film thickness versus pulse time for Sb ALD using $\text{Sb}(\text{SiEt}_3)_3$ and SbCl_3 on SiO_2/Si and H-Si at 95 °C	A28
FESEM images of films grown on H-Si using the $\text{Sb}(\text{SiR}_3)_3/\text{SbCl}_3$ ALD process at 35 °C (R = Me) vs 95 °C (R = Me or Et)	A28
Cross-sectional FESEM and AFM step analysis for film thickness verification	A29
Representative VASE measurements of Sb films	A30
Photo showing the precursor bubbler design used in this work	A31

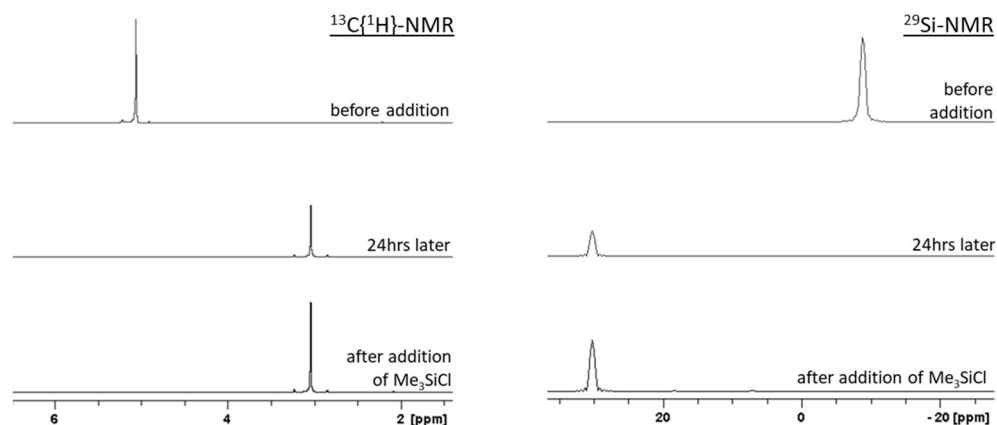


Figure A2.1: $^{13}\text{C}\{^1\text{H}\}$ and ^{29}Si NMR (1-dimensional projection from $^{29}\text{Si}/^1\text{H}$ -HMBC NMR) spectra of the NMR-scale reaction of $\text{Sb}(\text{SiMe}_3)_3$ (**2-1**) and SbCl_3 in C_6D_6 (151 and 119 MHz, respectively; 298 K). The reaction was monitored before (top) and after (middle) addition of 1 equivalent of SbCl_3 . After complete consumption of $\text{Sb}(\text{SiMe}_3)_3$, Me_3SiCl was added to the NMR tube to verify the identify the reaction product (bottom).

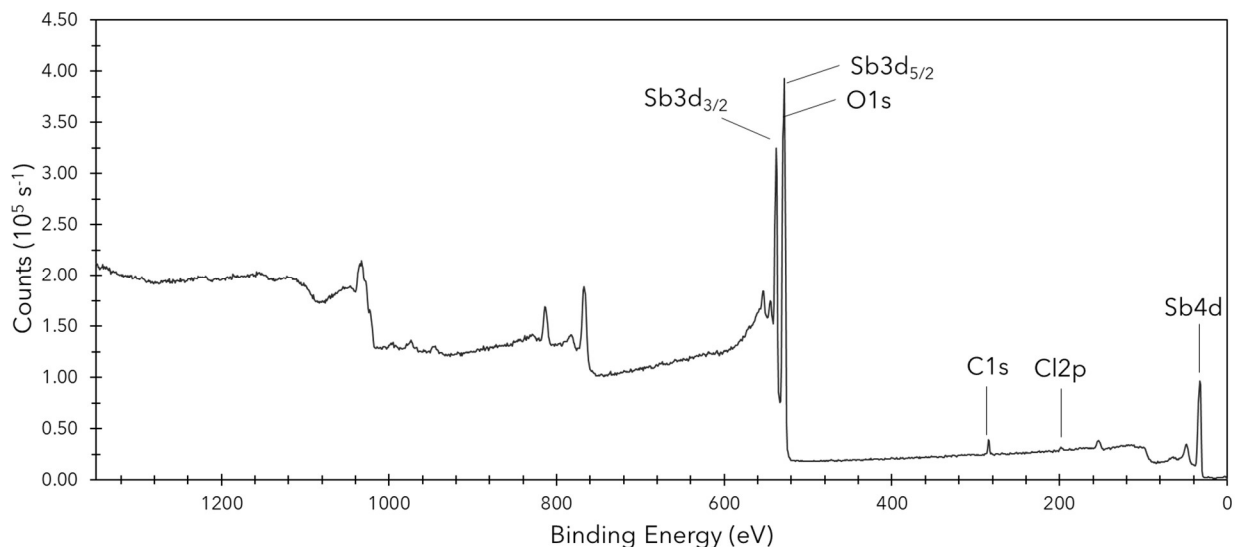


Figure A2.2: XPS survey spectrum of the surface of an Sb film (before sputtering into the film) grown on H-Si at 35 °C using 2000 cycles and 0.1 second pulses.

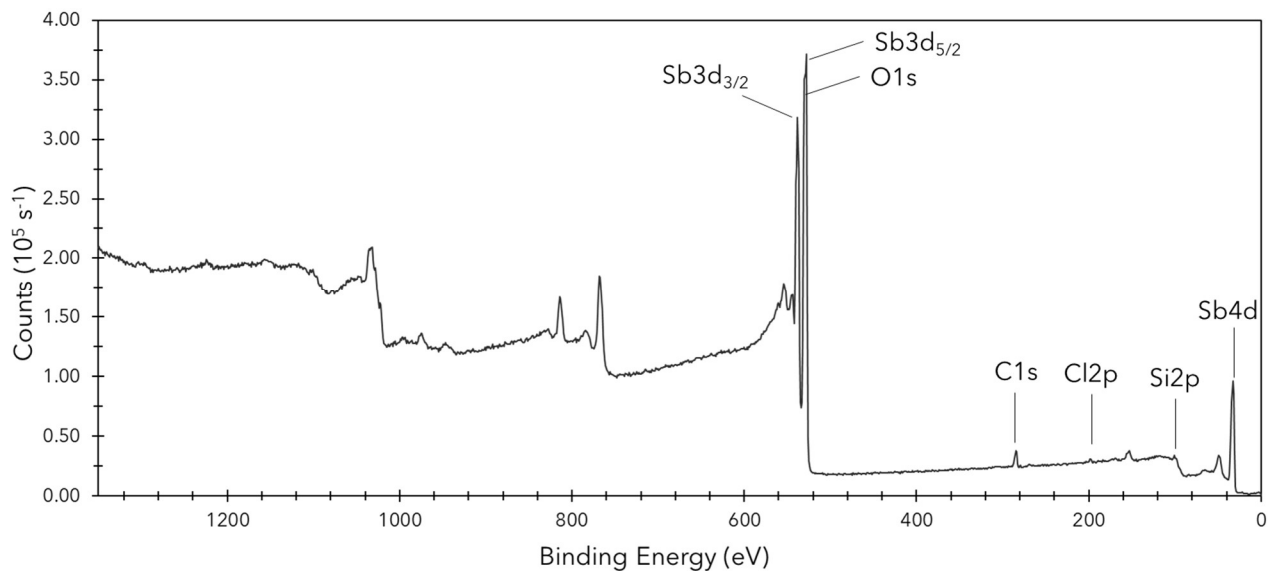


Figure A2.3: XPS survey spectrum of the surface of an Sb film (before sputtering into the film) grown on SiO₂/Si at 35 °C using 2000 cycles and 0.1 second pulses.

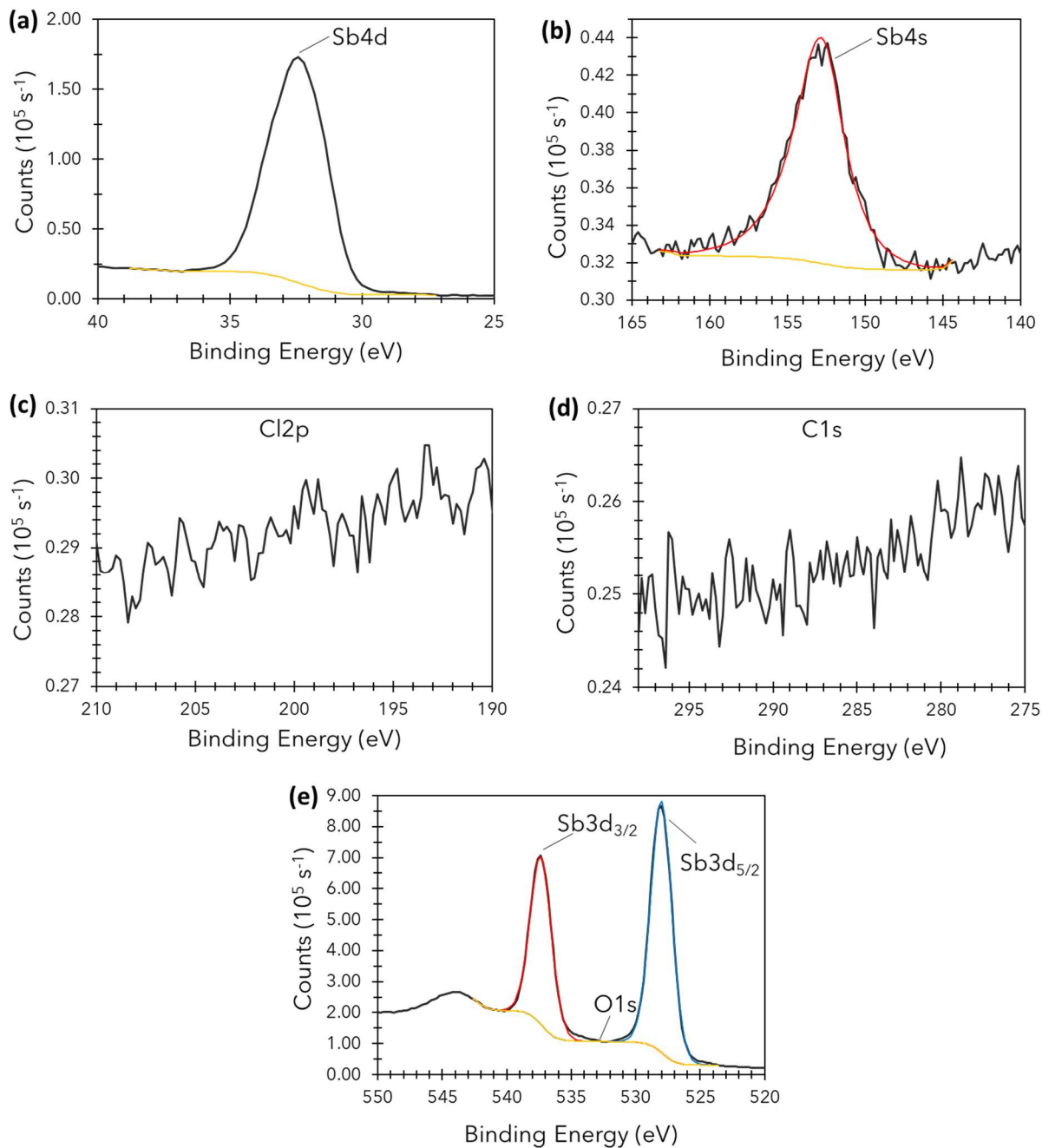


Figure A2.4: XPS data at Etch Level 3 of the Sb film grown on H-Si (35 °C, 2000 cycles, 0.1 second pulses) in the energy regions for (a) Sb4d, (b) Sb4s and Si2s, (c) Cl2p, (d) C1s, and (e) Sb3d and O1s. Orange lines represent the backgrounds, and red and blue lines represent the fitted model of the Sb peaks.

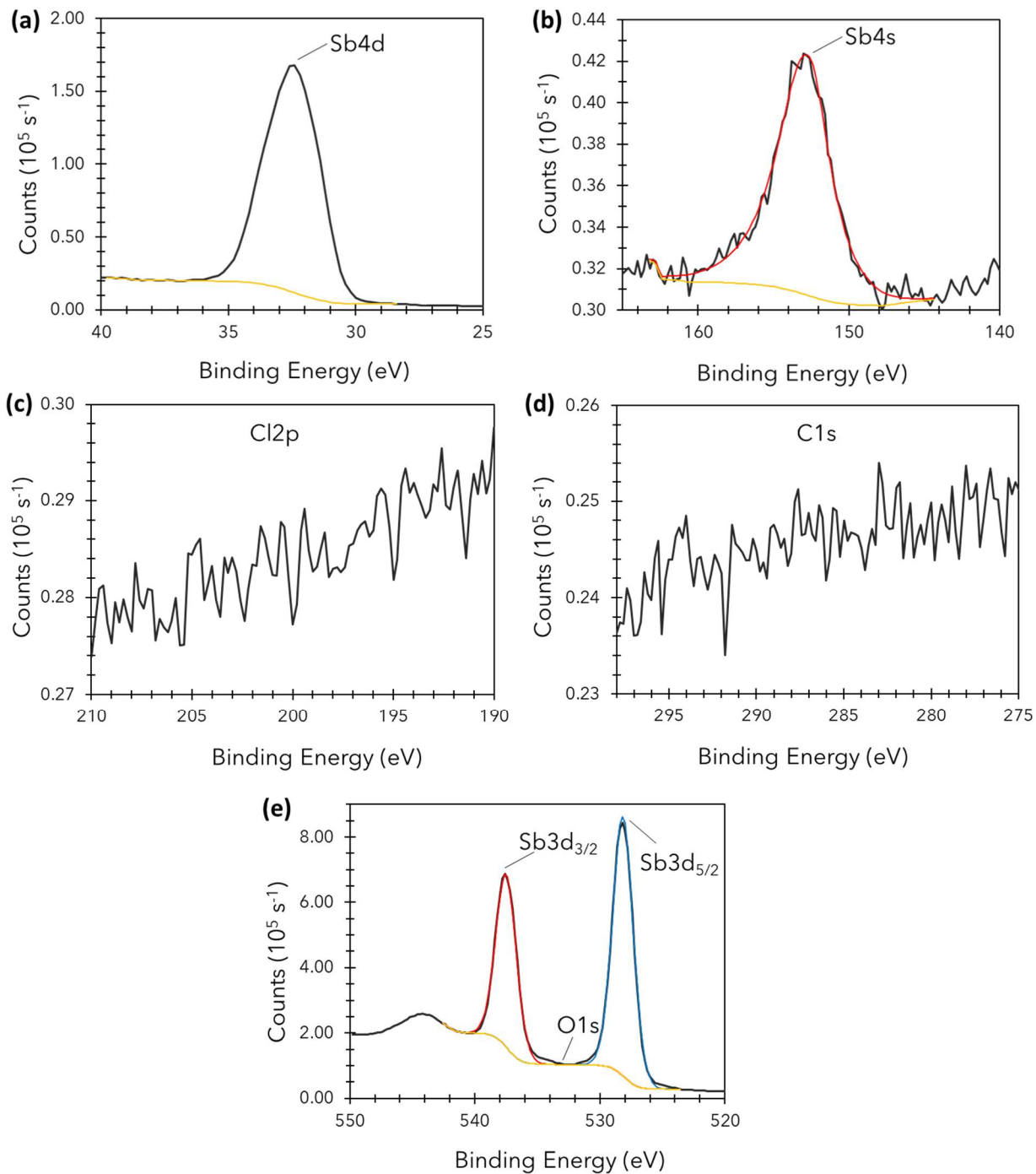


Figure A2.5: XPS data at Etch Level 2 of the Sb film grown on SiO₂/Si (35 °C, 2000 cycles, 0.1 second pulses) in the energy regions for (a) Sb4d, (b) Sb4s and Si2s, (c) Cl2p, (d) C1s, and (e) Sb3d and O1s. Orange lines represent the backgrounds, and red and blue lines represent the fitted model of the Sb peaks.

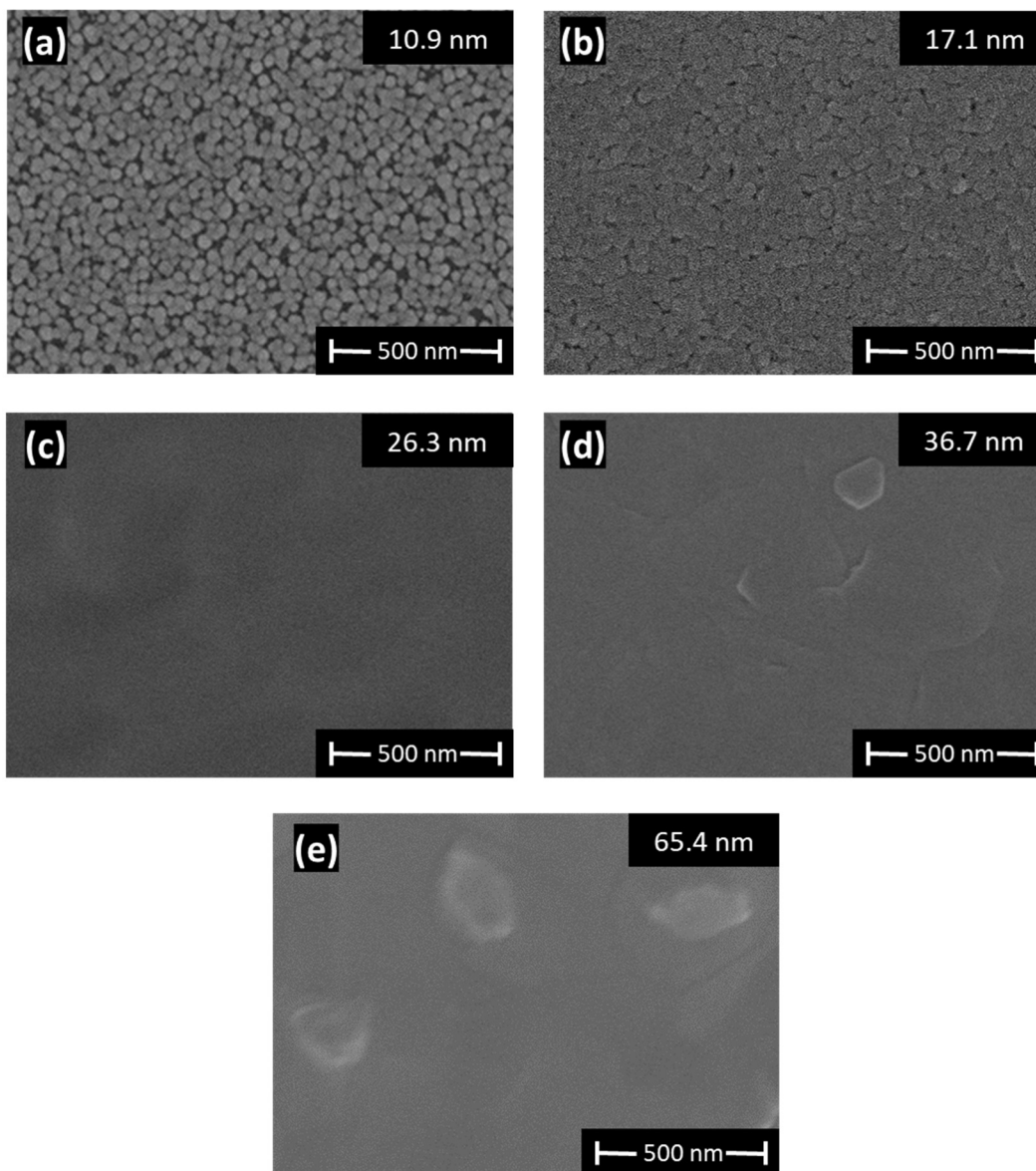


Figure A2.6: FESEM images of films grown on H-Si using (a) 125, (b) 250, (c) 500, (d) 1000, and (e) 2000 ALD cycles (35 °C deposition temperature; 0.1 second pulse times). Film thicknesses are average values determined by VASE.

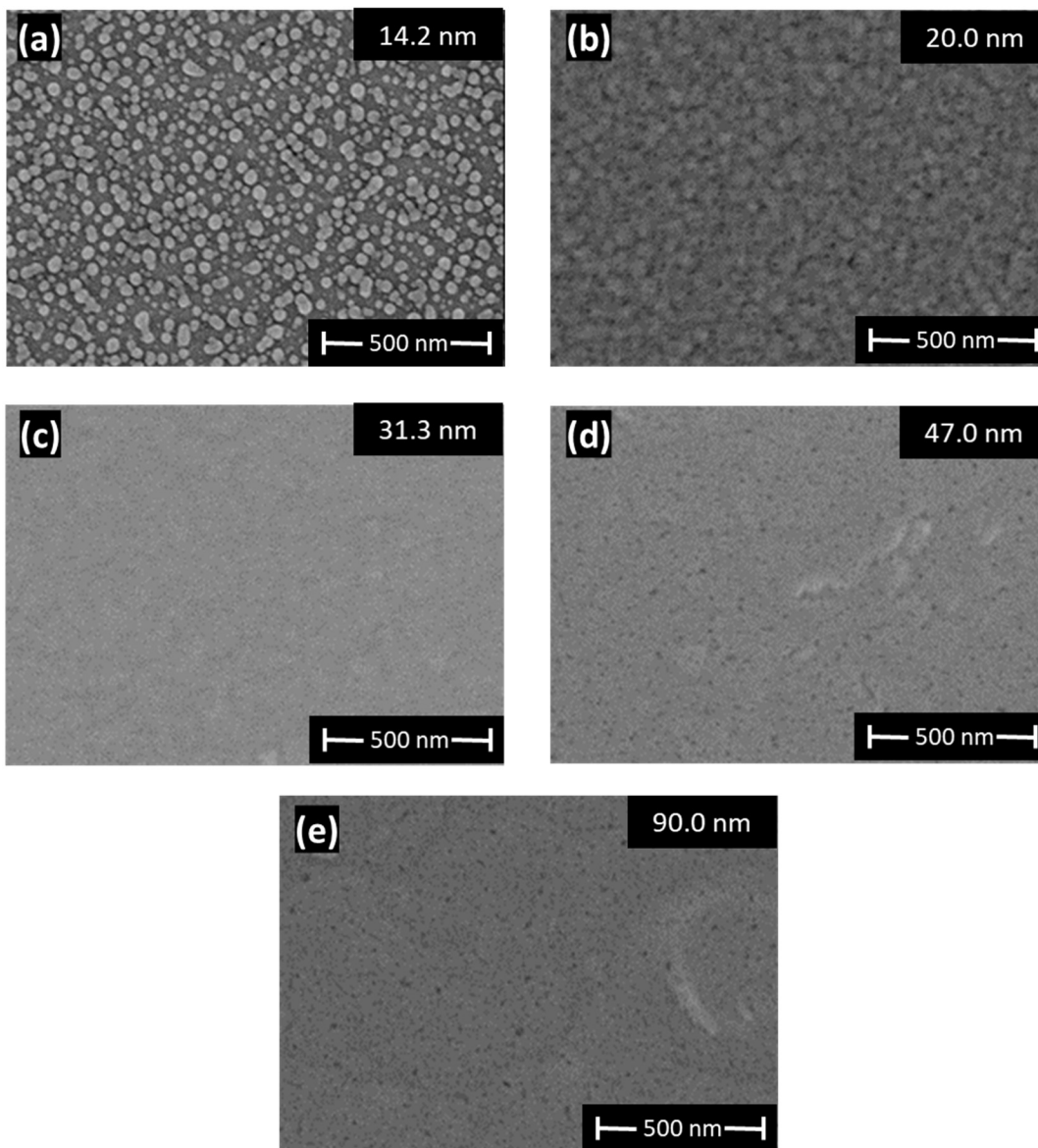


Figure A2.7: FESEM images of films grown on SiO₂/Si using (a) 125, (b) 250, (c) 500, (d) 1000, and (e) 2000 ALD cycles (35 °C deposition temperature; 0.1 second pulse times). Black dots in figures (b), (d), and (e) are due to post deposition surface contamination which developed over time from storage in a glove box (see Figure S9). Film thicknesses are average values determined by VASE.

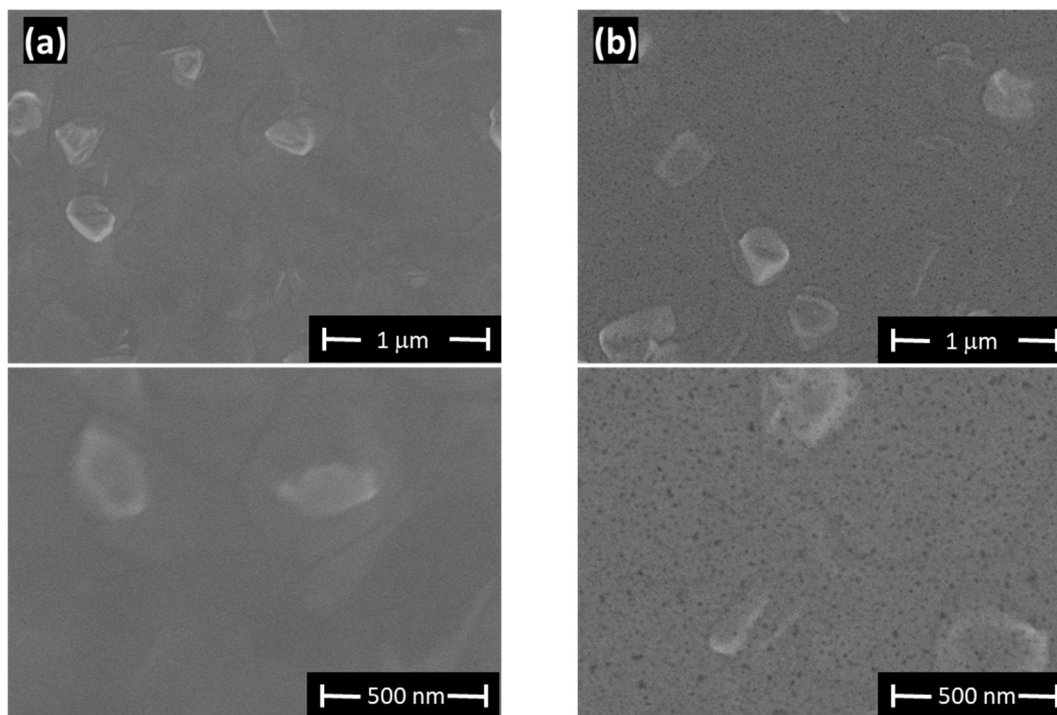


Figure A2.8: FESEM images of Sb films grown on H-Si using 2000 cycles (35 °C deposition temperature; 0.1 second pulse times). FESEM images (a) were obtained within 2 months of depositing the film, while (b) were taken after 5 months. In both cases, films were stored in a glove box. Therefore, black spots in films depicted here and in Figure S8 are most likely due to surface contamination from long storage times in a glove box.

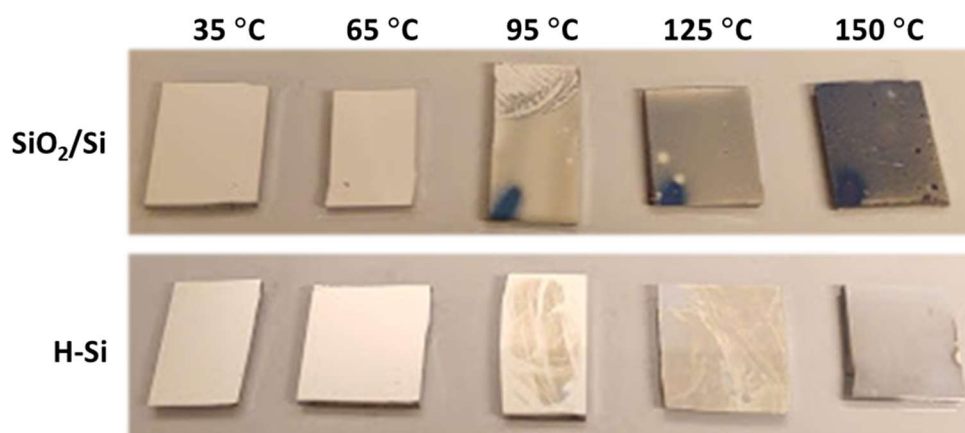


Figure A2.9: Photographs of films grown on SiO₂/Si and H-Si at variable growth temperatures. All films were grown using 1000 cycles and 0.4 second precursor and co-reactant pulse times. The loss of appearance of pristine, mirror-like silver films at higher

temperatures indicates a decay of uniformity (of the films photographed, ALD growth occurred only at 35 and 65 °C).

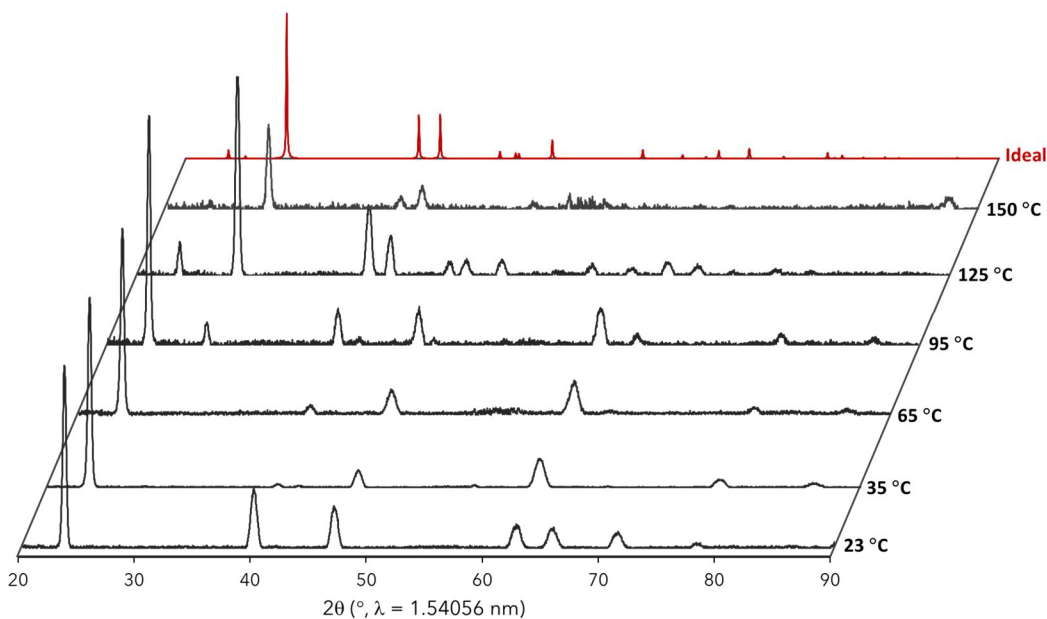


Figure A2.10: X-ray diffractograms of Sb films grown on H-Si at deposition temperatures ranging from 23 to 150 °C using 0.4 second reactant pulse times and 1000 cycles.

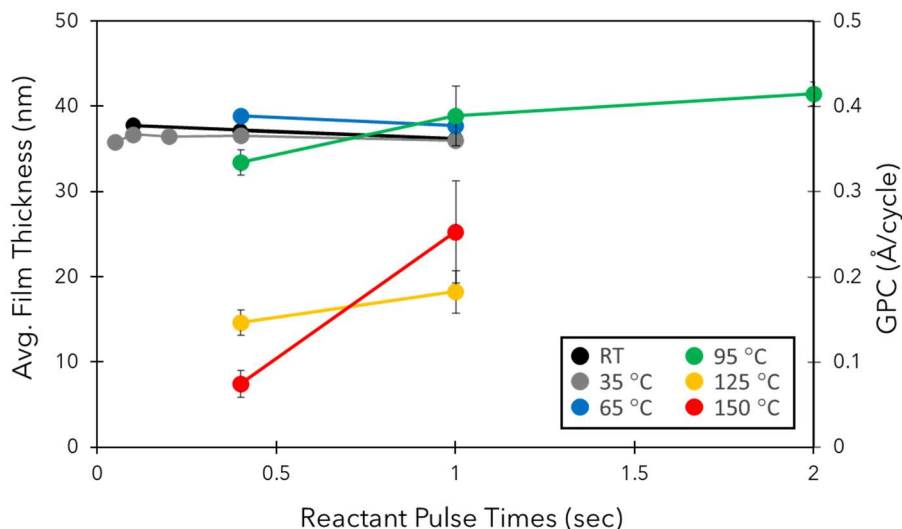


Figure A2.11: Dependence of average film thickness and growth rate on $\text{Sb}(\text{SiMe}_3)_3$ and SbCl_3 pulse times at a given deposition temperature. All films were deposited on H-Si using 1000 cycles.

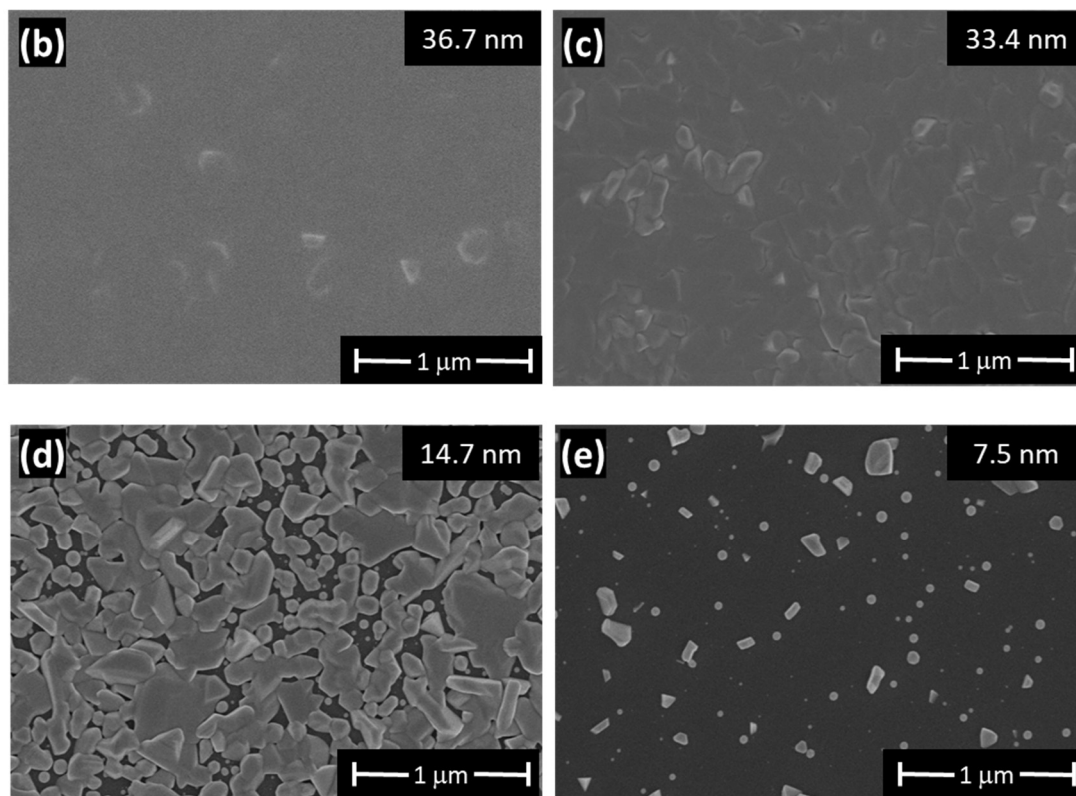


Figure A2.12: FESEM images of films grown on H-Si at (a) 35 °C, (b) 95 °C, (c) 125 °C, and (d) 150 °C using 1000 cycles and 0.4 second reactant pulse times (except for (a) which used 0.1 second pulses). Film thicknesses are average values determined by VASE.

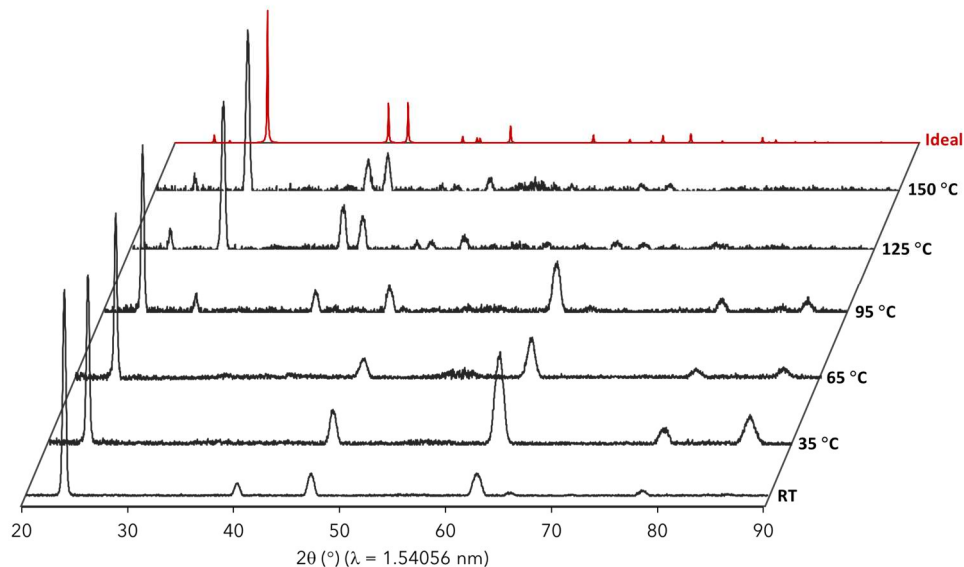


Figure A2.13: X-ray diffractograms of Sb films grown on SiO₂/Si at deposition temperatures ranging from 23 to 150 °C using 0.4 second reactant pulse times and 1000 cycles.

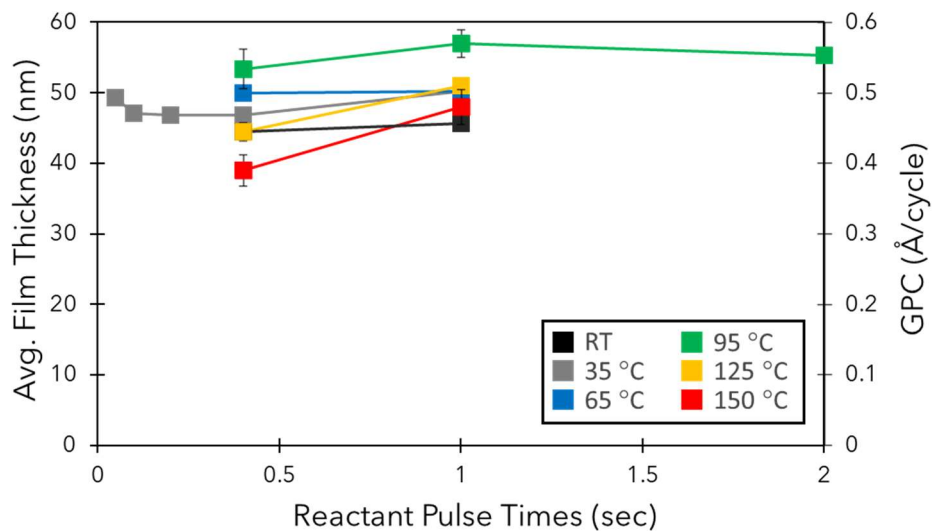


Figure A2.14: Dependence of average film thickness and growth rate on Sb(SiMe₃)₃ and SbCl₃ pulse times at a given deposition temperature. All films were deposited on SiO₂/Si using 1000 cycles.

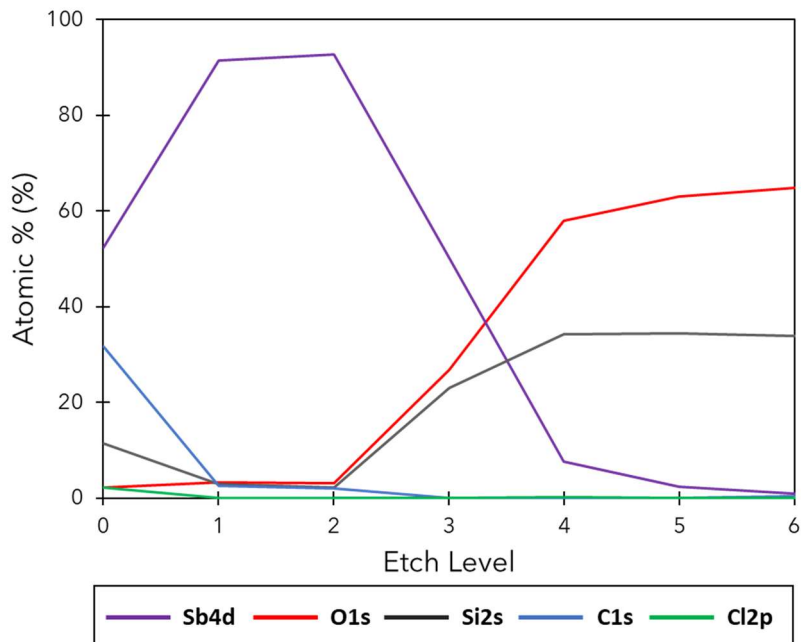


Figure A2.15: XPS depth analysis of a Sb film grown on SiO₂/Si at 95 °C using 1000 cycles and 0.4 second reactant pulse times.

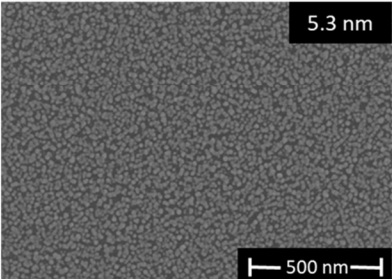
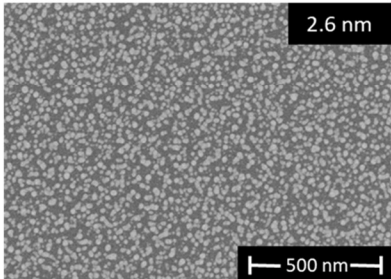
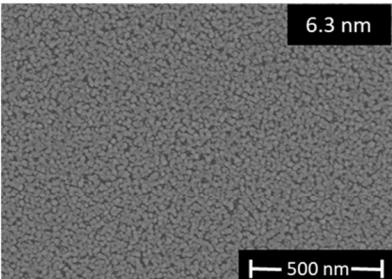
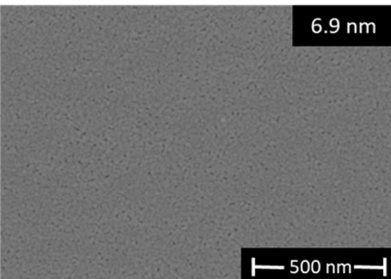
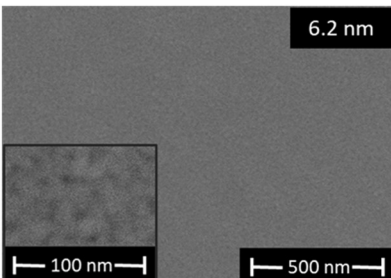
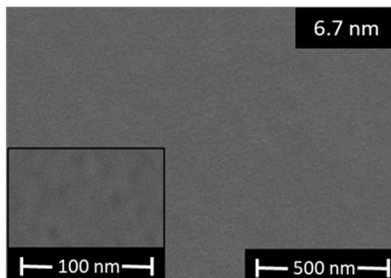
H-Si		SbCl ₃ Pre-Treatment Pulse Length		
		0.1 sec	0.4 sec	0.8 sec
ALD Pulse Length	0.1 sec			
	0.4 sec			
	0.8 sec			

Figure A2.16: Comparison of FESEM images of ultra-thin films deposited on H-Si at 35 °C using 50 pre-treatment cycles of SbCl₃ (pulse times are indicated in row headings) and 50 ALD cycles of Sb(SiMe₃)₃ and SbCl₃ (pulse times are indicated in column headings). Film thicknesses are average values determined by VASE.

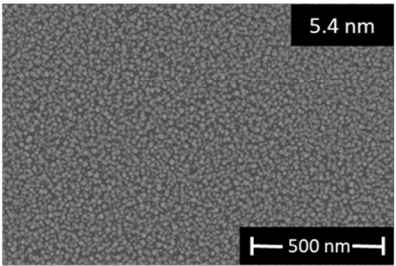
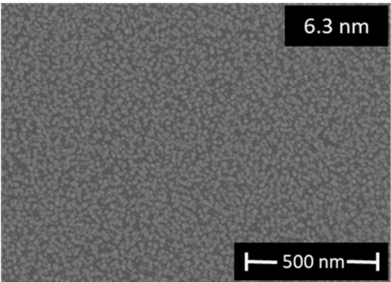
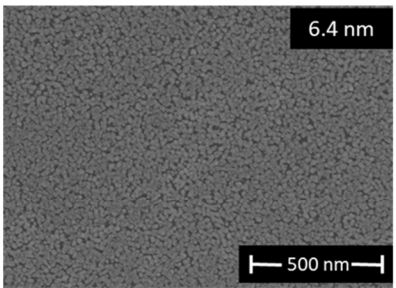
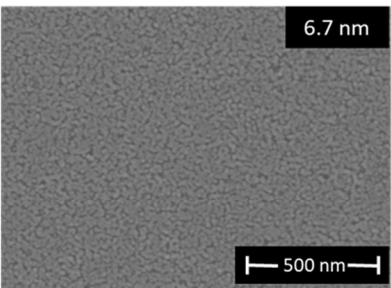
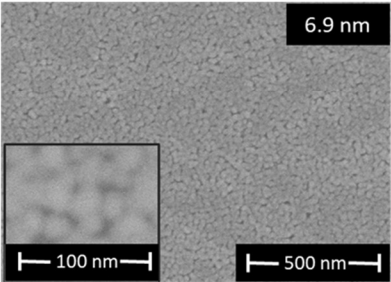
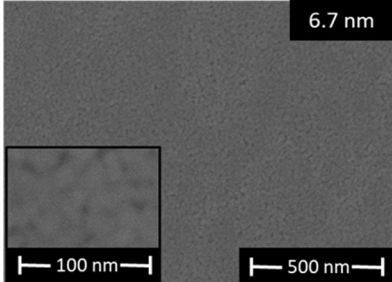
H-Si		Sb(SiMe ₃) ₃ Pre-Treatment Pulse Length		
		0.1 sec	0.4 sec	0.8 sec
ALD Pulse Length	0.1 sec			
	0.4 sec			
	0.8 sec			

Figure A2.17: Comparison of FESEM images of ultra-thin films deposited on H-Si at 35 °C using 50 pre-treatment cycles of Sb(SiMe₃)₃ (pulse times are indicated in row headings) and 50 ALD cycles of Sb(SiMe₃)₃ and SbCl₃ (pulse times are indicated in column headings). Film thicknesses are average values determined by VASE.

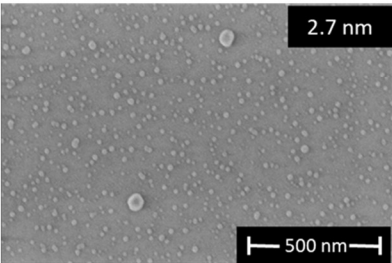
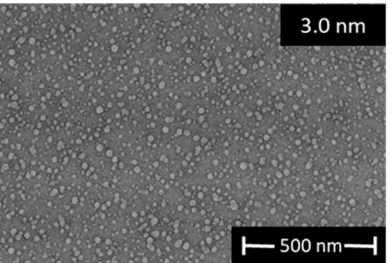
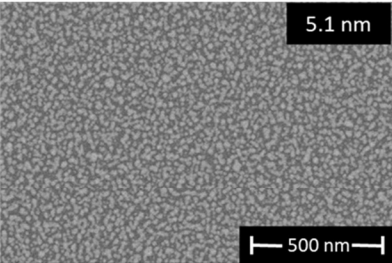
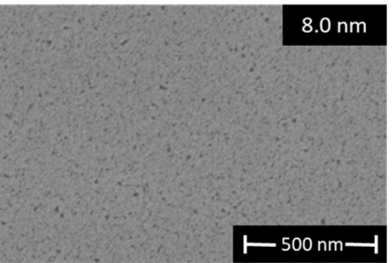
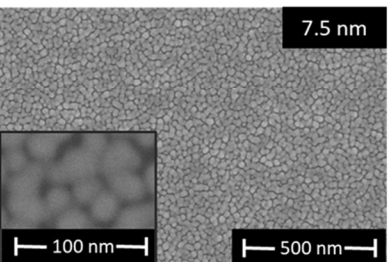
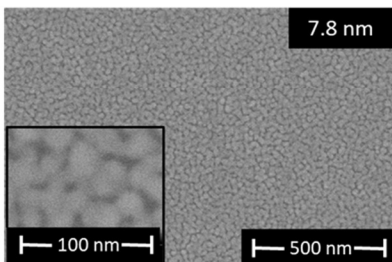
SiO ₂ /Si		SbCl ₃ Pre-Treatment Pulse Length		
		0.1 sec	0.4 sec	0.8 sec
ALD Pulse Length	0.1 sec			
	0.4 sec			
	0.8 sec			

Figure A2.18: Comparison of FESEM images of ultra-thin films deposited on SiO₂/Si at 35 °C using 50 pre-treatment cycles of SbCl₃ (pulse times are indicated in row headings) and 50 ALD cycles of Sb(SiMe₃)₃ and SbCl₃ (pulse times are indicated in column headings). Film thicknesses are average values determined by VASE.

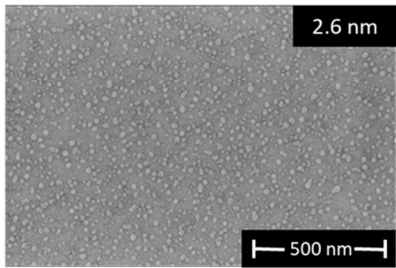
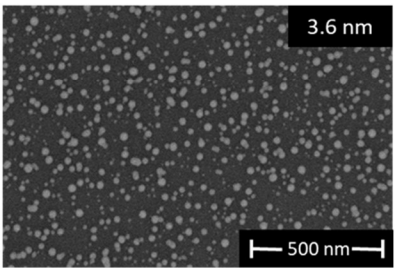
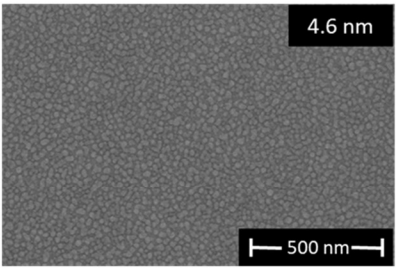
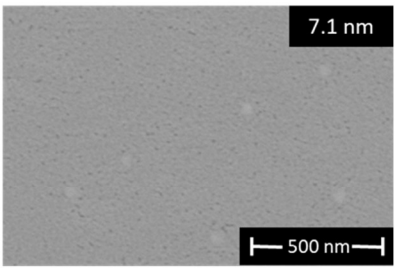
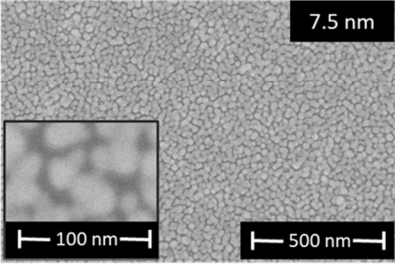
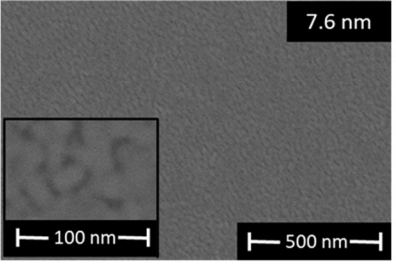
SiO ₂ /Si		Sb(SiMe ₃) ₃ Pre-Treatment Pulse Length		
		0.1 sec	0.4 sec	0.8 sec
ALD Pulse Length	0.1 sec			
	0.4 sec			
	0.8 sec			

Figure A2.19: Comparison of FESEM images of ultra-thin films deposited on SiO₂/Si at 35 °C using 50 pre-treatment cycles of Sb(SiMe₃)₃ (pulse times are indicated in row headings) and 50 ALD cycles of Sb(SiMe₃)₃ and SbCl₃ (pulse times are indicated in column headings). Film thicknesses are average values determined by VASE.

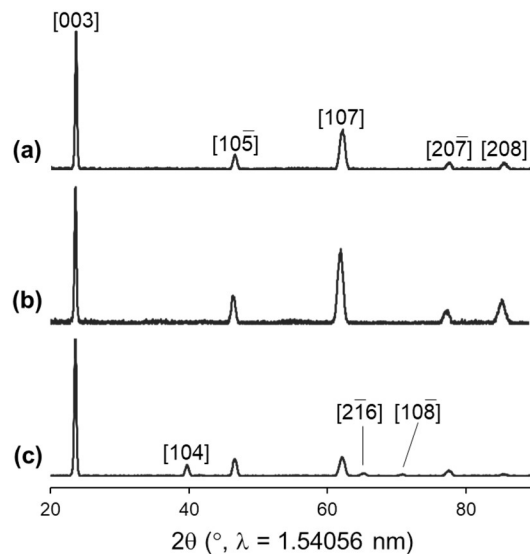


Figure A2.20: X-ray diffractograms of Sb films grown on SiO₂/Si (35 °C; 2000 cycles) using (a) the standard ALD method (no pre-treatment, all 0.1 s precursor pulses), (b) ALD with Sb(SiMe₃)₃ pre-treatment (surface pre-treatment with 50 × 0.4 s pulses of Sb(SiMe₃)₃, followed by 50 ALD cycles using 0.4 s pulses, and then 1950 ALD cycles using 0.1 s pulses), or (c) ALD with SbCl₃ pre-treatment (surface pre-treatment with 50 × 0.4 s pulses of SbCl₃, followed by 50 ALD cycles using 0.4 s pulses, and then 1950 ALD cycles using 0.1 s pulses).

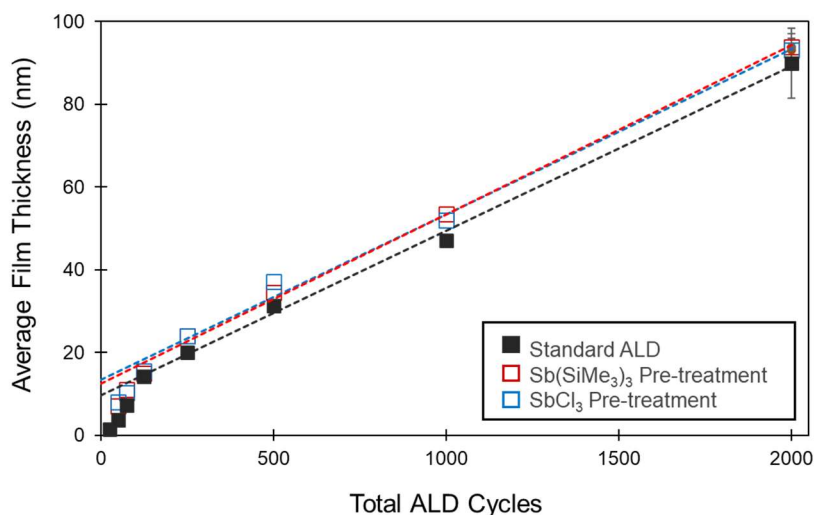


Figure A2.21: Film thickness versus the number of ALD cycles for 35 °C deposition on SiO₂/Si using: (i; black) standard ALD parameters (no pre-treatment, all cycles using 0.1

s pulses), (ii; red) ALD with $\text{Sb}(\text{SiMe}_3)_3$ pre-treatment (surface pre-treatment with 50 x 0.4 s pulses of $\text{Sb}(\text{SiMe}_3)_3$, followed by 50 ALD cycles using 0.4 s pulses, and all remaining ALD cycles using 0.1 s pulses), or (iii; blue) ALD with SbCl_3 pre-treatment (surface pre-treatment with 50 x 0.4 s pulses of SbCl_3 , followed by 50 ALD cycles using 0.4 s pulses, and all remaining ALD cycles using 0.1 s pulses).

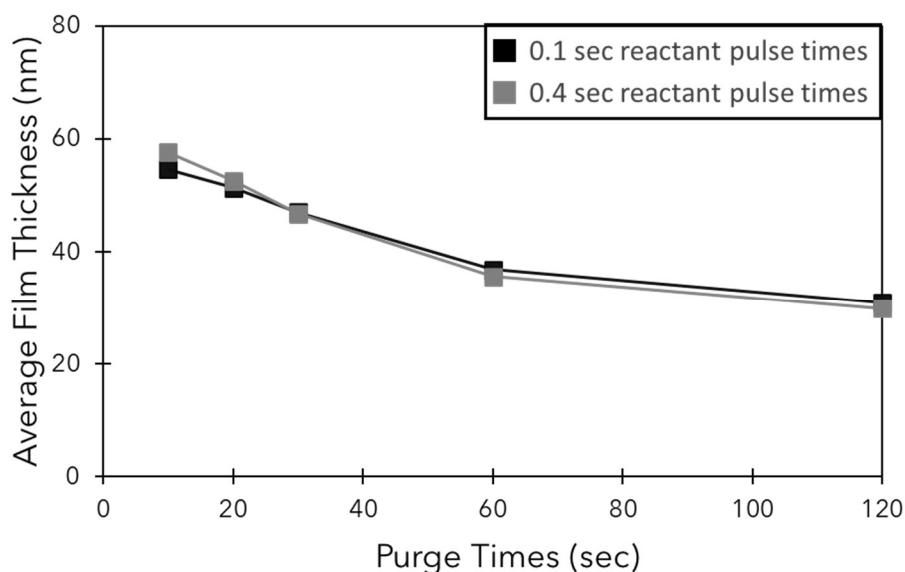


Figure A2.22: Dependence of film thickness on purge times (for each data point, purge times are those following each of the two precursor pulses). All films were grown on SiO_2/Si at 35 °C using 1000 cycles. Data points coloured black indicate films grown using 0.1 s reactant pulse times, while gray indicates films grown using 0.4 s pulse times.

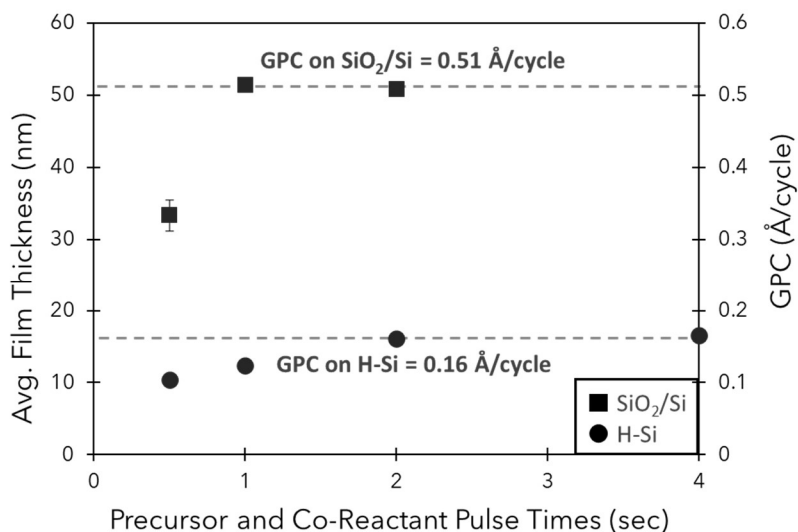


Figure A2.23: Dependence of film thickness and growth rate on $\text{Sb}(\text{SiEt}_3)_3$ and SbCl_3 pulse times on SiO_2/Si (squares) and H-Si (circles). Cycle number was kept constant (1000) as well as deposition temperature ($95\text{ }^\circ\text{C}$) and delivery temperatures ($85\text{ }^\circ\text{C}$ for $\text{Sb}(\text{SiEt}_3)_3$, $30\text{ }^\circ\text{C}$ for SbCl_3).

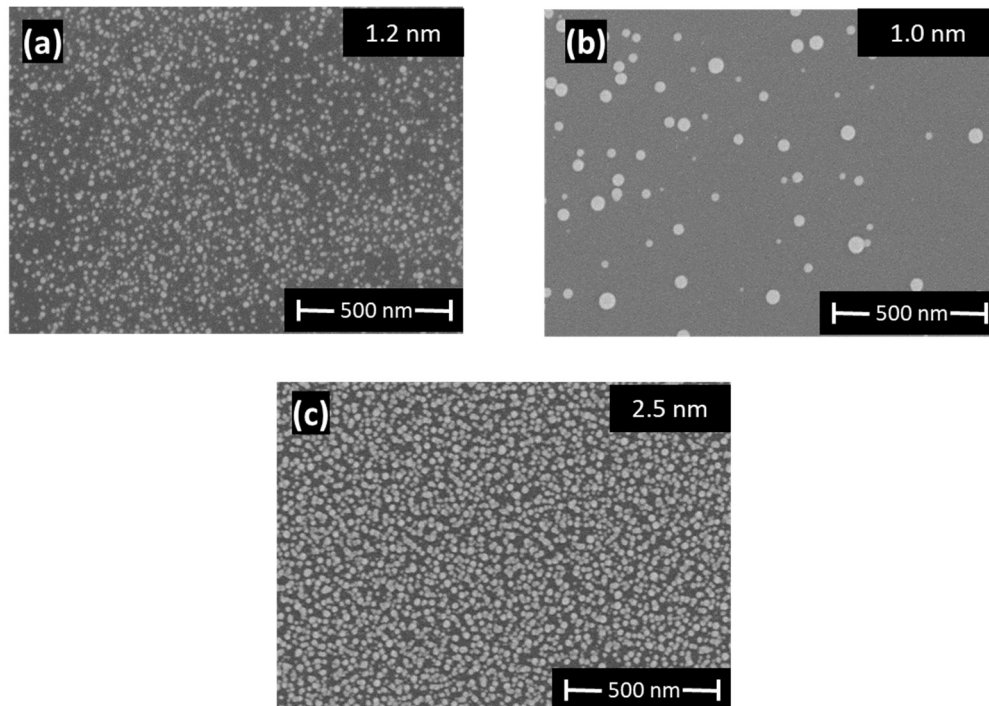


Figure A2.24: FESEM images of films grown on H-Si: (a) 50 $\text{Sb}(\text{SiEt}_3)_3/\text{SbCl}_3$ ALD cycles at $95\text{ }^\circ\text{C}$ (using 2 second pulse times); (b) 50 $\text{Sb}(\text{SiMe}_3)_3/\text{SbCl}_3$ ALD cycles at $95\text{ }^\circ\text{C}$ (using

0.1 second pulse times); (c) 50 Sb(SiMe₃)₃/SbCl₃ ALD cycles at 35 °C (using 0.1 second pulse times). Film thicknesses are average values determined by VASE.

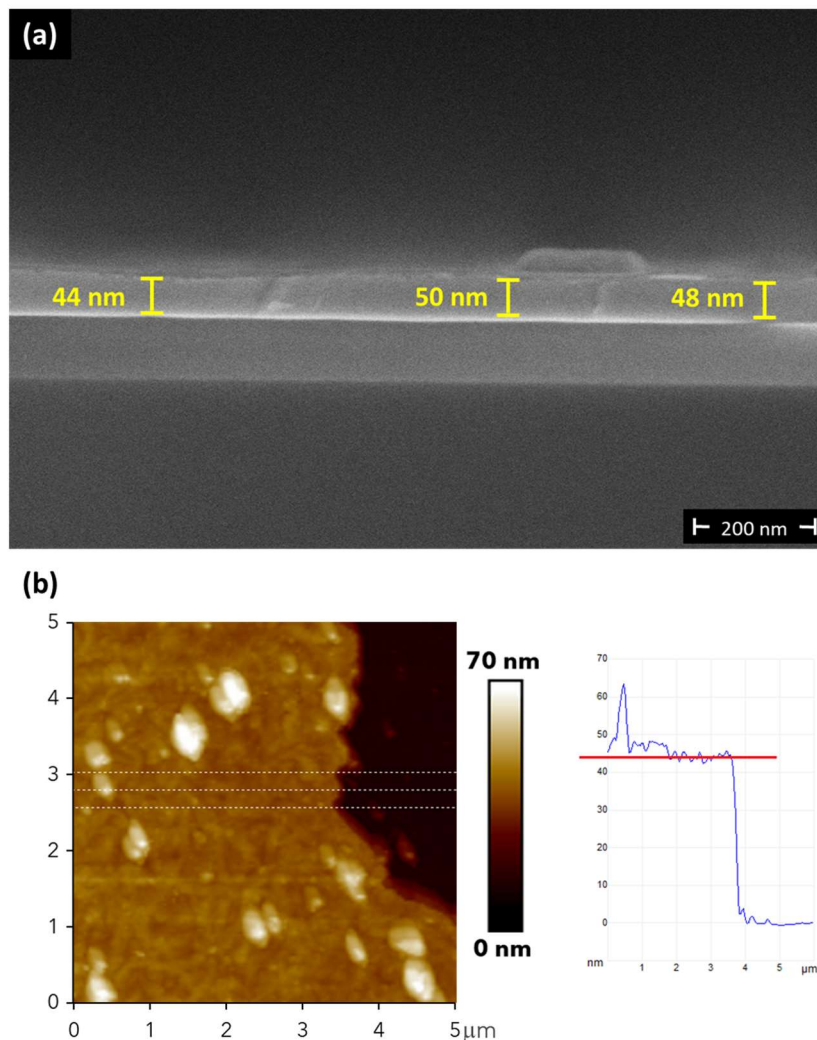


Figure A2.25: (a) Cross-sectional FESEM image of Sb film grown on SiO₂/Si at 35 °C using 1000 ALD cycles and 0.1 second and 30 second pulse and purge times, respectively. The average of three different thickness measurements along the film (47 nm) correlates well with the average thickness measurement obtained from VASE (47.03 nm). (b) AFM image of Sb film grown on SiO₂/Si at 35 °C using 1000 ALD cycles and 0.1 second and 30 second pulse and purge times, respectively (note: Kapton tape was adhered to the right side of the film before deposition and removed after deposition). The thickness measurement from AFM step analysis (44 nm) correlates well with the average thickness measured obtained from VASE (47.03 nm).

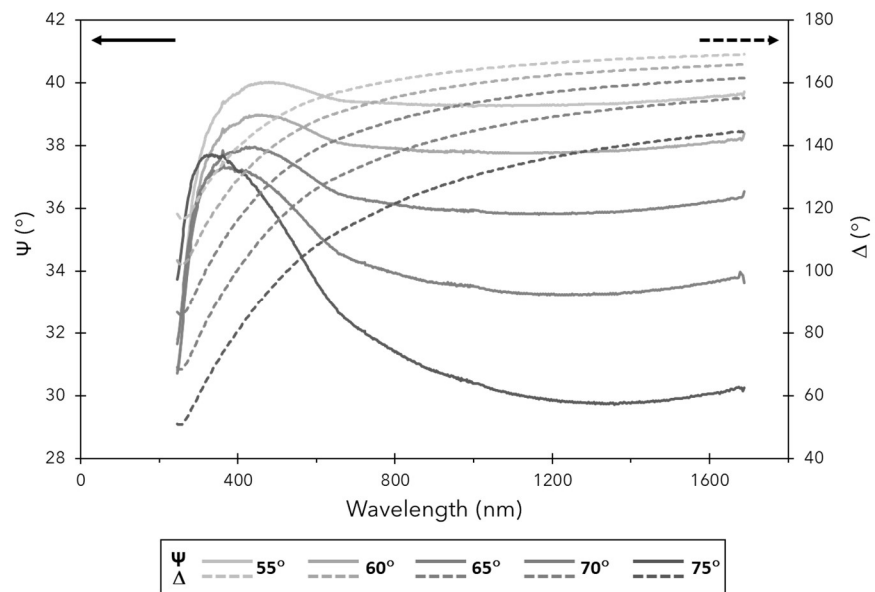


Figure A2.26: Measured values of Psi (Ψ , solid lines) and Delta (Δ , dashed lines) as a function of wavelength for a Sb film grown on H-Si at 35 °C (1000 cycles, 0.1 second pulse and 30 second purge times).

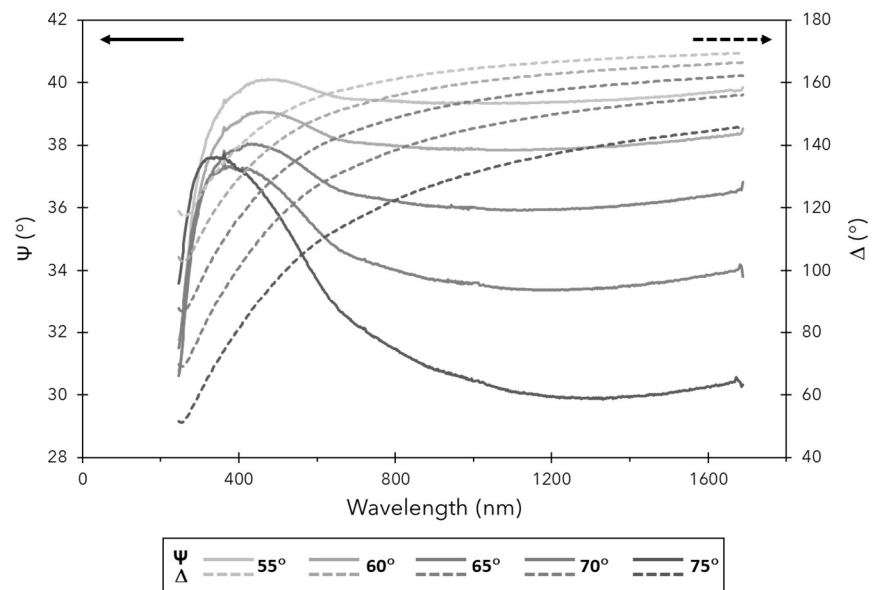


Figure A2.27: Measured values of Psi (Ψ , solid lines) and Delta (Δ , dashed lines) as a function of wavelength for a Sb film grown on SiO₂/Si at 35 °C (1000 cycles, 0.1 second pulse and 30 second purge times).

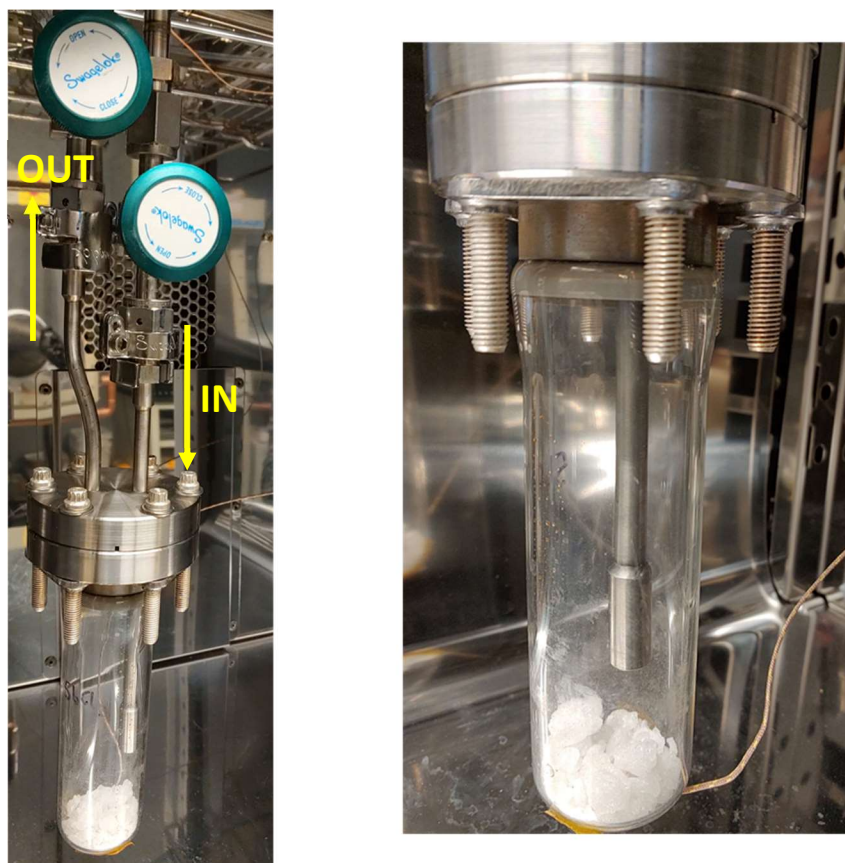


Figure A2.28: Photo showing the precursor bubbler design used in this work (in this case, the bubbler containing SbCl_3 is shown, but the same type was used for $\text{Sb}(\text{SiMe}_3)_3$). Bubblers are of a flow-through design, with a dip tube that is short enough to avoid contact with the precursor upon loading of the bubbler.

A3 – Supplementary Information Related to Chapter 3

Contents	Pages
Select NMR Spectra	A32-44
NMR Spectra of Select NMR-Scale Reactivity Tests Involving 3-8 or 3-12 and BX ₃ reagents	A45-46

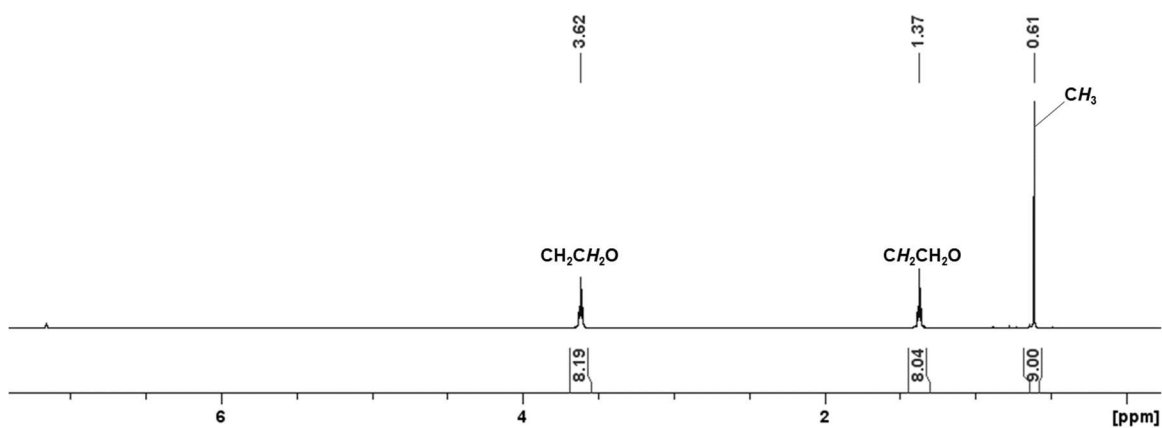


Figure A3.1: ¹H NMR spectrum of [Me₃GeLi(THF)₂]₂, **3-3** (C₆D₆, 600 MHz, 298 K).

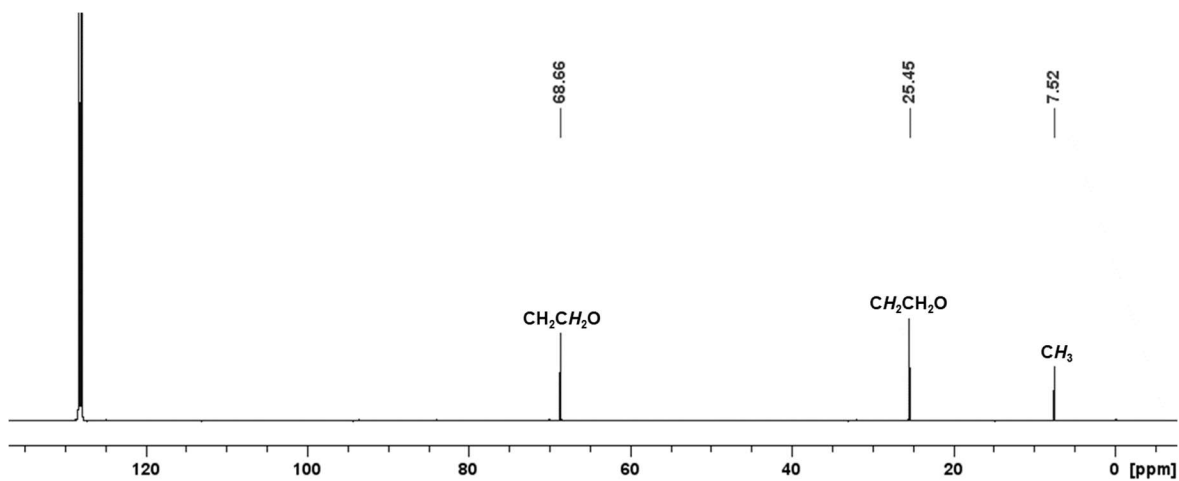


Figure A3.2: ¹³C{¹H} NMR spectrum of [Me₃GeLi(THF)₂]₂, **3-3** (C₆D₆, 151 MHz, 298 K).

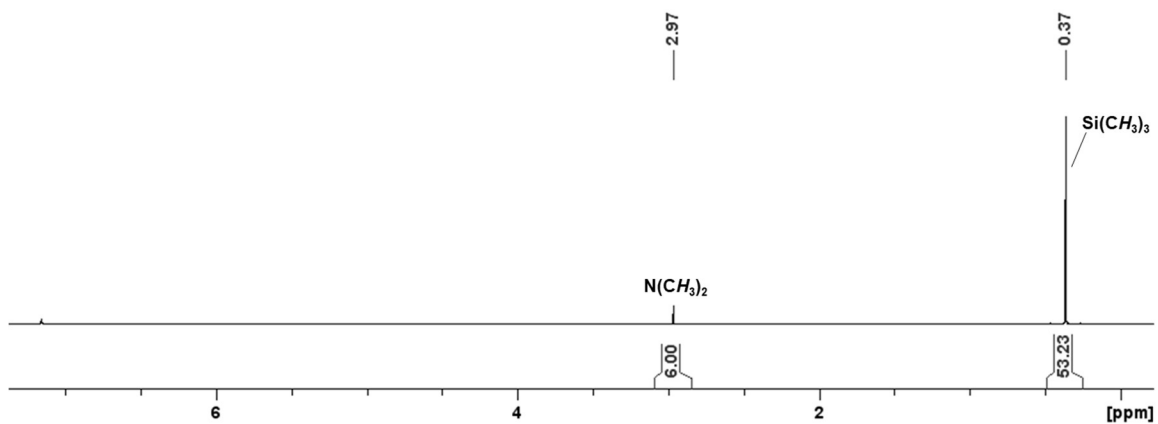


Figure A3.3: ^1H NMR spectrum of $\{(\text{Me}_3\text{Si})_3\text{Si}\}_2\text{B}(\text{NMe}_2)$, **3-8** (C_6D_6 , 600 MHz, 298 K).

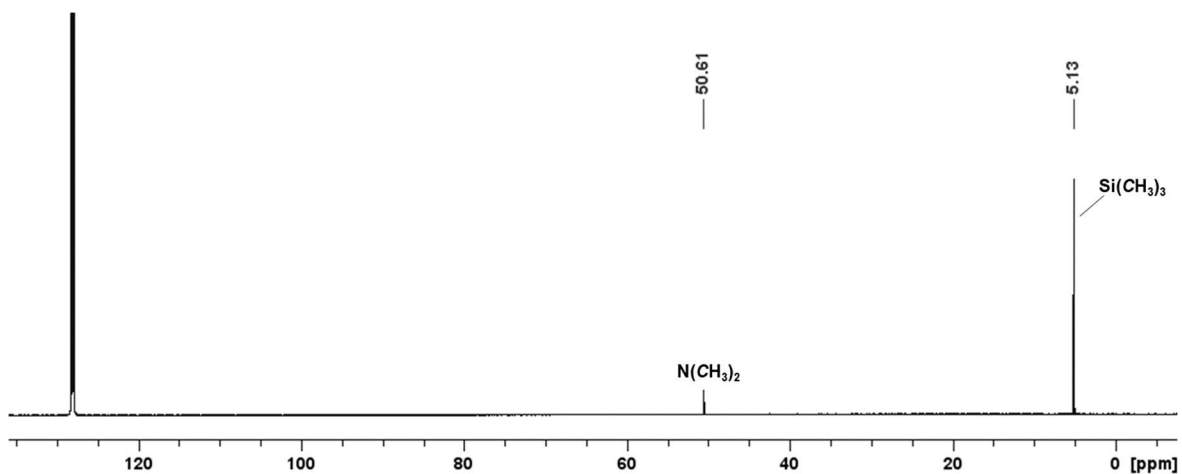


Figure A3.4: $^{13}\text{C}\{^1\text{H}\}$ NMR spectrum of $\{(\text{Me}_3\text{Si})_3\text{Si}\}_2\text{B}(\text{NMe}_2)$, **3-8** (C_6D_6 , 151 MHz, 298 K).

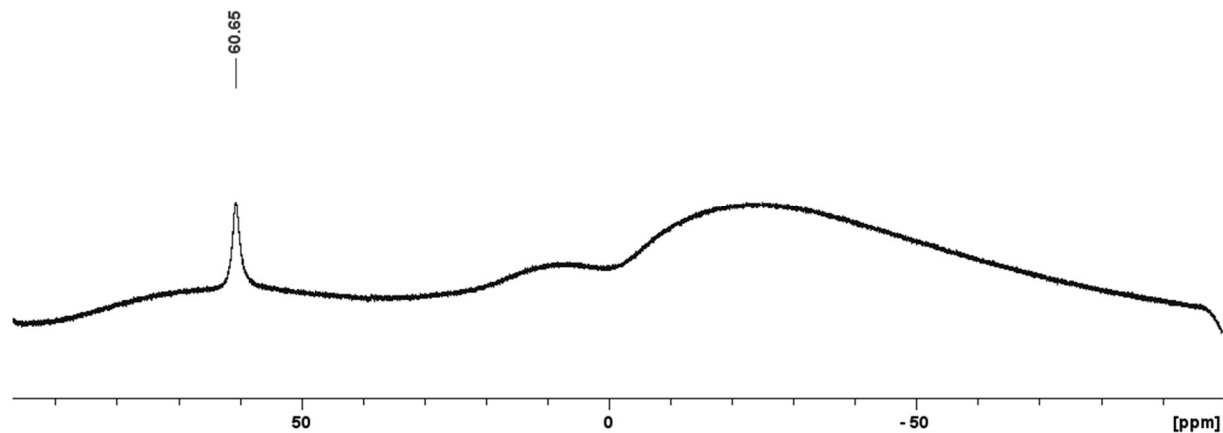


Figure A3.5: $^{11}\text{B}\{^1\text{H}\}$ NMR spectrum of $\{(\text{Me}_3\text{Si})_3\text{Si}\}_2\text{B}(\text{NMe}_2)$, **3-8** (C_6D_6 , 193 MHz, 298 K).

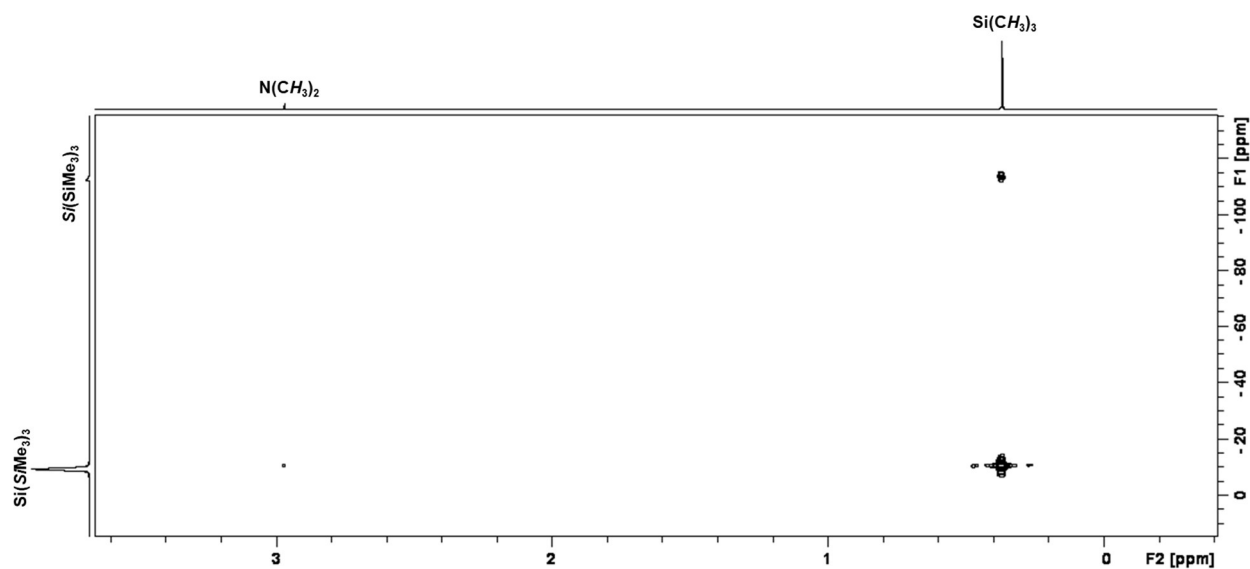


Figure A3.6: $^{29}\text{Si}-^1\text{H}$ HMBC NMR spectrum of $\{(\text{Me}_3\text{Si})_3\text{Si}\}_2\text{B}(\text{NMe}_2)$, **3-8** (C_6D_6 , 600/119 MHz, 298 K). F1 axis is an internal ^{29}Si NMR projection.

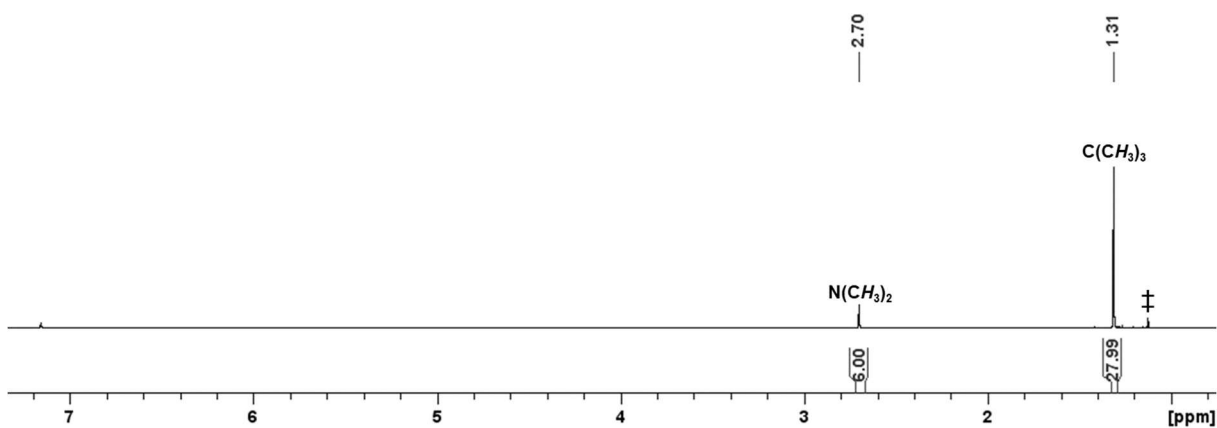


Figure A3.7: ^1H NMR spectrum of $(^t\text{Bu}_3\text{Si})\text{B}(\text{NMe}_2)\text{Cl}$, **3-9** (C_6D_6 , 600 MHz, 298 K). Peaks labeled with a double dagger correspond to the impurity that consistently arose during $(^t\text{Bu}_3\text{Si})\text{Na}(\text{THF})_n$ synthesis.

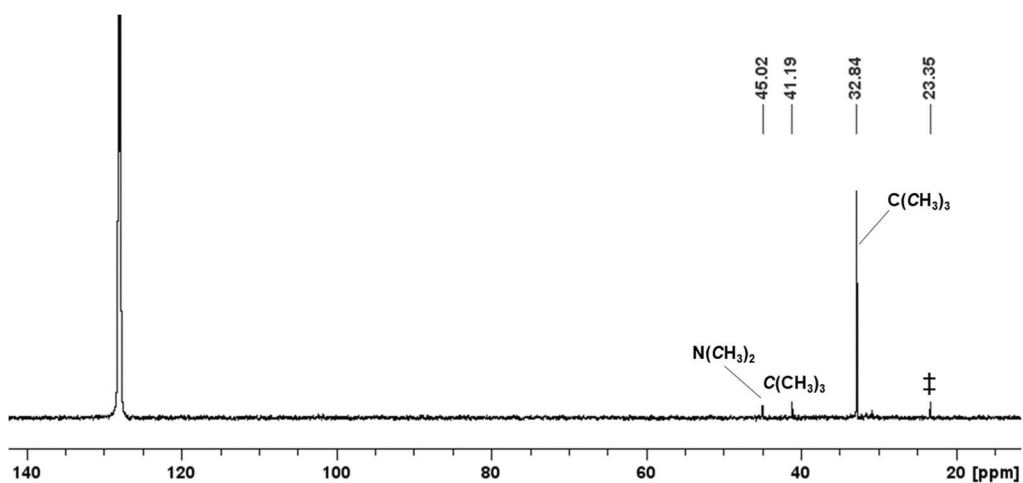


Figure A3.8: $^{13}\text{C}\{^1\text{H}\}$ NMR spectrum of $(^t\text{Bu}_3\text{Si})\text{B}(\text{NMe}_2)\text{Cl}$, **3-9** (C_6D_6 , 151 MHz, 298 K). Peaks labeled with a double dagger correspond to the impurity that consistently arose during $(^t\text{Bu}_3\text{Si})\text{Na}(\text{THF})_n$ synthesis.

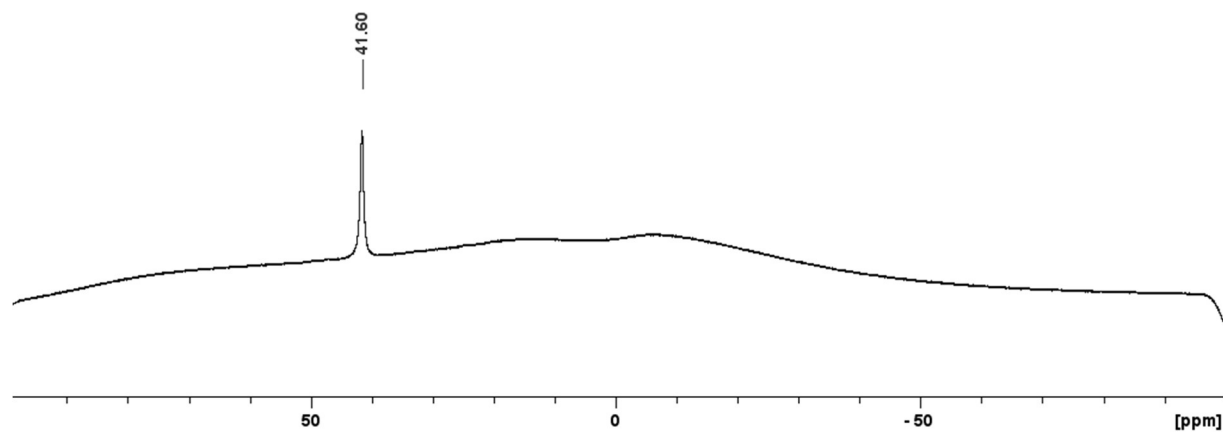


Figure A3.9: $^{11}\text{B}\{^1\text{H}\}$ NMR spectrum of $(t\text{Bu}_3\text{Si})\text{B}(\text{NMe}_2)\text{Cl}$, **3-9** (C_6D_6 , 193 MHz, 298 K).

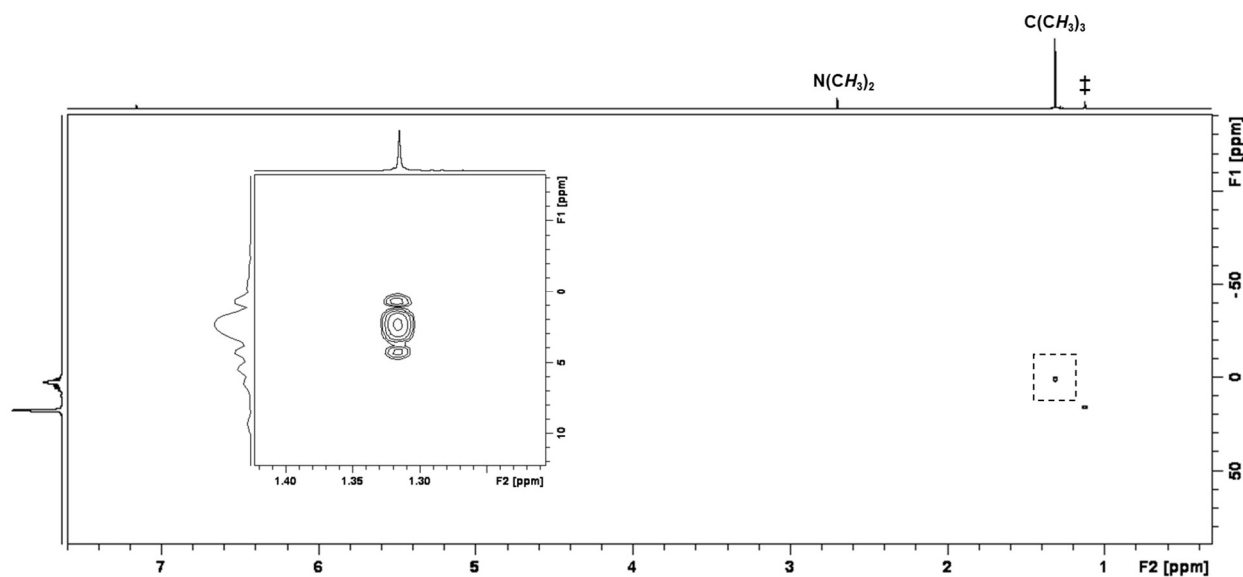


Figure A3.10: $^{29}\text{Si}-^1\text{H}$ HMBC NMR spectrum of $(t\text{Bu}_3\text{Si})\text{B}(\text{NMe}_2)\text{Cl}$, **3-9** (C_6D_6 , 600/119 MHz, 298 K). F1 axis is an internal ^{29}Si NMR projection. Peaks labeled with a double dagger correspond to the impurity that consistently arose during $(t\text{Bu}_3\text{Si})\text{Na}(\text{THF})_n$ synthesis.

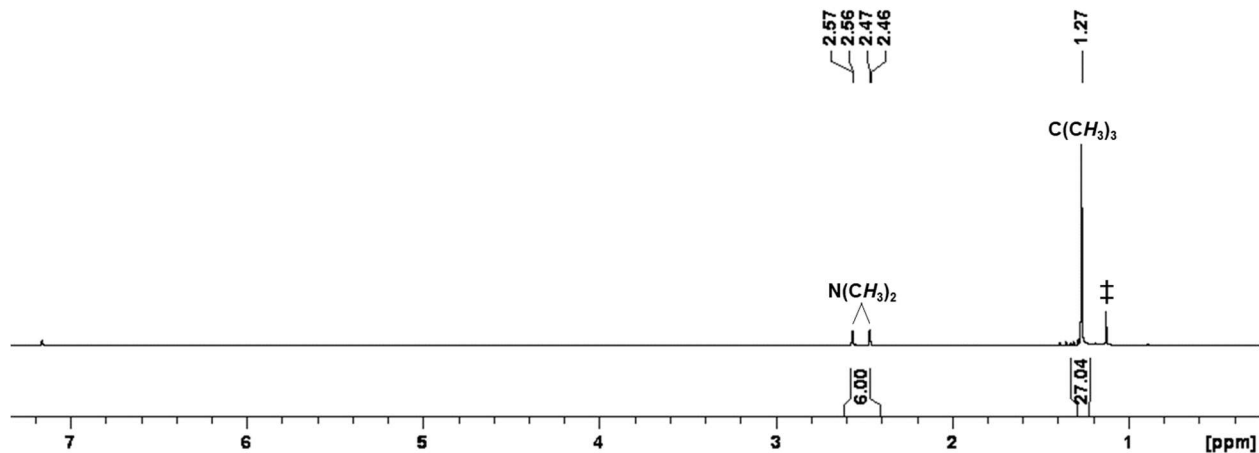


Figure A3.11: ^1H NMR spectrum of $(^t\text{Bu}_3\text{Si})\text{B}(\text{NMe}_2)\text{F}$, **3-10** (C_6D_6 , 500 MHz, 298 K). Peaks labeled with a double dagger correspond to the impurity that consistently arose during $(^t\text{Bu}_3\text{Si})\text{Na}(\text{THF})_n$ synthesis.

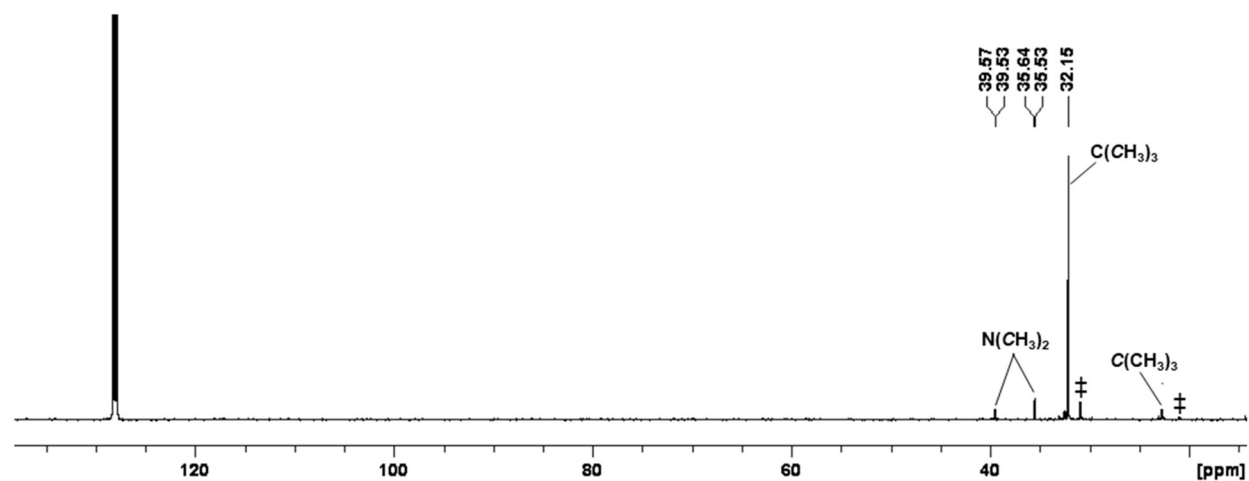


Figure A3.12: $^{13}\text{C}\{^1\text{H}\}$ NMR spectrum of $(^t\text{Bu}_3\text{Si})\text{B}(\text{NMe}_2)\text{F}$, **3-10** (C_6D_6 , 126 MHz, 298 K). Peaks labeled with a double dagger correspond to the impurity that consistently arose during $(^t\text{Bu}_3\text{Si})\text{Na}(\text{THF})_n$ synthesis.

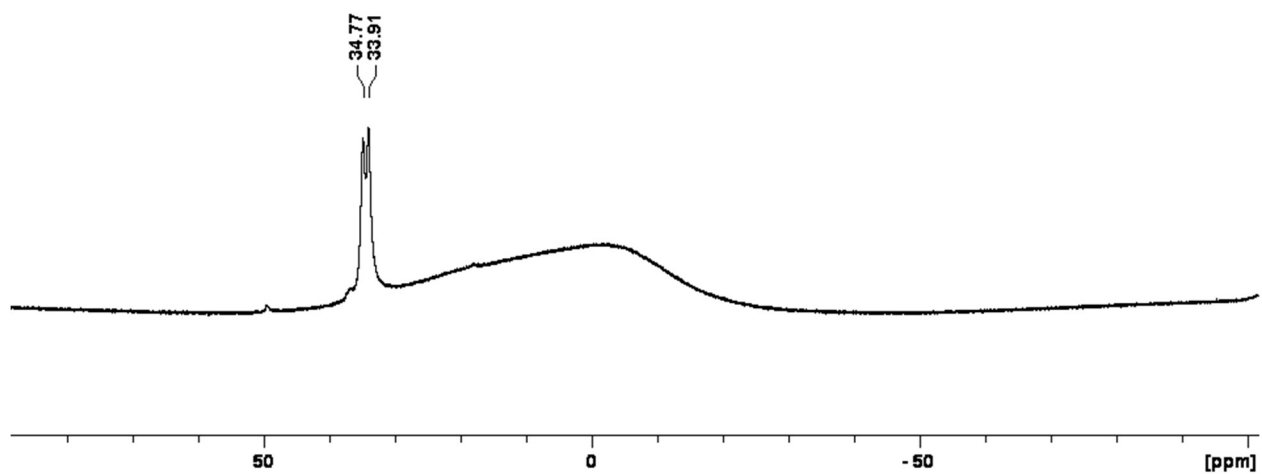


Figure A3.13: $^{11}\text{B}\{^1\text{H}\}$ NMR spectrum of $(t\text{Bu}_3\text{Si})\text{B}(\text{NMe}_2)\text{F}$, **3-10** (C_6D_6 , 161 MHz, 298 K).

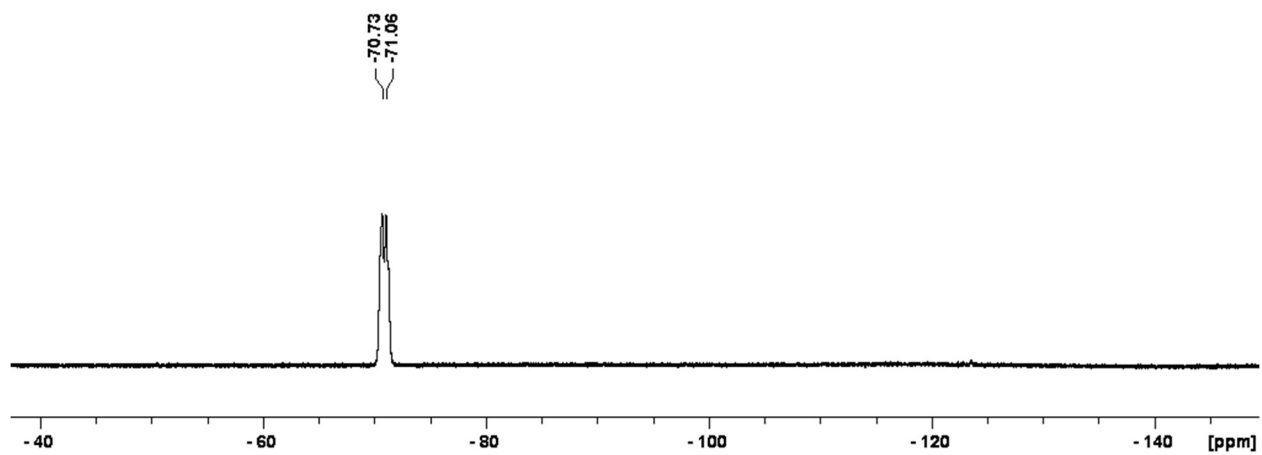


Figure A3.14: ^{19}F NMR spectrum of $(t\text{Bu}_3\text{Si})\text{B}(\text{NMe}_2)\text{F}$, **3-10** (C_6D_6 , 471 MHz, 298 K).

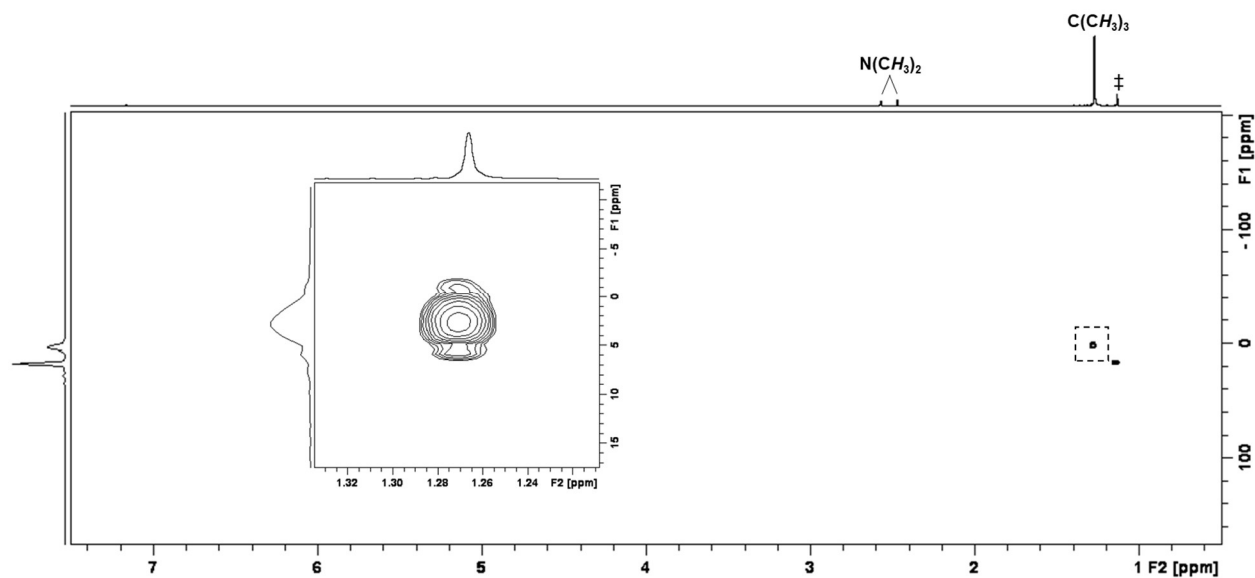


Figure A3.15: ^{29}Si - ^1H HMBC NMR spectrum of $(t\text{Bu}_3\text{Si})\text{B}(\text{NMe}_2)\text{F}$, **3-10** (C_6D_6 , 500/99 MHz, 298 K). F1 axis is an internal ^{29}Si NMR projection. Peaks labeled with a double dagger correspond to the impurity that consistently arose during $(t\text{Bu}_3\text{Si})\text{Na}(\text{THF})_n$ synthesis.

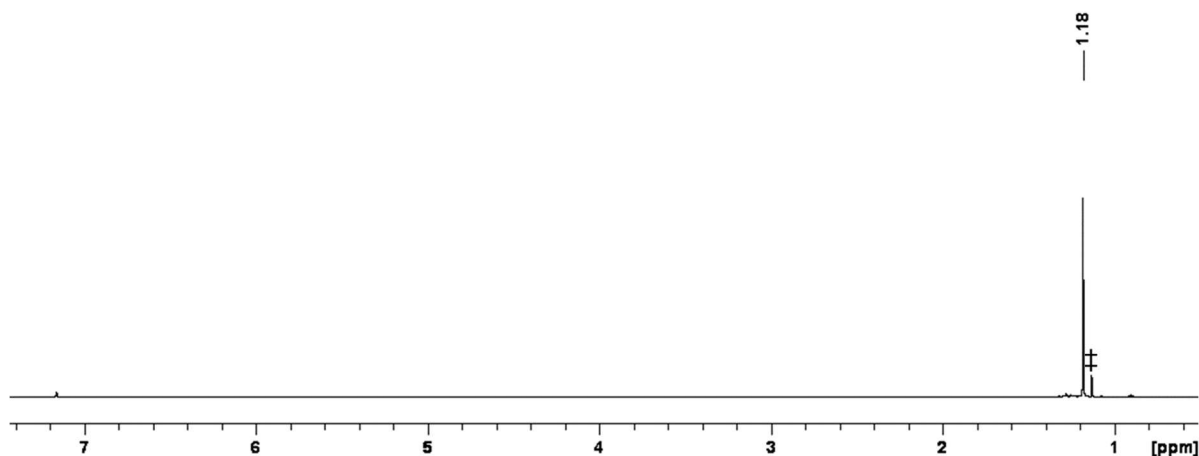


Figure A3.16: ^1H NMR spectrum of $(t\text{Bu}_3\text{Si})\text{BCl}_2$, **3-11** (C_6D_6 , 600 MHz, 298 K). Peaks labeled with a double dagger correspond to the impurity that consistently arose during $(t\text{Bu}_3\text{Si})\text{Na}(\text{THF})_n$ synthesis.

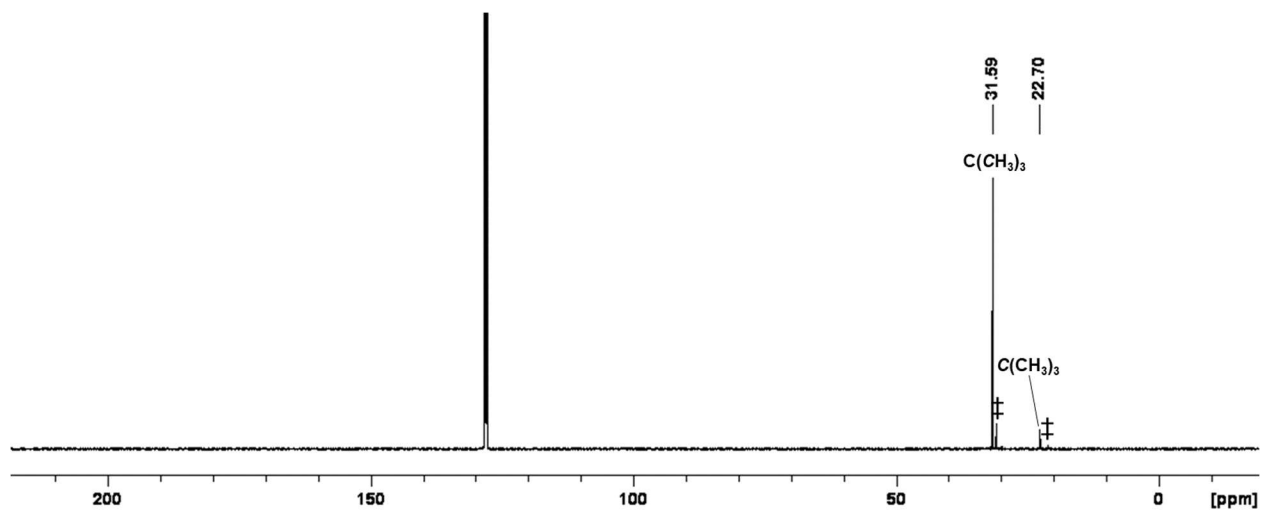


Figure A3.17: $^{13}\text{C}\{^1\text{H}\}$ NMR spectrum of $(^t\text{Bu}_3\text{Si})\text{BCl}_2$, **3-11** (C_6D_6 , 151 MHz, 298 K).

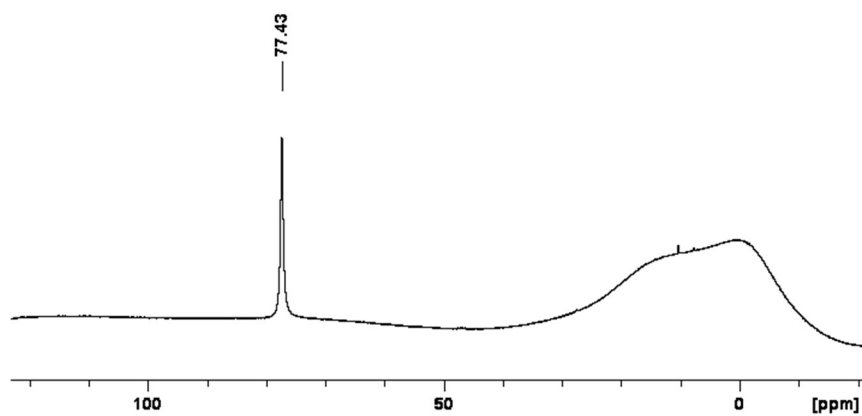


Figure A3.18: $^{11}\text{B}\{^1\text{H}\}$ NMR spectrum of $(^t\text{Bu}_3\text{Si})\text{BCl}_2$, **3-11** (C_6D_6 , 193 MHz, 298 K).

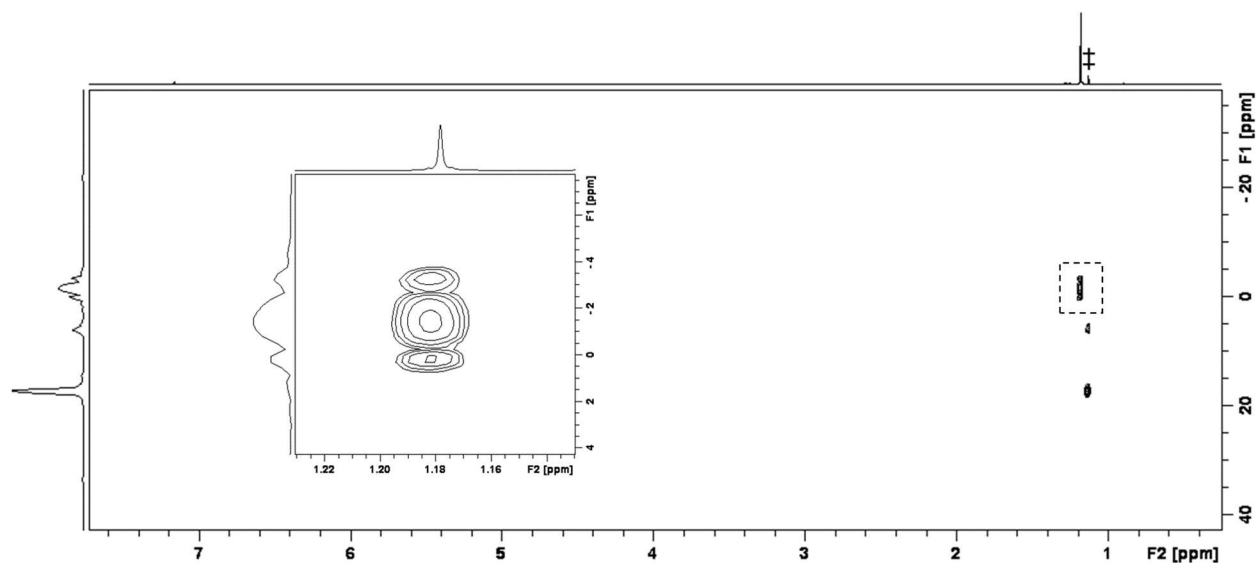


Figure A3.19: ^{29}Si - ^1H HMBC NMR spectrum of $(t\text{Bu}_3\text{Si})\text{BCl}_2$, **3-11** (C_6D_6 , 600/119 MHz, 298 K). F1 axis is an internal ^{29}Si NMR projection. Peaks labeled with a double dagger correspond to the impurity that consistently arose during $(t\text{Bu}_3\text{Si})\text{Na}(\text{THF})_n$ synthesis.

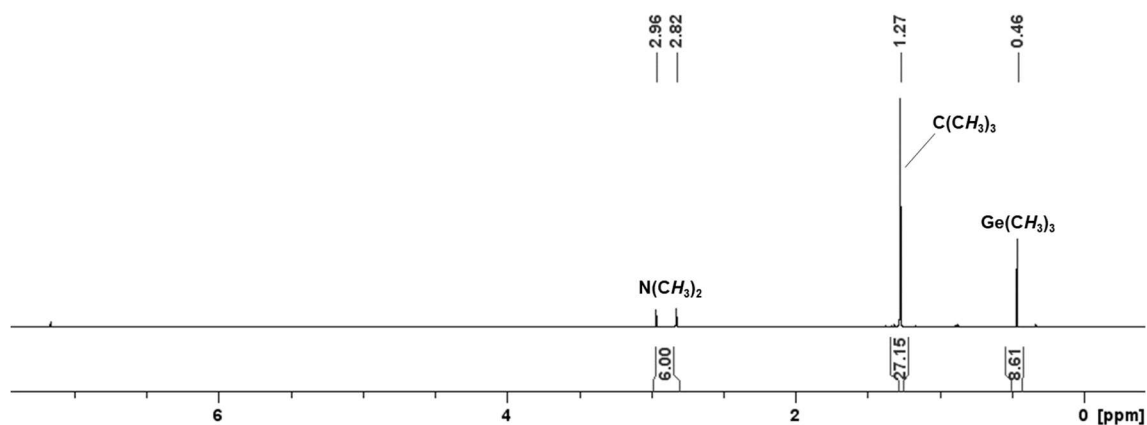


Figure A3.20: ^1H NMR spectrum of $(t\text{Bu}_3\text{Si})(\text{Me}_3\text{Ge})\text{B}(\text{NMe}_2)$, **3-12** (C_6D_6 , 600 MHz, 298 K).

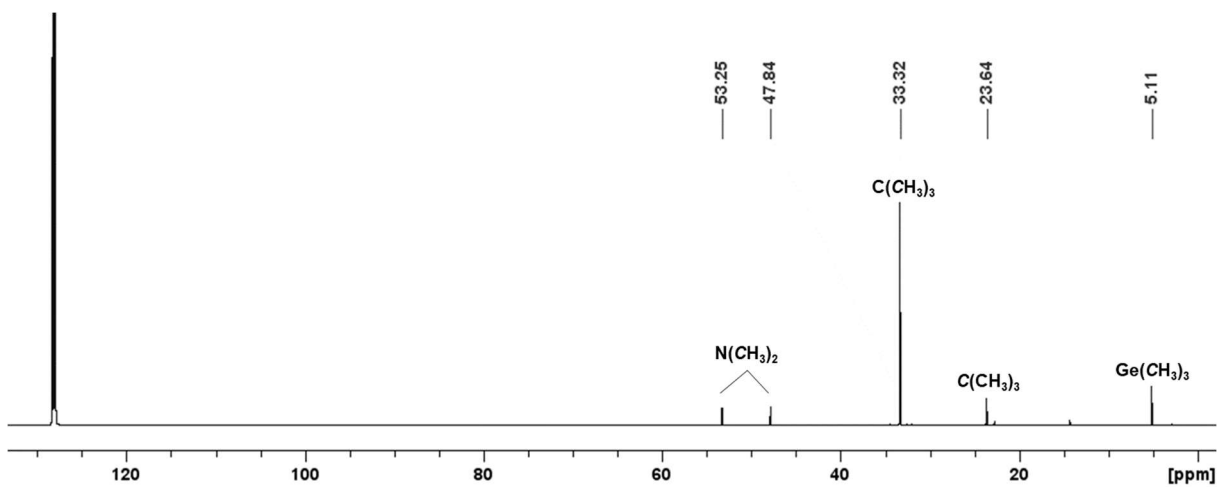


Figure A3.21: $^{13}\text{C}\{^1\text{H}\}$ NMR spectrum of $(t\text{Bu}_3\text{Si})(\text{Me}_3\text{Ge})\text{B}(\text{NMe}_2)$, **3-12** (C_6D_6 , 151 MHz, 298 K).

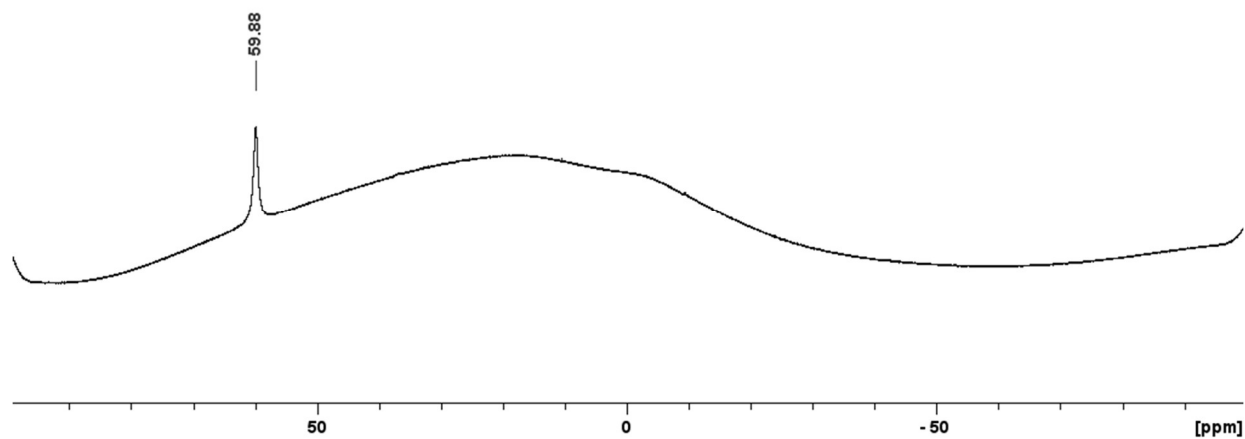


Figure A3.22: $^{11}\text{B}\{^1\text{H}\}$ NMR spectrum of $(t\text{Bu}_3\text{Si})(\text{Me}_3\text{Ge})\text{B}(\text{NMe}_2)$, **3-12** (C_6D_6 , 193 MHz, 298 K).

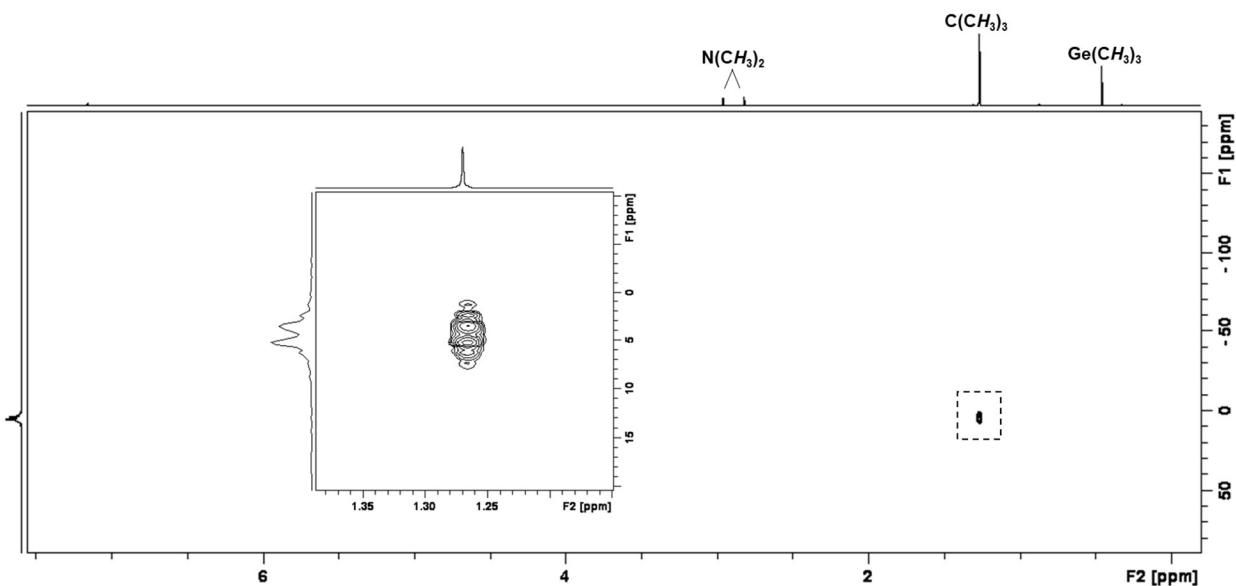


Figure A3.23: ^{29}Si - ^1H HMBC NMR spectrum of $(t\text{Bu}_3\text{Si})(\text{Me}_3\text{Ge})\text{B}(\text{NMe}_2)$, **3-12** (C_6D_6 , 600/119 MHz, 298 K). F1 axis is an internal ^{29}Si NMR projection.

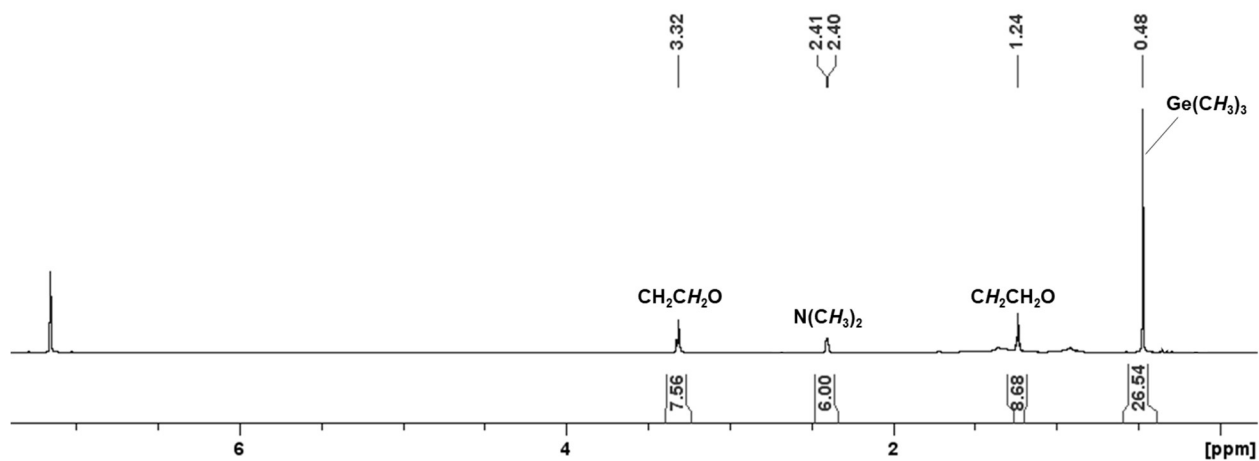


Figure A3.24: ^1H NMR spectrum of $\{(\text{Me}_3\text{Ge})_3\text{B}(\text{NMe}_2)\}\text{Li}(\text{THF})_2$, **3-13** (C_6D_6 , 600 MHz, 298 K).

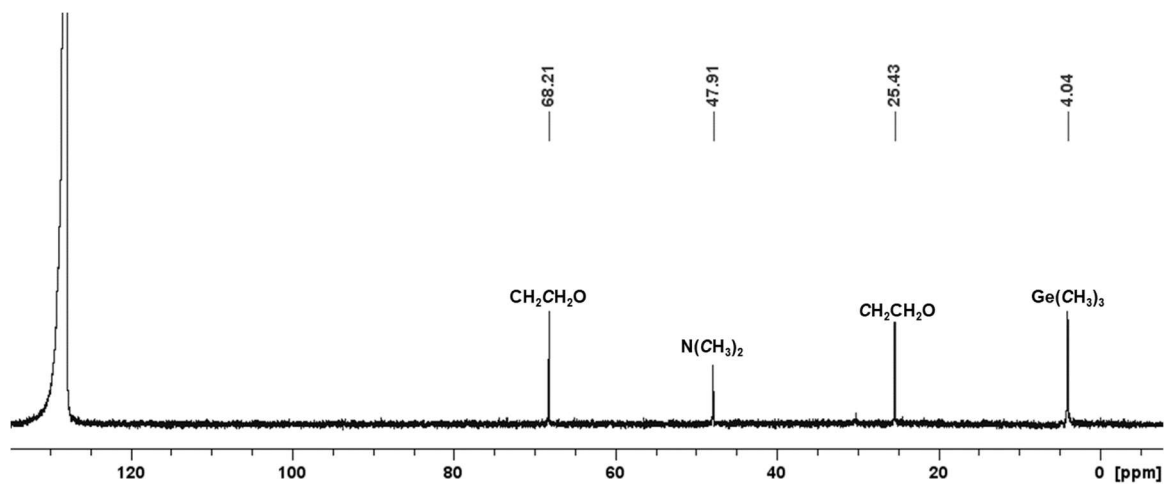


Figure A3.25: $^{13}\text{C}\{^1\text{H}\}$ NMR spectrum of $\{(\text{Me}_3\text{Ge})_3\text{B}(\text{NMe}_2)\}\text{Li}(\text{THF})_2$, **3-13** (C_6D_6 , 151 MHz, 298 K).

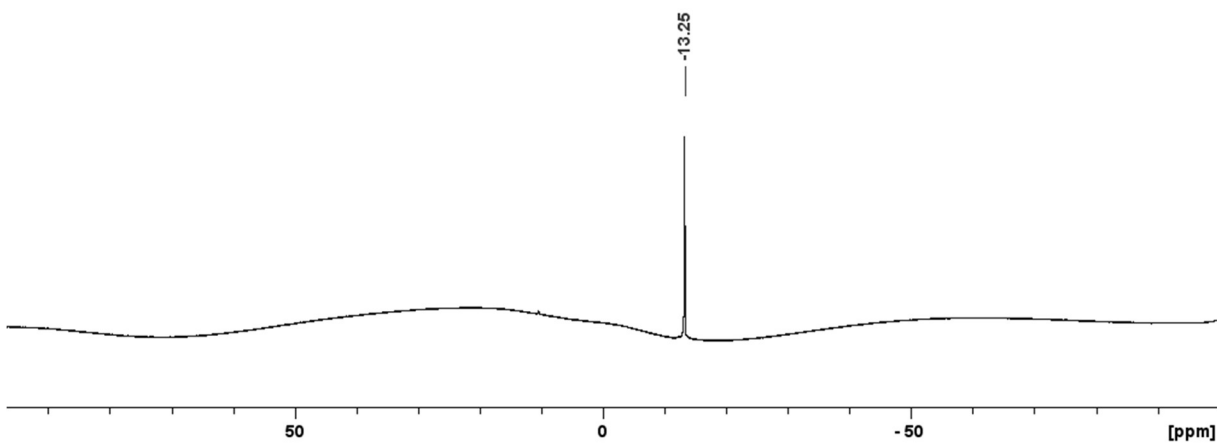


Figure A3.26: $^{11}\text{B}\{^1\text{H}\}$ NMR spectrum of $\{(\text{Me}_3\text{Ge})_3\text{B}(\text{NMe}_2)\}\text{Li}(\text{THF})_2$, **3-13** (C_6D_6 , 193 MHz, 298 K).

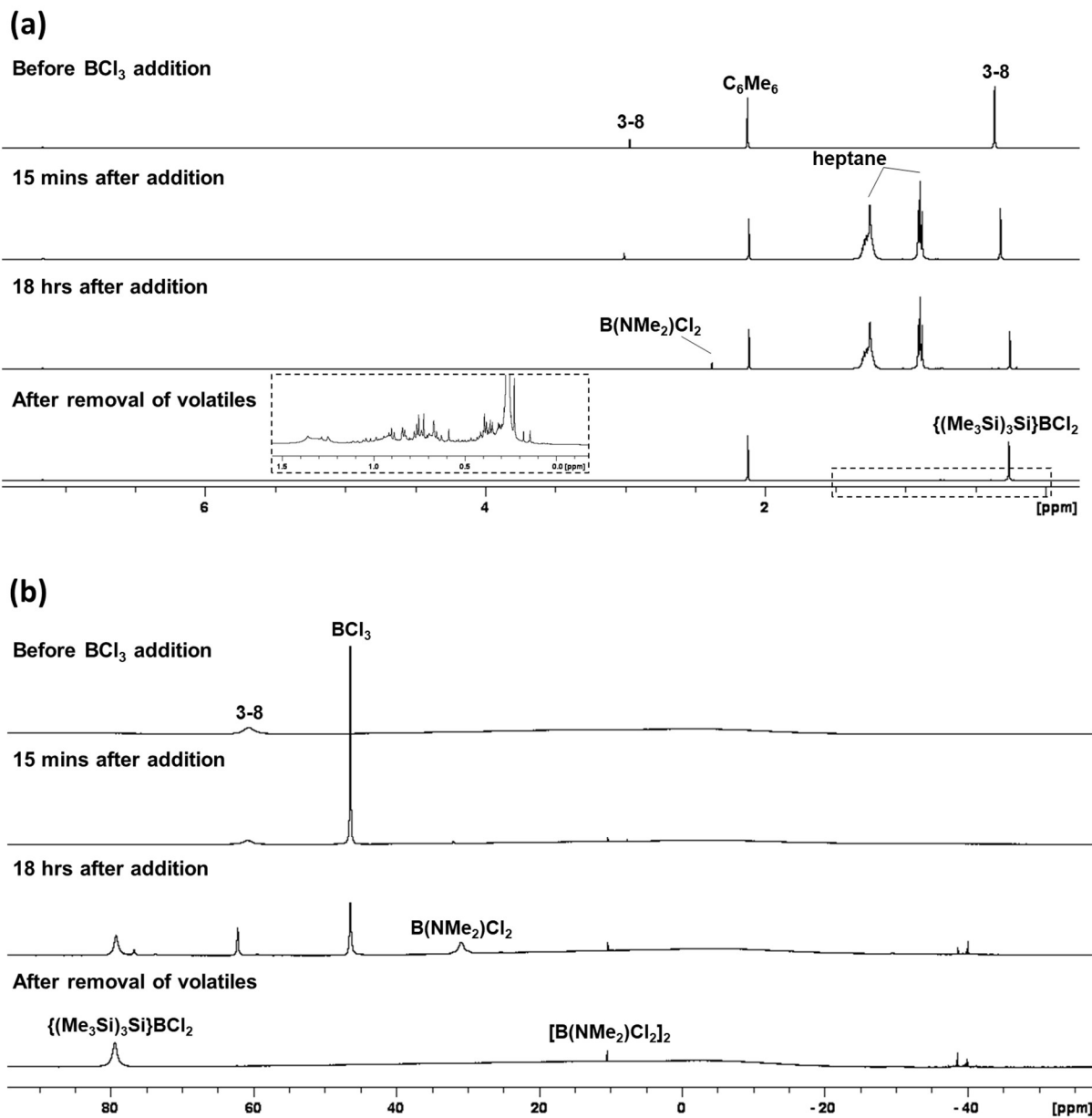


Figure A3.27: Monitoring the NMR-scale test reaction between $\{(\text{Me}_3\text{Si})_3\text{Si}\}_2\text{B}(\text{NMe}_2)$ (**3-8**) and excess BCl_3 (1M in heptane) in C_6D_6 , with C_6Me_6 as an internal standard. Identified NMR signals (based on known compounds in literature) are labelled throughout. (a) ^1H NMR spectra (500 MHz, 298 K); (b) $^{11}\text{B}\{^1\text{H}\}$ NMR spectra (126 MHz, 298 K).

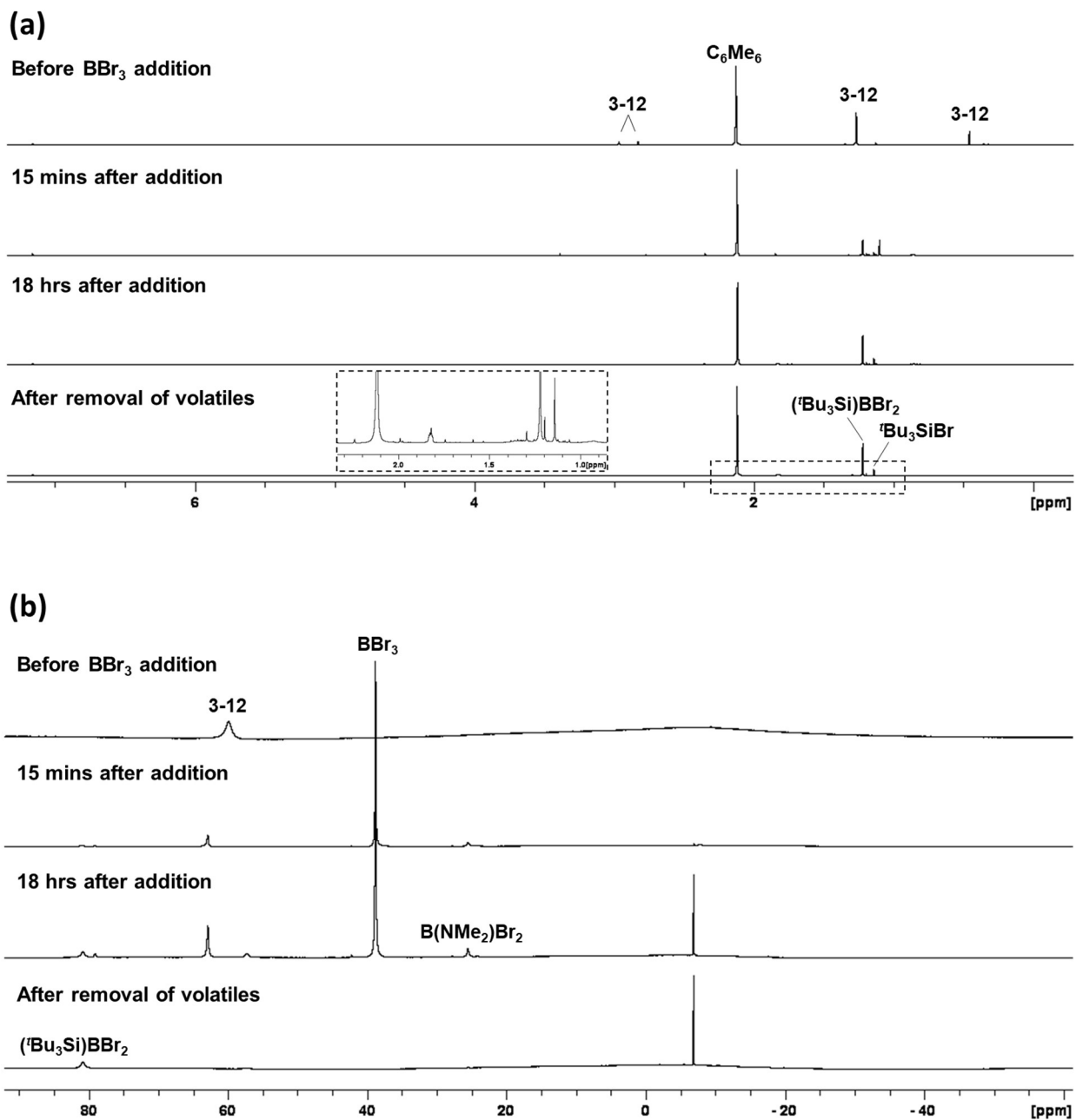


Figure A3.28: Monitoring the NMR-scale test reaction between ($t\text{Bu}_3\text{Si}$)(Me_3Ge) $\text{B}(\text{NMe}_2)$ (**3-12**) and excess BBr_3 in C_6D_6 , with C_6Me_6 as an internal standard. Identified NMR signals (based on known compounds in literature) are labelled throughout. (a) ^1H NMR spectra (500 MHz, 298 K); (b) $^{11}\text{B}\{^1\text{H}\}$ NMR spectra (126 MHz, 298 K).

A4.1 – Supplementary Information Related to Chapter 4

<u>Contents</u>	<u>Pages</u>
Plots of Film Thickness versus Reactant Pulse times for Annealed Films	A48
Representative VASE Measurements of Unannealed and Annealed Films	A48-49
XPS Data for Unannealed and Annealed Films	A50-51
Room Temperature and Low Temperature NMR spectra of 4-1 , 4-2(C₆H₆)₃ , and 4-2	A52-57
FT-IR Spectrum of 4-2	A58
¹³ C{ ¹ H} NMR Spectra of the Decomposition By-Products of 4-1	A58-59
Gas Chromatogram of the Non-Room Temperature-Volatile Decomposition By-Products of 4-1	A60
Mass Spectra of the Decomposition By-Products of 4-1	A61-65
X-ray crystal structures of 4-2(C₆H₆)₃ and 4-2	A66-68
Continuous Shape Measure (CSM) data for 4-1(C₆H₆)₃ , 4-1 , and 4-2	A69-70

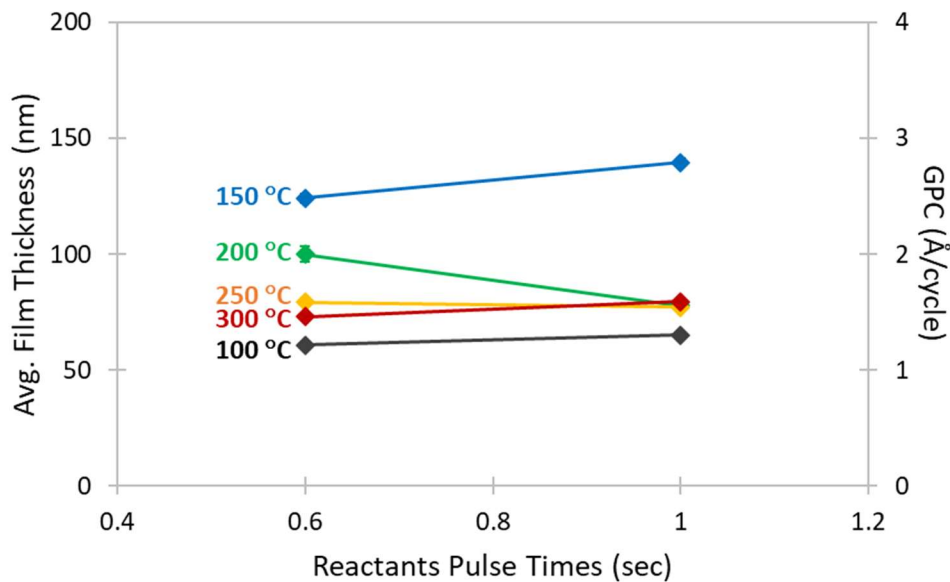


Figure A4.1: Dependence of average film thickness and growth rate on $[\text{Hf}(\text{NMeEt})_4]$ and IVA pulse times at a given deposition temperature. All films were deposited on SiO_2/Si using 500 cycles and annealed *in situ* at 400 °C for 1 hour.

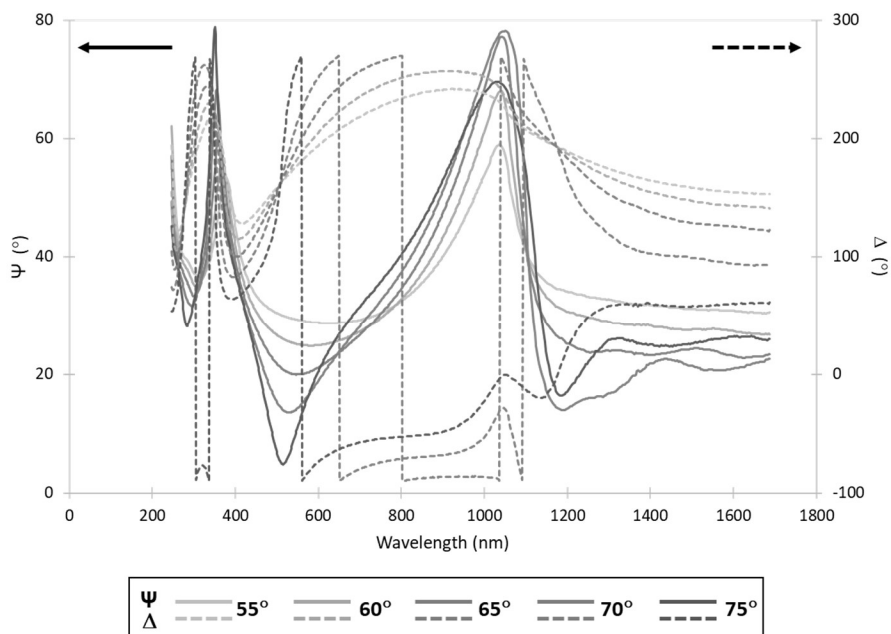


Figure A4.2: Measured values of Psi (Ψ , solid lines) and Delta (Δ , dashed lines) as a function of wavelength for an as-deposited HfO_2 film grown on SiO_2/Si at 100 °C (500 cycles, 0.6 second pulse and 60 second purge times).

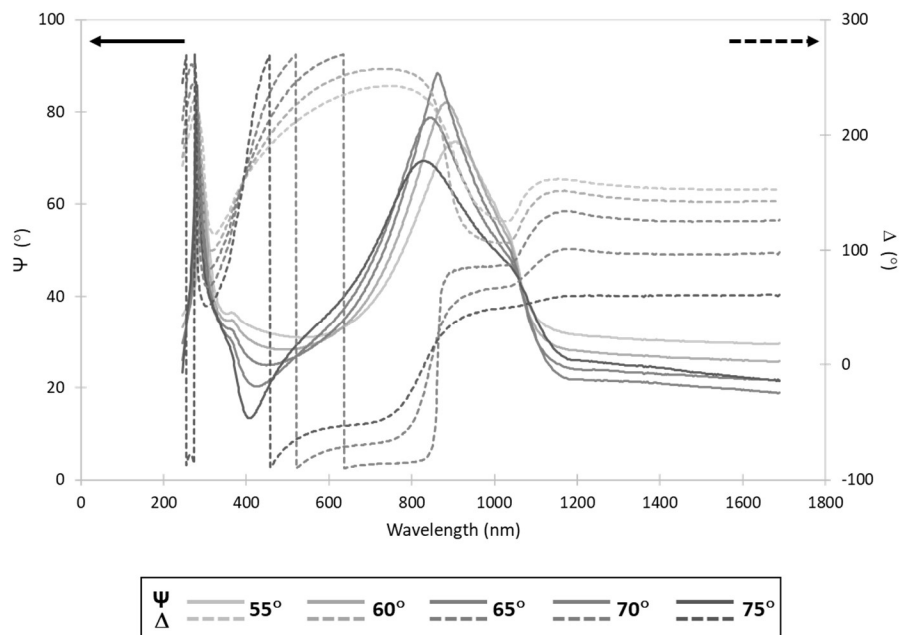


Figure A4.3: Measured values of Psi (Ψ , solid lines) and Delta (Δ , dashed lines) as a function of wavelength for an annealed HfO_2 film grown on SiO_2/Si at 100°C (500 cycles, 0.6 second pulse and 60 second purge times), followed by *in situ* annealing at 400°C for 1 hour.

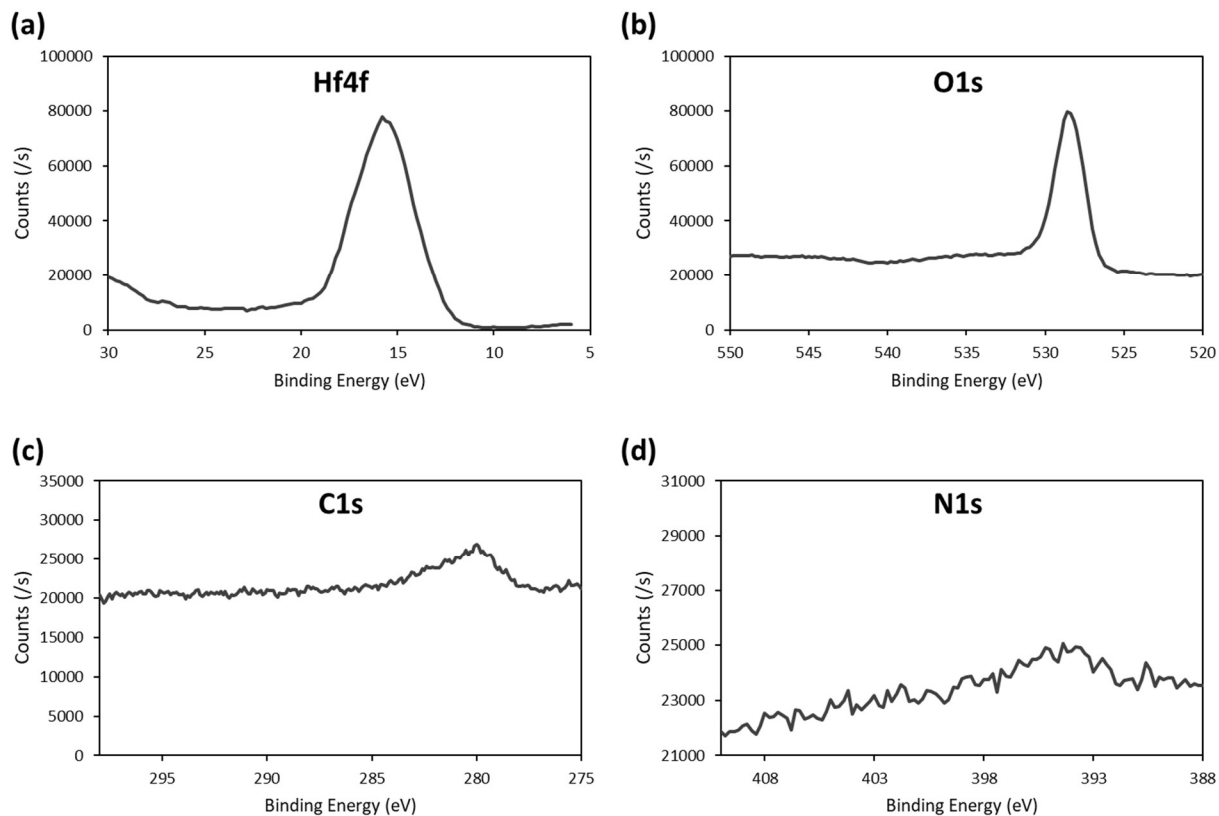


Figure A4.4: XPS data at Etch Level 20 of the as-deposited film grown on SiO₂/Si in the energy regions for (a) Hf4f, (b) O1s, (c) C1s, and (d) N1s. Thin films were grown at 100 °C using 500 cycles and 1 s reactant pulse times and 20 s purge times. For this preliminary data, initial deposition conditions used argon flow rates totaling 260 sccm (providing an internal pressure of 630 mTorr during operation), and IVA was delivered at 50 °C.

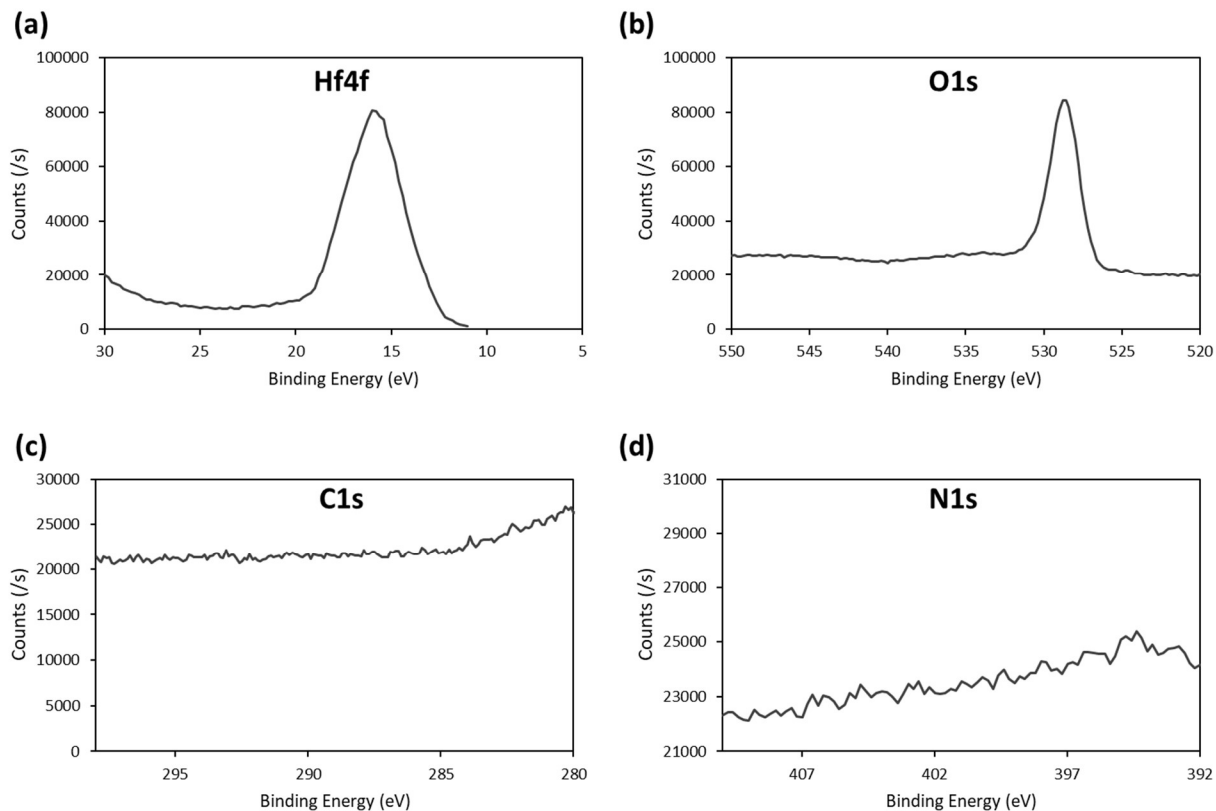


Figure A4.5: XPS data at Etch Level 12 of the thermally annealed film grown on SiO₂/Si in the energy regions for (a) Hf4f, (b) O1s, (c) C1s, and (d) N1s. Thin films were grown at 100 °C using 500 cycles and 1 s reactant pulse times and 20 s purge times. For this preliminary data, initial deposition conditions used argon flow rates totaling 260 sccm (providing an internal pressure of 630 mTorr during operation), and IVA was delivered at 50 °C.

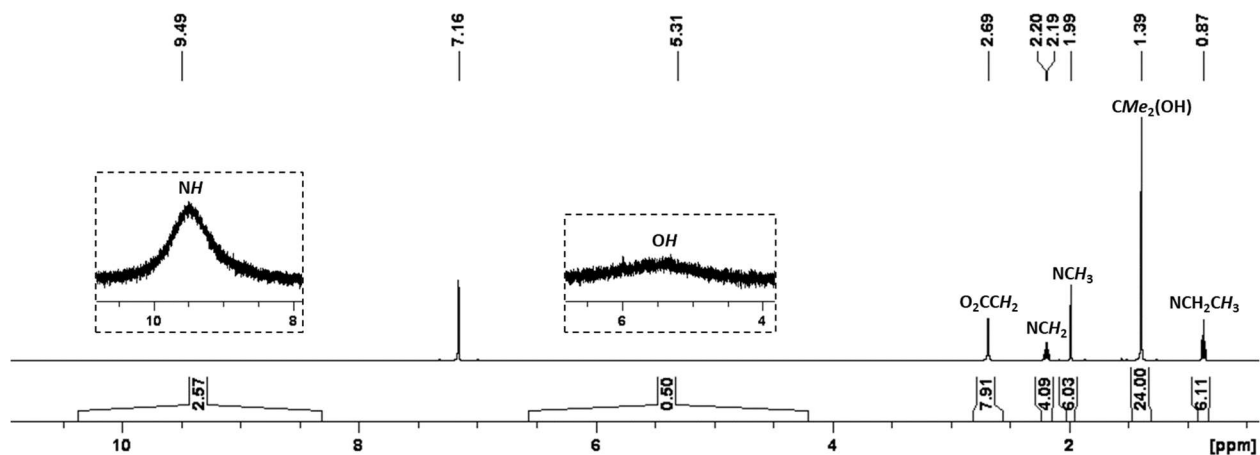


Figure A4.6: ^1H NMR spectrum of $[\text{EtMeNH}_2]_2[\text{Hf}(\kappa^2\text{-O}_2\text{CCH}_2\text{CMe}_2\text{OH})_2(\kappa^2\text{-OC(O)CH}_2\text{CMe}_2\text{O})_2]$ (**4-1**) in C_6D_6 (500 MHz, 298 K).

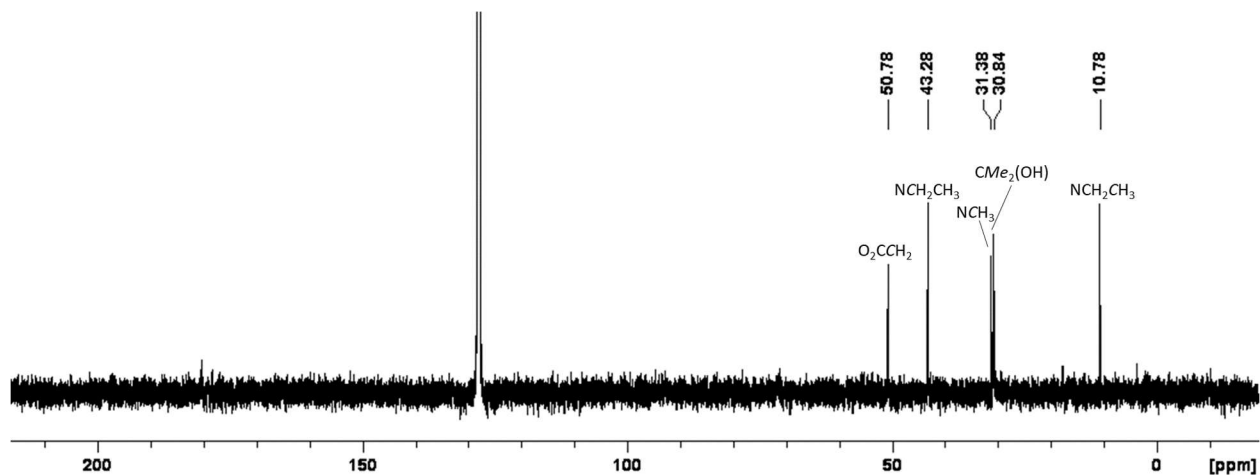


Figure A4.7: $^{13}\text{C}\{^1\text{H}\}$ NMR spectrum of $[\text{EtMeNH}_2]_2[\text{Hf}(\kappa^2\text{-O}_2\text{CCH}_2\text{CMe}_2\text{OH})_2(\kappa^2\text{-OC(O)CH}_2\text{CMe}_2\text{O})_2]$ (**4-1**) in C_6D_6 (126 MHz, 298 K).

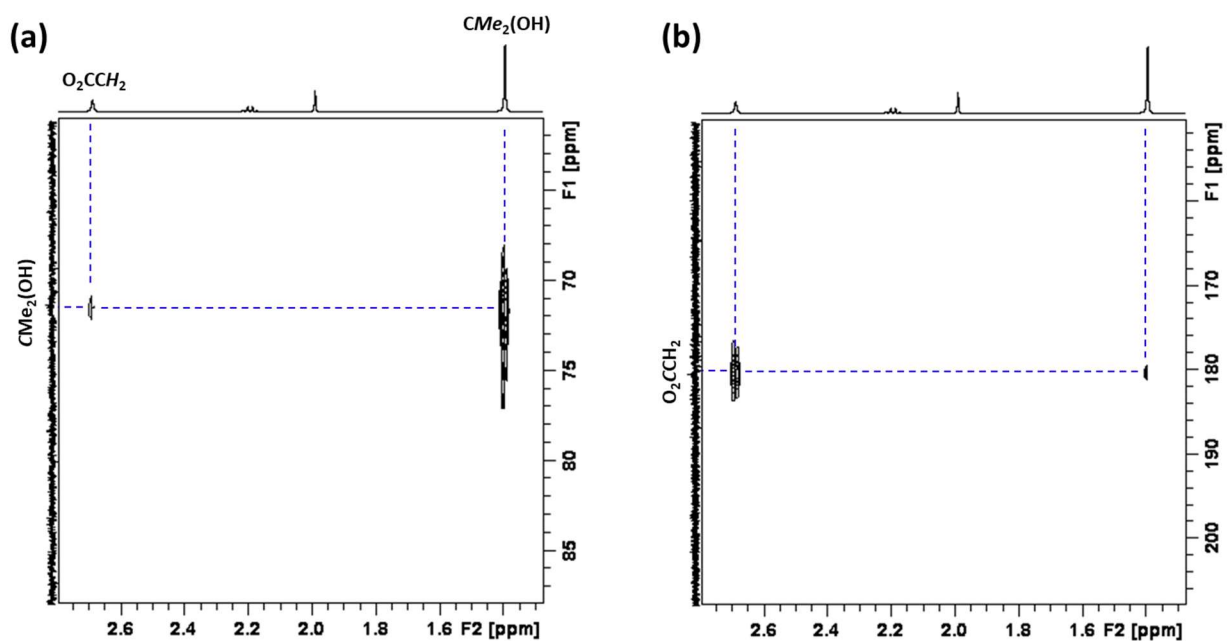


Figure A4.8: Select areas of the ^{13}C - ^1H HMBC NMR spectrum of $[\text{EtMeNH}_2]_2[\text{Hf}(\kappa^2\text{-O}_2\text{CCH}_2\text{CMe}_2\text{OH})_2(\kappa^2\text{-OC(O)CH}_2\text{CMe}_2\text{O})_2]$ (**4-1**) in C_6D_6 (600/151 MHz, 298 K) for the assignment of the (a) $\text{CMe}_2(\text{OH})\text{Me}_2$ and (b) O_2CCH_2 ^{13}C NMR signals.

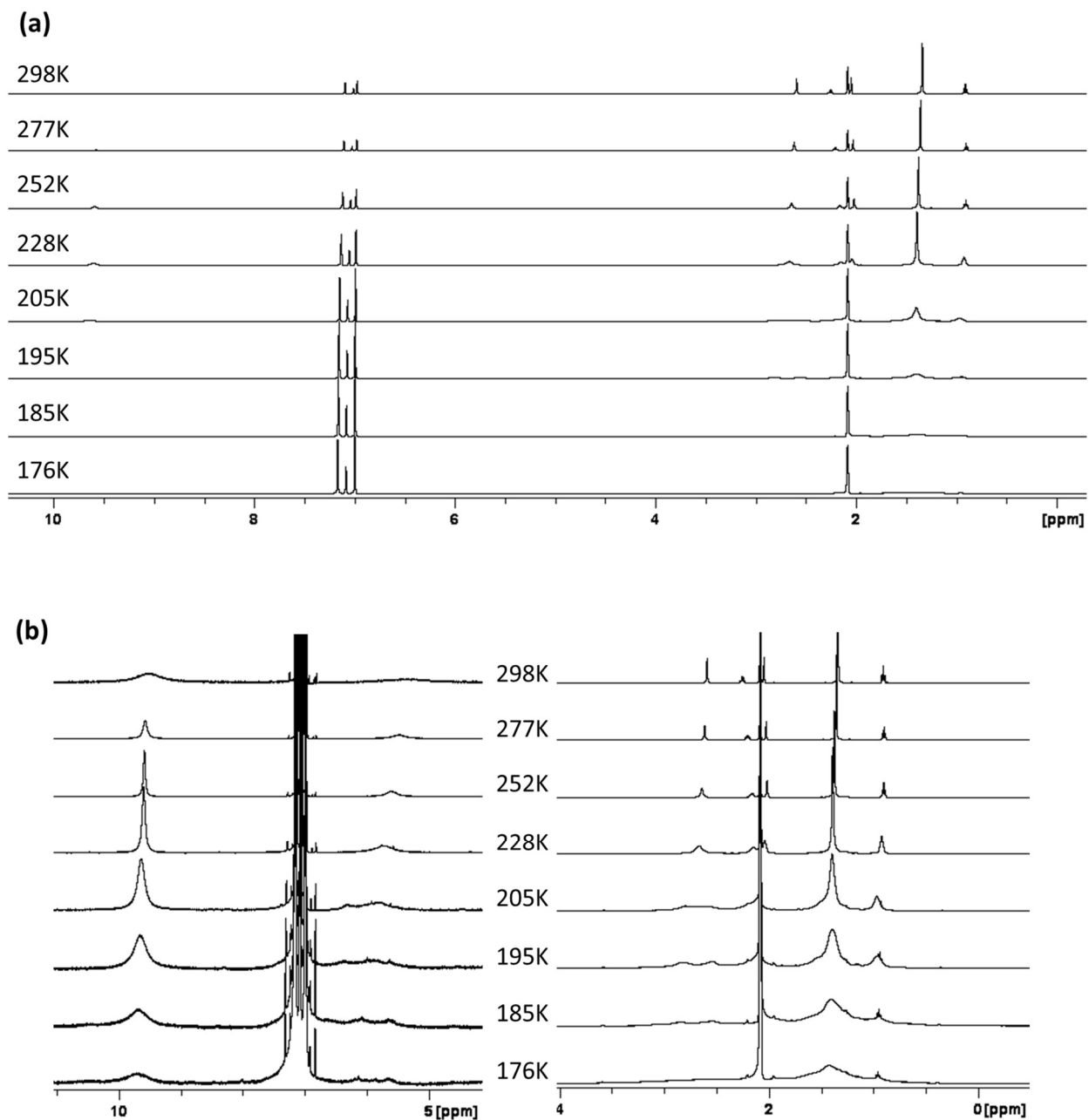


Figure A4.9: Variable temperature ^1H NMR spectra of $[\text{EtMeNH}_2]_2[\text{Hf}(\kappa^2\text{-O}_2\text{CCH}_2\text{CMe}_2\text{OH})_2(\kappa^2\text{-OC(O)CH}_2\text{CMe}_2\text{O})_2]$ (**4-1**) in $d_8\text{-tol}$ (500 MHz). (b) Magnified regions of the ^1H NMR spectra.

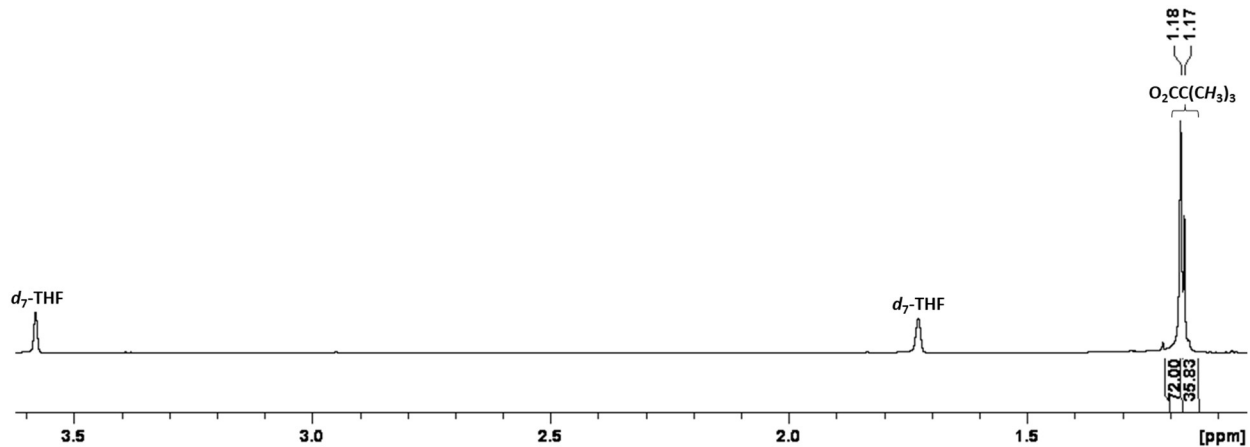


Figure A4.10: ^1H NMR spectrum of $[\text{Hf}_5(\text{O})_4(\mu\text{-O}_2\text{C}^t\text{Bu})_8(\kappa^2\text{-O}_2\text{C}^t\text{Bu})_4]$ (**4-2**) in d_8 -THF (600 MHz, 298 K).

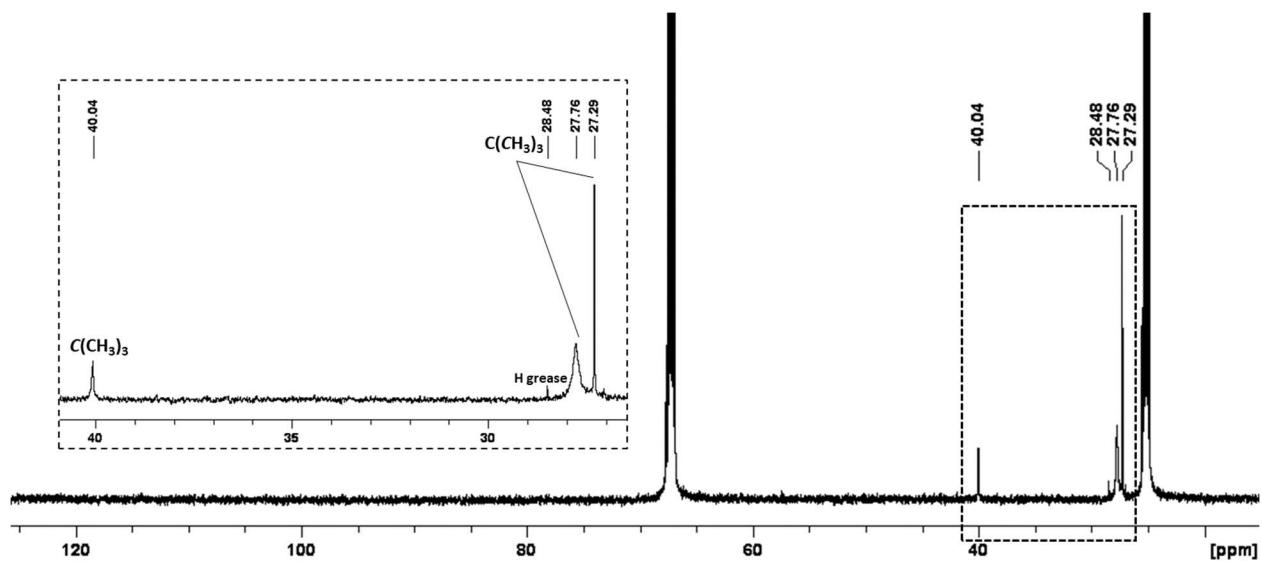


Figure A4.11: $^{13}\text{C}\{^1\text{H}\}$ NMR spectrum of $[\text{Hf}_5(\text{O})_4(\mu\text{-O}_2\text{C}^t\text{Bu})_8(\kappa^2\text{-O}_2\text{C}^t\text{Bu})_4]$ (**4-2**) in d_8 -THF (151 MHz, 298 K).

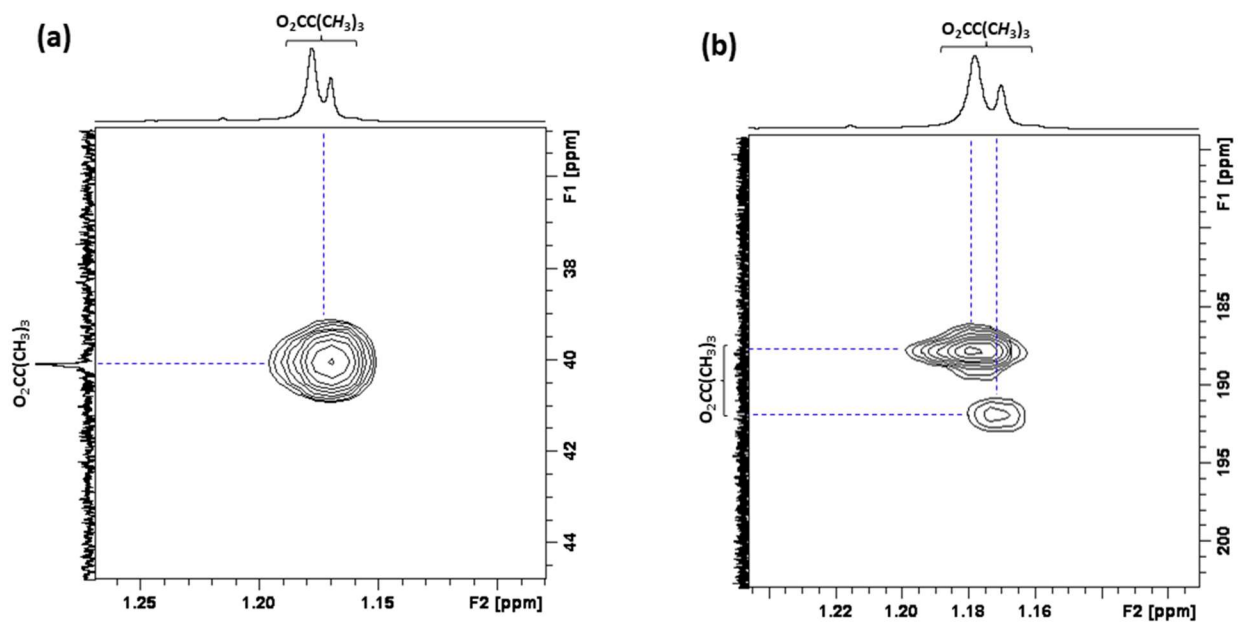


Figure A4.12: Select areas of the ^{13}C - ^1H HMBC NMR spectrum of $[\text{Hf}_5(\text{O})_4(\mu\text{-O}_2\text{C}^t\text{Bu})_8(\kappa^2\text{-O}_2\text{C}^t\text{Bu})_4]$ (**4-2**) in d_8 -THF (600/151 MHz, 298 K) for the assignment of the (a) $\text{O}_2\text{CC}(\text{CH}_3)_3$ and (b) $\text{O}_2\text{CC}(\text{CH}_3)_3$ ^{13}C NMR signals.

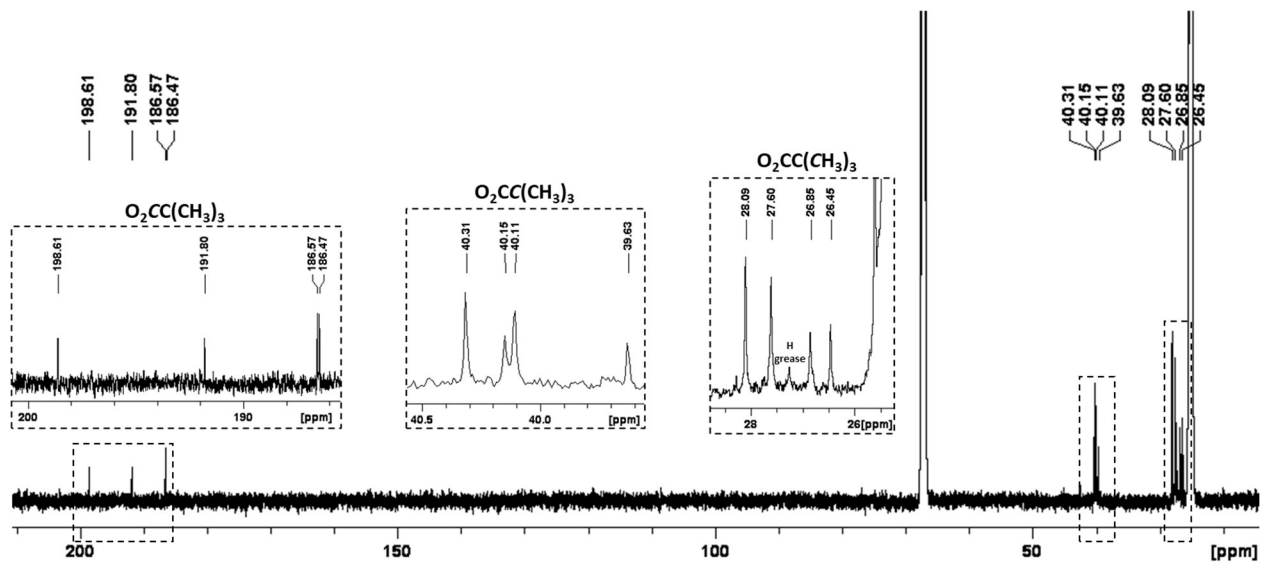


Figure A4.13: Low-temperature $^{13}\text{C}\{^1\text{H}\}$ NMR spectrum of $[\text{Hf}_5(\text{O})_4(\mu\text{-O}_2\text{C}^t\text{Bu})_8(\kappa^2\text{-O}_2\text{C}^t\text{Bu})_4]$ (**4-2**) in d_8 -THF (151 MHz, 176 K).

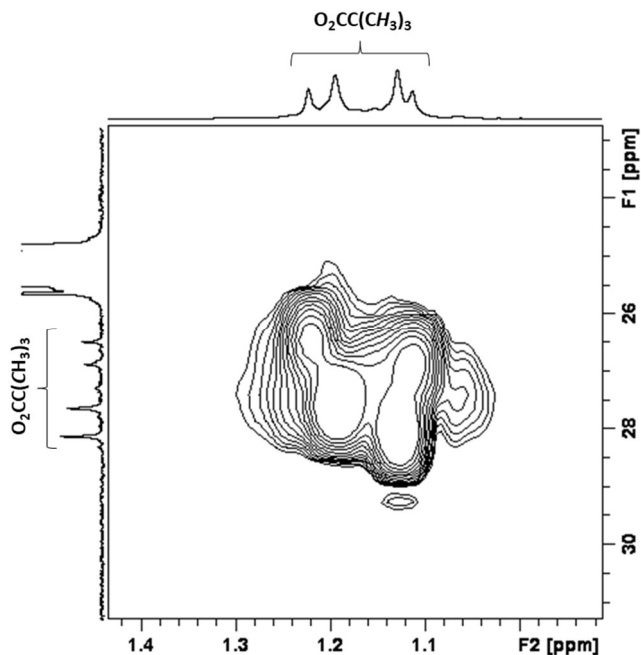


Figure A4.14: Select area of the low-temperature ^{13}C - ^1H HSQC NMR spectrum of $[\text{Hf}_5(\text{O})_4(\mu\text{-O}_2\text{C}^t\text{Bu})_8(\kappa^2\text{-O}_2\text{C}^t\text{Bu})_4]$ (**4-2**) in d_8 -THF (600/151 MHz, 176 K) for the assignment of the $\text{O}_2\text{CC}(\text{CH}_3)_3$ ^{13}C NMR signals.

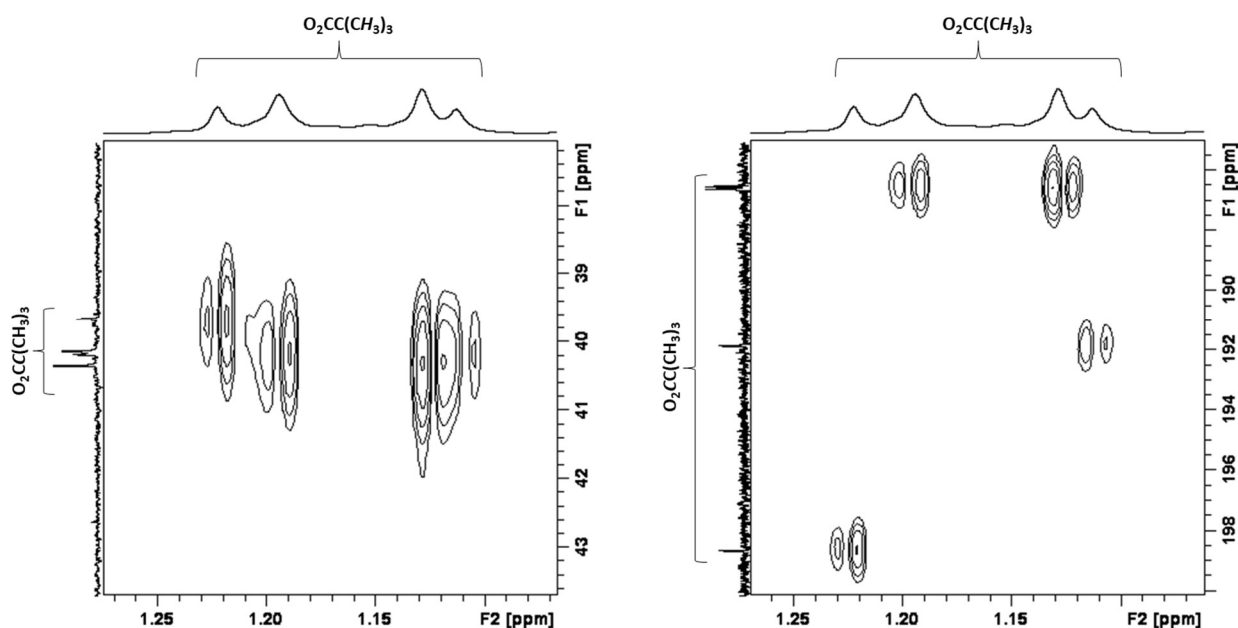


Figure A4.15: Select areas of the low-temperature ^{13}C - ^1H HMBC NMR spectrum of $[\text{Hf}_5(\text{O})_4(\mu\text{-O}_2\text{C}^t\text{Bu})_8(\kappa^2\text{-O}_2\text{C}^t\text{Bu})_4]$ (**4-2**) in d_8 -THF (600/151 MHz, 176 K) for the assignment of the (a) $\text{O}_2\text{CC}(\text{CH}_3)_3$ and (b) $\text{O}_2\text{CC}(\text{CH}_3)_3$ ^{13}C NMR signals.

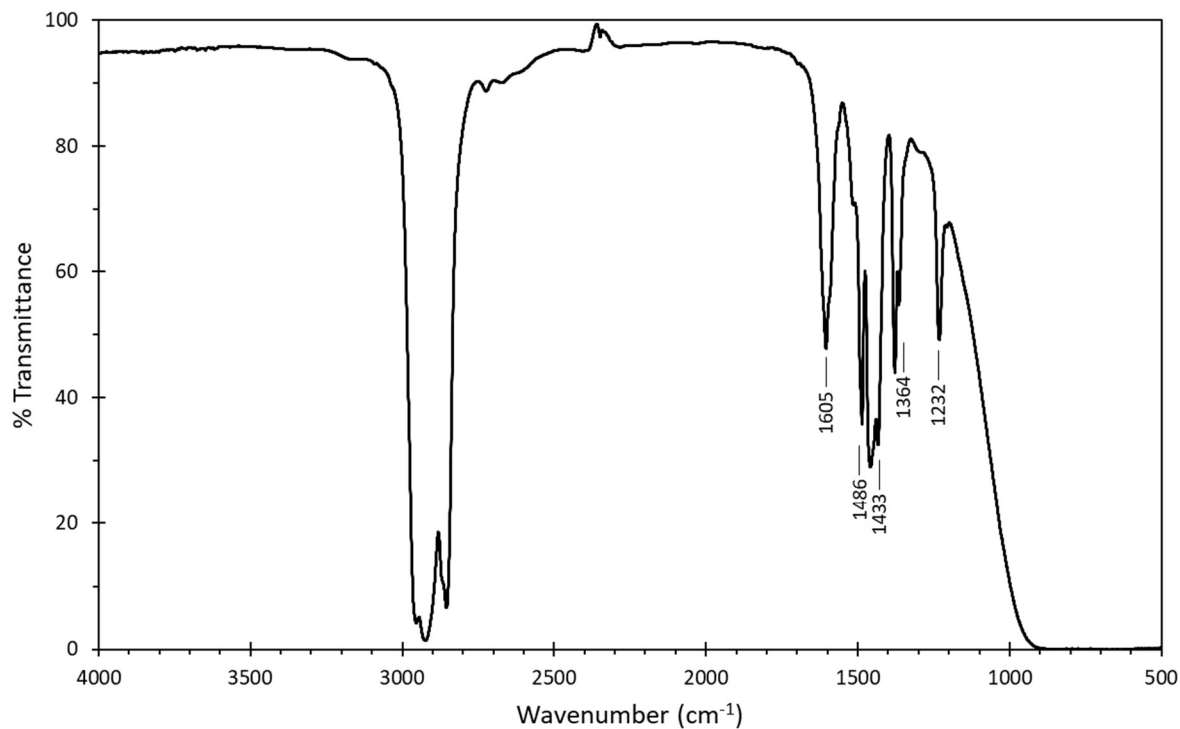
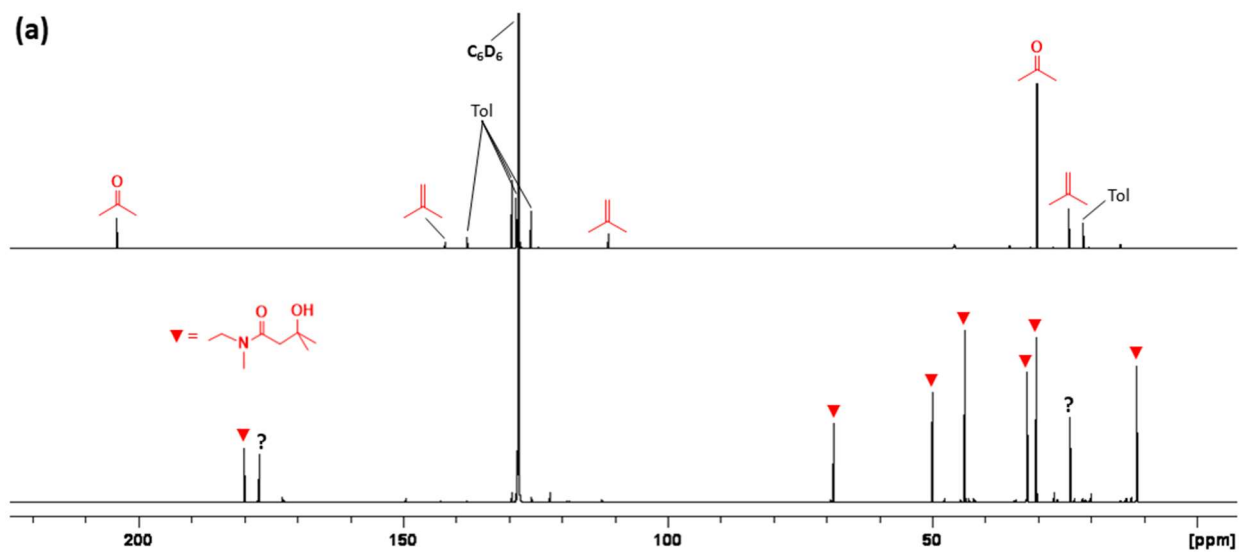


Figure A4.16: FT-IR spectrum of $[\text{Hf}_5(\text{O})_4(\mu\text{-O}_2\text{C}^t\text{Bu})_8(\kappa^2\text{-O}_2\text{C}^t\text{Bu})_4]$ (**4-2**) in a Nujol mull.



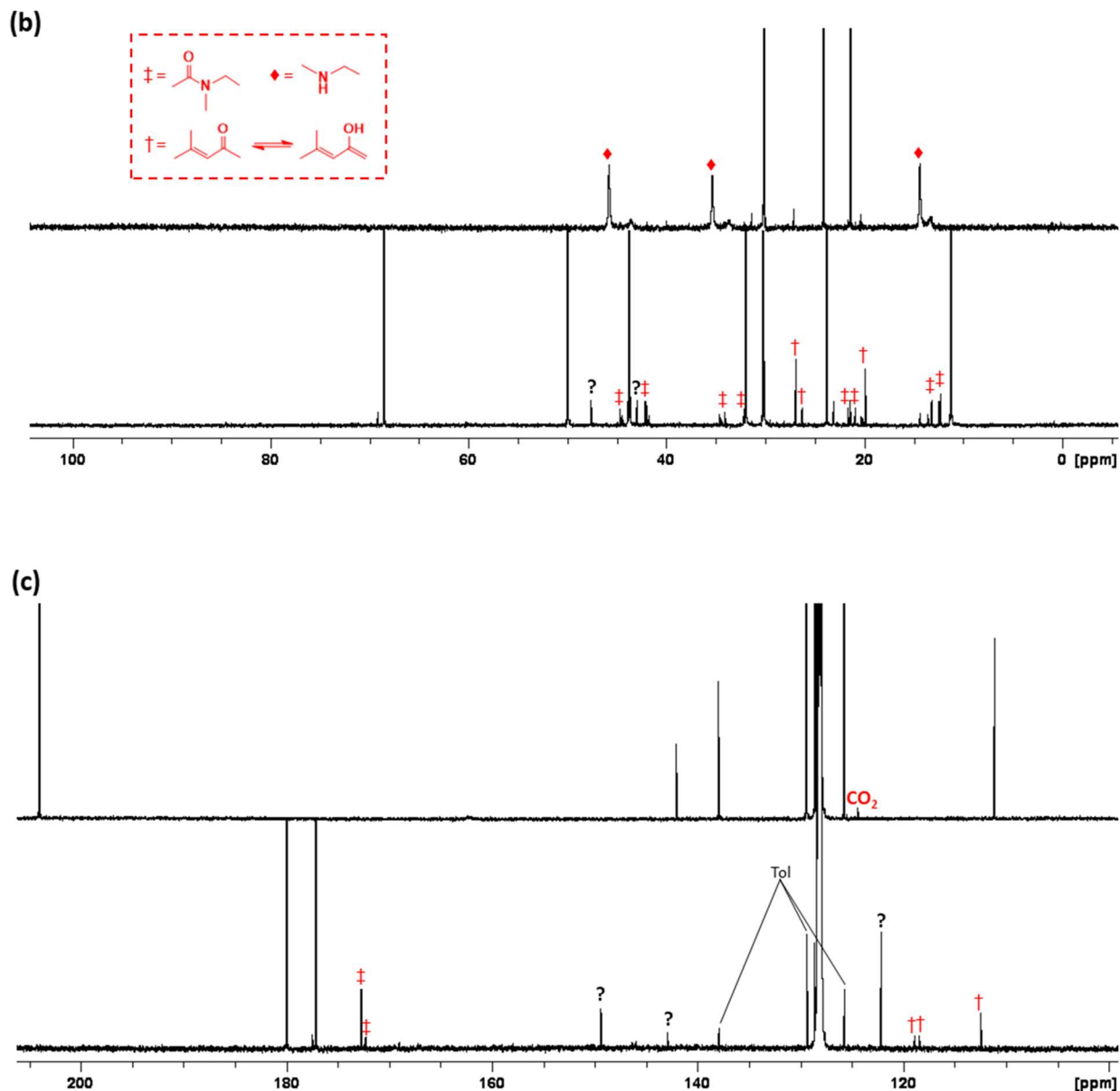


Figure A4.17: (a) $^{13}\text{C}\{^1\text{H}\}$ NMR spectra of the by-products (coloured red) from the thermal decomposition of a crude sample of **4-1** at 200 °C for 4 hours under dynamic vacuum (C_6D_6 , 151 MHz, 298 K). Top: Room temperature-volatile by-products vacuum transferred into a degassed J. Young tube containing C_6D_6 . Bottom: Non-room temperature-volatile by-products dissolved in C_6D_6 . (b and c) Magnified regions of (a). Unidentified peaks are labeled with a question mark.

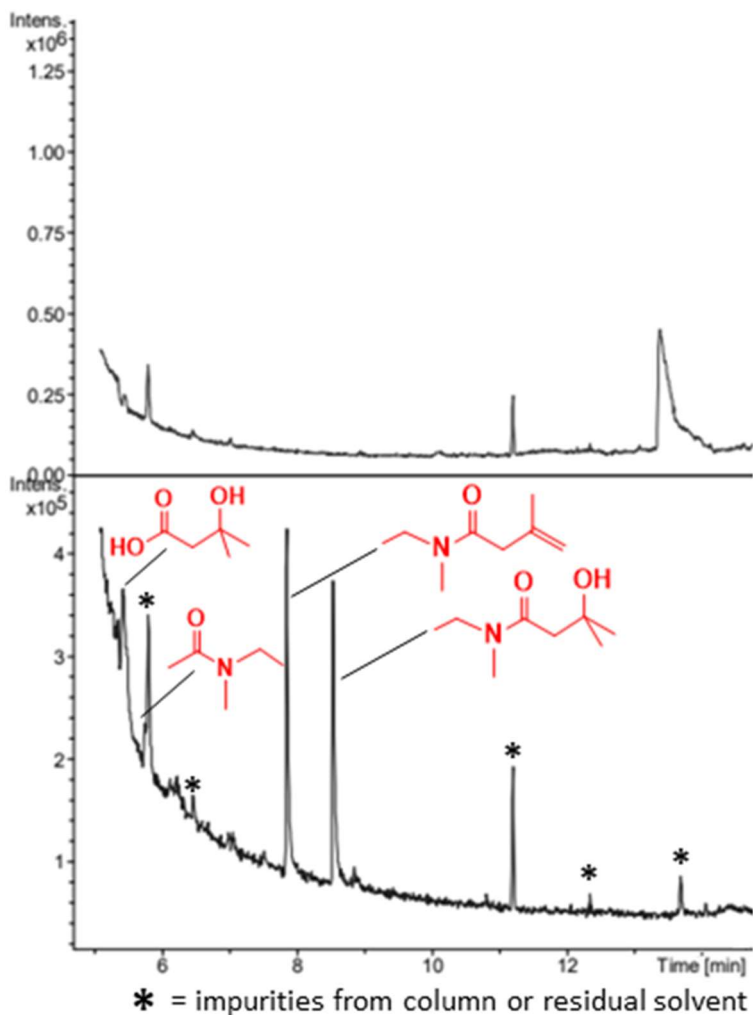


Figure A4.18: Gas chromatogram (mass selective detector) of non-room temperature-volatile by-products (coloured red) formed from heating a crude sample of **4-1** at 200 °C for 4 hours under dynamic vacuum (bottom) and of the experimental blank (top). Peaks at 7.9 and 8.5 min are tentatively assigned based on their MS fragmentation patterns.

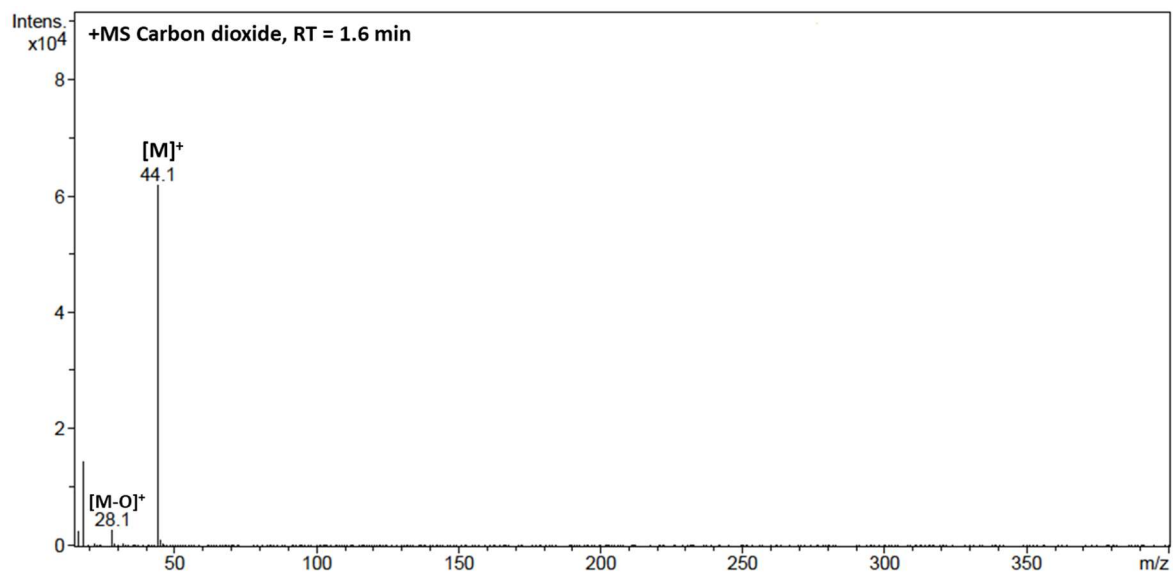


Figure A4.19: Mass spectrum of carbon dioxide detected in the headspace GC-MS sample after heating a crude sample of **4-1** at 200 °C for 4 hours under dynamic vacuum.

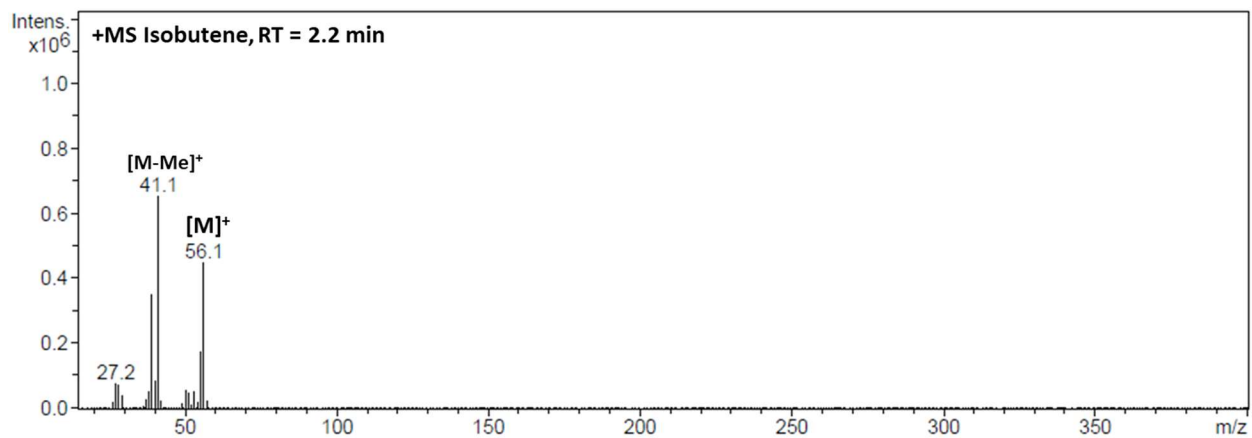


Figure A4.20: Mass spectrum of isobutene detected in the headspace GC-MS sample after heating a crude sample of **4-1** at 200 °C for 4 hours under dynamic vacuum.

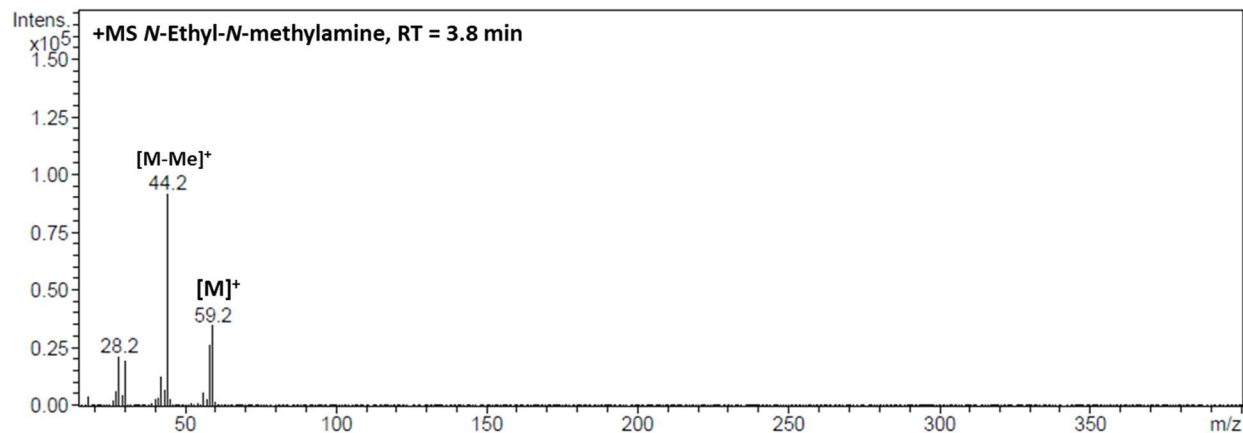


Figure A4.21: Mass spectrum of *N*-ethyl-*N*-methylamine detected in the headspace GC-MS sample after heating a crude sample of **4-1** at 200 °C for 4 hours under dynamic vacuum.

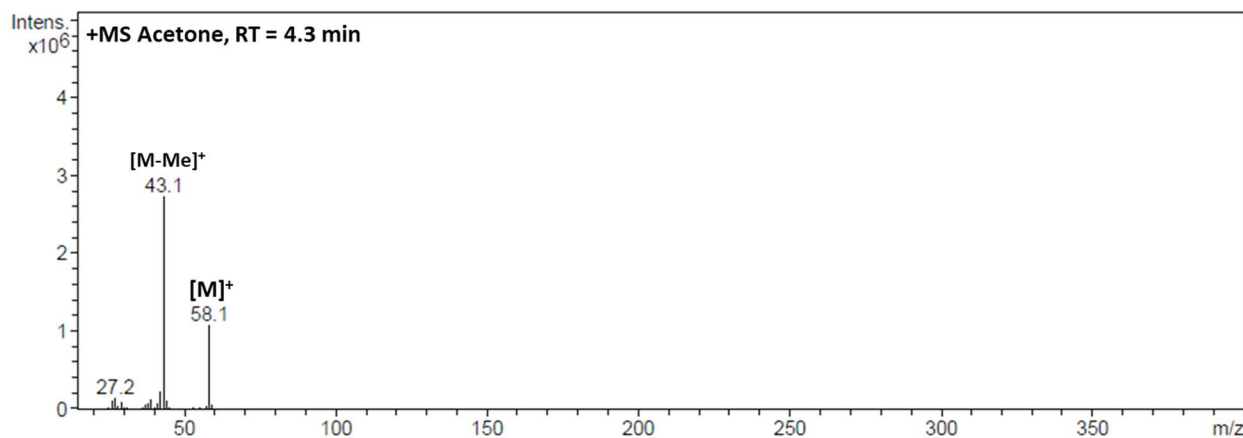


Figure A4.22: Mass spectrum of acetone detected in the headspace GC-MS sample after heating a crude sample of **4-1** at 200 °C for 4 hours under dynamic vacuum.

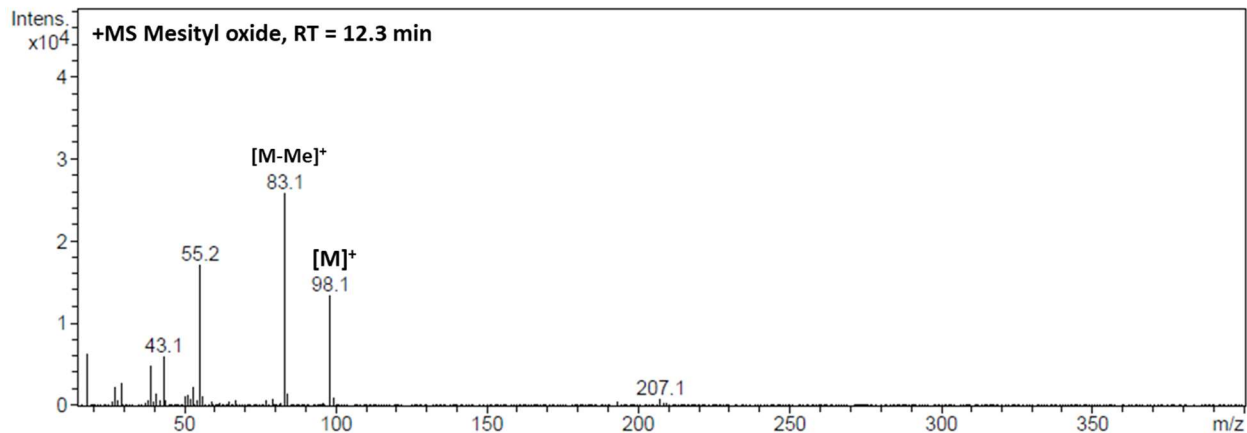


Figure A4.23: Mass spectrum of mesityl oxide detected in the headspace GC-MS sample after heating a crude sample of **4-1** at 200 °C for 4 hours under dynamic vacuum.

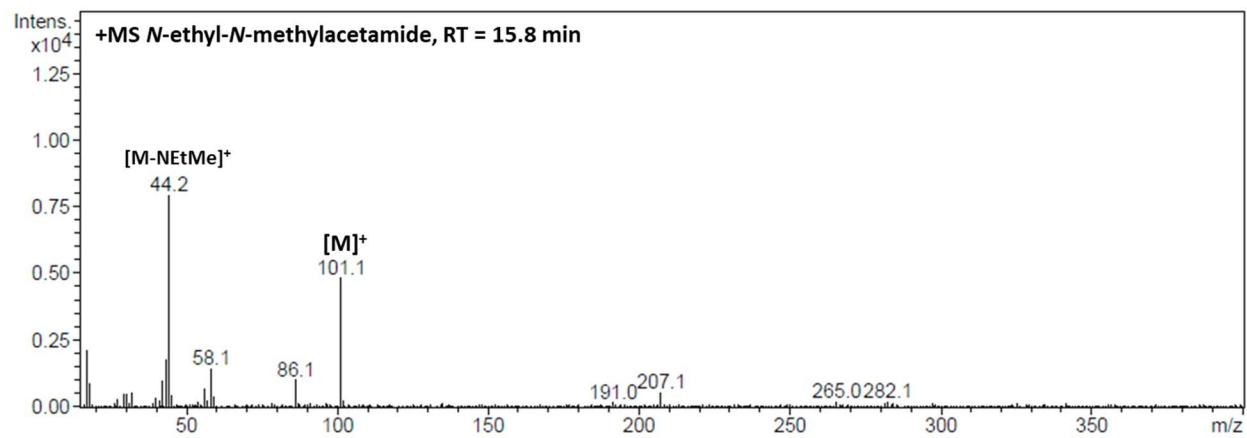


Figure A4.24: Mass spectrum of *N*-ethyl-*N*-methylacetamide detected in the headspace GC-MS sample after heating a crude sample of **4-1** at 200 °C for 4 hours under dynamic vacuum.

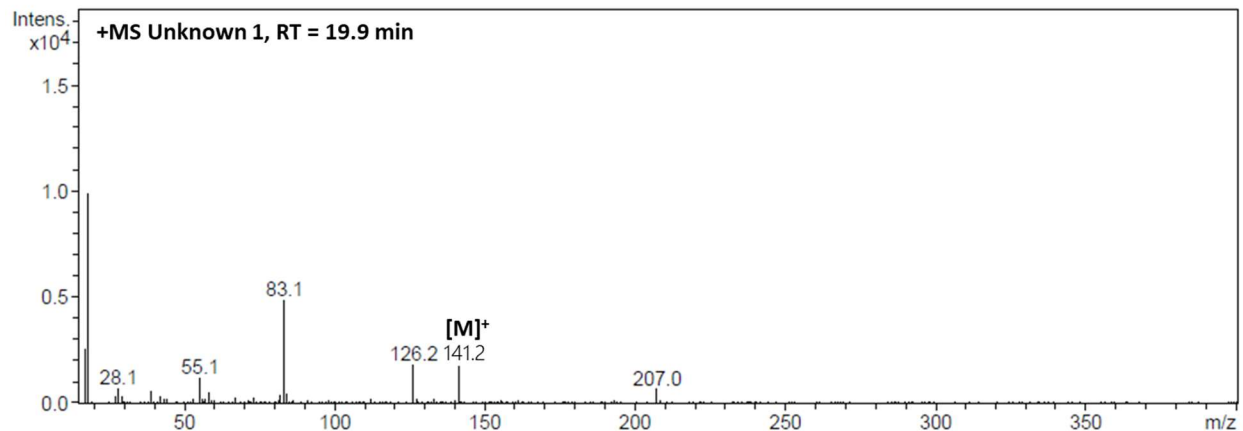


Figure A4.25: Mass spectrum of the unknown compound detected in the headspace GC-MS sample after heating a crude sample of **4-1** at 200 °C for 4 hours under dynamic vacuum.

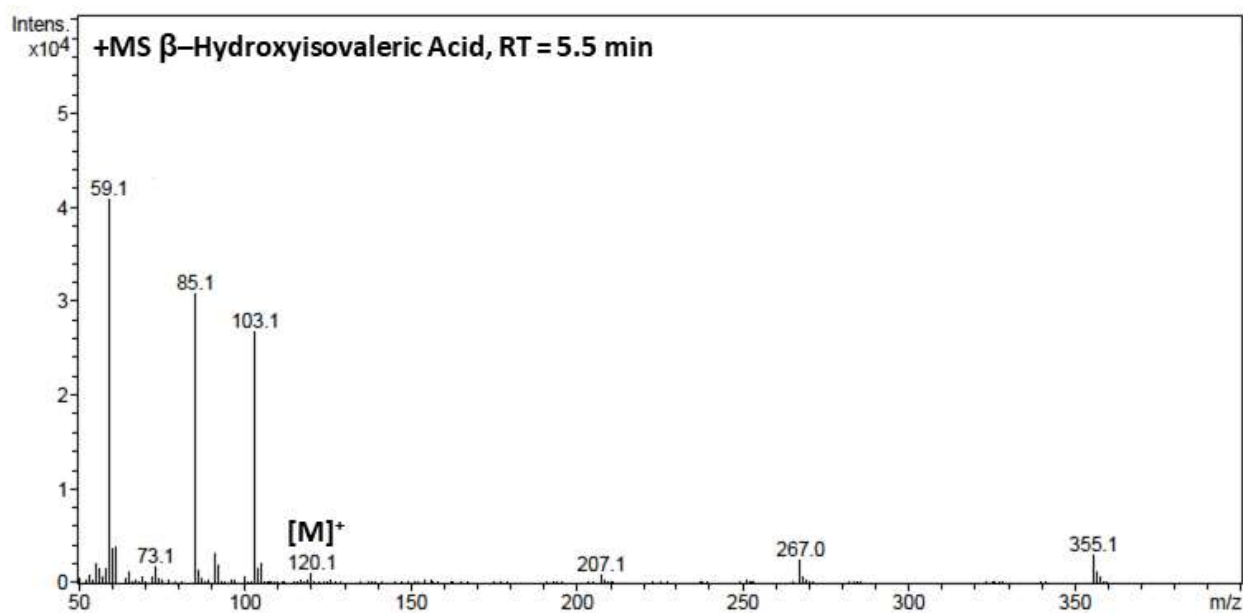


Figure A4.26: Mass spectrum of IVA detected in the GC-MS sample after heating a crude sample of **4-1** at 200 °C for 4 hours under dynamic vacuum.

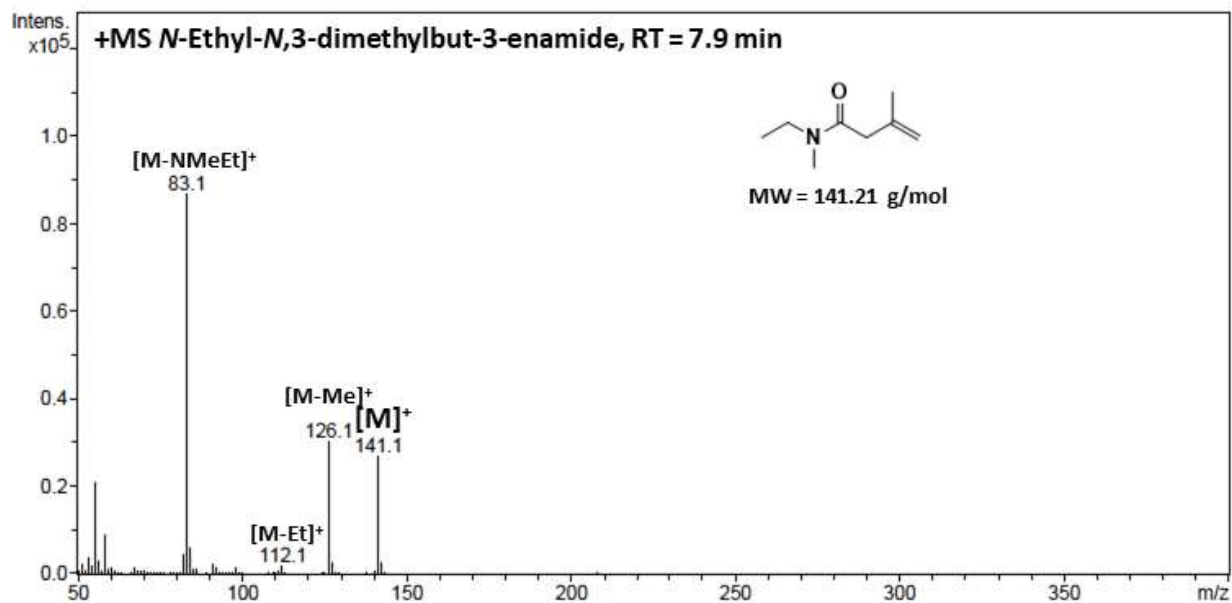


Figure A4.27: Mass spectrum of *N*-ethyl-*N*,3-dimethylbut-3-enamide detected in the GC-MS sample after heating a crude sample of **4-1** at 200 °C for 4 hours under dynamic vacuum. The identity of this compound is tentatively assigned based on the fragmentation pattern.

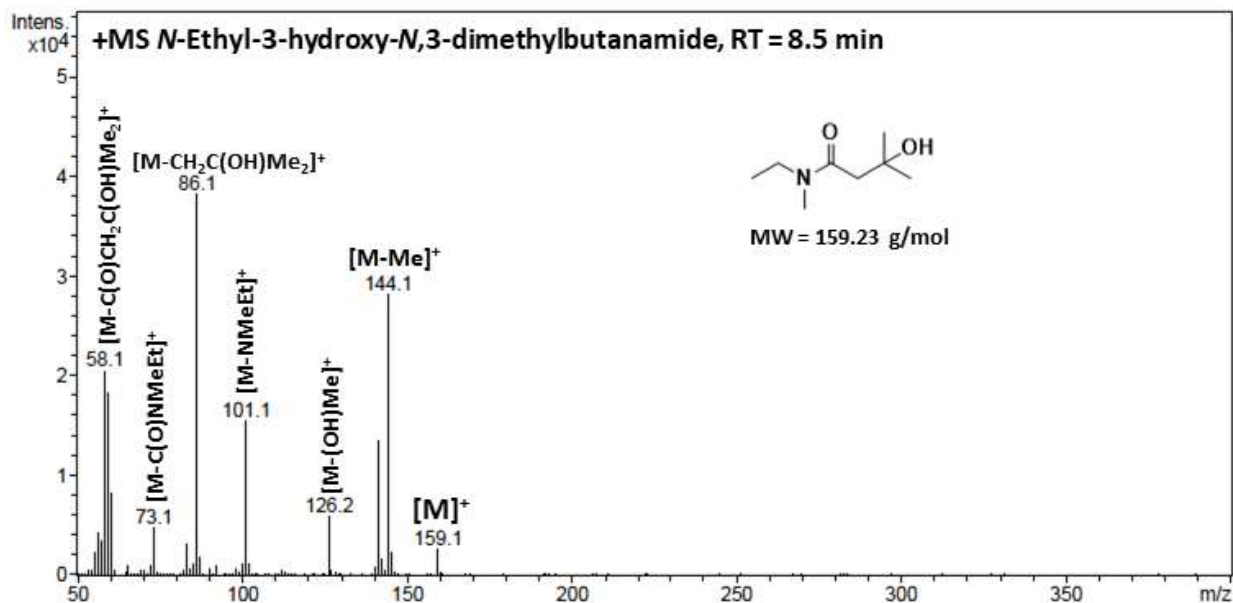


Figure A4.28: Mass spectrum of *N*-ethyl-3-hydroxy-*N*,3-dimethylbutanamide detected in the GC-MS sample after heating a crude sample of **4-1** at 200 °C for 4 hours under dynamic vacuum. The identity of this compound is tentatively assigned based on the fragmentation pattern.

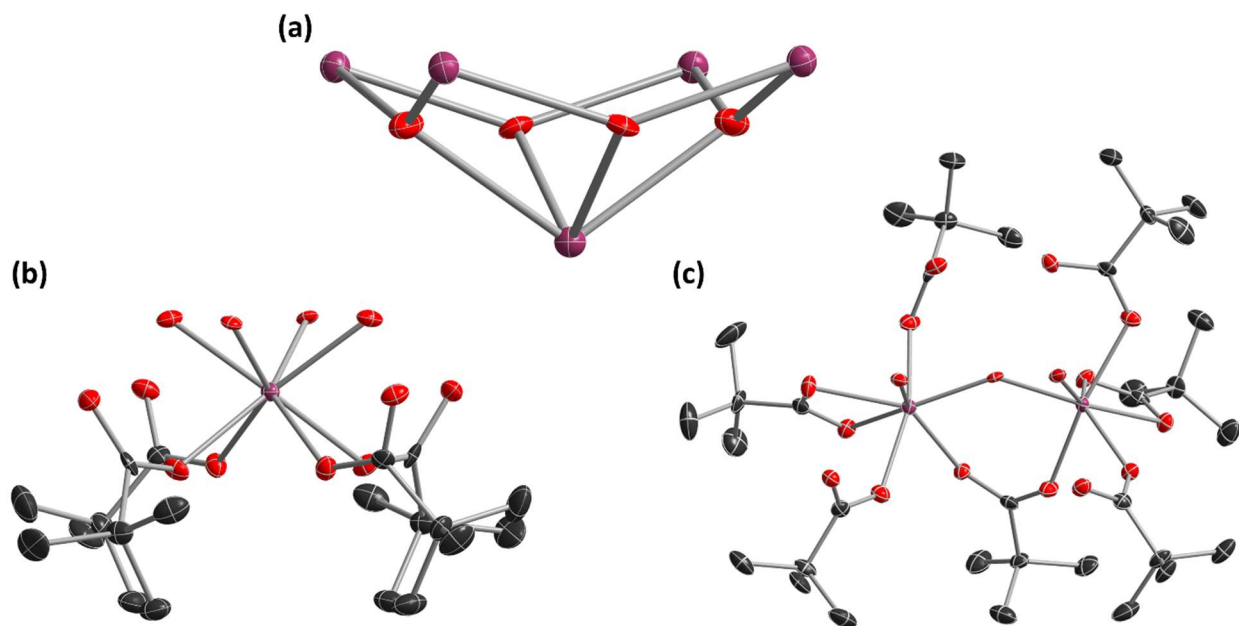


Figure A4.29: (a) Central coordination network of Hf metal centres and bridging oxo ligands observed in the X-ray crystal structure of **4-2(C₆H₆)₃**. (b) Coordination geometry about the apical, square antiprismatic Hf(1) centre of complex **4-2(C₆H₆)₃**. (c) Coordination geometry about the 7-coordinate Hf(2) and Hf(3) centres of complex **4-2(C₆H₆)₃**.

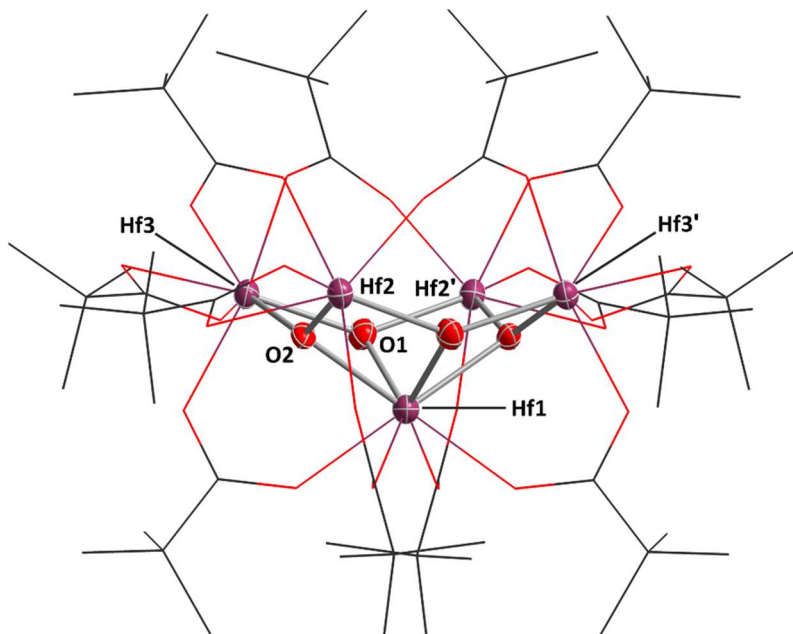


Figure A4.30: X-ray crystal structure of $[\text{Hf}_5(\mu_3\text{-O})_4(\mu\text{-Opiv})_8(\kappa^2\text{-Opiv})_4]$ (**4-2**) with ellipsoids set at 50% probability. Space group $C2/c$. Hydrogen atoms were refined isotropically and omitted for clarity. Pivalate ligands are depicted in wireframe for clarity. $R_1 = 0.0830$. Selected bond lengths (\AA) and angles ($^\circ$): Hf(1)-O(1) 2.14(1); Hf(1)-O(2) 2.151(9); Hf(2)-O(1) 2.108(8); Hf(2)-O(2) 2.047(8); Hf(3)-O(1) 2.019(8); Hf(3)-O(2) 2.071(9); O(1)-Hf(1)-O(2) 73.1(3); O(1)-Hf(1)-O(1') 114.0(5); O(2)-Hf(1)-O(2') 112.2(5); Hf(1)-O(2)-Hf(2) 104.2(4), Hf(1)-O(2)-Hf(3) 103.4(4), Hf(2)-O(2)-Hf(3) 142.6(5); Hf(2)-O(2)-Hf(3') 141.0(4).

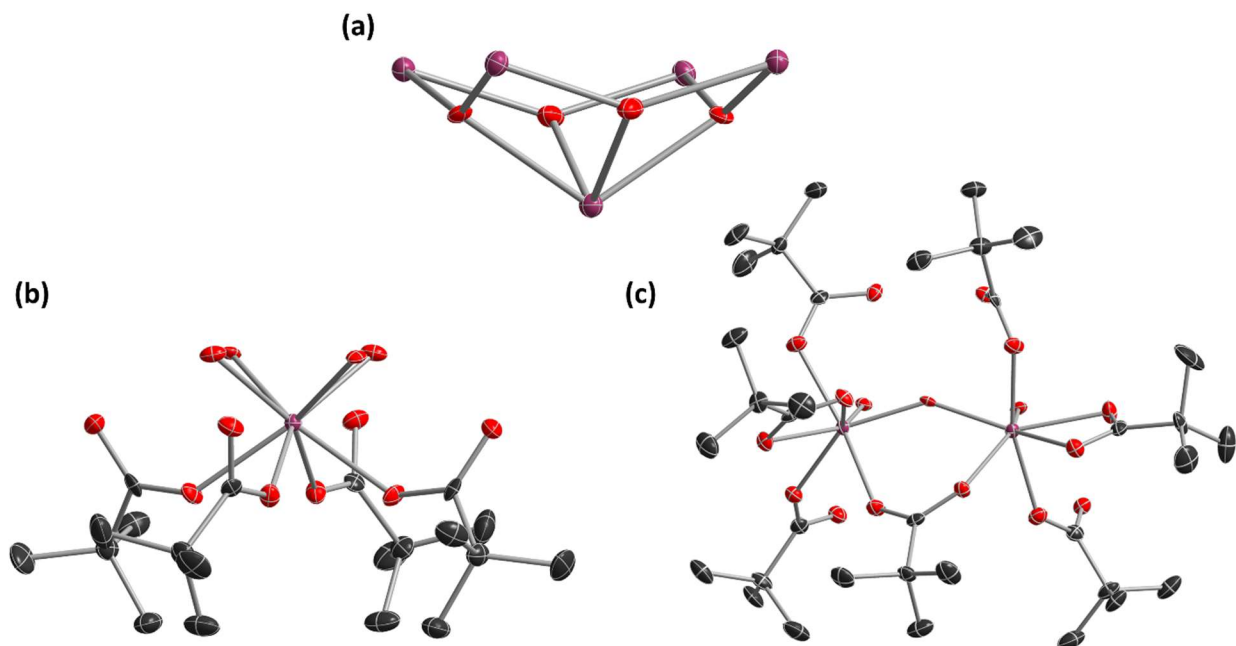


Figure A4.31: (a) Central coordination network of Hf ions and bridging oxo ligands observed in the X-ray crystal structure of **4-2**. (b) Coordination geometry about the apical, square antiprismatic Hf(1) centre of complex **4-2**. (c) Coordination geometry about the 7-coordinate Hf(2) and Hf(3) centres of complex **4-2**.

Table A4.1: Continuous shape measures (CSMs) of the 7-coordinate hafnium coordination polyhedra in the X-ray crystal structures of **4-1**, **4-2(C₆H₆)₃**, and **4-2**. The bolded values indicate the ideal polyhedron that best fit the coordination geometry.

Polyhedron	4-2(C ₆ H ₆) ₃		4-2	
	Hf(2)	Hf(3)	Hf(2)	Hf(3)
Heptagon HP-7, <i>D</i> _{7h}	33.649	32.954	32.966	32.262
Hexagonal Pyramid HPY-7, <i>C</i> _{6v}	19.803	19.714	19.877	19.810
Pentagonal Bipyramid PBPY-7, <i>D</i> _{5h}	3.198	3.844	3.252	3.822
Capped Octahedron COC-7, <i>C</i> _{3v}	2.714	2.213	2.861	2.443
Capped Trigonal Prism CTPR-7, <i>C</i> _{2v}	2.246	1.774	2.054	1.626
Johnson Pentagonal Bipyramid J13 JPBPY-7, <i>D</i> _{5h}	6.877	7.454	6.657	7.373
Johnson Elongated Triangular Pyramid J7 JETPY-7, <i>C</i> _{3v}	20.467	20.184	20.485	20.401

Table A4.2: Continuous shape measures (CSMs) of the 8-coordinate Hf(3) coordination polyhedra in the X-ray crystal structures of **4-1**, **4-2(C₆H₆)₃**, and **4-2**. The bolded values indicate the ideal polyhedron that best fit the coordination geometry.

Polyhedron	4-1	4-2(C ₆ H ₆) ₃	4-2
Octagon; OP-8, D_{8h}	34.042	31.802	31.643
Heptagonal Pyramid HPY-8, C_{7v}	24.001	23.466	23.419
Hexagonal Bipyramid; HBPY-8, D_{6h}	16.802	15.709	15.689
Cube; CU-8, O_h	11.326	8.088	8.106
Square Antiprism; SAPR-8, D_{4d}	4.024	0.518	0.497
Triangular Dodecahedron; TDD-8, D_{2d}	1.967	2.058	2.178
Johnson Gyrobifastigium J26; JGBF-8, D_{2d}	13.521	16.824	16.701
Johnson Elongated Triangular Bipyramid J14; JETBPY-8, D_{3h}	29.086	30.103	29.997
Biaugmented Trigonal Prism J50 JBTPR-8, C_{2v}	3.725	3.147	3.253
Biaugmented Trigonal Prism; BTPR-8, C_{2v}	3.856	2.480	2.526
Snub Diphenoid J84; JSD-8, D_{2d}	2.989	5.352	5.553
Triakis Tetrahedron; TT-8, T_d	11.119	8.897	8.958
Elongated Trigonal Bipyramid; ETBPY-8, D_{3h}	26.133	25.149	25.069

A5 – Supplementary Information Related to Chapter 5

Contents	Pages
NMR Spectra of 5-1 to 5-7	A71-83
Continuous Shape Measure (CSM) Data for 5-1 to 5-3 , 5-5 , and 5-7	A84

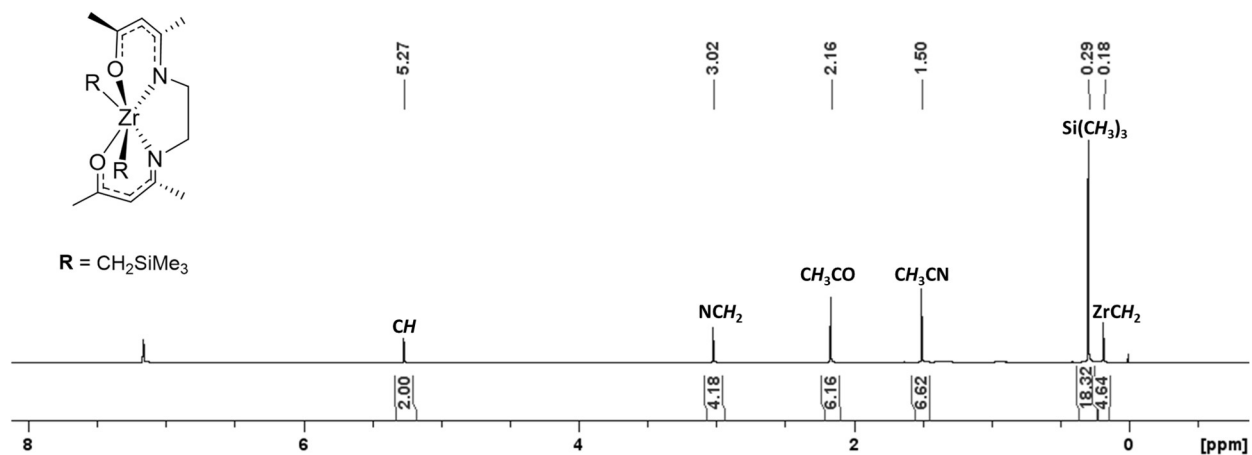


Figure A5.1: ¹H NMR spectrum of [Zr(acen)(CH₂SiMe₃)₂] (**5-1**) in C₆D₆ (500 MHz, 298 K). Unassigned peaks in the spectrum are the residual solvent signal, H grease, and tetramethylsilane.

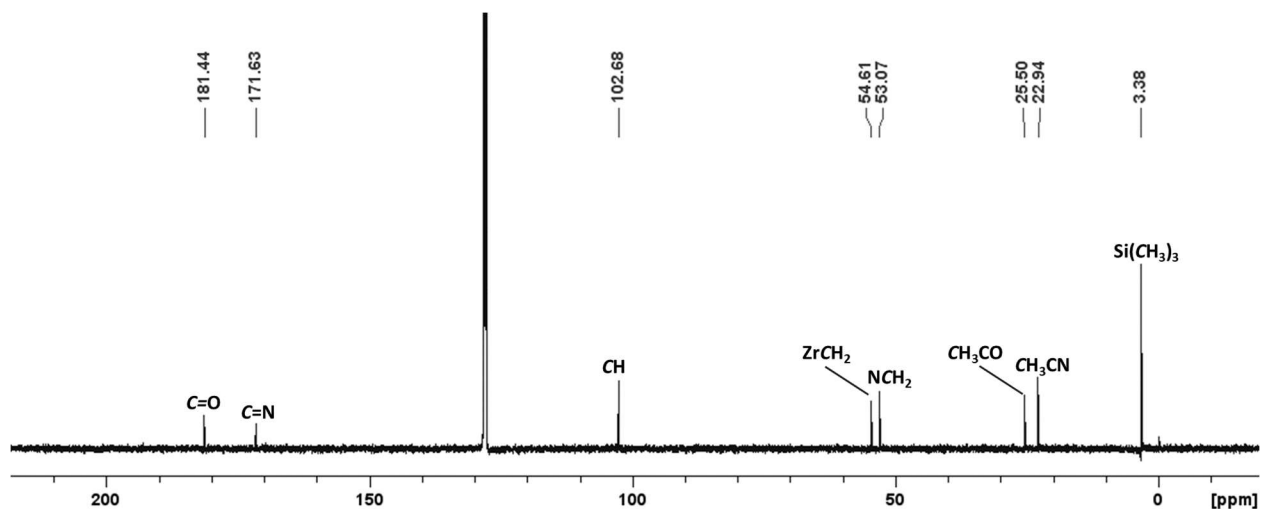


Figure A5.2: $^{13}\text{C}\{^1\text{H}\}$ NMR spectrum of $[\text{Zr}(\text{acen})(\text{CH}_2\text{SiMe}_3)_2]$ (**5-1**) in C_6D_6 (126 MHz, 298 K). Unassigned peaks in the spectrum are the residual solvent signal, and tetramethylsilane.

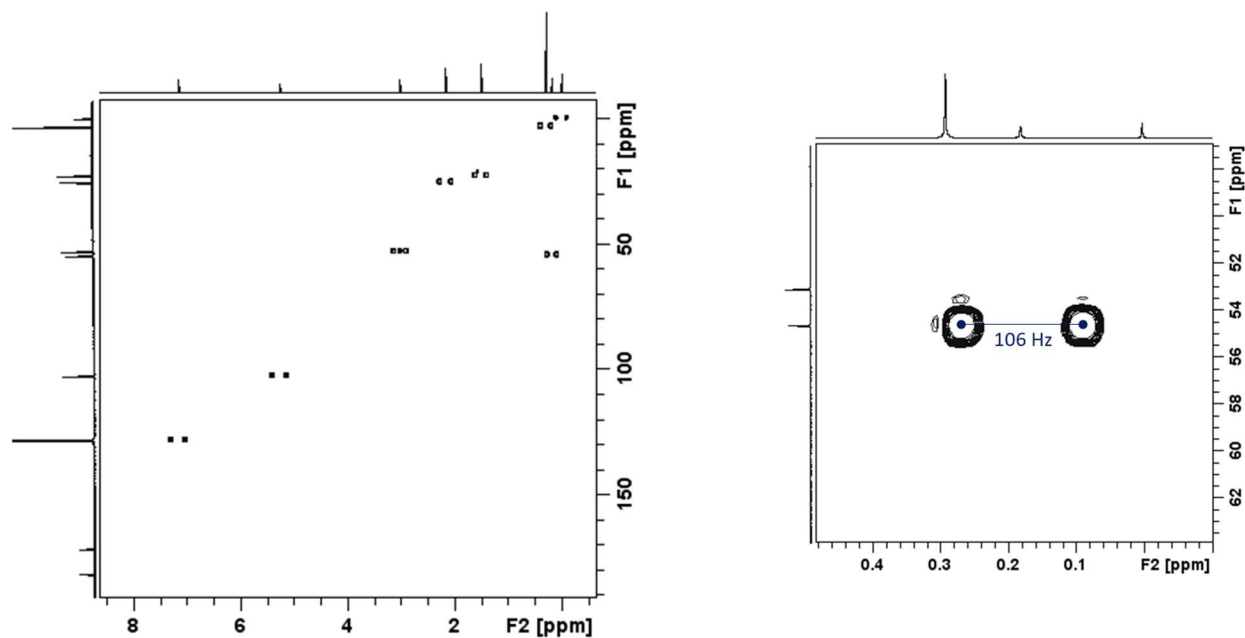


Figure A5.3: Non-decoupled $^{13}\text{C}-^1\text{H}$ HSQC NMR spectrum of $[\text{Zr}(\text{acen})(\text{CH}_2\text{SiMe}_3)_2]$ (**5-1**) in C_6D_6 (126/500 MHz, 298 K). The $^1J_{\text{CH}}$ coupling constant of the CH_2SiMe_3 group is displayed on the right.

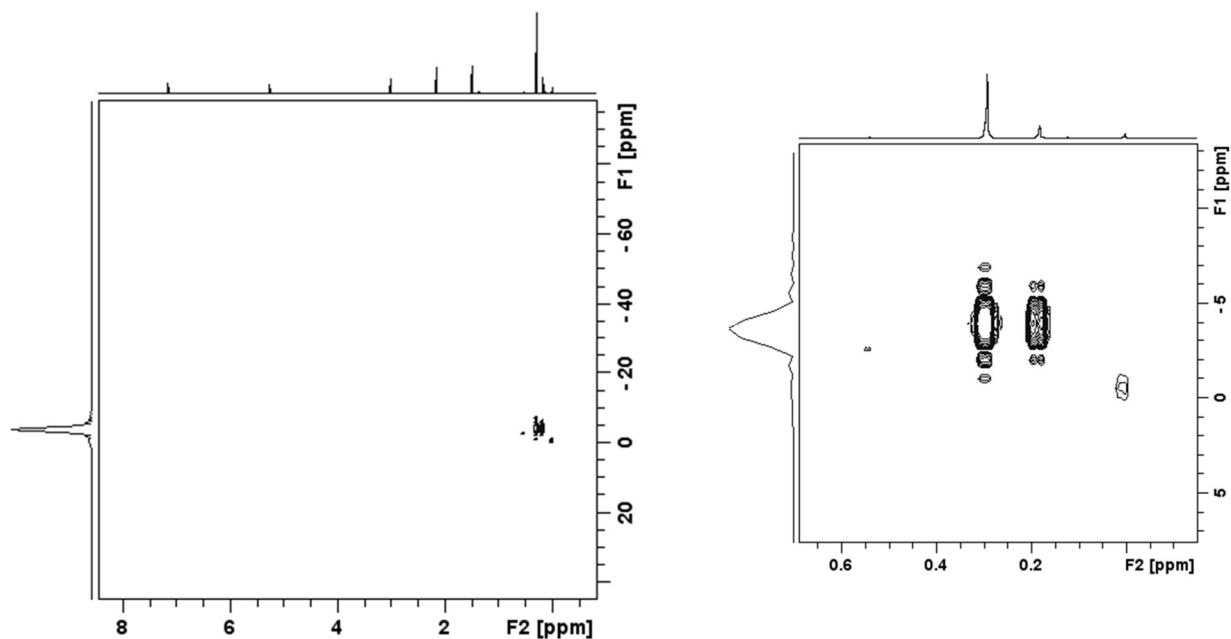


Figure A5.4: ^{29}Si - ^1H HMBC NMR spectrum of $[\text{Zr}(\text{acen})(\text{CH}_2\text{SiMe}_3)_2]$ (**5-1**) in C_6D_6 (99/500 MHz, 298 K). F1 axis is an internal ^{29}Si NMR projection.

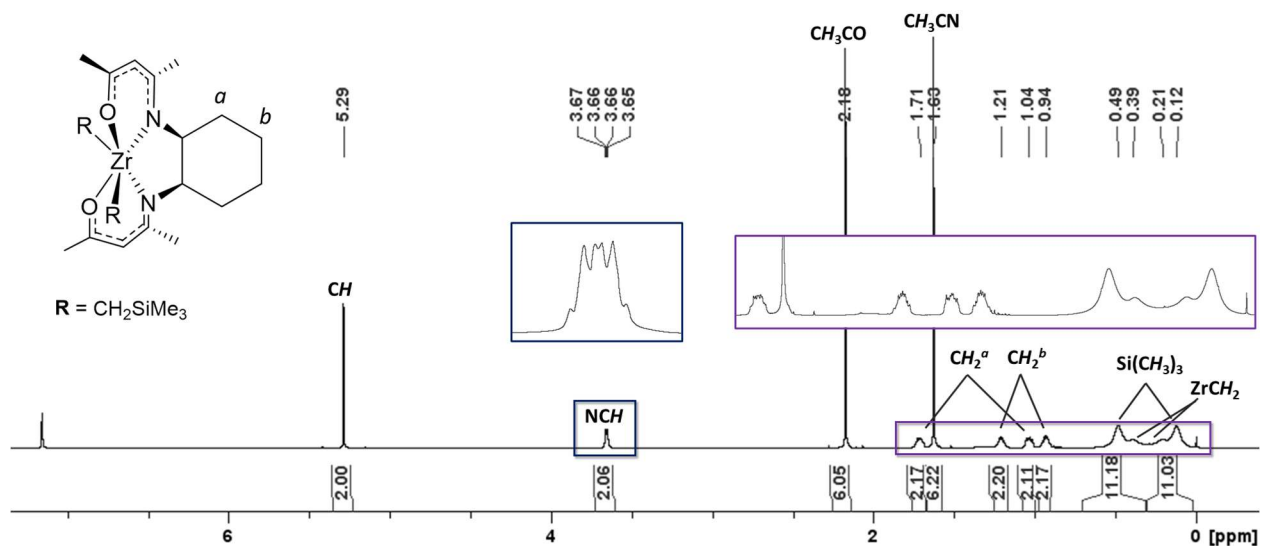
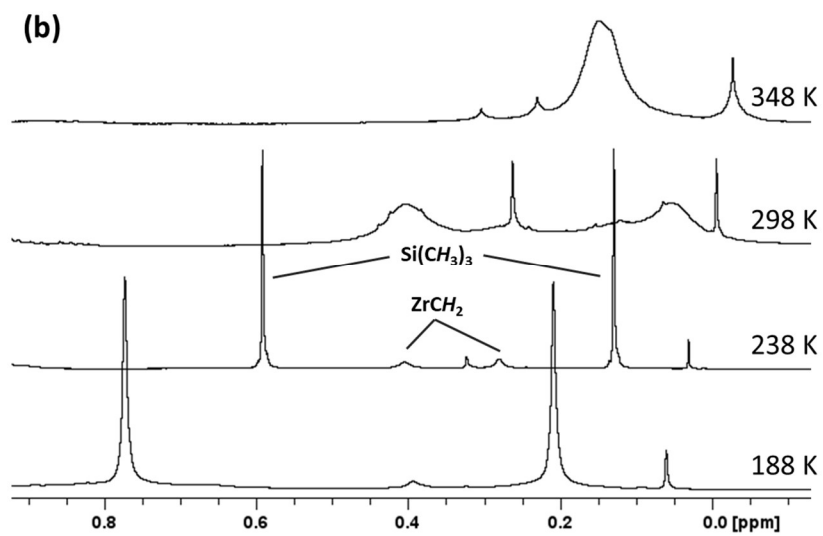
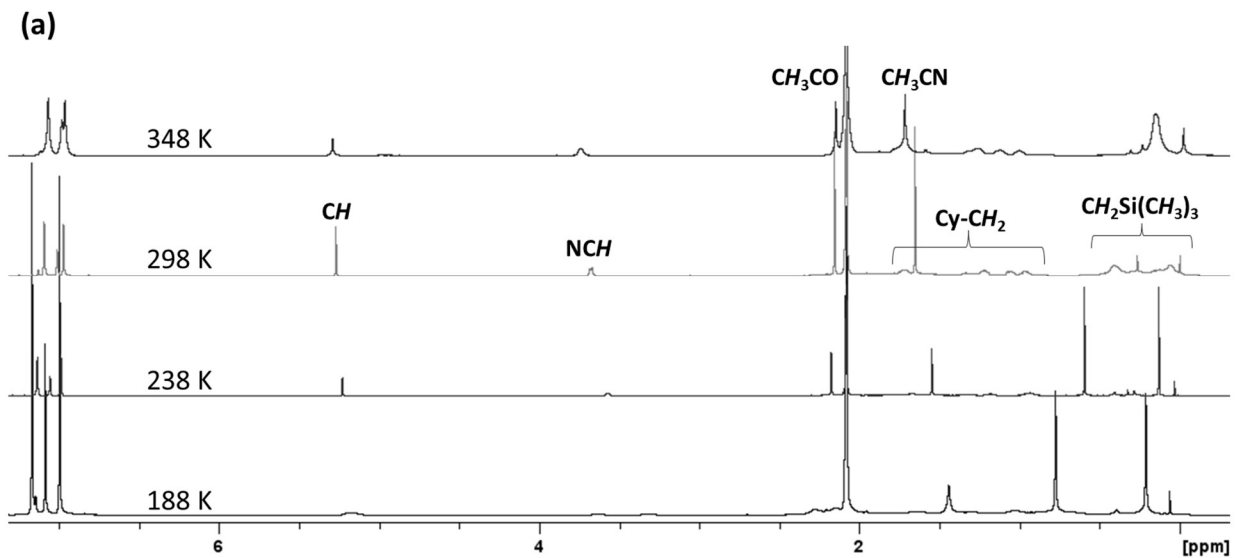


Figure A5.5: ^1H NMR spectrum of $[\text{Zr}(\text{cis-Cyacen})(\text{CH}_2\text{SiMe}_3)_2]$ (**5-2**) in C_6D_6 (600 MHz, 298 K). Unassigned peaks in the spectrum are the residual solvent signal, H grease, and tetramethylsilane.



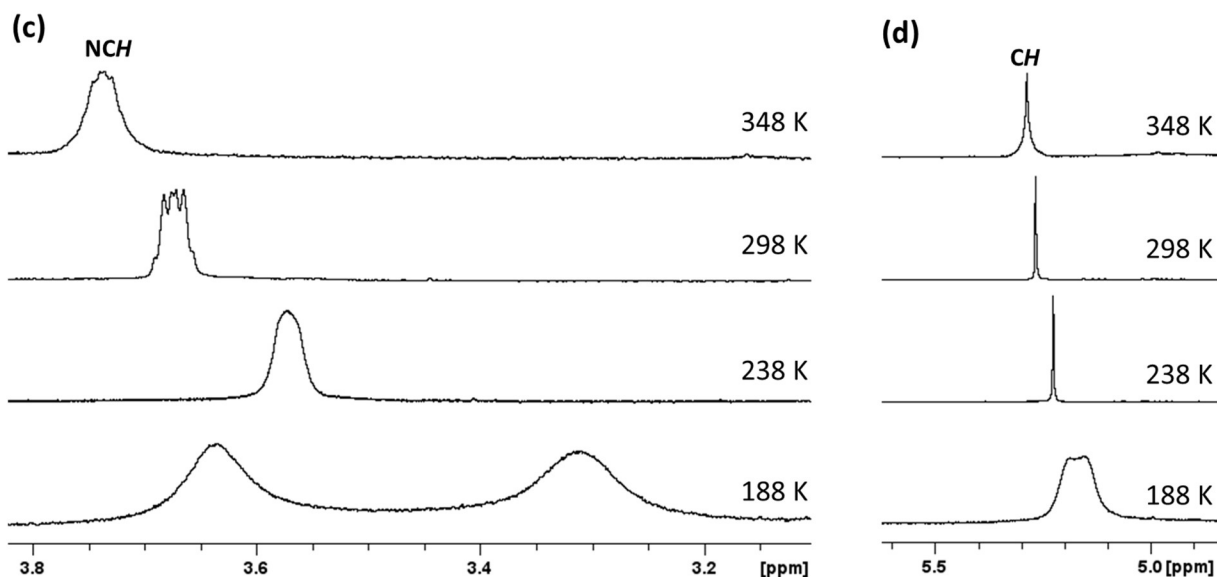


Figure A5.6: (a) Variable temperature ¹H NMR spectra of [Zr(*cis*-Cyacen)(CH₂SiMe₃)₂] (5-2) from 188-348 K in *d*₈-toluene (500 MHz). (b,c,d) Expanded regions of the ¹H NMR spectra featuring the (b) ZrCH₂Si(CH₃)₃, (c) NCH, and (d) CH proton peaks.

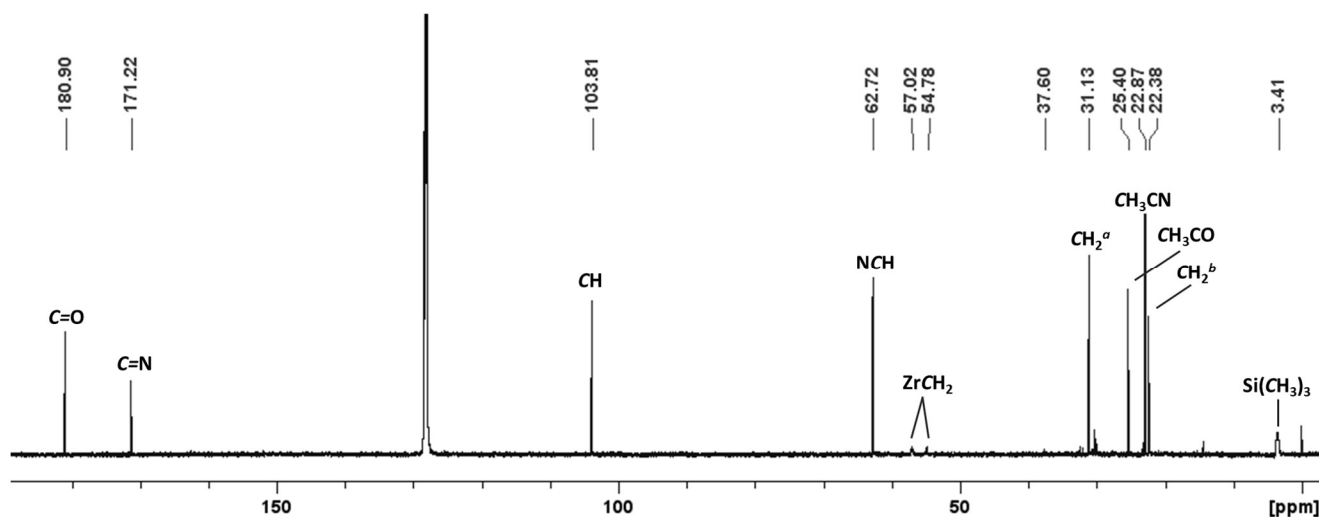


Figure A5.7: ¹³C{¹H} NMR spectrum of [Zr(*cis*-Cyacen)(CH₂SiMe₃)₂] (5-2) in C₆D₆ (151 MHz, 298 K). Unassigned peaks in the spectrum are the residual solvent signal, H grease, and tetramethylsilane.

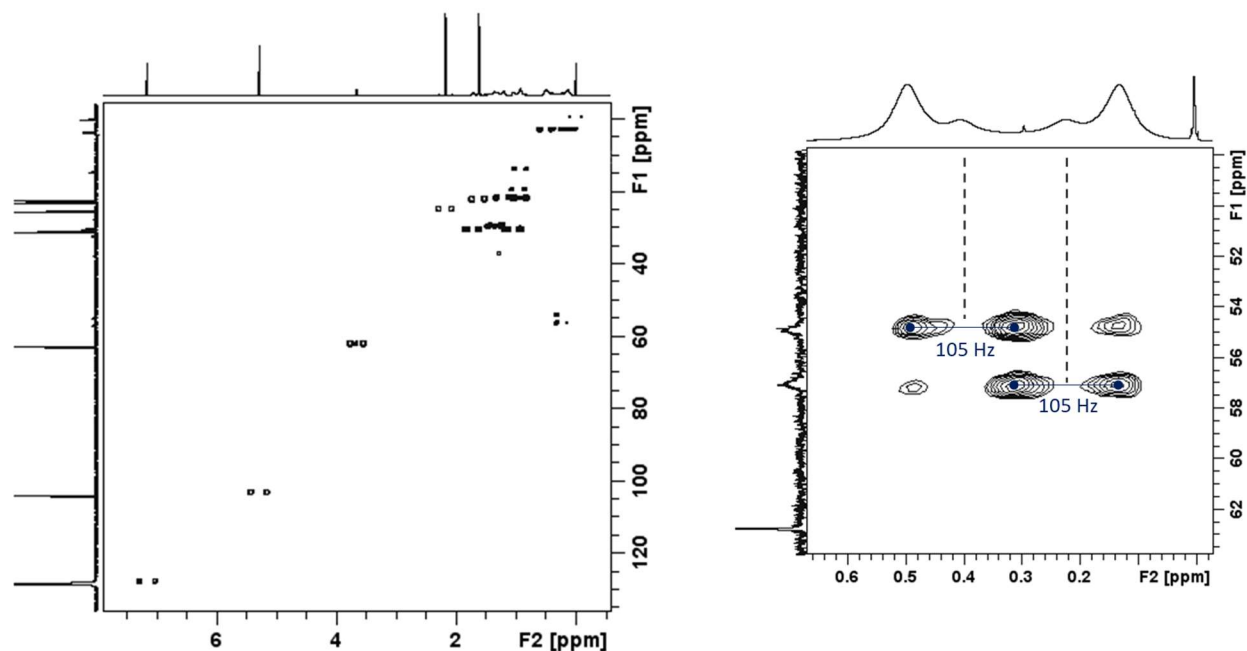


Figure A5.8: Non-decoupled ^{13}C - ^1H HSQC NMR spectrum of $[\text{Zr}(\text{cis-Cyacen})(\text{CH}_2\text{SiMe}_3)_2]$ (**5-2**) in C_6D_6 (126/500 MHz, 298 K). The $^1J_{\text{CH}}$ coupling constant of the CH_2SiMe_3 group is displayed on the right.

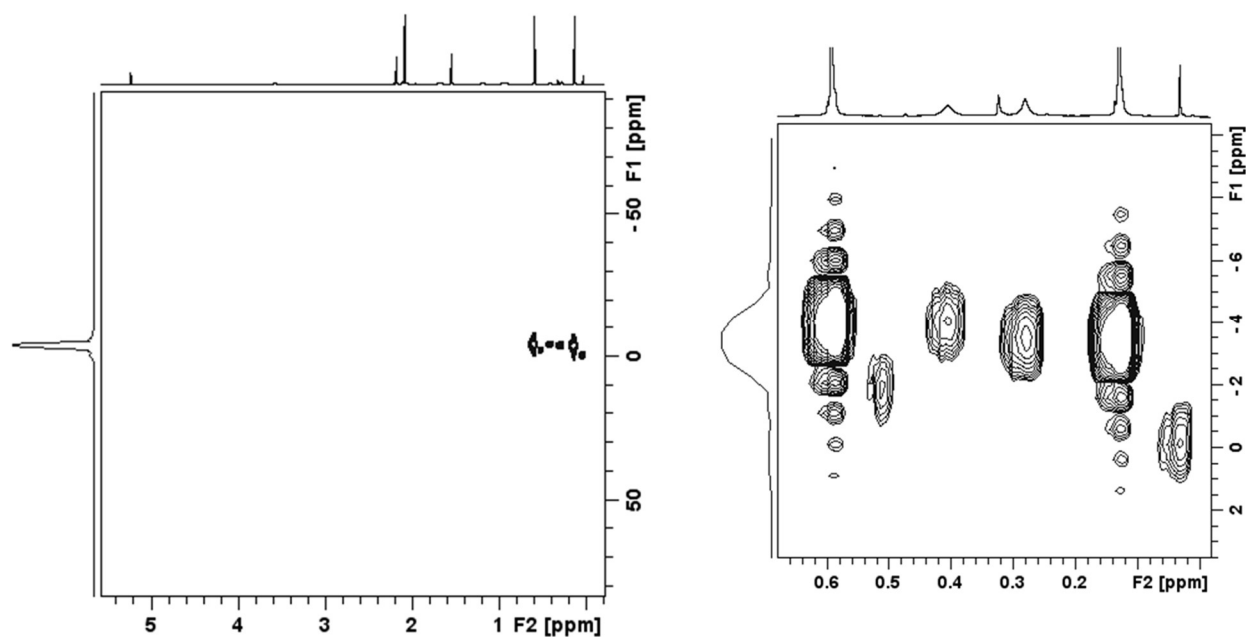
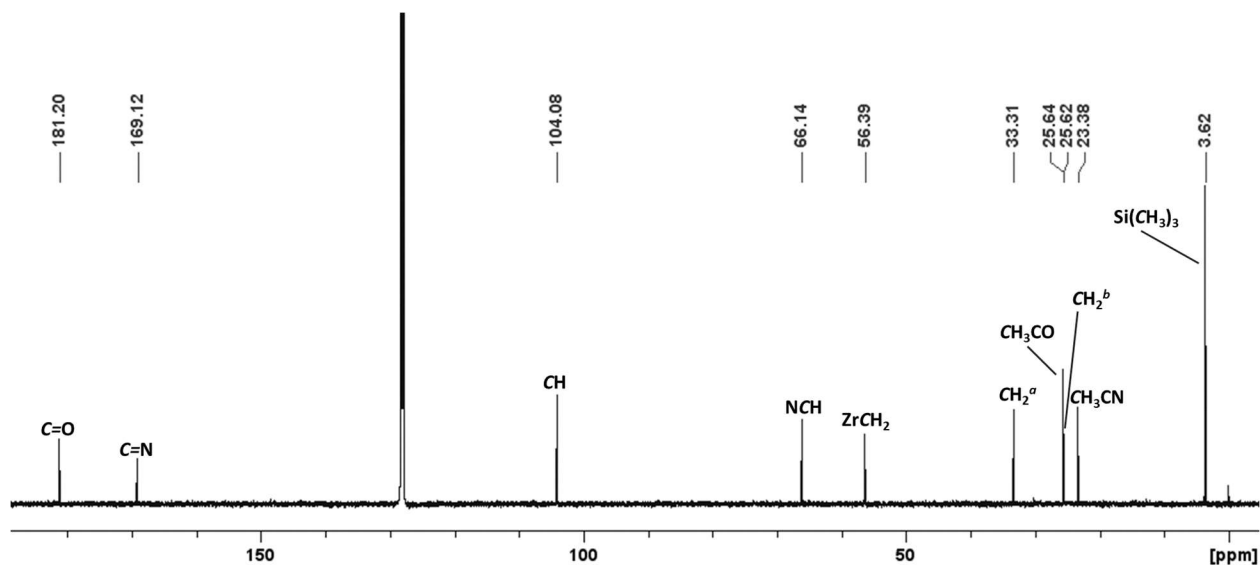
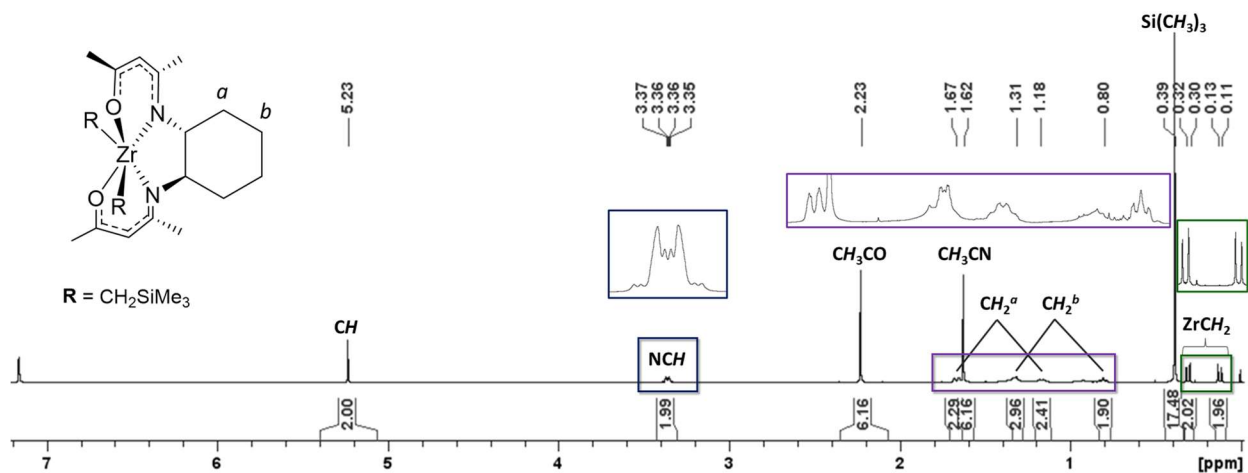


Figure A5.9: ^{29}Si - ^1H HMBC NMR spectra of $[\text{Zr}(\text{cis-Cyacen})(\text{CH}_2\text{SiMe}_3)_2]$ (**5-2**) in d_8 -toluene at 238 K (99/500 MHz). F1 axis is an internal ^{29}Si NMR projection.



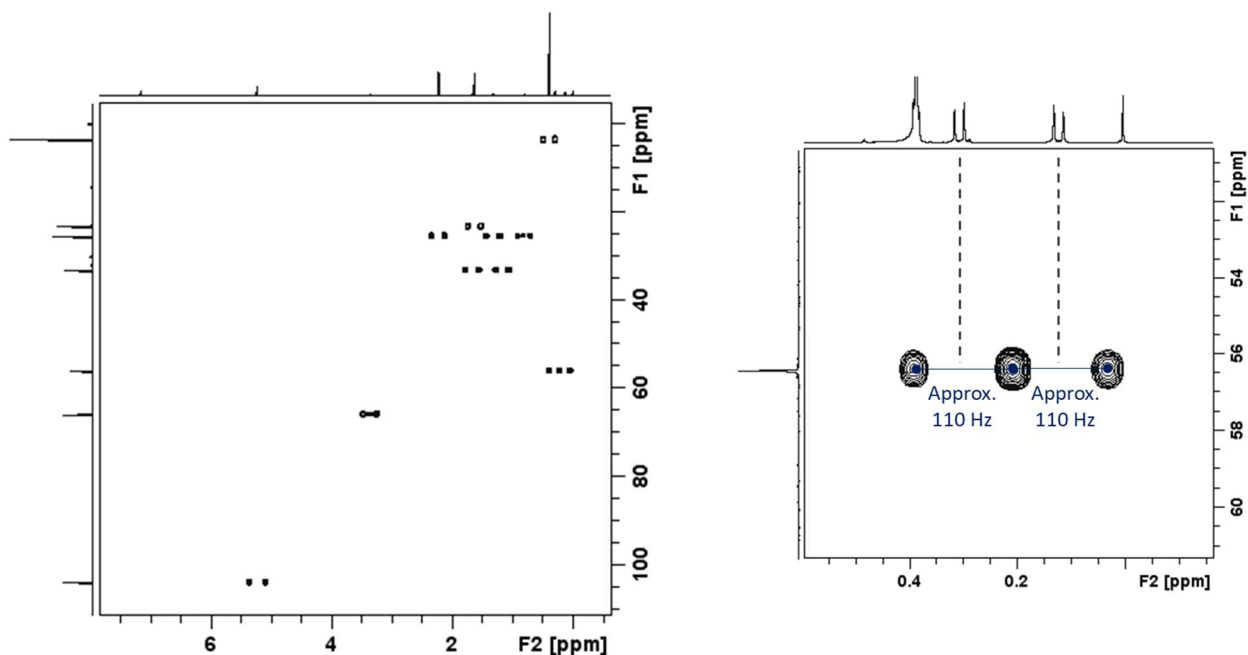


Figure A5.12: Non-decoupled ^{13}C - ^1H HSQC NMR spectrum of $[\text{Zr}(\text{trans-Cyacen})(\text{CH}_2\text{SiMe}_3)_2]$ (**5-3**) in C_6D_6 (126/500 MHz, 298 K). The $^1J_{\text{CH}}$ coupling constant of the CH_2SiMe_3 group is displayed on the right.

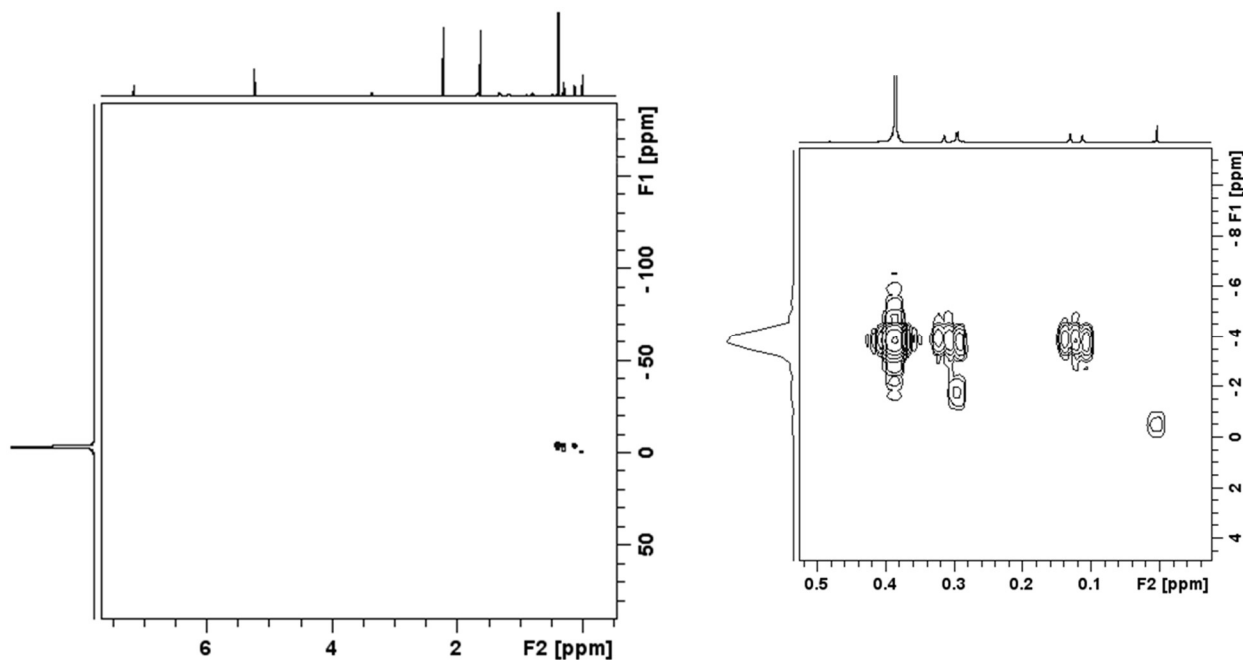


Figure A5.13: ^{29}Si - ^1H HMBC NMR spectrum of $[\text{Zr}(\text{trans-Cyacen})(\text{CH}_2\text{SiMe}_3)_2]$ (**5-3**) in C_6D_6 (99/500 MHz, 298 K). F1 axis is an internal ^{29}Si NMR projection.

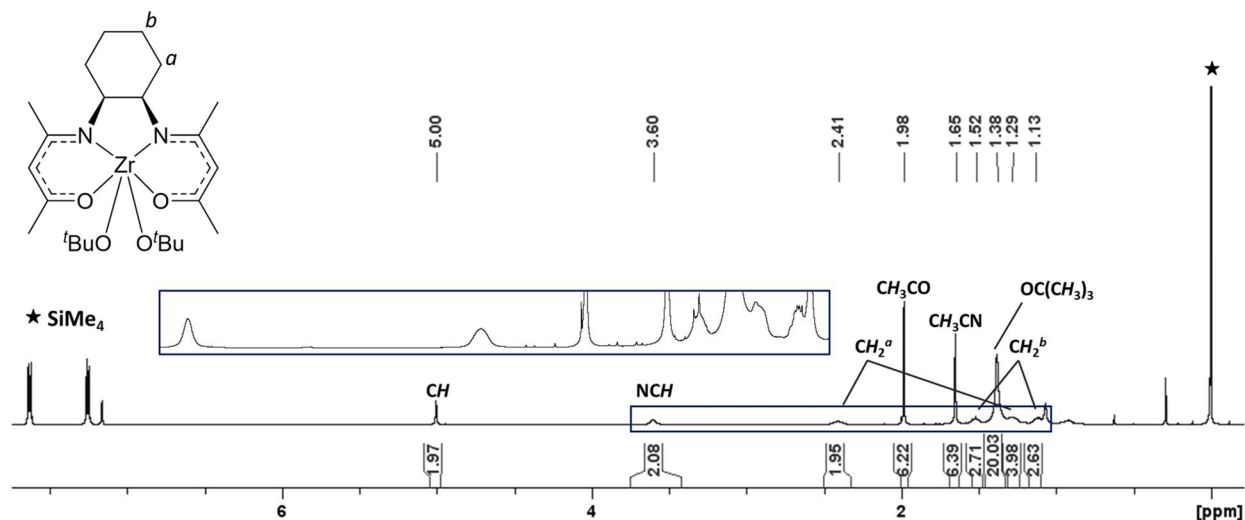


Figure A5.14: ^1H NMR spectrum of $[\text{Zr}(\text{cis-Cyacen})(\text{O}^t\text{Bu})_2]$ (**5-4**) generated in situ via the reaction of **2** with 2 equiv. of $^t\text{BuOH}$ in C_6D_6 in the presence of naphthalene as an internal standard (500 MHz, 298 K). Unassigned peaks in the spectrum are the residual solvent signal, naphthalene, and silicone grease.

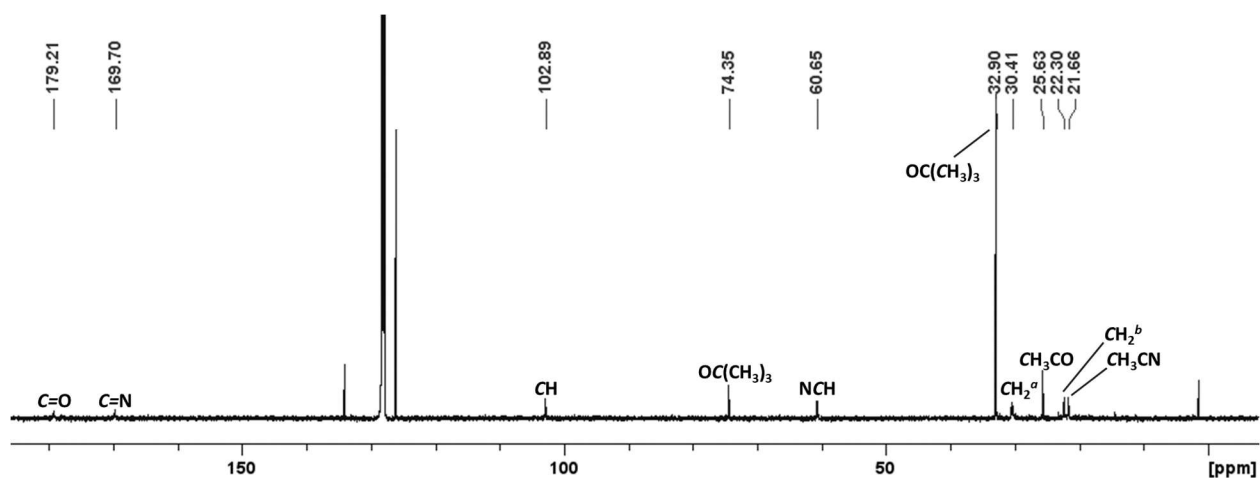


Figure A5.15: $^{13}\text{C}\{^1\text{H}\}$ NMR spectrum of $[\text{Zr}(\text{cis-Cyacen})(\text{O}^t\text{Bu})_2]$ (**5-4**) generated in situ via the reaction of **2** with 2 equiv. of $^t\text{BuOH}$ in C_6D_6 (126 MHz, 298 K). Unassigned peaks in the spectrum are the residual solvent signal, naphthalene, silicone grease, and tetramethylsilane.

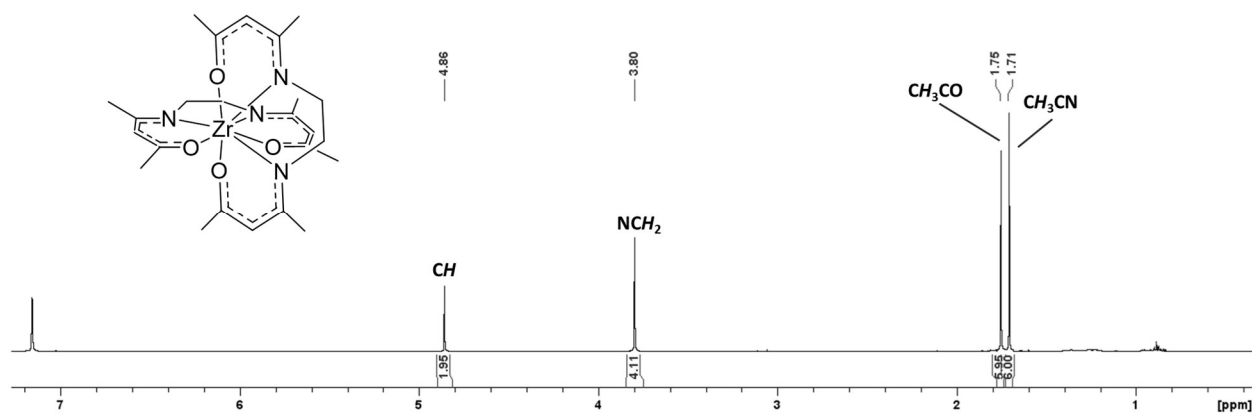


Figure A5.16: ^1H NMR spectrum of $[\text{Zr}(\text{acen})_2]$ (**5-5**) in C_6D_6 (600 MHz, 298 K). Unassigned peaks in the spectrum are the residual solvent signal and H grease.

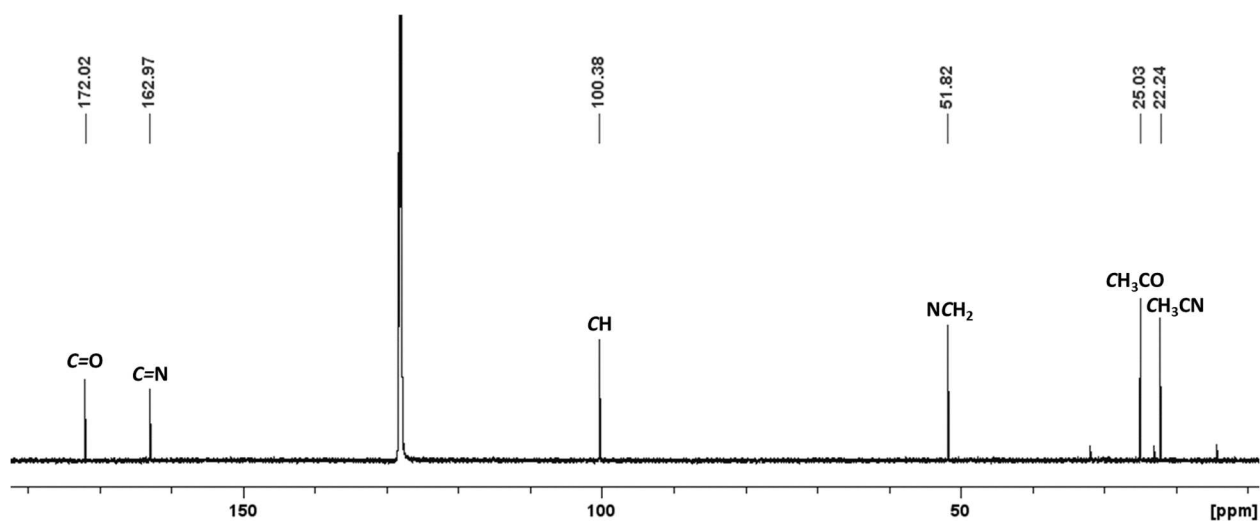


Figure A5.17: $^{13}\text{C}\{^1\text{H}\}$ NMR spectrum of $[\text{Zr}(\text{acen})_2]$ (**5-5**) in C_6D_6 (151 MHz, 298 K). Unassigned peaks in the spectrum are the residual solvent signal and H grease.

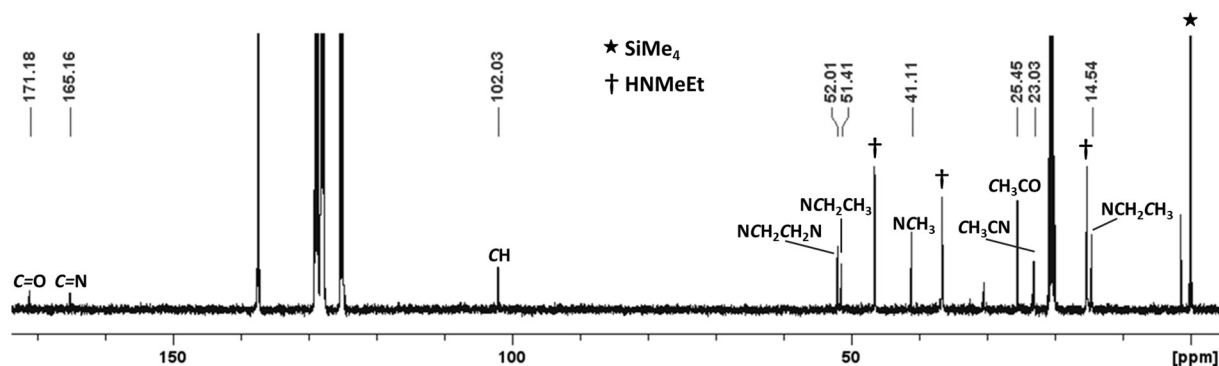


Figure A5.18: $^{13}\text{C}\{^1\text{H}\}$ NMR spectrum of $[\text{Zr}(\text{acen})(\text{NMeEt})_2]$ (**5-6**) generated in situ from the reaction of **1** with excess HNMeEt in d_8 -toluene (126 MHz, 249 K). Unassigned peaks in the spectrum are the residual solvent signal, H grease, and silicone grease.

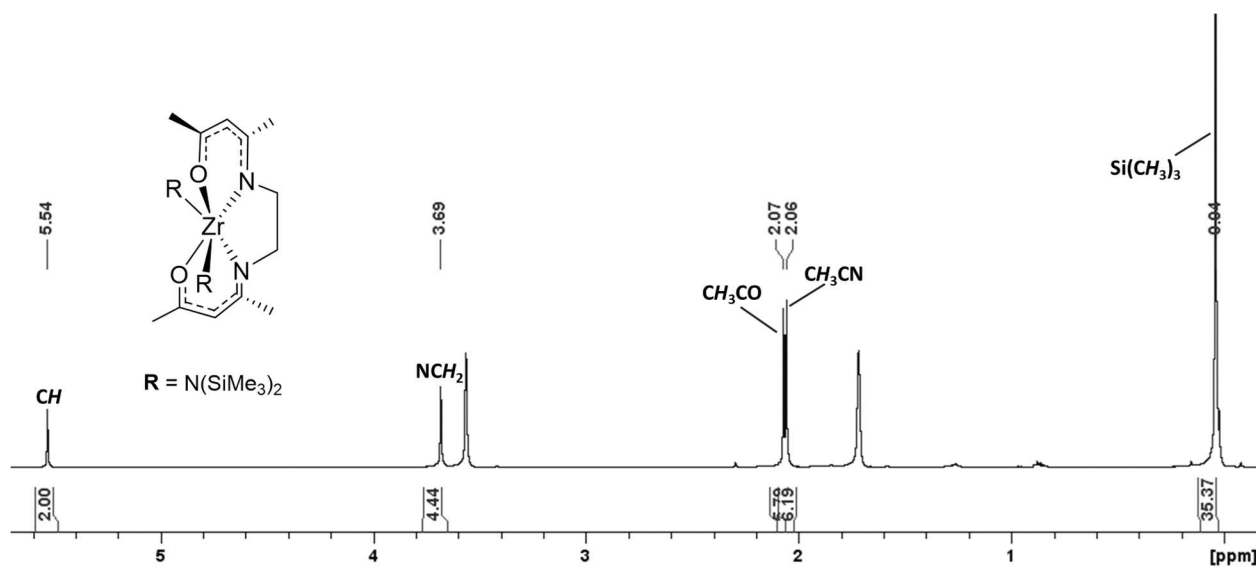


Figure A5.19: ^1H NMR spectrum of $[\text{Zr}(\text{acen})\{\text{N}(\text{SiMe}_3)_2\}_2]$ (**5-7**) in d_8 -THF (500 MHz, 249 K). Unassigned peaks in the spectrum are the residual solvent signal.

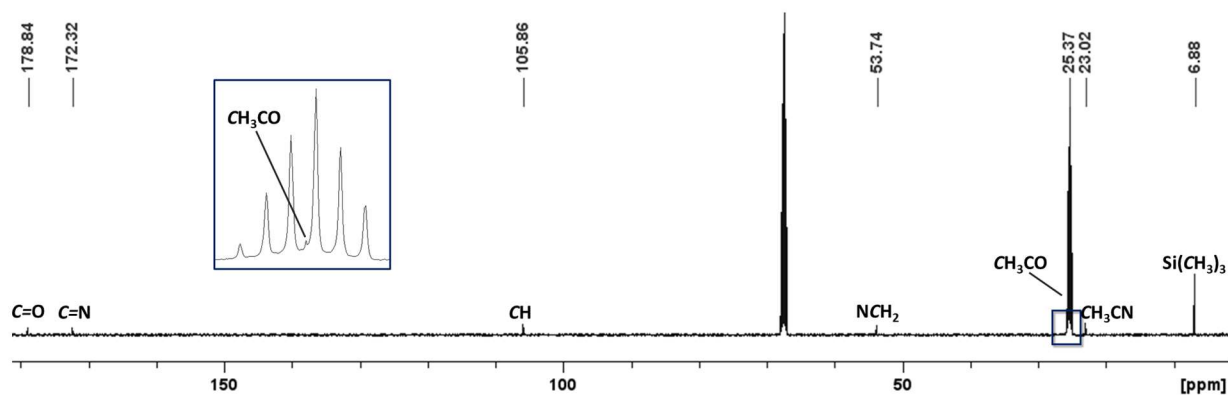


Figure A5.20: $^{13}\text{C}\{^1\text{H}\}$ NMR spectrum of $[\text{Zr}(\text{acen})\{\text{N}(\text{SiMe}_3)_2\}_2]$ (**5-7**) in d_8 -THF (126 MHz, 249 K). Unassigned peaks in the spectrum are the residual solvent signal.

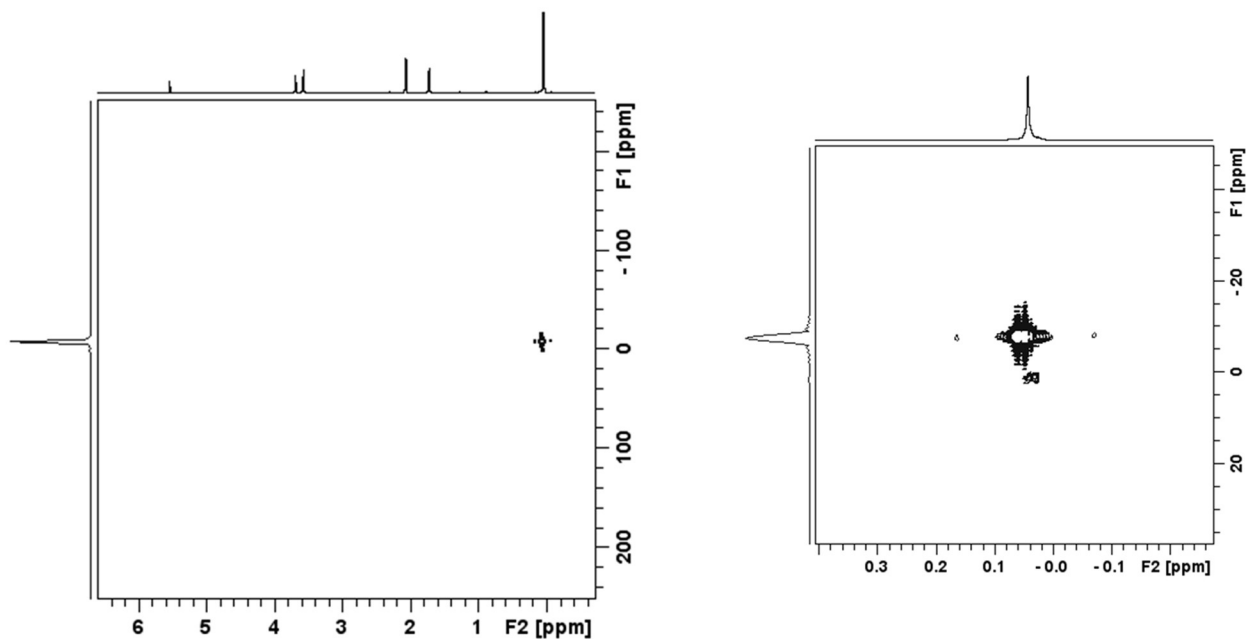


Figure A5.21: $^{29}\text{Si}\text{-}^1\text{H}$ HMBC NMR spectrum of $[\text{Zr}(\text{acen})\{\text{N}(\text{SiMe}_3)_2\}_2]$ (**5-7**) in d_8 -THF (99/500 MHz, 249 K). F1 axis is an internal ^{29}Si NMR projection.

Table A5.1: Continuous shape measures (CSMs) of the 6-coordinate zirconium coordination polyhedra in the X-ray crystal structures of **5-1** to **5-3** and **5-7**. The bolded values indicate the ideal polyhedron that best fit the coordination geometry.

Polyhedron	5-1	5-2	5-3	5-7
Hexagon HP-6, D_{6h}	34.813	34.463	34.615 34.866	29.815
Pentagonal Pyramid PPY-6, C_{5v}	13.712	11.554	10.619 10.433	13.638
Octahedron OC-6, O_h	11.532	15.785	11.225 10.911	8.508
Trigonal Prism TPR-6, D_{3h}	1.576	1.645	4.459 5.465	3.472
Johnson Pentagonal Pyramid J2 JPPY-6, C_{5v}	18.135	16.004	14.518 14.493	17.565